JOHANNES GUTENBERG-UNIVERSITÄT MAINZ
Institut für Kernphysik

Design and Development of the MAGIX Trigger Veto System

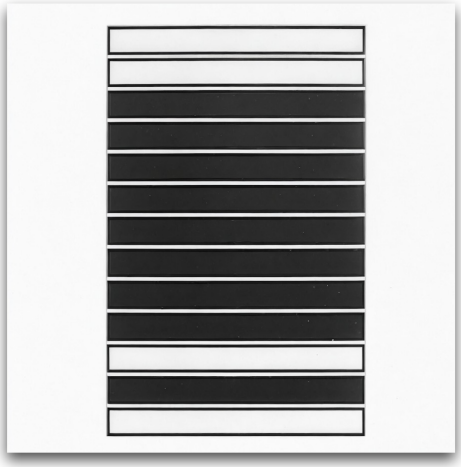

Dissertation

zur Erlangung des Grades
"Doktor der Naturwissenschaften"

am Fachbereich Physik, Mathematik und Informatik
der Johannes Gutenberg-Universität Mainz

Sebastian Stengel

MAINZ, 26. NOVEMBER 2024

Autor

Sebastian Stengel

MAGIX-Kollaboration

Institut für Kernphysik

Johann-Joachim-Becher-Weg 45

Johannes Gutenberg-Universität

D-55128 Mainz

sestenge@uni-mainz.de

Tag der mündlichen Prüfung

23. April 2025

Dancing in the wind as roses born again,
There you'll find me
Before the dawn of man in castles made of sand,
There you'll find me
Writing in the caves as fire lights the way,
There you'll find me
Mask of royal glow don in pharaoh's clothes,
There you'll find me

Avenged Sevenfold

Abstract

At the new high-intensity, low-energy electron accelerator MESA, the MAGIX setup will be used for high-precision scattering experiments including dark sector searches, the study of hadron structure and few-body systems, as well as investigations of reactions relevant to nuclear astrophysics. The MAGIX experiment features a window-less scattering chamber housing an internal gas jet target that can be operated with a variety of different gases, two high-precision magnetic spectrometers, as well as sophisticated detector systems positioned at the spectrometers' focal planes. This setup, combining a gas jet target with MESA's high-intensity electron beam, with a fully window-less design, allows for an exceptionally clean experimental environment, in which background effects like multiple scattering are drastically reduced. The focal plane detectors include a tracking detector realized by a time projection chamber and the MAGIX trigger veto system, which forms the central focus of this thesis.

The trigger veto system will provide a fast and reliable trigger decision for the data acquisition, and will furthermore allow for coincidence time measurements and particle identification information. Moreover, it will provide the basic hit and position information for the triggered readout of the time projection chamber. It comprises a segmented trigger layer made of 22 plastic scintillation detectors read out by photomultiplier tubes, complemented by a flexible veto system consisting of three layers of additional scintillation detectors read out by silicon photomultipliers and passive lead absorber layers, mounted below the trigger layer. Its data readout uses the ultrafast preamplifier-discriminator NINO chip, which encodes the signal amplitudes using the time-over-threshold method, followed by FPGAs programmed as TDCs.

During the course of this thesis, a finalized and optimized detector design for the MAGIX trigger veto system was successfully developed, which is now ready to be installed at the MAGIX experiment at MESA. Additionally, important detector properties, such as efficiency, coincidence time resolution, and spatial resolution, were characterized for the trigger layer using data collected during a dedicated beam time at MAMI. A detection efficiency of about 99.93 % was achieved, the coincidence time resolution reached values of around (180 ± 10) ps (FWHM), and the spatial resolution along a trigger scintillator was determined to be (25.07 ± 1.05) mm. The readout system's trigger rate tolerance was also evaluated, along with an assessment of its long-term stability. The entire readout system successfully withstood readout rates exceeding 4 MHz, with the individual channels reliably operating at rates above 700 kHz.

TABLE OF CONTENTS

INTRODUCTION

Since ancient times, humans have been trying to understand the fundamental questions about the nature and origin of the universe. Beyond our basic biological needs, it is curiosity and the pursuit of knowledge that motivate us and drive us forward. While philosophy approaches these questions in a qualitative and conceptual manner, physics seeks answers through quantitative and empirical methods. As physicists, we create models, conduct experiments, and utilize mathematical formulations to test and refine hypotheses. Different branches of physics address the fundamental questions from various perspectives and on different scales. In particle physics, for example, we operate on the smallest conceivable scale, asking the central question: "What are the fundamental particles that make up our universe, and how do they interact?" The deeper question of what a particle or interaction ultimately *is* in essence, however, belongs to the domain of philosophy. In physics, it is sufficient that these entities can be mathematically described and that their behaviour aligns with the observations we make in nature.

The discovery of the electron in 1897 laid the groundwork for a decades-long chase for particles, which culminated in what we call the Standard Model of Particle Physics since the late 1970s. It encompasses all known fundamental particles, including the electron, and unifies three of the four fundamental interactions: the electromagnetic, the weak, and the strong. To this day, the Standard Model stands as the most precise theoretical framework available for describing fundamental particle physics.

Yet, the Standard Model is not without limitations. It fails to explain important observations such as dark matter, dark energy, or neutrino oscillations, and it notably omits gravity, the fourth of the fundamental interactions. As a result, the Standard Model and its potential extensions are continually examined and tested through experiments in hopes of uncovering additional gaps and inconsistencies that expand our knowledge of the subatomic world. An important tool for this purpose are particle accelerators, at which, unlike for measurements in cosmology or astrophysics, the experimental conditions can be precisely designed and controlled. Presently, research at particle accelerators is progressing towards two complementary frontiers: the high-energy frontier and the low-energy precision frontier. While the high-energy frontier has been extensively probed in recent decades, primarily through the LHC at CERN, the efforts in this direction have yet to yield groundbreaking new discoveries. Meanwhile, fundamental questions

in nuclear, hadron, and particle physics that can only be addressed with low-energy electron beams have been largely overlooked.

At the Institute for Nuclear Physics at the Johannes Gutenberg University Mainz, Germany, a new particle accelerator is currently being developed, aimed at bridging precisely this gap. MESA, the **M**ainz **E**nergy-recovering **S**uperconducting **A**ccelerator, is a high-intensity, low-energy electron accelerator that will provide great opportunities to perform a new generation of high-precision scattering experiments. With two operational modes, an extracted beam mode and an energy-recovery mode, MESA will support three experiments: P2, DarkMESA, and MAGIX. The external P2 experiment will be operated with spin-polarized electrons in the extracted beam mode, allowing for sensitive tests of the Standard Model through parity-violating electron scattering, while the beam-dump experiment DarkMESA, located behind P2, is designed to search for light dark matter particles. The versatile **MA**inz **G**as **I**njection target e**X**periment, MAGIX, will utilize MESA's innovative energy-recovery mode to conduct high-precision electron scattering experiments across a range of fields, including nuclear astrophysics, hadron physics, dark sector searches, and few-body physics.

To achieve this, MAGIX uses an internal gas jet target and two high-resolution magnetic spectrometers, whose focal planes are equipped with specialized detector systems designed to precisely investigate the scattered electrons. These focal plane detectors include a tracking detector in the form of a time projection chamber, as well as the MAGIX trigger veto system, which forms the core subject of this thesis. The trigger veto system comprises a segmented trigger layer made of plastic scintillation detectors, complemented by a flexible veto system consisting of additional scintillation detectors and lead absorbers mounted below the trigger layer.

Outline

This thesis presents the comprehensive design and development of the MAGIX trigger veto system, tracing its progression from the initial concept through detailed design and development stages, alongside the determination of key detector properties. To do so, it is organized into three main parts.

Part One, *The MAGIX Experiment*, establishes the foundation for this thesis by situating the trigger veto system within the broader context of MAGIX. Chapter 1 begins by outlining the physics goals of MAGIX and its versatile applications made possible through the use of various target gases. Chapter 2 then details the experimental setup of MAGIX, including descriptions of the underlying electron accelerator MESA and the two other experiments, P2 and DarkMESA.

Part Two, *A Trigger Veto System for MAGIX*, gets more concrete on the trigger veto system itself and guides through its design and development. Chapter 3 starts with a high-level overview of the system's conceptual design and working principle. Chapter 4 follows with simulation studies performed using `Geant4`, in which multiple design parameters, such as the number and length of the scintillation detectors of the trigger layer, are evaluated and optimized. Subsequently, Chap-

ters 5 and 6 cover the individual development processes for the trigger layer and the veto system, respectively. Chapter 5 discusses the production of the trigger detectors, the development of the trigger layer's power supply and readout electronics, and the technical design of its mechanical setup. Chapter 6 describes the technical development of the veto system, along with preparatory studies for the veto detectors to finalize the design of the corresponding power supply and readout electronics.

Part Three, *The Readout of the MAGIX Trigger Veto System*, delves into the readout system of the trigger veto system, illustrating the path from signal to analysis, exemplified using the detector signals from the trigger layer. Chapter 7 provides a detailed description of the readout system's architecture and data acquisition process, while Chapter 8 addresses the data analysis procedure using data acquired during a beam time at the electron accelerator MAMI. Along the way, important detector properties, such as efficiency, coincidence time resolution, and spatial resolution, are extracted. Finally, Chapter 9 concludes this thesis with a summary of the most important findings and an outlook on future work and advancements.

Part I

The MAGIX Experiment

CHAPTER 1

THE PHYSICS OF MAGIX

The MAGIX experiment will, for the first time in accelerator-based science, carry out an experimental program in nuclear, hadron, and particle physics at an energy-recovering accelerator. The combination of the window-less gas jet target of MAGIX and the high-intensity electron beam of MESA results in competitive luminosities and at the same time a very clean experimental environment. Especially, effects of multiple scattering are drastically reduced, which enables experiments at a new level of precision.

The basic idea of MAGIX is the following: Provide a gas jet target perpendicular to the electron beam of MESA and perform electron scattering experiments with two high-precision magnetic spectrometers and an array of silicon strip detectors inside the scattering chamber. Its uniqueness lies in the use of different gases. By this, a rich physics program, including precision measurements of nuclear observables as well as high luminosity searches for rare events in the energy range from 20 MeV to 105 MeV, becomes accessible.

The following sections give an overview on the measurements proposed at MAGIX. For details on the MAGIX setup or the underlying electron accelerator MESA, see Chapter 2.

1.1 Nuclear Astrophysics

The question for the origin of the chemical elements and their abundance distribution in our Universe lies at the heart of nuclear astrophysics. In 1957, Burbidge, Burbidge, Fowler, and Hoyle [1], and independently Cameron [2], laid the foundation for this fascinating branch of physics. Based on their work, we know today that the elements and their isotopes were and still are forged via complex patterns of nuclear reactions, termed *nucleosynthesis*. In fact, astrophysics is capable of explaining the origin and to some extent also the abundance of all elements up to

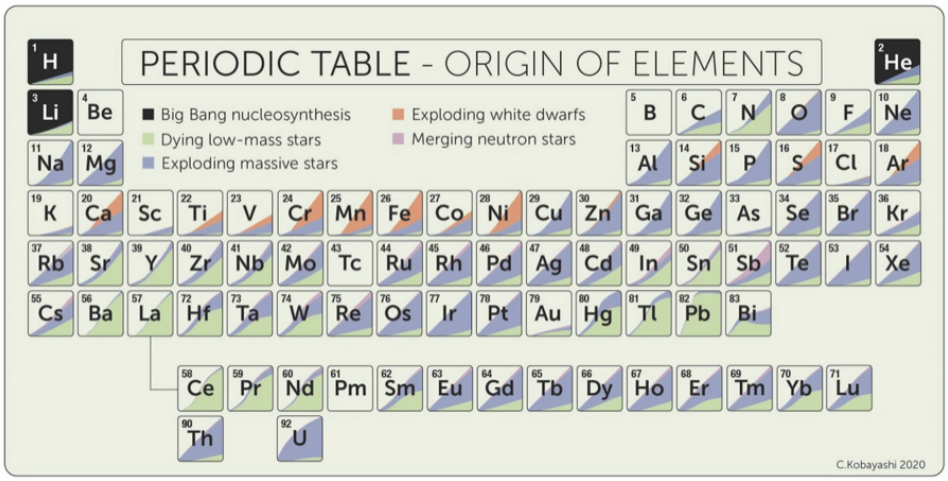

FIGURE 1.1. Astrophysical origin of the chemical elements. Figure from [3].

Uranium, see Fig. 1.1.

Starting from protons and neutrons produced shortly after the Big Bang, followed by the production of ^{1}H, the light nuclides ^{2}H, ^{3}He and ^{4}He, as well as traces of Lithium, Beryllium, and Bor, were formed within the first few minutes of the life of the Universe during *primordial nucleosynthesis*. As the Universe expanded, the production of new elements halted for a few hundred million years, until stars began to form from vast molecular clouds due to gravitational contraction. Since then, new generations of stars are constantly being born, aging by burning their fuel in *stellar nucleosynthesis*, and eventually dying by ejecting the ashes of their nuclear fires into the interstellar medium, known as supernovae, or by becoming white dwarfs. In addition to these two processes, the low-abundance nuclides ^{6}Li, ^{9}Be, ^{10}B, and ^{11}B are believed to be created via spallation reactions in the interstellar medium. [4, 5]

During stellar nucleosynthesis, about half of the gravitational energy of the collapsing gas cloud is converted into heat, thus increasing the gas temperature. Dependent on the mass of the initial gas cloud, sufficiently high temperatures can be reached in the hot interior of the star to trigger a sequence of nuclear fusion reactions. These more or less discrete nucleosynthetic processes involve *hydrogen burning* (conversion of H to He), *helium burning* (conversion of He to C, O, etc), as well as carbon, oxygen, neon, and silicon burning. By these, elements up to the Fe region ($A \sim 60$) are forged. For higher atomic mass numbers, fusion becomes energetically disfavored, and neutron capture processes must be considered. These are normally divided into slow and rapid processes (the s- and r-processes, respectively) and are followed by β^- decays, where an excess neutron in a nucleus is converted into a proton, thus leading to a new element. [4, 5]

The burning stages of a star mentioned above are only the net processes we observe. Actually, tens of thousands of different nuclear reactions are involved, some of which have a stronger impact on the overall evolution of the elements and others a smaller one. The initiation of these processes

happens by the thermal motion of the involved nuclei, hence they are called *thermonuclear reactions*. To describe such a process, two ingredients are needed: the relative velocity distribution of the interacting nuclei and the cross-section for the corresponding reaction. The former is characterized by the Maxwell-Boltzmann distribution ϕ, that describes the statistical distribution of the particle velocities inside an ideal gas or plasma. The relative velocity distribution is then given by

$$\phi(v)\,\mathrm{d}v = \phi(E)\,\mathrm{d}E \propto \sqrt{E}\exp(-E/kT), \tag{1.1}$$

where v and E are the relative velocity and the center-of-mass energy of the nuclei, respectively, $k = 8.6173 \times 10^{-5}\,\mathrm{eV/K}$ is the Boltzmann constant, and T is the temperature. The latter is described via

$$\sigma(E) = \frac{1}{E}\exp\left(-2\pi\eta\right)S(E), \tag{1.2}$$

where $1/E$ is a non-nuclear term, which involves the de Broglie wavelengths of the interacting nuclei, and $\exp\left(-2\pi\eta\right)$ represents the Coulomb penetration factor, i.e. the tunneling probability through the Coulomb barrier between the interacting nuclei. This exponentially decreasing factor appears since Eq. 1.1 reaches its maximum at an energy kT, which at stellar temperatures is always smaller than the repulsive Coulomb barrier. The nuclear reactions in stars are therefore only possible by quantum-mechanical tunneling. The parameter η is called the *Sommerfeld parameter* and is given by

$$\eta = Z_1 Z_2 \frac{\alpha c}{v}, \tag{1.3}$$

with Z_i being the atomic numbers of the involved nuclei, α the fine structure constant, and c the speed of light in vacuum. The remaining factor $S(E)$ is the so-called *astrophysical S-factor*, that contains all the nuclear physics effects of the interaction. It is normally given in the unit keVbarn and contributes most to the uncertainty of the cross-section. [5, 6, 7]

However, the key quantity of interest in astrophysics is the reaction rate per particle pair, which is defined as the integral over the reaction probability, which in turn is given by the product of Eqs. 1.2 and 1.1:

$$\langle\sigma v\rangle = \int_0^\infty \sigma(v)v\phi(v)\,\mathrm{d}v = \int_0^\infty \sigma(E)v\phi(E)\,\mathrm{d}E \propto \int_0^\infty S(E)\exp\left(-E/kT - 2\pi\eta\right)\mathrm{d}E. \tag{1.4}$$

The reaction probability as a function of the center-of-mass energy gives rise to a peak-shaped curve, which is normally referred to as the *Gamow peak*, see Fig. 1.2. In the energy region of the Gamow peak, the given reaction is most likely to occur, and to a first approximation, the reaction rate is proportional to the area under the Gamow peak. Note that the reaction rate drops by several orders of magnitude as the interacting nuclei get heavier, since the Sommerfeld parameter is increased and the tunneling probability through the Coulomb barrier is reduced. This behaviour can be seen in Fig. 1.2 and is the reason why the cross-sections of nuclear fusion

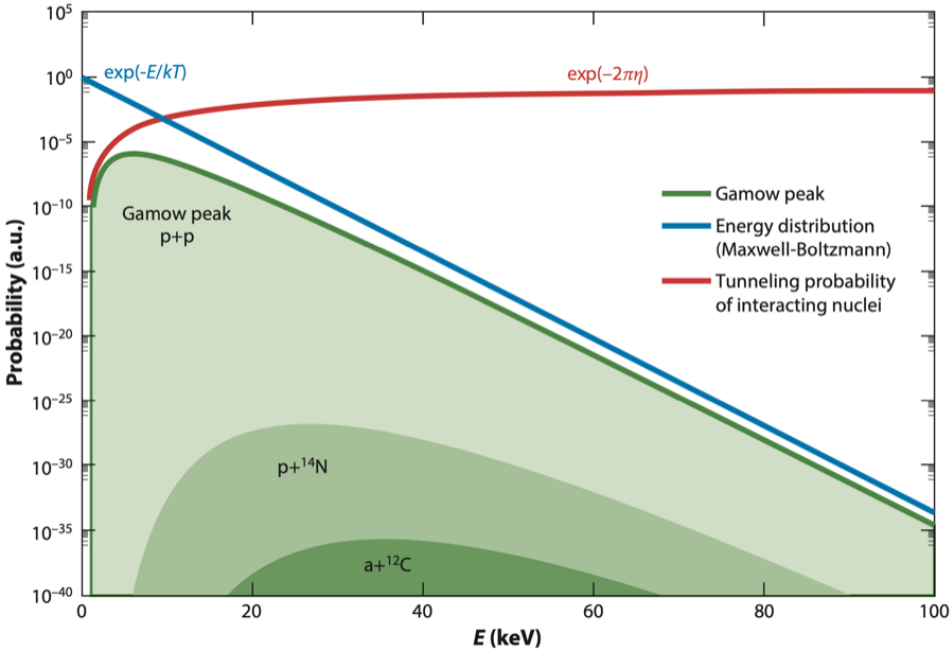

FIGURE 1.2. The reaction probability has the shape of a peak-shaped curve, the so-called Gamow peak (green). Note the many orders of magnitude on the ordinate and therefore the drastic drop of the reaction rate as the interacting nuclei get heavier. The blue curve represents the Maxwell-Boltzmann distribution and the red curve shows the tunneling probability of the interacting nuclei. The S-factor is not included in this plot. Figure from [5].

reactions of astrophysical interest are normally in the pico- to femtobarn range and thus are very hard to investigate. [5]

Of the many thousands of nuclear reactions involved in stellar nucleosynthesis, the reaction $^{12}C(\alpha,\gamma)^{16}O$ is of utmost interest and importance. It even has been dubbed "the holy grail of nuclear astrophysics" [6]. As a member of the helium burning stage, it competes with the 3α process ($3\alpha \rightarrow {}^{12}C+\gamma$) and several less important reactions, like $^{16}O(\alpha,\gamma)^{20}Ne$ or $^{20}Ne(\alpha,\gamma)^{24}Mg$, in defining the abundance ratio of ^{12}C and ^{16}O in our Universe. This ratio is the fundamental basis for all organic chemistry, as well as for the evolution of biological life, and has major implications, not only for stellar nucleosynthesis but for stellar structure and even the nature of the collapse and explosion of a star. More specifically, the reaction rate, or likewise the S-factor, of $^{12}C(\alpha,\gamma)^{16}O$ sensibly influences the abundance distribution of the heavier elements up to Iron, which can be seen from the *isotopic production factors* for certain elements in Fig. 1.3. The isotopic production factor describes the production of a certain isotope by nuclear fusion in the hot interior of a star and is defined as

$$P_{\text{iso}} := \frac{m_{\text{iso}}}{X^{\odot}_{\text{iso}} \times M_{\text{tot}}}, \tag{1.5}$$

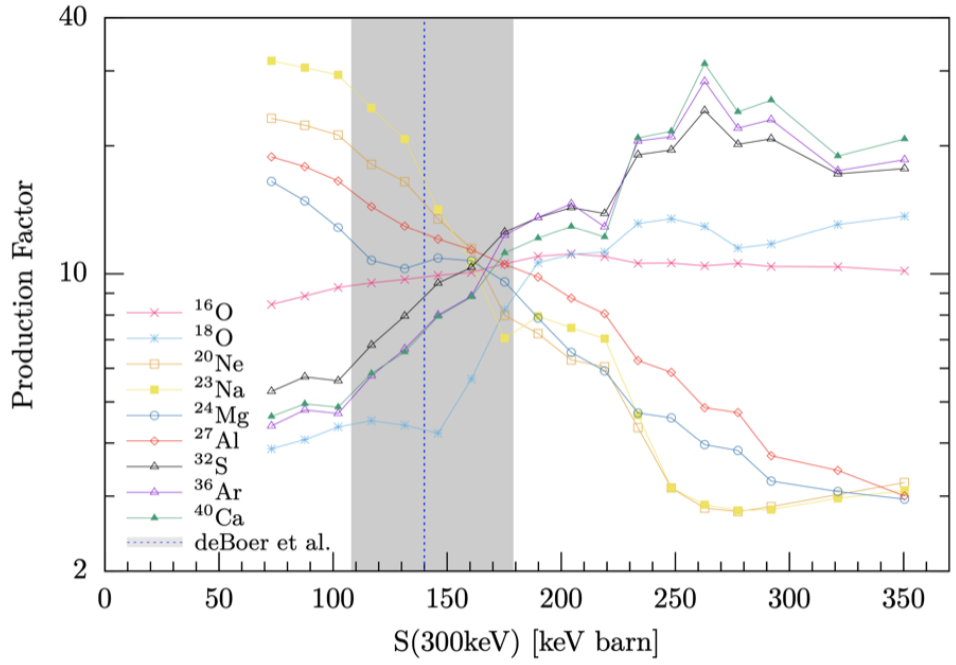

FIGURE 1.3. The isotopic production factors for certain isotopes as a function of S(300 keV) for the reaction $^{12}C(\alpha,\gamma)^{16}O$. The production factors and thus the resulting abundances are sensitively dependent on the S-factor, as shown by the result of deBoer *et al.* [6]. Figure from [7].

where m_{iso} is the total yield of the isotope in solar masses, $X^{\odot}_{\text{iso}}$ is the mass fraction of the isotope according to the solar metallicity pattern, and M_{tot} is the initial mass of the star [8]. Fig. 1.3 shows different isotopic production factors as a function of the astrophysical S-factor of the reaction $^{12}C(\alpha,\gamma)^{16}O$, which is taken at an energy of 300 keV, the representative energy for stellar helium burning. The vertical blue dashed line and the surrounding grey area illustrate the result and the uncertainty, respectively, of deBoer *et al.* [6]. It is clear that with such a large uncertainty, no robust prediction of the abundance of heavier elements can be made. In fact, an experimental error bar of $\leq 10\,\%$ is required for S(300 keV) to obtain reasonable results. [5, 6, 9, 8, 7]

The big problem of directly measuring S(300 keV) with the required accuracy is the tiny effective cross-section in the order of 10^{-17} barn. Therefore, there is no experiment so far that has measured the S-factor at center-of-mass energies much lower than 1 MeV. Instead, the results of the higher energy measurements must be extrapolated to the energy region of the Gamow peak. While doing so, potential extrapolation errors as well as the nuclear structure of ^{16}O with its resonances, a non-resonant contribution, and the interference between these components must be taken into account, which requires a high computational effort. One advantage is that almost 100 % of the resonant states of ^{16}O γ-decay to the ground state, thus the S-factor in the energy region of the Gamow peak is dominated by the two ground state transitions E1 and E2 with the respective

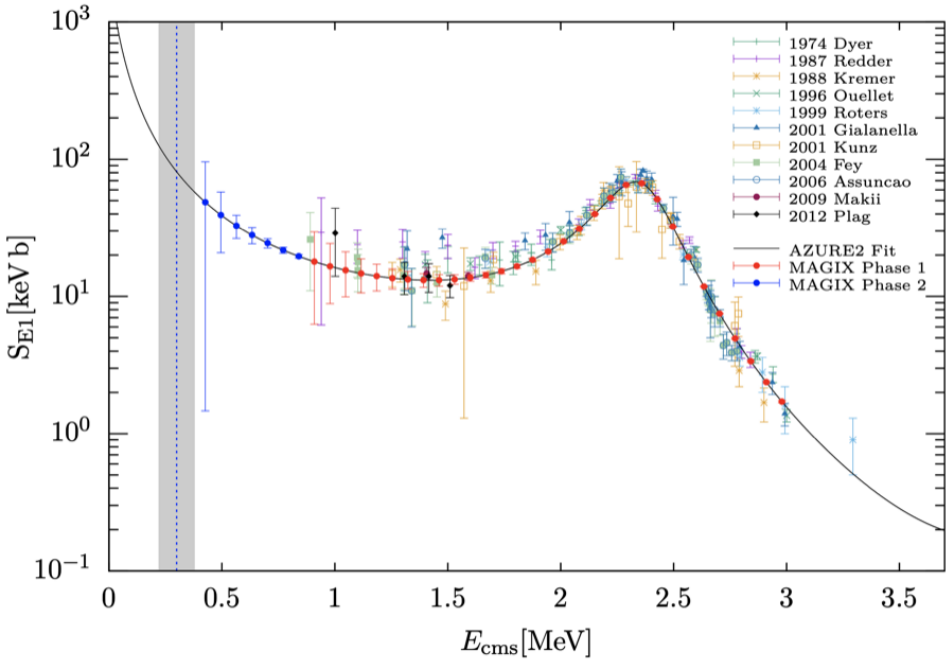

(a)

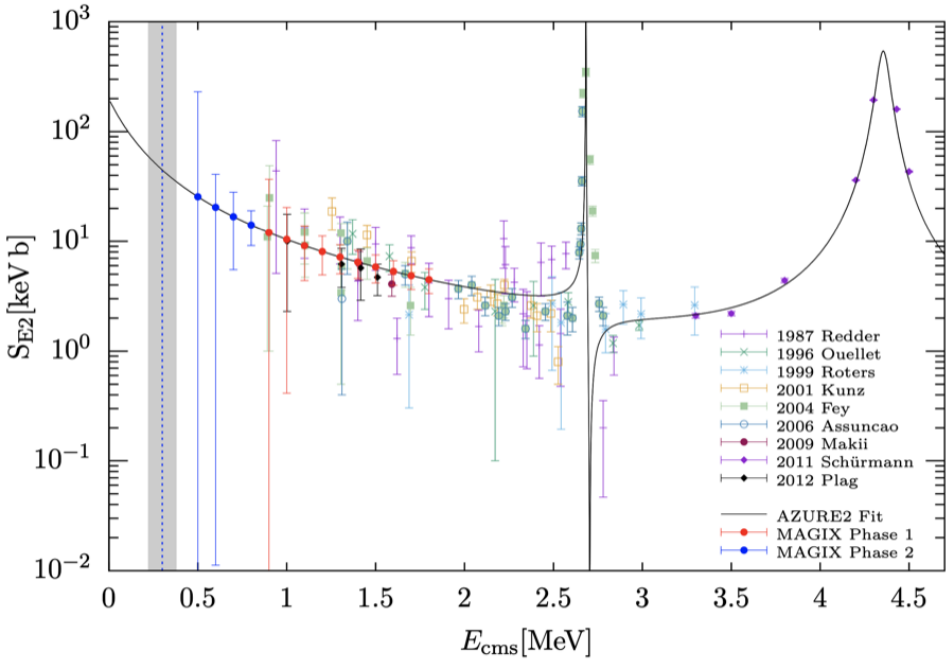

(b)

FIGURE 1.4. The MAGIX projections for the S-factor contributions S_{E_1} (a) and S_{E_2} (b) of the reaction $^{12}C(\alpha,\gamma)^{16}O$ are shown, together with existing measurements and a fit using the AZURE2 software. The MAGIX projections are separated into Phase 1 and Phase 2. Figures from [7].

S-factor contributions termed S_{E_1} and S_{E_2}. Nonetheless, the achievable accuracy for S(300 keV) is very limited. [7]

An alternative approach to a direct measurement of the $^{12}C(\alpha,\gamma)^{16}O$-reaction is the measurement of related nuclear reactions with much larger cross-sections, followed by the calculation of S(300 keV) using the reciprocity theorem. One possibility is the *photo-disintegration* method, in which the time-reversed reaction $^{16}O(\gamma,\alpha)^{12}C$ is measured. In this reaction, the oxygen is broken up by a photon and the recoiled α-particle has to be measured. In the energy region of the Gamow peak, the corresponding cross-section is ~ 50 times larger than the cross-section of $^{12}C(\alpha,\gamma)^{16}O$. [7]

An extension of this method is measuring the *electro-disintegration* reaction $^{16}O(e,e'\alpha)^{12}C$, in which the oxygen is broken up by the virtual photon emitted from the scattered electron, bringing MAGIX into play. Using ^{16}O as a target gas in combination with the MESA electron beam, the electro-disintegration reaction can be investigated at MAGIX. The four-momentum of the virtual photon can be determined by measuring the four-momentum transfer of the scattering process, which means that the recoil α-particle and the scattered electron have to be detected in coincidence. While the electron is detected in one of the magnetic spectrometers, the silicon strip detectors inside the scattering chamber are used for the detection of the α-particle. Due to the completely window-less design of MAGIX, the S-factor contributions S_{E_1} and S_{E_2} of the reaction $^{12}C(\alpha,\gamma)^{16}O$ can then be extracted more precisely than ever before. This can be seen in Fig. 1.4, in which the projections for MAGIX Phase 1 and MAGIX Phase 2 are shown. In Phase 1, the S-factor can be measured down to a center-of-mass energy of $E_{\mathrm{cms}} = 0.9\,\mathrm{MeV}$ using the above setup, but with an improved extrapolation into the energy region of the Gamow peak. In Phase 2, the setup will be expanded by a zero degree tagger that allows the detection of the electron at much smaller angles than in case of the spectrometers. By this, energies down to 0.4 MeV can be reached for the first time ever, improving the accuracy of the extrapolation even further. [7]

1.2 Electromagnetic Form Factors of the Proton

As found in 1933 [10, 11], the proton is no fundamental particle but has an internal structure, which was later identified to be composed of quarks and gluons. The electromagnetic structure can be described by the two Sachs form factors G_E and G_M, which are related to the charge and magnetization distributions inside the proton. Accordingly, the proton has a non-zero charge radius r_E^p and a non-zero magnetic radius r_M^p. [12]

In the case of the charge radius r_E^p, three methods are used for determination: (a) measuring the electric form factor $G_E(Q^2)$ in electron-proton scattering experiments at low four-momentum transfer Q, (b) measuring various atomic transitions in hydrogen, and (c) measuring the lamb shift of the 2S - 2P transition in muonic hydrogen. Before 2010, the results of methods (a) and (b) were consistent with each other. The results from method (c), which first appeared in 2010,

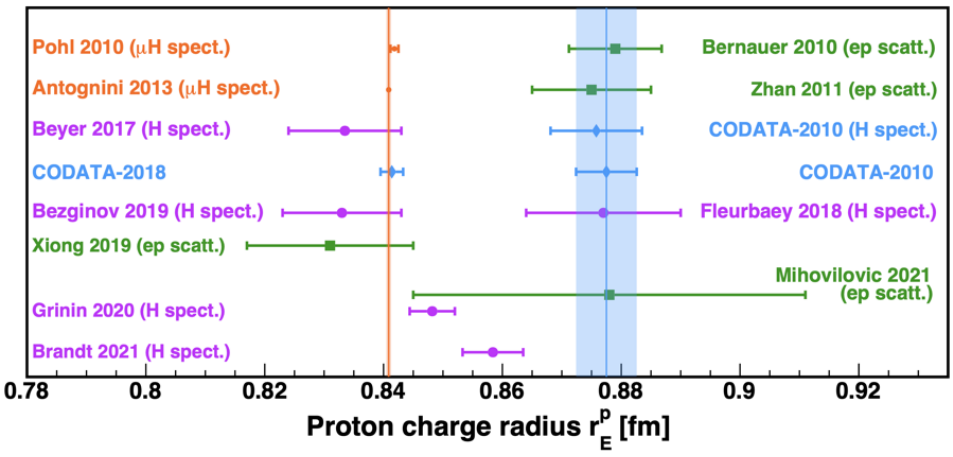

FIGURE 1.5. Selection of recent r_E^p measurements. Results using methods (a)-(c) are shown in green squares, purple dots, and orange dots, respectively. In addition, the CODATA compilations are shown as blue diamonds. Figure from [13].

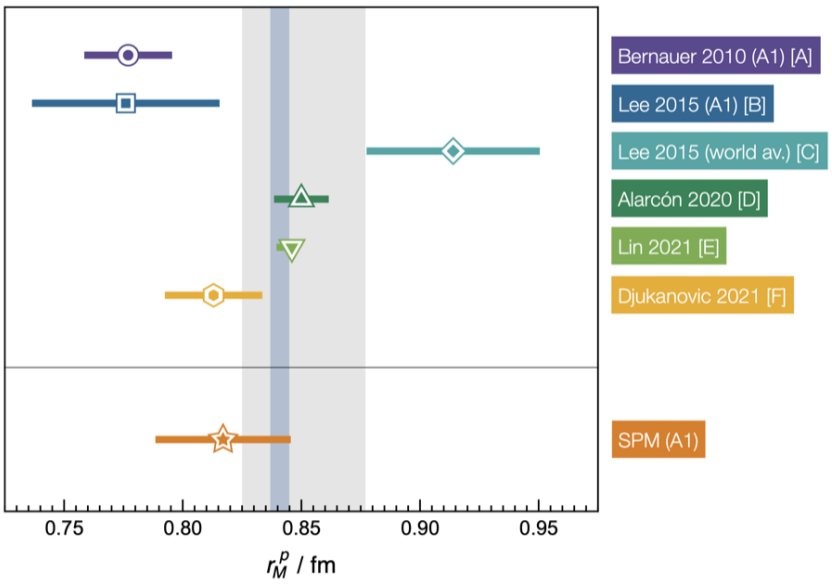

FIGURE 1.6. Results for the magnetic radius of the proton using various analysis techniques. All shown results are based on electron-proton scattering data either from A1 at MAMI [14] or from PRad at JLab [15] except (F), which is a prediction using lattice QCD. Figure from [16].

showed a dramatic difference with respect to the other two. This contradictory situation was named the *proton radius puzzle*. Since then, several new measurements and reanalyses were published, which made the situation even more puzzling, see Fig. 1.5. [17, 13]

For the magnetic radius of the proton, r_M^p, a contradictory situation arises as well, even among electron-proton measurements, as can be seen in Fig. 1.6. To obtain r_M^p, usually two methods are used: (a) using electron-proton scattering to measure $G_M(Q^2)$ analogous to method (a) for measuring r_E^p and (b) measuring the ratio G_E/G_M in double polarization experiments. [18]

MAGIX is ideally suited to contribute significantly to the above mentioned puzzles by measuring both the electric and the magnetic form factor at very low four-momentum transfers Q with high precision, using hydrogen as a target gas and detecting the scattered electrons in one of the two magnetic spectrometers. The conventional way to do this is the method of *Rosenbluth separation*, which is based on the unpolarized elastic electron-proton scattering cross-section described by the Rosenbluth formula:

$$\left(\frac{\mathrm{d}\sigma}{\mathrm{d}\Omega}\right)_{ep} = \left(\frac{\mathrm{d}\sigma}{\mathrm{d}\Omega}\right)_{\mathrm{Mott}} \frac{\epsilon G_E^2 + \tau G_M^2}{\epsilon(1+\tau)}. \tag{1.6}$$

Here,

$$\left(\frac{\mathrm{d}\sigma}{\mathrm{d}\Omega}\right)_{\mathrm{Mott}} = \frac{4\alpha^2}{Q^4}\frac{E'^3}{E}\cos^2\left(\frac{\theta_e}{2}\right) \tag{1.7}$$

is the Mott cross-section with α being the fine structure constant; Q^2 the negative squared four-momentum of the transferred virtual photon; E and E' the energies of the incoming and outgoing electron, respectively; and θ_e the electron scattering angle. The squared four-momentum transfer Q^2 in turn is given by

$$Q^2 = 4EE'\sin^2\left(\frac{\theta_e}{2}\right); \tag{1.8}$$

E' can be calculated via

$$E' = \frac{E}{1+\frac{2E}{m_p}\sin^2\left(\frac{\theta_e}{2}\right)}; \tag{1.9}$$

$\tau = Q^2/(4m_p^2)$ is a dimensionless variable, where m_p is the proton mass; and ϵ is the polarization of the transferred virtual photon given by

$$\epsilon = \left(1+2(1+\tau)\tan^2\left(\frac{\theta_e}{2}\right)\right)^{-1}. \tag{1.10}$$

The form factors can be written as an expansion in terms of Q^2,

$$\frac{G_{E/M}(Q^2)}{G_{E/M}(0)} = 1 - \frac{1}{6}\left(r_{E/M}^p\right)^2 Q^2 + 120\left(r_{E/M}^p\right)^4 Q^4 - ..., \tag{1.11}$$

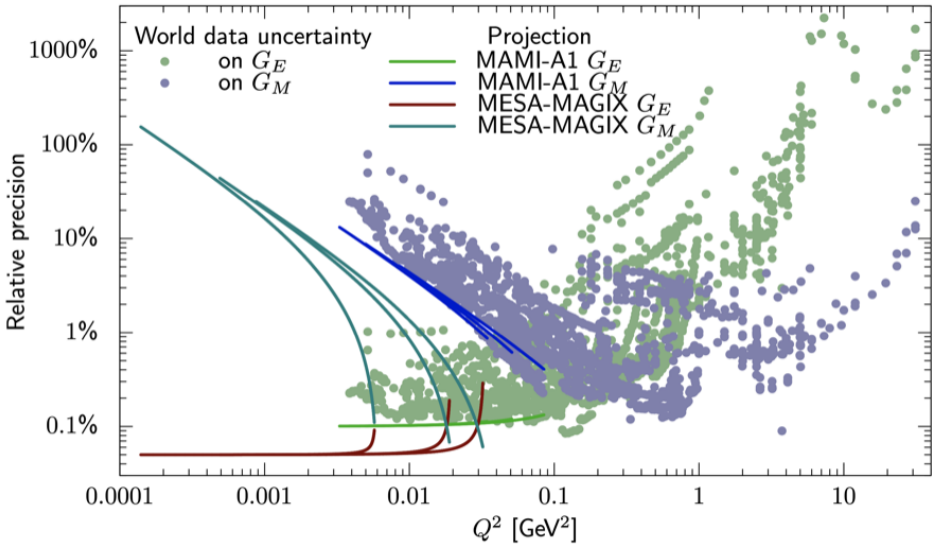

FIGURE 1.7. The cross-section sensitivity to G_E and G_M. The relative precision of the cross-section is mapped to the respective form factor, assuming the other one is fixed. The existing cross-section data, as well as projections for MAGIX and an updated version of the earlier A1 measurement at MAMI are shown. Figure from [20].

and are normalized at $Q^2 = 0$ to the charge and magnetic moment of the proton in units of the electron charge $|e|$ and of the nuclear magneton $\mu_N = e\hbar/(2m_p)$, such that

$$G_E(0) = 1, \quad \text{and} \quad G_M(0) = \mu_p \approx 2.793. \tag{1.12}$$

By defining the reduced cross-section

$$\left(\frac{\mathrm{d}\sigma}{\mathrm{d}\Omega}\right)_{\text{reduced}} := \epsilon(1+\tau)\frac{\left(\frac{\mathrm{d}\sigma}{\mathrm{d}\Omega}\right)_{ep}}{\left(\frac{\mathrm{d}\sigma}{\mathrm{d}\Omega}\right)_{\text{Mott}}} = \epsilon G_E^2 + \tau G_M^2, \tag{1.13}$$

one yields a linear dependence in ϵ with G_E^2 as the slope and τG_M^2 as the intercept. By taking cross-section data for different ϵ values but fixed values for Q^2, the form factors G_E and G_M can be separated. Note that both θ_e and E have to be varied for this, which is done by changing the spectrometer angle and the beam energy, respectively.

From Eq. 1.11 follows that the charge and magnetization radii $r^p_{E/M}$ can be extracted using

$$r^p_{E/M} = \left[-\frac{6}{G_{E/M}(Q^2)}\frac{\mathrm{d}}{\mathrm{d}Q^2}G_{E/M}(Q^2)\right]_{Q^2=0}, \tag{1.14}$$

which shows the importance to measure the form factors at low values of Q^2. [12, 13, 19]

Following Eq. 1.13, the limitations of this method can be seen. The contribution of G_E^2 to the reduced cross-section scales with ϵ and hence vanishes for large Q^2. In contrast, the contribution

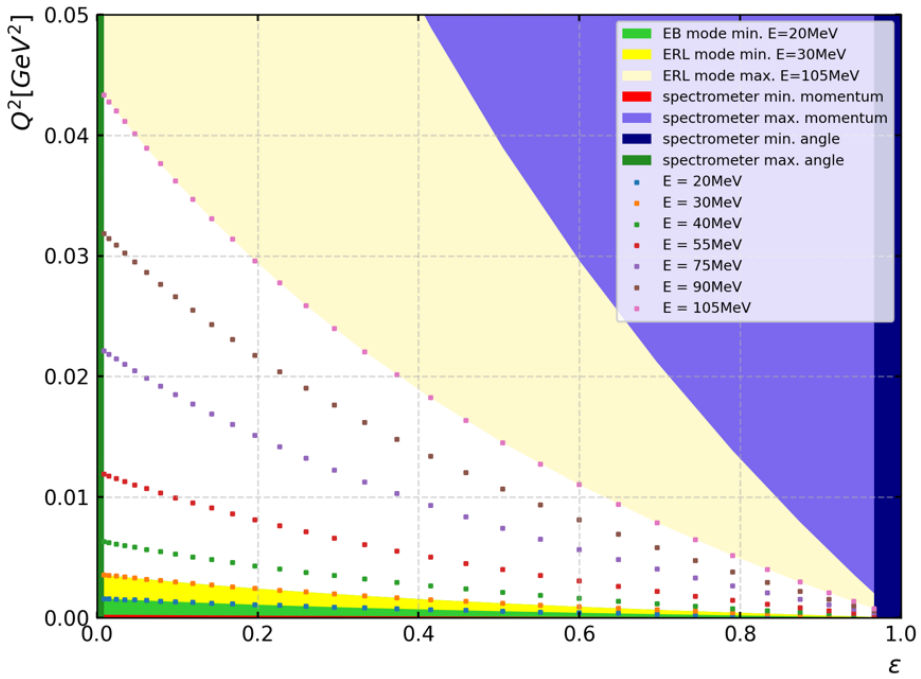

FIGURE 1.8. The accessible kinematical region in the $\epsilon - Q^2$-plane for MAGIX. The colored regions are excluded due to the beam energy range in ERL mode (30 MeV to 105 MeV), the beam energy range in EB mode (20 MeV to 105 MeV), the angular range of the spectrometers (15 ° to 165 °), and the central momentum range of the spectrometers (3 MeV to 282 MeV).

of G_M^2 is suppressed by τ which vanishes as Q^2 goes to zero. Therefore, the electric form factor can be extracted with the highest precision at low Q^2 values, while a magnetic form factor extraction is more precise for high Q^2 values. This circumstance can be seen in Fig. 1.7, especially by the green and blue dots representing the uncertainty of cross-section world data on G_E and G_M as of August 2019, respectively. Also shown are the former projections for an updated version of the earlier A1 measurement at MAMI [14] which were partly confirmed in 2022 [21], as well as the projections for MAGIX. The unprecedented precision of G_E will be achieved through the low beam energy of MESA and the window-less design of the MAGIX setup, leading to a drastically reduced background environment. On the other hand, the only possibility to measure G_M at low Q^2 values with such precision, is to choose a kinematic regime with a large backward scattering angle. Then, ϵ effectively approaches to zero as well. If done correctly, ϵ is even smaller than τ and the contribution of G_M to the reduced cross-section is enhanced. [18]

Fig. 1.8 shows the accessible kinematical region in the $\epsilon - Q^2$-plane for MAGIX. The various colored areas are excluded due to experimental limitations on the beam energy, the adjustable spectrometer angles, and the designed central momentum range of the spectrometers. Also shown is a possible set of measurements for different beam energies.

1.3 Dark Sector Searches

A variety of astrophysical and cosmological observations suggest the existence of dark matter (DM) and there are many different theoretical models that try to explain the observed discrepancies [22]. From a particle physics perspective, these models usually describe DM as an extension of the Standard Model of Particle Physics (SM) via new particles of a dark sector, that interact only partially with the known baryonic SM matter. Over the last years, the search for such dark sector particles has become a prime focus of fundamental physics and has led to numerous experimental searches - unfortunately, all with negative results so far[1].

The large number of DM models allows for a very broad range of DM masses (from $\sim 10\,\mathrm{keV}$ to $\sim 10\,\mathrm{TeV}$) and cross-sections for interactions with SM particles, which does not make the search any easier [26, 27]. With the non-finding of massive dark sector particles in the high-energy regime at the LHC at CERN and in underground-experiments in the past years, the focus has moved to searches for light dark matter (LDM) candidates (below $\sim 1\,\mathrm{GeV}$) and the messenger particles of the hypothetical dark sector [28]. A promising approach to discover these are fixed-target electron-scattering experiments in the low-energy regime [29, 30], which brings us to MESA. Its beam energy in the MeV to GeV region coupled with the high luminosity reached at MAGIX is ideally suited for the search for a dark sector messenger particle.

One simple but popular model extends the SM by an additional $U(1)_D$ group. The model is comprised by a massive vector mediator particle, the *dark photon* γ', and the dark matter candidate χ with masses $m_{\gamma'}$ and m_χ, respectively. The particles couple to each other via a dark fine structure constant α_D and the dark photon couples to the ordinary SM photon very weakly with a mixing parameter ϵ. The dark matter particle χ exists only within the dark sector and does not couple to SM matter. In this model, the dark photon can decay via different decay channels and becomes therefore measurable. *Visible decays* are all decays in which the end products are SM particles, e.g. a lepton pair. In the case of an *invisible decay*, the dark photon produces dark matter particles that do not interact with SM particles, e.g. $\gamma' \to \chi\bar{\chi}$, which is of course only kinematically feasible if the dark photon is heavier than twice the mass of the dark matter particle, i.e. $m_{\gamma'} > 2m_\chi$. [26]

The MAGIX setup will be sensitive to both types of decays. Assuming a production of the dark photon through a mechanism similar to the Bremsstrahlung process, a dark photon γ' could radiatively be produced off a nuclear target Z via the reaction $e^- Z \to e^- Z \gamma'$. The corresponding cross-section scales with Z^2 [29], and the e^- and Z represent the MESA beam and the atomic nuclei of the target gas of MAGIX, respectively. Dark photon searches at MAGIX are therefore preferably performed using a high-Z target gas, like Argon or Xenon.

[1] In fact, there is one exception. The so-called *ATOMKI anomaly* [23] in the internal pair creation isoscalar transition $^8\mathrm{Be}(18.15) \to {}^8\mathrm{Be}\, e^+e^-$ could be explained by a hypothetical gauge boson with a mass of $\sim 17\,\mathrm{MeV}$, termed the X17. But since there are also possible SM explanations for this anomaly [24, 25], it is not seen as a positive result here.

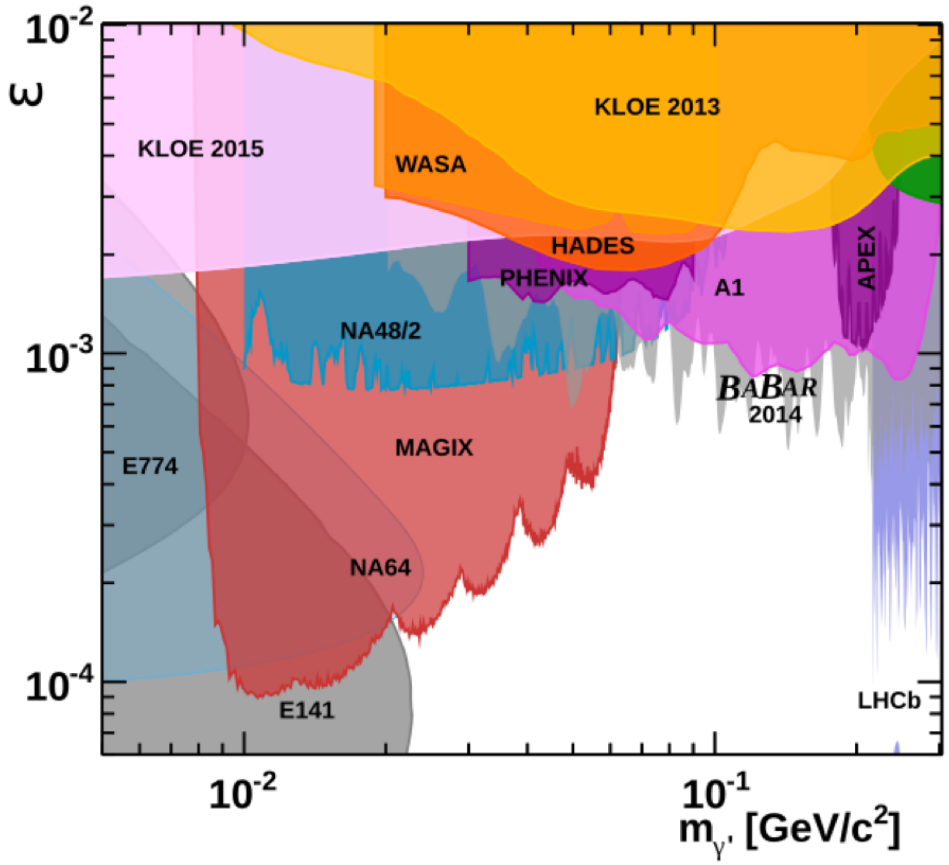

FIGURE 1.9. The γ' parameter space spanned by $m_{\gamma'}$ and ϵ for the visible dark photon decay $\gamma' \rightarrow e^+e^-$. The achievable exclusion limits of MAGIX are shown in red, together with existing exclusion limits of several other experiments. Figure from [31].

The most likely visible decay of the dark photon that is kinematically allowed at MAGIX is $\gamma' \rightarrow e^+e^-$, where the final state can be detected in coincidence in the two magnetic spectrometers. After reconstructing the invariant mass of the e^+e^- pair, the dark photon would manifest itself as a sharp resonance above the radiative background. If no peak is found, MAGIX is able to exclude regions in the γ' parameter space spanned by its mass $m_{\gamma'}$ and its mixing parameter ϵ. These projected exclusion limits are depicted in Fig. 1.9, assuming the use of a solid tantalum target[2].

For investigating the invisible decay channel $\gamma' \rightarrow \chi\bar{\chi}$, the decay products of the dark photon cannot be detected. Instead, the scattered beam electron is measured together with the recoil target nucleus and the missing mass compared to the initial state is computed. Analogous to the S-factor measurement in Section 1.1, the electron is therefore detected in one of the spectrometers, while the recoil nucleus is detected via the silicon strip detectors inside the scattering chamber [26, 32]. To avoid the complex excitation spectra of high-Z materials, which

[2]The dark sector searches at MAGIX will commence with a 55 MeV electron beam using a tantalum target, in order to obtain competitive data even before the MESA ERL mode and the gas jet target are commissioned.

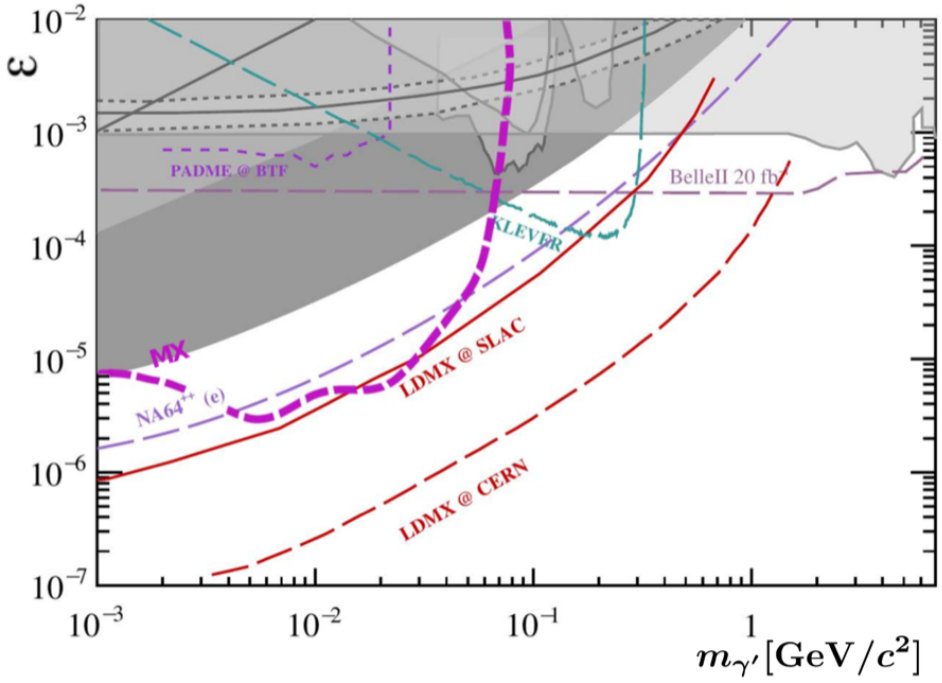

FIGURE 1.10. The γ' parameter space for the invisible dark photon decay $\gamma' \rightarrow \chi\bar{\chi}$. The anticipated MAGIX exclusion limits (MX) are shown in addition to the limits of several other experiments. Figure from [31].

would complicate the measurement of the recoil nucleus, this search is best done using the most simplest target gas, i.e. hydrogen. The reduction in cross-section in this case has to be compensated by longer data taking periods. Analogous to the case of the visible decay, MAGIX is able to provide exclusion limits in the γ' parameter space if no invisibly decaying dark photon is found. These are shown in Fig. 1.10 for the use of a hydrogen target.

1.4 Few-Body Physics

Quantum chromodynamics (QCD) is the underlying theory of the strong force - one of the three fundamental forces described by the Standard Model of Particle Physics (SM) - and describes the interaction between quarks mediated by gluons. These do not occur individually but are confined into hadrons, of which the proton and neutron are the elementary building blocks to the increasingly heavy nuclei forming the chemical elements we know. While QCD is capable of explaining the composition of protons, neutrons, and other light hadrons using *ab-initio* calculations starting from quarks and gluons as degrees of freedom [33], this approach currently fails for larger few-body systems, i.e. heavier nuclei. [34, 33]

However, considerable progress has been made by describing nuclei using chiral effective field theory (χEFT), a perturbation theory that obeys the relevant conservation laws and symmetries

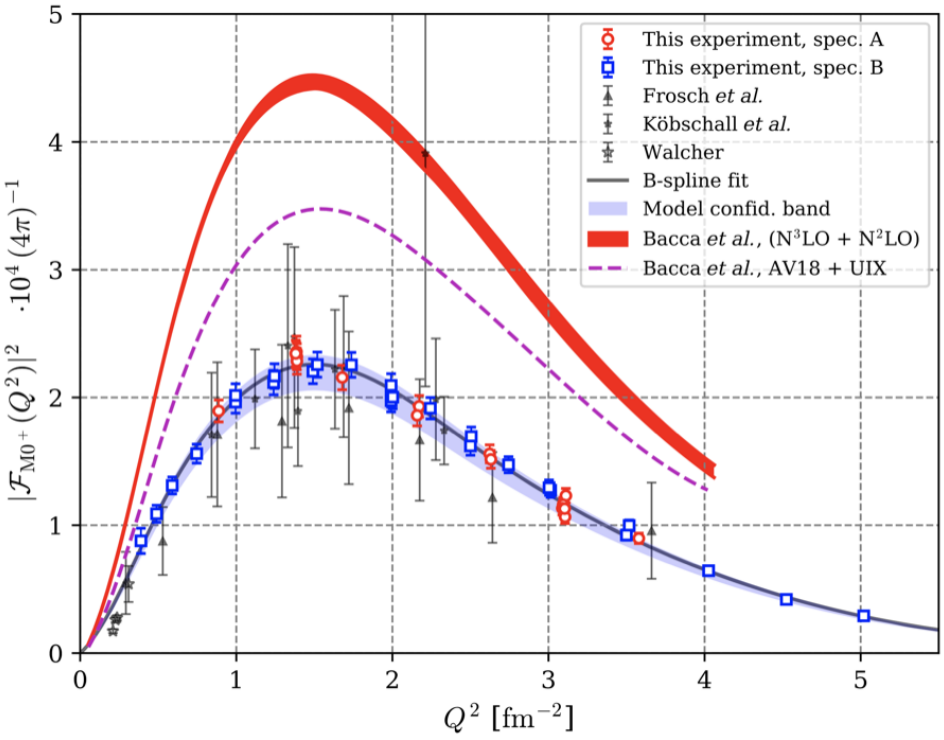

FIGURE 1.11. The transition form factor for the α-particle monopole transition $0_1^+ \rightarrow 0_2^+$ as a function of the squared four-momentum transfer Q^2. Theoretical calculations by Bacca *et al.* are shown, together with data from inelastic electron scattering. The most recent data by Kegel *et al.*, taken with the A1 spectrometers in Mainz, reaffirms the discrepancy between theory and experiment. Figure from [37].

of QCD in the low-energy domain, which is characteristic for the nuclear binding. This allows the description of nuclei not only by phenomenological approaches, but starting from first principles. Nonetheless, χEFT is not entirely without uncertainties and the theoretical predictions heavily depend on the included contributions [35, 36], e.g. from nucleon-nucleon forces (NN), three-nucleon forces (3N), final-state interactions (FSI), or meson exchange currents (MEC). This is why precise experimental data in the low-energy regime is needed to calibrate the theory and to systematically verify or falsify new theoretical developments. [37, 36]

MAGIX can do exactly that by studying the excitation of light nuclei using the high-intensity electron beam of MESA. With the use of different target gases, certain inclusive as well as exclusive reactions can be investigated, testing different aspects of the theoretical description of nuclei. In the following, two of the several feasible and planned few-body measurements are discussed in more detail.

One extensively studied few-body system so far is the α-particle, the nucleus of ^{4}He, consisting of two protons and two neutrons. While its ground state 0_1^+ can be accurately described at the subpercent level using χEFT [37], the calculations for its first excited state 0_2^+ are heavily

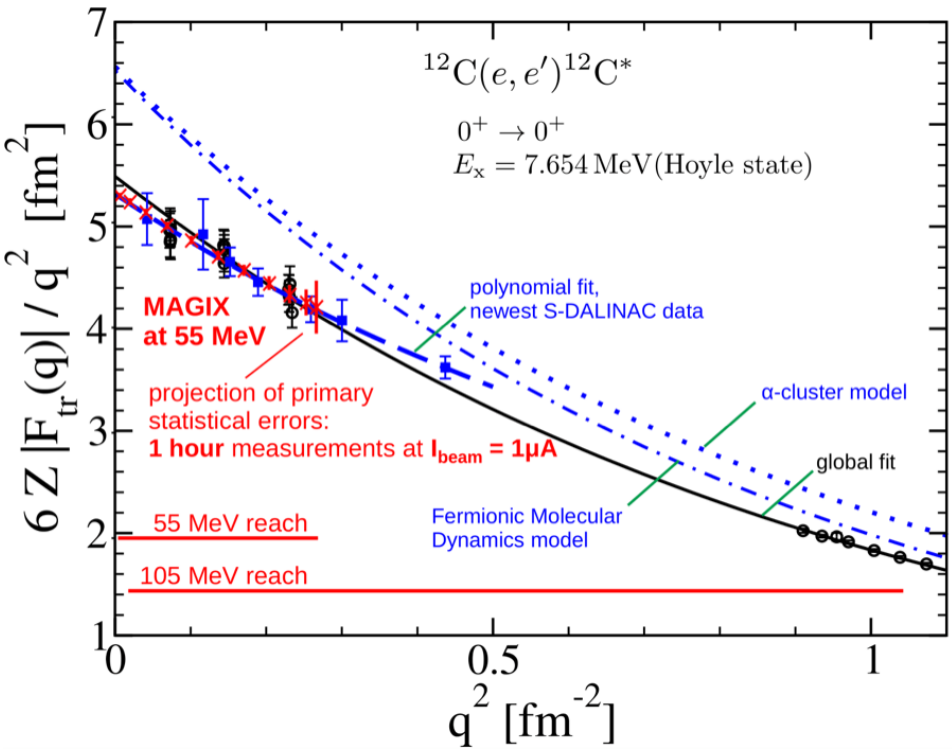

FIGURE 1.12. The transition form factor of the Hoyle state in ^{12}C as a function of the squared three-momentum transfer q^2. Fitted experimental data from the S-DALINAC in Darmstadt (blue squares and blue dashed line) is compared to two model approaches: an α-cluster model (blue dotted line) and a fermionic molecular dynamics (FMD) model (blue dashed-dotted line). Also some older data is shown (black circles), together with a global fit (black line). The possible reach of MAGIX is indicated in red. Figure from [39].

dependent on the included model contributions [35]. The transition form factor $\left|\mathcal{F}_{M0^+}\left(Q^2\right)\right|$ of this isoscalar monopole resonance provides insight into the nuclear structure of the α-particle and can serve as a test for ab-initio methods. Latest χEFT calculations for $\left|\mathcal{F}_{M0^+}\left(Q^2\right)\right|$ by Bacca *et al.* [36] have shown a factor of 2 disagreement with existing experimental data from inelastic electron scattering. Recently, this discrepancy has been reaffirmed with the most precise electron scattering data measured to date by Kegel *et al.* [37, 38]. The extent of the deviation can be seen in Fig. 1.11. Due to its design and the conditions at MESA, MAGIX can contribute to this situation by providing even more accurate electron scattering data on ^{4}He in an even lower Q^2 region, further narrowing down the constraints for the theoretical models of few-body physics.

A similar problem arises for ^{12}C, which also exhibits an excited 0^+ state, known as the *Hoyle state*. Its radiative decay width Γ_{rad} influences the reaction rate of the 3α process ($3\alpha \rightarrow {}^{12}\mathrm{C} + \gamma$), the fundamental reaction in stellar nucleosynthesis for producing carbon in our Universe. For a long time, Γ_{rad} was only known with an uncertainty of $\pm 12\,\%$ [40], which limited its applications

in astrophysics. In fact, an accuracy of $\pm 5\,\%$ is needed to yield convenient results [40]. Although this limit could be crossed by Chernykh *et al.* in 2010 [40], further precision measurements are required to check and improve the findings. Besides, the Hoyle state plays a prominent role as a prototype of α-cluster states in light nuclei. By describing ^{12}C as a system of three α-particles using a cluster EFT, new features of nuclear forces might be discovered. However, even the most advanced models fail to explain the transition to the Hoyle state accurately to this day, see Fig. 1.12. [41, 40]

A more precise experimental determination of Γ_{rad} will bring more clarity into the understanding of the Hoyle state. Unfortunately, Γ_{rad} cannot be accessed directly in an experiment, but has to be determined as a product of quantities measured in different experiments, one of which being Γ_π, the pair decay width of the $e^\pm$-decays of the Hoyle state. Γ_π can be determined via inelastic electron scattering by measuring the transition form factor $F_{\mathrm{tr}}(q)$, see Fig. 1.12. The extrapolation of $F_{\mathrm{tr}}(q)$ to zero momentum transfer then yields the monopole matrix element, which in turn defines Γ_π. By contributing data to $F_{\mathrm{tr}}(q)$ in the low q-regime with the use of a solid ^{12}C target, see Fig. 1.12, MAGIX is able to improve the experimental uncertainty of Γ_{rad} and, supplementary, to deliver valuable data as input for future EFT calculation developments.

CHAPTER 2

THE MAGIX SETUP

Often, electron scattering cross-sections $\mathrm{d}\sigma/\mathrm{d}\Omega$ to first order are proportional to the Mott cross-section, cf. Eq. 1.6, and in turn inversely proportional to the fourth power of the four-momentum transfer Q during the scattering process, cf. Eq. 1.7, hence

$$\frac{\mathrm{d}\sigma}{\mathrm{d}\Omega} \propto \frac{1}{Q^4}.$$

Furthermore, Q^2 is related to the electron scattering angle θ_e according to

$$Q^2 = 4EE' \sin^2\left(\frac{\theta_e}{2}\right),$$

where E and E' are the electron energies before and after the scattering process, respectively. This relation shows the high level of precision that is needed in electron scattering experiments: A resolution for the cross-section of $< 1\%$ requires an angular resolution of $\Delta\theta_e < 0.05^\circ$ and, when using nuclear targets, a precise relative energy resolution of $\Delta E'/E < 10^{-4}$. [18]

An effective approach to meet these requirements is by using high-resolution magnetic spectrometers [18, 42]. This is why MAGIX, the acronym for **MA**inz **G**as **I**njection Target E**X**periment, employs two multi-purpose magnetic spectrometers surrounding a gas jet target at its center. The gas jet target is chosen to minimize the effects of multiple scattering, which is also supported by the completely window-less design of the MAGIX scattering chamber. Low-energy electron scattering is performed with competitive luminosities in the order of $10^{35}\,\mathrm{cm}^{-2}\mathrm{s}^{-1}$, employing the beam of the electron accelerator MESA. The focal planes of the spectrometers are each equipped with dedicated detector systems, including a tracking detector realized by a time projection chamber (TPC) and a sophisticated trigger veto system. In addition, an array of silicon strip detectors is placed around the interaction point for the detection of heavy charged recoil particles.

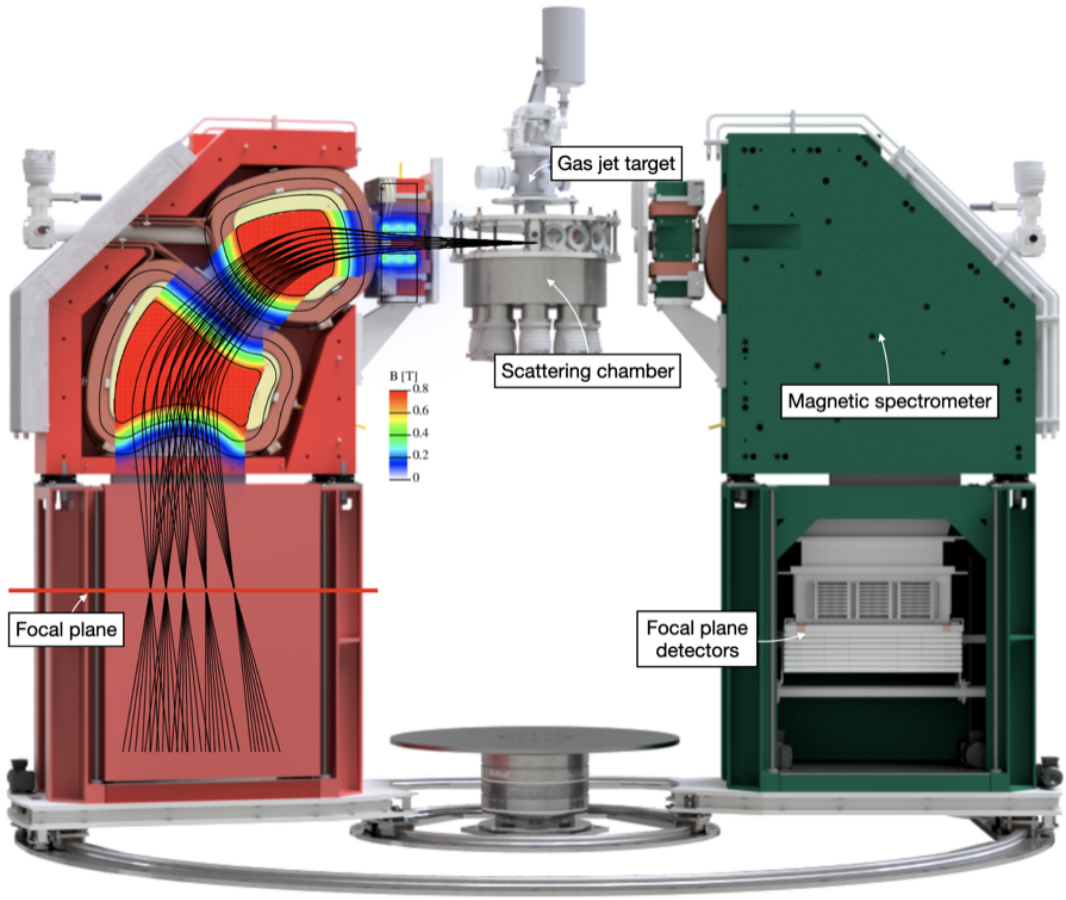

FIGURE 2.1. The schematic setup of MAGIX. A completely window-less scattering chamber, housing a gas jet target and an array of silicon strip detectors, is surrounded by two high-resolution magnetic spectrometers, whose focal planes are equipped with dedicated tracking, trigger, and veto detectors.

Fig. 2.1 shows the schematic setup of MAGIX. The upcoming sections guide through each of the individual components, including the electron accelerator MESA.

2.1 The Electron Accelerator MESA

MESA is the low-energy quasi-continuous-wave recirculating electron linac that is currently being built at the Institute for Nuclear Physics on the campus of the Johannes Gutenberg University in Mainz, Germany. For this, the underground halls of the decommissioned A4 experiment at MAMI[1] are employed, as well as newly constructed halls, which were completed at the end of 2023. The first electron beam is expected in early 2025. The acronym MESA stands for **M**ainz **E**nergy-recovering **S**uperconducting **A**ccelerator and emphasizes the accelerator's core principle

[1] **MA**inz **MI**crotron

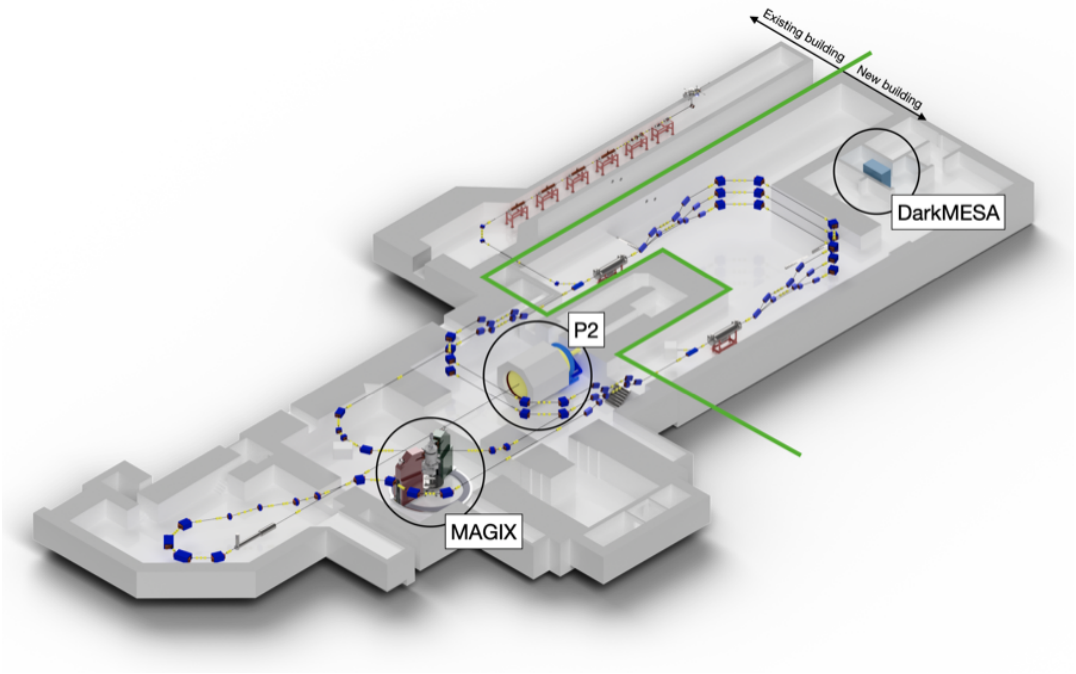

FIGURE 2.2. The floor plan of MESA including the three experiments MAGIX, P2, and DarkMESA. The green line shows the boundary between the existing and the newly constructed parts of the underground halls.

of energy-recovery. The accelerator is designed to provide a high-intensity electron beam with high polarization and excellent beam quality for high-precision particle physics experiments.

MESA will be used in two different modes: the extracted beam (EB) mode and the energy-recovery linac (ERL) mode. In EB mode, the electron beam will have a maximum beam energy of 155 MeV, a maximum beam current of 0.15 mA, and a maximum beam polarization of $> 85\,\%$, serving the external experiments P2 and, parasitically to P2, DarkMESA. In contrast, the ERL mode will provide the internal MAGIX experiment with an unpolarized electron beam with a maximum beam energy of 105 MeV and a maximum beam current of 1 mA up to 10 mA[2]. After interacting with the MAGIX target, the beam electrons can then be recaptured and fed back into the superconducting accelerator modules, where the largest part of their kinetic energy can be regained.

The floor plan of MESA is shown in Fig. 2.2, including the three experiments MAGIX, P2, and DarkMESA. The boundary between the existing and newly constructed underground halls is depicted by the green line. [32]

[2]The increase to 10 mA will be realized in a later construction stage of MESA [43]. Beyond that, a second upgrade has been discussed, in which the beam current shall be increased to 100 mA by converting the MAGIX beam layout into a storage ring [44].

2.1.1 Accelerator Layout

The general layout of MESA can be separated into several more or less individual passages, which are shortly described in the following. If not stated otherwise, the information in this section is based on the PhD thesis of D. Simon [45], which provides a much more detailed and complete discussion on MESA.

Injector The beam layout of the MESA injector can be seen in Fig. 2.3a. It starts with the polarized dc photogun STEAM[3] [46], where a laser beam is used to emit polarized electrons from a GaAs photocathode. The electrons are then accelerated to 100 keV and directed into the beam preparation system MELBA[4] [47], which consists of a spin-manipulation system followed by a chopper-buncher section. The spin manipulation system is built from two Wien-filters and allows a freely adjustable polarization direction, whereas the chopper-buncher system is used to improve the overall beam quality and to match the beam into the normal-conducting booster linac MAMBO[5] [48]. In MAMBO, the electrons are accelerated by four normal-conducting injector cavities to energies of up to 5 MeV and beam currents of up to 10 mA. The electron beam then passes a 180° arc, the MARC[6] 0, and goes through an injection-extraction-chicane, before it reaches the first super-conducting cryomodule of the main accelerator, the MEEC[7] 1.

Main Accelerator and Return Arcs The main accelerator follows the concept of a double-sided accelerator design with two super-conducting linac modules in the form of modified ELBE[8] cryomodules [49], the so-called MEECs, as well as five vertically stacked recirculation arcs termed MARC[6] 1-5. A closer look on the layout is given in Fig. 2.3b. Each cryomodule consists of two TESLA[9]-type SRF[10] cavities with a resonance frequency of 1.3 GHz, each of which provides a maximum energy gain of 12.5 MeV per passage. The beam electrons therefore can gain a maximum of 25 MeV per turn or 50 MeV per complete circulation. The recirculation arcs are arranged such that the beam with the lowest energy is transported to the highest arc and the one with the highest energy to the arc on the bottom.

By adjusting the energy gain of the cryomodules and by varying the number of circulations through the main accelerator, the beam energy can be flexibly tailored to the needs of the experiment. For serving the external P2 experiment, one to three circulations are possible, and the accessible energy range in EB mode goes from somewhere below 30 MeV[11] up to 155 MeV.

[3] **S**mall **T**hermalized **E**lectron Source **At** **M**ainz
[4] **ME**SA **L**ow-energy **B**eam **A**pparatus
[5] **M**illi**AM**pere **BO**oster
[6] **M**ESA **ARC**
[7] **M**ESA **E**nhanced **E**LBE **C**ryomodule
[8] **E**lectron **L**inac for Beams with High **B**rilliance and Low **E**mittance
[9] **T**eraelectronvolt **E**nergy **S**uperconducting **L**inear **A**ccelerator
[10] **S**uper-conducting **R**adio **F**requency
[11] At the time of writing this thesis, it is not clear what the minimal beam energy in EB mode will be, but the circulating value is 20 MeV.

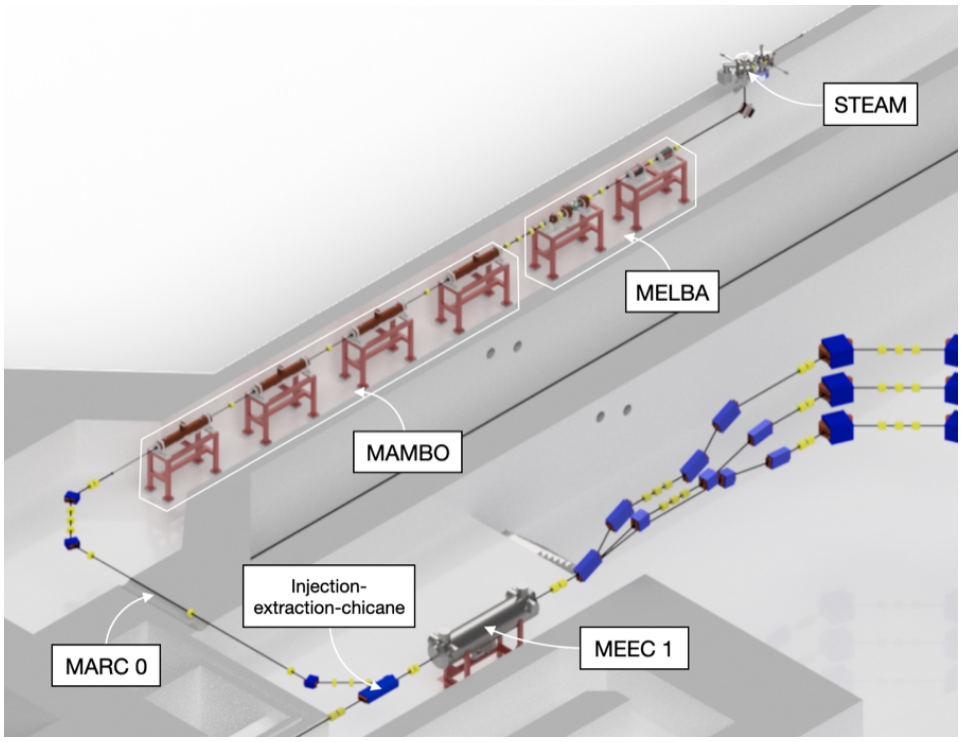

(a)

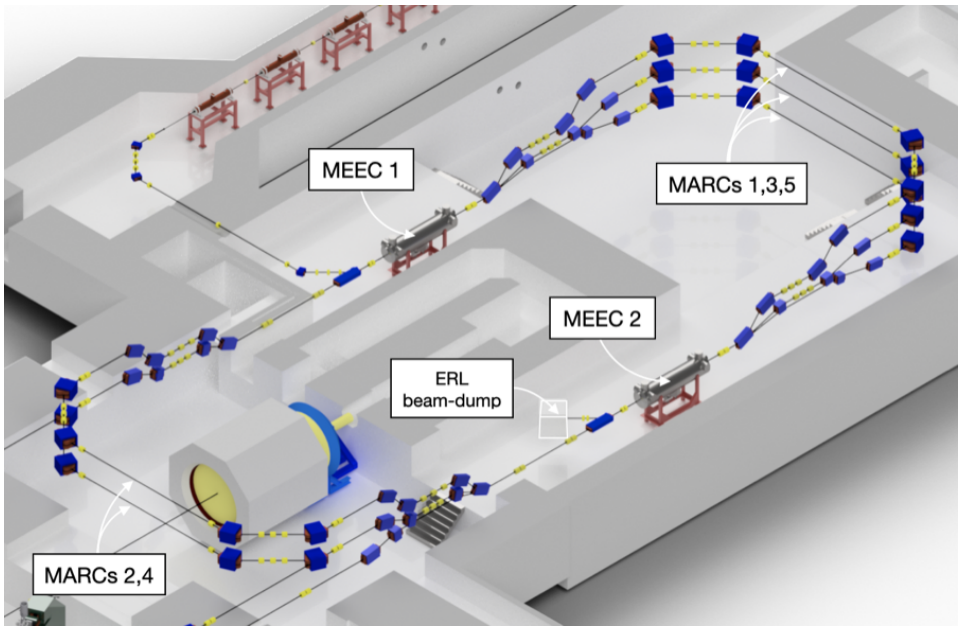

(b)

FIGURE 2.3. The beam layout of MESA. Closer looks on the individual parts of the MESA injector (a) and the main accelerator with the return arcs (b) are given. Beam lines are shown in black, dipole magnets in blue, and quadrupoles in yellow.

The internal MAGIX experiment, on the other hand, can only be reached after a maximum of two circulations, setting an upper limit to the beam energy in ERL mode of 105 MeV. In addition, a lower limit of 30 MeV is defined by the injection-extraction-chicane, whose design does not allow electrons with an energy of less than 30 MeV to pass. Hence, these electrons would be lost before being returned to the SRF cavities for energy-recovery. As an alternative, the MAGIX experiment can also be operated in EB mode[12], for which an individual beam-dump is available [50], see Fig. 2.4. In this mode of operation, the beam energies below 30 MeV are also available for MAGIX. With a possible future upgrade, one may extend the range of accessible beam energies by adding two more recirculation arcs and therefore increasing the number of possible circulations by one [51]. As a result, the maximum beam energies in EB and ERL mode would be raised to 205 MeV and 155 MeV, respectively.

The unique feature of the MESA main accelerator is the capability for energy-recovery. After the interaction with the internal MAGIX target, the beam electrons are recaptured and reinjected into the SRF cavities. If this is done using a phase shift of 180° with respect to the resonance frequency of the SRF cavities, the beam enters the cavities in the decelerating phase and the beam energy can be restored down to injection energy. The remaining 5 MeV beam is then dumped inside the ERL beam-dump. To allow for this method, a very thin gas jet target with minimized containment material is used, details on which are given in Section 2.2. Conversely, the high beam current of MESA is indispensable for the reasonable operation of such a target, i.e. for achieving competitive luminosities and count rates.

2.1.2 The P2 Experiment

The purpose of the external P2 experiment is to provide a high-precision determination of the weak mixing angle $\sin^2\Theta_W$, also called Weinberg angle, to a precision of 0.15 % at a four-momentum transfer $Q^2 = 4.5 \times 10^{-3}\,\mathrm{GeV}^2$. The precise knowledge of $\sin^2\Theta_W$ provides a stringent test of the SM and enables the exploration of New Physics models with mass scales up to 50 TeV. In the SM, the weak mixing angle is connected to the weak charge of the proton $Q_W(p)$, which in turn can be extracted from a measurement of the parity-violating cross-section asymmetry A^{PV} in elastic electron-proton scattering. This tiny symmetry lies in the order of 10^{-8} [52] and will be the smallest asymmetry measured so far in electron scattering experiments.

To achieve the intended precision, a measurement time of 11 000 h is required, employing MESA in EB mode with a high beam polarization of $> 85\,\%$, a beam energy of 155 MeV, and a beam current of 0.15 mA. The high beam polarization must be ensured and quantified at all times, which is why three polarimeters are used along the beam layout of MESA: a double Mott polarimeter at 100 keV as part of the dc photogun STEAM, a single Mott polarimeter at 5 MeV at the outlet of the booster linac MAMBO, and a Møller polarimeter at 155 MeV in front of the P2 experiment. The beam layout towards P2 is illustrated in Fig. 2.4.

[12] In fact, the commissioning phase of MESA will limit the beam operation to EB mode with an energy of 55 MeV.

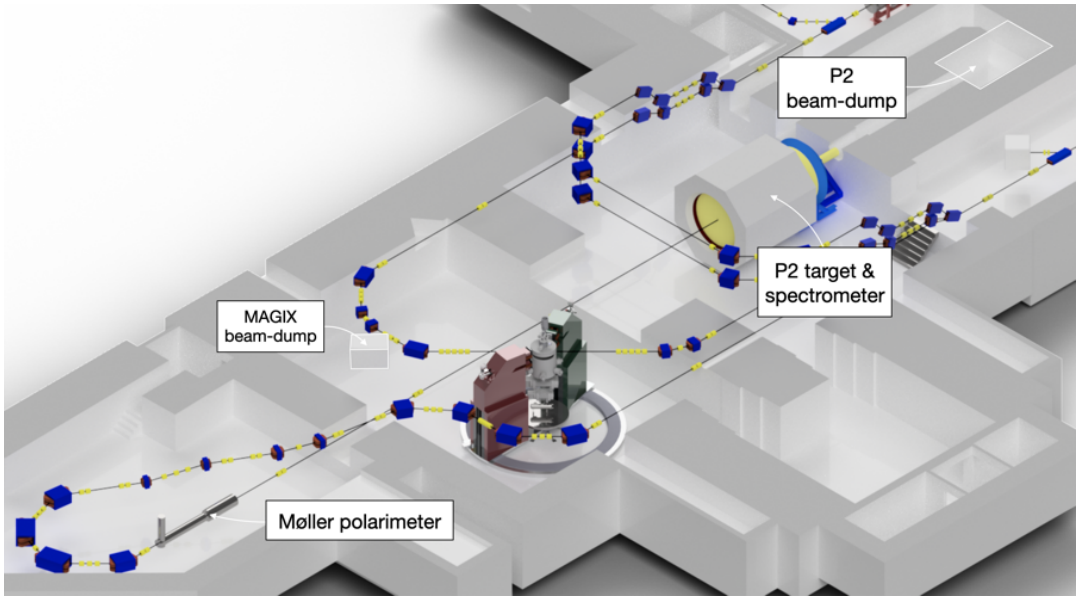

FIGURE 2.4. Beam layout towards the P2 experiment. The MESA beam is extracted from the main accelerator and directed towards the Møller polarimeter. The beam electrons then interact with the P2 target, some of which get detected inside the P2 spectrometer, while the residual beam is dumped into the P2 beam-dump. Additionally, the MAGIX beam-dump is shown, which enables MAGIX the operation in EB mode.

The protons are provided in form of a 60 cm long high-power liquid hydrogen target. After the interaction, the elastically scattered electrons are detected for each helicity state using a super-conducting solenoid spectrometer with 100 % azimuthal-acceptance. A closer look on the experimental setup can be found in Fig. 2.5. The beam electrons enter the evacuated scattering chamber through the beam line and interact with the liquid hydrogen target. The forward-scattered electrons then leave the scattering chamber through a ring-shaped Kevlar window into the helium-filled tracking section based on HV-MAPS detectors, with the help of which the Q^2 of the electrons is reconstructed. After passing a lead shield to suppress background processes such as Møller scattering and Bremsstrahlung, the scattered electrons are detected in a Cherenkov ring detector for the measurement of the parity-violating asymmetry. The electrons that do not interact with the target, leave the spectrometer and are dumped into the P2 beam-dump.

In the future, several extensions of the measurement program at P2 are foreseen, which include a backward-angle measurement of the parity-violating asymmetry in electron-proton scattering and the determination of the weak charge of the ^{12}C nucleus. Moreover, it is planned to measure the neutron skin of the ^{208}Pb nucleus in cooperation with the MREX[13] collaboration. [52]

[13] **M**ainz **R**adius **EX**periment

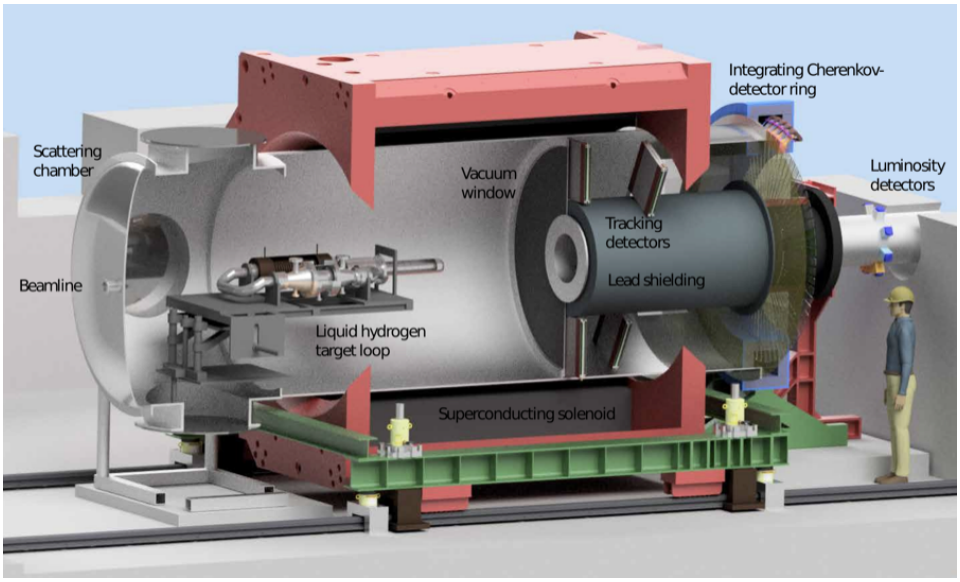

FIGURE 2.5. CAD model of the experimental setup of P2. Figure from [53].

2.1.3 The Beam-Dump Experiment DarkMESA

Located on the beam-axis of the P2 experiment and employing its beam-dump as a target, DarkMESA is the third experiment operated at MESA. As the name suggests, DarkMESA performs measurements investigating the hypothetical dark sector that could explain the phenomenon of dark matter as an extension of the SM. More precisely, it explores the low-energy parameter space for the invisible dark photon decay as described in Section 1.3, thus providing additional exclusion limits to the measurement landscape. The assumption is that dark photons γ' could be produced in the P2 beam-dump before they decay invisibly into pairs of dark matter particles $\chi\bar{\chi}$, see Fig. 2.6a. After passing about 15 m of air and 8 m of concrete, a small portion of the dark matter particles could be detected in the DarkMESA detector. Depending on the detection method, both electron recoil or nucleon recoil could in principle be used for this, as depicted in Figs. 2.6b and 2.6c, respectively.

However, following extensive simulation studies [27], it was decided to build the DarkMESA detector in the form of a traditional calorimeter that measures the electron recoil[14]. Due to the low interaction probability of the dark matter particles, the number of scattering centers in the detector should be maximized. High Z materials are therefore preferred and the calorimeter is built from high-density Cherenkov crystals.

The calorimeter is hermetically enclosed by a dedicated veto system made from lead absorbers and plastic scintillation detectors read out by silicon photomultipliers (SiPMs), so that background events from cosmogenic muons can be identified and suppressed. Background contributions

[14] For DarkMESA phase C, other detector concepts are still being discussed at the time of writing this thesis.

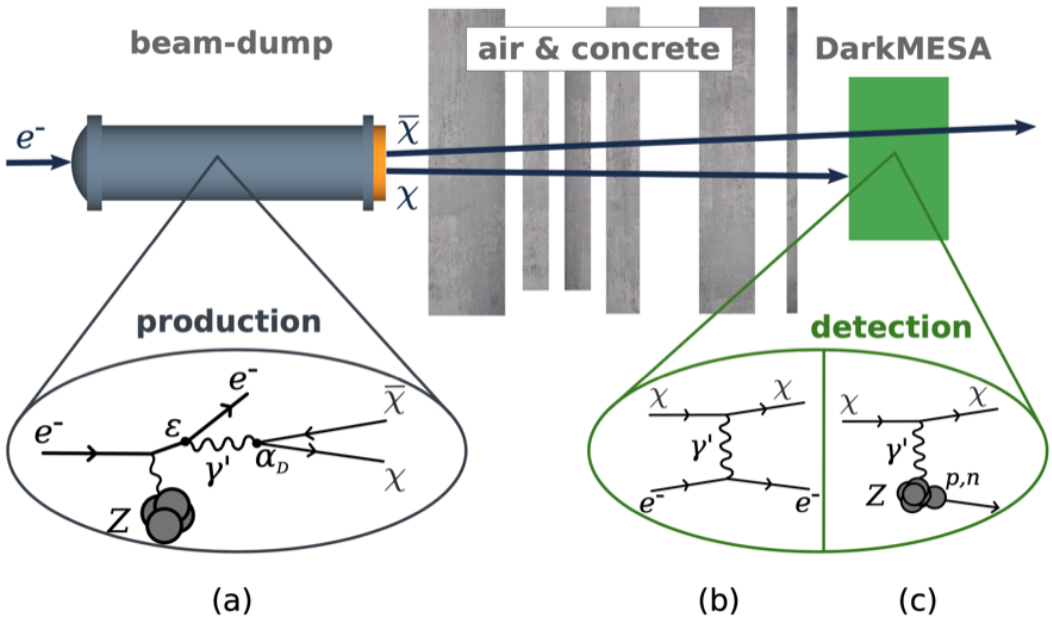

FIGURE 2.6. The concept of DarkMESA including the Feynman graphs of production and detection. Dark photons γ' could be produced in the P2 beam-dump and decay into pairs of dark matter particles $\chi\bar{\chi}$ (a). In the DarkMESA detector, the dark matter particles could then scatter off electrons (b) or nucleons (c), before they are detected by measuring the respective recoil. Figure from [27].

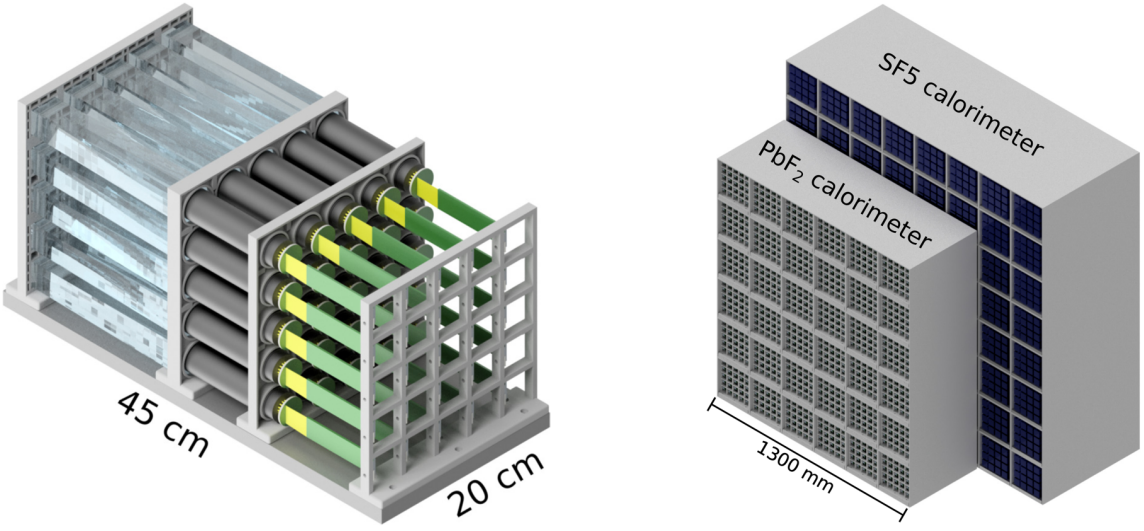

FIGURE 2.7. The DarkMESA calorimeters for Phase A (a) and Phase B (b). A prototype module made from 25 PbF_2 crystals is used for Phase A. In Phase B, 900 PbF_2 and 1,024 SF5 crystals will be combined into two walls, drastically increasing the active detector volume. Figures from [27].

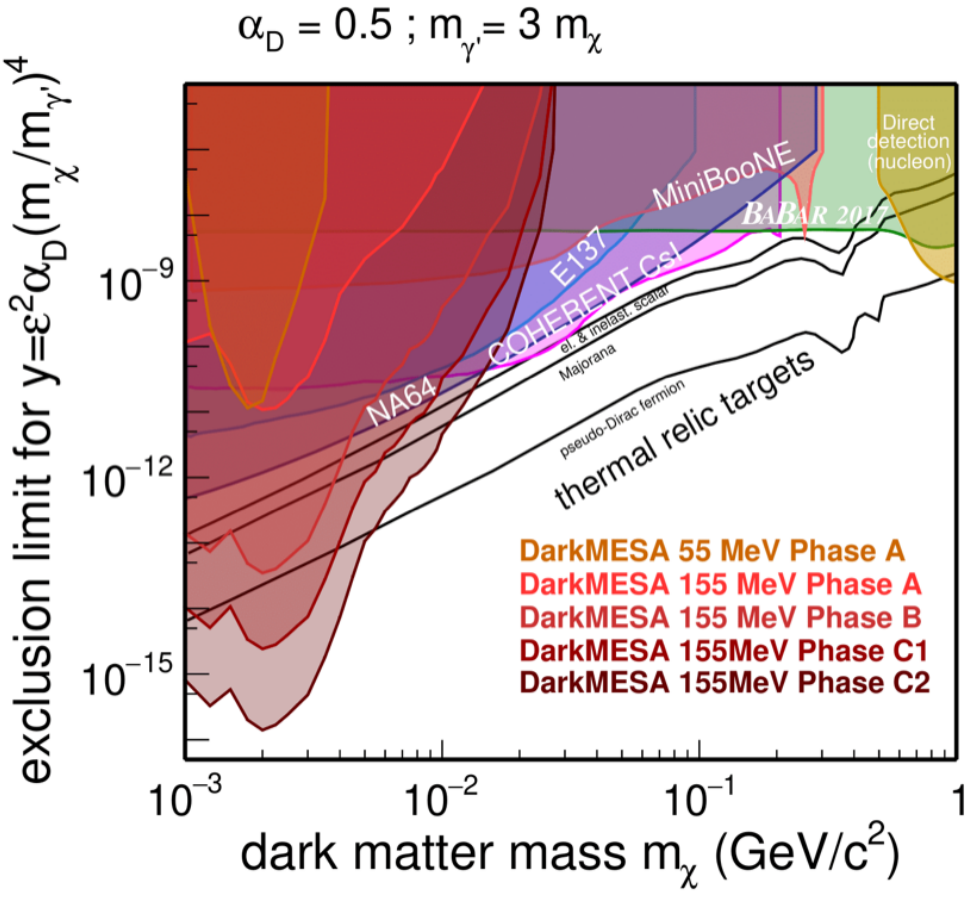

FIGURE 2.8. The parameter space for the invisible dark photon decay $\gamma' \rightarrow \chi\bar{\chi}$ with m_χ on the x-axis and the dimensionless parameter y on the y-axis. The achievable exclusion limits for the individual DarkMESA phases are shown in red, together with the exclusion limits of several other experiments. The thermal relic targets correspond to predictions assuming a thermal origin of dark matter. Figure provided by M. Christmann.

from beam-related neutrons and neutrinos will be negligible [27], but could be counteracted by evaluating the calorimeter signals with and without MESA beam operation. A closer look on the veto system is given in Appendix A.1, since the use of plastic scintillators in combination with SiPMs opens up the possibility for valuable synergy effects between DarkMESA and MAGIX.

Based on dedicated beam times at MAMI [54, 55, 56], extensive laboratory research [57, 58], as well as the already mentioned extensive simulation studies [27], the following phased approach for the DarkMESA detector setup was concluded. With each phase, the active detector volume will be enlarged and more and more dark matter particles will be able to reach the DarkMESA detector, which in turn increases the interaction probability.
In Phase A, the calorimeter consists of a prototype module made from 25 PbF_2 crystals read

out by photomultiplier tubes (PMTs) that are arranged in a 3D-printed 5x5 grid as shown in Fig. 2.7a. The active detector volume of the module is 3.6 L. Together with the veto system, this setup allows for characterization studies in the laboratory or at MAMI, and can be used for first background measurements during the commissioning phase of MESA.
For Phase B, the detector volume of the calorimeter will be drastically increased by combining 36 of the above mentioned modules (900 PbF_2 crystals) into a wall with an active detector volume of around 120 L. In addition, a second wall with an active detector volume of about 580 L, made from 1,024 SF5 crystals combined into 64 modules, will be placed right behind the first. The calorimeter setup for Phase B is illustrated in Fig. 2.7b.
To increase the detector volume even further, an additional Phase C is proposed. By using thin sheets of commercially available radiation shielding glass, active detector volumes of 1 m^3 (Phase C1) and even 9 m^3 (Phase C2) are foreseen. Other options for Phase C, for instance based on the technique of opaque scintillators, are under investigation.

Fig. 2.8 shows the regions of the parameter space for the invisible dark photon decay that will be covered by the individual phases of DarkMESA[15]. In contrast to Section 1.3, the yield variable $y = \epsilon^2 \alpha_D \left(m_\chi / m_{\gamma'}\right)^4$ is shown on the y-axis, which is a dimensionless combination of the dark photon model parameters ϵ, α_D, m_χ, and $m_{\gamma'}$. To obtain the illustrated results, the conservative assumptions of $\alpha_D = 0.5$ and $m_{\gamma'} = 3m_\chi$ were used. As can be seen, from Phase B on, DarkMESA will be able to provide exclusion limits that are accessible for the first time ever. [27]

2.1.4 The Beam Layout for MAGIX

Fig. 2.9 schematically shows the beam layout for the internal MAGIX experiment. At the bottom right, the MESA beam enters the recirculation arc of MAGIX after the completion of two circulations through the main accelerator. It then passes the beam separation of MARC 4 and gets directed towards the interaction point of MAGIX using a double bend achromat. The beam height at the interaction point is 3715 mm above the hall floor. Behind the MAGIX setup, two routes are possible: If MAGIX employs the EB mode of MESA, the beam is guided to the MAGIX beam-dump and is destroyed. If MAGIX is operated in ERL mode, on the other hand, the beam follows a return arc and a chicane, before it is returned to the main accelerator for energy-recovery. [45]

The first dipole of the return arc behind the MAGIX setup fulfills multiple purposes. Besides the usage as a bending dipole, it will be operated as a forward spectrometer, called FORE [7]. This will be part of the zero degree tagger mentioned in Section 1.1, which is needed to expand the accessible energy range in the measurement of the astrophysical S-factor of the reaction $^{12}C(\alpha,\gamma)^{16}O$. Additionally, FORE will serve as a luminosity monitor, making use of the Bremsstrahlung process [59].

The straight beam line section around MAGIX, running from the double bend achromat to the re-

[15] The commissioning phase of MESA will only allow for a beam energy of up to 55 MeV instead of the final 155 MeV. Phase A is therefore subdivided into "Phase A 55 MeV" and "Phase A 155 MeV".

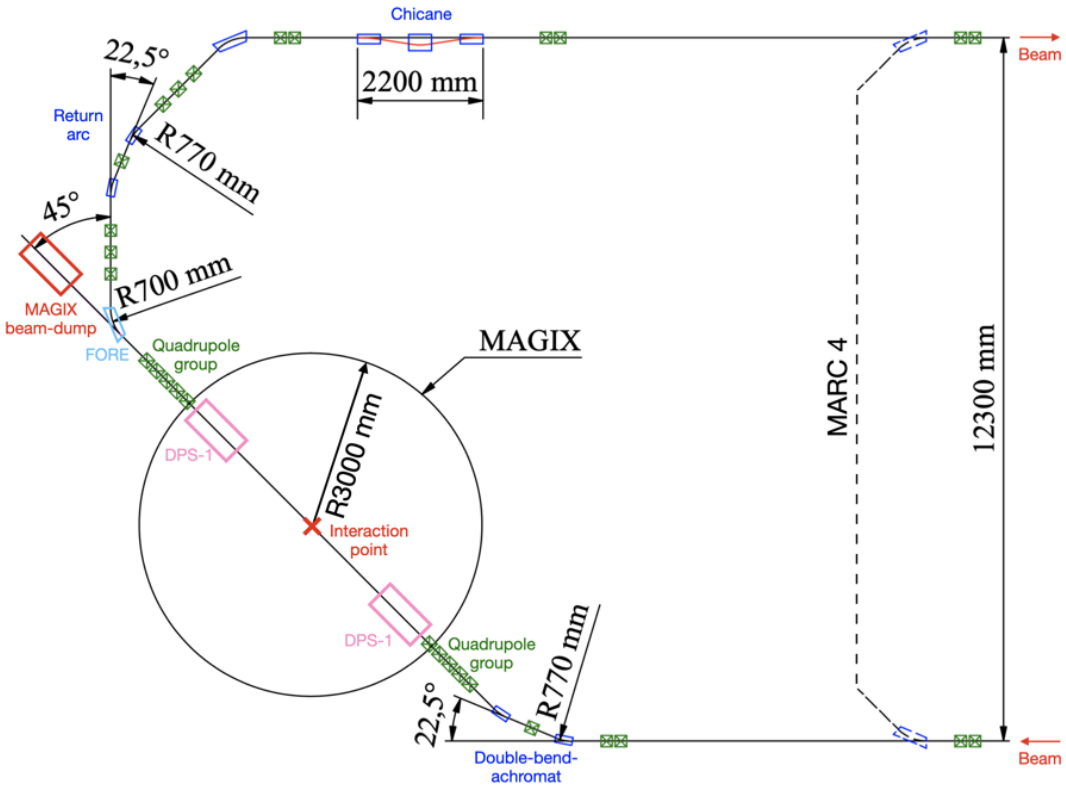

FIGURE 2.9. The beam layout for the internal MAGIX experiment. Beam lines are shown in black, dipole magnets in blue, quadrupoles in green. Figure adapted from [45].

turn arc, will be tightly packed. Supplementary to the scattering chamber and the spectrometers of MAGIX, a group of quadrupoles is installed both upstream and downstream of the internal MAGIX target, so that the MESA beam can be focused on the interaction point in a precise but still flexible way. At the time of writing this thesis, the quadrupole group size is set to five but could in the future still be reduced. Beyond that, the differential pumping system DPS-1, cf. Appendix A.2, must be implemented into this beam line section, also both upstream and downstream of the internal target. The DPS-1 is inevitable due to the completely window-less design of MAGIX and the therefore shared vacuum of the scattering chamber, the spectrometers, and the MESA beam lines.

2.2 The MAGIX Gas Jet Target

The core piece of MAGIX, located at the heart of the window-less scattering chamber and enclosing the interaction point, is the cryogenic supersonic cluster-jet target that was developed and initially tested at the University of Münster [60]. By expanding a pre-cooled gas through a fine convergent-divergent nozzle, i.e. a Laval nozzle, it provides a continuous stream of target

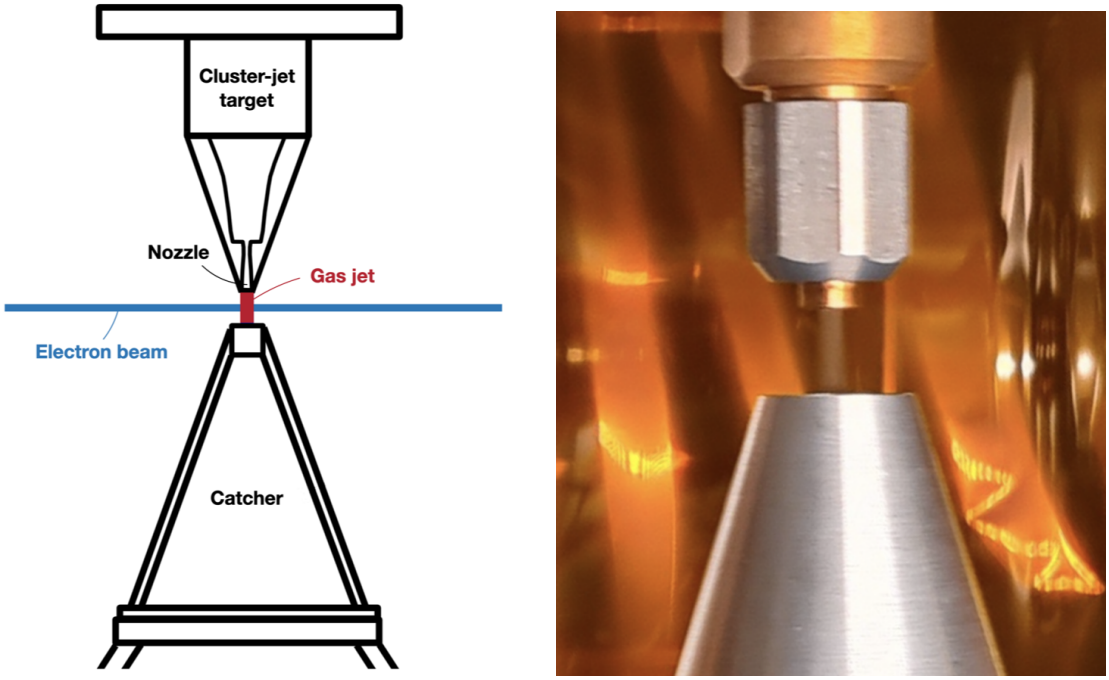

(a) (b)

FIGURE 2.10. A sketch of the interaction region at MAGIX (a) and its realization inside the scattering chamber (b). A gas jet is ejected from the nozzle of the cluster-jet target, perpendicular to the electron beam of MESA. After the interaction, the gas jet is caught by the catcher and pumped away. Photograph in (b) taken by P. Brand.

material with a high and constant gas jet thickness. In 2017, it was successfully operated at MAMI using hydrogen [61], which represented the proof of concept for the usage of this type of target at MAGIX. Dependent on the experimental needs, it can be operated with many different target gases, such as H_2, Ar, O_2, N_2, or Xe, and is therefore highly suited for the rich physics program discussed in Chapter 1.

Fig. 2.10a shows a sketch of the interaction region at MAGIX. The cluster-jet target is located at the top and its nozzle ejects a gas jet perpendicular to the horizontally incoming electron beam of MESA. After the interaction, the gas jet is extracted from the scattering chamber by a funnel-shaped catcher, which is placed directly underneath the interaction point and connected to a powerful pumping cascade, cf. Appendix A.2. By this, the constancy of the optimized vacuum conditions inside the scattering chamber can be assured throughout the experiment. An actual photo of the interaction region is shown in Fig. 2.10b, taken during a second characterization beam time at MAMI in 2021 with argon as the target gas [62]. In addition to nozzle and catcher, the argon jet can be faintly seen.

The use of a cluster-jet target at MAGIX is motivated by several reasons. First, as discussed above, to allow for the operation of MESA in ERL mode, MAGIX has to provide a target that is thin

enough to enable the recapture of the electron beam after the interaction. In fact, this requirement limits the areal thickness of the target to less than $\rho_{\text{areal}} \approx 10^{20}\text{atoms/cm}^2 \times 1/Z^2$ [61], with Z being the atomic number of the target material. Otherwise, the effect of multiple scattering would be too large. Furthermore, when minimizing the systematic uncertainties in electron scattering experiments, a typical limiting factor are the energy straggling and multiple scattering contributions from scattering off a considerable thick target. These effects can be avoided by using a relatively low-density and window-less gas target, which drastically improves the cleanliness of the experimental environment. Note that a gas target enclosed in a cell represents no alternative, since the interaction of the electron beam with the cell walls or foils would introduce irreducible background contributions. The cluster-jet target is therefore the natural choice to achieve the aspired precision at MAGIX.

At MAGIX, the low-density target is compensated by the high-intensity electron beam of MESA. The anticipated beam current of $I = 10\,\text{mA}$ corresponds to a possible interaction rate of $\dot{N}_{\text{int}} = I/e \approx 6.2 \times 10^{16} s^{-1}$, i.e. the number of beam electrons per second, which can be used to specify the required areal thickness of the MAGIX target. Following the relation $L = \dot{N}_{\text{int}} \cdot \rho_{\text{areal}}$ for the luminosity, the design luminosity of $L \approx 10^{35}\,\text{cm}^{-2}\text{s}^{-1}$ for MAGIX can be achieved with an areal thickness for the MAGIX target of $\rho_{\text{areal}} = 1.6 \times 10^{18}\text{atoms/cm}^2$. With the use of a cluster-jet target, this value is totally achievable if the interaction between the electron beam and the gas jet takes place directly behind the nozzle [60]. Nonetheless, the areal thickness of the MAGIX target should still be tried to be maximized in order to achieve the highest luminosity possible - of course, within the given limit to enable the operation in MESA's ERL mode.

The areal thickness of a cluster-jet target sensitively depends on the temperature and pressure in front of its Laval nozzle, as well as the narrowest inner diameter and the outlet diameter of the nozzle [60]. To maintain a given areal thickness of the gas jet, the volume flow through the nozzle, i.e. the gas flow rate q_{v}, has to be increased if the temperature or the pressure increases. Similarly, the gas flow rate has to be raised if wider nozzle diameters are used. The temperature in front of the nozzle also affects the cluster formation process inside the gas jet - the lower the temperature, the better the cluster-jet. At MAGIX, a well defined cluster-jet is preferred compared to a conventional gas jet, since it is less divergent in the lateral direction and its areal thickness does not decrease as rapidly with the distance from the nozzle. In addition, the gas flow rate at MAGIX should be as small as possible, in order to not mar the vacuum conditions inside the scattering chamber. Both requirements can be met by operating the MAGIX cluster-jet target with the lowest manageable temperature pressure pair that achieves the desired areal target thickness, as well as by using comparably small nozzle diameters. One nozzle design for the MAGIX setup has a narrowest inner diameter of $d^* = 0.5\,\text{mm}$ and an outlet diameter of $d = 1\,\text{mm}$, for which the temperature pressure pair of $T_0 = 40\,\text{K}$ and $p_0 = 1.73\,\text{bar}$ corresponds to a gas flow rate of $q_{\text{v}} = 2400\,\text{L/h}$ and an areal target thickness of $\rho_{\text{areal}} = 5 \times 10^{18}\text{atoms/cm}^2$. Thus, the design luminosity of MAGIX is indeed achievable.

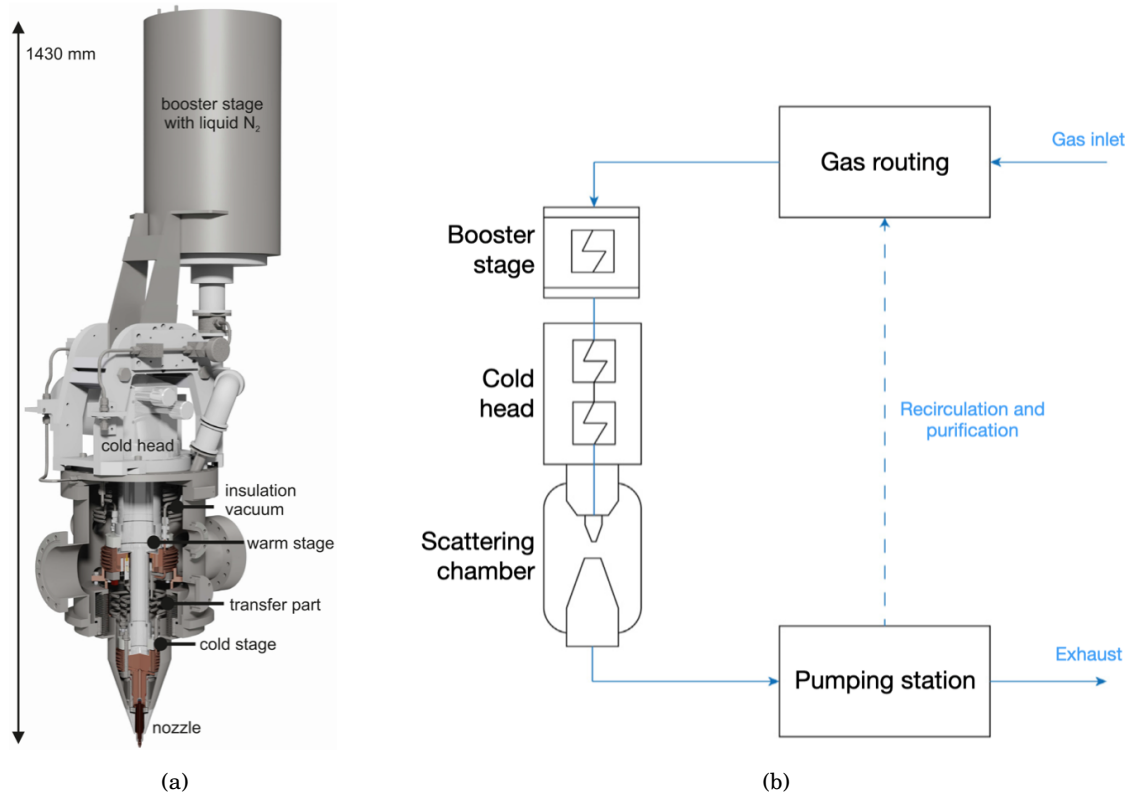

(a) (b)

FIGURE 2.11. CAD model of the MAGIX cluster-jet target developed at the University of Münster (a) and a simplified sketch of the gas flow at MAGIX (b). Figure (a) from [61], figure (b) adapted from [61].

The actual design of the MAGIX cluster-jet target can be seen in Fig. 2.11a. The necessary cooling power is provided by two systems: a booster stage and a two-stage cryogenic cold head. The booster stage can be filled with liquid nitrogen and thereby be used to pre-cool the inserted gas. The gas is then directed through copper pipes around the two stages of the cold head, the warm stage and the cold stage, both of which are surrounded by an insulation vacuum and connected by a transfer part made from stainless steel. The Laval nozzle sits at the lower end of the cold stage. It is assembled to an adaptable extension that enables the adjustment of the nozzle position and allows for a simple exchange of the nozzle. When the gas passes the convergent part of the nozzle, it is compressed and accelerated to supersonic velocities, before it is adiabatically cooled during the expansion in the divergent part. A few mm beneath the nozzle, the gas is then caught by the catcher and pumped away by the connected pumping station. At the time of writing this thesis, it is not possible to reuse the target gas thereafter, but it is planned to extend the system by a recirculation and purification system to enable the use of rare and expensive target gases. A sketch of the gas flow at MAGIX is shown in Fig. 2.11b. [60, 61]

2.3 The MAGIX Scattering Chamber

As seen in Fig. 2.1, the scattering chamber of MAGIX surrounds the interaction point and sits in the middle of the spectrometer setup. It has the cluster-jet target at its center, as well as an array of silicon strip detectors for the detection of heavy charged recoil particles. Furthermore, a veto detector is installed to suppress background contributions from the scattering reactions of beam halo electrons with the target's nozzle and catcher, the so-called beam halo veto.

The scattering chamber has a completely window-less design, i.e. the same vacuum is shared by the scattering chamber, the MESA beam lines, and the MAGIX spectrometers. This is of great benefit to the measurement accuracy, as the first material that a scattered electron encounters is the entrance foil of the MAGIX TPC, see Section 2.5.2, hence minimizing the effects of multiple scattering. On the other hand, it gives rise to several technical challenges. As an example, a sophisticated connection between the scattering chamber and the spectrometers has to be designed, that allows the spectrometer angles to be continuously changed without considerably corrupting the vacuum conditions inside the scattering chamber. For this, a sliding seal connection is foreseen, as it was realized at a number of locations before [63, 64, 65, 66, 67, 68, 69, 70, 71, 72, 73]. Besides, a great deal of effort is required to enable the intended vacuum conditions in the order of 10^{-6} mbar. An overview on the vacuum system of MAGIX can be found in Appendix A.2.

2.3.1 Chamber Design

At the time of writing this thesis, the design of the scattering chamber is not entirely finalized. For this reason, only the design idea and its most important points are outlined here.

The MAGIX scattering chamber will be assembled out of three individual modules [74], as can be seen in Fig. 2.12a. The *interaction module* sits at the top, connecting the inside of the scattering chamber with the MESA beam lines and the MAGIX spectrometers. The cluster-jet target is mounted on the upper side of the module with the target nose protruding through a hole into the chamber. A hexapod will be used as a connecting piece, allowing the target nozzle to be perfectly aligned to the electron beam and the target catcher. In addition, a bellows will be used to ensure a vacuum-tight connection. At the outside of the module, two flanges are used to connect the scattering chamber to the beam lines of MESA. Moreover, two large cutouts are realized for the transition to the spectrometers, which will be covered with the planned sliding seal construction. As an alternative, covers with flanges at discrete angle positions can be used.

The *feed-through module* builds the middle part of the scattering chamber. As its name suggests, this module provides feed-throughs for the signal, power, and control cables of the detector systems mounted inside the chamber. Additionally, the beam halo veto will be mounted to the inner wall of the module.

The last module is the *pump module*. It forms the bottom of the scattering chamber and connects the target catcher to its powerful pumping cascade. In addition, eight turbomolecular pumps are

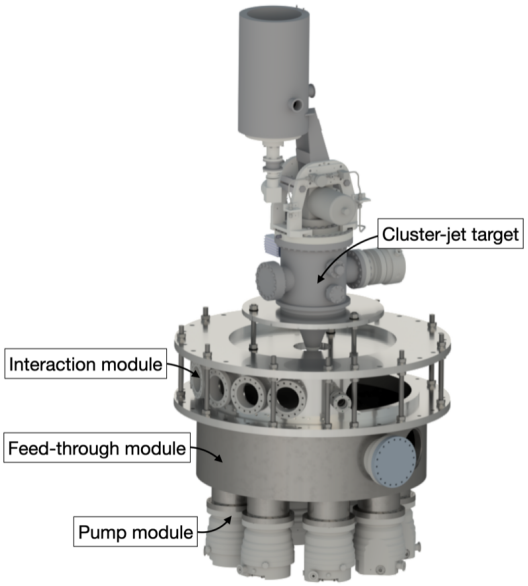

(a)

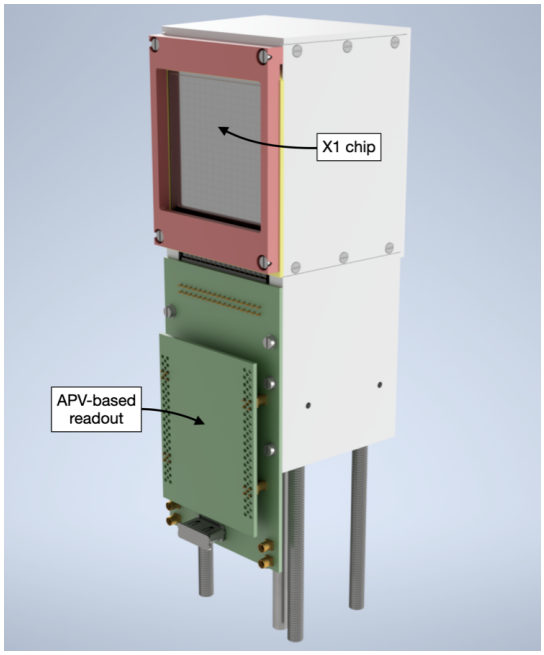

(b)

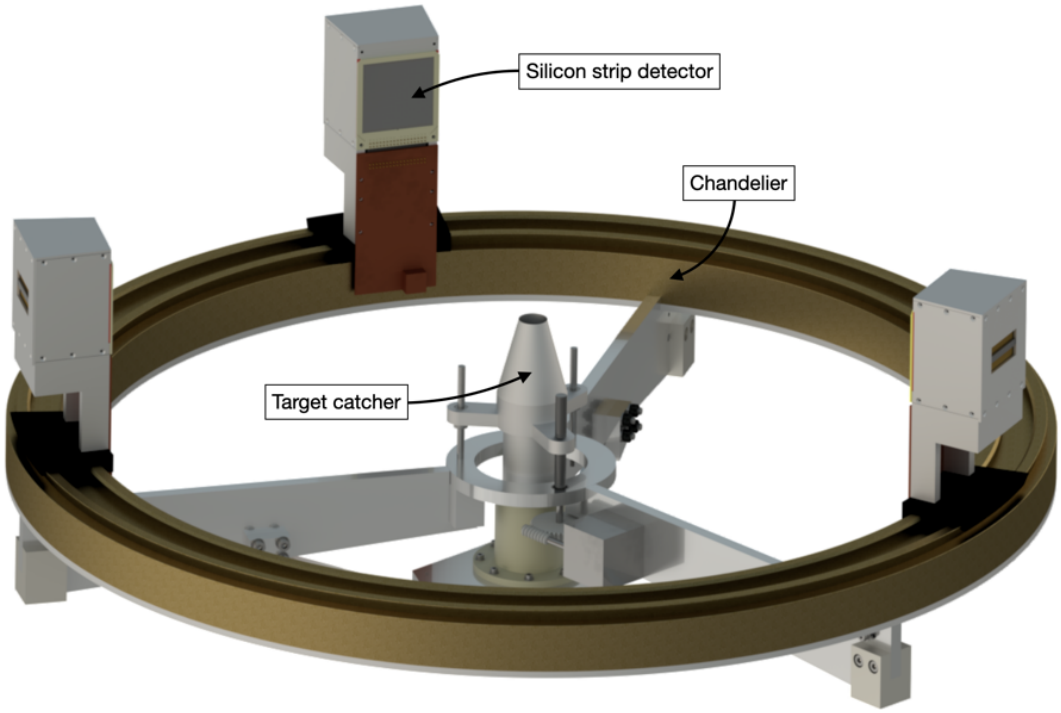

(c)

FIGURE 2.12. The MAGIX scattering chamber (a) and one of the silicon strip detectors (b), an array of which is movably mounted onto the chandelier (c) inside the scattering chamber. Technical designs by S. Aulenbacher, M. Biroth, and J. Geimer.

mounted directly to the bottom side of the module, ensuring that the residual gas pressure inside the scattering chamber is kept at a minimum. Besides, the chandelier, see Section 2.3.2, will be mounted to the module.

2.3.2 Silicon Strip Detectors

For some of the experiments described in Chapter 1, it is essential to measure the recoil particles in coincidence with the scattered electrons. While the electrons are detected in one of the two magnetic spectrometers, an array of silicon strip detectors, see Fig. 2.12b, is placed inside the scattering chamber for detecting the recoil particles. Because of their low kinetic energy, it is imperative that the recoil particles do not pass any material prior to their detection and the only available and accessible location at MAGIX to do so is inside the vacuum of the scattering chamber. The detector array surrounds the interaction point in a distance of approximately 30 cm and is movably mounted onto the so-called chandelier as shown in Fig. 2.12c.

The silicon strip detectors make use of the X1 chip by Micron Semiconductor [75], which provides a total active area of 50 mm × 50 mm divided into 16 silicon strips. If a recoil particle hits the detector area, the energy loss of the recoil particle leads to the creation of electron-hole pairs, which are in the following separated by the voltage difference applied between the cathode, i.e. the silicon strips, and the anode of the detector. The holes then get detected at the cathode, the electrons at the anode. By measuring the charge asymmetry between the two ends of a silicon strip, one of the position coordinates of the hit can be determined. The second coordinate is given by the chip segmentation into strips.

The readout of the silicon strip detectors is based on the APV25-S1 [76, 77], which was developed for the CMS experiment at CERN. The actual signals of the silicon strip detectors come from the strip ends, each of which is connected to its own readout channel, including a preamplifier, an inverter, and a shaper. The charges collected at the anode are used as the trigger signal for the APV.

At the time of writing this thesis, a scintillator telescope extension is being developed that will be directly attached to the rear side of the silicon strip detector. This 50 mm thick plastic scintillator layer will be read out by 16 SiPMs, arranged in a grid of 4×4, and will serve as an electron veto for recoil α-particles, e.g. when measuring the electro-disintegration reaction $^{16}\mathrm{O}(e,e'\alpha)^{12}\mathrm{C}$ as described in Chapter 1. Moreover, the scintillator telescope will help to distinguish between protons and deuterons, which is crucial for some of the other experiments proposed at MAGIX. [78, 79, 80]

2.3.3 Beam Halo Veto

The second detector system placed inside the scattering chamber is the beam halo veto. Beam tests at A1 at MAMI using the cluster-jet target [61] showed that part of the observed background is

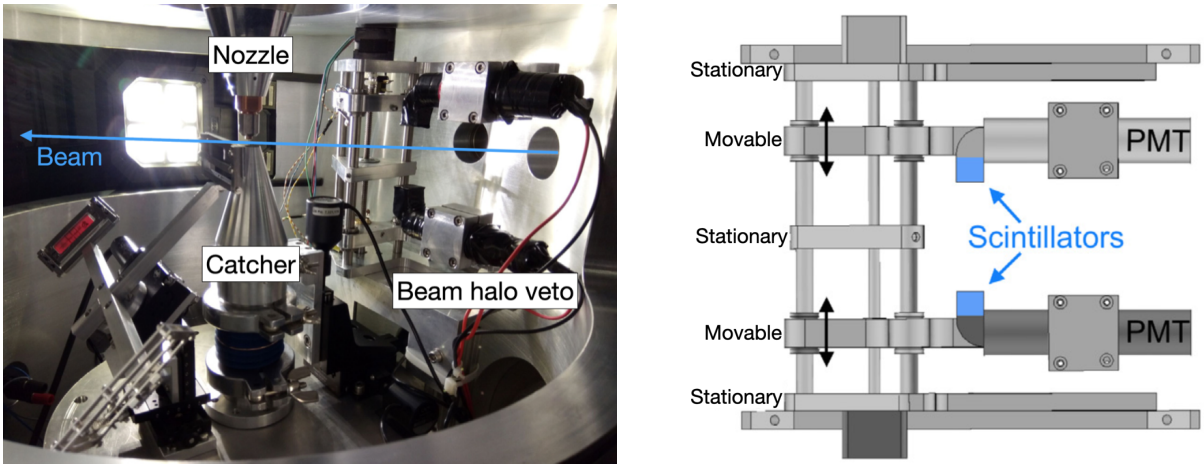

(a) (b)

FIGURE 2.13. The beam halo veto during the beam tests at A1 at MAMI (a) and a sketch of the beam halo veto (b). Figures adapted from [61].

attributable to beam halo electrons scattering off the target's nozzle and catcher. This background contribution will also be present at MESA and, unfortunately, it cannot be avoided. A beam halo inevitably forms following the scattering reactions of beam electrons and residual gas atoms inside the beam line vacuum. What can be done, however, is to counteract the beam halo with a veto detector[16].

The beam halo veto is built from two scintillation detectors, that can be vertically moved into the beam halo as needed. The detector is positioned upstream of the cluster-jet target and is mounted to the inner wall of the scattering chamber, as shown in Fig. 2.13a. It consists of a stationary frame, as well as two movable platforms to which the scintillation detectors are mounted, see Fig. 2.13b. The platforms each run along a spindle, actuated by a stepper motor. The scintillation detectors are made from a cuboidal scintillator, a right-angle prism light guide, and a PMT. [61, 81]

2.4 The MAGIX Spectrometers

The two high-resolution magnetic spectrometers of MAGIX, named STAR and PORT, surround the scattering chamber as shown in Fig. 2.1. They are individually mounted on movable steel platforms running on two ring rails and driven by three-phase motors, and are located on the opposite sides of the MESA beam line. The green spectrometer STAR is placed on the right hand side in the direction of the electron beam, the red spectrometer PORT on the left hand side.[17]

[16] Another option is to use a collimator, which will be done at MAGIX as well [61]. The collimator is built from two vertically movable 13 cm thick tungsten absorbers and is integrated into the beam line of MESA, upstream of the MAGIX target.

[17] This is an allusion to the colors of the navigation buoys when entering a port.

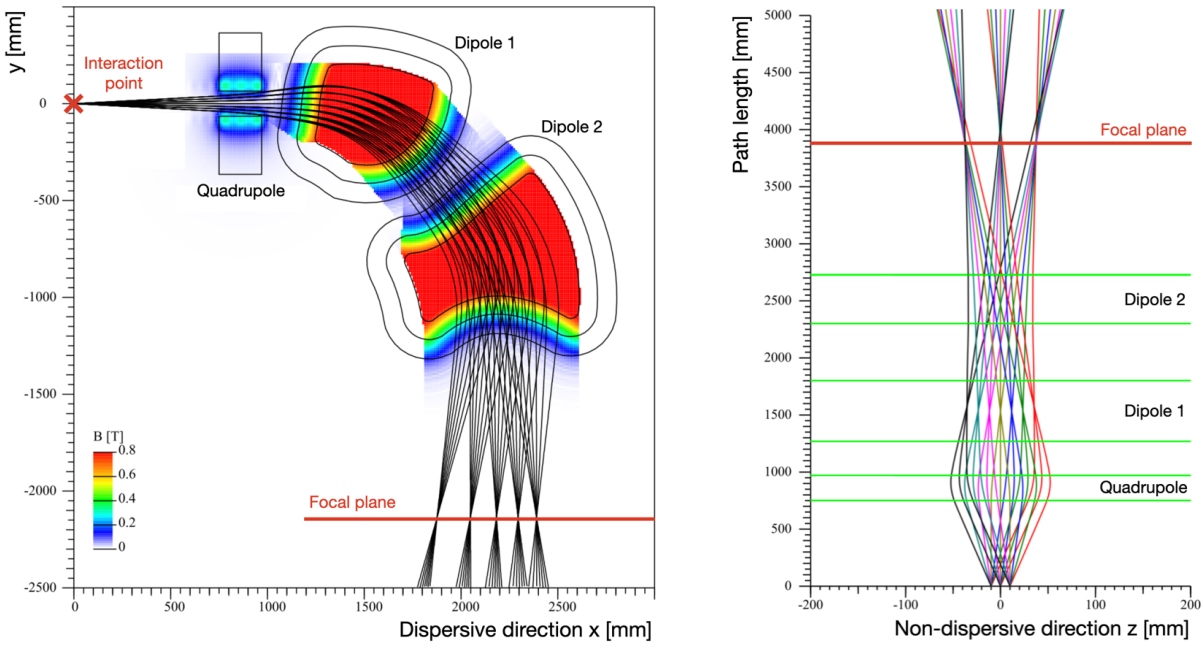

(a) (b)

FIGURE 2.14. The MAGIX spectrometers map the target coordinates onto the focal plane coordinates. In the dispersive direction x, the scattered electrons are sorted according to their momenta $|\vec{p}|$ (a), the coordinate in the non-dispersive direction z is a combination of the target coordinates (b). Figures adapted from [82].

Both spectrometer arms can be independently rotated around the common vertical axis through the interaction point with an accessible angular range for the center planes of the spectrometers from 15° to 165°, where 0° corresponds to the direction of the electron beam, i.e. the forward direction.

The completely window-less design of MAGIX requires the spectrometers to be connected to the scattering chamber in a way that allows for changing the spectrometer angle without considerably breaking the vacuum. To achieve this, the before mentioned sliding seal construction is foreseen. Alternatively, flanges at discrete angle positions can be used. To support the vacuum system of MAGIX, a dedicated pumping section is connected to each spectrometer, cf. Appendix A.2.

The spectrometers are realized in a double-focusing quadrupole-dipole-dipole configuration, employing a common return yoke for both dipoles, and are constructed mirror-symmetrically with respect to their center plane, not identically. This means that the spectrometer setup will be mirror-symmetrical to the MESA beam line. Following the magnetic field lines of the spectrometer optics, the scattered electrons[18] are focused onto a rectangular, horizontal focal plane, where they are mapped according to their target coordinates, see Fig. 2.14. In the so-called *dispersive*

[18]If the polarities of the magnets are switched, positrons can be detected as well. This allows MAGIX the investigation of e.g. the visible decay channel of the dark photon as described in Section 1.3.

direction, the scattered electrons are sorted according to their momenta $|\vec{p}|$, and in the *non-dispersive direction*, the focal plane coordinate is a combination of the target coordinates. More details on the coordinate mapping can be found in the Diploma thesis of J. Müller [83] or the Bachelor's thesis of F. Hówelberend [82]. The coordinate system of the MAGIX spectrometers is chosen in a way, that the x-axis goes along the dispersive direction, the z-axis matches the non-dispersive direction, and the origin lies at the interaction point. The y-axis then results from the requirement of a right-handed coordinate system.

The design parameters of the spectrometers are a central momentum range of $3 - 282\,\mathrm{MeV/c}$ with an acceptance of $\pm 15\,\%$ around the central momentum, a relative momentum resolution of $\Delta p/p < 10^{-4}$, a circular angular acceptance with a 2.5° opening angle, and an angular resolution of $\Delta\theta_e < 0.05°$. The design reference momentum is 200 MeV. The lower limit of the central momentum range results from the power supply units that are used for the spectrometer magnets and the upper limit is due to saturation effects inside the magnet iron. The resolutions are based on the precision requirements for MAGIX as described in the introduction to this chapter, where the energy resolution translates to the momentum resolution by neglecting the mass of the electron. To fulfill these challenging design goals, a precise knowledge of the spectrometer optics is essential, so that the mapping from target coordinates to focal plane coordinates, and vice versa, can be modeled as accurately as possible. Moreover, the focal plane detectors, see Section 2.5, must allow the reconstruction of the focal plane coordinate (x, z) and the corresponding particle track with a spatial resolution of 100 µm or better [84], as well as an angular resolution of a few mrad. And of course, the resolution of the motors, that move the spectrometer arms along the two ring rails, has to enable the aspired angular resolution as well. [18, 85, 82, 83]

2.5 The MAGIX Focal Plane Detectors

As shown in Fig. 2.1, the focal planes of the MAGIX spectrometers are each equipped with dedicated tracking, trigger, and veto detectors. In combination, the detector systems are responsible for the detection and the identification of incoming particles, which include the scattered particles coming from the interaction point, but also unwanted background contributions from e.g. cosmogenic muons or beam-induced neutrons. In order to reduce the effects of those contributions, each spectrometer arm includes a shielding house, inside of which the individual detectors are mounted, and which also serves as the mechanical connection piece between the spectrometer and the movable steel platform. The focal plane detectors of the two spectrometer arms are, just like the spectrometers, built mirror-symmetrically with respect to their center plane, not identically, to provide a mirror-symmetrical setup with respect to the MESA beam lines. The tracking detectors are built in the form of an open field cage time projection chamber, the MAGIX TPC, and the trigger and veto detectors are, per spectrometer arm, integrated into one combined setup, the MAGIX trigger veto system.

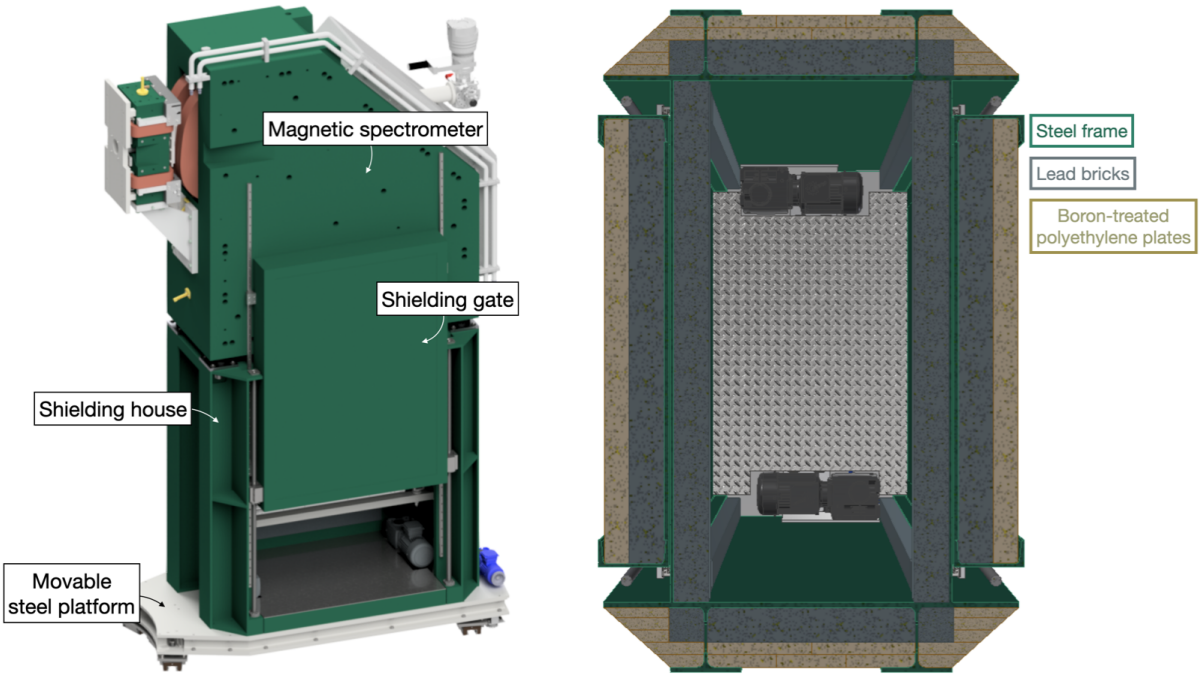

(a) (b)

FIGURE 2.15. The two spectrometer arms of MAGIX both include a shielding house, that mechanically connects the spectrometer and the movable steel platform (a). The frame of the shielding house is filled with lead bricks, as well as boron-treated polyethylene plates (b), protecting the focal plane detectors on the inside from electromagnetic radiation and neutrons, respectively.

2.5.1 Shielding Houses

Fig. 2.15a exemplarily shows the spectrometer arm of the magnetic spectrometer STAR. The spectrometer is mounted on top of a shielding house, mechanically connecting it to the movable steel platform. The frame of the shielding house is manufactured as a welded steel construction, comprising two vertically movable shielding gates for providing access to the focal plane detectors on the inside. The steel frame is filled, see Fig. 2.15b, with a 100 mm thick lead shielding against electromagnetic radiation, built from individual lead bricks made from the antimonial lead alloy PbSb4, as well as a 70 mm thick neutron shielding, composed of boron-treated polyethylene plates with a boron content of 5 % by weight. In the final assembly, the exterior of the steel frame will be clad with additional cover sheets.

2.5.2 The MAGIX TPC

Enclosing the horizontal focal plane of the spectrometer optics, the MAGIX TPC is responsible for the track reconstruction of the incoming particles. It is built in form of a time projection chamber and designed to achieve a spatial resolution of 100 µm or better, allowing for the

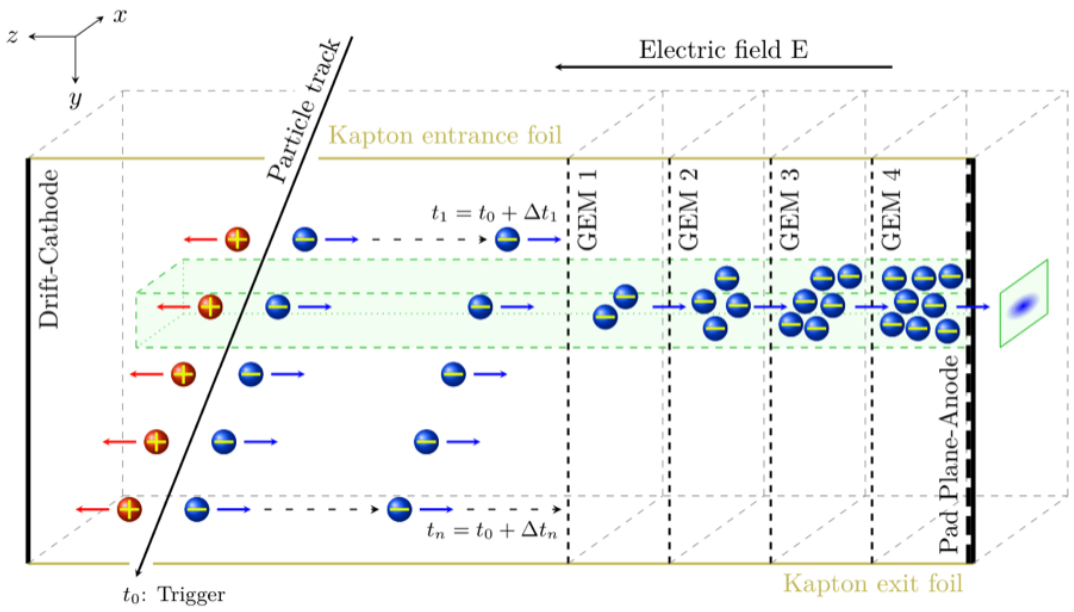

FIGURE 2.16. The working principle of the MAGIX TPC. An incoming charged particle causes an ionization trace and the generated electrons and ions drift towards the anode and cathode, respectively. The electrons pass an amplification stage made of four GEMs, before they leave clustered signals on the pad plane of the anode at times $t_i = t_0 + \Delta t_i$, where t_0 is the trigger time of the particle track and Δt_i is the drift time of the individual electron. The positions of the weighted centers of the clusters represent the projected x- and y-coordinates of the ionization trace, whereas the drift times correspond to the z-coordinates. The particle track can therefore be fully reconstructed. The path of an individual electron-ion pair is illustrated as the green block. Figure adapted from [7].

aspired momentum and angular resolutions of the MAGIX spectrometers, cf. Section 2.4. For this, particular attention must be paid to the reduction of material in between the spectrometer vacuum and the TPC's sensitive volume, so that the effects of multiple scattering are minimized. The MAGIX TPC is therefore directly mounted to the lower spectrometer flange, see Fig. 2.18, and a novel open field cage concept is utilized, reducing the introduced material budget to a minimum. In the following, the most important design aspects of the MAGIX TPC are described. For further details on how a TPC works and what needs to be considered when building one, please refer to the Master's theses of D. Markus [86] or J. Rausch [87].

Fig. 2.16 shows the working principle of the MAGIX TPC in the coordinate system of the MAGIX spectrometers. A charged particle enters the sensitive gas volume of the TPC and causes an ionization trace. If the particle originates from the interaction point, it comes in from the y-direction through the 75 µm thick Kapton entrance foil - which is the first and foremost material it encounters in the window-less design of MAGIX, and also the only one between the vacuum system of MAGIX and the sensitive TPC volume - and leaves through the 125 µm thick Kapton

exit foil towards the MAGIX trigger veto system. The electric field along the z-direction separates the electron-ion pairs of the ionization trace and the electrons and ions drift towards the anode and cathode, respectively. Since the primary ionisation inside a TPC is usually too low to yield signals that are distinguishable from electronic noise [87], the electrons are amplified by a cascade of four Gas Electron Multiplier (GEM) foils, before they yield clustered signals on the pad plane of the anode, which is oriented parallel to the xy-plane. The timestamp of an individual electron signal, $t_i = t_0 + \Delta t_i$, where t_0 is the trigger time of the particle track (given by the trigger veto system) and Δt_i is the electron's drift time[19], corresponds to the z-position of the point, where the initial electron-ion pair has been generated - provided, that the drift velocity inside the TPC gas is known. The projected positions in x and y, on the other hand, can be extracted as the weighted center of the cluster on the pad plane. Thus, by merging all the electron signals of the ionization trace, a complete 3D reconstruction of the particle track is possible.

Compared to other TPCs, the MAGIX TPC has a rather small gas volume, which helps reducing space-charge effects and improves the overall spatial resolution [88]. Its dimensions in x and y are 782.0 mm and 213.7 mm, respectively. The sensitive drift volume, which goes from the cathode to the surface of the first GEM foil, has a width of 177.3 mm along the z-direction and hence a volume of 29.6 L results. The total gas volume is roughly 31.0 L with a distance of 185.5 mm between cathode and anode. The active areas of the cathode, the GEM foils, and the anode are each 768 mm × 192 mm in x and y. The largest possible area in x and z that is traversable for incoming particles is 782.0 mm × 140.3 mm.

As seen in Section 2.4, the spatial resolution in x (dispersive direction) directly impacts the momentum resolution of the MAGIX spectrometers. Besides, both the spatial resolution in x and the spatial resolution in z (non-dispersive direction) contribute to the overall reconstruction of the target coordinates and therefore influence the angular resolution of the MAGIX spectrometers. Whereas the resolution in z is determined by the time resolutions of the trigger time and the drift time of the electrons, the resolution in x depends on the anode pad size along the x-direction and the accuracy of the cluster weighting. With the exception of the trigger time resolution, which is specified by the MAGIX trigger veto system, all these parameters are determined by the design decisions for the MAGIX TPC. These will be discussed in the following paragraphs.

Gas Composition A TPC gas is usually composed of two components, a *counting gas* and a *quenching gas*[20]. The counting gas is responsible for the ionization trace if a charged particle passes through the sensitive volume, but not the entire energy loss of the particle is used for the generation of electron-ion pairs. Instead, a percentage of the counting gas atoms is only excited, followed by relaxation under the emission of photons. Some of these photons can have enough energy to excite or even ionize further counting gas atoms. To prevent an avalanche effect

[19] The later measured timestamp t_i also includes the time required to pass the whole signal processing chain from the amplification onwards in the form of a constant offset that can be corrected for.

[20] It is also possible that the two components are mixtures of several gases.

	Lower field limit	**Upper field limit**
Electric field strength [V/cm]	220	800
Drift velocity v_{drift} [m/μs]	0.016	0.051
Transversal diffusion [μm/$\sqrt{\text{cm}}$]	220	330
Longitudinal diffusion [μm/$\sqrt{\text{cm}}$]	255	180

TABLE 2.1. The two limits of the operating range of the MAGIX TPC. The optimal working point lies at the lower limit, where the drift velocity and the transversal diffusion parameter are both at their minimum.

and thus delayed signals elsewhere, the quenching gas is deployed. It absorbs the high-energy photons and re-emits their energy through nonradiative processes. For the MAGIX TPC, a gas mixture of 90 % argon and 10 % carbon dioxide is used, where Ar acts as the counting gas and CO_2 as the quenching gas.

Electric Drift Field Strength The electric field strength applied along the drift volume, together with the choice of the TPC gas mixture, sensitively influences the drift behavior of the electrons, which is parameterized by the drift velocity, as well as the longitudinal and transversal diffusion parameters. When the electrons are accelerated by the electric field in the direction of the anode, their movement does not follow a straight line, but rather a kind of statistic trembling motion around the direct path towards the anode, called diffusion. Therefore, electrons generated at a distance z from the anode will not raise signals after the exact same drift time. Instead, their drift times will cause a distribution, that can also be interpreted as a drift velocity distribution, if the distance z is taken as the constant drift length of the electrons. The mean value of this distribution is called the *drift velocity* and the width of the distribution corresponds to the *longitudinal diffusion* parameter. Moreover, the diffusion also causes a deviation of the x and y coordinates of an electron hit on the first GEM foil from those of the electron-ion pair creation, which is a measure for the *transversal diffusion* parameter.

Fig. 2.17 shows these three gas transport properties for the Ar/CO_2 (90 %/10 %) mixture used at MAGIX in dependence of the electric field strength E applied inside the sensitive drift volume. The operating range for the MAGIX TPC is shown as the two green dashed lines and goes approximately from the minimum of the transversal diffusion at an electric field strength of $220\,\text{V}\,\text{cm}^{-1}$ to the maximum of the drift velocity at $800\,\text{V}\,\text{cm}^{-1}$. Below this range, the effects of electron attachment get too large, i.e. too many drift electrons are lost due to recombination or accumulation near the gas atoms. Above this range, the contributions from flashovers grow too significant and the MAGIX TPC approaches the limit of its readout electronics. Besides, a technical limit of $1000\,\text{V}\,\text{cm}^{-1}$, shown as the grey dashed line, is set by the utilized power supplies.

The drift velocity and the transversal diffusion parameter loosely translate into limits to the spatial resolutions along z and x, respectively. The lower the drift velocity, the better the relative

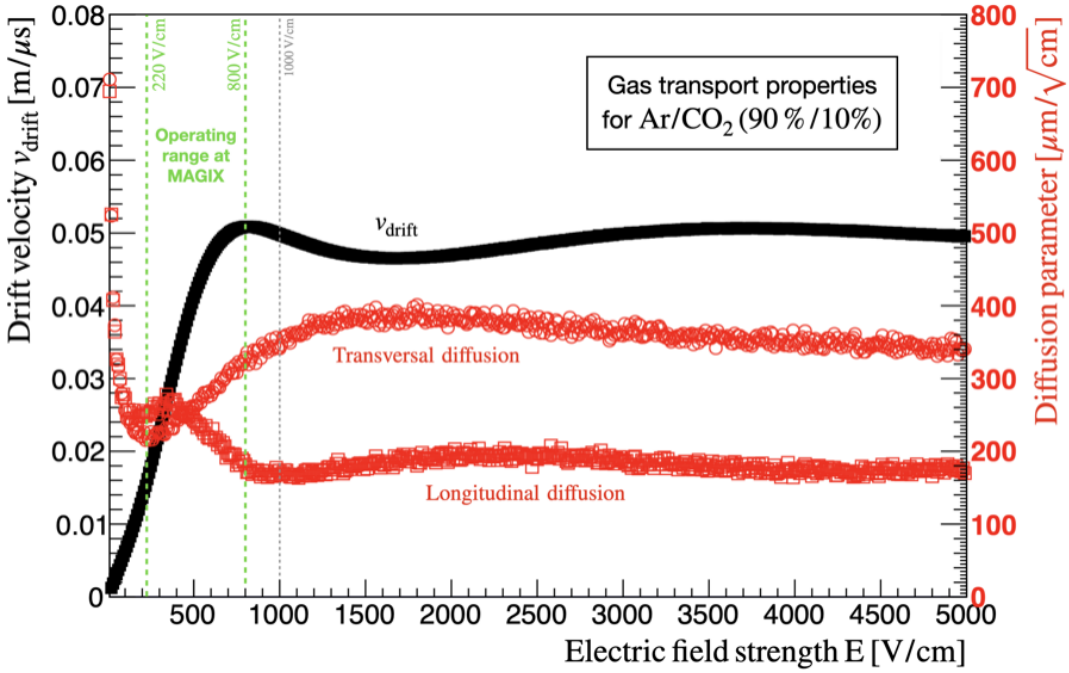

FIGURE 2.17. The gas transport properties of the MAGIX TPC in dependence of the electric field strength applied along the drift volume. The operating range of the MAGIX TPC goes from the minimum of the transversal diffusion parameter to the maximum of the drift velocity and is marked by the two green dashed lines. Figure adapted from [88].

drift time resolution and therefore the spatial resolution along the non-dispersive z-direction.[21] The lower the transversal diffusion parameter, the better the spatial resolution along x and y, and therefore in particular along the dispersive x-direction. Considering these parameters, the optimal working point for the MAGIX TPC therefore lies at the lower end of the operating range, i.e. at 220 $\mathrm{V\,cm^{-1}}$, where the drift velocity and the transversal diffusion parameter both are at their minimum within the feasible range. However, the operation of the MAGIX TPC will start at the higher limit of the operating range, i.e. at 800 $\mathrm{V\,cm^{-1}}$, where the drift velocity has its maximum. Here, the operation of the TPC is the most stable, since the drift velocity stays more or less constant if the electric field strength slightly deviates from its set point. The optimal operating point can then be approached over time. The corresponding values of the gas transport properties for the two limits of the operating range are listed in Tab. 2.1. [88]

Homogeneity of the Electric Field To ensure that the electric field along the sensitive drift volume is as homogeneous as possible, the MAGIX TPC requires a surrounding field cage, which would typically be constructed using a set of strips or wires that surround the sensitive volume

[21] The longitudinal diffusion parameter also influences the drift time resolution and thus the spatial resolution along z. However, as its effect is lower than that of the drift velocity, it is rather unimportant for the MAGIX TPC [88].

from all sides. But given the criteria to minimize the material budget in between the spectrometer vacuum and the sensitive TPC volume, such field cage design is not viable. Instead, the MAGIX TPC is realized with a novel open field cage, that only surrounds the sensitive volume from three sides, leaving open the face towards the spectrometer. The field shaping elements of the open field cage are extended well into the spectrometer vacuum, in order to mitigate the effects of static field distortions that are inevitably introduced by this design. The orientation and the mounting of this field cage extension can be seen in Fig. 2.18. For more details on the open field cage concept, please refer to the paper of Caiazza *et al.* [84].

Nevertheless, the MAGIX TPC is susceptible to field distortions. Both static distortions due to remaining field inhomogeneities and dynamic distortions based on space-charge effects must be taken into account and should be counteracted. For this reason, a dedicated calibration system has been developed [89], called Starry Night, that can be used both dynamically, in parallel to a running measurement, and statically, i.e. in between data taking periods. It allows for the scanning of the electric field by releasing electrons at fixed, known positions and measuring their drift times and deflections. 814 UVC-LEDs are used to create photoelectrons in a grid-like pattern on the aluminum-coated fused silica behind the cathode. The coating has a thickness of 11 nm and almost entirely oxidizes to Al_2O_3 [90]. The wavelength of the UVC-LEDs is 255 nm and is chosen such that photoelectrons are only released from the aluminum oxide layer and not from the surrounding other materials, like copper or Kapton. [90]

Amplification Stage The amplification stage of the MAGIX TPC is built from four GEM foils, which are stacked one behind the other and aligned parallel to the anode, see Fig. 2.16. A GEM foil consists of an insulating layer that is coated with a conducting layer on each side, equipped with a dense and regular hole pattern. If a high potential difference is applied to the two conducting layers, a high electric field is generated inside the holes that can be used to accelerate impinging drift electrons, which in turn ionize secondary electrons and therefore cause a charge amplification. By stacking multiple GEMs behind each other, competitive gain values of 10^5 and higher can be achieved.

The GEMs used for the MAGIX TPC are made from a 50 µm Kapton foil, coated with a 5 µm copper layer on each side and equipped with holes of 50 µm diameter[22]. By using a cascade of four of these GEMs, an amplification of 10^5 is achieved. The distance between the holes is 280 µm for the two outer GEMs of the cascade and 140 µm for the two inner ones. A summary of the voltages applied to the four GEMs, the resulting electric fields inside the holes, as well as the distances between the GEMs, is given in Tab. 2.2.

The amplification by the four GEM foils contributes to the spatial resolution along the dispersive x-direction. The charge amplification consecutively turns a single drift electron into an ever larger electron avalanche that is measured as the clustered signal on the anode's pad plane. The size of

[22] In fact, the holes are biconical, 50 µm at the center plane of a GEM foil and 70 µm at the surfaces.

	GEM 1	**GEM 2**	**GEM 3**	**GEM 4**
Potential towards cathode [V]	3950	2880	2230	1940
Potential towards anode [V]	3680	2630	1960	1600
Potential difference [V]	320	310	300	300
Thickness [cm]	0.005	0.005	0.005	0.005
Electric field strength [V/cm]	64000	62000	60000	60000
Distance to next GEM or anode [cm]	0.2	0.2	0.2	0.4

TABLE 2.2. The applied potentials at the surfaces of the four GEM foils of the MAGIX TPC and the resulting electric field strengths inside the GEM holes. "GEM 1" is the most inner foil, i.e. the foil towards the cathode, "GEM 4" the most outer one, i.e. the foil closest to the anode. The potentials are given with respect to the anode's potential at 0 V. [88]

the cluster is defined by the gain of the amplification stage, as well as the transversal diffusion in between the individual GEM foils, and the larger the cluster, the more accurate the extraction of the projected x- and y-coordinates by the cluster weighting. In contrast to the situation inside the drift volume of the TPC, a large transversal diffusion is therefore helpful at this point. [88]

Pad Plane Readout The active area of the anode is segmented into 9216 gold-coated copper pads of size 2 mm × 8 mm in x and y, respectively, arranged in 384 columns and 24 rows. Each pad is connected to a signal processing chain composed of an inverting preamplifier, a shaper, an ADC[23], and a discriminator, corresponding to one readout channel. The channels are read out using the VMM[24] Hybrid 3a, developed at the Brookhaven National Laboratory [91] and advanced by the RD51 working group [92]. Each VMM provides 128 readout channels, thus 72 VMMs are needed for the readout of one complete MAGIX TPC. The signals from eight VMMs are routed onto a hybrid board, which combines a DVMM[25] board and a FEC[26] card. The DVMM was developed in combination with the VMMs and is responsible for their data collection. The FEC synchronizes the eight connected VMMs and is connected via Ethernet to a DAQ computer. More details on the readout of the MAGIX TPC can be found in the Master's thesis of D. Markus [86].

The spatial resolution along the dispersive x-direction is directly influenced by the pad size of the anode. The size of 2 mm along x provides a kind of "coarse resolution", which can be improved by weighting the responsive pads of a cluster with the collected charges per pad. By this, the weighted center of the cluster can be calculated, that gives the projected x- and y-coordinates of the initially generated electron-ion pair. [88]

[23] **A**nalog to **D**igital **C**onverter
[24] **V**innie **M**icro **M**egagas
[25] **D**igital **VMM**
[26] **F**ront-**E**nd **C**oncentrator

FIGURE 2.18. The positioning and mounting of the MAGIX focal plane detectors inside the shielding house. The spectrometer adapter flange is used to mount the field cage extension of the MAGIX TPC to the lower spectrometer flange. The trigger layer is directly attached to the lower flange of the TPC frame and the veto system is assembled to the shielding house walls using a cradle made of steel beams. Space for power supplies and readout electronics is available below the detector systems.

2.5.3 The MAGIX Trigger Veto System

Placed directly below the Kapton exit foil of the MAGIX TPC, each spectrometer arm houses a trigger veto system, see Fig. 2.18, combining the tasks of triggering and vetoing in one integrated setup. It consists of a dedicated trigger layer made of plastic scintillation detectors, as well as a modular veto system composed of veto layers, also made of plastic scintillation detectors, and lead absorber layers. The trigger layer provides the fast timing and energy loss measurements, that are required for the proposed physics program discussed in Chapter 1, and is responsible for starting the data acquisition. Moreover, it gives the basic hit and position information for a triggered readout of the MAGIX TPC. The veto system, on the other hand, is responsible for the separation of signal from background events. Dependent on the response pattern of the veto layers, an event can be classified accordingly. Since the MAGIX trigger veto system is the central topic of this thesis, all the details on its design and development are presented in the coming chapters.

2.6 The MAGIX Slow Control System

The setup of MAGIX entails manydifferent parameters, such as voltages, pressures, or flow rates, all of which have to be monitored, controlled, and recorded. The data rate and the amount of data for these kind of control parameters, that normally stay more or less constant during a measurement, are typically considerably lower than for the readout of particle detector systems. Therefore, two important readout domains are usually distinguished: *data acquisition* (DAQ) and *slow control*. The DAQ is responsible for reading out all the detector systems and its data rate can easily reach the kHz to MHz regions. The slow control, on the other hand, covers the readout of the above mentioned control parameters and its data rate reaches only a few Hz at maximum. This "slow" readout of the control parameters also implicates that the amount of slow control data is several orders of magnitude lower than the amount of DAQ data.

At MAGIX, the slow control of all involved components is integrated into one common software stack, the MAGIX Slow Control System `MXSlowControl`. It is based on the *Experimental Physics and Industrial Control System* (EPICS) and its first version has been developed as part of the PhD thesis of S. Lunkenheimer [7]. Before that, however, the decision had to be made whether a custom-made or an already existing slow control system should serve as a basis. The advantages of an already existing one, such as documentation or long-term support, are obvious, and a feasibility study of an EPICS-based slow control system [93] showed that EPICS meets all the requirements for the application at MAGIX. Another driver towards this decision has been the fact that MESA and P2 use an EPICS-based slow control system as well. Overall important parameters, such as vacuum conditions or beam quality, can therefore be accessed by all parties involved.

EPICS is supported by a large international collaboration and therefore widely used and well

documented. Its architecture is decentralized, meaning that the servers and clients run independently from each other and communicate via a shared network. The idea is that each server or client runs an *Input-Output-Controller* (IOC), the main program of EPICS, that communicates with the network using the protocol *Channel Access* (CA). In the case of a server, the IOC also communicates with the connected devices and provides all control parameters to the network in the form of so-called EPICS *process variables* (PVs). A client, in contrast, is not connected to any devices, but has access to all EPICS PVs via the network. Of course, a network participant can be both server and client.

The behaviour of an IOC is specified inside an individual command file, where, among other things, the device drivers of the connected devices can be modularly loaded as needed. The slow control system can thus be easily expanded or updated. An example for a device driver, that has been written for the MAGIX trigger layer as part of this thesis, is given in Appendix C.2. For more details on EPICS or `MXSlowControl`, please refer to the EPICS documentation [94, 95, 96] or the PhD thesis of S. Lunkenheimer [7].

Part II

A Trigger Veto System for MAGIX

CHAPTER 3

THE CONCEPT OF THE MAGIX TRIGGER VETO SYSTEM

The MAGIX trigger veto system combines four tasks that are crucial for the success of the electron scattering experiments planned at MAGIX. First, it delivers a fast and reliable trigger decision signal that is used to start the data DAQ and which in addition defines the inter-detector timing of the overall experiment. Furthermore, the trigger signal provides the timing reference for the MAGIX TPC, or in other words, the anchor point for the track reconstruction. Beyond that, the trigger veto system is responsible for separating signal from background events by raising particular response patterns for the different incoming particles.

These four tasks are accomplished by combining two detector systems into one integrated setup: A dedicated trigger layer, as well as a veto system composed of three veto and several lead absorber layers. During the course of this chapter, it is shown how the MAGIX trigger veto system is conceptually designed and what requirements and constraints have led to the decisions involved.

3.1 The Need for a Veto System

As seen in Chapter 2, MAGIX enjoys a very clean experimental environment due to its completely window-less design and the comparably low density of its gas jet target. Moreover, the low beam energy of MESA drastically reduces the background sources that MAGIX will face compared to high-energy electron scattering experiments. The low MESA beam energy of 20 MeV to 105 MeV lies below the pion production threshold, thus drastically restricting the possible interaction channels of the beam electrons.In addition, the MAGIX focal plane detectors are placed inside the shielding houses beneath the spectrometers, see Section 2.5.1, reducing the effects of possible background sources even further.

Nonetheless, two relevant background sources remain that will be present at MAGIX: The portion

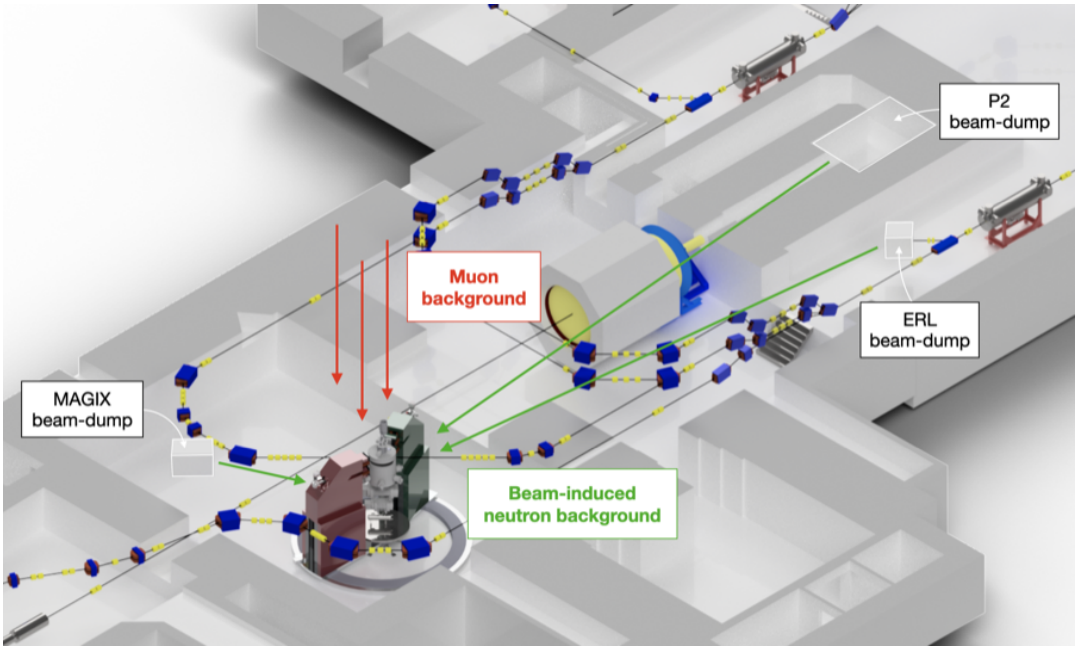

FIGURE 3.1. The background sources present at MAGIX: Cosmogenic muons, as well as beam-induced neutrons originating from the three beam-dumps that are located inside the MESA halls.

of cosmogenic muons that are not stopped inside the concrete ceiling of the MESA halls, the above soil, or the shielding house walls or magnet yokes, as well as beam-induced background particles, of which neutrons are the ones that will directly influence the MAGIX focal plane detectors due to their penetrating nature[1]. Fig. 3.1 illustrates this circumstance, where the muon and neutron backgrounds are depicted in red and green, respectively. Also shown are the three beam-dumps located inside the MESA halls, which are the main origin of the beam-induced neutron background[2]: the P2 beam-dump, the ERL beam-dump, and the MAGIX beam-dump.

In the P2 beam-dump, the MESA beam is dumped after interacting with the P2 target. As described in Chapter 2, this does not happen simultaneously to data taking at MAGIX[3], since the MESA beam can only be delivered to one experiment at a time. Therefore, the naive thought would be that the P2 beam-dump is unproblematic for MAGIX. Nevertheless, the P2 beam-dump will need time to deactivate after a measurement period, and dependent on the MESA beam time schedule, MAGIX may be affected by this to a certain extent.

In the ERL mode of MESA, only the energy gained inside the SRF cavities can be restored from

[1]The beam-induced background particles also include e.g. scattered electrons, produced photons, or recoil nuclei. However, those particles that do not originate from the interaction point are effectively blocked by the 100 mm lead shielding of the shielding houses.

[2]Provided the MESA beam does not mistakenly hit parts of the beam optics devices or so.

[3]The exception to this are background and calibration measurements at MAGIX, where no MESA beam is needed. These could generally be performed in parallel with data collection at P2.

the beam electrons, which means that after the deceleration process, the electrons will still have the 5 MeV gained in the pre-accelerator MAMBO. For dumping these electrons, the ERL beam-dump is installed. However, due to its positioning and the low energy of the electrons, the effects on MAGIX are expected to be negligible.

The most problematic source for beam-induced neutron background will probably be the MAGIX beam-dump. If MAGIX is operated in MESA's EB mode, which will be the case especially during the commissioning phase of MESA, it will be used to dump the beam electrons after their interaction with the MAGIX target. Additionally, it would be used for a potential future storage ring upgrade of MESA [44]. At the time of writing this thesis, it is not totally clear what impact the beam-dump will have on the background situation at MAGIX, although it has been simulated to a certain extent [50]. But of the three beam-dumps, the MAGIX beam-dump will definitely contribute the most.

To address the above mentioned background sources, it is of utmost importance that MAGIX comprises an additional veto system per spectrometer, which is capable of distinguishing between signal electrons or positrons, background muons, and background neutrons[4].

3.2 The Working Principle of the Trigger Veto System

In addition to a dedicated veto system, MAGIX requires a trigger system per spectrometer that is responsible for starting the DAQ and whose timing characteristics define the time resolution of the overall experiment. At a very early stage, the idea came up to combine these two detector systems into one setup, which is now the MAGIX trigger veto system.

Together with the MAGIX TPC, the trigger veto system makes up the focal plane detectors that provide the necessary information for investigating the electron scattering interactions occurring inside the scattering chamber. Since the magneto-optics of the MAGIX spectrometers focus the scattered electrons onto a horizontal focal plane, the trigger veto system is built in form of a sandwich detector composed of individual horizontally placed layers. It consists of one segmented trigger layer at the top, followed by a flexible veto system of three segmented veto layers and several lead absorber layers directly underneath it, where the first veto layer should be placed at the uppermost position of the veto system, so that it can function as a second trigger layer as well. While the trigger layer is segmented along the dispersive direction of the spectrometer, the veto layers are segmented along the non-dispersive direction, improving the overall rate capability and spatial resolution of the system. A conceptual drawing of the trigger veto system is shown in Fig. 3.2.

The trigger layer provides the rapid and reliable signals, which, after digitization, are used to trigger the DAQ, but also provide the option of analog energy loss measurements. Its timing

[4]The shielding houses also include a layer of 70 mm boron-treated polyethylene to support the protection from penetrating neutrons.

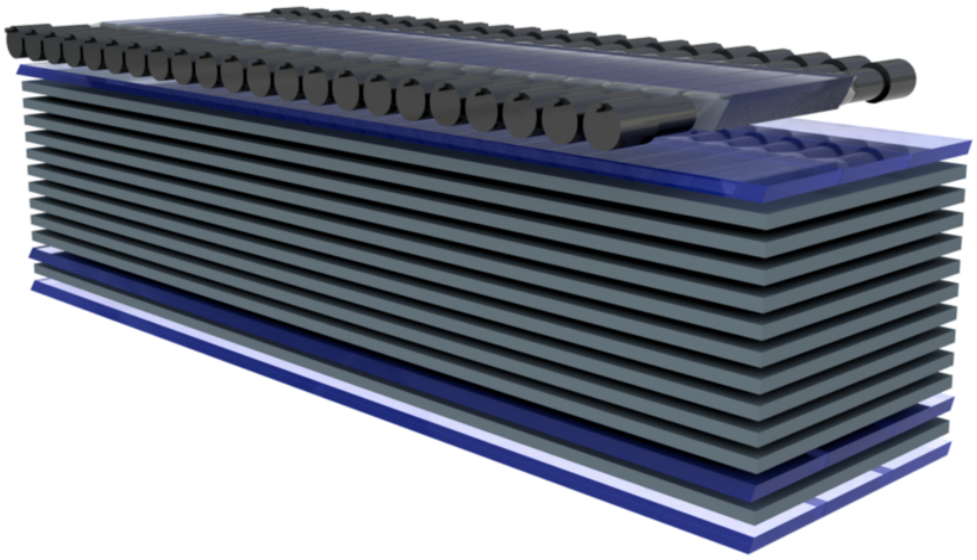

FIGURE 3.2. Conceptual CAD model of the trigger veto system. It is built as a sandwich detector composed of individual horizontally placed layers. The trigger layer sits at the top and the veto system is placed directly underneath it.

properties define the time resolution of a single-spectrometer event, as well as the coincidence time resolution of an event also including signals in the trigger layer of the second spectrometer or in an additional detector system like the silicon strip detectors inside the scattering chamber. Furthermore, it gives the basic hit and position information for a triggered readout of the TPC, or in other words, the anchor point for the TPC track reconstruction. In order to perform these tasks in the best possible and most reliable way, the following criteria have been set for the trigger layer: A detection efficiency very close to 100 %, an intrinsic timing resolution goal enough to achieve a coincidence time resolution of ≤ 1 ns, a trigger rate tolerance up into the MHz region, an almost dead time free readout, as well as long-term stability.

The veto system, on the other hand, is responsible for the separation of signal and background events. As discussed in Section 3.1, the two troublesome background sources present at MAGIX are cosmogenic muons and beam-induced neutrons. Due to the orientation of the MAGIX spectrometers, the muons travel in similar directions as the scattered electrons inside the trigger veto system, which is why the lead absorber layers are used. Electrons and electron-initiated electromagnetic showers are stopped inside the lead absorber layers, while the penetrating muons are detected by the veto layers afterwards. The beam-induced neutrons are counteracted by coincidence conditions between the different detector layers. Thus, the different incoming particles each raise individual response patterns inside the trigger veto system, which is illustrated in Fig. 3.3. The electrons raise signals in the trigger layer T and the first veto layer V1 and are then

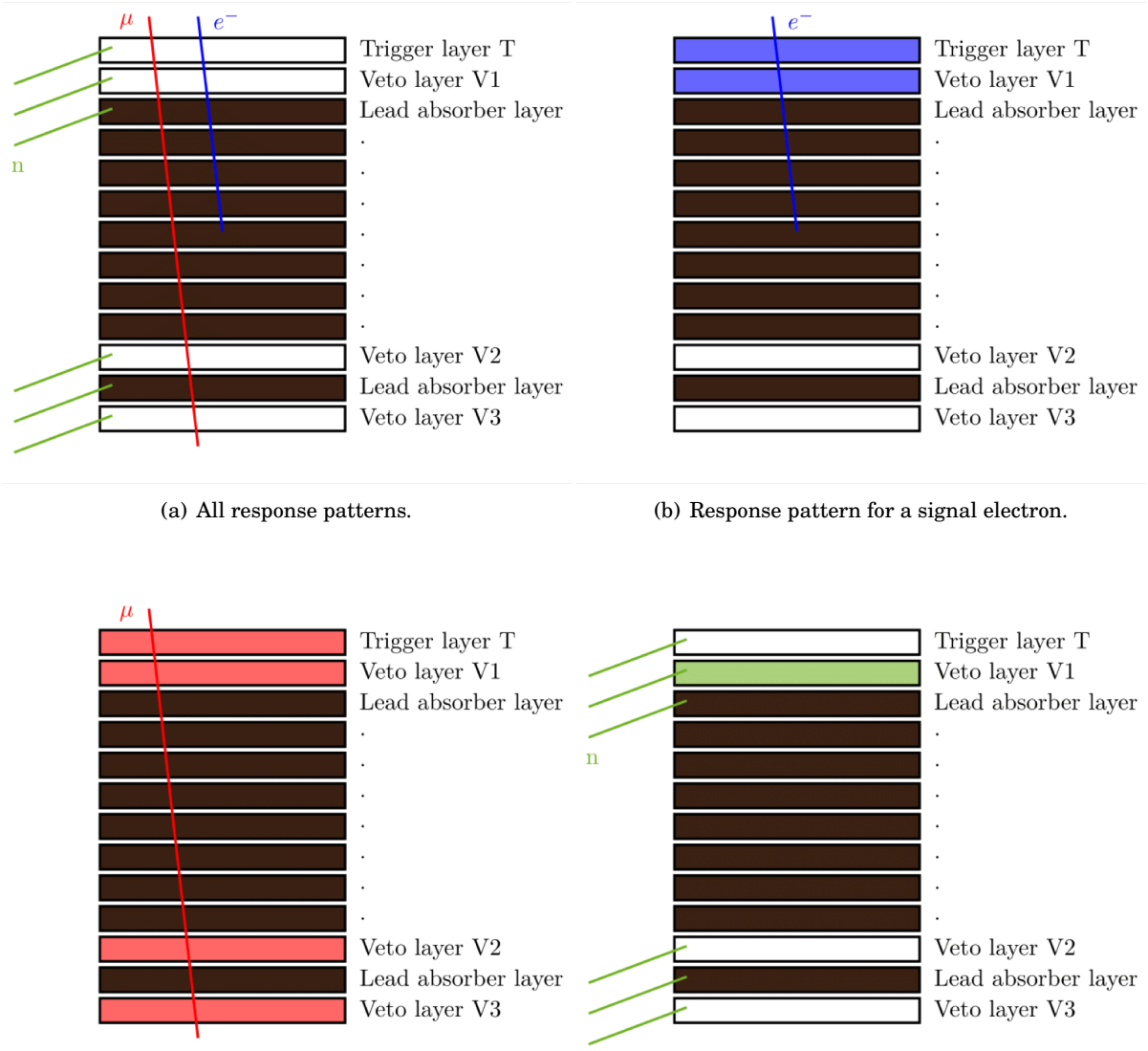

(a) All response patterns.

(b) Response pattern for a signal electron.

(c) Response pattern for a background muon.

(d) Response pattern for a background neutron.

FIGURE 3.3. Working principle of the veto system. The different incoming particles raise individual response patterns and can therefore be classified as signal or background.

stopped for the most part inside the lead absorber layers between the veto layers V1 and V2. The penetrating muons leave signals in all four detector layers, which is why the veto response pattern `V1&V2&V3` is planned to be used to distinguish electrons and muons. The beam-induced neutrons typically yield signals in only one of the detector layers due to their low interaction probability. To minimize the amount of falsely identified events, the response probability of the pattern `V1&V2&V3` must be maximized for muons and minimized for electrons, which will be

addressed in Chapter 4. This includes that the efficiency of the veto layers has to be as close to 100 % as possible. In contrast, the time resolution of the veto layers is secondary.

3.3 Conception of the Trigger Layer

The trigger layer is composed of individual plastic scintillation detectors that are placed next to each other along the dispersive direction of the spectrometer. The detectors each consist of a plastic scintillator bar that is read out coincidentally by a photomultiplier tube (PMT) on each side, where scintillator and PMT are connected by a light guide.

The choice of plastic scintillators is based on their high light yield, fast signal characteristics, machinability, robustness, and comparatively low cost. Cherenkov radiators had been discussed in an initial phase but quickly discarded, since the directional emission of Cherenkov light would introduce a significant detector response dependence on the angles of incoming particles and therefore would not be helpful for the purpose of the trigger detectors. Besides, Cherenkov radiators are typically heavier, more expensive, and less easily machined and shaped.

Due to their higher geometric fill factor, PMTs are the preferential choice compared to silicon photomultipliers (SiPMs). Moreover, PMTs typically have a lower dark current, a better radiation hardness, and the advantage that their dynamic range is directly determined by their gain, which can be controlled by varying the PMT supply voltage. In contrast, the dynamic range of a SiPM is limited by its number of microcells [97].

When the plastic scintillators of the individual layers are chosen too thin, this can result in a too small light yield and eventually in an efficiency loss. To accommodate for a possible, additional degradation of the light yield through aging under experimental conditions, as it was for instance observed at A1 [34, 98], which has later been fixed by implementing an additional amplifier stage into every readout channel, especially the trigger detectors must have a high enough light yield with some head room. This is achieved by using rather thick plastic scintillator bars for the trigger layer with a thickness of 26 mm and by almost completely covering their end faces with 25.4 mm PMTs. In fact, the exact thickness of 26 mm has been chosen due to the availability of this PMT size of 1 inch, in combination with the criterion to cover as much of the scintillator faces as possible.

In order to avoid gaps between the trigger detectors in the incident direction of the scattered electrons, and thus to avert losing efficiency, the profile of the plastic scintillator bars has a rhombic shape[5]. Fig. 3.4 shows the schematic side view of three trigger scintillator bars placed side by side along the dispersive direction of the spectrometer. The rhombic profile has a base of 36 mm, a height of 26 mm, and an interior angle of 60°. The angle of 60° creates enough overlap between the individual scintillator bars to cover the 16° track divergence of the scattered

[5]Actually, the profile is only a parallelogram, not a rhombus. However, the terminology has evolved this way and is now commonly used in this form.

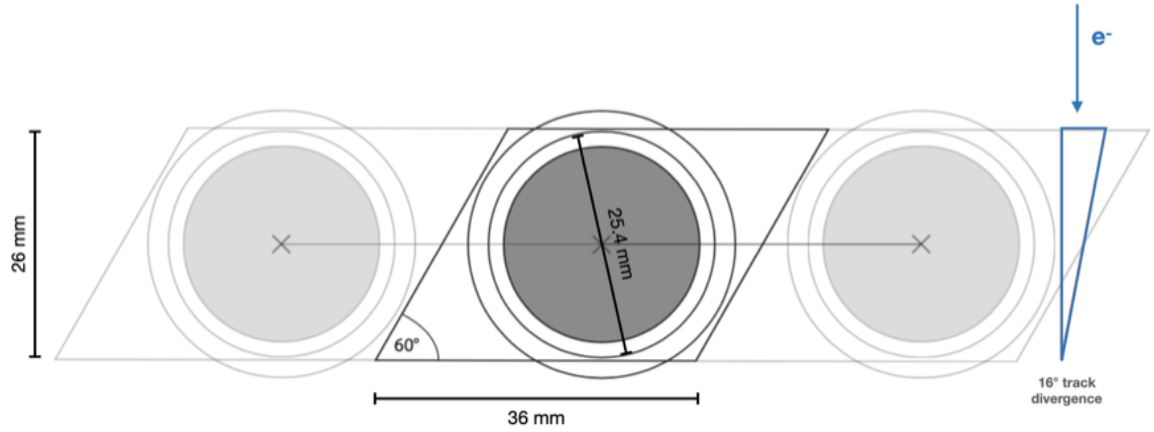

FIGURE 3.4. The profile of the trigger scintillator bars has a rhombic shape. By this, gaps in the incident direction of the scattered electrons are avoided. The scintillators are coincidentally read out using PMTs.

electrons, which will be motivated in Chapter 4. The base of 36 mm is chosen such that there is enough space between the PMTs for the assembly of high-voltage sockets and cables. In order not to lose the scintillation light arriving in the sharp corners of the rhombic profile, the light guides are used, which translate the rhombic profile of the scintillator bars onto the circular profile of the PMTs.

The determination of all further trigger layer parameters and the selection of the exact components for the trigger detectors has been an essential part of this thesis and will be covered in the coming chapters.

3.4 Conception of the Veto System

The veto system consists of three segmented veto layers and several lead absorber layers, which are arranged above each other and combined into a modular system. The idea arose that the veto system could be built as a flexible drawer system, which eventually has been implemented this way, see Chapter 6. By this, the configuration of veto and lead absorber layers is highly customizable and individual layers can even be easily excluded by just pulling out the respective drawer.

Out of space constraints - the overall height of the trigger veto system should not significantly exceed 300 mm due to the available space in the shielding houses - the veto system has been designed to be built out of 14 layers with a thickness of 10 mm each, thus providing space for the

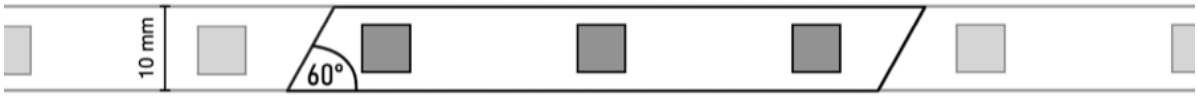

FIGURE 3.5. The profile of the veto scintillator segments is rhombic as well.

three veto layers and eleven lead absorber layers[6]. The areal dimensions are the same for all layers, in order to simplify the overall setup.

Each veto layer is made from three individual plastic scintillation detectors that partition the layer along the non-dispersive direction of the spectrometer, where each detector is composed of a plastic scintillator segment that is read out coincidentally by three SiPMs on each end face. The decision to use plastic scintillators is again based on their high light yield, fast signal characteristics, machinability, robustness, and comparatively low cost. SiPMs are used because of their compact form factor, which is extremely helpful due to the space constraints inside the shielding houses. Moreover, the use of SiPMs allows for promising synergy effects between MAGIX and DarkMESA as shown in Appendix A.1. The veto detectors of DarkMESA are read out by SiPMs as well and a lot of effort has already been invested in the development of the corresponding electronics. The geometry of the DarkMESA readout cards also determines the division of the MAGIX veto layers into three segments.

As for the trigger layer, the profile of the plastic scintillator segments is rhombic with an interior angle of 60°, as can be seen in Fig. 3.5. This is again so that gaps between the detectors in the incident direction of the scattered electrons are avoided.

The determination of the remaining parameters of the veto system will be topic of the coming chapters, as will be the selection of the specific components.

[6]At a later point, the space constraints proved not to be as significant as expected and the total number of layers could be increased to 18. This gives space to 15 lead absorber layers in the final setup, which further improves the veto efficiency as will be shown in Chapter 4.

CHAPTER 4

SIMULATION STUDIES WITH GEANT4

Chapter 3 explained the general concept of the MAGIX trigger veto system. For the final construction of the trigger veto system, questions like "How many trigger detectors are necessary?" or "What dimensions do the veto layers need to have?" must be answered. To do so, the `Geant4` simulation of the trigger veto system, started by M. Christmann as part of his PhD thesis [27], has been pursued and expanded. The idea is to investigate how the numbers of produced optical photons in the individual scintillators of the trigger and veto layers are influenced by changes in the detector geometry, described by so-called *design parameters*, and optimize the design of the trigger veto system accordingly. For this purpose, 105 MeV electrons and 1 GeV muons have been simulated and the detector responses of the individual scintillators of the trigger veto system have been studied. The results of these simulation studies are laid out in this chapter. Please note that at this stage of geometry optimization, not all possible effects have been taken into account. As an example, instead of varying the electron energy along the dispersive direction of the spectrometer, as it will be the case in the final MAGIX setup according to momentum dispersion, one fixed energy has been used for all electrons of a dataset.

Section 4.1 starts with an overview on the `Geant4` simulation of the trigger veto system, where the detector model is motivated, the active physics processes are listed, and the analysis procedure is described. Subsequently, Section 4.2 shows some necessary preparatory studies that have been performed to obtain several essential inputs for optimizing the design parameters of the trigger veto system. Section 4.3 then guides through the design parameter optimization of the trigger layer, the veto layers, and the lead absorber layers, followed by a summary of the most important simulation results, as well as the final agreed on values for the design parameters.

In addition, Appendix B provides further information to the simulation studies presented in this chapter. If you are interested in an introduction to the `Geant4` software framework, please refer to

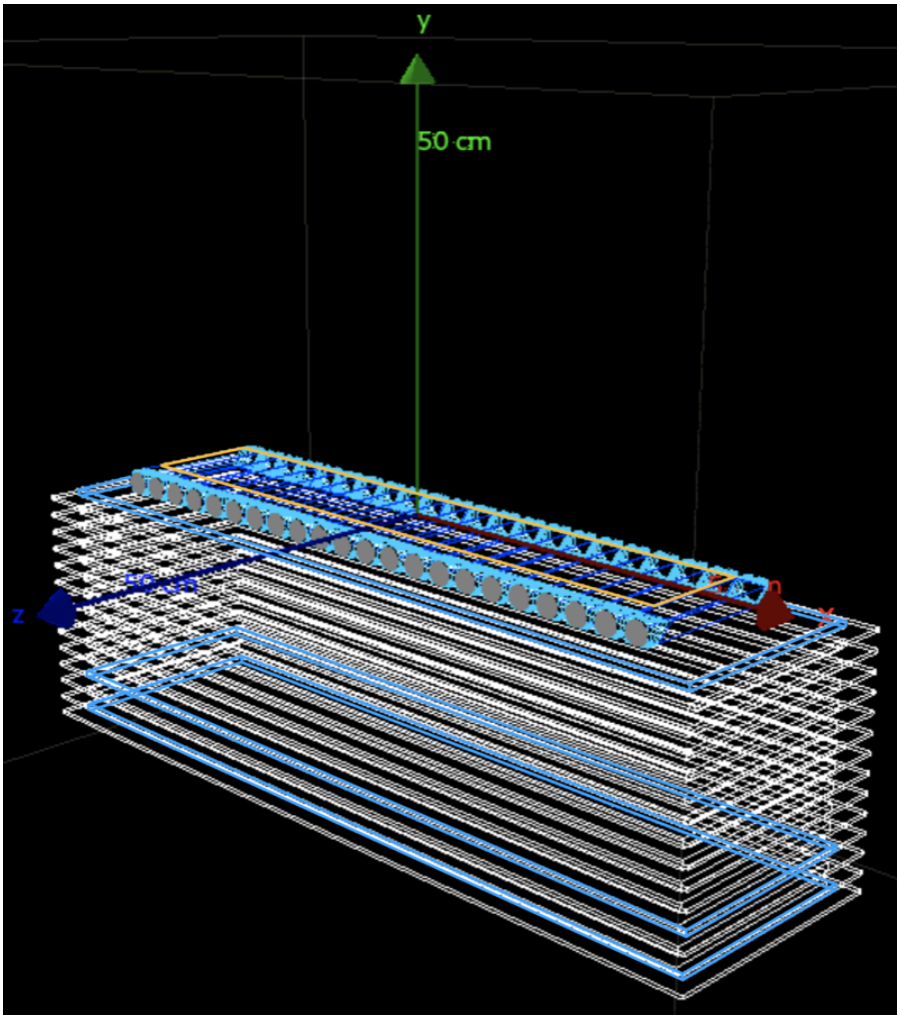

FIGURE 4.1. Geant4 model of the trigger veto system. The Geant4 coordinate system is chosen such that its axes match those of the spectrometer coordinate system described in Section 2.4.

Appendix B.1; details on the GitLab repository of the simulation, i.e. MXTriggerVetoSimulation, can be found in Appendix B.2; and Appendix B.3 contains an additional study on the placement of the second veto layer V2. Moreover, Appendix B.4 provides complementing tables and plots to the simulation studies in this chapter.

4.1 The MAGIX Trigger Veto Simulation

4.1.1 Modeling the Trigger Veto System

For modeling the trigger veto system in Geant4, only its most important parts are considered and implemented, as can be seen in Fig. 4.1.

The uppermost element of the model is the exit window of the MAGIX TPC made from a Kapton foil, which is shown as the thin orange rectangle. It sits around the origin of the Geant4 coordinate system, such that the axes of the spectrometer coordinate system, cf. Section 2.4, match those of the Geant4 coordinate system. Thus, x is the dispersive direction of the spectrometer (red axis), y is the height (green axis), and z is the non-dispersive direction of the spectrometer (blue axis). The dimensions of the Kapton foil are 768 mm × 0.125 mm × 130 mm (xyz), which are the latest numbers for the dimensions of the TPC exit window at the time of performing the simulation studies in this chapter[1]. The electrons and muons are generated at $y = 10$ mm and a random position in the xz-plane of the Kapton foil. Their starting angles in the dispersive and non-dispersive directions, respectively, follow the angular distributions exhibited by the electrons hitting the trigger veto system after propagating through the spectrometer optics, as they will be motivated in Section 4.2.1. Thus, homogeneous distributions for the incident angles and impact positions of the generated electrons and muons are assumed instead of specific distributions as they are to be expected for individual measurement campaigns.

The trigger layer T is placed 5 mm beneath the TPC exit window, which is as close as it will be possible in the final setup due to the technical realization of the TPC. The trigger layer is segmented along the x-axis by using individual scintillation detectors, which are composed of a plastic scintillator bar (shown with dark blue outlines) coupled to a light guide made of acrylic glass (shown in light blue) and a PMT (shown in grey) on each side, as described in Chapter 3. The scintillator bars have the already known rhombic profile with a base length of 36 mm, a height of 26 mm, and an interior angle of 60°, and are made from the plastic scintillator BC-404[2] by Saint-Gobain [100]. The light guides transform the profile of the scintillators onto the circular PMT profile with a diameter of 25.4 mm, which happens over a length of 20 mm along the z-axis. To consider a reflective layer around the scintillators and light guides, both are surrounded by a 0.1 mm thick layer of air followed by a 0.2 mm thick layer of PTFE tape[3].

The veto system is placed below the trigger layer, such that a 4 mm gap remains between them, which will be necessary for properly mounting the individual layers in the final setup of the trigger veto system, see Chapter 6. In total, the veto system consists of 14 layers, each of which has a 4 mm gap towards the upper. Three of these layers are the veto layers V1, V2, and V3 (shown with light blue outlines), also made from the plastic scintillator BC-404[4], and the remaining eleven

[1] Later on, the dimensions of the Kapton exit foil were changed to 782.0 mm × 0.125 mm × 140.3 mm. As a result, the simulation does not include particles generated at the very edges of the final foil. However, given the conservative selection of assumed incident positions and angles of the particles, cf. Section 4.2.1, no issues are foreseen by this change.

[2] This is the scintillator material of choice at the time of performing the studies presented in this chapter. Later on, it was decided to use the material EJ-230 by Eljen Technology [99] instead, see Section 5.1.2. Nevertheless, as scintillation yield and attenuation length are very similar for the two materials, cf. Tab. 5.1, this aspect can be dismissed.

[3] Note that these layers are not needed for the studies in this chapter, since only the numbers of produced optical photons are studied. However, the layers are implemented and can be used for possible future studies.

[4] Also for the veto layers, at some point it was decided to use EJ-230 as the scintillator material instead of BC-404, see Section 6.2.1. But again, the differences in scintillation yield and attenuation length are rather small, cf. Tab. 5.1,

are lead absorber layers made from the antimonial lead alloy PbSb4 (shown in white). Both layer types are modeled as one large sheet with a thickness of 10 mm. As the trigger scintillators, the veto layers have a rhombic profile with an interior angle of 60°. If not stated otherwise, all eleven lead absorber layers are placed between the veto layers V1 and V2 for the studies in this chapter. In addition to the 4 mm gaps between the individual layers, each layer of the veto system is supported by a 4 mm steel sheet with an area of 1000 mm × 300 mm in the xz-plane (also shown in white). These are implemented for modeling the drawers that will be used for supporting the individual layers of the veto system in the final assembly, where each will be made from a 4 mm steel sheet and a frame of aluminum profiles.

The goal of simulating the trigger veto system is to investigate how the numbers of produced optical photons in the individual scintillators of the trigger layer and the veto layers are influenced by changes in the detector geometry, where optical photons are all those photons produced by scintillation or the Cherenkov effect. The so-called design parameters, e.g. the number of trigger scintillators per trigger layer or the dimensions of the veto layers, must be known to finalize the design of the trigger veto system. Only then components can be ordered or parts be commissioned to assemble the trigger veto system. Together with many other required input parameters, the design parameters are defined inside a steering file as described in Appendix B.2. The most important ones for modeling the trigger layer, the veto layers, and the lead absorber layers, as well as some others, are listed in Tabs. 4.1–4.4, respectively, together with the corresponding steering file variables and their values. If no value is assigned to a listed parameter, it is a design parameter, whose optimization will be topic of Section 4.3. For that, all other parameters had to be fixed beforehand. Most of them have been decided upon at an earlier stage based on results from lab measurements or technical constraints, as laid out in Chapters 5 and 6, and some others have been determined within the preparatory studies presented in Section 4.2.

4.1.2 Active Physics Processes

As described in the literature [101] -, there are many mechanisms how particles can interact with a medium. For each of these processes, there is a corresponding `Geant4` class that can be activated, and which will then be taken into account during the simulation.

For the simulation studies in this chapter, electrons and muons are used to study the numbers of produced optical photons inside the individual scintillators of the trigger veto system. Therefore, the interaction mechanisms of electrons, muons, and photons are of utmost interest, as well as the mechanisms that are relevant for the consideration of optical photons. The active processes for each of these are listed in Tabs. 4.5–4.8, respectively, together with the corresponding `Geant4` classes.

so that this aspect has no impact on the outcomes of the simulation studies in this chapter.

Parameter description	Steering file variable	Value
Number of trigger scintillators along x	`MAGIXDetectorLayersX`	
Length of the trigger scintillators along z	`scinti_length`	
Exterior angle of the trigger scintillator rhombus	`scinti_angle`	30°
Height of the trigger scintillator rhombus along y	`scinti_height`	26 mm
Base of the trigger scintillator rhombus	`scinti_width`	36 mm
Length of the trigger light guides along z	`lightGuideLength`	20 mm
Diameter of the trigger PMTs	`pmt_diameter`	25.4 mm

TABLE 4.1. Important input parameters for modeling the trigger layer T.

Parameter description	Steering file variable	Value
Number of veto layers along y	`MAGIXVetoLayersY`	3
Veto layer length along x	`veto_scinti_length`	
Veto layer width along z	`veto_scinti_width`	
Exterior angle of the veto scintillator rhombus	`veto_scinti_angle`	30°
Height of the veto scintillator rhombus along y	`veto_scinti_height`	10 mm

TABLE 4.2. Important input parameters for modeling the veto layers V1, V2, and V3.

Parameter description	Steering file variable	Value
Lead absorber layer length along x	`Pb_dx`	
Lead absorber layer width along z	`Pb_dz`	
Thickness of lead absorber layers along y	`Pb_dy`	10 mm
Number of lead absorber layers between V1 and V2	`Pb1_elements`	11
Number of lead absorber layers between V2 and V3	`Pb2_elements`	0

TABLE 4.3. Important input parameters for modeling the lead absorber layers.

Parameter description	Steering file variable	Value
Length of the steel sheets along x	`steel_dx`	1000 mm
Steel sheet thickness along y	`steel_dy`	4 mm
Width of the steel sheets along z	`steel_dz`	300 mm
Length of TPC window along x	`vacuumFoil_dx`	768 mm
Thickness of TPC window along y	`vacuumFoil_dy`	0.125 mm
Width of TPC window along z	`vacuumFoil_dz`	130 mm
Gap between TPC window and T along y	`foilScinti_distance`	5 mm
Gap between layers T and V1 along y	`veto1_distance_to_trigger`	4 mm
Distance between veto and lead layers along y	`pb_distance_to_veto`	8 mm*
Distance between lead layers along y	`pb_distance_to_pb`	8 mm*

*: These values include both the gap between the individual layers and the steel sheet thickness.

TABLE 4.4. Other important input parameters for modeling the trigger veto system.

Physics process	**Geant4 class**
Bremsstrahlung	`G4eBremsstrahlung`
Ionisation	`G4eIonisation`
Multiple scattering	`G4eMultipleScattering`
Positron annihilation	`G4eplusAnnihilation`

TABLE 4.5. Active physics processes for electrons (and positrons).

Physics process	**Geant4 class**
Bremsstrahlung	`G4MuBremsstrahlung`
Ionisation	`G4MuIonisation`
Multiple scattering	`G4MuMultipleScattering`, `G4WentzelVIModel`
Single Coulomb scattering	`G4CoulombScattering`
e^+e^- pair production	`G4MuPairProduction`

TABLE 4.6. Active physics processes for muons.

Physics process	**Geant4 class**
Photoelectric effect	`G4PhotoElectricEffect`
Compton scattering	`G4ComptonScattering`
Pair production	`G4GammaConversion`

TABLE 4.7. Active physics processes for photons.

4.1.3 Figures of Merit and Analysis Procedure

For the optimization of the design parameters in Section 4.3, it has to be defined what "optimal" actually means. For this purpose, a handful of *figure of merits* have been defined, the maximization or minimization of which represents the optimization.

For each trigger configuration C, a *trigger response probability* $\epsilon_{\mathrm{T,C}}$ can be defined, which is calculated as

$$\epsilon_{\mathrm{T,C}} = \frac{\text{number of events registered by C}}{\text{number of all simulated events}}. \tag{4.1}$$

The corresponding error $\Delta\epsilon_{\mathrm{T,C}}$ is estimated as

$$\Delta\epsilon_{\mathrm{T,C}} = \frac{\sqrt{\text{number of events registered by C}}}{\text{number of all simulated events}}, \tag{4.2}$$

since obtaining the numerator of $\epsilon_{\mathrm{T,C}}$ is a simple Poisson distributed counting problem. $\epsilon_{\mathrm{T,C}}$ is equivalent to a trigger efficiency and its maximization, or alternatively the minimization of the difference $1-\epsilon_{\mathrm{T,C}}$, ensures that the trigger configuration C geometrically accepts as many events as possible. All implemented trigger configurations are listed in Tab. 4.9. While the configurations `T`, `V1`, `V2`, and `V3` simply represent a response by the respective scintillator layer, regardless of how the other layers respond, the configuration `T && V1` requires a logical AND of layers T and V1,

Physics process	**Geant4 class**
Scintillation	`G4Scintillation`
Cherenkov radiation	`G4Cerenkov`
Absorption	`G4OpAbsorption`
Reflection, refraction	`G4OpBoundaryProcess`
Rayleigh scattering	`G4OpRayleigh`
Mie scattering	`G4OpMieHG`

TABLE 4.8. Additional active physics processes for the consideration of optical photons.

Trigger configuration C	**Description**
`T`	layer T responded
`T && V1`	layers T and V1 responded
`V1`	layer V1 responded
`V2`	layer V2 responded
`V3`	layer V3 responded

TABLE 4.9. All implemented trigger configurations.

which will be a possible trigger setting in the final setup of MAGIX. Note that the configurations `V1`, `V2`, and `V3` will not be used as trigger settings in the final setup, but are only used to indicate whether the individual veto layers respond or not.

For characterizing the veto system, several veto patterns P have been implemented, which are listed in Tab. 4.10. For each, one can define a *veto response probability* $\epsilon_{\mathrm{V,P}}$,

$$\epsilon_{\mathrm{V,P}} = \frac{\text{number of events registered by P}}{\text{number of all simulated events}}, \tag{4.3}$$

which is equivalent to a veto efficiency. The corresponding error $\Delta\epsilon_{\mathrm{V,P}}$ is estimated, analogously to $\Delta\epsilon_{\mathrm{T,C}}$, by

$$\Delta\epsilon_{\mathrm{V,P}} = \frac{\sqrt{\text{number of events registered by P}}}{\text{number of all simulated events}}. \tag{4.4}$$

For electrons, $\epsilon_{\mathrm{V,P}}$ represents the portion of events that is mistakenly rejected by the veto system and is also referred to as *false electron rejection*. If the veto system is conceptualized as a hypothesis test, it corresponds to the type II error, i.e. the false negatives. For muons, on the other hand, $1-\epsilon_{\mathrm{V,P}}$ is the fraction of events erroneously accepted by the veto system, which is referred to as *false muon acceptance* and corresponds to the type I error, i.e. the false positives. By minimizing the false electron rejection, as well as the false muon acceptance, it can be assured that the veto system works as intended and is able to separate signal electrons from background muons. As an alternative, the difference $1-\epsilon_{\mathrm{V,P}}$ can be maximized for electrons or $\epsilon_{\mathrm{V,P}}$ can be maximized for muons.

Unfortunately, it is not possible to optimize both the false electron rejection and the false muon acceptance at the same time. In practice, a compromise has to be found between the two,

Veto pattern P	Description
`no V`	no veto layer responded
`only V1`	only V1 responded
`only V2`	only V2 responded
`only V3`	only V3 responded
`only V1 and V2`	V1 and V2 responded, V3 not
`only V1 and V3`	V1 and V3 responded, V2 not
`only V2 and V3`	V2 and V3 responded, V1 not
`all V`	all veto layers responded
`V1&V2 new`	see Appendix B.3

TABLE 4.10. All implemented veto patterns.

dependent on the experiment at hand. For MAGIX, this can be illustrated using two of the intended experiments described in Chapter 1. When measuring the electric form factor $G_E(Q^2)$ of the proton, cf. Section 1.2, a signal rate up into the MHz region is expected so that the comparably low rate of cosmogenic muons[5] can be safely neglected. Besides, the intended precision during this experiment necessitates detecting the scattered electrons with an efficiency as close to 100 % as possible. Minimizing the false electron rejection therefore has the highest priority in this case and a slightly larger false muon acceptance is of no consequence. When looking for the visible decay channel of the dark photon, however, cf. Section 1.3, the expected signal rate is lower than the rate of cosmogenic muons. Consequently, mistakenly accepted muons exert a significant impact on the performance of the experiment and must be actively counteracted. Moreover, the exact value for the detection efficiency of the scattered electron holds less significance. For this experiment, the minimization of the false muon acceptance is thus to be prioritized. Please note that, on purpose, no exact figures for the false electron rejection and the false muon acceptance are given here. The precise compromise between the two must be decided specifically for each experiment.

In the final setup of MAGIX, the veto pattern where all three veto layers respond, i.e. `all V`, is planned to be used. This pattern is therefore of specific interest in the coming sections and is used to make statements about the results of the individual studies. All other veto patterns are included in the studies for the sake of completeness, but are not particularly interesting for the required results. The veto pattern `V1&V2 new` is only needed for the additional study on the placement of the veto layer V2 presented in Appendix B.3.

With the above definitions of the response probabilities, the simulation data can be analyzed accordingly. As described in Appendix B.2, the stored datafiles contain the numbers of produced optical photons inside the individual scintillators of the trigger veto system, where each line in a

[5] With the rule of thumb for the rate of cosmogenic muons being one muon per minute per square centimeter at sea-level [101], a trigger layer with its sensitive area of 817.5 mm × 150 mm, cf. section 5.4, is exposed to a cosmogenic muon rate of roughly 20 Hz if placed in the laboratory. Underground, inside the MAGIX hall, this value will obviously be even lower.

datafile represents one simulated event. By scanning a datafile line by line, the numerators of the trigger and veto response probabilities can be obtained. This is done by increasing a counter for each of the trigger configurations and veto patterns, if the number of produced optical photons inside the corresponding scintillators exceed a certain threshold, the before defined variable *Photon cut*. A closer look on the influence of this variable can be found in Section 4.2.2. The response probabilities and their errors can then be calculated and plotted against the design parameter being optimized.

4.2 Preparatory Studies

When starting the simulation studies for the trigger veto system, not all of the required input parameters described in Section 4.1.1 had already been defined. Besides the design parameters, a few input parameters had to be determined within the scope of several dedicated preparatory studies, which are laid out in the following sections.

4.2.1 Incident Angle Distributions

To correctly simulate the electrons and muons hitting the trigger veto system, their angular distributions in the dispersive and non-dispersive directions of the spectrometer have to be known. Of course, the angular distribution of the cosmogenic muons is known to approximately follow a $\cos^2\theta$ distribution, where θ is the Zenith angle of the incident muons [102]. But for the scope of the simulation studies in this chapter, it is better to use the same angular distributions for both electrons and muons. Since the track reconstruction of the TPC contains the determination of the dispersive and non-dispersive angles, a track that does not match the angular distribution of the electrons can immediately be identified as background. Therefore, only electrons and muons with the same incident angles are of particular interest, since the trigger veto system must be capable of distinguishing between the two of them.

To determine the angular distributions of the electrons, already simulated electron tracks that had been used for the characterization of the spectrometers proved to be helpful. The electrons originate from the interaction point inside the scattering chamber, pass a collimator, and propagate through the magneto-optics of the spectrometer. The electrons then exit the spectrometer with angular distributions, that do not change anymore due to the absence of a magnetic field below the spectrometer. These angular distributions are therefore the same as those for the electrons hitting the trigger veto system.

Using the same coordinate axes as described in Section 4.1.1, but with the origin at the interaction point inside the scattering chamber[6], the simulated electrons are created at $y = 0\,\text{mm}$ at three different positions along the non-dispersive direction, $z = -5\,\text{mm}$, $z = 0\,\text{mm}$, and $z = 5\,\text{mm}$. According to the design reference momentum of the spectrometers of 200 MeV, where magnet

[6]This is the spectrometer coordinate system described in Section 2.4.

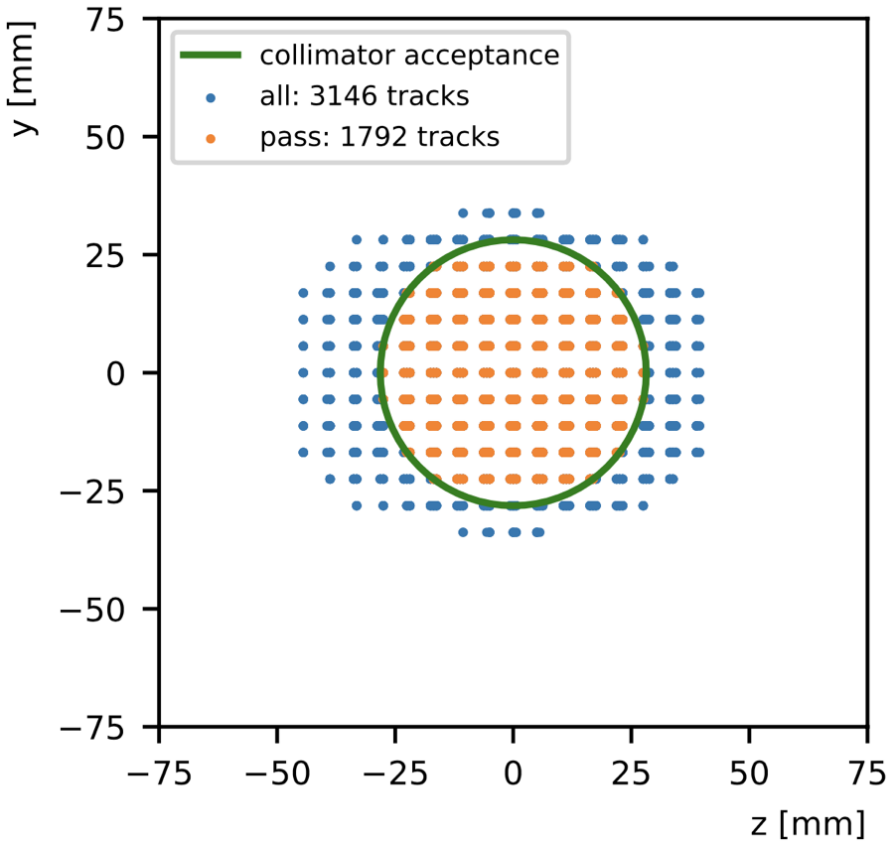

FIGURE 4.2. Simulated electron tracks in the yz-plane of the collimator. The electrons that are able to pass the collimator are shown in orange. The circular collimator is placed at a distance of 645 mm from the interaction point with an opening angle of 2.5°.

saturation effects should not yet be significant, the momenta of the particles are chosen between 167 MeV and 225 MeV, representing a spectrometer central momentum of 195 MeV and a central momentum acceptance of roughly ± 15 %. The collimator is placed at $x = 645\,\text{mm}$, $y = 0\,\text{mm}$, and $z = 0\,\text{mm}$, and has an acceptance of 2.5° with respect to its center, thus being a circle with a radius of approximately 28.16 mm. Fig. 4.2 shows the collimator acceptance, together with the simulated electron tracks in the yz-plane of the collimator. Obviously, only a limited set of different tracks has been used for the studies in this section. For actual physics measurements, the angular distributions will significantly differ according to the cross-sections being involved. However, the angular range that is accepted is the same. After passing the collimator and the spectrometer, the electrons then show the angular distributions as can be seen in Fig. 4.3. Both the dispersive and the non-dispersive angle are measured against the y-axis. The former in the xy-plane, the latter in the yz-plane. The angle ranges $(-16.4°, 7.3°)$[7] and $(-1.4°, 1.5°)$ of the electrons passing

[7]The absolute value of −16.4° has been rounded to 16° and appears in Fig. 3.4 as the expected track divergence of the scattered electrons.

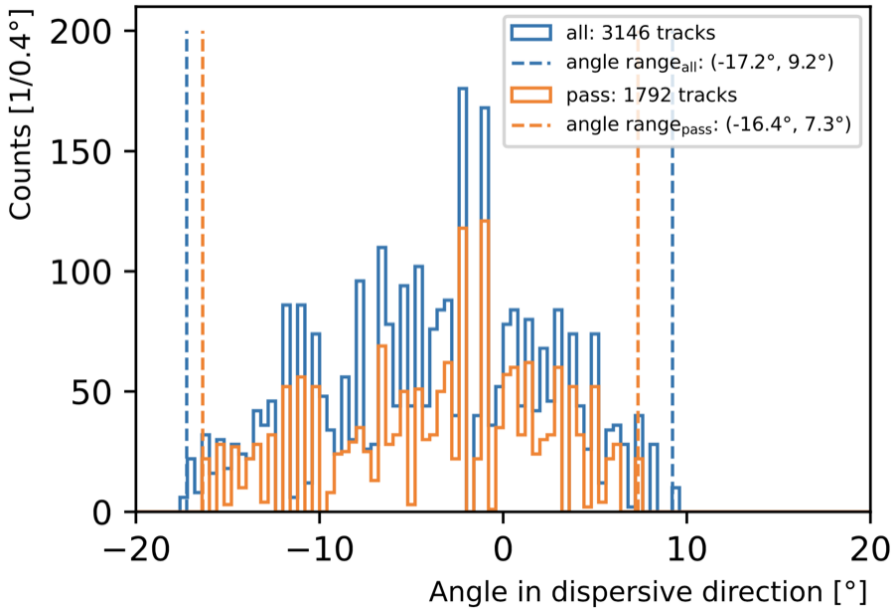

(a)

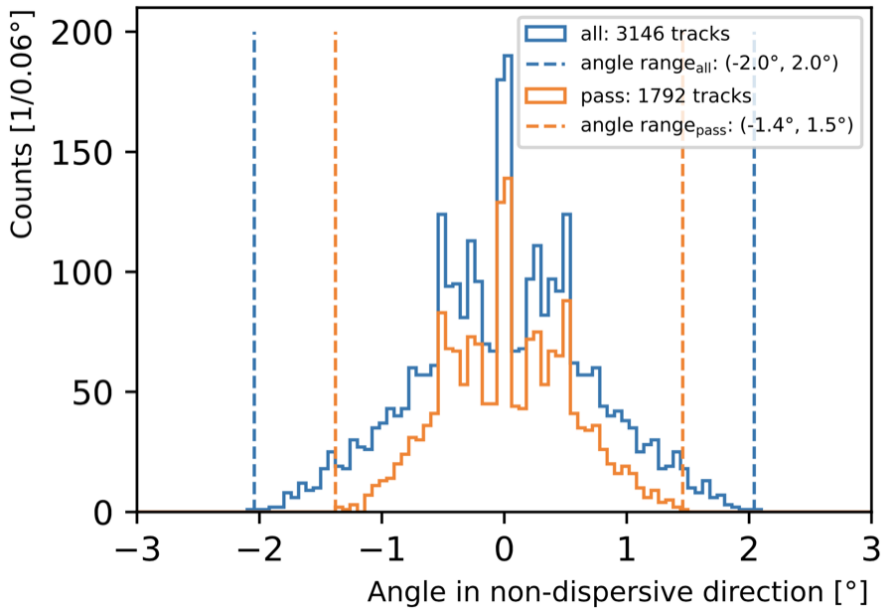

(b)

FIGURE 4.3. The angular distributions of the electrons hitting the trigger veto system in the dispersive (a) and non-dispersive (b) directions of the spectrometer. The observable binning artifacts result from the relatively low number of simulated electron tracks and the arbitrary choice of 100 bins for the plotted ranges. The distributions of the electrons passing the collimator are used as an input for the design parameter optimizations in Section 4.3.

the collimator have been used as the inputs for the angular distributions of the dispersive and non-dispersive angles, respectively, in the optimization studies shown in Section 4.3.[8]

4.2.2 Impact of the Variable *Photon cut*

One flexible input parameter is the variable *Photon cut*. It sets the threshold, from which number of produced optical photons inside a scintillator an event is taken into account for the calculation of the trigger and veto response probabilities. One can compare it to a signal threshold in the later setup of MAGIX, be it in the form of a discriminator threshold or an applied software cut in an analysis.[9] In principle, it can be set individually for each detector layer, but for the scope of the studies in this chapter, the same value is used everywhere.

To make the variable *Photon cut* more intuitive, Fig. 4.4a shows the numbers of produced optical photons in the individual detector layers for 100,000 electron events with an energy of 105 MeV. For this study, the trigger layer is implemented as 22 trigger scintillators, each with a length of 150 mm; the veto layers are modeled with a length of 950 mm and a width of 250 mm; and the lead absorber layers are given the same dimensions as the veto layers. For the trigger layer, the peak of the distribution is at around 50,000, while the distribution of the veto layer V1 peaks at around 19,000. This difference is expected and can be explained by the different layer thicknesses, i.e. 26 mm for the trigger layer and 10 mm for the veto layers. With a scintillation yield of 10,400 photons per 1 MeV of deposited energy[10] and a density of 1.023 g/cm^3 [100] for BC-404, the approximate energy loss by ionization of a minimum ionizing particle in a plastic scintillator of 1.9 MeV/g cm^{-2} [101] holds true quite well. The distributions of the veto layers V2 and V3 peak at 0 due to their placement beneath the eleven lead absorber layers. In contrast, Fig. 4.4b shows the optical photon distributions for 100,000 muon events with an energy of 1 GeV. Here, the three distributions for the veto layers all peak at around 19,000, since the muons have enough energy to pass the eleven lead absorber layers between layers V1 and V2. From comparing the distributions for electrons and muons, one can see that a reasonable cut value on the variable *Photon cut* lies in the range from 0 to 18,000. By this, electrons and muons can be effectively distinguished using, for example, `all V` as the veto pattern.

The same can be deduced from Fig. 4.5. Here, the variable *Photon cut* is varied from 100 to 20,000 and the different veto response probabilities are plotted against it. For each dataset, 100,000 electron events with an energy of 105 MeV are simulated, which sets a lower limit for

[8] Since performing the study presented in this section, the collimator acceptance has been decreased to 1.75°. The angle ranges used for the optimization studies are therefore quite conservative compared to those in the final setup of MAGIX.

[9] Obviously, this is a simplified picture. The later measurable signals are a superposition of the contributions along the whole signal chain, starting with the light production inside the scintillator and ending with the signal transmission to the measurement device. However, qualitatively it is the same.

[10] Unfortunately, the scintillation yield of BC-404 is not directly available, cf. [100]. However, the characteristics of BC-404 are almost identical to those of EJ-204 by Eljen Technology [103], whose scintillation yield is given as 10,400 photons per 1 MeV of deposited energy.

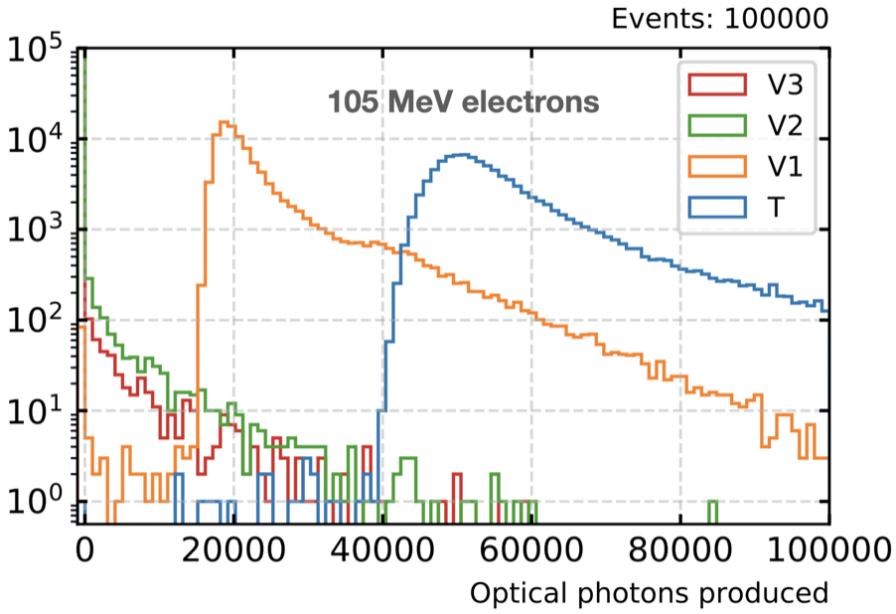

(a)

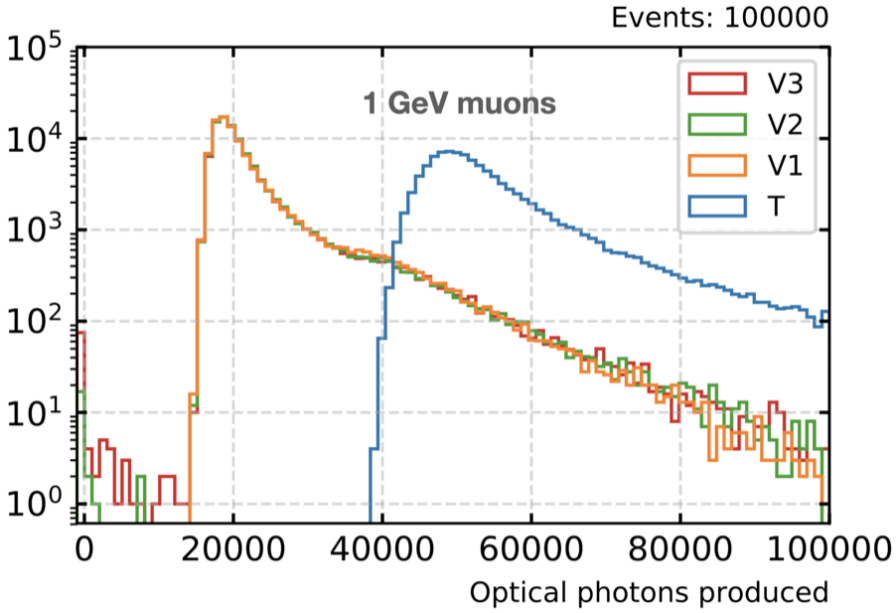

(b)

FIGURE 4.4. Produced optical photons inside the individual detector layers of the trigger veto system for 105 MeV electrons (a) and 1 GeV muons (b).

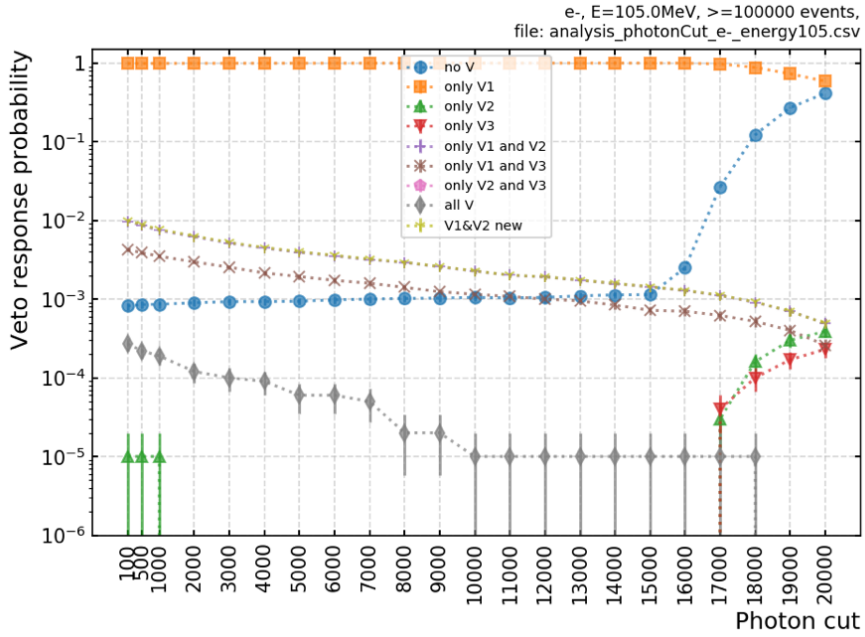

FIGURE 4.5. The individual veto response probabilities against the variable *Photon cut*. $\epsilon_{\mathrm{V,all\,V}}$ steadily decreases and reaches its minimum for a *Photon cut* value of 10,000.

the investigation of the veto response probabilities down to 10^{-5}. Note also that if a veto pattern would respond to no events at all, the corresponding response probability and its error would be evaluated as 0, cf. Eqs. 4.3 and 4.4, not allowing for a meaningful statement other than that the veto response probability is $\leq 10^{-5}$. As *Photon cut* is increased, the veto pattern of interest, i.e. `all V`, steadily decreases until it reaches a plateau of 10^{-5} for a *Photon cut* value of 10,000. The exact numbers to this plot can be found in Tab. B.5 in Appendix B.4.1.

Fig. 4.5 also shows that the choice of the variable *Photon cut* has a significant impact on the resulting veto response probability $\epsilon_{\mathrm{V,all\,V}}$. Therefore, it is recommended to invest some time for accurately setting the signal thresholds in the final setup of MAGIX, so that the best possible veto efficiency can be obtained. For the simulation studies in the coming sections, *Photon cut* is set to 1,000, although significantly better results for the response probabilities can be achieved if a value of, for example, 10,000 is chosen. This decision is made to yield more conservative results.

4.2.3 Amount of Lead Absorber Layers

Due to space limitations in the final MAGIX setup, the design of the trigger veto system includes 14 layers, three of which are veto layers and eleven are lead absorber layers. In case there should be more space available than anticipated, it could be worthwhile to add more lead absorber layers between the veto layers V1 and V2 in order to further reduce the false electron rejection.

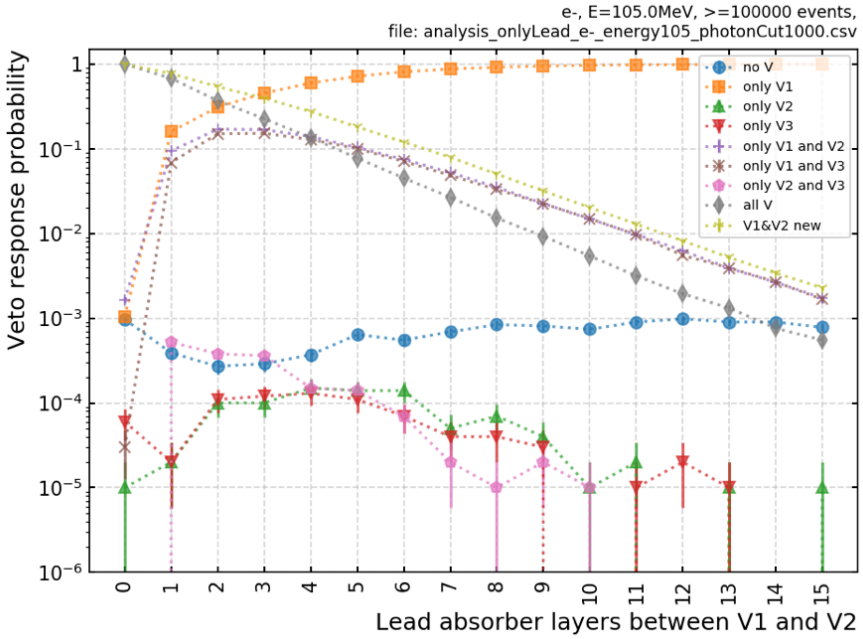

FIGURE 4.6. The individual veto response probabilities for electrons against the amount of lead absorber layers between the veto layers V1 and V2. $\epsilon_{\mathrm{V,all\,V}}$ continually decreases as the amount of lead absorber layers is increased.

To quantify this, the amount of lead absorber layers between the veto layers V1 and V2 has been varied between 0 and 15, without placing a lead absorber layer between the layers V2 and V3. For this study, the trigger layer consists of 22 trigger scintillators, each with a length of 150 mm, and the veto and lead absorber layers are both implemented with a length of 1000 mm and a width of 500 mm. 100,000 electron events with an energy of 105 MeV are simulated per dataset. Note that this again limits the quantification possibility of the veto response probabilities to 10^{-5} or higher. The results can be seen in Fig. 4.6. For the planned eleven lead absorber layers between V1 and V2 and the veto pattern of interest, i.e. `all V`, a veto response probability of $(4.44 \pm 0.21) \times 10^{-3}$ is achieved for electrons. If one were to increase the number of lead absorber layers to 15, this number can be improved to $(8.00 \pm 0.89) \times 10^{-4}$. Thus, it is recommended to consider more than eleven lead absorber layers between V1 and V2, if the space should be available. Of course, this only holds true if the false electron rejection is the prioritized parameter for the experiment at hand. For experiments in which minimizing the false muon acceptance has a higher priority, cf. Section 4.1.3, an increase in the number of lead absorber layers will probably be disadvantageous. The detailed numbers regarding the behaviour of $\epsilon_{\mathrm{V,all\,V}}$ in Fig. 4.6, please refer to Tab. B.6 in Appendix B.4.1.

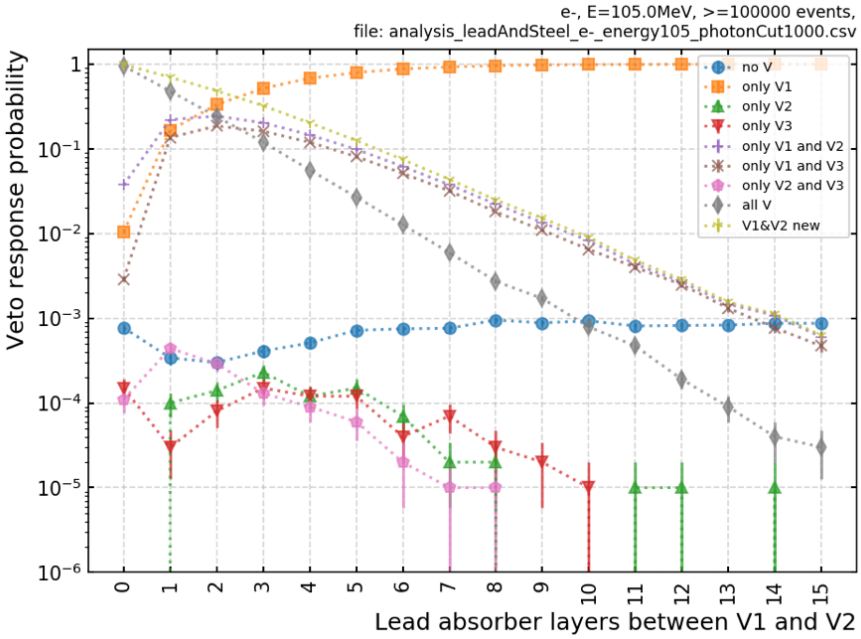

FIGURE 4.7. The individual veto response probabilities against the amount of lead absorber layers between V1 and V2, again for electrons. This time, additional 4 mm steel sheets are used for each layer of the veto system.

4.2.4 Impact of the Steel Sheets

In the later setup of the trigger veto system, the veto and lead absorber layers will be placed inside drawers made from 4 mm steel sheets supported by frames made of aluminum profiles. As an alloy of iron and carbon, steel is a very dense material (cf. $\rho_{\mathrm{Fe}} = 7.87\,\mathrm{g/cm^3}$ [104]) with a rather short radiation length (cf. $X_{0,\mathrm{Fe}} = 1.76\,\mathrm{cm}$ [104]), which additionally contributes to stopping the incident electrons between the veto layers V1 and V2. With this in mind, the steel sheets should be considered during the simulation and their contribution should be quantified.

For this purpose, the steel sheets are implemented with a thickness of 4 mm and an area of 500 mm × 1200 mm, which is larger than they will be in the final setup. By this, the drawer frames made of aluminum profiles and the mounting rack made of steel beams that will be necessary for the final assembly of the trigger veto system are approximated. All other input parameters are chosen as in Section 4.2.3. The steel sheets are placed directly beneath each of the veto and lead absorber layers. The impact of the steel sheets on the veto response probabilities is shown in Fig. 4.7, where the study from Section 4.2.3 has been repeated, but with the steel sheets included. Again, 100,000 electrons with an energy of 105 MeV are simulated for each dataset. For the veto pattern `all V`, it can be seen that for the eleven planned lead absorber layers between V1 and V2, an improved veto response probability of $(4.70 \pm 0.69) \times 10^{-4}$ is achieved, which is approximately a factor of 10 better compared to the result from Section 4.2.3. If the space for four more lead

absorber layers should be available, even values of $(3.00 \pm 1.73) \times 10^{-5}$ are possible. If needed, the exact numbers for $\epsilon_{\mathrm{V,all\,V}}$ can be found in Tab. B.7 in Appendix B.4.1.

4.3 Design Parameter Optimization

Using the figures of merit defined in Section 4.1.3, the optimization of the design parameters of the trigger veto system can be performed in a systematic manner. Since some of the design parameters need to be fixed before several others can be optimized, the studies presented in this section are conducted in the following order.

First, the design parameters of the trigger layer, i.e. the number of trigger scintillators and their length, are optimized by minimizing the difference of the trigger response probability for the trigger layer T, i.e. $1 - \epsilon_{\mathrm{T,T}}$, for 105 MeV electrons with the angular distributions shown in Section 4.2.1. By this, the trigger layer gets large enough to accept all incident particles coming through the TPC exit window, setting the geometric acceptance of the trigger layer as close to 100 % as possible. Note that with the sole focus on geometric acceptance, the outcomes of this optimization are equally applicable to electrons of lower energy.

Subsequently, the difference of the trigger response probability for the veto layer V3, i.e. $1 - \epsilon_{\mathrm{T,V3}}$, is minimized for the optimization of the design parameters of the veto layers, i.e. their length and width. For this, 1 GeV muons are used and the lead absorber layers between the veto layers, as well as the steel sheets underneath the veto and lead absorber layers, are included in the simulation. This results in the veto layer V3 being large enough to respond to all incident particles hitting the trigger veto system from the direction of the TPC, hence maximizing its geometric acceptance. Since all three veto layers will have the same dimensions, this step includes maximizing the geometric acceptances of V1 and V2.

Finally, the minimization of the veto response probability for the pattern `all V`, i.e. $\epsilon_{\mathrm{V,all\,V}}$, represents the optimization of the design parameters of the lead absorber layers, i.e. their length and width. Using 105 MeV electrons, the lead absorber layers become as small as possible without increasing the false electron rejection. Note that the use of 105 MeV electrons represents the worst case scenario for the veto system as no higher beam energies will be available for MAGIX in the near future. For lower energy electrons, even lower values for the false electron rejection will be achieved, as it is more likely that the electrons will be stopped inside the lead absorber layers.

For all of the above steps, the minimization goal is to bring the respective figure of merit below 10^{-3}. This value represents the anticipated statistical uncertainty in the form factor measurement discussed in Section 1.2, which, at the time of writing this thesis, is the experiment planned at MAGIX with the highest precision requirements. Thus, to avoid being the limiting factor in future experiments, the trigger and veto efficiencies should be closer to 100 % as this value. Moreover,

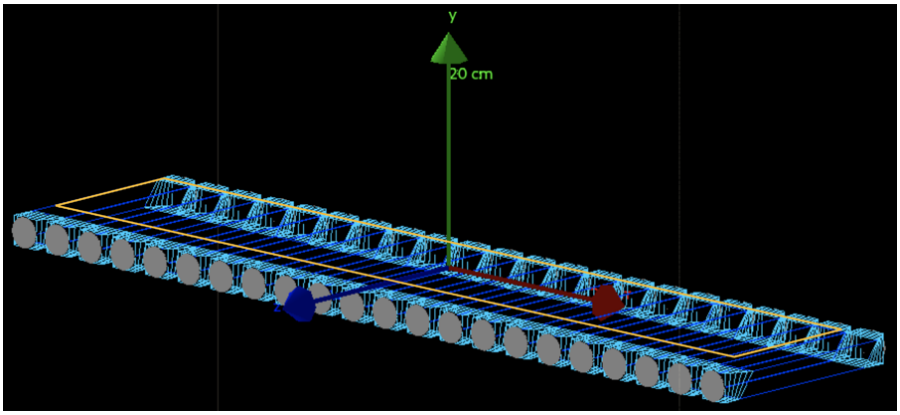

FIGURE 4.8. Only the TPC exit window and the trigger layer are loaded into `Geant4` for optimizing the design parameters of the trigger layer.

the second requirement regarding the trigger and veto efficiencies is their uniform distribution across the individual detector layers.

4.3.1 Optimization for the Trigger Layer

The number of trigger scintillators and their length are the two design parameters of the trigger layer. Since the trigger scintillators are placed side by side along the dispersive direction of the spectrometer, their number defines the dimension of the trigger layer along the x-axis. Analogously, the length of the trigger scintillators defines the dimension of the trigger layer along the non-dispersive direction of the spectrometer, i.e. the z-axis. Anyway, optimizing these two design parameters means choosing them large enough, so that all incident particles exiting the TPC window are geometrically accepted by the trigger layer. To quantify this, only the TPC exit window and the trigger layer are loaded into `Geant4`, see Fig. 4.8, where the `Geant4` world volume[11] is set to 90 cm × 150 cm × 40 cm (xyz) and the gap along the x-axis between two trigger scintillators is set to 0.5 mm. The number of trigger scintillators and their length are then varied one after the other, while the other parameter is kept constant.

In the first step, the number of trigger scintillators is varied between 15 and 24, which corresponds to a trigger layer width between 562.0 mm and 890.5 mm, and a plateau for $1-\epsilon_{\mathrm{T,T}}$ is searched for. The length of the trigger scintillators is fixed to 300 mm, which easily covers the TPC exit window along the z-axis, and 100,000 electron events with an energy of 105 MeV are simulated for each dataset. The results are shown in Fig. 4.9. As expected, $1-\epsilon_{\mathrm{T,T}}$ decreases with an increasing number of trigger scintillators, as a larger and larger fraction of the TPC exit window is covered by the trigger layer. The minimum is reached for 21 trigger scintillators, which corresponds to a trigger layer width of 781.0 mm, covering the whole TPC exit window along the x-axis. The goal

[11] The concept of the `Geant4` world volume is described in Appendix B.1.

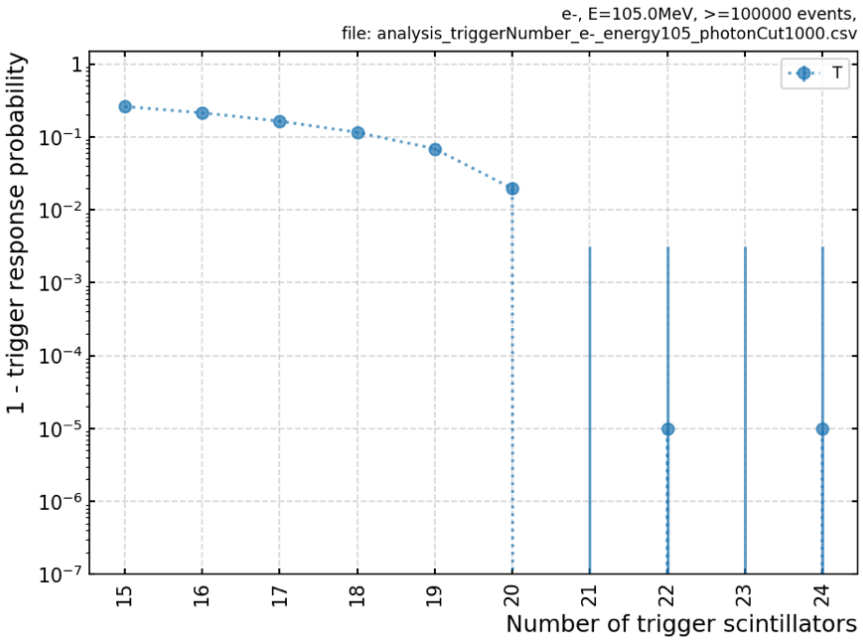

FIGURE 4.9. The number of trigger scintillators is varied between 15 and 24, while the scintillator length is fixed to 300 mm. The minimum for $1-\epsilon_{T,T}$ is reached for 21 trigger scintillators, which corresponds to a trigger layer width of 781 mm.

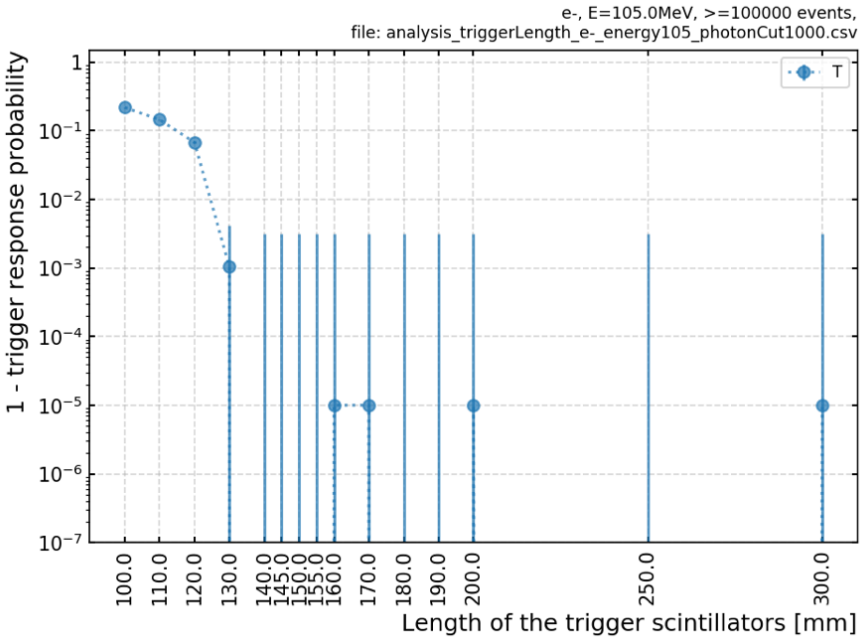

FIGURE 4.10. The number of trigger scintillators is fixed to 22 and their length is varied from 100 mm to 300 mm. $1-\epsilon_{T,T}$ reaches its minimum for a scintillator length of 140 mm.

of 10^{-3} is met. If you are interested in the exact numbers to Fig. 4.9, please refer to Tab. B.8 in Appendix B.4.2. In addition to the values for $1-\epsilon_{\mathrm{T,T}}$, also the values for $\epsilon_{\mathrm{T,T}}$ and $\Delta\epsilon_{\mathrm{T,T}}$ are listed.

Next, the trigger scintillator length is varied between 100 mm and 300 mm. The number of trigger scintillators is fixed to 22 and again, 100,000 electron events with an energy of 105 MeV are simulated for each dataset. Fig. 4.10 shows the results. As with varying the number of trigger scintillators, $1-\epsilon_{\mathrm{T,T}}$ decreases as the length of the trigger scintillators is increased. This can again be explained by the larger and larger fraction of the TPC exit window that is covered as the length of the trigger scintillators is increased. The minimum is reached for a length of 140 mm, which is reasonable, given the dimension of the TPC exit window of 130 mm along the z-axis. Again, the goal of 10^{-3} is reached and the exact numbers to Fig. 4.10 can be found in Tab. B.9 in Appendix B.4.2.

4.3.2 Optimization for the Veto Layers

The design parameters of the veto layers are their length along the dispersive direction, i.e. the x-axis, and their width along the non-dispersive direction, i.e. the z-axis. As with the trigger layer, the goal is to choose these parameters large enough so that all incident particles coming from the TPC can geometrically be detected inside the veto layers. Since all three veto layers will have the same dimensions and the veto layer V3 is the furthest away from the trigger layer, maximizing the geometric acceptance of V3 automatically includes doing the same for V1 and V2. Thus, $1-\epsilon_{\mathrm{T,V3}}$ is the chosen figure of merit for the optimization of the dimensions of the veto layers.

Fig. 4.11 illustrates how the trigger veto system is implemented in `Geant4` for this purpose. The world volume is changed to 150 cm × 100 cm × 100 cm (xyz) and the trigger layer is modeled as 22 trigger scintillators, each with a length of 150 mm. The lead absorber layers and the steel sheets are implemented, where the lead absorber layers are enlarged to an area of 1200 mm × 500 mm to ensure that no secondary particles are able to yield a signal in one of the veto layers by reentering the trigger veto system from one of the sides. As incident particles, muons with an energy of 1 GeV are used[12], a representative energy of the cosmogenic muon spectrum [102]. For each dataset, 100,000 events are simulated and both design parameters are varied one after the other, while the other one is kept constant.

The length of the veto layers is varied first. Since the TPC exit window is 768 mm long along the x-axis and the maximal available space in this direction is approximately 1000 mm, the length of the veto layers is varied between 600 mm and 1000 mm. The width of the veto layers is fixed to 500 mm. The results are shown in Fig. 4.12. As expected, the trigger response probabilities for the individual veto layers increase with increasing veto layer length, because a larger and larger fraction of the simulated particles yield signals inside the veto layers. Since the veto layer

[12] Other muon energies have been simulated as well, but for a better readability of this chapter, the results have been outsourced to Appendix B.4.3.

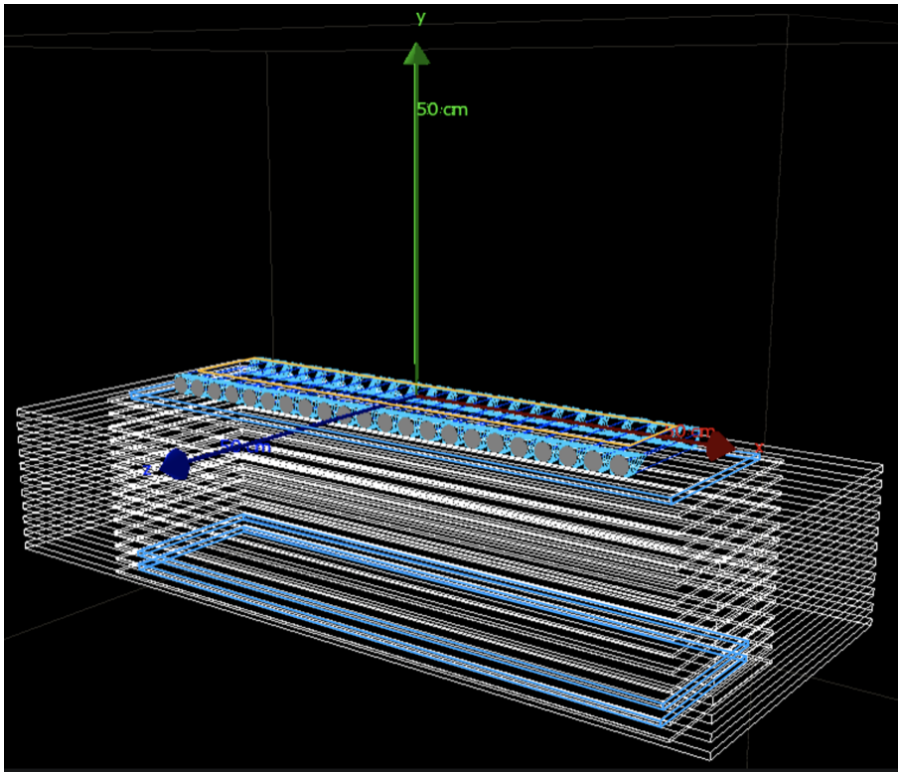

FIGURE 4.11. For optimizing the veto layer dimensions, the complete trigger veto system is implemented in `Geant4`. The steel sheets are used and the lead absorber layers are enlarged.

V1 is placed directly beneath the trigger layer, $1-\epsilon_{\mathrm{T,V1}}$ and $1-\epsilon_{\mathrm{T,T\&\&V1}}$ reach the minimum already for a veto layer length of 800 mm, where the length of the TPC exit window is just exceeded. In contrast, $1-\epsilon_{\mathrm{T,V2}}$ and $1-\epsilon_{\mathrm{T,V3}}$ decrease with increasing veto layer length up until its highest value of 1000 mm, where the figure of merit of particular interest, i.e. $1-\epsilon_{\mathrm{T,V3}}$, falls below the goal of 10^{-3} for a veto layer length of 950 mm. The reason that a minimum is not reached is the fact that the 1 GeV muons do not pass the lead absorber layers unaffected but are subject to energy loss and thus multiple scattering. The muons can, dependent on their incident position and angle, therefore be scattered onto a path leaving the trigger veto system, which is exemplarily shown for the second veto layer V2 and a veto layer length of 950 mm in Fig. 4.13. Exactly those 1 GeV muons that are generated with a large negative dispersive angle close to the left edge of the TPC window are not able to reach the second veto layer.[13] However, with the decreased collimator acceptance in the final MAGIX setup, cf. Section 4.2.1, this effect will be notably reduced. Moreover, the positioning of the veto layers along the dispersive direction of the spectrometer does not necessarily need to be symmetrical with respect to the trigger layer and

[13]The impact of this effect is less significant for higher energy muons, as can be seen in Figs. B.8 and B.10 in Appendix B.4.3.

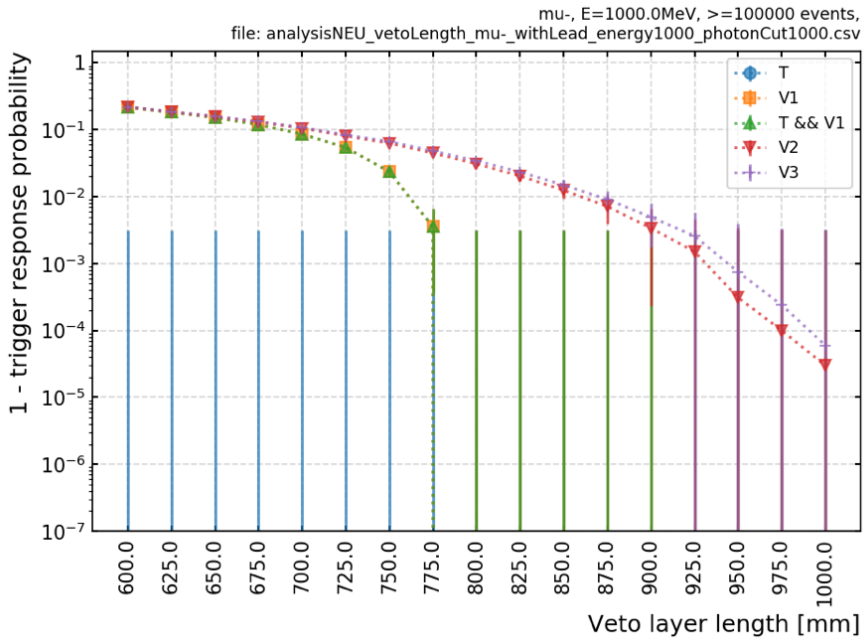

FIGURE 4.12. The veto layer length is varied from 600 mm to 1000 mm, while the width of the veto layers is fixed to 500 mm. $1-\epsilon_{\mathrm{T,V3}}$ steadily decreases with increasing veto layer length. From a length of 950 mm on, it lies below 10^{-3}.

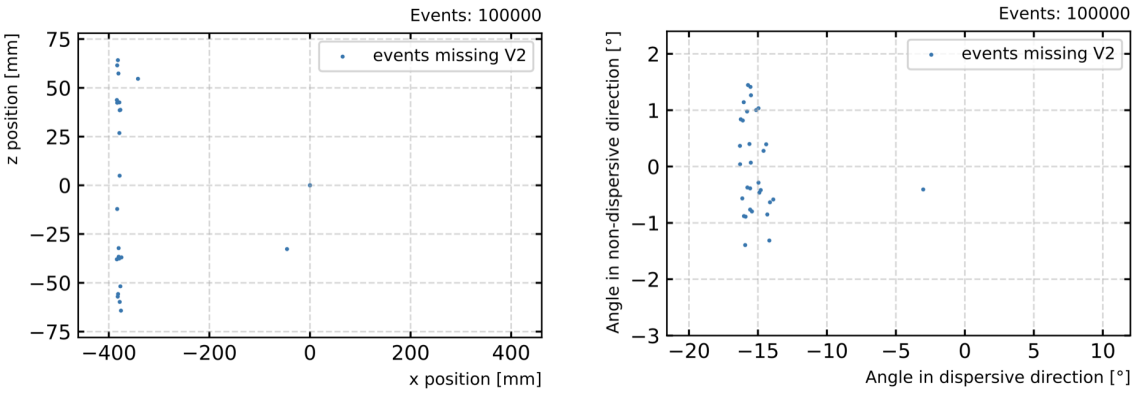

(a) (b)

FIGURE 4.13. The acceptance for 1 GeV muons with incident positions x and z (a), as well as incident angles in the dispersive and non-dispersive directions (b), is exemplarily shown for the second veto layer V2 and a veto layer length of 950 mm. As can be clearly seen, the muons that are generated with a large negative dispersive angle close to the left edge of the TPC window lie outside the acceptance.

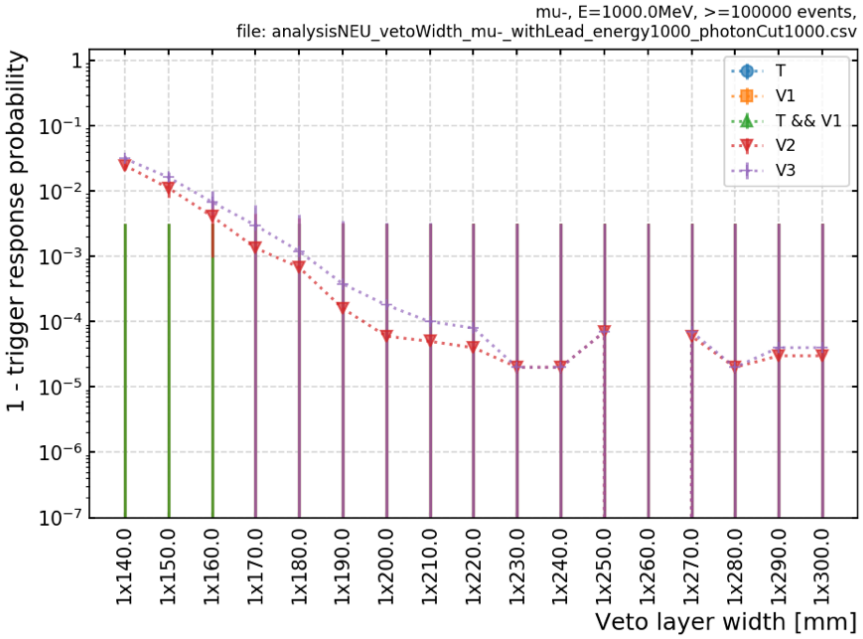

FIGURE 4.14. The width of the veto layers is varied between 150 mm and 300 mm with a fixed veto layer length of 1200 mm. $1-\epsilon_{T,V3}$ reaches its minimum for a width of 230 mm after falling below 10^{-3} for a width of 190 mm.

the TPC window. Instead, given the considerable negative shift in the angular distribution of the dispersive angle, cf. Section 4.2.1, the veto system can and will be shifted accordingly.

The second step is to vary the width of the veto layers between 150 mm and 300 mm, while their length is kept constant at 1200 mm. The lower value is chosen so that the veto layer V1 covers the complete trigger layer along the non-dispersive direction of the spectrometer and the higher value is chosen due to space constraints in the final MAGIX setup. The results are shown in Fig. 4.14. $1-\epsilon_{T,V1}$ and $1-\epsilon_{T,T\&\&V1}$ are at their minimum for all veto width values, since the width of 150 mm already covers the trigger layer at the position of V1. $1-\epsilon_{T,V2}$ and $1-\epsilon_{T,V3}$ decrease with increasing veto layer width as expected. The minimum is reached at around 230 mm, where the goal of 10^{-3} is exceeded by approximately one and a half orders of magnitude.

As with the studies for the trigger layer, the tables with the exact numbers to Figs. 4.12 and 4.14 can be found in Appendix B.4.3, i.e. Tabs. B.10 and B.11.[14]

4.3.3 Optimization for the Lead Absorber Layers

For optimizing the design parameters of the lead absorber layers, i.e. their length and width, the trigger veto system is loaded as shown in Fig. 4.15. The trigger layer is implemented as 22

[14]The plots and tables for the other muon energies are given there as well.

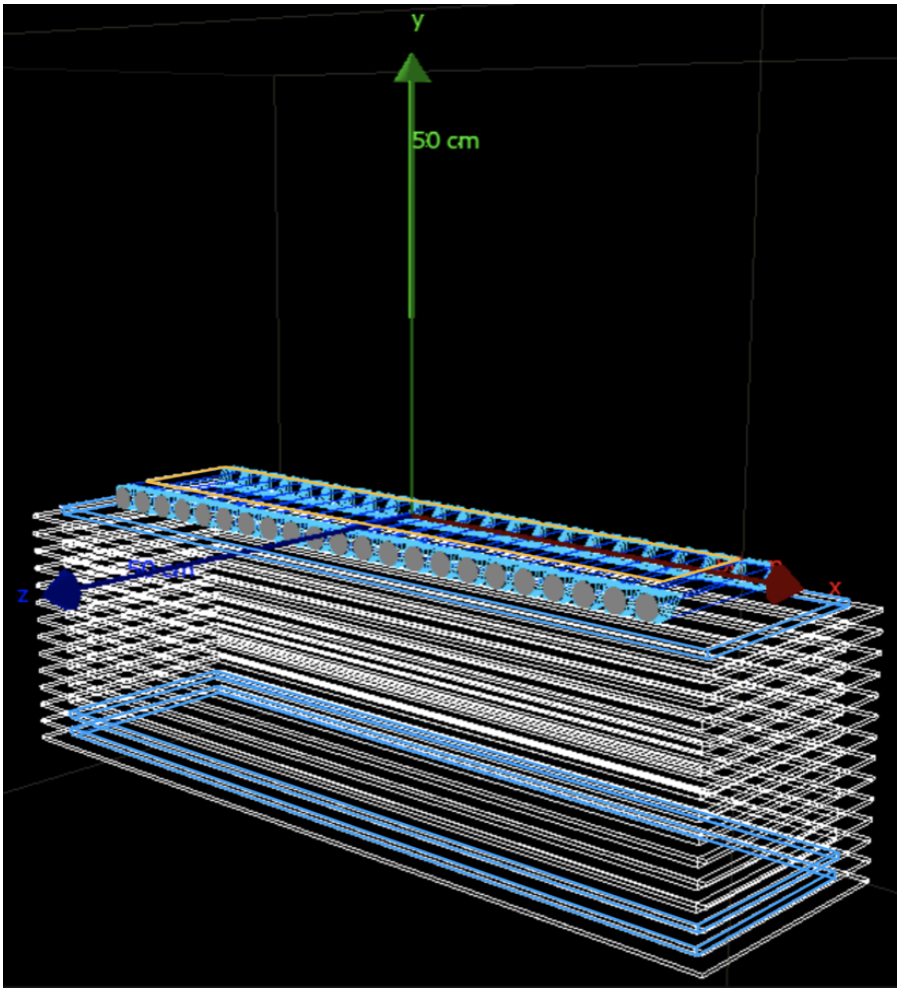

FIGURE 4.15. The model of the trigger veto system for the optimization of the design parameters of the lead absorber layers. The steel sheets are implemented and the dimensions of the lead absorber layers are varied.

150 mm long trigger scintillators and the dimensions of the veto layers are set to a length of 950 mm and a width of 250 mm. The `Geant4` world volume is set to 150 cm × 100 cm × 100 cm (xyz) and the steel sheets are implemented to support the individual veto and lead absorber layers. After optimizing the design parameters of the trigger and veto layers, the lead absorber layers should be dimensioned as small as possible without increasing the false electron rejection. Thus, the length and width of the lead absorber layers are varied one after the other, while the other is kept constant. For each dataset, 100,000 electrons with an energy of 105 MeV are simulated and the veto response probability for the veto pattern `all V`, i.e. $\epsilon_{\mathrm{V,all\,V}}$, is chosen as the figure of merit.

First, the length of the lead absorber layers along the dispersive direction of the spectrometer is varied between 1000 mm and 600 mm. As for the veto layers, these boundaries are chosen due to

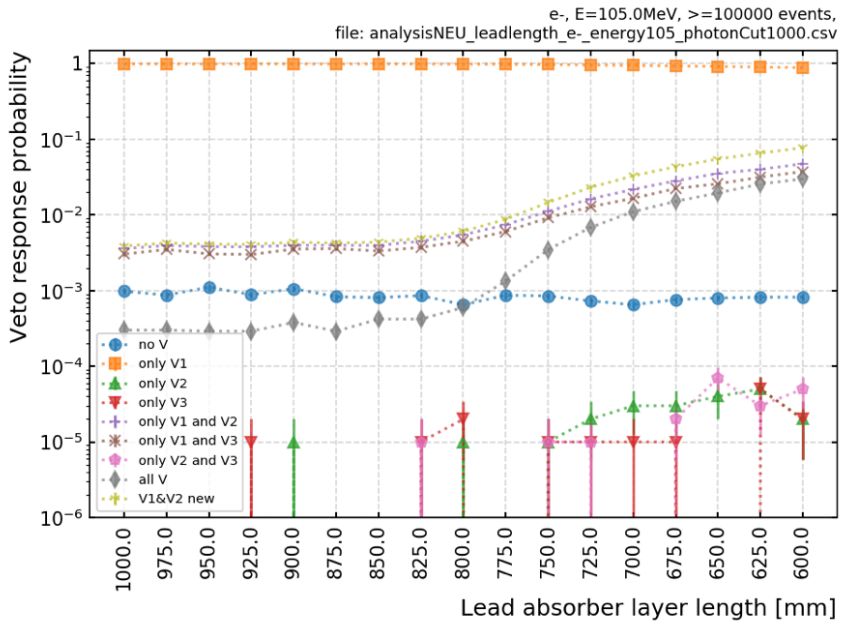

FIGURE 4.16. The length of the lead absorber layers is varied from 1000 mm to 600 mm. Their width is fixed to 280 mm. The minimum of $\epsilon_{\mathrm{V,all\,V}}$ can be held down to a length of around 850 mm. From a length of 775 mm on, the goal of 10^{-3} is not exceeded anymore.

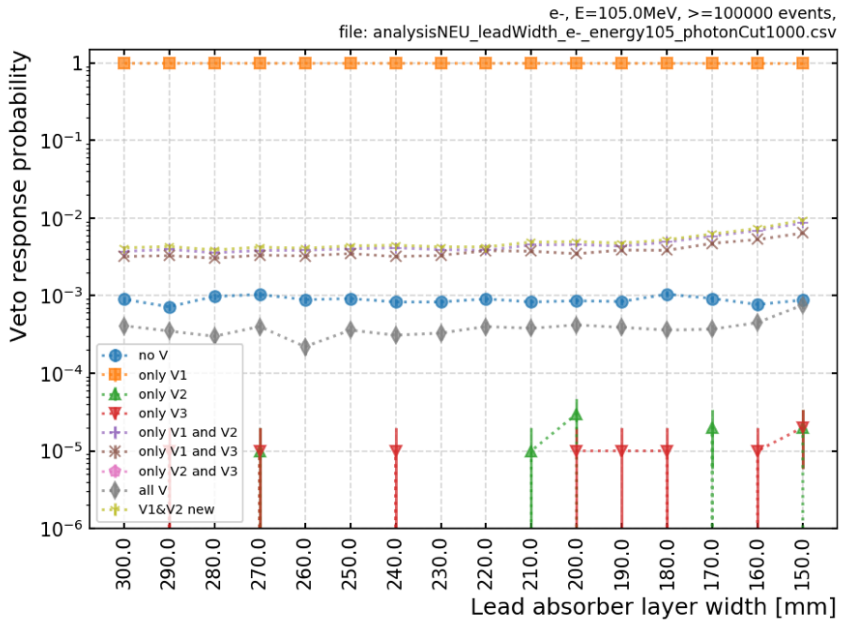

FIGURE 4.17. The length of the lead absorber layers is fixed to 1000 mm and their width is varied from 300 mm to 150 mm. From a width of 180 mm, the minimum of $\epsilon_{\mathrm{V,all\,V}}$ cannot be held anymore. The goal of 10^{-3} is achieved for all width values.

the maximal available space and the dimensions of the TPC exit window. The width of the lead absorber layers is fixed to 280 mm and the results are shown in Fig. 4.16. As expected, at some point $\epsilon_{\mathrm{V,all\,V}}$ increases as the length of the lead absorber layers is decreased, since the layers are less and less able to stop the electrons between the veto layers V1 and V2. The minimum for $\epsilon_{\mathrm{V,all\,V}}$ can be held down to a length of between 850 mm and 900 mm, and from a length of 775 mm, the goal of 10^{-3} is not achieved anymore. The exact numbers to Fig. 4.16 can be found in Tab. B.20 in Appendix B.4.4.

Fig. 4.17 shows the results for varying the width of the lead absorber layers from 300 mm to 150 mm, while the length of the layers is fixed to 1000 mm. The behaviour of $\epsilon_{\mathrm{V,all\,V}}$ is again a slight increase as the width of the lead absorber layers is increased. The minimum is held down to a width of 180 mm, while the goal of 10^{-3} is achieved for all width values. The exact numbers to Fig. 4.17 are given in Tab. B.21 in Appendix B.4.4.

4.3.4 Summary and Conclusions from the Optimization Studies

In the previous sections, the simulation studies for the MAGIX trigger veto system using `Geant4` have been presented. One after the other, the design parameters of the trigger layer, the veto layers, and the lead absorber layers have been varied and the corresponding figure of merits have been optimized. In the following, the most important results of the simulation and the decisions that have been made based on these results shall be summarized. An even more condensed summary can be found in Tab. 4.11.

For the trigger layer, the design parameters are the number of scintillators as well as their length, determining the dimensions of the trigger layer in the dispersive and non-dispersive directions of the spectrometer, respectively. The chosen figure of merit, i.e. $1-\epsilon_{\mathrm{T,T}}$, is minimized for scintillator numbers of ≥ 21 and scintillator lengths of ≥ 140 mm. For both parameters, $1-\epsilon_{\mathrm{T,T}}$ reaches 10^{-5}, which is the best quantification possible, given that only 100,000 events have been simulated for each dataset. The set goal of 10^{-3} is therefore exceeded by two orders of magnitude.
Based on these results, it has been decided to use 22 scintillators per trigger layer, each with a length of 150 mm. The number 22 has been chosen so that the trigger layer acceptance in the dispersive direction ranges from center to center of the two outermost trigger scintillators, rather than from edge to edge, in which case not the entire scintillator thickness would be available at the acceptance boundaries due to the rhombic profile of the trigger scintillators. The length of 150 mm along the non-dispersive direction has been chosen to include some safety margin between the trigger layer acceptance and the light guides coupled to the trigger scintillators. Subsequently, a total of 50 trigger scintillators has been ordered, of which 22 will be incorporated into the final MAGIX setup per spectrometer and six will serve as spare parts.

The design parameters of the veto layers are their length along the dispersive direction and their width along the non-dispersive direction of the spectrometer. $1-\epsilon_{\mathrm{T,V3}}$ has been chosen as the figure of merit, which steadily decreases with increasing veto layer length down to a value of

Design parameter	**Possible range**	**Final agreed on value**
Number of trigger scintillators along x	≥ 21	22
Length of the trigger scintillators along z	140 mm to 300 mm	150 mm
Veto layer length along x	950 mm to 1000 mm	950 mm
Veto layer width along z	230 mm to 300 mm	250 mm
Lead absorber layer length along x	850 mm to 1000 mm	950 mm
Lead absorber layer width along z	180 mm to 300 mm	250 mm

TABLE 4.11. Summary of the design parameter optimizations. The possible parameter ranges for the design parameters are given, together with their final agreed on values.

6×10^{-5} for a length of 1000 mm. The set goal of 10^{-3} is exceeded for lengths ≥ 950 mm. When varying the width of the veto layers, $1 - \epsilon_{\mathrm{T,V3}}$ reaches its minimum in the 10^{-5} region for widths of ≥ 230 mm. The set goal of 10^{-3} is exceeded for widths ≥ 190 mm.
As a consequence, the length of the veto layers has been set to 950 mm, which gives enough space along the dispersive direction of the spectrometer for the readout of the veto layers as well as for mounting the frames of the drawers, in which the layers of the veto system will be placed. As described in Chapter 3, the veto layers will be segmented along the non-dispersive direction into three individual scintillators in order to allow for additional spatial resolution along this direction. Each of the segments will have a rhombic profile with a height of 10 mm and an interior angle of 60°. Based on the simulation results, the base length of the rhombus has been set to 85 mm. Accounting for a gap of 0.5 mm between the segments, this results in a veto layer width of 256 mm. In the following, 24 of these scintillator segments have been ordered, which is equivalent to eight complete veto layers. Three of these will be installed per spectrometer in the final MAGIX setup and two will be kept as a reserve.

The length and width along the dispersive and non-dispersive directions of the spectrometer, respectively, are the design parameters of the lead absorber layers. The chosen figure of merit has been $\epsilon_{\mathrm{V,all\,V}}$, which holds its minimum in the 10^{-4} region for lengths ≥ 850 mm and widths ≥ 180 mm. The set goal of 10^{-3} is exceeded for length values of ≥ 800 and all tested width values from 150 mm to 300 mm.
Although the results allow for even smaller lead absorber layers, it has been decided to dimension the lead absorber layers in the same way as the veto layers. Thus, the length has been set to 950 mm and the width to 250 mm. By this, it is ensured that the veto layers are additionally shielded against background particles from the exterior of the trigger veto system. In the following, 24 lead absorber layers have been ordered in total. Per spectrometer, eleven of these will be installed in the final MAGIX setup and the remaining two are kept as a reserve[15].

[15] At a later point, the space limitations for assembling the trigger veto system turned out to be not as critical as expected. Therefore, the number of lead absorber layers per spectrometer could be increased to 15 so that six additional layers were ordered. Thus, 30 lead absorber layers are available, 15 of which will be installed per spectrometer in the

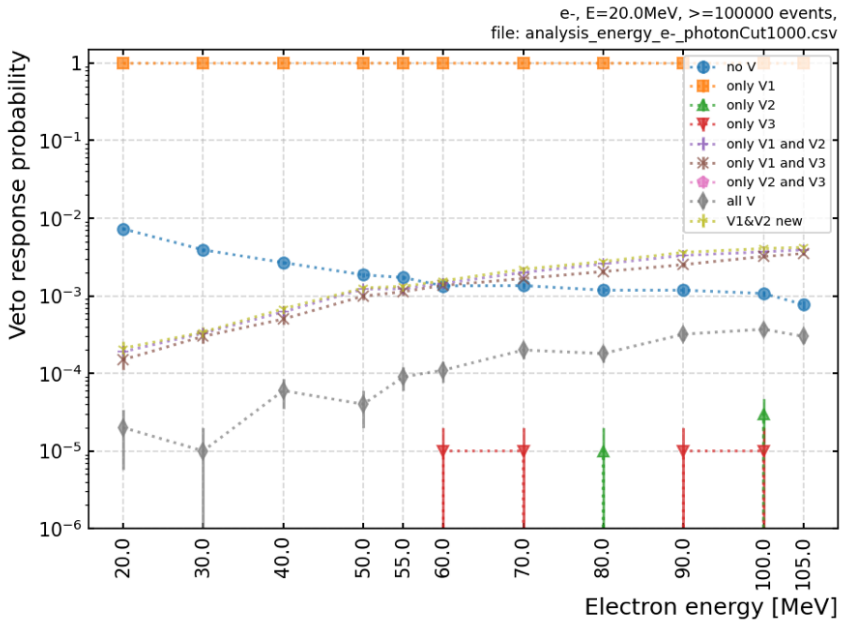

FIGURE 4.18. The individual veto response probabilities against the electron energy.

With respect to the final MAGIX setup, one additional study has been performed. As mentioned before, the use of 105 MeV electrons for the optimization of the design parameters represents the most challenging scenario for the veto system as it will occur at MAGIX. If the requirements for the false electron rejection are met under this extreme circumstance, they must also apply to electrons with lower energies. Nevertheless, to gain insight into the performance of the veto system, electrons with different energies in the MESA beam energy range that will be available for MAGIX, i.e. from 20 MeV to 105 MeV, are simulated using the final decided upon values for the design parameters of the trigger veto system. For each dataset, 100,000 electrons are generated and the veto response probability for the veto pattern `all V`, i.e. $\epsilon_{\mathrm{V,all\,V}}$, is chosen as the figure of merit. The results are shown in Fig. 4.18. As expected, the behaviour of $\epsilon_{\mathrm{V,all\,V}}$ features a slight, continuous increase within the error bars as the electron energy is increased. While for 105 MeV electrons, $\epsilon_{\mathrm{V,all\,V}}$ amounts to $(3.00 \pm 0.55) \times 10^{-4}$, it decreases to $(2.00 \pm 1.41) \times 10^{-5}$ for 20 MeV electrons. Please note that these values for $\epsilon_{\mathrm{V,all\,V}}$ are once more rather conservative due to the low chosen value of 1000 for the variable *Photon cut*. The exact numbers to Fig. 4.18 are given in Tab. B.22 in Appendix B.4.5.

final setup of MAGIX. No layers are stored as a reserve.

CHAPTER 5

DESIGN AND DEVELOPMENT OF THE TRIGGER LAYER

During the simulation studies in Chapter 4, the basic design parameters of the MAGIX trigger veto system have been finalized. However, many concrete questions like "What PMT model to use for the trigger detectors?" or "How to mount the trigger veto system inside the shielding house?" remain open. During the course of this and the following chapter, answers to such hardware questions shall be given, resulting in a fully developed and ready-to-build design of the trigger veto system. For clarity reasons, the design and development process has been divided into two parts, with this chapter covering the trigger layer and the subsequent one, Chapter 6, dealing with the veto system. The readout and analysis parts of the trigger veto system will then be discussed in Chapters 7 and 8, respectively, including the extraction of essential detector properties for the trigger detectors.

At this stage, the trigger layer is built from 22 plastic scintillation detectors, which are placed next to each other along the dispersive direction of the spectrometer. The scintillators are 150 mm long bars with a rhombic profile, cf. Chapter 3, and each bar is read out coincidentally by two PMTs, using light guides in between. However, this amount of information is obviously not sufficient to actually build the trigger layer and install it inside the shielding house. The following sections therefore explain the individual components of the trigger detectors, the slow control and readout electronics for the trigger layer, as well as its mounting. Please note that a basic knowledge of scintillation detectors is assumed and a theoretical overview is not provided at this point. Detailed descriptions of scintillation detectors can be found e.g. in Refs. [105, 101, 106, 107].

5.1 The Trigger Detectors

5.1.1 PMTs

The PMTs of the trigger layer are from the model R1924A-03 by Hamamatsu [108], see Fig. 5.1a, where the suffix "-03" denotes the variant with an integrated 0.2 mm thick magnetic shield, as well as Hamamatsu's "HA treatment". The PMTs have a stated diameter of 25.4 mm (1 inch) with a housing diameter of 26.2 mm and an effective photocathode area of 22.0 mm. Their entry windows are made from borosilicate glass with a refractive index of approximately 1.5[1] and their spectral response ranges from 300 nm to 650 nm with a maximum at 420 nm. The quantum efficiency at this peak wavelength is 26 %. The PMTs' time response is comparably fast with an anode pulse rise time of 1.5 ns, an electron transit time of 17 ns, and a transit time spread of 0.9 ns. The PMTs employ a cascade of 10 dynodes and provide a gain of 2.0×10^6 for a supply voltage of −1000 V between cathode and anode. The PMTs are therefore operated in the anode grounding scheme, where the anode is grounded and a high negative voltage is applied to the cathode. A supply voltage of −1250 V should not be exceeded. Operating the PMTs in the cathode grounding scheme, i.e. grounding the cathode and applying a high positive voltage to the anode, has been discussed but not pursued any further. The anode grounding scheme has the great advantage that it eliminates the potential difference between an PMT's anode and the external circuit. Additionally, baseline shifts may occur for high counting rates if the PMTs are operated in the cathode grounding scheme [109]. The output signals of the PMTs have negative polarity.

High-voltage sockets of the model C13003-01 by Hamamatsu [110], see Fig. 5.1b, are used in combination with the PMTs. These include a high-voltage power supply and thus allow the operation of the PMTs by applying a low supply voltage of only +15 V. This allows for the omission of bulky, cumbersome high-voltage cables and connectors and therefore saves valuable space inside the shielding house. Besides, the sockets enable fast voltage programming by upscaling a separately applied control voltage in the range from 0 V to +5 V by a factor of −250 to the required negative supply voltage between a PMT's cathode and anode. The typical response time after a change in control voltage is 80 ms. The signal cables of the sockets are equipped with SMA[2] connectors[3] - the decision to use SMA connectors instead of BNC[4] connectors has been made due to their smaller size and higher frequency range - and the four power supply cables for voltage programming (1× control voltage, 1× supply voltage, 2× ground) are combined into 4-pin connectors[5], see Fig. 5.1c. Besides voltage programming, the sockets can be operated by resistance programming, where a variable resistor is used to adjust the control voltage. For this, the sockets provide a fifth, blue cable, which is permanently connected to the reference voltage

[1] Unfortunately, even when asked, Hamamatsu does not provide any more detailed information on this.
[2] **S**ub**M**iniature version **A**
[3] Telegärtner SMA Straight Plug J01150A0011
[4] **B**ayonet **N**eill-**C**oncelman
[5] 3M Mini Clamp II Plug 37104-B122-00E MB

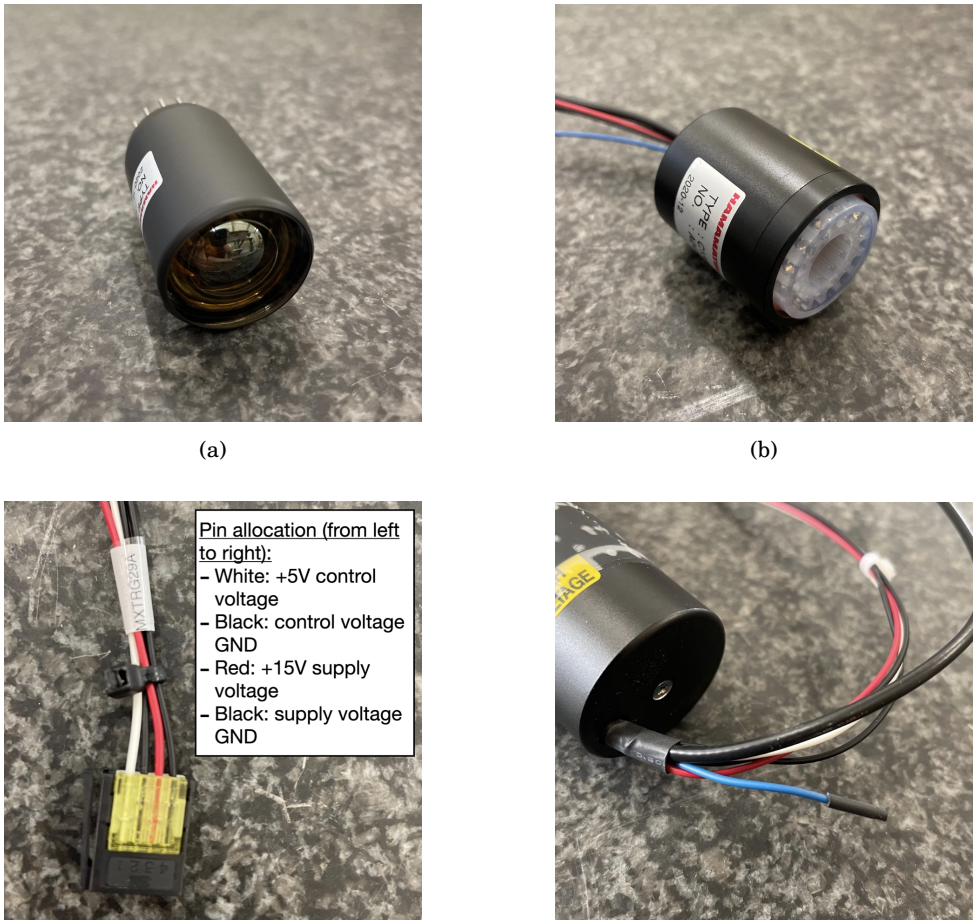

(a) (b) (c) (d)

FIGURE 5.1. The trigger detectors are read out by Hamamatsu's R1924A-03 PMTs (a), which are operated with the corresponding high-voltage sockets C13003-01 (b). The four cables for voltage programming are combined in a 4-pin connector (c) and the additional blue cable for resistance programming is shortened and insulated (d).

of +5 V. But since these are not employed for the trigger detectors of MAGIX, they have been shortened and insulated, see Fig. 5.1d.

One important question that had to be answered is whether to use the PMTs with an integrated magnetic shield or not. Without special precautions, a PMT is very sensitive to an external magnetic field since it easily disturbs the electron transit inside the PMT. Already a small magnetic field of 1 mT is sufficient to massively disturb the PMT's gain process [109]. Although the magnetic fields of the MAGIX spectrometers rapidly decrease in strength towards their focal planes, cf. Fig. 2.14a, it cannot be ruled out that small magnetic field tails of a few μT or even mT will still be present in the region of the trigger layer. In this scenario, modifying the magnetic fields of the spectrometers, e.g. when changing the experimental setting of MAGIX during a measurement period, could lead to alterations in the gains of the PMTs, consequently affecting

the effective thresholds of the trigger layer readout channels and thus the overall efficiency of the trigger layer. A high-precision experiment would therefore suffer tremendously under such an effect. For this reason, the behaviour of the PMTs under the influence of a weak magnetic field has been studied in more detail, which will be the topic of the coming paragraphs.

Tested PMT Models and Magnetic Shields Two PMT models have been compared to each other: the Hamamatsu R1924A [111] and the Hamamatsu R1924A-03 [108].[6] The most important parameters of both models have already been discussed above, since the only difference between the two are the magnetic shield and Hamamatsu's "HA treatment" incorporated into the R1924A-03.

The integrated magnetic shield has a thickness of 0.2 mm and is made from a permalloy with a high relative magnetic permeability in the 10^5 range. Unfortunately, Hamamatsu does not further specify its composition.

The "HA treatment" covers the outside of the glass bulb of the PMT with conductive black paint that is connected to the cathode potential, which is a technique that proves beneficial for PMTs operated in the anode grounding scheme [109]. In this scheme, if some grounded component is brought near the glass bulb of the PMT or even makes contact with it, the electrons inside the PMT are attracted by the ground potential, deviate from their actual transit path, and strike the inner wall of the bulb. This may produce a glass scintillation and, as a result, a significant increase in noise. The "HA treatment" compensates for this effect by repelling the electrons from the inner wall of the bulb, thus drastically decreasing the noise level. Since now a negative high voltage is applied to the outside of the glass bulb, the whole PMT should be covered with an insulating layer for safety, typically a heat-shrinkable tube. Of course, the introduction of these additional layers increases the diameter of the PMT, which is why the R1924A-03 has a housing diameter of 26.2 mm compared to the 25.4 mm of the R1924A.

In addition to the two PMT models, a mu-metal cylinder with a thickness of 1 mm has been used for the comparison of the integrated magnetic shield of the R1924A-03 with a separate outer one, and beyond that, whether a second magnetic shield could prove advantageous. In total, the following four combinations have been tested:

- Combination A: Hamamatsu R1924A without any magnetic shield
- Combination B: Hamamatsu R1924A with the outer mu-metal cylinder
- Combination C: R1924A-03 with its incorporated magnetic shield
- Combination D: R1924A-03 plus the outer mu-metal cylinder.

[6] These two models are the pre-selection based on previous laboratory measurements that are not part of this thesis.

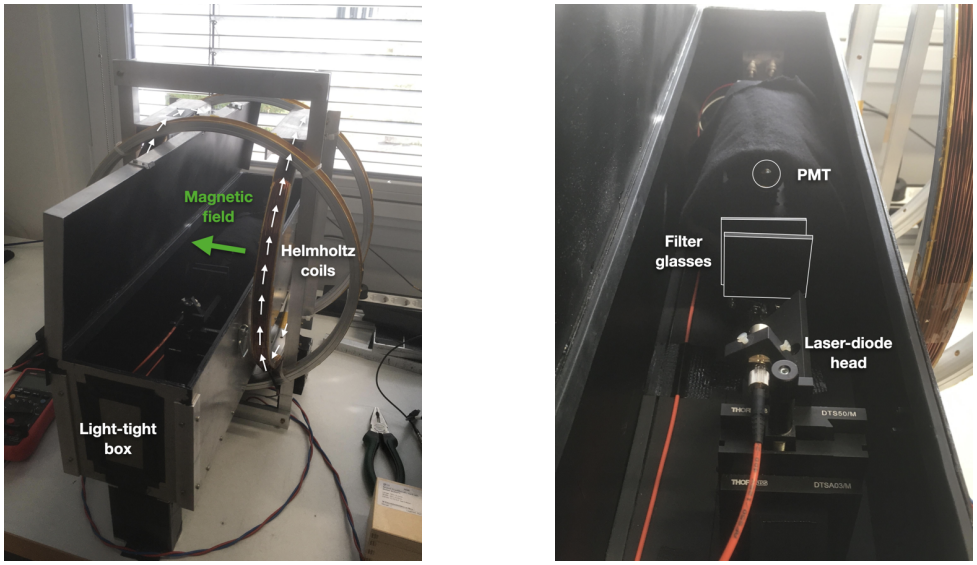

(a) (b)

FIGURE 5.2. Magnetic field tests for the trigger PMTs. The combination being tested is placed at the center of a pair of Helmholtz coils (a), where the magnetic field lines run in parallel to the indicated large green arrow. The second pair of coils is not used. PMT signals are obtained using a pulsed light source with a laser-diode head shooting at the photocathode and reducing its intensity with the help of optical filter glasses (b).

Setup for the Magnetic Field Tests The setup that has been used for the magnetic field tests is shown in Fig. 5.2. A pair of Helmholtz coils, which is designed for fields just above 2 mT, see Fig. 5.2a, generates a nearly uniform magnetic field at the position of the combination being tested. Positioned at the center of the coil pair, the combination is placed inside a light-tight box, whose long side aligns with the tube axis of the PMT. Both coils are powered by an equal electric current, which is chosen to circulate as indicated by the small white arrows. The magnetic field lines therefore align in the direction indicated by the large green arrow and thus are perpendicular to the PMT tube axis.[7] The direction of the field lines is defined as the z-direction with $z = 0$ being the center of the coil pair. Each coil has 120 turns and a radius of $R = 9.5\,\text{cm}$ with a distance between the coils of 19 cm. The coils are therefore positioned at $z = \pm R$.

The magnetic field $\vec{B}$ is tuned by adjusting the amount of current I flowing through the coils following

$$\vec{B}(z) = \frac{\mu_0 N I}{2}\left(\frac{R^2}{\left(R^2+\left(z+\frac{R}{2}\right)^2\right)^{\frac{3}{2}}}+\frac{R^2}{\left(R^2+\left(z-\frac{R}{2}\right)^2\right)^{\frac{3}{2}}}\right)\vec{e}_z, \tag{5.1}$$

[7] One could also test the influence of a magnetic field, whose field lines run in parallel to the PMT tube axis. However, according to [109], the effects of such fields can hardly be counteracted anyway. This residual risk is therefore tolerated for MAGIX.

where μ_0 is the permeability of the vacuum, N is the number of coil turns, R is the radius of the coils, and $\vec{e}_z$ is the unit vector along the direction of the field lines [112]. At the position of the PMT ($z = 0$) and ignoring the direction of the magnetic field, Eq. 5.1 simplifies to

$$B(0) = \frac{\mu_0 N I}{2} \left(\frac{2R^2}{\left(\frac{5}{4}R^2\right)^{\frac{3}{2}}} \right),$$

which results in

$$B(0) = 567.85 \times 10^{-6} \, \frac{\mathrm{N}}{\mathrm{A^2 m}} \times I$$

when the numbers for the above setup are used ($\mu_0 = 1.257\,\mathrm{N\,A^{-2}\,m^{-1}}$, $N = 120$, and $R = 0.095\,\mathrm{m}$). However, the even simpler form

$$B(0)\,[\mathrm{mT}] = 0.568 \times I\,[\mathrm{A}] \tag{5.2}$$

can been used, where the set current is inserted in A and the resulting magnetic field is given in mT. In fact, after Eq. 5.2 had been checked and verified with a Foerster probe, it has been used to obtain the magnetic field strength at the position of the PMT throughout the tests in this section.

To generate signals inside the PMT being tested, a pulsed light source[8] with an adjustable pulse rate between 1 Hz and 1 MHz is used. The utilized laser-diode head is from the model N-635L with a stated wavelength of 633 nm, a typical pulse width of < 200 ps, and a typical power of 18 pJ per pulse. To reduce and vary the intensity of the laser light impinging on the photocathode of the PMT even further, a set of 50 mm × 50 mm filter glass sheets in different optical densities[9] from the material NG9 by Schott [114] is available. The resulting rate of photons impinging on the photocathode of the PMT therefore depends on the pulse rate of the laser and the choice of filter glasses. A closer look on the setup inside the light-tight box is given in Fig. 5.2b. For the tests in this section, the pulse rate of the laser is set to 5 kHz and two filter glasses are combined to obtain an optical density of 4. The PMT signals are read out using a 5 GS/s digitizer[10] with a dynamic range of 1 Vpp.

Altering the Magnetic Field Strength For investigating the effects of different magnetic field strengths, the current through the Helmholtz coils is varied between 0.0 A and approximately 3.8 A, representing magnetic field strengths between 0.00 mT and 2.16 mT following Eq. 5.2. The control voltage of the PMT being tested is set to 4.0 V, which corresponds to a supply voltage of −1000 V between the PMT's cathode and anode. The PMT is rotated such that the cable exit

[8] HORIBA JOBIN YVON NanoLED

[9] Optical density (OD), also denoted as absorbance A, is a logarithmic measure of the attenuation experienced by light as it passes through matter. It can be calculated by $\mathrm{OD} = -\log_{10}(I/I_0)$, where I_0 is the intensity of the light before the passage and I is the intensity of the light after the passage. The ratio I/I_0 is also termed the transmittance τ or T, which describes the light's linear attenuation. An optical density of 1 therefore means the attenuation to a tenth, an optical density of 2 means the attenuation to a hundredth, and so on. [113]

[10] CAEN V1742

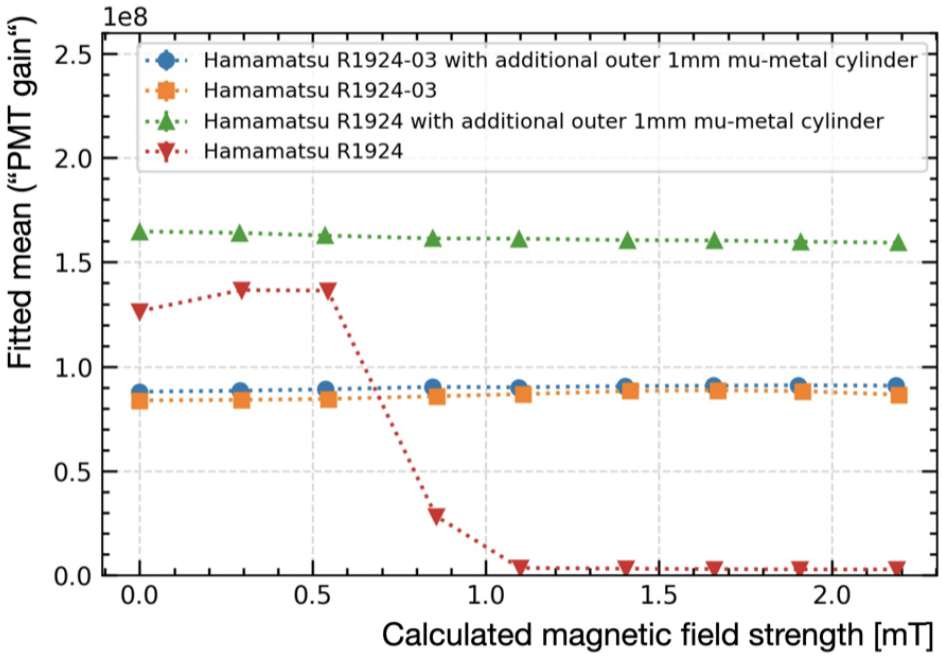

FIGURE 5.3. The fitted mean values of the "PMT gain" distributions are plotted against the magnetic field strength. The drop for combination A (red down pointing triangles) shows that some sort of magnetic shield must be used for the PMTs of the trigger layer.

of the high-voltage socket points upwards, which is defined as an orientation of 0° and will be important for the coming paragraph.

For each magnetic field strength, 3 min of data are collected to accumulate a meaningful amount of statistics. For each recorded PMT pulse in such a dataset, its waveform is integrated to obtain the stored charge, which is then divided by the elementary charge to get the "PMT gain". More precisely, this parameter is the product of the number of photoelectrons created at the photocathode and the gain of the PMT. The wording here goes back to initial tests that actually measured the gain of the PMT by resolving the first photoelectron peak of the PMT with a drastically reduced laser intensity. Probably, it is best throughout the tests in this section to just view the parameter "PMT gain" as a yield with arbitrary values.

All "PMT gain" values of the dataset are stored in a histogram, which is then fitted with a Gauss distribution. Eventually, the mean values, together with the corresponding errors, of the Gauss fits for the different datasets are plotted against the magnetic field strength. Fig. 5.3 shows the results for the four tested combinations, where the data points of the individual curves are connected to guide the eye.

The major thing to notice is the drop for combination A (red down pointing triangles) for a magnetic field strength of just over 0.5 mT, which highlights why this investigation is so crucial.

From here on, less and less electrons are able to make the transit through the PMT, until the point when no charge is collected at the anode anymore. The use of the R1924A without any magnetic shield is therefore not an option, since magnetic field tails of this magnitude cannot be ruled out for the final setup of MAGIX.

In contrast, combination B (green up pointing triangles) shows a much better performance, where the "PMT gain" stays nearly constant up to beyond 2 mT. The outer mu-metal cylinder shields the PMT from the magnetic field and prevents the "PMT gain" from dropping. The use of an outer magnetic shield in this form could thus be an option for MAGIX.

A similarly stable performance can be seen for combinations C and D (orange squares and blue circles), respectively. Both are not affected by the magnetic field, so that the integrated magnetic shield of the R1924A-03 and the outer mu-metal cylinder both seem to fulfil their purpose in an equally effective manner. Moreover, it can be seen that a second magnetic shield does not provide any benefits. Both combinations B and C are therefore plausible options for MAGIX. Yet, to save space as well as the effort and cost that would be involved in installing the mu-metal cylinders, the R1924A-03 with only its integrated magnetic shield is to be preferred.

If one compares the curves for combinations A and B to those for combinations C and D, there is another observation to make. For the latter two, the PMT gain is reduced by almost a factor of 2, which is most probably caused by Hamamatsu's "HA treatment" that is incorporated into the R1924A-03. As discussed above, this procedure drastically reduces noise for PMTs operated in the anode grounding scheme, which is the case for both tested PMTs. This noticeable difference in gain has not been further investigated as part of this thesis, but nevertheless, the "HA treatment" is an important feature and should be utilized for the PMTs of the trigger layer.

Rotating the PMT Around Its Tube Axis Following the magnetic field strength tests from the previous paragraph, it has also been investigated whether the rotation angle of the PMT around its tube axis makes a significant difference to the PMT's performance inside the field, so that in case some certain angle proves favorable, the result can later be taken into account when coupling the components of the trigger detectors. For this purpose, different angles between 0° and 360° are tested, where the angle is increased by rotating the PMT in a clockwise manner when looking at the setup in Fig. 5.2b from the front. 0° again corresponds to the angle at which the cable exit of the high-voltage socket points upwards. Since the magnetic field strength tests showed that some kind of magnetic shield for the PMTs of the trigger layer is necessary and desired, combination A (R1924A without any shield) is not considered for the study in this paragraph. The magnetic field strength is set to approximately 1.5 mT, which corresponds to a coil current of 2.64 A. The control voltage of the PMT being tested is again set to 4.0 V and filter glasses with a total optical density of 4 are used in between the PMT and the laser head. The procedure for collecting and plotting the data is the same as for the magnetic field strength tests.

As shown in Fig. 5.4, no problematic dependence on the rotation angle has been found. Of course,

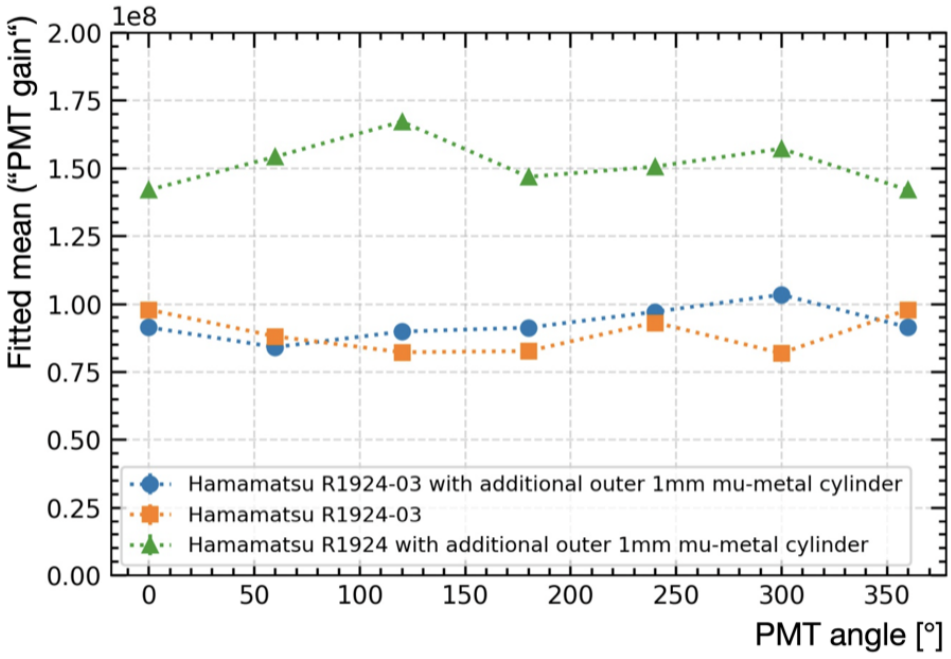

FIGURE 5.4. The PMT rotation angle is varied and the fitted mean values of the "PMT gain" distributions are plotted. No problematic dependence is found, although the PMTs' performances are clearly influenced by the orientation of the dynodes towards the magnetic field.

there are some variations that can be explained by the changing orientation of the PMT dynodes towards the magnetic field, but due to the high gain of the PMTs and the large available head room in adjusting the supply voltages of the PMTs, this does not pose any limitations. When building the trigger detectors at a later point, however, it should be ensured that the rotation angle between the PMT and the scintillator is the same for all detectors.

5.1.2 Scintillators

The trigger scintillators have the form of 150 mm long bars with the rhombic profile described in Section 3.3. They are made from the plastic scintillator material EJ-230 by Eljen Technology (Scionix) [99], which has been decided upon especially due to its fast timing characteristics. A comparison of EJ-230 to other plastic scintillators can be found in Tab. 5.1, where the properties of Saint-Gobain's general purpose scintillator BC-400 [100] are given as a reference. While basic properties like light output and refractive index are almost identical for the different scintillators, parameters like the light attenuation length or the pulse width can be fine-tuned to specific applications. For MAGIX, the timing characteristics are of utmost significance for achieving good timing properties for the trigger layer and the whole MAGIX setup. In contrast, the light attenuation length, for example, plays a rather subordinate role for the trigger scintillators due

	EJ-230	**BC-404**	**EJ-200**	**BC-400**
Light output [% Anthracene]	64	68	64	65
Scintillation yield [photons/1 MeV e^-]	9700	10400 [103]	10000	10000 [103]
Wavelength of maximum emission [nm]	391	408	425	423
Light attenuation length [cm]	120	160	380	250
Signal Rise time [ns]	0.5	0.7	0.9	0.9
Decay time [ns]	1.5	1.8	2.1	2.4
Signal Pulse Width, FWHM [ns]	1.3	2.2	2.5	2.7
Polymer base	PVT	PVT	PVT	PVT
Refractive index	1.58	1.58	1.58	1.58
Manufacturer	Eljen Technology	Saint-Gobain	Eljen Technology	Saint-Gobain
Principal applications	fast timing / high count rates	fast counting	fast timing / long scintillators	general purpose

TABLE 5.1. Comparison of different plastic scintillator materials. Data taken from the corresponding datasheets [99, 100, 103]. For BC-404 and BC-400, the scintillation yields are not directly available, but since their characteristics are almost identical to those of Eljen Technology's EJ-204 and EJ-212, respectively, these values are given here.

to their short length. The polymer base of EJ-230 is polyvinyltoluene (PVT) and its light output amounts to 64 % anthracene with a wavelength of maximum emission of 391 nm, which lies in the vicinity of the spectral response maximum of the trigger PMTs. The fast timing is expressed by a signal rise time of 0.5 ns, a decay time of 1.5 ns, and a signal pulse width (FWHM[11]) of 1.3 ns. The refractive index of the scintillators is specified as 1.58[12]. One specimen of the trigger scintillators is shown in Fig. 5.5a.

5.1.3 Light Guides

The light guides that connect the PMTs to the scintillators are made from optical quality acrylic glass (PMMA) with a refractive index of approximately 1.51 at a wavelength of 391 nm [115], produced by Grünke Acryl and milled into shape by the institute's in-house mechanical workshop. The light guides are designed such that the rhombic profile of the scintillators is translated into the circular form of the PMTs, see Fig. 5.5b. The circular surface of the light guides has a diameter of 25.0 mm and is therefore slightly larger than the effective area of the PMTs' photocathode. Their rhombic surfaces exactly match those of the scintillators. Note that due to the mirror-symmetry of the scintillator end faces, two mirrored versions of the light guides are required. The height of the light guides, if you look at them as in Fig. 5.5b, i.e. the distance

[11] **F**ull **W**idth **H**alf **M**aximum

[12] Unfortunately, Eljen Technology does not state the wavelength at which the refractive index has been measured. But most likely, it corresponds to the wavelength of maximum emission, i.e. 391 nm.

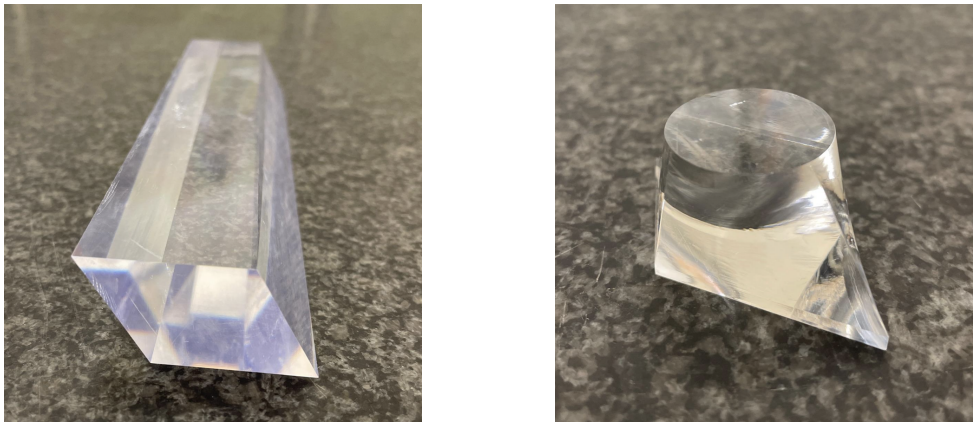

(a) (b)

FIGURE 5.5. The trigger scintillators (a) are made from Eljen Technology's material EJ-230 and the light guides (b) are milled from optical quality acrylic glass.

between scintillator and PMT, is 22 mm, of which 2 mm are a rhombic plateau so that a workpiece can be clamped before getting milled and 20 mm correspond to the gradual form transition from rhombic to circular.

If the rhombic and circular surfaces of the light guides are compared, it is apparent that the input area of the light guides is larger than their output area. In fact, the circular surface has an area of 491 mm^2 and therefore amounts to only 52.46 % of the 936 mm^2 large rhombic surface. Following the phase space arguments by Garwin for the "incompressibility" of the flux density of photons in a light guide [116], only this fraction of input light at best can be transferred by the light guides. The remaining percentage is subject to imperfect total internal reflection. However, there are several reasons why the design of the light guides has been chosen this way. First of all, the above statement assumes that the input area of the light guides is entirely illuminated, which in scintillation counting need not be the case. Secondly, the space constraints inside the shielding house and the desired tight packing of the trigger detectors do not allow for the use of larger PMTs. Thus, there has been no possibility to effectively increase the output area of the light guides. Another option would have been to leave out the light guides and couple the PMTs directly to the scintillator. This would have significantly simplified the production of the trigger detectors, but would have just replaced the above problem with that of reading out only a portion of the scintillator end faces. And especially the direct light from the sharp corners of the rhombic profile of the trigger scintillators, which form the important overlapping regions of the trigger layer, would have been neglected.

So it is clear that the usage of light guides leads to light losses, and yet it is a good idea to use them due to the significance of the sharp corners of the trigger scintillators' rhombic profile. To proof this statement, either a sophisticated simulation could have been written or the performance with and without light guides in this special geometry could have been compared by measurement.

To save time, as most of the experimental setup already existed from first laboratory tests, the decision was made to perform dedicated measurements. These will be covered in the coming paragraph.

Light Yield Measurements With and Without Light Guides The setup that has been used can be seen in Fig. 5.6a. A scintillator bar with the familiar rhombic profile, which at the time of performing these tests has been 220 mm long and made from the plastic scintillator BC-404 by Saint-Gobain[13] [100], is placed inside a light-tight box. Directly attached to the scintillator, without the use of a coupling material such as e.g. optical grease, are the two light guides, if used, and the two PMTs, termed "PMTLeft" and "PMTRight". None of the parts are wrapped with a reflective layer of e.g. PTFE tape. As holding structures, several 3D-printed components are used. For obtaining signals, a well collimated ^{90}Sr source with an activity of 20 MBq is used[14], which is placed on different positions along the scintillator as indicated in Figs. 5.6b and 5.6c. Two measurement series with seven locations each are performed, where the source is moved from "PMTLeft" towards "PMTRight". One along the center of the scintillator (cyan colored locations) and one along the scintillator edge (purple colored locations).

The procedure for data collection and analysis is similar to that used for the magnetic field strength tests - the observable under consideration is again the "PMT gain" that should be viewed as a yield with arbitrary values -, but with a few minor differences. The control voltages of both PMTs are set to 3.5 V, which corresponds to a supply voltage between cathode and anode of −875 V, and 2 min of data are collected per source location. The resulting histograms for both PMTs are then not fitted with a standard Gauss distribution, but with a Gauss with a linearly increasing sigma on the right side of its peak. The choice for this fit model is motivated by the fact that it captures the histogram tails towards high light yield values, one possible explanation for which are geometric effects that enhance the reflection behaviour during light transport. Details on the fit model can be found in the Master's thesis of M. Lauß [57]. The results for the two measurement series are shown in Figs. 5.7a and 5.7b, respectively, where the data points are again connected to guide the eye. Four different curves are shown: "PMTLeft" without light guides (blue diamonds), "PMTLeft" with light guides (green up pointing triangles), "PMTRight" without light guides (yellow squares), and "PMTRight" with light guides (red down pointing triangles).

For the measurement series along the scintillator center, the curves show the behaviour that is expected when considering light attenuation by the scintillator material and light losses due to imperfect total internal reflection. For "PMTLeft", the gain decreases as the source is

[13] As described in Section 5.1.2, the scintillator material for the final trigger detectors is EJ-230 by Eljen Technology [99]. Nevertheless, as the properties of BC-404 and EJ-230 are quite similar, cf. Tab. 5.1, the outcomes of these tests retain their significance.

[14] In more detail, the institute's ^{90}Sr source #43 has been used. ^{90}Sr is a beta-emitter that decays with a half-life of 28.5 a into ^{90}Y under the emission of an electron with a maximum energy of 546 keV. ^{90}Y then further decays with a half-life of 64.1 h into ^{90}Zr by emitting an electron with a maximum energy of 2274 keV. [117]

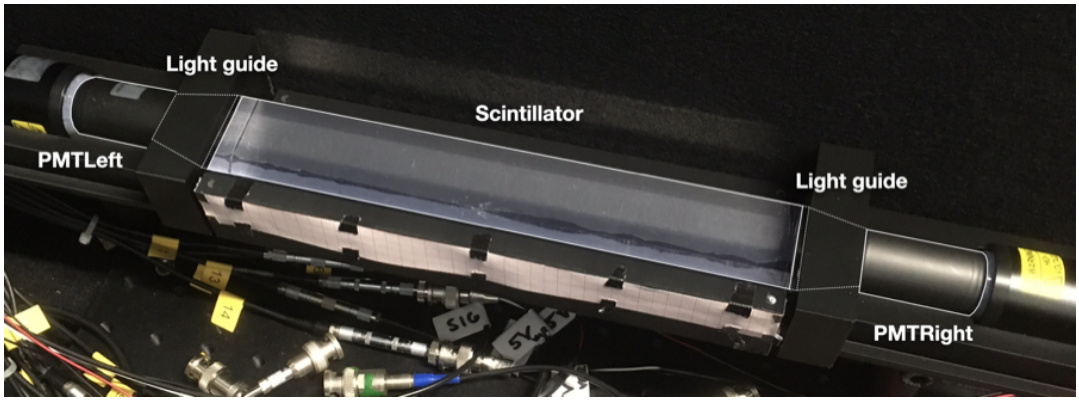

(a)

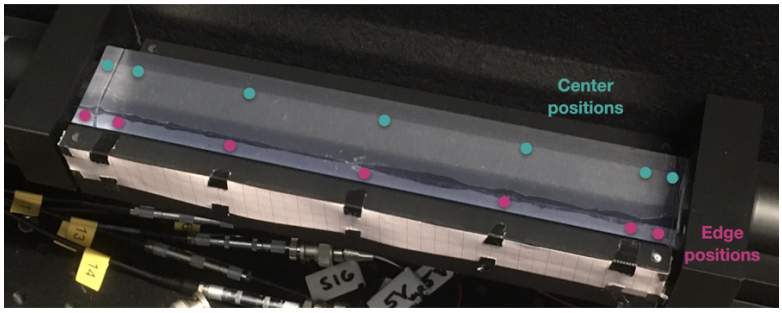

(b)

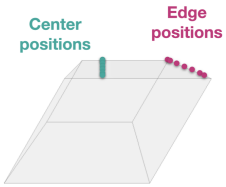

(c)

FIGURE 5.6. Setup for the comparison measurements with and without light guides (a). Different locations along the scintillator center and edge are radiated with a collimated ^{90}Sr source (b and c).

moved towards "PMTRight", both for with and without the light guides. The same is observed for "PMTRight" but consistently the other way around. The differences in "PMT gain" for with and without the light guides differ for the two PMTs, which could be due to non-optically coupling of the individual parts. By this, no smooth light transition is ensured between the parts and small deviations in placing and clamping the parts give different results. In addition, two different PMTs have been used, for which different intrinsic gains are to be expected. Nonetheless, note that the major goal of this study is the comparison between performance with and without light guides, where larger differences are expected and therefore potential issues result from the sharp corners of the rhombic profile of the trigger scintillators, so that no further quantitative investigations have been performed towards this observation.

For the positions along the scintillator edge, the basic behaviour is the same as for the center positions but with significant drops in gain directly in front of the two PMTs if no light guides are used. This proofs the expectation since the PMTs just do not cover the complete rhombic scintillator end faces. The light produced in the sharp corners directly in front of a PMT can therefore only reach the PMT's photocathode by undergoing several reflections inside the scintllator, thereby

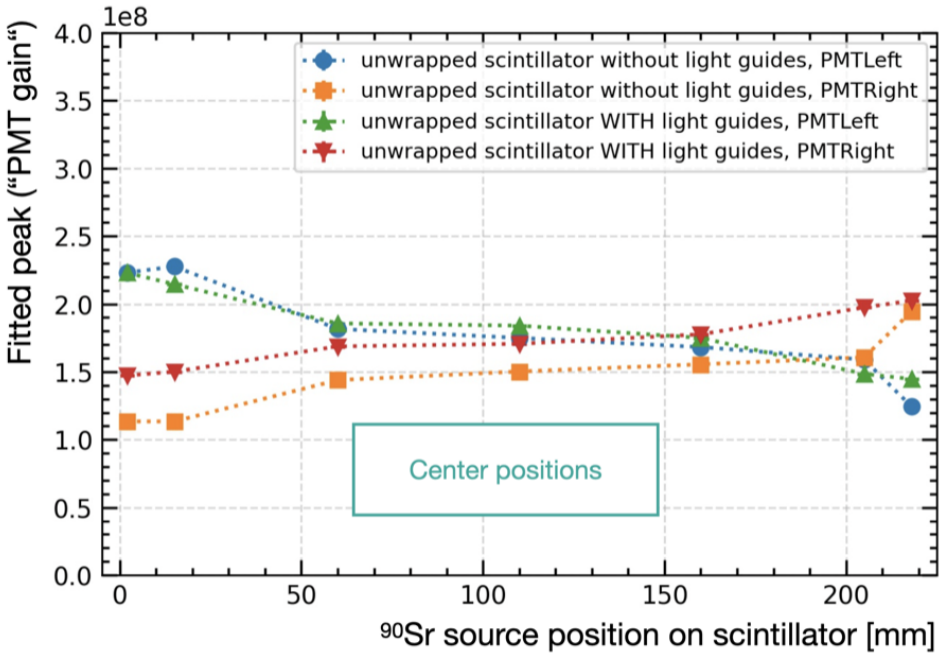

(a)

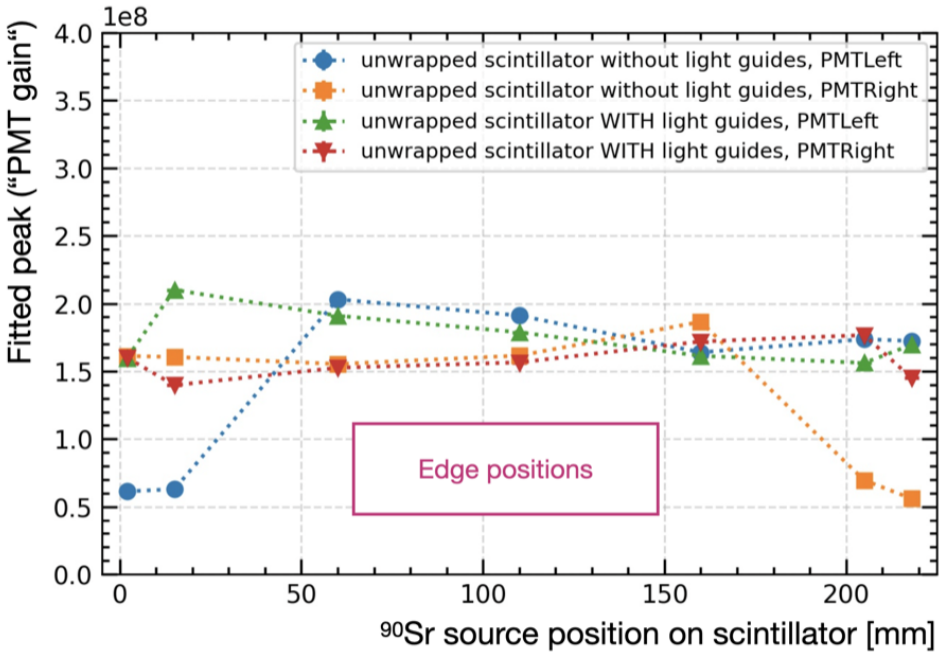

(b)

FIGURE 5.7. The fitted peak values of the "PMT gain" distributions are plotted against the position of the ^{90}Sr source on the scintillator. As expected for the center positions (a), the values decrease as the source is moved away from the respective PMT. For the positions along the edge (b), significant gain drops are observed close to the scintillator end faces if no light guides are used.

drastically decreasing the "PMT gain". As a consequence, since a consistent high efficiency for electron tracks going through the sharp corners of the scintillators are of utmost importance to ensure a consistent efficiency of the trigger layer especially at the overlapping regions of the scintillators, the trigger detectors must be used with light guides in order to perform the physics measurements presented in Chapter 1 with the envisaged accuracy.

5.1.4 Optical Coupling and Wrapping

After having all components of the trigger detectors in place, they first have to be optically and mechanically coupled to maximize the performance. For this purpose, the transparent optical epoxy EPO-TEK 301-2 by Epoxy Technology [118] with a refractive index of 1.53 is used, which impresses with its practicability and mechanical stability. The reasoning to use this material, its most important characteristics, and a comparison of the refractive indexes of the individual components of the trigger detectors can be found in Appendix C.1.1. The epoxy layers between the scintillator and the light guides have a thickness of roughly 0.1 mm. Between the light guides and the PMTs, epoxy layers with a thickness of approximately 0.2 mm are introduced. The exact procedure of coupling the individual parts is described in detail in Appendix C.1.2.

As a final step, the trigger detectors have to be wrapped. To enhance their light yield, a diffusely reflective layer of PTFE tape is used to cover the scintillator and the light guides, see Fig. 5.8a. By this, the light transport to the PMTs is improved by statistically reflecting the light back in that does not undergo total internal reflection but is scattered to the outside and would otherwise be lost. The tape has a thickness of 75 µm and two layers are used to completely cover every part of the scintillator and light guide surfaces. The decision to use PTFE tape has been made following the Bachelor's thesis of S. Fechner [119], where different wrapping materials have been tested and compared, and the PTFE tape convinced with its reflectivity and practicability. Besides the reflective wrapping, the trigger detectors have to be shielded from ambient light. To do so, the detectors are wrapped by two layers of black polyethylene foil with a thickness of 70 µm to achieve light-tightness, see Fig. 5.8b. As for the coupling process, the detailed procedure of wrapping the trigger detectors is not described here but can be found in Appendix C.1.3.

5.1.5 Summary and Conclusions for the Trigger Detectors

As a consequence from the studies presented in this section, the trigger detectors are built as follows: A 150 mm long EJ-230 plastic scintillator bar with the rhombic profile described in Section 3.3 is coincidentally read out by two PMTs with light guides in between. For the PMTs, the model R1924A-03 by Hamamatsu with its integrated magnetic shield and Hamamatsu's beneficial "HA treatment" is used, operated with the corresponding high-voltage socket C13003-01. To save space, cost, and effort, an additional outer magnetic shield is not applied. As coupling material, the optical epoxy EPO-TEK 301-2 is employed, and the PMTs are coupled to the light guides with an orientation angle between the two PMTs and the scintillator of 90° and 270°,

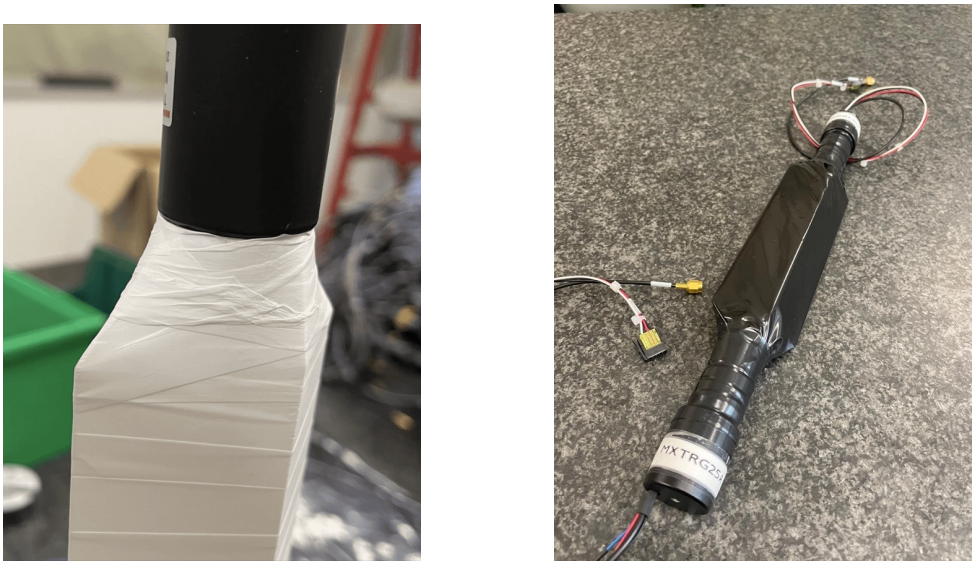

(a) (b)

FIGURE 5.8. The coupled detectors are wrapped by two layers of reflective PTFE tape (a) and covered in two layers of black polyethylene foil for light-tightness (b).

respectively, dependent on the scintillator side. As a reflective layer, PTFE tape is wrapped around the scintillator and the light guides, and for light-tightness, the complete detector is covered in light-tight, black polyethylene foil. After production, a trigger detector looks like as shown in Fig. 5.8b. The weight of a trigger detector, including the cables and connectors, is roughly 365 g and its total length amounts to about 355 mm.

During the course of this thesis, 51 trigger detectors have been produced[15], 22 of which will be installed in the final MAGIX setup per spectrometer and seven will serve as spare detectors. Both the high-voltage sockets of the detectors and the corresponding cables have been labeled as indicated in Fig. 5.8b. The naming convention is "MXTRG**#", where the "**" denotes the 51 trigger detectors ranging from "00" to "50" and the "#" denotes the two PMTs of a trigger detector, termed "A" and "B". An overview on which specific PMTs and which specific sockets have been used for the individual trigger detectors can be found in the Bachelor's thesis of K. Bent [120].

5.2 The Power Supply of the Trigger Layer

The power supply for the trigger layer is realized as shown in Fig. 5.9. The high-voltage sockets of the trigger detectors are supplied by so-called *DAC boards*, which are placed close to the trigger detectors as will be shown in Section 5.4. Each DAC board can operate up to ten high-voltage

[15] As described in Section 4.3.4, it was originally planned to have only 50 trigger detectors available. But since one scintillator showed a small kink when being delivered, Scionix provided one additional scintillator as a gesture of goodwill, so that one additional detector could be produced.

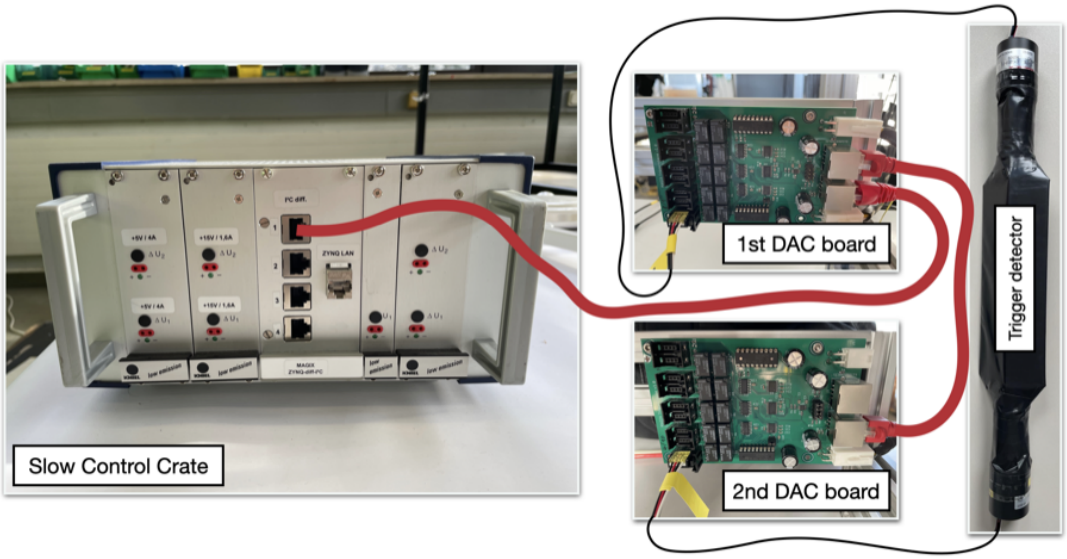

FIGURE 5.9. The concept for the power supply of the trigger layer. The trigger detectors are operated using so-called DAC boards that provide the required voltages to the individual high-voltage sockets. The DAC boards are fed and controlled by a slow control crate, housing the power devices and a control unit.

sockets and the voltages for each socket are individually controllable via the network. The DAC boards are fed and controlled by a half-size 19-inch slow control crate, housing the required power devices and a control unit for the operation of up to eight DAC boards. Four of the DAC boards can be directly connected to the crate, to each of which a second DAC board can be "daisy-chained". In total, the trigger layer power supply can thus be operated with 80 high-voltage sockets, i.e. 40 trigger detectors, which provides more than enough spare channels for the operation of a trigger layer with its 22 trigger detectors. In the following, the individual components of the trigger layer power supply shall be described in more detail.

5.2.1 DAC Boards

Fig. 5.10a shows a photo of a DAC board. At the top of the picture, the ten available jacks (yellow box) for connecting the 4-pin power supply connectors of the high-voltage sockets can be seen. For each jack, the +15 V supply voltage can be turned on and off individually by remotely switching the respective relay (orange box). The control voltages of the jacks can be adjusted between 0 V and +5 V employing 16-bit DACs[16] (pink boxes), which corresponds to a control voltage resolution of roughly 76 µV or 0.00152 % (relative). Both the relays and the DACs are controlled via differential I^2C.

The bottom of the picture shows the input and output connectors for the communication and

[16] **D**igital-to-**A**nalog **C**onverters

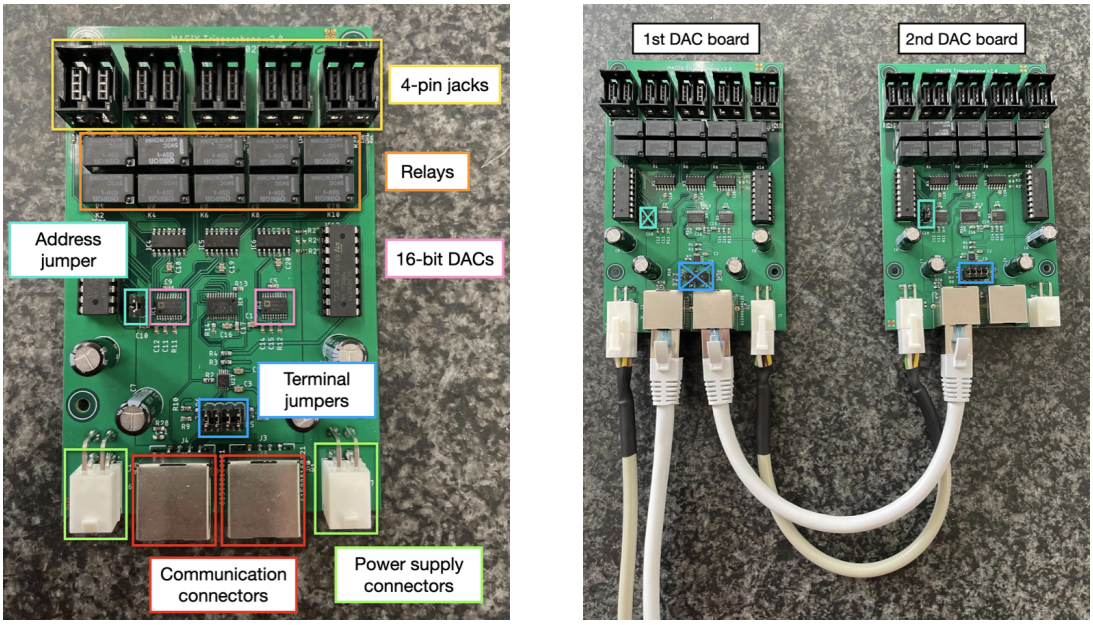

(a) (b)

FIGURE 5.10. Photo of a trigger layer DAC board (a), with the most important components labeled. A maximum of two DAC boards can be connected as a "daisy-chain" (b), where the labeled terminal and address jumpers have to be set accordingly.

power supply cables coming from the slow control crate and going to the potentially connected second, "daisy-chained" DAC board. Which side, left or right, is used for input and which for output does not matter. For communication, standard RJ-45 connectors are used (red boxes), and for power supply, the four individual lines (+5 V for the control voltages, +15 V for the supply voltages, and 2× GND) are combined into 4-pin connectors (green boxes).

The four terminal jumpers (blue boxes) denote whether a DAC board is the last link in a "daisy-chain". Thus, if a "daisy-chain" consists of two DAC boards, the terminal jumpers have to be set on the second one and remain open on the first one, as can be seen in Fig. 5.10b. In contrast, if the "daisy-chain" is composed of only one DAC board, its terminal jumpers have to be set.

Dependent on how a DAC board is connected to the slow control crate, each of the ten 4-pin jacks is assigned its own unique address between 0 and 79, where the control and supply voltage of each address can be individually controlled via a differential I^2C bus. The address range that is assigned to a specific DAC board is determined by the port of the slow control crate the DAC board is connected to and whether the address jumper of the DAC board (turquoise boxes) is set or not. For a second, "daisy-chained" DAC board, the address jumper has to be set, while the jumper remains open for a DAC board that is directly connected to the slow control crate, see Fig. 5.10b. The exact assignment of the addresses is illustrated in the documentation of the trigger layer power supply [121], which can also be consulted if any further information on the

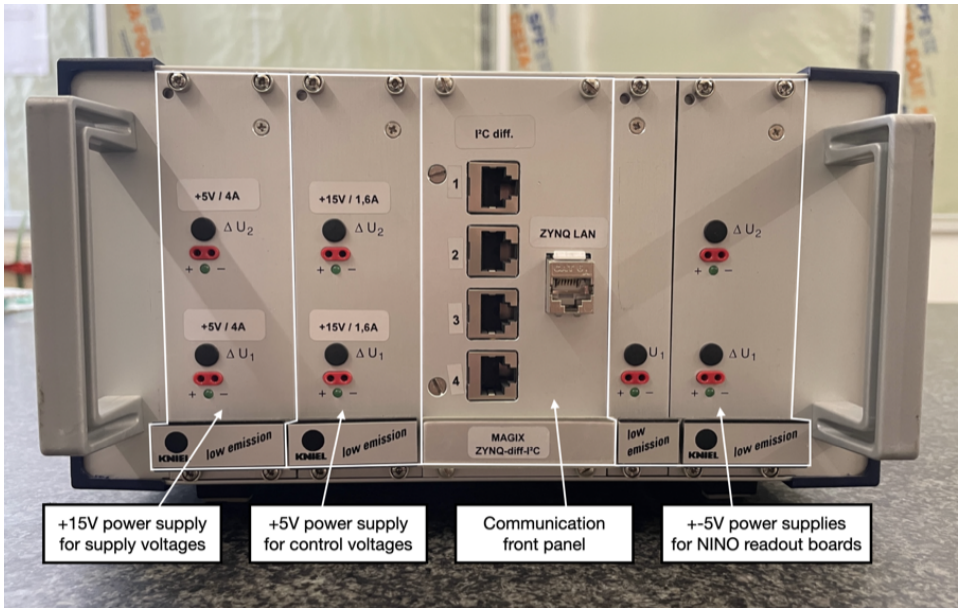

(a)

(b)

FIGURE 5.11. The front (a) and rear (b) panels of the slow control crate.

DAC boards is needed.

5.2.2 Slow Control Crate

The front and rear panels of the half-size 19-inch slow control crate are shown in Figs. 5.11a and 5.11b, respectively. The crate houses the double-channel power supply CAD15.1,6 by Kniel

System-Electronics [122] for providing the +15 V supply voltages of the high-voltage sockets of the trigger detectors, as well as Kniel's double-channel +5 V power supply CAD5.4 [123] for the control voltages. The Kniel power supplies have been chosen due to their extremely low-noise behaviour and good radiation hardness compared to other devices. A Z-turn board by MYiR [124] serves as the control unit, which is mounted behind the communication front panel, labeled "MAGIX ZYNQ-diff-I^2C". The Z-turn board supports the control of the +15 V power supply and the addresses on the DAC boards via SSH, TCP/IP, SFTP, or a web server. The communication front panel includes one RJ-45 connector for the Z-turn board's network connection, labeled "ZYNQ LAN", as well as four RJ-45 connectors for the communication connections to the DAC boards, labeled "I^2C diff. 1-4". Furthermore, the crate houses one additional Kniel CAD5.4 power supply, as well as a one-channel Kniel CAA5.4 [125] to provide ±5 V for the operation of two NINO readout boards, which will be described in Section 5.3. The ±5 V power supplies can be controlled by the Z-turn board as well. The rear panel accommodates all the power supply outputs, employing robust XLR connectors, together with the mains plug and switch. The four outputs labeled "XLR1-4" are intended for connecting the DAC boards and the two labeled "NINO 1-2" are used for the operation of the two NINO readout boards. If more detailed information on the slow control crate is needed, please refer to the documentation of the trigger layer power supply [121].

5.2.3 Slow Control via EPICS and CSS

Employing the TCP/IP server of the slow control crate's Z-turn board, together with the differential I^2C busses, the supply and control voltages of each 4-pin jack address on a DAC board can be controlled via dedicated TCP/IP commands that set or read the corresponding TCP/IP variables. Moreover, the +15 V and ±5 V power supplies of the slow control crate can be globally switched on or off, which is also controllable via dedicated TCP/IP commands. Please note that only the TCP/IP variables are set and read out. If, due to hardware problems, a variable is set but the corresponding hardware does not respond, this is not necessarily noticeable when reading the variable. A list of all available TCP/IP commands can be found in the documentation of the slow control crate [121].

As described in Section 2.6, MAGIX uses the EPICS-based software stack `MXSlowControl` to combine the slow control parameters of all involved components in a common system. For the power supply of the trigger layer, a dedicated EPICS driver has been written to translate the individual TCP/IP commands into EPICS *process variables* (PVs) so that each control parameter is addressable via the network. The corresponding files can be found in Appendix C.2.

For better usability, the EPICS PVs have been integrated into a graphical user interface (GUI) created with Control System Studio (CSS). A screenshot is given in Fig. 5.12. The supply voltages can be controlled via simple switches and the control voltages can be set by passing the respective values in mV. Besides, it is possible to assign GUI elements with the execution of external scripts, as can be seen from the differently labeled buttons. For automated measurement programs, the

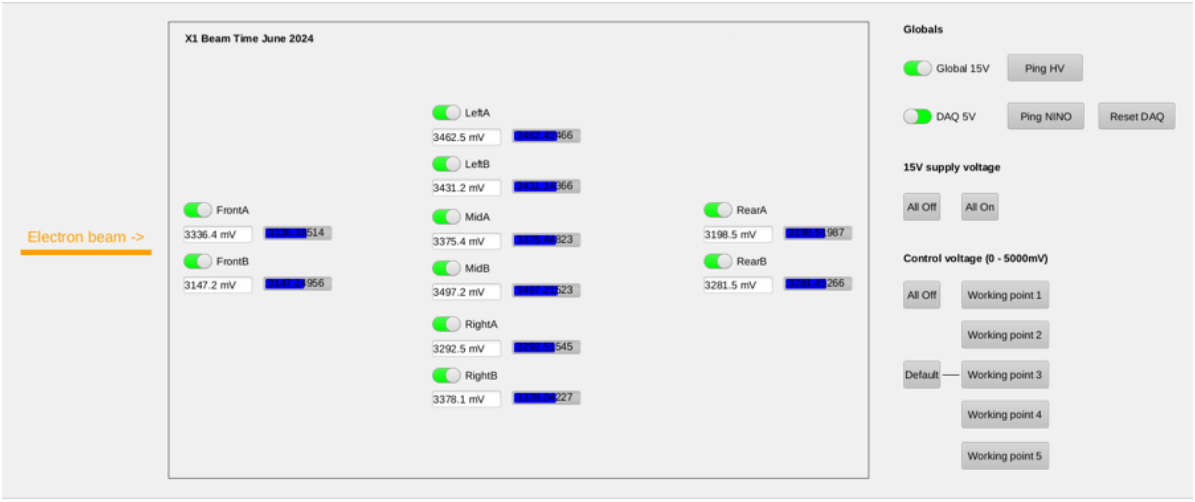

FIGURE 5.12. Screenshot of the trigger layer slow control in CSS as it has been used for the MAMI beam time mentioned in Chapter 8. EPICS PVs, but also whole scripts, as can be seen from the differently labeled buttons, e.g. "Reset DAQ", can be assigned to GUI elements, significantly simplifying the operability.

external scripts can of course also be used without CSS.

5.2.4 Outlook on the Power Supply in the Final MAGIX Setup

In the final MAGIX setup, six DAC boards will be used per trigger layer, as will be shown in Section 5.4. In total, 20 DAC boards have been produced, eight of which will serve as spare boards.

The half-size 19-inch slow control crate described in Section 5.2.2 will not be utilized in the final setup, but will be kept available for future lab measurements. Instead, a full-size 19-inch crate is being developed[17] at the time of writing this thesis that will be built twice, once for each spectrometer. It will house the power supplies for the supply and control voltages of the high-voltage sockets of the trigger detectors, as well as the necessary power supplies for the operation of four NINO readout boards[18], each of which will get its own Kniel CAD5.4 power supply. To save complexity and cost, the control unit will be changed from the Z-turn board to an in-house developed Ethernet controller, which supports the control via TCP/IP, SFTP, or a webserver. Two of these controllers will be installed in the crate to separately control the power supplies for the trigger detectors and those for the NINO readout boards. Note that the exchange of the control unit might necessitate making adjustments to the EPICS driver of the trigger layer power supply.

[17] This decision has been made so that the available height underneath the veto system can be utilized as efficiently as possible.

[18] The reason why four NINO readout boards are required will be given in Chapter 6.

The crate will be mounted inside a 19-inch rack that will exploit the empty space directly underneath the veto system, cf. Fig. 2.18. The front of the rack will show in the direction of small spectrometer angles, i.e. the forward direction of MAGIX, which is defined as the *trigger veto side*. In contrast, the direction towards large spectrometer angles, i.e. the backward direction of MAGIX, is termed the *TPC side*. All electronics components of the MAGIX trigger veto system will be oriented towards the *trigger veto side*, whereas the components of the MAGIX TPC electronics will face towards the *TPC side*. The mirror-symmetrical design of the spectrometers and the focal plane detectors with respect to the MESA beam lines is therefore also adopted when installing the corresponding electronics. By this, both detector systems are accessible independently of each other and can be worked on at the same time.

5.3 The Readout of the Trigger Layer

To fulfill the purposes of the trigger layer described in Chapter 3, it has to provide a very precise timestamp for any incoming particle that interacts with one or more of the trigger scintillators and generates signals in the corresponding PMTs. Additionally, by recording the time difference between the two PMT pulses of a trigger detector, the interaction point coordinate along the non-dispersive direction can be reconstructed. The second coordinate of the interaction point is given by the segmentation of the detector plane. Furthermore, by measuring the deposited energy of an incoming particle, additional information is available that will support the veto system in distinguishing between different particle types. Thus, the readout of the trigger layer should provide a precise time-pickoff, as well as magnitude determination of the recorded PMT pulses.

The in-house developed NINO readout board [126] meets the above requirements by combining leading-edge triggering and the Time-over-Threshold (ToT) method with a very accurate and fast TDC[19] programmed on an FPGA[20]. It is based on the NINO ASIC[21] developed by CERN and has originally been designed for the A1 neutron polarimeter, which has been successfully operated during a first measurement campaign in 2019 [127]. The following Section 5.3.1 will discuss the NINO readout board in more detail, whereas Section 5.3.2 will give an outlook on the readout for the trigger veto system in the final MAGIX setup, which will employ an upgraded second version of the NINO readout board.

5.3.1 NINO Readout Board

A specimen of the NINO readout board can be seen in Fig. 5.13. It fits the 19-inch standard and is based on the ultrafast discriminator-amplifier NINO chip [128, 129] developed for the ALICE experiment at CERN, which provides eight input channels. Each channel includes a differential

[19] **T**ime-to-**D**igital-**C**onverter
[20] **F**ield **P**rogrammable **G**ate **A**rray
[21] **A**pplication-**S**pecific **I**ntegrated **C**ircuit

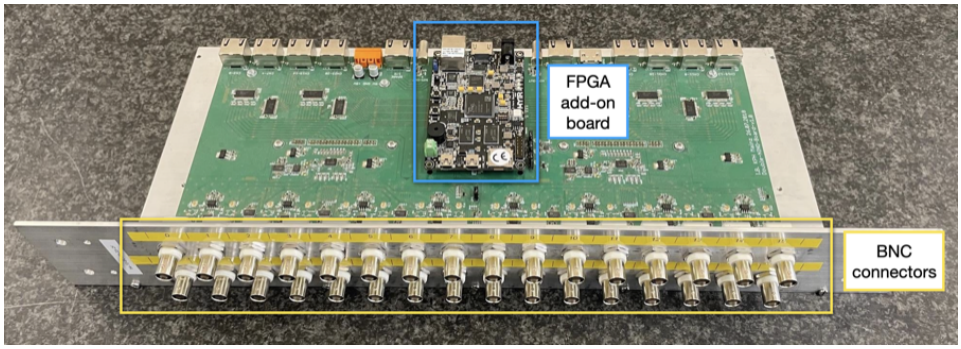

(a)

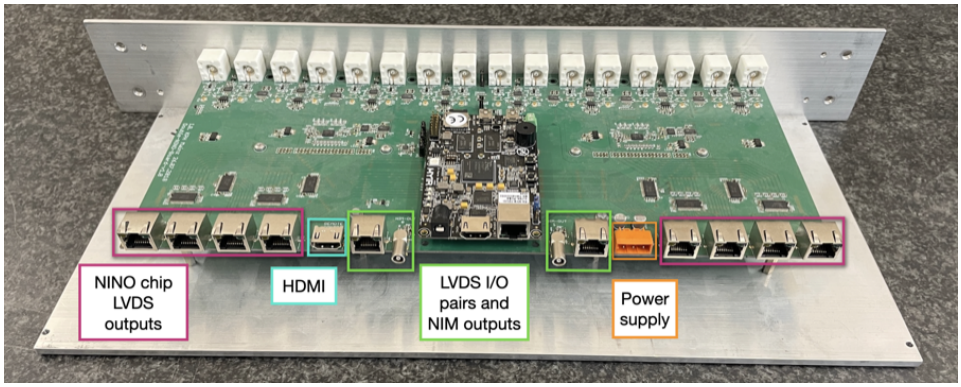

(b)

FIGURE 5.13. Front (a) and rear (b) views on the NINO readout board developed for A1.

input stage, a fast amplification stage, a very precise discriminator, as well as ToT encoding in the differential LVDS[22] output signal. On the NINO readout board, however, the NINO chips are operated in their single-ended mode, i.e. only negative signals are fed to the differential inputs, to work with the negative output pulses of the trigger PMTs. The positive inputs are internally terminated with 50 Ω.

The NINO readout board incorporates four NINO chips and therefore provides 32 readout channels that are equipped with BNC connectors at the front side of the board (yellow box). The BNC connectors are arranged in two rows of 16, the first and last eight of which belong to one NINO chip. The two PMT signals of a trigger detector should be connected to input channels of two different NINO chips - for example along a column of the 2×16 BNC connector grid -, as crosstalk between the channels of a NINO chip can occur from time to time [130]. To guarantee the operation within the NINO chip specifications, each readout channel includes an active attenuator[23] in front of its NINO chip input that can be programmed via a 12-bit DAC. At the

[22] **L**ow-**V**oltage **D**ifferential **S**ignaling
[23] NXP BAP64Q Quad PIN diode attenuator [131]

NINO chip input, the analog output signal of the active attenuator can additionally be monitored and checked using an MML[24] connector. The discriminator threshold of a NINO chip can be set using a 12-bit DAC as well, where the threshold is applied to all eight NINO chip input channels at once. Therefore, by combining the NINO chip threshold with the adjustable active attenuators, an individual signal threshold can effectively be set for each readout channel. More details on this will be given in Chapter 7.

Two operation modes are available for the NINO readout board: a local mode and a remote mode. In the local mode, all settings are controlled by an FPGA add-on board, which is plugged onto the NINO readout board using two 80-pin SMT connectors (blue box). In this mode, the LVDS output signals of the NINO chips are routed to the pins connecting the FPGA add-on board with the NINO readout board. In the remote mode, on the other hand, all settings can be controlled from an external computer via an I^2C connection employing an HDMI connector at the rear side of the board (turquoise box). The LVDS output signals of the NINO chips are routed to RJ-45 connectors in this mode, also located at the back of the NINO readout board (purple boxes). Dependent on the experimental needs, both operation modes can prove useful. The local mode allows for a fast and immediate signal processing in the close vicinity of the experimental setup, especially by employing the FPGA of the FPGA add-on board, and drastically reduces the amount of required cabling. In fact, if the FPGA add-on board is configured accordingly, only one Ethernet cable is needed for readout. On the other hand, the software installed on the FPGA add-on board cannot simply be reprogrammed in case this should become necessary during a measurement period. This flexibility is provided by the remote mode, where the entire software runs on the external computer and can be changed as required. However, significantly more cabling is required for the remote mode. The remaining connections at the rear side of the NINO readout board are a $\pm 5\,V$ power supply connector (orange box), as well as two programmable LVDS I/O pairs using RJ-45 connectors and two programmable NIM[25] outputs employing LEMO[26] connectors (green boxes).

For choosing between the two operation modes, the NINO readout board includes the three mode jumpers JP1, JP2, and JP3 (red box), see Fig. 5.14a. If the mode jumpers are set to the left, i.e. towards the BNC input connectors, the remote mode is chosen. If they are set to the right, the NINO readout board is operated in the local mode.[27] In addition, the test pulse jumpers JP4 and JP5 (yellow box) can be used to generate test pulses on different input channels of the NINO readout board.[28] Whereas jumper JP4 enables the test pulses for the first seven input channels of each NINO chip, i.e. channels 0 to 6, 8 to 14, 16 to 22, and 24 to 30, jumper JP5 enables them for the last channels of each NINO chip, i.e. channels 7, 15, 23, and 31. If the jumpers are set to

[24] MML is a special micro-miniature coaxial connector format produced by Radiall [132].

[25] **N**uclear **I**nstrumentation **S**tandard

[26] LEMO connectors are special coaxial connectors produced by the LEMO group [133].

[27] The jumpers JP1 and JP2 configure the serial data (SDA) and serial clock (SCL) lines of the I^2C bus, respectively. Jumper JP3 sets the reset pin (nRES) for all I^2C members.

[28] The test pulses are generated in parallel to the BNC connectors and are present at the inputs of the active attenuators.

the left, the test pulses are activated, if they are set to the right, the test pulses are set inactive. The amplitudes of the test pulses are controllable by 12-bit DACs.[29]

For MAGIX, the NINO readout board is operated in the local mode, using an MYiR Z-turn board [124] as the FPGA add-on board, see Fig. 5.14b. The Z-turn board is a high-performance single board computer that is built around the Xilinx Zynq-7020[30] System-On-Chip, featuring an integrated dual-core processor with Xilinx 7-series FPGA logic and rich peripherals such as USB-to-UART, Mini USB OTG, TF (MicroSD), JTAG, or Ethernet. It can be booted from the TF card interface (pink box) - this is how it is done at MAGIX - or a 16 MB flash memory, which can be decided via the two boot select jumpers (green box). If the upper jumper JP1 is set, the Z-turn board boots from the flash memory, if it is left open, the TF card interface is used for booting. The lower jumper JP2 has to be set in both cases. The power supply of the Z-turn board is provided through the SMT connections to the NINO readout board, a separate supply is not required. The control and readout of the Z-turn board is handled via an Ethernet connection to the network (blue box).

The FPGA of the Z-turn board is programmed to incorporate a *Tapped Delay Line TDC* with 256 cells and a typical delay time of approximately 18 ps for each readout channel. A TDC is started when a corresponding input signal occurs and is read out with a clock frequency of 250 MHz, providing a so-called *coarse time*, which is the product of a counter that is incremented every clock cycle and the clock period of 4 ns. The *coarse time* therefore represents the timing information of the input signal to an accuracy of 4 ns. The information stored inside the TDC, i.e. the number of delay line cells that the input signal has propagated through before the TDC is read out, corresponds to a so-called *fine time*, which is in principle accurate to within the delay time of a single delay line cell, i.e. 18 ps. A more detailed explanation of the *Tapped Delay Line TDCs* will be given in Chapter 7.

5.3.2 Outlook on the Readout in the Final MAGIX Setup

For the use in the final MAGIX setup, an upgraded second version of the NINO readout board has been developed as can be seen in Fig. 5.15. Several changes have been implemented, the most important of which are:

- the BNC input connectors have been changed to SMA connectors to avoid the use of additional adapters between the trigger detectors and the NINO readout board;
- since the NINO readout board will only be operated in local mode at MAGIX, the LVDS output signals of the NINO chips are only routed to the pins of the Z-turn board, thus the RJ-45 connectors at the rear of the board have been removed;

[29] The inputs of these DACs are termed *TP*, which appears in the NINO readout board's schematic [134], as well as when configuring the NINO readout board, cf. Code 7.1. Up to the point of writing this thesis, no experience has been gained with the test pulses and only the default value $TP = 0$ has been used.

[30] There is also a Zynq-7010 version available.

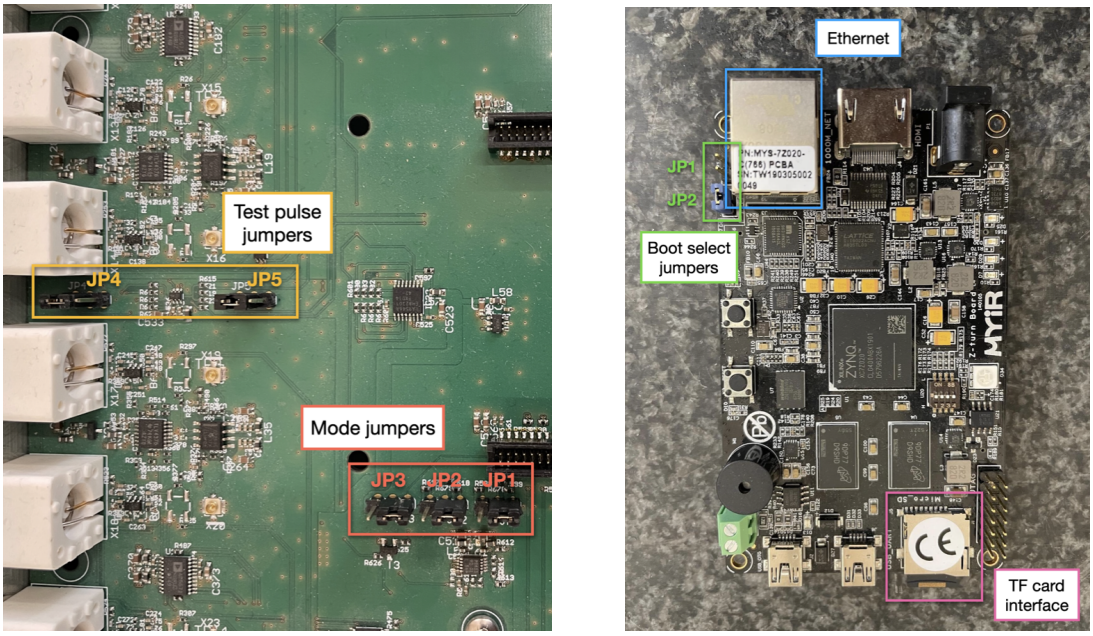

(a) (b)

FIGURE 5.14. The NINO readout board includes five jumpers (a) for setting the operation mode and enabling test pulses onto different input channels. As the FPGA add-on board, the MYiR Z-turn board is used (b).

- the amount of programmable LVDS I/O pairs has been increased from two to eight to provide more flexibility for merging the readout systems of the different detector systems of MAGIX;
- the second generation of the MYiR Z-turn board [135] is used as the FPGA add-on board, since the production of the first generation has been discontinued at some point.

In total, 10 of the upgraded NINO readout boards will be available[31], four of which will be installed per spectrometer and two will serve as spare boards. The upgraded NINO readout boards will be mounted inside a MayTec frame that is directly attached to the veto system cradle, cf. Section 6.1.2, and will be accessible from the *trigger veto side* as defined in Section 5.2.4. The corresponding control unit and power supplies will be placed inside the full-size 19-inch slow control crate for the trigger layer as described in Section 5.2.4.

The upgraded NINO readout boards will be used both for the trigger layer signals and the signals of the veto layers. Due to the huge magnitudes of the trigger layer signals, additional in-house produced passive 20 dB attenuators, see Section 7.2.1, will be used in front of the SMA inputs of the NINO readout boards to prevent the active attenuators from operation outside

[31] Unfortunately, the number of upgraded NINO readout boards is limited by the amount of available NINO chips, which are not being produced anymore.

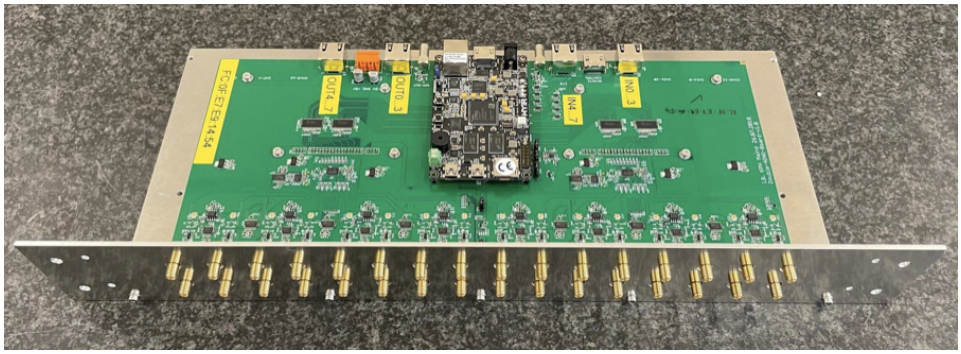

FIGURE 5.15. A first look on an upgraded NINO readout board.

their specifications. The four upgraded NINO readout boards per spectrometer correspond to 128 available readout channels, of which 44 will be used for the trigger layer and 54 are required for the three veto layers, cf. Section 6.2.4. The remaining 30 channels will serve as spare channels.

5.4 The Mounting of the Trigger Layer

After finalizing the trigger detectors, their power supply, and the readout, one detail still needs to be taken care of, namely the mounting of the trigger layer. As already brought up in Chapter 3, the veto system is built as a customizable drawer system and it seems reasonable to apply this design idea for the trigger layer as well. The trigger layer mounting is therefore directly attached to the lower flange of the TPC frame using a pair of horizontally mounted telescopic rails, see Fig. 5.16a, and is installed such that it opens towards the *trigger veto side* as defined in Section 5.2.4.

The mounting holds the 22 trigger detectors that are placed next to each other along the dispersive directon of the spectrometer, as well as the DAC boards that are needed to power the 44 high-voltage sockets, see Fig. 5.16b, and is built from a 4 mm steel sheet and a frame of different aluminum profiles. The steel sheet includes a large rectangular cut-out of size 837 mm × 150 mm, so that the material budget between the trigger layer and the first veto layer is kept at a minimum, see Fig. 5.16c. In order to ensure the positioning of the trigger layer to be as plane as possible, a target value of 0.25 mm for the maximal sagging of the trigger layer was set in advance. To provide enough stability and to prevent the drawer from too much sagging, two quadratic 10 mm × 10 mm aluminum profiles are mounted along the edges of the cut-out. By using the quadratic aluminum profiles, this target value has been beaten by roughly a factor of two, see Fig. 5.17. Meeting this requirement came at the expense of other aspects, as during the design process a compromise had to be found between the maximal sagging, the overall weight of the drawer due to the available telescopic rail models, and the vertical distance between the trigger layer and the first veto layer. The final weight of the trigger drawer is 15.1 kg, which increases

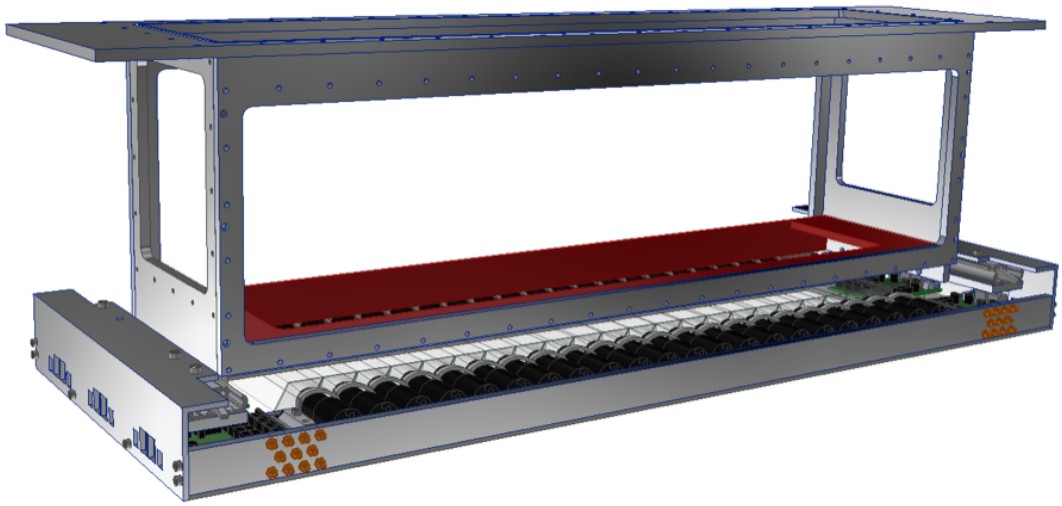

(a) The trigger layer mounting is directly attached to the lower flange of the TPC frame.

(b) 22 trigger detectors and six DAC boards are held by the trigger layer mounting.

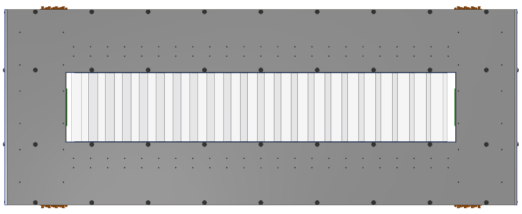

(c) A rectangular cut-out is incorporated into the steel sheet for minimizing the material budget between the trigger layer and the first veto layer.

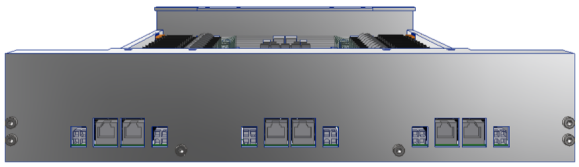

(d) Cut-outs in the short side walls of the drawer are used to route the DAC board cabling.

FIGURE 5.16. CAD model of the trigger layer mounting.

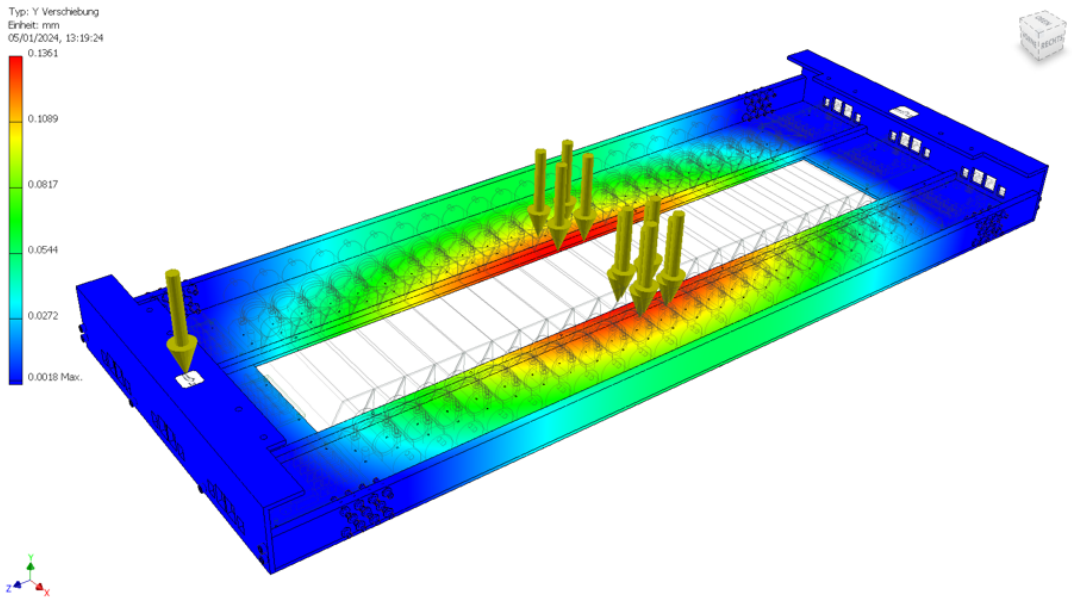

FIGURE 5.17. Stability analysis of the trigger layer mounting using Autodesk Inventor 2019. The weight of the 22 trigger detectors is roughly 8 kg and is modeled as a pressure of 0.4 kPa on the upper sides of the aluminum bars along the rectangular cut-out. The weight of the DAC boards and the 3D-printed components sums up to about 3 kg and is modeled as a pressure of 0.1 kPa applied to the upper side of the steel sheet. In addition, gravity is taken into account. A maximal sagging of 0.1361 mm is predicted within the red areas.

to 27.2 kg if the trigger detectors and the DAC boards are added. A concession had to be made regarding the vertical distance between the trigger layer and the first veto layer. In the final design, this distance amounts to 18 mm (10 mm aluminum profile, 4 mm steel sheet, 4 mm gap), which is significantly higher than the simulated 4 mm in Chapter 4. Still, the dimensions of the veto and lead absorber layers are chosen large enough to compensate for this change.

44 SMA feed-throughs are embedded in the long side walls of the drawer to enable a fixed cabling from the drawer to the NINO boards. Individual trigger detectors can therefore be exchanged without changing the readout cabling. The power supply and control cables of the DAC boards are routed through cut-outs in the short side walls of the drawer, see Fig. 5.16d. Six DAC boards are used for a symmetric channel assignment and cabling for the trigger detectors. Thus, 60 power supply channels are provided, 16 of which are spare channels.

The trigger detectors lie on the two aluminum profiles that are mounted along the edges of the rectangular cut-out and are held in place by dedicated 3D-printed molds embracing the light guides and PMTs. Additional 3D-printed clamps are used for fixation. Between the trigger detectors, a gap of 0.5 mm along the dispersive direction is incorporated, resulting in a tightly arranged trigger layer while giving enough space for the wrapping materials. With this, the

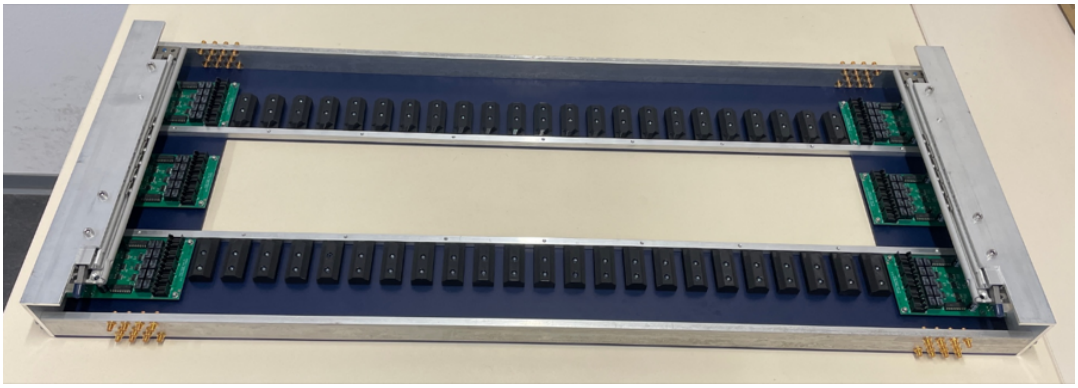

FIGURE 5.18. A fully assembled trigger layer mounting. For corrosion protection, the steel sheet is powder-coated (RAL 5011, steel blue, semi-matt).

sensitive area of the trigger layer amounts to 817.5 mm × 150 mm. The orientation of the trigger detectors is such that the upper sharp edges of the rhombic scintillator profiles point in the direction of the interaction point of MAGIX.

Three copies of the trigger layer mounting have been assembled as part of this thesis, one of which is shown in Fig. 5.18. Two will be installed in the final MAGIX setup and one will be kept as a laboratory twin. A guide on how to assemble the trigger layer mounting can be found in Appendix C.3.

CHAPTER 6

DESIGN AND DEVELOPMENT OF THE VETO SYSTEM

The veto system is an arrangement of horizontally placed, 10 mm thick veto and lead absorber layers, to be placed underneath the trigger layer. As for the trigger layer in Chapter 5, this chapter delineates the design and development process of the veto system, so that it can actually be built and incorporated into the final setup of MAGIX. Please note that the development of the veto system is not completely finished at the time of writing this thesis. Whereas the mechanical setup already exists in its final form, not all details regarding the veto detectors have been addressed at this point. Nevertheless, progress is ongoing. For instance, important results from a beam time at MAMI in October 2023 concerning the readout concept have been obtained as part of the Bachelor's thesis of H. Keßler [136].

Section 6.1 starts with the technical implementation of the veto system, together with a few words on the lead absorber layers. Section 6.2 then provides details on the veto layers and the individual veto detectors.

6.1 Technical Implementation of the Veto System

As mentioned in Chapter 3, the veto system is built in the form of a flexible drawer system. The arrangement and the amount of the individual layers of the veto system are therefore highly adaptable to the needs of the experiment. The drawer system consists of nine drawers, each of which is composed of two individual levels. Each level provides space for one veto layer or one lead absorber layer, resulting in 18 available slots for arranging the layers of the veto system. Three slots will be used for the veto layers V1, V2, and V3 and the remaining 15 slots will be equipped with lead absorber layers. The drawers are mounted to the shielding house walls using a cradle made of steel beams and open towards the *trigger veto side* as defined in Section 5.2.4. A

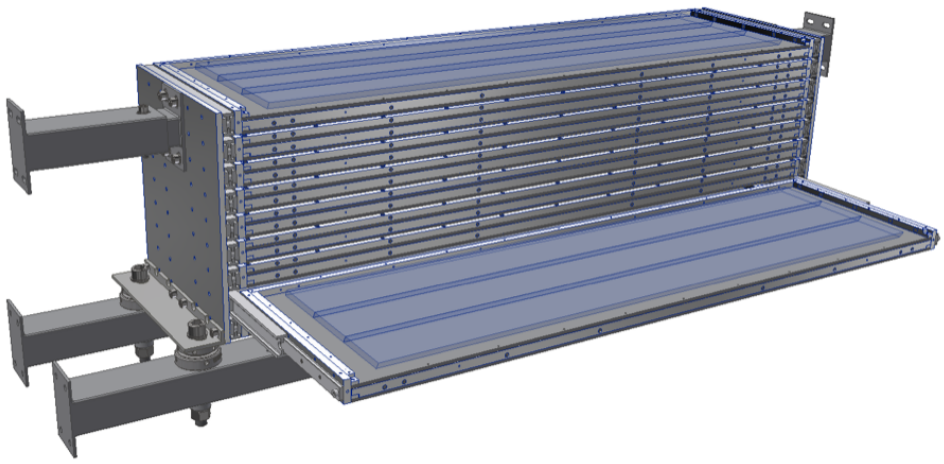

FIGURE 6.1. CAD model of the veto system. Nine drawers provide 18 slots for arranging the veto and lead absorber layers. The drawers are installed using a cradle made of steel beams.

rendering of the veto system based on a CAD model is shown in Fig. 6.1.

Apparently, there is no finalized, optimum arrangement of the veto and lead absorber layers due to the veto system's design criterion of flexibility and customizability. Nonetheless, a few thoughts on possible arrangements shall be given here. Obviously, the first veto layer V1 should be at the uppermost position so as to not miss out on the benefits of operating it as a second trigger layer and to use it for measurements dedicated to the efficiency estimate of the trigger layer. For the veto layers V2 and V3, however, there are different possibilities. One would be the arrangement as it has been used in the simulation studies in Chapter 4, i.e. all lead absorber layers are placed between the veto layers V1 and V2. Nevertheless, a different arrangement could be chosen for better practicability, where the veto layers V2 and V3 are put into the upper levels of the two lowest drawers as it is shown in Fig. 6.1. Since the upper levels of the drawers are easier accessible, this would prove helpful for the cable routing of a veto layer, as well as the potential exchange of individual veto detectors. Also, the veto layer V3 would be additionally shielded by the one lead absorber layer underneath it. Calibration measurements with the final MAGIX setup will finally show what arrangements will be optimal for the different kinds of intended experiments.

6.1.1 Design of the Veto System Drawers

A closer look to the design of the veto system drawers is given in Fig. 6.2a. The two levels of a drawer are each built from a 4 mm steel sheet and a frame of aluminum profiles that are screwed to a pair of vertically mounted telescopic rails. The rear and side profiles are permanently attached to the steel sheets and the telescopic rails, whereas the front profiles are used as

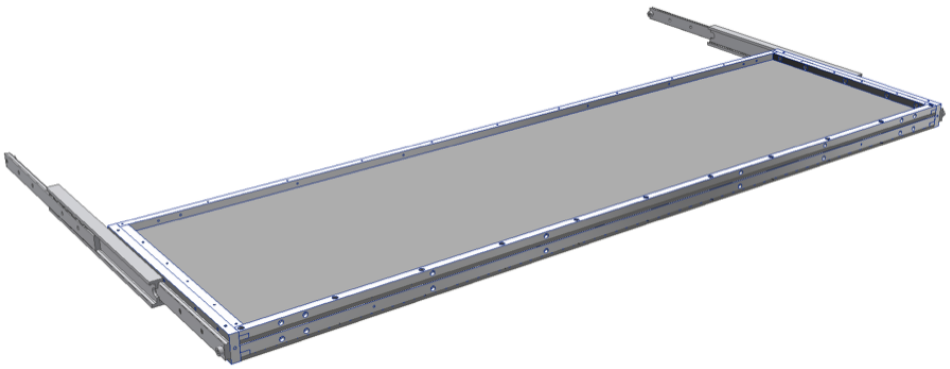

(a)

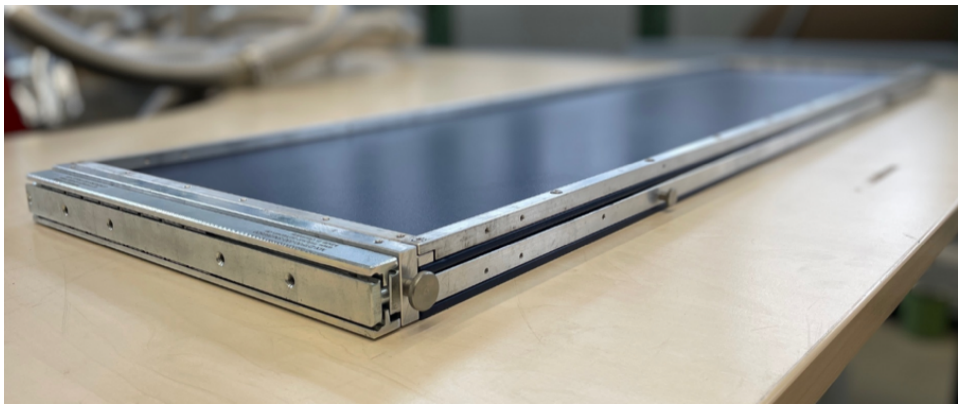

(b)

FIGURE 6.2. Design of the veto system drawers: CAD model (a) and the assembled version (b). Each drawer consists of two levels, each of which is built from a 4 mm steel sheet and a frame of aluminum profiles. The steel sheets are powder-coated for corrosion protection (RAL 5011, steel blue, semi-matt).

required. If a level is equipped with a lead absorber layer, the corresponding front profile has to be attached for stability. Without it, the steel sheet of the level would show too much sagging. If the level carries a veto layer, on the other hand, the front profile can be excluded, cf. Fig. 6.1, to provide space for the amplifier boards, which will be described in Section 6.2.4, and the cabling. Further details on the drawer design, a stability analysis, as well as an assembly guide can be found in Appendix D.1.

For properly mounting the drawers to the veto system cradle and for counteracting the slight sagging of the steel sheets, cf. Appendix D.1, 4 mm gaps are accounted for between the drawers and also between the two levels of a drawer. Each drawer therefore occupies a height of 36 mm, of which 32 mm correspond to the drawer itself and 4 mm to the gap towards the drawer above it. The 32 mm in turn result from the two 10 mm layers placed inside a drawer, its two 4 mm steel sheets, and the 4 mm gap between the two levels of the drawer. The individual layers of the veto

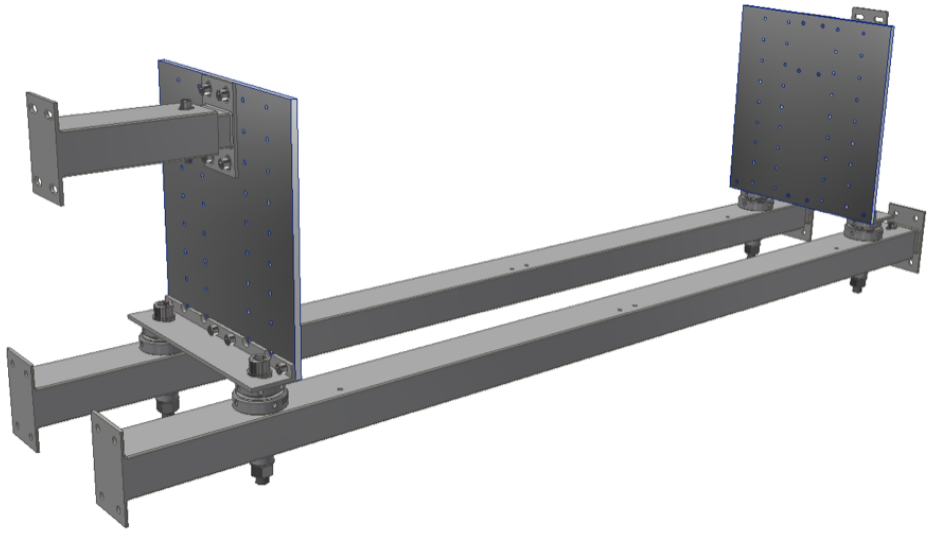

FIGURE 6.3. The steel beam cradle for installing the veto system. For a concise positioning of the drawers, two plates with a precisely produced hole pattern are used. The steel beams of the cradle are directly attached to the shielding house walls.

system thus have a nominal vertical distance of 8 mm between each other, which is the exact number as has been used for the simulation studies in Chapter 4.

In the context of this thesis, 18 drawers, nine of which will be used per veto system, have been assembled and are ready to be installed in the final MAGIX setup. A photo of an assembled drawer is shown in Fig. 6.2b.

6.1.2 Design of the Veto System Cradle

The cradle that holds the drawers, see Fig. 6.3, is based on two rectangular steel beams that are mounted to the inner walls of the shielding house, cf. Fig. 2.18. Two precisely manufactured aluminum hole plates ensure the concise positioning of the drawers in relation to each other. Four adjustable chocks connect the hole plates to the steel beams and provide adjustability in the vertical direction. Additionally, the position of the chocks can be changed along the dispersive direction of the spectrometer, by which the placement of the veto system can be adjusted so that the geometric acceptance of the veto layers matches the acceptance of the trigger layer, cf. Section 4.3.2. At the upper edges of the hole plates, two short steel beams are introduced as additional struts, one of which is a little longer than the other. This is due to the fact, that the MAGIX TPC and the MAGIX trigger veto system will not be positioned exactly in the middle of the shielding house, since the optics of the MAGIX spectrometers guide the scattered electrons slightly towards the interaction point of MAGIX, cf. Figs. 2.1 and 2.14. The orientation of the cradle therefore will be such that the shorter upper steel beam shows in the direction of the

MAGIX interaction point. Along the dispersive direction of the spectrometer, the position of the two short steel beams can be adjusted using elongated holes. The holes inside the lower steel beams will be used to attach the MayTec frame, which holds the four NINO readout boards that will be used per trigger veto system. More details on the veto system cradle, as well as an assembly guide, are provided in Appendix D.2.

During the course of this thesis, the parts for both copies of the veto system cradle have been produced and are available for being assembled into the final MAGIX setup. For corrosion-protection, all steel parts have been powder-coated (RAL 5011, steel blue, semi-matt).

6.1.3 Lead Absorber Layers

The 10 mm thick lead absorber layers are made from the hard lead alloy PbSb4 (96 % lead and 4 % antimony) due to its higher rigidity and load capacity compared to pure lead. The layers are therefore easier to handle and show less sagging. The areal dimensions of the layers are 950 mm × 250 mm in the dispersive and non-dispersive directions of the spectrometer, respectively, based on the results from the simulation studies in Chapter 4. With the density of PbSb4 being 11.21 g/cm^3, the weight of a single lead absorber layer amounts to 26.62 kg.[1]

For the final setup of MAGIX, 30 lead absorber layers are available, 15 of which will be used per veto system. For industrial safety, all lead absorber layers are painted (RAL 7035, light grey, matt).

6.2 The Veto Detectors

At this stage, each veto layer comprises three individual plastic scintillator segments that are placed next to each other along the non-dispersive direction of the spectrometer. The segments have a length of 950 mm and exhibit the rhombic profile described in Section 3.4. Each end face of a segment is read out by three SiPMs, totaling 18 SiPMs per veto layer or 54 SiPMs per veto system.

As described in Section 2.1.3 and Appendix A.1, the veto detectors of DarkMESA utilize plastic scintillation detectors read out by SiPMs as well. A lot of effort has already been invested into the development of the detectors themselves, as well as the corresponding readout and power supply electronics, so that the initial idea has been to integrate as many aspects as possible from the concept of DarkMESA into the veto layer design of MAGIX. Moreover, the NINO readout board - as it is used for the readout of the trigger layer, cf. Section 5.3.1 -, is intended to be used for also reading out the veto layers, ensuring a standardized readout across all detector layers of the trigger veto system.

Regarding the choices of scintillator material and SiPM model, MAGIX follows the concept of

[1] These values are based on the delivery notes for the lead absorber layers that have been ordered for the MAGIX trigger veto system.

DarkMESA one-to-one as it is described in Sections 6.2.1 and 6.2.2, respectively. Besides, the veto detectors of DarkMESA also serve as an example when it comes to coupling and wrapping the individual veto scintillators for MAGIX. In terms of the corresponding electronics, however, several modifications have been implemented compared to the ideas discussed in Appendix A.1. For answering the involved design questions, several preparatory studies have been necessary, which are outlined in Section 6.2.3. An outlook on the veto layers in the final MAGIX setup is then given in Section 6.2.4. Please note that as for Chapter 5, a basic knowledge of scintillation detectors is assumed and no theoretical overview is provided at this point.

6.2.1 Scintillators

As mentioned before, the individual plastic scintillator segments of the veto layers are 950 mm long and show the rhombic profile described in Section 3.4. Due to their comparatively large length, a scintillator material with a long attenuation length must be used that still meets the high requirements for fast timing, which is why EJ-200 by Eljen Technology [103] has been chosen. It is explicitly designed with a long attenuation length and fast timing, and is also the scintillator material of choice for the DarkMESA veto detectors. A comparison of EJ-200 to several other plastic scintillators can be found in Tab. 5.1 in Chapter 5. Its polymer base is polyvinyltoluene (PVT) and the light output amounts to 64 % anthracene with a wavelength of maximum emission of 425 nm. The long attenuation length and fast timing are expressed in a light attenuation length of 380 cm, a signal rise time of 0.9 ns, a decay time of 2.1 ns, and a signal pulse width (FWHM) of 2.5 ns. A photo of a veto scintillator is shown in Fig. 6.4a.

6.2.2 SiPMs

For the readout of the veto scintillators, the same SiPM model as for the DarkMESA veto system is used, i.e. the MicroFJ-60035-TSV by onsemi [137].[2] It has an active area of 6.07 mm × 6.07 mm with a microcell fill factor of 75 %. The number of microcells is 22,292. Its spectral range goes from 200 nm to 900 nm with a peak PDE[3] at 420 nm, which almost perfectly matches the wavelength of maximum emission of the veto scintillators. At this peak wavelength, the PDE ranges from 38 % to 50 %, dependent on the applied overvoltage. The overvoltage should be chosen between 1 V and 6 V, which corresponds, together with the SiPM's typical breakdown voltage between 24.2 V and 24.7 V, to a bias voltage range going from 25.2 V to 30.7 V. Achievable gains lie in the order of 10^6.

Each microcell of the MicroFJ-60035-TSV features a Single Photon Avalanche Diode (SPAD), a quench resistor, and a fast capacitor. All microcells are connected in parallel, which provides

[2] The initial motivation for DarkMESA to use this particular SiPM model is based on two main reasons: First, onsemi was chosen as the manufacturer because it is the only one that offers SiPMs with a dedicated, separate fast output. Second, the specific model MicroFJ-60035-TSV was selected for its high active area and high fill factor.

[3] **P**hoton **D**etection **E**fficiency

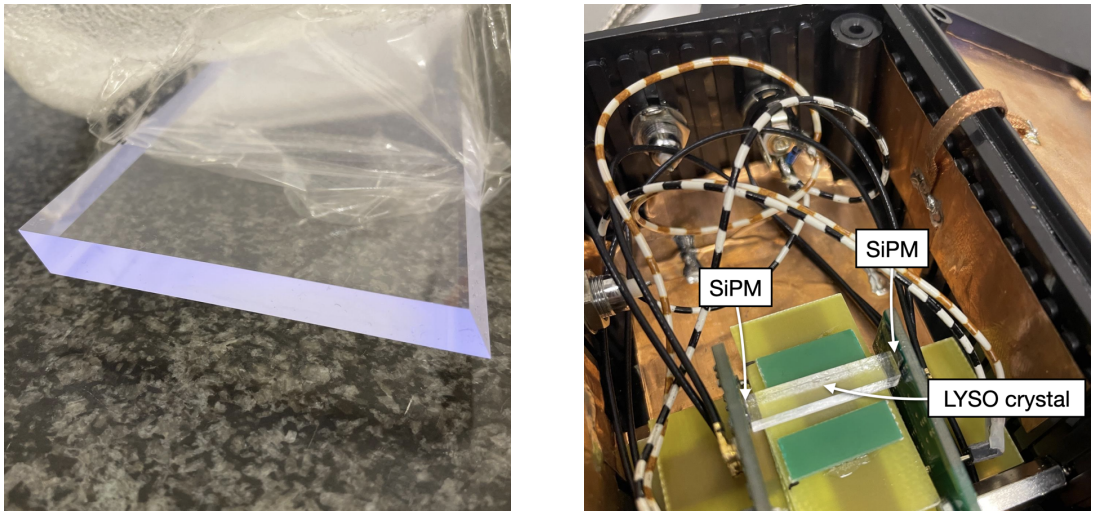

(a) (b)

FIGURE 6.4. The veto scintillators (a) are made from Eljen Technology's material EJ-200. To arrive at a final design for the readout and power supply electronics for the veto layers, dedicated preparatory studies have been performed using two SiPMs mounted in a small light-tight housing (b).

the SiPM with three terminals: Cathode, anode, and *fast output*. In contrast to the capacitively coupled fast output, the *slow output* is the output of the cathode or anode, dependent on which one is chosen for readout, showing a positive or negative output polarity, respectively. Whereas the slow output provides output pulses with a pulse width (FWHM) of ~ 50 ns, the output pulses of the fast output are significantly faster with a pulse width (FWHM) of ~ 3 ns. Conversely, the slow output provides significantly higher signals. Between cathode and anode, the bias voltage is applied, where different biasing circuits are possible, cf. [138].

6.2.3 Preparatory Studies for the Veto Electronics

As mentioned above, the veto layers are still in the development stage at the time of writing this thesis.What has been done as part of this thesis, is to tackle the unresolved questions that stood in the way of a final design of the veto electronics. Based on the found answers, the veto electronics are now being produced and will soon be available for testing and further development of the veto detectors.

The following questions have been addressed to arrive at a final design for the veto electronics:

- Do the SiPM signals of the veto layers work with the NINO readout board? Specifically, can events where only a few photons reach a SiPM be reliably detected?
- What is the influence of the NINO readout board's active attenuators on the SiPM signals? Should they be removed from the readout channels that are used for the veto detectors?

- Should the SiPMs be operated using their fast or slow output?
- Should the SiPMs be read out individually, or is the adoption of the DarkMESA design with SiPM groups of three more suitable?

To answer the above questions, a series of dedicated tests involving two SiPMs and a NINO readout board have been conducted, which are described in the following paragraphs.

Setup, Data Acquisition, and Data Analysis Fig. 6.4b shows the setup that has been used. Two SiPMs are each located on a small PCB[4] that was designed in-house by the institute's electronics workshop, and are mounted facing each other inside a small light-tight housing. The PCBs include a biasing circuit for the SiPMs that is similar to circuit B on page 3 of onsemi's application note "Biasing and Readout of ON Semiconductor SiPM Sensors" [138], but where the sense resistor R_S is chosen to be only 10 Ω instead of 50 Ω to further reduce the microcell recovery time. The SiPMs thus need to be operated with a positive bias voltage and both fast and slow outputs show positive output pulse polarities. For the tests in this section, bias voltages of 27.5 V are applied, corresponding to overvoltages between 2.8 V and 3.3 V, dependent on the specific breakdown voltage of the individual SiPM[5].

To produce signals inside the SiPMs, two different methods are used. First, coupled with optical grease, a LYSO crystal[6] with a quadratic profile of 4 mm × 4 mm and a length of 22 mm is placed between the two SiPMs, see Fig. 6.4b, and a ^{60}Co source with an activity of 84.4 kBq is used[7] to produce scintillation light inside the crystal. By this, signals with a rather high light yield are generated as they will occur for a SiPM in the final MAGIX setup if a particle interacts with a veto scintillator close to its end face to which the SiPM is coupled. A SiPM on the opposite end face will only experience tiny signals in this case, which are generated by only a handful of photons. To mimic this behaviour, the second method is used, where SiPM dark counts are measured without utilizing the LYSO crystal and the ^{60}Co source. To collect a meaningful amount of statistics per dataset, two different data taking durations are chosen for the two methods. If the LYSO crystal is employed in combination with the ^{60}Co source, only 1 min of data taking is sufficient due to the comparably high rate of ^{60}Co decays. For the SiPM dark counts, on the other hand, 5 min of data taking is necessary to accumulate enough statistics.

[4] **P**rinted **C**ircuit **B**oard

[5] For the preparatory tests in this section, the breakdown voltages of the two SiPMs have not been determined.

[6] Unfortunately, details on the exact material of the crystal are not available. But typically, LYSO crystals exhibit very fast signal rise times in the ps-region [139], while showing longer decay times compared to plastic scintillators. Moreover, LYSO crystals show a higher light yield than plastic scintillators, while the wavelengths of maximum emission are comparable, cf. [140].

[7] More precisely, the institute's ^{60}Co source "SR755" has been used. ^{60}Co is a beta-emitter that decays with a half-life of 5.3 a into ^{60}Ni under the emission of an electron. Due to the excited states of ^{60}Ni, the decay scheme of ^{60}Co shows several decay modes involving a number of gamma-ray emissions subsequent to the beta-decay. The most prominent decay mode with a branching ratio of 99.88 %, however, emits an electron with a maximum energy of 317 keV and ends on the 2.5 MeV 4^+ level of ^{60}Ni. [141]

The positive output pulses of the SiPMs are fed into passive inverters and routed to input channels 0 and 1 of the NINO readout board. For testing the influence of the active attenuators of the NINO readout board on the SiPM signals, the active attenuator of input channel 0 is bridged so that it does not affect the channel's signal flow, whereas the attenuator of channel 1 is controllable via the corresponding 12-bit DAC as normal. Details on the active attenuators will be given in Section 7.2, but the following information shall already be communicated here for better contextualization: The attenuation is the highest if the corresponding DAC value is set to 0 and is the lowest if the DAC value is 4095. In between, the attenuation follows a characteristic S-curve, cf. Fig. 7.4b. The 12-bit DAC that controls the discriminator threshold of the utilized NINO chip is set to 600, which in previous laboratory measurements has proven to be a solid working point. More details on the discriminator threshold of the NINO chips will be provided in Section 7.2 as well.

Each recorded SiPM pulse in a dataset results in a discriminated output pulse from the NINO chip, whose length encodes the time-over-threshold (ToT) of the SiPM pulse, representing a measure for its stored charge. The path from an analog pulse to the charge it contains entails numerous steps, which will be described in Section 7.1. At this point, it suffices to know that a charge value is extracted for each SiPM pulse, for which a calibrated, non-linear conversion from ToT to charge is required. However, please note that since the initial conversion from ToT to charge[8] has been conducted for an attenuator DAC value of 575, cf. Section 7.2, which corresponds to a relatively high attenuation compared to that obtained with a DAC value of 4095, the calculated charge values will be shifted to higher values for the data presented in this section.[9] The calculated charge values for the two NINO input channels are then stored in histograms and can be plotted. As a last step, a software coincidence between the two input channels is implemented, which is only exploited if the LYSO crystal and the ^{60}Co source are employed. By this, dark noise from the individual SiPMs, as well as electronics noise from the individual input channels of the NINO readout board can be filtered.

Compatability of the NINO Readout Board with the SiPM Signals of the Veto Layers
A simulation for the veto layers performed by M. Biroth has shown that when a particle interacts with a veto scintillator close to one of its end faces, a SiPM attached to the opposite end face is exposed to merely a handful of photons, typically in the order of around ten [78]. This scarcity is due to the substantial length of the veto scintillator segments, leading to a significant attenuation of the scintillation light. Consequently, the expected SiPM signals for such events exhibit very low magnitudes. Nevertheless, to ensure the ability of reading out the veto detectors in coincidence from both end faces, regardless of the incident position of the incoming particle, it is essential to ensure that the NINO readout boards are capable of effectively measuring and processing such

[8] The conversion has later been redone, see Section 7.2.3.

[9] In hindsight, this issue could have been addressed by introducing a conversion factor. However, due to time constraints, it has been relied solely on the already existing analysis framework.

signals.

To validate this capability, SiPM dark counts are used to mimic SiPM signals that are generated by only a few photons. The LYSO crystal and the ^{60}Co source are not employed. In this test, the fast output of the SiPM connected to channel 1 of the NINO readout board is utilized, with the corresponding attenuator DAC set to 4095, ensuring that the attenuation is as low as possible.

The charge histogram of the acquired data is shown in Fig. 6.5. As illustrated, the individual photoelectron (PE) peaks of the connected SiPM can be resolved, however, a 10× amplifier stage[10] is required for this purpose in this configuration. Without the amplifier, the SiPM signals are too weak for detection by the NINO readout board. The peaks at approximately 35 pC, 155 pC, and 260 pC correspond to the 1 PE, 2 PE, and 3 PE, respectively, peaks of the SiPM's gain distribution. When using the 1 PE peak to estimate the gain of the SiPM, with a value of 35 pC and taking into account the utilized 10× amplifier stage, the calculated gain amounts to approximately 21.9×10^6. Comparing this with the specified gain in the SiPM datasheet, which should be around 3.5×10^6 for the set overvoltage between 2.8 V and 3.3 V [137], the calculated gain is too high by about a factor of 6, showing the above mentioned shift of the charge values towards higher values.[11]

Hence, the NINO readout board effectively resolves the photoelectron peaks of the connected SiPM, employing a 10× amplifier stage in combination with the SiPM's fast output, and therefore the NINO readout board is capable of detecting the anticipated SiPM signals generated by only a handful of photons. Accordingly, the NINO readout board is well-suited for reading out the veto detectors of MAGIX.

Impact of the Active Attenuators on the SiPM Signals of the Veto Layers For the production of the upgraded NINO readout boards, cf. Section 5.3.2, the question has to be answered whether the active attenuators can be used in combination with the SiPM signals of the veto detectors or not. If this were not the case, the upgraded NINO readout boards would need to be equipped with two different types of input channels: One for reading out the trigger layer signals, including the active attenuator, and another without it for the signals of the veto layers. While the last paragraph has already demonstrated that small SiPM signals can be detected with the NINO readout board including the active attenuators, their influence on the SiPM signals is studied somewhat more precisely.

As a first step, the NINO readout board's channel 0 with its bridged attenuator is compared to channel 1 with the attenuator set to the most open configuration, i.e. its DAC value is set to 4095. Fig. 6.6 presents the resulting charge histograms, both for SiPM signals generated using the LYSO crystal and the ^{60}Co source, Figs. 6.6a and 6.6b, as well as for SiPM dark counts amplified by a 10× amplifier, Figs. 6.6c and 6.6d.

[10] Throughout the tests in this section, the gain block AD8354 by Analog Devices [142] has been used for this purpose.

[11] If compared to the base attenuation of the active attenuators that roughly amounts to a factor of 4 when considering the charge, cf. Section 7.2.1, this approximate result seems reasonable.

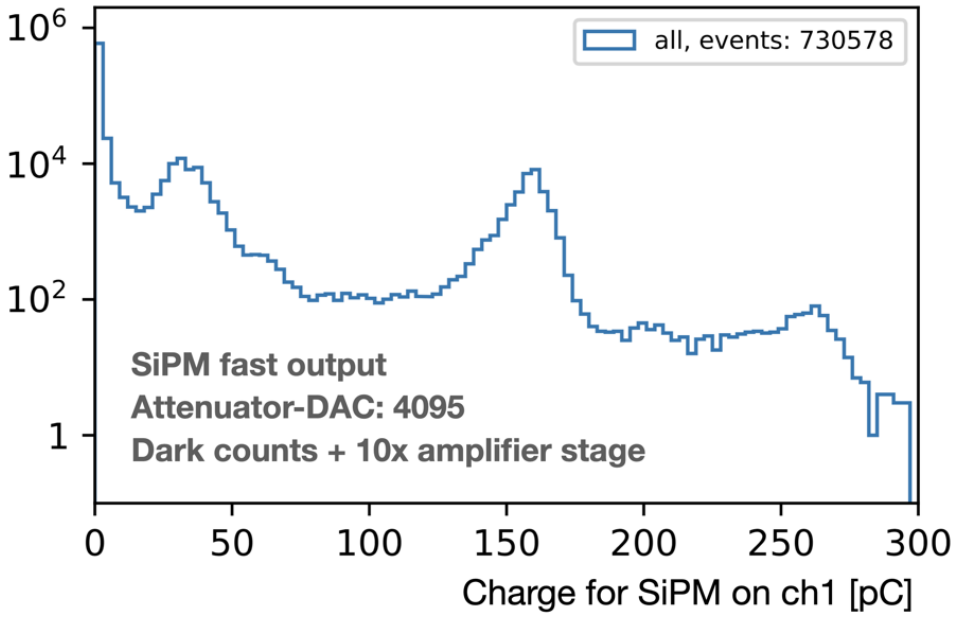

FIGURE 6.5. The charge histogram for the SiPM connected to channel 1 of the NINO readout board, when SiPM dark counts and a 10× amplifier stage are utilized. The clearly identifiable peaks at around 35 pC, 155 pC, and 260 pC correspond to the first three photoelectron (PE) peaks of the SiPM gain spectrum. The peak at 0 pC is referred to as the pedestal or noise edge [143].

For SiPM signals generated with the LYSO crystal and the ^{60}Co source, two distinctions are apparent between the charge histograms for the bridged attenuator, Fig. 6.6a, and the open attenuator, Fig. 6.6b. First, the charge histogram for the bridged attenuator is slightly shifted towards higher charge values. This is due to the fact that the open attenuator introduces a base attenuation for channel 1, which is absent for the bridged attenuator of channel 0. Secondly, the charge histogram for the bridged attenuator displays more noise compared to that for the open attenuator. The base attenuation of the open attenuator therefore helps reducing noise and thus appears to be advantageous. Similar observations can be made for the SiPM dark counts. The PE peaks in the charge histogram for the bridged attenuator, Fig. 6.6c, are less pronounced than those in the charge histogram for the open attenuator, Fig. 6.6d, further highlighting the noise reduction provided by the base attenuation. Regarding the position of the PE peaks, no definitive conclusion can be drawn. While the first and third PE peaks seem to be at the same locations for both charge histograms, the second PE peak has shifted to a lower charge value for the bridged attenuator. The expected shift towards higher charge values for all three PE peaks is not observed. Nonetheless, this discrepancy likely arises from the conversion from ToT to charge, which provides incorrect charge values since it has been performed for a considerably higher attenuation. Therefore, this issue has not been studied any further.

In a subsequent test, the dynamic range of the active attenuator of the NINO readout board's

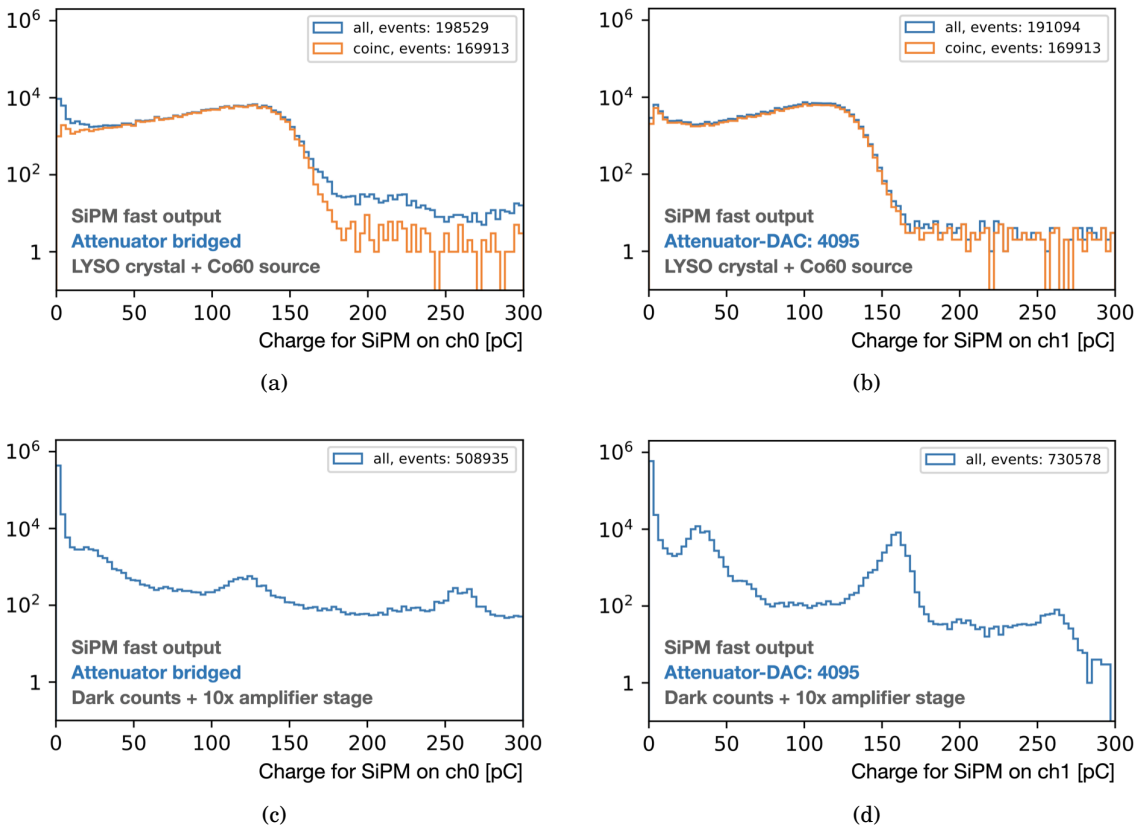

FIGURE 6.6. The charge histograms for signals generated with the LYSO crystal and the ^{60}Co source (a and b), as well as for SiPM dark counts (c and d), both for the bridged attenuator of channel 0 and the open attenuator of channel 1. The open attenuator clearly introduces a base attenuation that helps reducing noise.

channel 1 is investigated by varying the attenuator DAC value while using SiPM dark counts to generate SiPM signals. Exemplarily, the charge histograms for the four attenuator DAC values 1000, 1100, 1115, and 1500 are shown in Figs. 6.7a–6.7d, respectively. For a DAC value of 1000, the attenuation is so high that only two PE peaks surpass the effective signal threshold. If the DAC value is increased, i.e. the attenuation is decreased, more and more PE peaks can be resolved. The difference between the charge histograms for the DAC values 1100 and 1115 demonstrates how sensitively the attenuator affects the SiPM signals in this region. A DAC value of 1500 then represents a relatively open setting for the attenuator again, as the PE peaks closely resemble those in Fig. 6.6d. Thus, it can be stated that the use of the active attenuators leaves enough head room for adjusting the signal thresholds for the veto detectors.

In conclusion, the active attenuators can be effectively used with the SiPM signals of the veto detectors. Their base attenuation reduces noise, and their dynamic range enables the flexible adjustment of the signal thresholds of the NINO readout board's input channels, while offering enough head room towards both higher and lower attenuation levels. The upgraded NINO readout

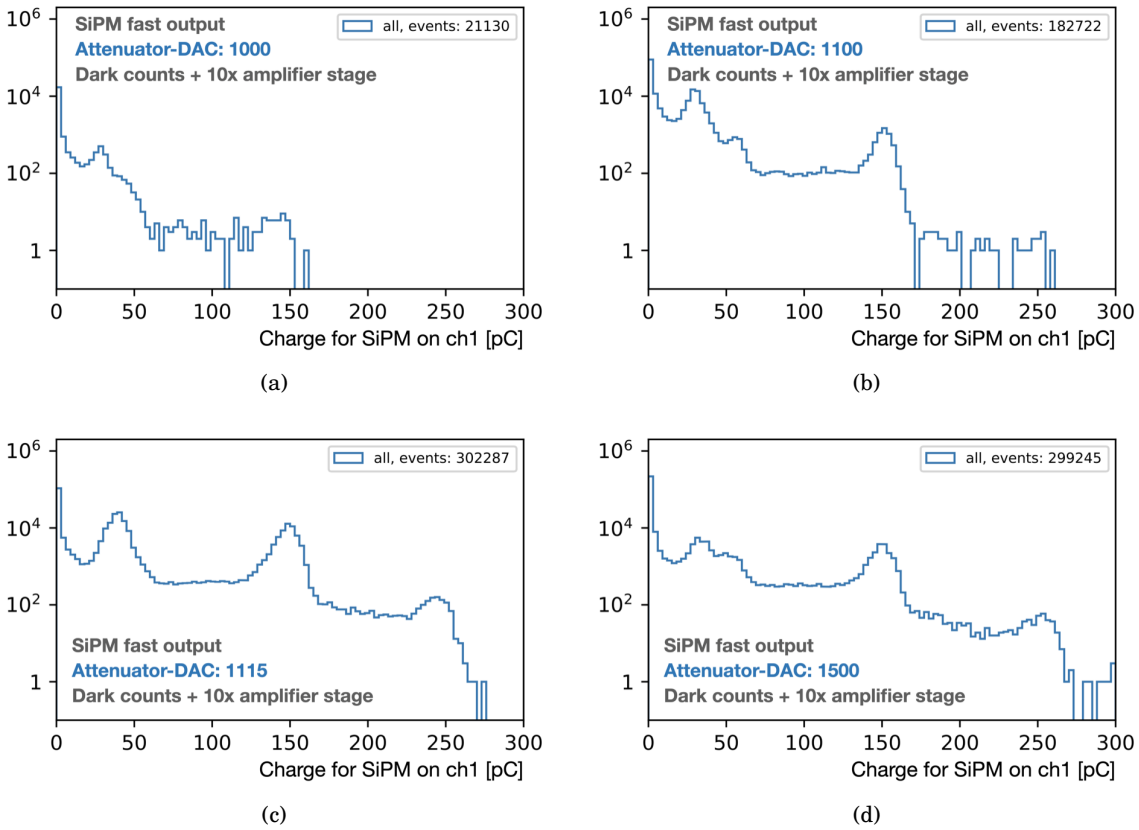

FIGURE 6.7. The charge histograms for different attenuator DAC values for channel 1 using SiPM dark counts. As the DAC value is increased, i.e. the attenuation decreased, more and more PE peaks surpass the effective signal threshold. The active attenuators thus appear to offer enough head room to be used with the SiPM signals of the veto layers.

board will therefore incorporate an active attenuator in every readout channel.

Choice between the SiPM's Fast and Slow Output As demonstrated in the previous two paragraphs, SiPM signals generated by only a few photons necessitate a 10× amplifier stage to be detected by the NINO readout board, if the fast output of the SiPM is utilized. This prompts the consideration whether omitting the additional amplifier per veto layer readout channel could be feasible by employing the SiPM's slow output instead. While this approach would sacrifice the superior timing characteristics of the fast output, it could potentially streamline the design and production of the readout electronics for the MAGIX veto layers, reducing both cost and effort.

To explore this possibility, the performance of the slow output is compared to that of the fast output operated with a 10× amplifier stage, both for SiPM dark counts and SiPM signals generated with the LYSO crystal and the ^{60}Co source. SiPM dark counts are used to determine whether the additional amplifier stage can indeed be omitted, while the signals generated with the LYSO

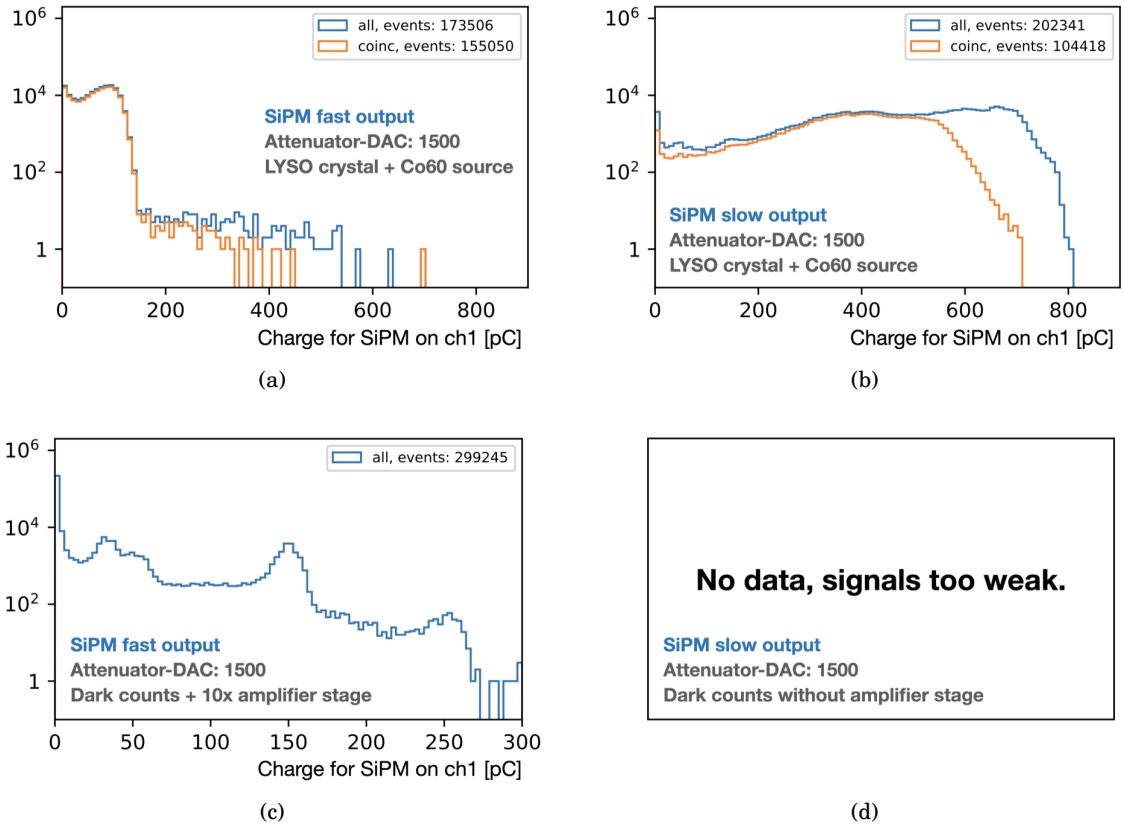

FIGURE 6.8. The charge histograms for signals generated with the LYSO crystal and the ^{60}Co source (a and b), as well as for SiPM dark counts (c and d), both for the SiPM's fast and slow output. When using SiPM dark counts, the fast output is operated in combination with a 10× amplifier stage. In comparison to the output signals from the fast output, those from the slow output exhibit significantly larger charge values. However, the increase is not sufficient to dispense with the need for the 10× amplification.

crystal and the ^{60}Co source provide insight into the behaviour of the slow output. Both types of signals are read out with channel 1 of the NINO readout board, where the DAC of the active attenuator is set to 1500.

The resulting charge histograms are depicted in Fig. 6.8. For the signals generated with the LYSO crystal and the ^{60}Co source, Figs. 6.8a and 6.8b, there is a clear distinction between reading out the SiPM's fast or slow output, respectively. The output signals from the slow output show significantly larger charge values than those from the fast output. However, both outputs can be read out and processed, rendering no clear preference based on the signals generated with the LYSO crystal and the ^{60}Co source. Conversely, for SiPM dark counts, the outcomes differ. As in the previous paragraphs, the PE peaks of the SiPM can be resolved using the fast output and the 10× amplifier stage, Fig. 6.8c, but not when utilizing the slow output, Fig. 6.8d. The SiPM signals

remain too weak to be processed by the NINO readout board.

Hence, regardless of whether the fast or slow output is employed, an additional 10× amplification is imperative for processing the SiPM signals of the veto layers with the NINO readout board. Given this necessity, it would be imprudent to forego the superior timing characteristics of the fast output. Consequently, the SiPMs of the veto detectors will be read out using their fast output.

Individual vs. Summed SiPM Signal Readout: Decision for MAGIX As previously discussed, DarkMESA's veto detectors are read out using SiPM groups of three, a choice made to reduce the overall channel count for readout and slow control. Another motivation behind this decision was to amplify the signal charge, as it was not clear what the lower limit of the signal threshold of the DarkMESA readout would be. Initially, adopting this approach for MAGIX seemed like a straightforward choice. However, employing SiPM groups presents several drawbacks.

First, the additional spatial resolution that is available by using more than one SiPM, cf. Bachelor's thesis by H. Keßler [136], cannot be capitalized, as it cannot be discerned from the signal sum, which SiPM yielded a larger or smaller signal. Secondly, summing the three individual SiPM signals increases the detector capacitance by a factor of three, consequently reducing the signal rise time by the same factor. Thirdly, employing a single bias voltage for all three SiPMs of a group, all of which will have slightly different breakdown voltages, leads to different overvoltages and gains. Gain-matching the three SiPMs is simply not possible.

For MAGIX, a critical question arises: What holds greater importance? Is it worthwhile to reduce the channel count to save cost and effort and to enhance the SiPM signal charges, even at the expense of compromising on the three above aspects? The immediate response tends towards a resounding no. With only 54 SiPMs across all three veto layers of a trigger veto system, the channel count becomes virtually inconsequential nowadays. Moreover, the tests of the previous paragraphs have shown the feasibility of reading out individual SiPM signals using the NINO readout board, making charge amplification unnecessary.

Nonetheless, to assess the performance of the SiPM signal sum in conjunction with the NINO readout board, a comparative measurement between individual SiPM signals and their sum is conducted. Using a T-piece to sum the signals, the combined signal is directed to channel 1 of the NINO readout board, with the DAC value of the active attenuator set to 1500. Again, both SiPM dark counts and SiPM signals generated with the LYSO crystal and the ^{60}Co source are used.

The resulting charge histograms, shown in Figs. 6.9a–6.9d, reveal no significant distinctions for the SiPM signals generated with the LYSO crystal and the ^{60}Co source. Although the charge values for the summed signal are shifted towards higher values, this remains the only notable disparity observed. Similarly, for the SiPM dark counts, while the PE peaks for the summed signal are shifted towards higher charge values compared to the individual SiPM signals, they remain resolvable.

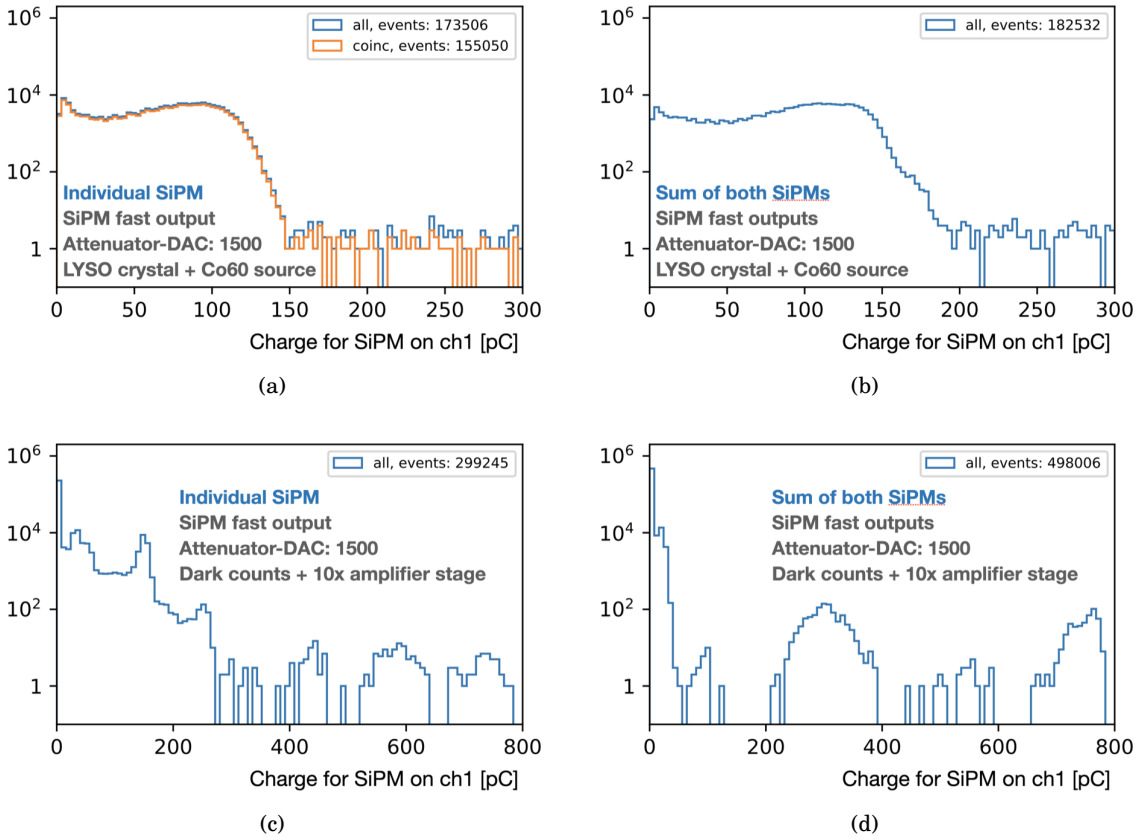

FIGURE 6.9. The charge histograms for signals generated with the LYSO crystal and the ^{60}Co source (a and b), as well as for SiPM dark counts (c and d), once for both SiPMs being read out individually and once for their summed signal. The charge values for the summed signal are shifted to higher values but this is the only notably observation.

In conclusion, employing SiPM groups of three fails to outweigh its drawbacks for the purposes of MAGIX. Therefore, 54 veto layer signals per trigger veto system can comfortably be handled, and charge amplification is unnecessary for the SiPM signals of the veto detectors. Instead, when reading out each SiPM individually, MAGIX benefits from the enhanced spatial resolution along the non-dispersive direction of the spectrometer, from a faster signal rise time for the veto detectors and thus from an improved time resolution, as well as from the possibility to individually adjust the bias voltages of the SiPMs for gain-matching.

Summary and Conclusions for the Veto Electronics Based on the preceding analyses, the following conclusions can be drawn:

- The SiPM signals of the veto detectors can be effectively read out using the NINO readout board with the incorporation of an additional 10× amplifier stage. Notably, when measuring with SiPM dark counts, it is possible to resolve the individual photoelectron peaks of the

charge spectrum. The NINO readout board therefore proves suitable for detecting events involving only a handful of photons reaching a SiPM, as anticipated in the final setup of MAGIX. Consequently, the NINO readout board will be employed for processing both trigger layer and veto layer signals, thereby unifying the overall readout strategy of the trigger veto system.

- The active attenuators of the NINO readout board do not detrimentally affect the SiPM signals of the veto detectors. While they introduce a base attenuation, it is not substantial enough to adversely impact the SiPM signals. On the contrary, the active attenuators aid in noise reduction. Overall, they offer a broad dynamic range, providing considerable flexibility for setting an effective signal threshold. Therefore, all input channels of the NINO readout boards will be equipped with active attenuators, considerably simplifying the production complexity of the NINO readout boards.

- Both the fast and the slow outputs of the SiPMs necessitate a 10× amplification for detecting SiPM signals with the NINO readout board. As a result, the slow output no longer holds any advantage over the fast output for MAGIX. It is thus advisable to leverage the faster timing characteristics of the fast output whenever possible. Hence, the SiPMs of the veto detectors will be operated using their fast outputs.

- The summation of several SiPM signals, similar to the SiPM groups of three at DarkMESA, does not offer any advantages for the veto detectors of MAGIX. In contrast, using individual SiPM signals provides additional spatial resolution along the non-dispersive direction of the spectrometer, improves the rise time of the veto layer signals by reducing the detector capacitance, and offers the flexibility of individually adjusting the SiPM bias voltages. Moreover, given the limited number of 54 SiPMs per veto system, the argument of reducing the channel count by grouping the SiPMs holds far less significance compared to DarkMESA. Due to these considerations, it has been decided to read out the SiPMs of the veto detectors individually.

Building upon these decisions for the veto electronics, dedicated *SiPM boards*, *amplifier boards*, and a *slow control crate* designated for the veto layers in the final MAGIX setup are currently being developed in-house at the time of writing this thesis.

The SiPM boards will be directly attached to the end faces of the veto scintillators and carry the three SiPMs and a temperature sensor. To simplify the later wrapping process of the veto detectors, the shape of the SiPM boards precisely conforms to the rhombic profile of the veto scintillators, resulting in the need of two mirrored versions of the SiPM boards. The layouts of the two versions are shown in Fig. 6.10.

The amplifier boards will act as an intermediary component between the SiPM boards, the NINO readout boards, and the slow control crate. The nine SiPM signals from the three SiPM boards

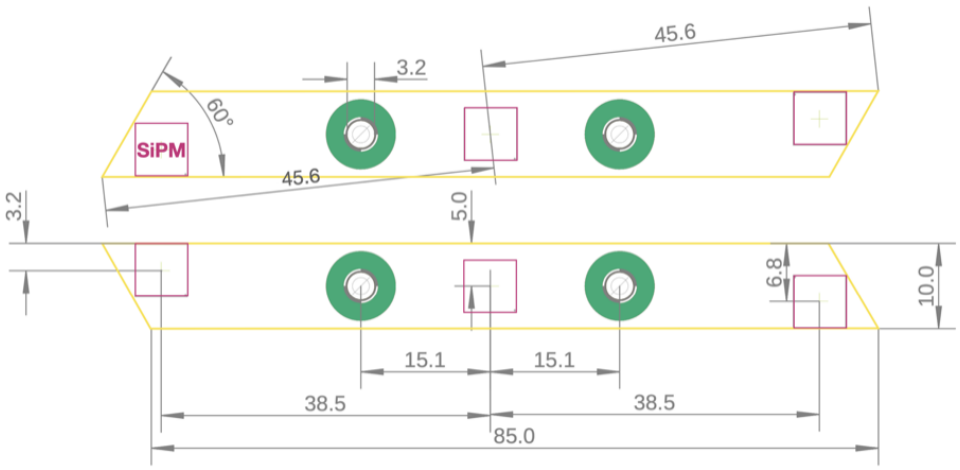

FIGURE 6.10. The layouts of the two mirrored versions of the SiPM boards. The boards carry three SiPMs, with the two outer ones placed towards the sharp corners of the rhombic profile. Two M3 through-holes can be used to attach the boards to the end faces of a veto scintillator. The temperature sensors are located at the rear sides of the boards and are not shown here. Figure from [144].

of a single veto layer side are guided through MML cables to one amplifier board, where they undergo a 10× amplification[12] and can then be accessed via SMA connectors for the connection to a NINO readout board. As such, two amplifier boards are used per veto layer, meaning that six boards are required per veto system. For mounting the two amplifier boards of a veto layer, the unused holes along the front edge of the respective drawer level will be used. In addition to the readout aspect, the amplifier boards also forward the required voltages to the SiPM boards, also via MML cables, and serve as a communication interface between the SiPM boards and the slow control crate. For instance, the amplifier boards house the DACs that allow for the adjustment of the bias voltages of the individual SiPMs. The control of the amplifier boards in turn happens via a Display Port connection from the slow control crate. The layout of the amplifier boards is depicted in Fig. 6.11.

The slow control crate will be built in the form of a full-size 19-inch crate, housing a double-channel power supply CAD36.0,65 by Kniel System-Electronics [145] to provide the bias voltages for the SiPMs, one in-house developed Ethernet controller as the control unit, cf. Section 5.2.4, and one Kniel CAD5.4 serving as the power supply for the Ethernet controller. Additionally, front panels will be available that provide the Display Port outputs for controlling the amplifier boards. Similar to the slow control crate of the trigger layer, the Kniel power supplies have been chosen due to their extremely low-noise behaviour and good radiation hardness compared to other devices.

[12] The gain block AD8354 by Analog Devices [142] will also be employed for this purpose.

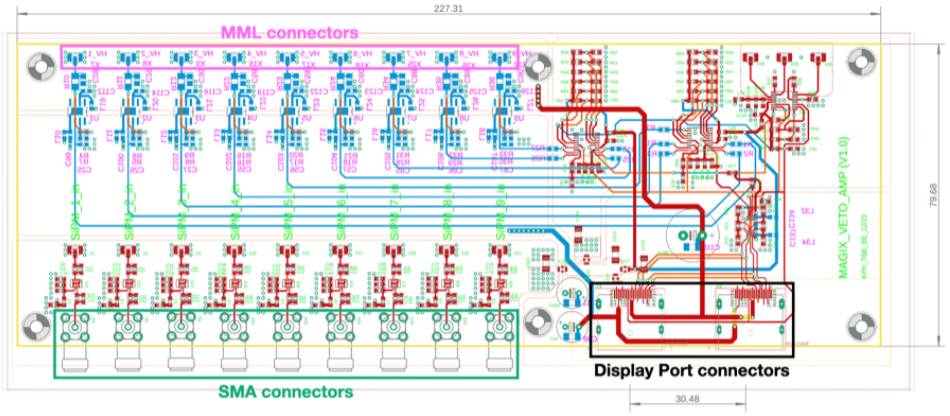

FIGURE 6.11. The layout of the amplifier boards. At the rear side of the board, MML connectors are available for connecting the SiPM boards; the SMA connectors at the front side are used for routing the amplified SiPM signals to the NINO readout boards; and two redundant Display Port connectors are provided for the communication with the slow control crate. Figure from [130].

6.2.4 Outlook on the Veto Layers in the Final MAGIX Setup

Summarizing the decisions from the previous sections, the veto layers will be built as follows: Each veto layer comprises three individual veto detectors positioned adjacent to each other along the non-dispersive direction of the spectrometer. Each veto detector consists of a 950 mm long EJ-200 plastic scintillator segment with the rhombic profile described in Section 3.4, read out by three individual SiPMs per end face. The SiPMs are from onsemi's model MicroFJ-60035-TSV and are located on dedicated in-house developed SiPM boards that will be optically and mechanically coupled directly to the end faces of the scintillator segments. The exact coupling procedure and wrapping process remain undetermined at the time of writing this thesis.

For the readout of the veto layer signals, the upgraded NINO readout board, cf. Section 5.3.2, will be utilized. Per spectrometer, 54 readout channels are required for the three veto layers, and together with the 44 readout channels for the trigger layer, this explains the necessity for installing four NINO readout boards per trigger veto system. Unlike the readout channels that handle the signals of the trigger layer, those processing the veto layer signals will not employ the in-house developed passive 20 dB attenuators, cf. Section 7.2, due to the comparatively low magnitudes of the SiPM signals.

In-house developed amplifier boards will serve as the interface between the SiPM boards, the NINO readout boards, and the full-size 19-inch slow control crate designated for the veto layers in the final setup of MAGIX. The amplifier boards provide the 10× amplification for the SiPM signals and forward the required voltages to the SiPM boards. The slow control crate houses all necessary power supplies and is responsible for controlling all amplifier boards and SiPM boards. The crate will be mounted inside the rack underneath the trigger veto system and will be

accessible from the *trigger veto side* as defined in Section 5.2.4.

For the final setup of MAGIX, 24 veto scintillators are available, nine of which will be used for the three veto layers of a veto system. The remaining six scintillator segments, which is the equivalent of two complete veto layers, will serve as spare parts. All 24 veto scintillators will be equipped with SiPM boards, fully wrapped, and prepared for immediate use as backup veto detectors. This implies the need for 48 SiPM boards, 24 of each mirrored version. However, to secure sufficient spare boards for the future operation of MAGIX, 30 SiPM boards will be produced of each version, totaling 60 altogether. With three SiPMs per SiPM board, a total of 180 SiPMs are thus required for equipping all 60 SiPM boards. During the course of this thesis, 320 SiPMs have been procured, with the remaining 140 earmarked for potential use in the veto detectors of DarkMESA. Regarding the amplifier boards, six boards are required per spectrometer, totaling twelve overall. Yet, as with the SiPM boards, a reserve of additional boards will be necessary to ensure replacement availability for the future operation of MAGIX. Thus, 15 amplifier boards will be produced in total. The full-size 19-inch slow control crate will be built twice, once for each spectrometer, and will provide Display Port outputs for the connection of up to eight amplifier boards, six of which will be needed per spectrometer. The remaining two will serve as spare channels.

Part III

The Readout of the MAGIX Trigger Veto System

CHAPTER 7

FROM SIGNAL TO DATA

During the design and development process of the trigger veto system presented in Chapters 5 and 6, a fully developed and ready-to-build design of the trigger veto system has been successfully achieved. What is missing, however, is the actual data acquisition, i.e. readout and analysis. The present chapter therefore begins with a detailed description of the readout process, following the path of PMT signals from the trigger detectors as they are processed by the NINO readout board and the MYiR Z-turn board, until data is recorded and available for analysis. Along the way, particular attention will be given to the *control parameters* that significantly affect the signal flow along a readout channel. Signals from the veto layers are not considered, as the development of the veto detectors is not yet fully complete at the time of writing this thesis.[1] The following Chapter 8 will then build upon this data, discussing key aspects of the analysis process and extracting essential detector properties for the trigger detectors.

Section 7.1 of this chapter begins with an introduction to the PMT signals from the trigger detectors and their characteristics. Section 7.2 then covers the signal processing on the NINO readout board, including the passive 20 dB attenuators, the active attenuators, and the NINO chips. The role of the Z-turn board is described in Section 7.3, with particular attention to the *Tapped Delay Line TDC* implemented on the Z-turn board's FPGA. Finally, Section 7.4 concludes the chapter with an overview on how to acquire data.

Please note that for most of the measurements in this chapter, the upgraded second version of the NINO readout board has been used, along with the passive 20 dB attenuators. By doing so, consistency and comparability with the results presented in Chapter 8 are ensured. In the rare

[1] Nevertheless, the majority of the readout chain is identical. Although the amplitudes and shapes of the veto layer signals will differ from those of the trigger detectors, this only necessitates adjustments to the settings of the corresponding readout channels.

(a) (b)

FIGURE 7.1. An exemplary signal of the trigger detector "MXTRG25" for a control voltage of 3000 mV (a), as well as the corresponding Fourier spectrum from 0 Hz to 1.2 GHz (b). The signal has been obtained with a digital oscilloscope, using one of the passive 20 dB attenuators, as they will be used in the final MAGIX setup.

cases, where the passive 20 dB attenuators have not been utilized, or the original version of the NINO readout board has been employed, it is explicitly stated.

7.1 The PMT Signals of the Trigger Detectors

Following the development of the trigger layer in Chapter 5, all required components are available to extract signals from the trigger detectors. At this point, the signals can be influenced by only one *control parameter*, i.e. the PMT control voltage that adjusts the applied voltage between a PMT's cathode and anode and therefore the applicable gain of the PMT. In the following, this parameter is called *control voltage* or, in short, *cv*.

An exemplary signal for a control voltage of 3000 mV is shown in Fig. 7.1a, obtained using cosmogenic muons[2] and recorded with PMT "A" of the trigger detector "MXTRG25", a digital oscilloscope[3], and, in between, one of the passive 20 dB attenuators that will be used for the trigger layer readout channels in the final MAGIX setup. Details on the passive attenuators will be given in Section 7.2.1. As can be seen, the PMTs of the trigger detectors yield sharp peaks with a pulse width (FWHM) of only a few ns, which can be directly translated into a rough estimate for the detector system's dead time. The stringent dead time criterion specified for the trigger layer, cf. Section 3.2, is therefore effectively fulfilled. Furthermore, for illustration, Fig. 7.1b displays the Fourier spectrum of the signal, whose frequency components need to be considered for the frequency response of the adjustable active attenuators, as will be covered in Section 7.2.1 as well.

[2]Since both the MESA beam electrons and cosmogenic muons are minimium ionizing particles, their average energy depositions inside a trigger scintillator are practically identical. The PMT signals of both particle types thus have comparable amplitudes and shapes.

[3]Rohde & Schwarz RTM3004 [146]

To get a better feeling for the behaviour of the signals from the trigger detectors, Fig. 7.2 shows exemplary histograms of several characteristic variables of the PMT pulses, as well as how they change with the applied control voltage. Again, the data has been obtained with cosmogenic muons, using the PMT "MXTRG25A" in combination with the above mentioned digital oscilloscope and one of the passive 20 dB attenuators, where each analog PMT pulse is recorded as an array of voltage values and corresponds to one event. After determining and subtracting the signal baseline for a PMT pulse, its pulse height, charge, and FWHM can be extracted[4]. Figs. 7.2a, 7.2c, and 7.2e, respectively, show the histograms of these three characteristic variables for the case of self-triggered events. In contrast, Figs. 7.2b, 7.2d, and 7.2f show the histograms for events triggered by a coincidence between the two PMTs "A" and "B" of the trigger detector "MXTRG25".[5] Per histogram and control voltage, 10 000 events have been recorded.[6] Besides, the histograms for the individual control voltages have been stacked for better visualization.

As expected, the pulse height of the PMT pulses increases with increasing control voltage, as does the charge. For the self-triggered events, see Figs. 7.2a and 7.2c, both the pedestal - also referred to as the noise edge [143] - and the muon peaks are clearly visible. Whereas the pedestal stays at a constant position, the muon peak shifts towards higher values as the control voltage is increased. For the coincidence-triggered events, in contrast, see Figs. 7.2b and 7.2d, only the muon peaks are discernible, as the random noise events of the pedestal hardly cause coincident events in both PMTs of the trigger detector. The mere sight of these histograms therefore highlights why a coincident readout of the trigger detectors is so crucial.

A similar picture arises for the FWHM distributions. As the control voltage is increased, the PMTs get more and more noisy, which shows itself in a broadening of the FWHM distribution for the self-triggered events, see Fig. 7.2e, towards low FWHM values. In addition, an increased gain of the PMT of course leads to higher pulse heights and thus to higher FWHM values. For the coincident events, on the other hand, see Fig. 7.2f, only the latter can be observed. As the control voltage is increased, the FWHM distribution is shifted towards higher FWHM values.

[4] Since the PMT pulses are negative signals, the pulse height is just the minimum of the voltage array. The charge can be calculated by the following notation of Ohm's law, $Q = \frac{U \times t}{R}$, where the current I is expressed as Q/t, U is the integrated voltage of the PMT pulse, $R = 50\,\Omega$ is the characteristic impedance, and $t = 0.1\,\text{ns}$ is the timescale of the oscilloscope, i.e. the time difference between two voltage values of the array. The FWHM can be extracted by scanning the voltage array and taking the time difference between the points, at which the voltage is equal to half the pulse height.

[5] To ensure the same setup for both the self-triggered and the coincidence-triggered events, the NINO readout board has been used to create the trigger signal for the oscilloscope. The signals of PMTs "MXTRG25A" and "MXTRG25B" have been guided through passive signal splitters before being routed to readout channels 0 and 16 of the NINO readout board, respectively, and the oscilloscope. This fact has not been corrected for! Therefore, the unaffected PMT pulses of the trigger detectors exhibit a power that is twice as high as shown in Figs. 7.2 and 7.3. For the self-triggered events, the oscilloscope has been triggered with the logical OR of the two used input channels of the NINO readout board, assigned to one of the two NIM outputs at the rear of the NINO readout board. For the coincidence-triggered events, the logical AND has been employed. In both cases, the NINO readout board has been configured with *att* and *thr* values of 700 and 600, respectively. More details on these two DAC values will be given in Section 7.2.

[6] Note that the peaks in the histograms thus exhibit varying degrees of prominence. In hindsight, it would have been preferable to gather data for an equal duration of time.

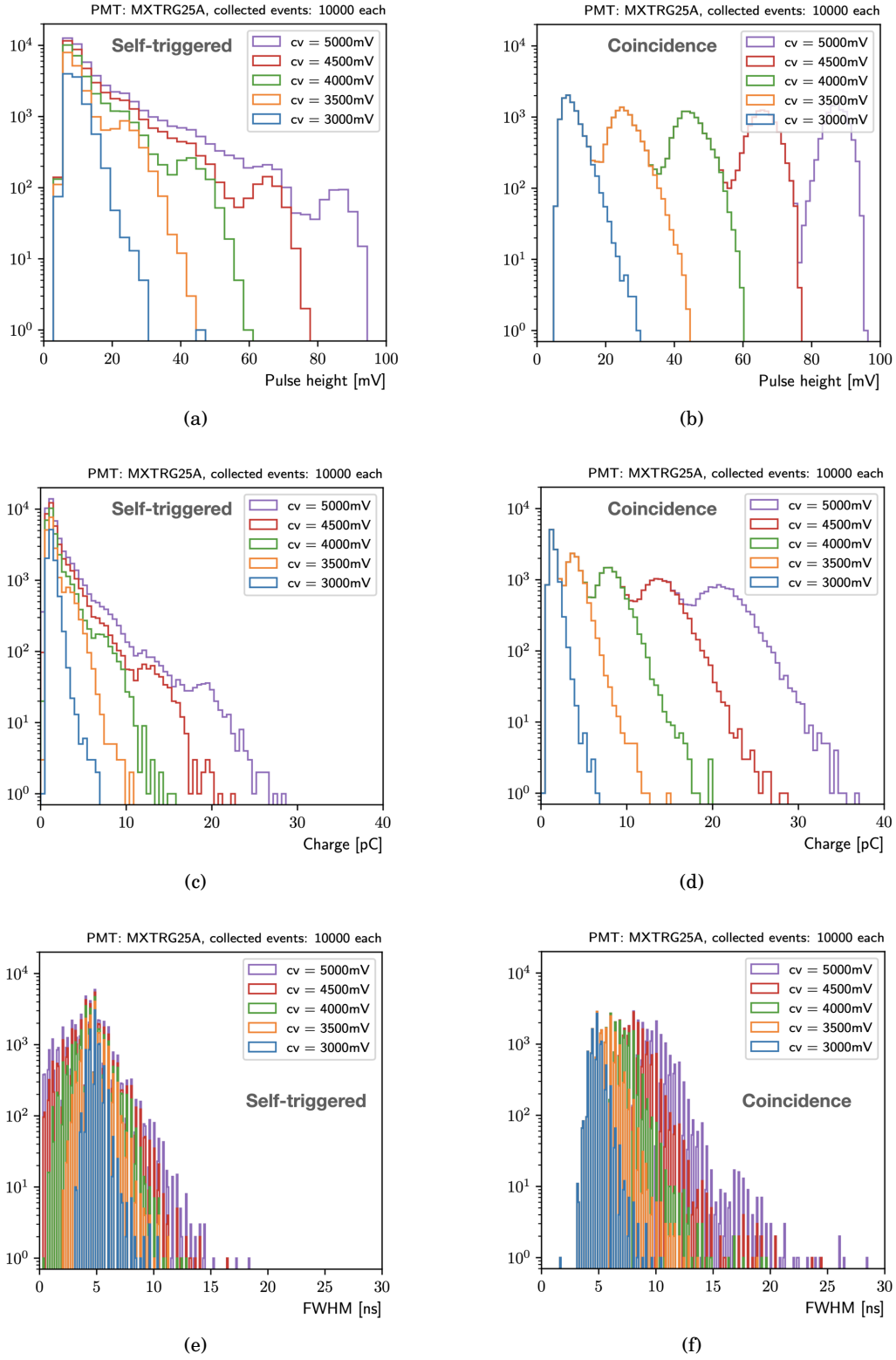

FIGURE 7.2. Pulse height, charge, and FWHM distributions of the trigger PMT pulses for different control voltages, both for self-triggered events (left) and coincidence-triggered events (right).

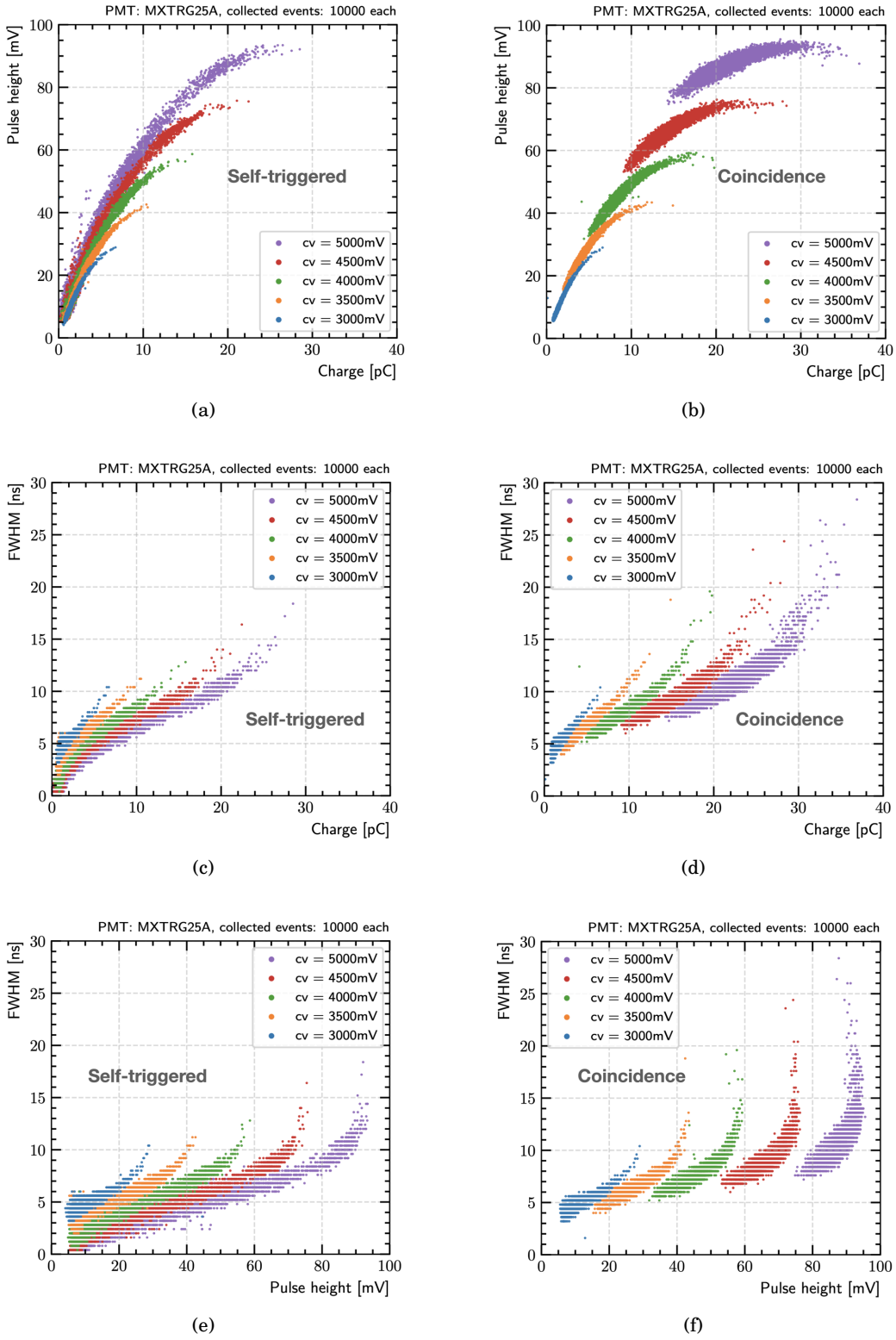

FIGURE 7.3. Scatter plots of pulse height, charge, and FWHM of the trigger PMT pulses for different control voltages, both for self-triggered events (left) and coincidence-triggered events (right). The observable discretization corresponds to the binning of the data acquisition.

Once again, this illustrates how crucial the coincident readout of the trigger detectors is for the quality of the trigger data.

As an additional illustration that the coincident readout of the trigger detectors works as intended, Fig. 7.3 displays the 2D scatter plots of the three characteristic variables pulse height, charge, and FWHM. Again, once for self-triggered events, see Figs. 7.3a, 7.3c, and 7.3e, and once for coincidence events, see Figs. 7.3b, 7.3d, and 7.3f. Clearly, the coincident readout ensures that noise is filtered out and only the events caused by cosmogenic muons are recorded.

7.2 Signal Processing on the NINO Readout Board

The analog PMT signals of the trigger detectors are routed onto the readout channels of a NINO readout board, where they are first attenuated and then processed by its four NINO chips. The resulting output signals are Time-over-Threshold (ToT) encoded, differential LVDS logic pulses. Thus, the magnitude of an analog input signal gets encoded into the width of the output signal. The signal flow along a readout channel can be influenced by several *control parameters*, i.e. by setting several 12-bit DACs[7], that are controllable via the Z-turn board, as will be shown in Section 7.4. Especially those for adjusting the amount of attenuation and for setting the discriminator threshold of the corresponding NINO chip are of special interest, because when combined, an individual effective signal threshold can be set per readout channel. The following paragraphs provide details about the signal processing along a readout channel and how it can be influenced, with an emphasis on the *control parameters* that will later be relevant during data acquisition.

7.2.1 Attenuation

The first stage of the signal processing along a readout channel is the attenuation of the relatively high signal amplitudes from the trigger detectors. Given the NINO chip's sensitive input signal range of 100 fC to 2 pC [128], this step is essential to ensure the operation of a NINO chip within its specifications. Each readout channel of the NINO readout board therefore features an adjustable active attenuator that is controllable by a 12-bit DAC. Additionally, a passive 20 dB attenuator is included in each readout channel[8] so that the active attenuators can also be operated within their specifications.

Active Attenuators The adjustable active attenuators are from the model BAP64Q, a four-pin diode attenuator by NXP [131]. Its schematics is shown in Fig. 7.4a, where $RF_{in/out}$ are the two

[7] All DACs in this section are from the model AD5671RB by Analog Devices [147].

[8] Please note that only the readout channels used for the trigger detector signals will utilize the passive 20 dB attenuators in the final setup of MAGIX, as the signal amplitudes from the veto detectors are sufficiently low to eliminate the need for additional attenuation.

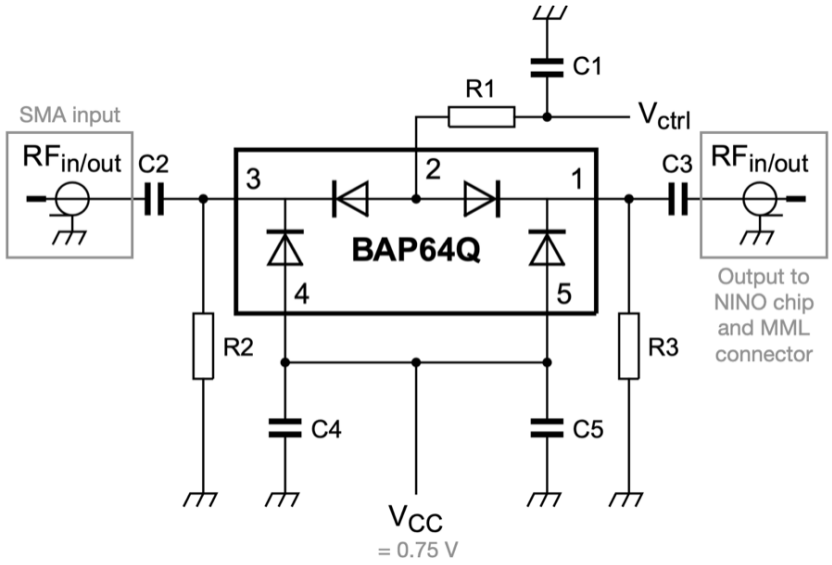

(a)

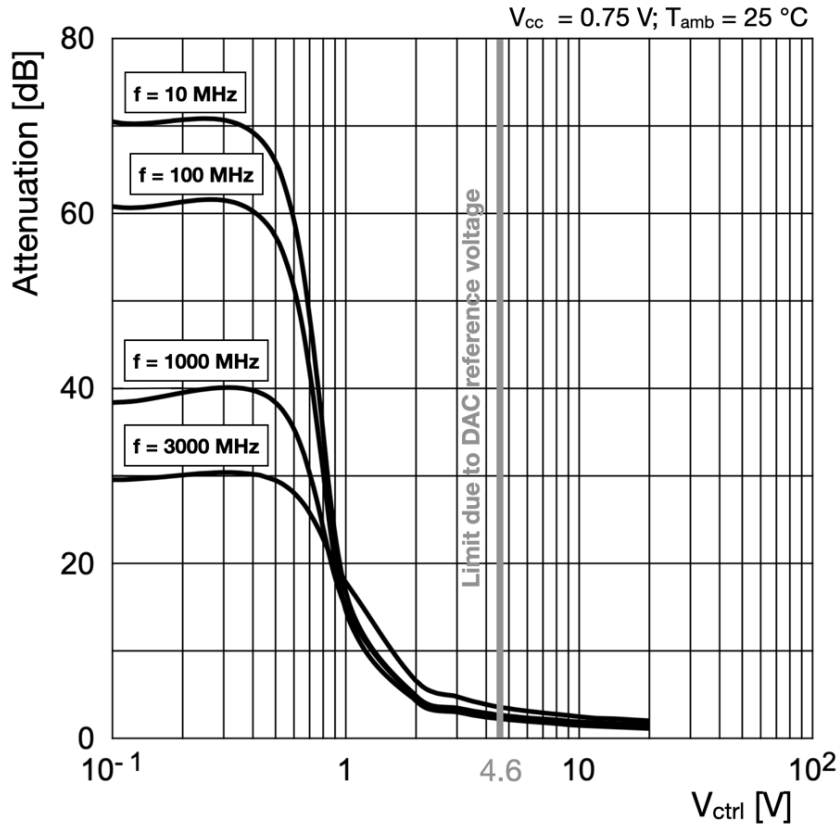

(b)

FIGURE 7.4. The schematics (a) and the attenuation behaviour (b) of the adjustable active attenuator BAP64Q, which is incorporated into each readout channel of the NINO readout board. Figures adapted from [131].

analog input/output connections of the circuit[9], $V_{CC} = 0.75\,V$ is a reference voltage applied to bias the diodes, and V_{ctrl} is the adjustable voltage that actually defines the attenuation. On the upgraded second version of the NINO readout board, the left $RF_{in/out}$ is used as the input and is directly connected to the SMA input connector of the corresponding readout channel. The right $RF_{in/out}$ serves as the output, which is routed onto the negative input of the corresponding NINO chip channel. Additionally, it is available buffered via an MML connector.[10] The specific values for each resistor and capacitor can be found in the schematics of the NINO readout board [134].

The voltage V_{ctrl}, which determines the amount of attenuation, is set by a 12-bit DAC and can therefore be controlled via an input value between 0 and 4095. The DAC's reference voltage is roughly 4.6 V, giving a voltage resolution for V_{ctrl} of 1.126 mV. From now on, the input value of this attenuation DAC is referred to as *att*[11]. As a *control parameter* that significantly influences the behaviour of a readout channel, it will be frequently referenced throughout the upcoming sections and chapters.

Fig. 7.4b illustrates the attenuation behaviour of the active attenuators, i.e. the amount of attenuation in dB versus the voltage V_{ctrl} in V. The upper limit for V_{ctrl} on the NINO readout board, determined by the reference voltage of its DAC, is indicated by the grey vertical line. The attenuation is highest at low V_{ctrl} values and lowest at high values of V_{ctrl}. In other words, the attenuation is highest when $att = 0$ and is minimal when $att = 4095$. Between these values, the attenuation follows a characteristic S-curve. Below approximately 0.9 V, the attenuation exhibits a noticeable frequency dependency: it is higher for lower frequencies and lower for higher frequencies. So far, no negative impacts of this frequency dependency have been observed in combination with the PMT signals of the trigger detectors. However, should any issues arise in the future, this frequency dependency can be mitigated by choosing *att* values greater than 800, as the dependency is far less pronounced for V_{ctrl} values above 0.9 V. Besides, it is important to note that the attenuation never reaches zero, which explains the base attenuation that has been observed for the active attenuators in Section 6.2.3.

Additional Passive 20 dB Attenuators During a test beam time for the MAGIX silicon strip detector at MAMI in February 2024, an issue was identified that could ultimately be traced back to the active attenuators. Four MAGIX trigger detectors were used to trigger the silicon strip detector, marking the first time both detector systems were combined. From rates of a few kHz onwards, a pile-up of the PMT signal tails was observed. Initially, it was suspected that the frequency dependence of the active attenuators was to blame, but this could later be disproven by the institute's electronics workshop. Instead, the issue was due to the PMT signal amplitudes

[9] Because of the circuit's symmetry, either connection can be used as the input or output.

[10] This buffered analog output of the attenuator involves an offset that can be controlled via its own 12-bit DAC. On the NINO readout board, the input of this DAC is termed *OFS*, which appears in the NINO readout board's schematic [134], as well as when configuring the NINO readout board, cf. Code 7.1. Up to the point of writing this thesis, only its default value $OFS = 0$ has been used.

[11] In the NINO readout board's schematic [134], it is termed *ATT_CTRL*.

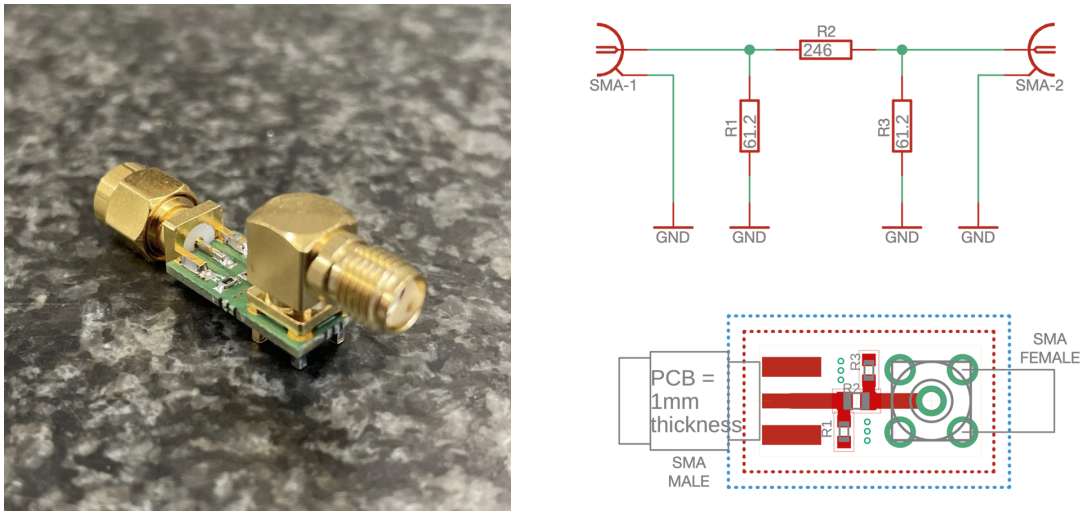

(a) (b)

FIGURE 7.5. One of the passive 20 dB attenuators (a) and the corresponding schematics (b). The passive attenuators are realized in the pi pad configuration and ensure the operation of the active attenuators within their specifications. Additionally, they mitigate the effects of impedance mismatches. In the final MAGIX setup, passive attenuators will be utilized across all trigger layer readout channels. Figure (b) from [130].

being too large for the active attenuators, so that the diodes were essentially overloaded, and the diode depletion regions couldn't keep up. [130] To address this problem, additional passive 20 dB attenuators have been developed, as shown in Fig. 7.5, which can be inserted at the SMA inputs of the upgraded second version of the NINO readout board or directly at the SMA feed-throughs of the trigger layer mountings. The passive attenuators are realized in the pi pad configuration, i.e. a resistive network consisting of one series resistor[12] and two shunt resistors, matching the 50 Ω characteristic impedance of a readout channel for both input and output of a passive attenuator. The frequency dependence of this attenuator type is generally flat as only resistors are used. Utilizing the passive 20 dB attenuators, the active attenuators can operate within their specifications, resolving the pile-up issue and ensuring overall cleaner PMT signals, see Fig. 7.6. The latter is an additional benefit, which can be explained by the fact that the passive attenuators mitigate impedance mismatches caused by the variable impedance of the active attenuators[13] and the fixed input impedance of the NINO chips. By further attenuating the input signals, these mismatches become less significant, reducing signal reflections.

[12] Actually, the circuit contains two series resistors, one for the input and one for the output. However, in practice, these are combined into a single resistor to minimize the number of components.

[13] The impedance of an active attenuator depends on V_{ctrl} and therefore the chosen *att* value of the readout channel.

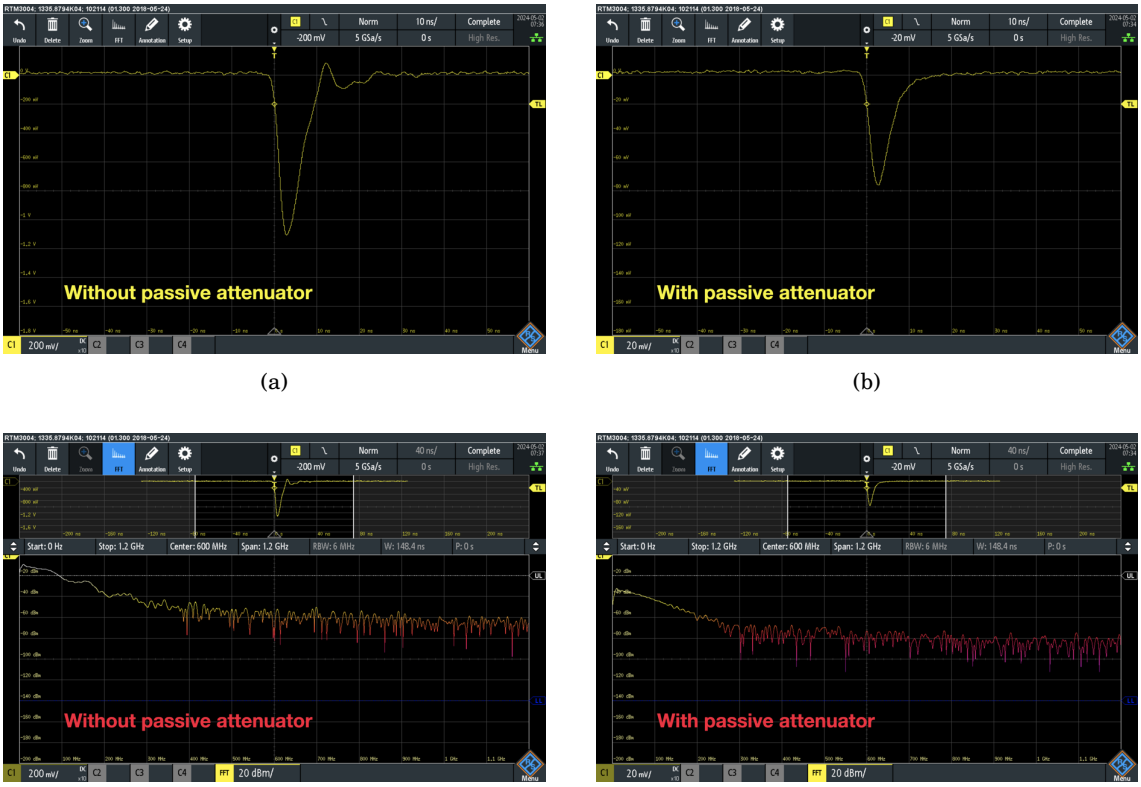

(a) (b)

(c) (d)

FIGURE 7.6. Exemplary signals of the trigger detector "MXTRG25" without (a) and with (b) a passive 20 dB attenuator for a control voltage of 3000 mV, as well as the corresponding Fourier spectra from 0 Hz to 1.2 GHz (c and d), respectively. Clearly, the passive attenuators mitigate impedance mismatches, providing overall cleaner PMT signals.

7.2.2 NINO Chip

The signal processing along a readout channel proceeds with the amplification and discrimination of the attenuated PMT signals from the trigger detectors by a channel of a NINO chip. As briefly described in Section 5.3.1, the NINO chip is an ultrafast 8-channel discriminator-amplifier ASIC that was developed for the ALICE experiment at CERN. Each of the eight NINO channels includes a differential input stage, a fast amplification stage, a very precise discriminator, as well as ToT encoding in its differential LVDS output signal. A block diagram of the NINO chip is shown in Fig. 7.7. In the following, the individual components of a NINO channel, along with their associated *control parameters*, are briefly addressed. For further details on the design of the NINO ASIC, please refer to the corresponding publications [128, 129].

Differential Input Stage On the NINO readout board, the NINO chips are operated in their single-ended mode, i.e. only one polarity of the differential input stages is utilized. Since both

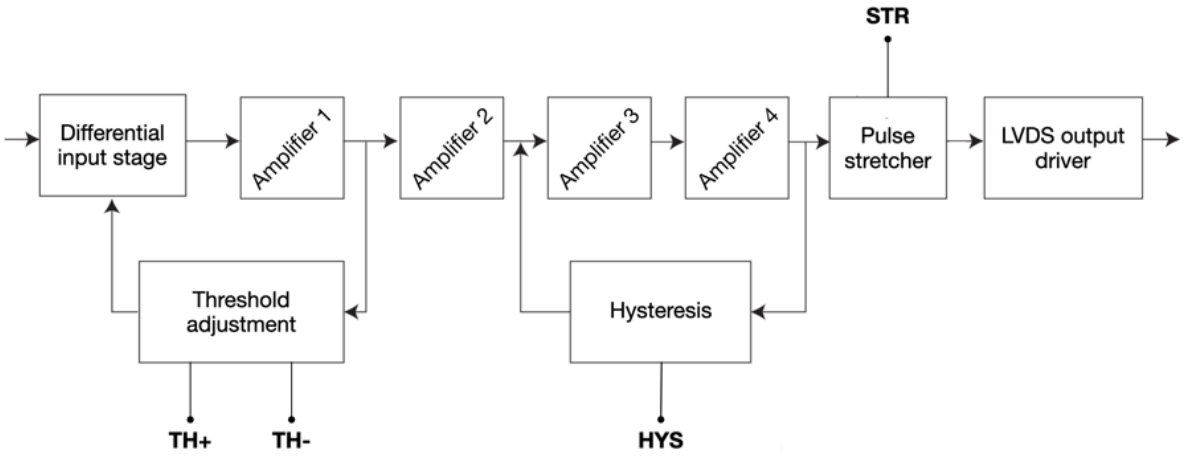

FIGURE 7.7. Block diagram of the 8-channel NINO chip. Each channel incorporates a differential input stage, a fast amplification stage composed of four identical, cascaded amplifiers, a pulse stretcher, and an LVDS output driver. Several inputs are available to influence a channel's behaviour. Figure adapted from [129].

the PMT pulses from the trigger detectors and the SiPM pulses from the MAGIX veto detectors exhibit a negative polarity, the outputs of the active attenuators are routed onto the negative inputs of the NINO channels, whereas their positive inputs are internally terminated with 50 Ω. The output logic pulses of a NINO channel therefore have a negative polarity as well. An exemplary logic pulse is shown in Fig. 7.8a, obtained with the same digital oscilloscope and the same setup as for the self-triggered events in Section 7.1. The two small spikes following the logic pulse are caused by signal reflections from the NIM output's LEMO connector and the corresponding output circuit, which can be eliminated by terminating the LEMO connector with an additional 50 Ω resistor, see Fig. 7.8b. However, this results in a halving of the NIM output signal's amplitude.[14]

Amplification Stage The amplification stage of a NINO channel incorporates four identical, cascaded amplifiers that provide sufficient gain to enable leading-edge discrimination. Each amplifier introduces a voltage gain of six, resulting in a total gain of 1296. While the gain is fixed, the amplification stage offers two adjustment options to fine-tune the signal processing of a NINO channel: the discriminator threshold and a hysteresis circuit.

The discriminator threshold is set by a voltage difference applied to two symmetrical inputs, *TH+* and *TH-*, both of which can be adjusted via their own 12-bit DAC, and which simultaneously

[14]Although the amplitude is halved, the ToT remains unchanged. Consequently, a potential ToT measurement using a NIM output of the NINO readout board is not negatively impacted. For the measurements in Sections 7.1 and 7.2.3, no termination resistor has been used, while the measurements in this section and those in Section 7.2.3 have been conducted with the termination resistor.

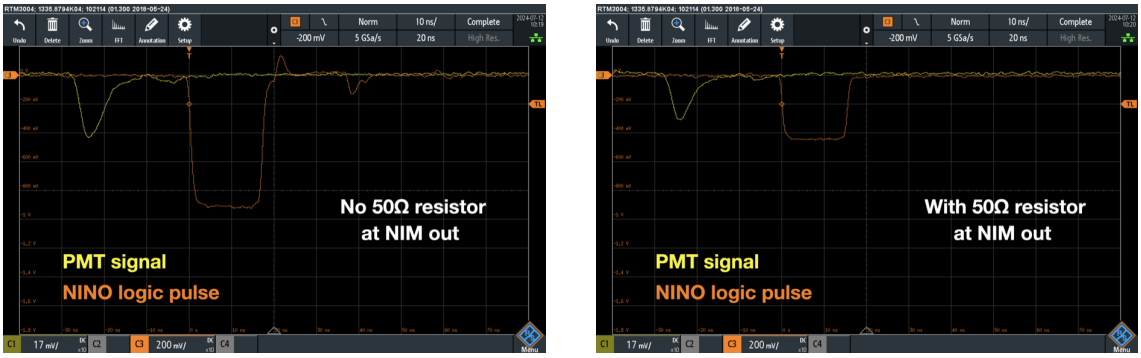

(a) (b)

FIGURE 7.8. Exemplary logic pulses of a NINO chip channel, measured at one of the two NIM outputs of the NINO readout board. The two small spikes that follow the logic pulse (a) are caused by signal reflections and can be eliminated (b) if a 50 Ω termination resistor is used at the NIM output.

affect all eight channels of a NINO chip. Unfortunately, the inner schematics and functionality of the NINO chip are not fully available and understood, making the exact purpose of the two inputs unclear.[15] For the NINO readout board, it has therefore been decided to use the same input value for both DACs and calibrate the readout channels of the NINO readout board accordingly. In the following, the common input value of the two DACs is termed *thr*, which is the *control parameter* that simultaneously sets the discriminator threshold for all eight channels of a NINO chip. Together with the attenuation parameter *att*, it determines the behaviour of a readout channel and allows for the adjustment of an individual, effective signal threshold, details on which will be given in Section 7.2.3.[16] It will therefore frequently reappear throughout the upcoming sections and chapters.

The hysteresis circuit of a NINO channel allows for the introduction of a small hysteresis between the output of the fourth amplifier and the input of the third amplifier. Essentially, this splits the discriminator threshold of the channel, defined by *thr*, into two separate thresholds: one for the leading edge and one for the trailing edge of the analog input signal. As a result, the switching of the discriminator becomes less susceptible to noise components in the input signal. Unfortunately, the available literature on the NINO chip does not provide a detailed explanation of how the hysteresis of a NINO channel precisely works. Consequently, no practical experience

[15] Still, several test measurements conducted by the institute's electronics workshop are available in the NINO readout board's documentation [126].

[16] In principle, the NINO chip also allows for setting an individual threshold per channel without consulting the active attenuators. For this, each NINO chip channel has an additional operating point input that can be controlled via its own 12-bit DAC. On the NINO readout board, the input of this DAC is termed *OP*, which appears in the NINO readout board's schematic [134], as well as when configuring the NINO readout board, cf. Code 7.1. However, using this method was discarded since it sensitively influences the dynamical behaviour of a NINO chip channel by pushing the operating point of the channel's input transistor out of its optimum [130]. Instead, the active attenuators were chosen. As a result, the outputs of the operating point DACs are not connected to the NINO channels, and their default value is $OP = 0$.

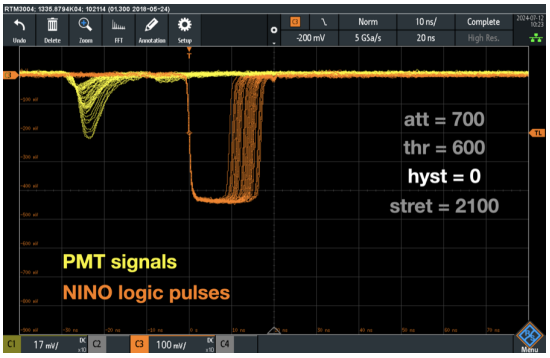

(a)

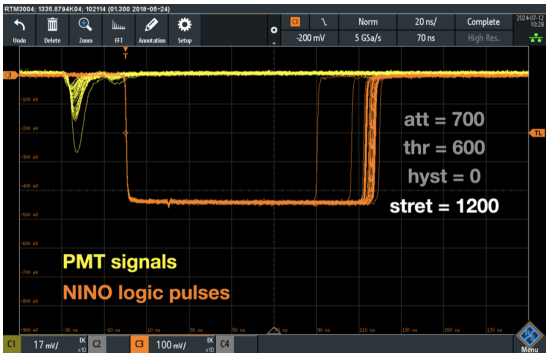

(b)

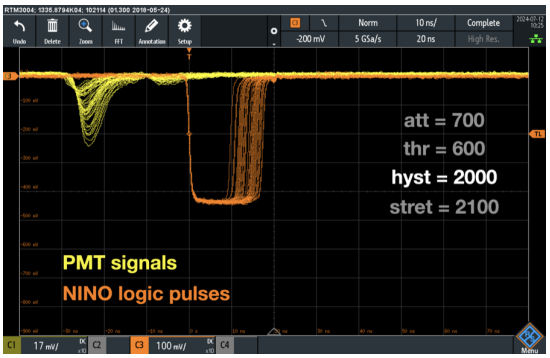

(c)

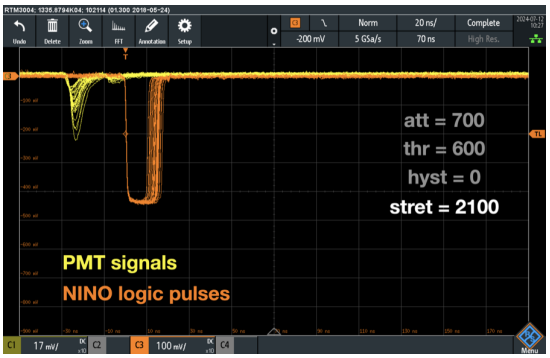

(d)

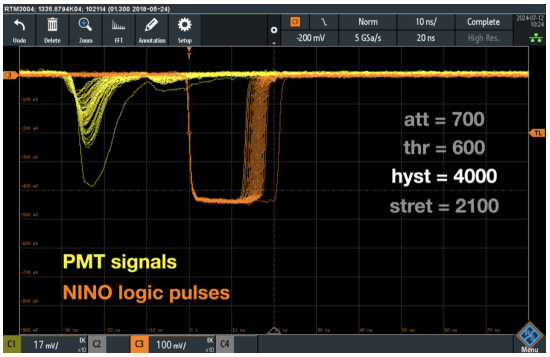

(e)

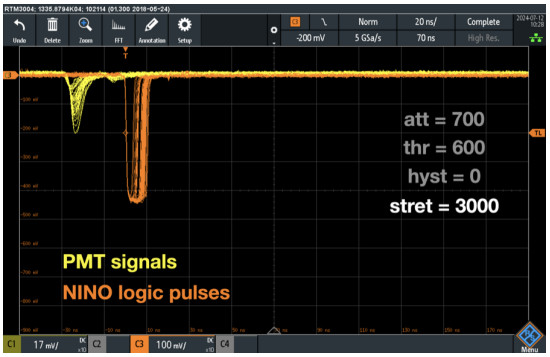

(f)

FIGURE 7.9. Influence of the *control parameters hyst* (a, c, e) and *stret* (b, d, f) on the output logic pulses of a NINO channel. The signals have been obtained using the same digital oscilloscope as in Section 7.1, using an infinite display persistence and collecting cosmogenic muon data for roughly 30 s.

with this parameter has been sought up to the point of writing this thesis. Moreover, the PMT pulses from the trigger detectors exhibit relatively low-noise, cf. Fig. 7.8, so that noise in the input signal has not been an issue so far. Nevertheless, the hysteresis of a NINO chip channel is controlled by its own 12-bit DAC, whose input is referred to as *hyst* when configuring the NINO readout board, cf. Code 7.1. Alternatively, it is termed *HYS* in Fig. 7.7 and in the NINO readout board's schematic [134]. A high value for this *control parameter* corresponds to a large amount of hysteresis, and vice versa. Its impact can be surmised in Figs. 7.9a, 7.9c, and 7.9e, where the increasing amount of hysteresis slightly compresses the ToT distribution of the resulting logic pulses by influencing the behaviour of the discriminator switching. Except for the measurements in Fig. 7.9, only the default value $hyst = 0$ has been used throughout this thesis.

Pulse Stretcher The ToT encoding in the LVDS output signal of a NINO channel can be influenced by a pulse stretcher that artificially prolongs the output logic pulse. The amount of stretching is controlled by a 12-bit DAC, whose input value is referred to as *stret* when configuring the NINO readout board, cf. Code 7.1, or as *STR* in Fig. 7.7 and in the NINO readout board's schematic [134]. A calibration plot for converting the DAC's input value into the stretch time is available in the NINO readout board's documentation [126], while Figs. 7.9b, 7.9d, and 7.9f visualize the impact of this *control parameter*. A high stretch time, reaching into the µs region, is achieved with low *stret* values, while no pulse stretching is obtained at $stret = 4095$. Throughout the studies in this thesis, the default value $stret = 2100$ has been used, corresponding to a stretch time of just below 10 ns. This value is motivated by the signal processing on the Z-turn board, whose clock signal with a clock period of 4 ns is used to read out the Tapped Delay Line TDCs programmed on the Z-turn board's FPGA, cf. Section 7.3.1. The stretch time of 10 ns therefore corresponds to two and a half clock cycles, preventing the two edges of a logic pulse from entering a readout channel's TDC within the same clock cycle.

7.2.3 Setting an Effective Signal Threshold

For each readout channel of a NINO readout board, the combination of the *control parameters* *thr* and *att* determines an individual, effective signal threshold. While *thr* sets the discriminator threshold of a NINO chip, *att* effectively compresses the amplitude range of input signals at the input of a NINO channel. At maximum attenuation, i.e. $att = 0$, the amplitude range is maximally compressed, making the discriminator threshold set by *thr* correspond to the highest possible signal threshold for this specific *thr* setting. Reducing the attenuation, i.e. increasing *att*, then decompresses the amplitude range, thereby lowering the signal threshold. Another way to view this is in terms of a range of achievable signal thresholds. Whereas *thr* defines the maximum of the range[17], *att* determines a specific value within the range.

[17] The minimum of the range is given by the minimal input signal charge processable by a NINO channel, i.e. 100 fC [128], which corresponds to an input signal amplitude of several mV for the pulse shape of the trigger PMTs.

If needed, the relationship between the value pairs of *thr* and *att* and the corresponding signal thresholds can be precisely calibrated. To do so, one has to determine the exact mV value of an input signal's amplitude, which, for a given value pair of *thr* and *att*, just exceeds the signal threshold and evokes a logic pulse in the corresponding NINO channel. However, since the performance of each readout channel of a NINO readout board exhibits slight variations due to production-related differences in the numerous components incorporated into a readout channel, a separate calibration has to be performed for each readout channel on every NINO readout board.

Clearly, this is a time-consuming process, and it is worth questioning whether knowing the exact mV value of the signal threshold for a given value pair of *thr* and *att* actually provides any benefit. When considering the MAGIX trigger veto system, it becomes clear that this is indeed not needed. In the final setup of MAGIX, the signal thresholds of the individual readout channels will not be set to specific mV values, but will be adjusted based on more emergent detector properties such as efficiency and coincidence time resolution. The knowledge of a mV value is not beneficial, as long as the signal thresholds can be tuned such that the detector properties fulfill certain requirements.

Nevertheless, an exemplary calibration was conducted for one readout channel during the early days of this thesis, which will be briefly described at the end of this section. Prior to that, it shall be demonstrated that the signal threshold of a readout channel can be adjusted by both *thr* and *att* in a similar manner, despite them affecting different stages of the signal processing along a readout channel. It will be shown how the set signal threshold affects the input signal distribution from the trigger detectors and influences the ToT distribution of the output logic pulses of a NINO channel. The latter is crucial, as ToT will be the only parameter available in the later experimental operation of MAGIX to characterize the magnitude of an analog PMT signal from the trigger detectors, the knowledge of which is essential to the planned energy loss measurements with the trigger layer.

Impact of the Signal Threshold To demonstrate the influence of the effective signal threshold set, Figs. 7.10 and 7.11 show its impact on the PMT pulses' characteristic variables charge and pulse height, as well as on the ToT of a NINO channel's logic pulses. For the plots in Fig. 7.10, a fixed *thr* value has been chosen while varying the attenuation parameter *att*. Conversely, for Fig. 7.11, *att* has been held constant and *thr* has been varied. The measurements discussed in this paragraph have again been conducted using cosmogenic muons and PMT "A" of the trigger detector "MXTRG25". A setup similar to the one used for the self-triggered events described in Section 7.1 has been employed[18]. The PMT's control voltage has been fixed to 3000 mV, and 1000 events have been recorded for each value pair of *thr* and *att*. If needed, alternative plots to the

[18]The subtle difference is that the digital oscilloscope's TTL trigger signal has been employed, which has been routed to the AUX OUT port, converted to a NIM signal, and then sent to a readout channel of the NINO readout board. For more details on this setup, please refer to the Bachelor's thesis of D. Schmitt [148].

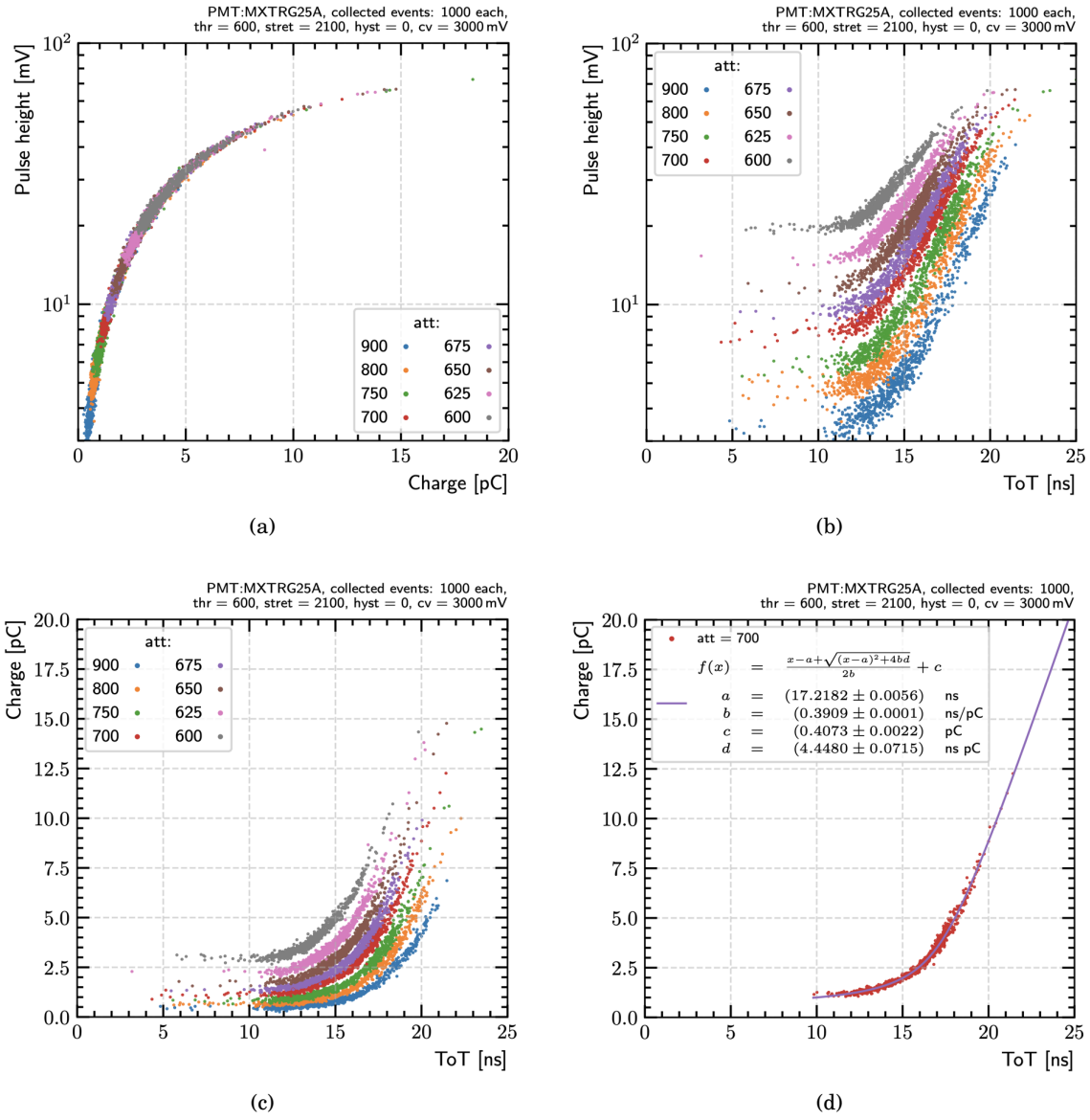

FIGURE 7.10. Impact of the signal threshold on the PMT pulses' characteristic variables charge and pulse height, as well as on the ToT of the output logic pulses. A fixed *thr* value of 600 has been used and *att* has been varied.

ones shown in Figs. 7.10 and 7.11 can be found in Appendix E.1, where the pulse height has been plotted with a linear scale.

Fig. 7.10a shows the 2D scatter plot of the PMT pulses' characteristic variables pulse height and charge for various values of *att*, with a fixed *thr* value of 600. As the *att* value decreases, the signal threshold increases, causing more and more input signals to be excluded and the resulting distributions to shift towards higher charge and pulse height values. The effective signal threshold therefore functions as a true signal threshold.

Figs. 7.10b and 7.10c confirm that the ToT encoding of the NINO chip works as expected: as pulse height and charge increase, so does the ToT. Additionally, as before, the distributions shift to higher charge and pulse height values as *att* is decreased and the signal threshold is increased. Notably, the ToT distributions begin at approximately 10 ns, which is consistent across all *att* values. This starting point is due to the pulse stretcher setting of *stret* = 2100, which corresponds to a stretch time of roughly 10 ns, cf. Section 7.2.2. The consistency across varying *att* values is expected and highlights the inherent nature of the parameter ToT: Time-over-Threshold. The relationship between the characteristic variables charge and pulse height of a PMT pulse and the resulting ToT is therefore not absolute, but depends on the signal threshold determined by a value pair of *thr* and *att*. Another point to note are the occasional events at ToT values below 10 ns, which, in principle, should not occur given the set stretch time. At the time of writing this thesis, the origin of these events has not been further investigated and they are excluded during data analysis by applying a variable cut on ToT, as will be described in Chapter 8. It remains unclear whether these events are due to noise in the LVDS output driver of a NINO channel, a malfunction in the pulse stretcher, or issues with merging the leading and trailing edges of an output logic pulse[19].

In the later operation of MAGIX, only the parameter ToT will be available to characterize the magnitude of an analog PMT signal from the trigger detectors. Typically, the magnitude of a signal from a scintillation detector is quantified by the charge contained in the corresponding pulse. This charge can be used to estimate the number of optical photons produced in the scintillator[20], and, if the scintillation yield of the scintillator material is known[21], it is possible to calculate the deposited energy of an incoming particle, i.e. its energy loss. Hence, a precise understanding of the relationship between ToT and charge is essential, which unfortunately depends on the set signal threshold and therefore has to be measured individually for each threshold setting. Fig. 7.10d exemplarily shows the measured relation for one readout channel of a NINO readout board and the value pair *thr* = 600 and *att* = 700, where the data points have been fitted using a function including both linear and square root terms[22]. By utilizing the fit parameters, recorded ToT values can be converted to the corresponding charge values of the PMT pulses, allowing for the calculation of the energy loss of the incoming particles. This fitted relationship will be applied

[19] On the NINO readout board, the output logic pulses from a NINO channel are routed to the Z-turn board, where they are processed by a TDC programmed on the board's FPGA. Details on this are provided in Section 7.3. However, the TDC is sensitive to both the leading and the trailing edge of a logic pulse, recording a dedicated timestamp for each edge. During data analysis, these timestamps then have to be merged again to calculate their difference, i.e. the ToT of the readout channel.

[20] The charge represents the number of electrons in the PMT pulse. By considering the PMT's gain and the quantum efficiency of the PMT's photocathode, the number of optical photons reaching the PMT window can be extracted. To further determine the total number of optical photons produced in the scintillator, geometric considerations have to be taken into account. For this, a dedicated simulation will be worthwhile in the future.

[21] For the scintillator material used for the trigger detectors, i.e. EJ-230 by Eljen-Technology (Scionix), it is listed in Tab. 5.1.

[22] Up to the point of writing this thesis, the accuracy of this fit function has been sufficient. However, in the future, it may be beneficial to adopt a more physically motivated model.

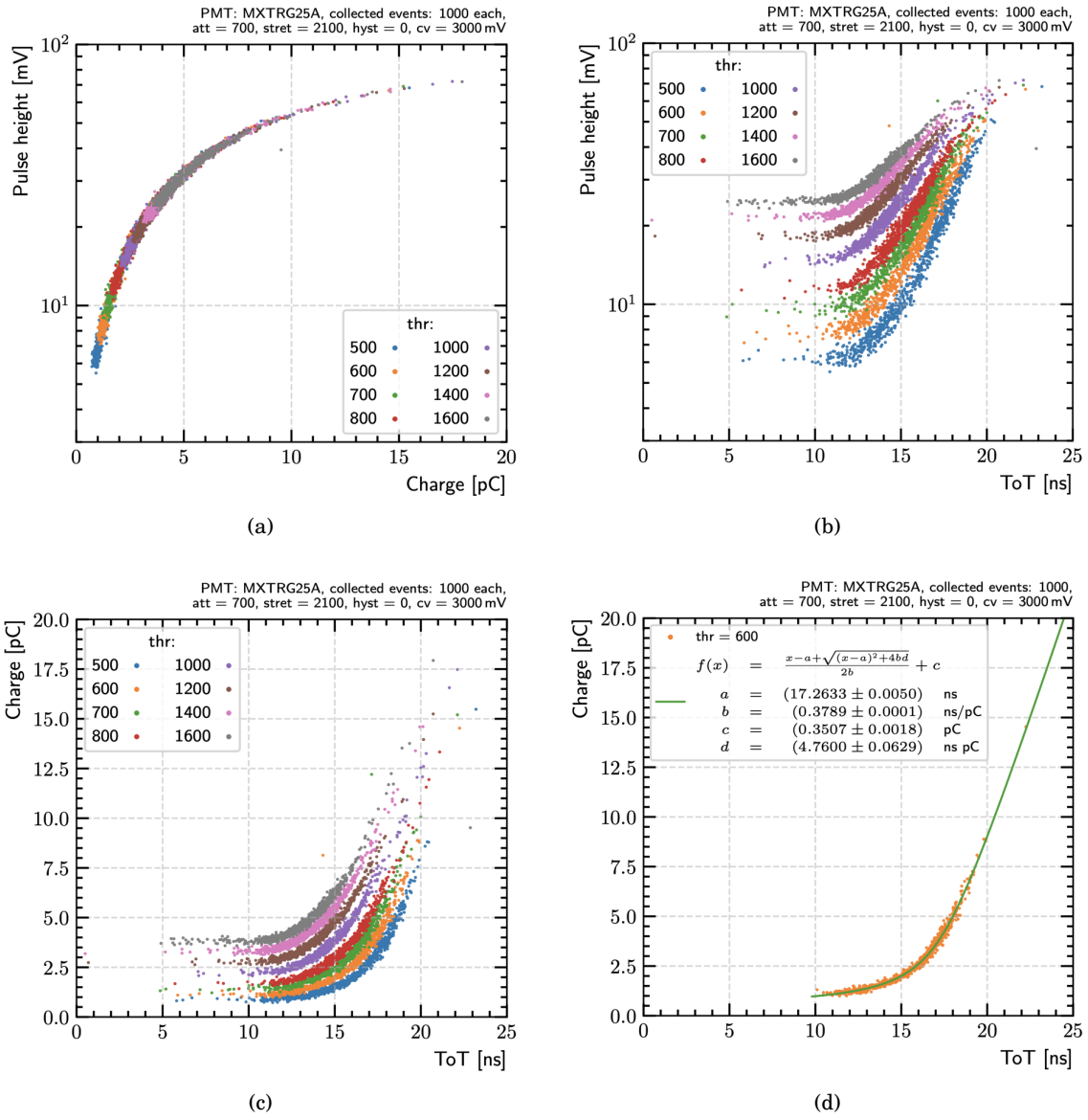

FIGURE 7.11. Impact of the signal threshold on the PMT pulses' characteristic variables charge and pulse height, as well as on the ToT of the output logic pulses. *thr* has been varied and *att* has been held constant at *att* = 700.

during data analysis, see Chapter 8, with the relationship being individually determined for each readout channel.

Finally, Fig. 7.11 illustrates the same relationships with a fixed *att* value of 700, while *thr* has been varied. The results match the previous observations[23], reaffirming that both *thr* and *att* can be used interchangeably to set the signal threshold of a readout channel.

[23] Comparing the fits from Figs. 7.10d and 7.11d, which have been performed on two distinct datasets obtained with identical *control parameters*, the results are not consistent within the given errors. This inconsistency can be explained by the limited statistics, with only 1000 events collected.

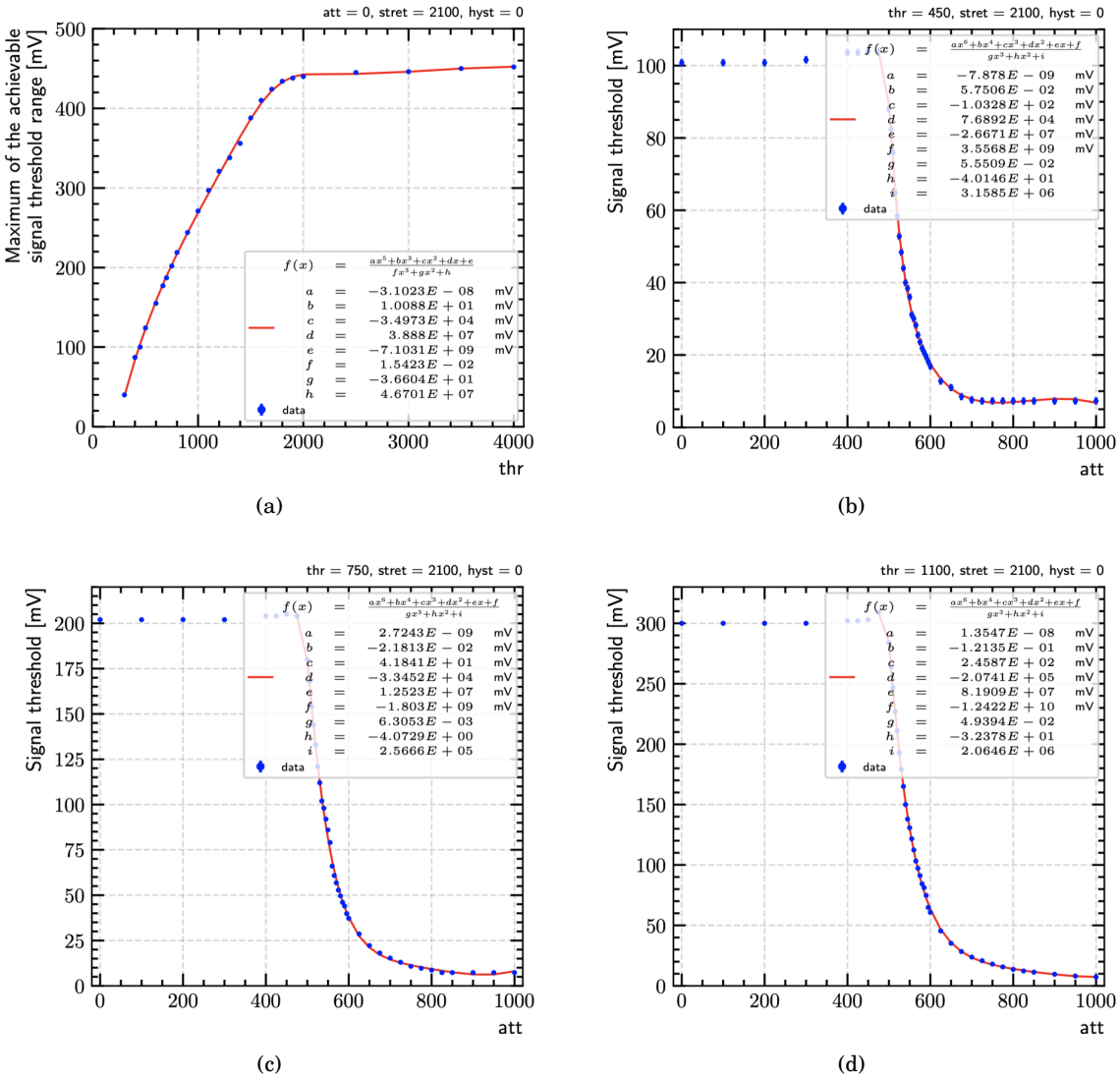

FIGURE 7.12. Exemplary effective signal threshold calibration. The maximum of the achievable signal threshold range is defined by *thr* (a), while *att* determines a specific signal threshold within the range (b, c, d).

Calibration of the Effective Signal Threshold As mentioned above, an exemplary calibration of the effective signal threshold has been performed for one readout channel of a NINO readout board during the initial stages of this thesis. Please note that the corresponding measurements have been conducted employing one of the first generation NINO readout boards without utilizing a passive 20 dB attenuator. The upcoming calibration therefore only serves as a proof of concept and should only be used as a first reference.

As signal source, a programmable function generator[24] has been used. Negative rectangular

[24] HAMEG HM8130 [149]

pulses with a frequency of 10 kHz, a pulse width of 100 ns, and an offset of 0 mV have been employed as input signals, which have been routed onto one channel of the NINO readout board. The logical OR of all input channels has been assigned to one of the two NIM outputs at the rear of the NINO readout board and monitored with a digital oscilloscope[25]. For a given value pair of *thr* and *att*, the effective signal threshold could now be found by increasing the amplitude of the input signals until the logical OR raised a signal.

Four calibration curves have been obtained, which are shown in Fig. 7.12: the maximum of the achievable signal threshold range versus *thr*, see Fig. 7.12a, and the effective signal threshold versus *att* for the three different *thr* values 450, 750, and 1100, corresponding to maximally achievable signal thresholds of 100 mV, 200 mV, and 300 mV, respectively, see Figs. 7.12b–7.12d. As can be seen, the relationships are highly non-linear, requiring fractional function fits with fifth and sixth-order polynomials, respectively, to accurately represent the dependencies.[26] Another notable aspect is the shape of the calibration curves in Figs. 7.12b, c, and d, which represents the attenuation behaviour of the adjustable active attenuators, cf. Fig. 7.4b.

During the later laboratory work for this thesis, a value pair of *thr* and *att* has crystallized that has proven to be a solid working point when utilizing the passive signal splitters[27], which is why it has been used throughout this chapter: $thr = 600$ and $att = 700$. It corresponds to a maximum of the achievable signal threshold range of approximately 150 mV and a signal threshold set to roughly 7 % to 8 % of this[28], i.e. 10 mV to 12 mV. Without the signal splitters, the working point $thr = 600$ and $att = 475$ has proven to be reliable, where $att = 475$ already sets the signal threshold to roughly 100 % of the maximum of the achievable signal threshold range, i.e. 150 mV. This working point will therefore reappear in Section 7.4, as well as in Chapter 8.

7.3 Signal Processing on the Z-Turn Board

Following the signal processing on the NINO readout board, the ToT-encoded logic pulses from the NINO chips are available at the SMT connectors that connect the NINO readout board to the FPGA add-on board. As a reminder, MAGIX operates the NINO readout board in its local mode, cf. Section 5.3, utilizing the second generation of the MYiR Z-turn board [135] as the FPGA add-on board. The Z-turn board employs a Xilinx XC7Z020 SoC[29] with an Artix-7 FPGA, which exhibits

[25] SIGLENT SDS1204X-E [150]

[26] Given that this is only a rough calibration, a physically motivated fit function has not been pursued, and fractional functions have been used instead. The fitting errors are so large that they are not reported here. However, the fractional function fits are visibly sufficient to represent the relationships.

[27] As a reminder, the passive signal splitters have been used so that the PMT pulses of a trigger detector could be routed onto both the digital oscilloscope and the NINO readout board.

[28] This information can be extracted from the three calibration curves in Figs. 7.12b–7.12d, where $att = 700$ sets the signal thresholds to 7.6 mV, 15.3 mV, and 23.8 mV, respectively, corresponding to 7.60 %, 7.65 %, and 7.93 % of the respective maximum of the achievable signal threshold range. The influence of *att* on the effective signal threshold is therefore rather independent from the set discriminator threshold.

[29] **S**ystem-**O**n-**C**hip

85 000 logic cells, 53 200 LUTs[30], and 220 DSP[31] slices. The Z-turn board therefore provides a high degree of flexibility, allowing functionality to be implemented on the FPGA or run on the SoC part of the board.

The FPGA of the Z-turn board is programmed to incorporate a highly accurate and fast TDC with a precision of approximately 18 ps for each readout channel. The individual TDCs are read out at the Z-turn board's clock frequency of 250 MHz, i.e. every 4 ns, and the TDC information from all channels is then merged, before being processed on the SoC part of the Z-turn board, resulting in a continuous data stream that can be processed by a frontend computer. The TDCs are sensitive to both the leading edge and the trailing edge of a logic pulse, and provide a precise timestamp per edge. The time difference between the two timestamps of a logic pulse then reconstructs the vital parameter ToT, which is already known from the previous section. Moreover, the two timestamps are used to assign a point in time to the original analog signal of a trigger detector, which can then be set into context to other detector systems at MAGIX. The time resolution achieved with the trigger layer therefore sensitively depends on the accuracy of the TDCs implemented on the Z-turn board.

In the following, the principle and realization of the TDCs implemented on the Z-turn board's FPGA will be explained in more detail. Subsequently, the readout architecture on the Z-turn board, both on its FPGA and the SoC part, will be described, i.e. how the TDC information from all 32 readout channels of a NINO readout board is merged and processed into a continuous data stream. The employed data structure will be presented as well. Please note that only the key aspects relevant for recording data will be provided. Code snippets of the TDC implementation in `VHDL`, for example, are not included. For details on this, please refer to the `GitLab` repository `MAGIX-FPGA/NINO`, which is accessible to all members of the MAGIX collaboration.

7.3.1 TDC Implementation on the FPGA

Technically, each TDC comprises two components: a *coarse TDC* and a *fine TDC*. Fig. 7.13 illustrates the idea behind this approach.

The *coarse TDC* uses the Z-turn board's clock signal to define a so-called *coarse time* for each edge of a logic pulse. The accuracy of the *coarse TDC* is limited to the clock period of $t_{CLK} = 4\,\text{ns}$, as only with every rising edge of the clock signal, it can be checked whether the status of the input signal has changed, i.e. an edge of a logic pulse has occurred. Typically, the edges of a logic pulse do not coincide with a rising edge of the clock signal, as indicated by the two timestamps t_L and t_T of the logic pulse's leading edge and trailing edge, respectively. Consequently, the edges of the logic pulse are only registered with the rising edges of the following clock cycles

[30] **L**ook**U**p **T**able
[31] **D**igital **S**ignal **P**rocessing

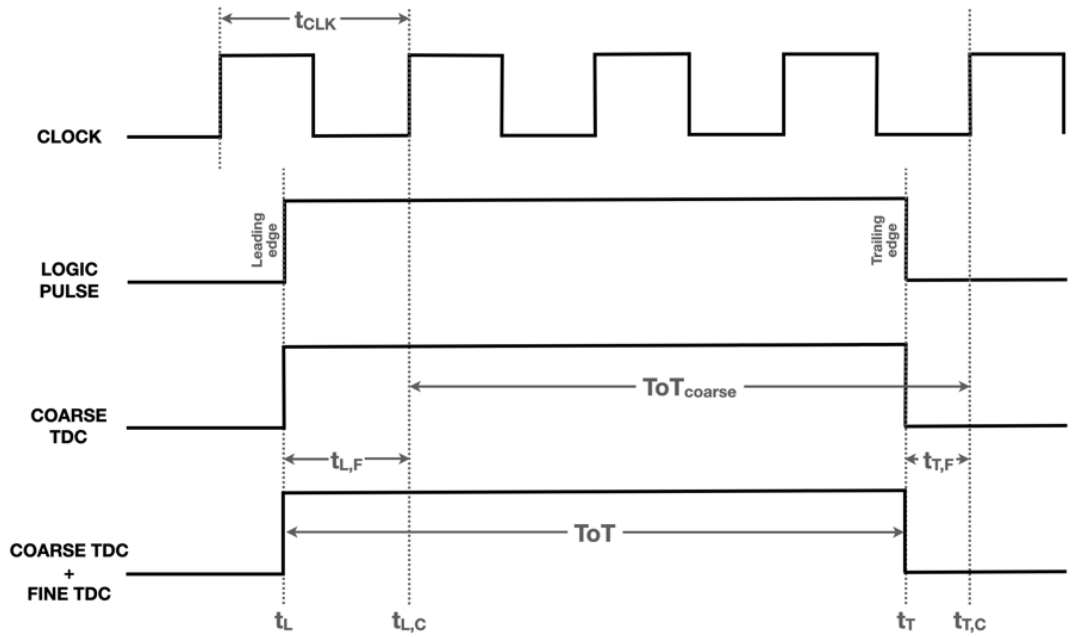

FIGURE 7.13. The combination of a *coarse TDC* and a *fine TDC* allows for the reconstruction of the parameter ToT to within the accuracy of the *fine time* measurement.

and the measured *coarse times*[32] represent the timestamps $t_{\mathrm{L,C}}$ and $t_{\mathrm{T,C}}$ rather than the logic pulse's actual timestamps t_{L} and t_{T}. As a result, the ToT encoded into the logic pulse is only reconstructed to within the accuracy of the *coarse time* measurement, i.e. 4 ns, as can be seen from $\mathrm{ToT}_{\mathrm{coarse}}$.

Adding a *fine TDC* corrects for this limitation. The *fine TDC* provides a *fine time* measurement for the two edges of the logic pulse, representing the time differences $t_{\mathrm{L,F}}$ and $t_{\mathrm{T,F}}$, respectively. When combined with the *coarse time* measurement, the timestamps of the logic pulse can be accurately determined using $t_{\mathrm{L}} = t_{\mathrm{L,C}} - t_{\mathrm{L,F}}$ and $t_{\mathrm{T}} = t_{\mathrm{T,C}} - t_{\mathrm{T,F}}$. More generally, any timestamp t is given by $t = \textit{coarse time} - \textit{fine time}$. Using this method, the accuracy of reconstructing the ToT encoded into the logic pulse is enhanced to within the accuracy of the *fine time* measurement.[33]

One common method for implementing a *fine TDC* is the so-called *Tapped Delay Line*, the idea of which is illustrated in Fig. 7.14a. The delay line consists of a fixed number N of delay line cells, each with a constant delay time τ. The outputs of these cells are connected to the data inputs of D-type flip-flops, whose outputs Q_1, Q_2, ..., Q_{N} constitute the output of the *fine TDC*. When a START signal is fed into the delay line, it propagates through the delay line cells, present to the data inputs of the flip-flops, until a common STOP signal enables the outputs of the flip-flops. The

[32] Technically, the *coarse time* is just the product of a counter that is incremented every clock cycle and the clock period of 4 ns. The counter is initialized during system startup, so the *coarse time* represents the elapsed time since system start in ns.

[33] Obviously, this approach is only effective if the accuracy of the *fine time* measurement is better than the clock period.

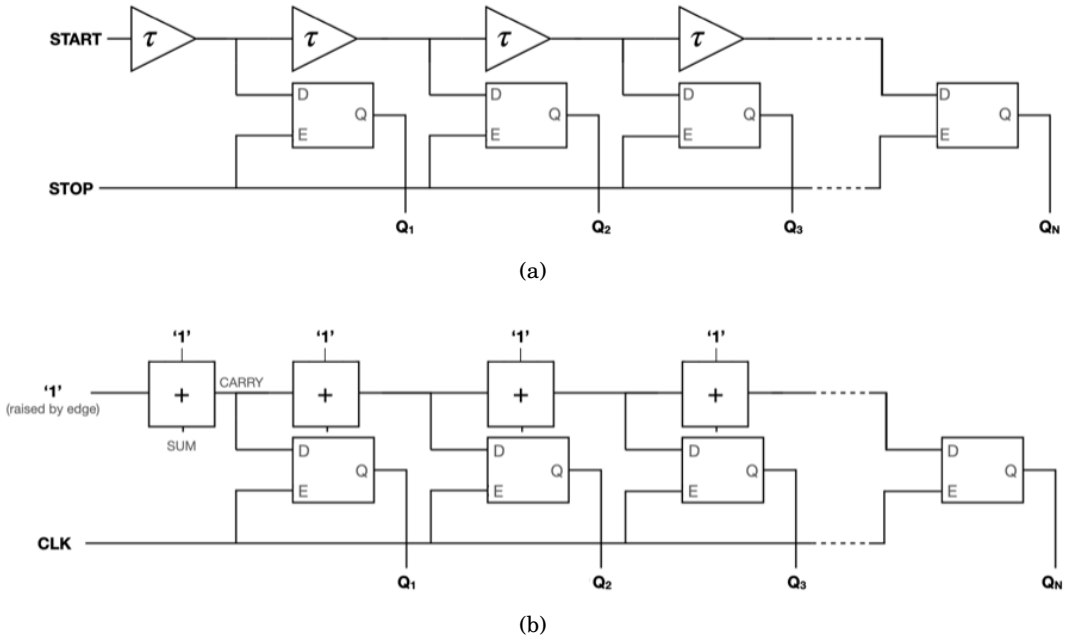

FIGURE 7.14. The principle of a Tapped Delay Line TDC (a) and its implementation on the FPGA of the Z-turn board (b). Figures adapted from [151].

travelled distance of the signal, i.e. the number of delay line cells the signal propagates through before the STOP signal occurs, also termed *fine time bin*, is then represented by the output of the *fine TDC*, providing a measure of the time difference between the STOP signal and the START signal.

For MAGIX, the Tapped Delay Line is implemented using 256 binary half-adders[34] as the delay line cells[35] and the clock signal of the Z-turn board serves as the common STOP signal, see Fig. 7.14b. The START signal is a binary 1 raised by either the leading edge or the trailing edge of a logic pulse.[36] The first half-adder adds the input signal to a binary 1, and the resulting carry bit is stored in the first flip-flop while being forwarded to the second half-adder. The sum bit is discarded. This process continues down the delay line, with the carry bit propagating through each half-adder until the *fine TDC* is read out with the rising edge of the next clock cycle and the flip-flops are reset. Thus, the delay line effectively represents the addition of a binary 1 to a

[34]A half-adder is a digital logic circuit that performs the binary addition of two single-bit binary numbers. The result of the addition is given via two outputs, SUM and CARRY, where SUM is the least significant bit of the addition result and CARRY is its most significant bit, indicating a carry-over from the addition.

[35]At the programming level, the delay line is realized with 64 `CARRY4` blocks [152], i.e. four-channel carry blocks. This results in a more efficient implementation compared to using 256 half-adders.

[36]At the hardware level, it is more intricate. Each delay line incorporates a sophisticated input stage, which includes a dedicated circuit for identifying the START signal as a leading or trailing edge, as well as an input buffer that provides a binary 1 to start the delay line. Moreover, the input buffer provides a second signal, which indicates a valid input signal and tells the system to read out the delay line with the next rising edge of the clock cycle. For further details on the input stage, please refer to Ref. [153].

binary 2^{256}, where the carry bit sequentially propagates through the delay line. The position of the carry bit at the occurrence of the STOP signal corresponds to the *fine time bin* and represents the *fine time* measurement of the delay line. The accuracy of this measurement is determined by the delay time of a delay line cell, i.e. the calculation time of a half-adder, which is roughly 18 ps for the Z-turn board [154]. Hence, adding the *fine TDC* drastically improves the TDC accuracy and, consequently, the time resolution of the whole readout system.

At this point, two important considerations must be addressed. First, with each half-adder introducing a calculation delay of 18 ps, the cumulative delay of the entire delay line totals around 4.6 ns. This exceeds the 4 ns period of the Z-turn board's clock, meaning that the delay line is read out before the propagating carry bit is able to reach the end of the delay line. Consequently, the *fine TDC* should not yield *fine time bins* greater than $256 \times 4.0/4.6 \sim 222$. Second, the calculation times of the individual half-adders will exhibit slight variations that must be accounted for. Taken together, these two aspects necessitate a precise calibration to accurately relate the *fine time bin* to the actual *fine time* in ns for each readout channel. This *fine time calibration* is integral to the data analysis and will be described in Chapter 8.

7.3.2 Readout Architecture on the Z-Turn Board

Before delving into the nuances of recording data, which will be covered in the next section, it is useful to first explore the readout architecture that is programmed onto the Z-turn board. Fig. 7.15 illustrates the corresponding block diagram.

The outputs of the *fine TDCs* are each buffered in an `AXI-Stream`[37] FIFO[38] register with a capacity of 512 hits, the outputs of which are then combined by two 512-hit `AXI-Stream-Interconnect` FIFOs. The precise definition of a *hit* is not important at this point and will be provided in the coming Section 7.3.3. A 32 768-hit `AXI-Stream-Interconnect` FIFO then merges the outputs of the second stage FIFOs with the information from a dedicated *coarse TDC* FIFO. Additionally, optional LVDS and trigger inputs can be included at this stage. In future MAGIX operations, these inputs will be used to include signals from other detector systems, such as the silicon strip detectors in the scattering chamber or the trigger signal from the second spectrometer, enabling online trigger decisions to be made directly on a Z-turn board. The merged *hits* then pass through a DMA[39] block and are processed by the Z-turn board's CPU[40], on which a ring buffer provides a continuous data stream over a 1 GBit/s Ethernet connection. While the CPU is located on the SoC part of the Z-turn board, all other components are implemented on the Z-turn board's FPGA. Further information on the readout architecture on the Z-turn board, as well as the general trigger concept planned for MAGIX, can be found in various presentations by H. Merkel [153, 155, 156].

[37] **A**dvanced e**X**tensible **I**nterface is a standardized interface protocol of ARM processors.
[38] **F**irst **I**n - **F**irst **O**ut
[39] **D**irect **M**emory **A**ccess
[40] **C**entral **P**rocessing **U**nit

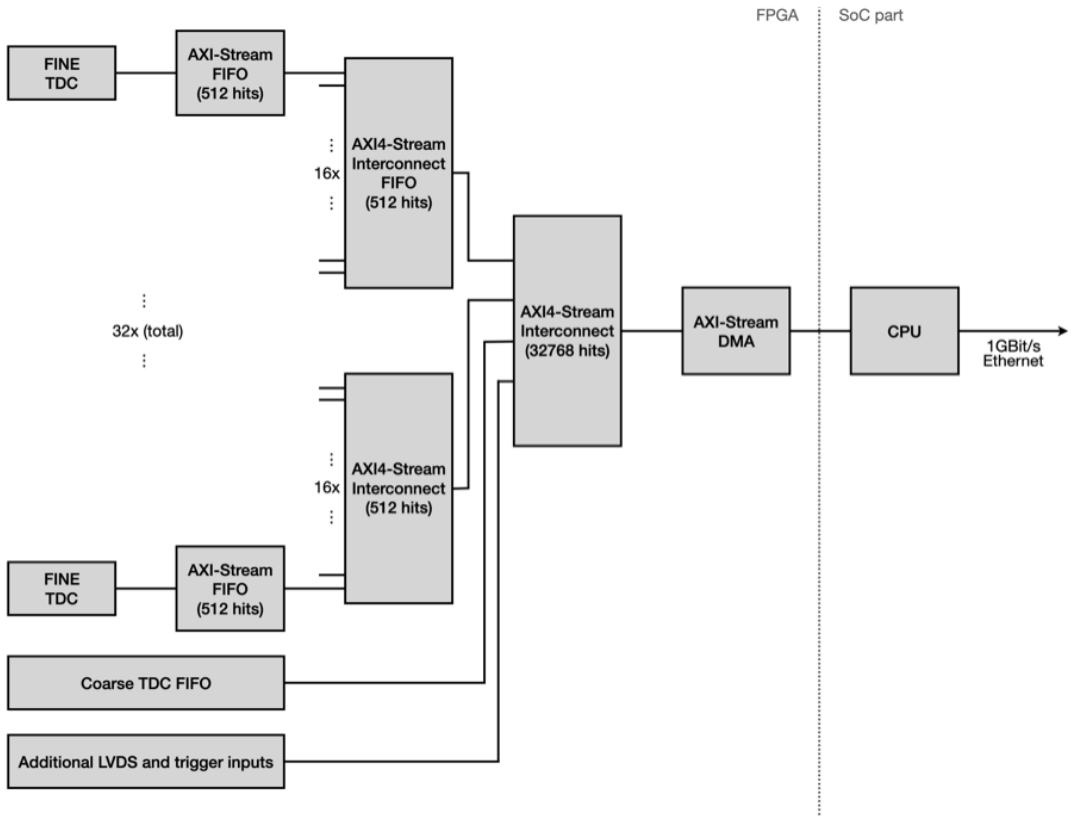

FIGURE 7.15. Block diagram of the readout architecture on the Z-turn board. The *fine TDC* and *coarse TDC* information is merged with additional LVDS and trigger inputs, before being processed into a continuous data stream that is available via a 1 GBit/s Ethernet connection. All components, except for the CPU, are fully implemented on the Z-turn board's FPGA.

7.3.3 Data Structure

The continuous data stream provided by the Z-turn board via the 1 GBit/s Ethernet connection is composed of individual *hits*, where each *hit* corresponds to the timestamp of one edge of a logic pulse. Each *hit* contains the TDC information, i.e. *coarse time* and *fine time bin*, of the corresponding timestamp, along with the number of the readout channel and whether the timestamp belongs to a leading or trailing edge. The *hits* exhibit a certain data structure, which is illustrated in Fig. 7.16.

A *hit* is represented by a 64-bit word, i.e. eight bytes, which is transmitted as two 32-bit subwords in little-endian byte order. The information contained in a *hit* is assigned to different sections of the 64-bit word:

- The first bit represents the edge of the logic pulse: a 0 indicates a leading edge, a 1 denotes a trailing edge.

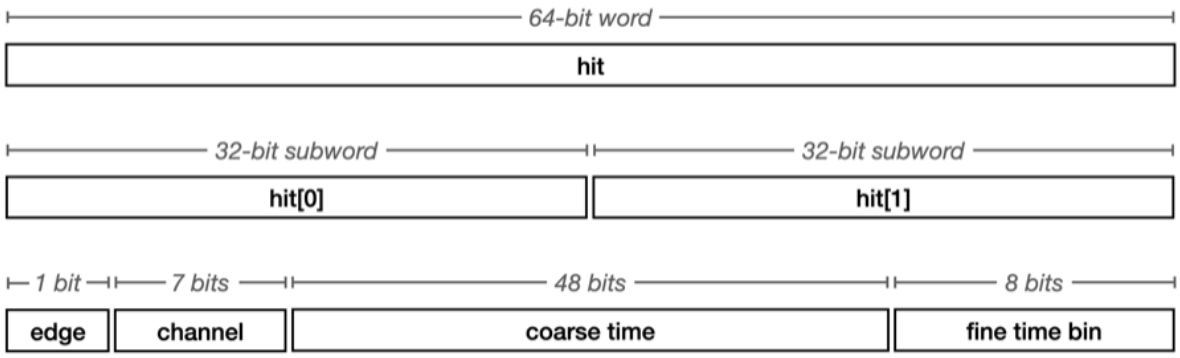

FIGURE 7.16. The Z-turn board's continuous data stream is composed of individual *hits*, each corresponding to the timestamp of a logic pulse edge. A *hit* contains the TDC information of a timestamp, i.e. *coarse time* and *fine time bin*, along with the readout channel number and whether the timestamp corresponds to a leading or trailing edge.

- Bits 1 to 7 encode the number of the readout channel. Technically, five bits would be sufficient, as they already provide a channel range from 0 to 31, but seven bits have been chosen instead. This provides a channel range from 0 to 127 and allows for the combination and simultaneous readout of four NINO readout boards.
- The subsequent 48 bits express the *coarse time* of the corresponding timestamp. Given that the *coarse time* measures the elapsed time since system startup in ns, a substantial number of bits is required. The 48 bits offer a *coarse time* range from 0 to 281 474 976 710 655, equivalent to a maximum *coarse time* of roughly 3 d, 6 h, and 11 min. After this, the *coarse time* has to be reset to 0.
- The last eight bits contain the *fine time bin* of the timestamp. This provides a *fine time bin* range from 0 to 255, perfectly matching the 256 cells composing the Tapped Delay Line TDCs.

Alongside the various possible combinations to assemble a *hit* from the information of a logic pulse timestamp, several 64-bit status words are reserved for signaling specific scenarios. They are defined on the SoC part of the Z-turn board and are raised as required under specific conditions. Tab. 7.1 lists those currently in use at the time of writing this thesis, denoted in hexadecimal notation.

The START and STOP words mark the beginning and end of a data file, respectively. They will be encountered again during data acquisition, which will be the topic of the coming section. The SYNC word is used to verify the response of the `sync()`-function that will be used in later MAGIX operations for synchronizing the clocks of multiple Z-turn boards. Although not utilized

Word name	Hexadecimal notation	Status
START	\xFF\xFF\xFF\xFF\x01\x00\x00\x00	Beginning of data file
STOP	\xFF\xFF\xFF\xFF\x02\x00\x00\x00	End of data file
SYNC	\xFF\xFF\xFF\xFF\x04\x00\x00\x00	Correct `sync()`-response
FIFO ERROR	\xFF\xFF\xFF\xFF\x08\x00\x00\x00	FIFO full
BUFFER ERROR	\xFF\xFF\xFF\xFF\x10\x00\x00\x00	Ring buffer full

TABLE 7.1. Reserved 64-bit status words that are used to signal specific scenarios, denoted in hexadecimal notation.

in this thesis, it is mentioned here for completeness. The two error words are used to signal issues encountered on the Z-turn board. FIFO ERROR indicates that one of the FIFOs is full, comprising the merging of the *hits* and thus necessitating a reduction in the signal rate. BUFFER ERROR signifies that the ring buffer on the Z-turn board's CPU is full, a problem that can also be mitigated by lowering the signal rate.

7.4 Data Acquisition

After the ToT-encoded logic pulses from the NINO chips have been processed by the the Z-turn board, a continuous stream of *hits* is available that can be fed to a frontend computer. However, simply connecting a computer is not sufficient. Several software steps are necessary to establish a connection with the Z-turn board, configure the NINO readout board, and initiate data acquisition. The present section outlines these steps, along with explaining how to record data and how to read the stored data for analysis.

All steps are performed using several `Python3` scripts, but for better clarity, only excerpts from the used code will be shown. The complete scripts are available in the `GitLab` repository `MAGIX_DarkMESA/MXTriggerReadout`, which is accessible to all members of the MAGIX collaboration.

7.4.1 Configuring the NINO Readout Board

Code 7.1 shows the `Python3`-functions used for configuring the NINO readout board, as well as for establishing and terminating a connection from a frontend computer to the Z-turn board[41].

Calling the function `NINOconnect()` establishes a connection with the Z-turn board using `Python3`'s `socket`-module [157], which is commonly used for low-level networking interfaces. First, an instance of the `socket` class, termed *nino*, is created invoking the `socket()`-function (line 5), where the *address family* and the *socket type* have to be specified as the first and second

[41] When no connection is established, the inputs of the Tapped Delay Line TDCs are disabled. If analog input signals are present, the NINO readout board processes them as usual, but the logic pulses generated by the NINO chips are not forwarded for further processing.

Code 7.1: Connecting to the Z-turn board and configuring the NINO readout board.

```
1  import socket as s
2
3  ### Create socket for Z-turn board and connect to it
4  def NINOconnect(host='Zynq3', port=5001):
5      nino = s.socket(s.AF_INET, s.SOCK_STREAM)
6      nino.connect((host, port))
7      return nino
8
9  ### Disconnect from Z-turn board
10 def NINOdisconnect(nino):
11     nino.close()
12
13 ### Define config for NINO readout board and send to Z-turn board
14 def NINOconfig(nino, att=475, thr=600, hyst=0, stret=2100):
15     config = [[  att]*32, # ATT_CTRL, attenuation, 4095 is lowest
16               [    0]*32, # OFS, default=0
17               [    0]*32, # OP, default=0
18               [  thr]*4,  # TH+, discriminator threshold, 0 is lowest
19               [  thr]*4,  # TH-, default=TH+
20               [ hyst]*4,  # HYS, hysteresis, default=0
21               [stret]*4,  # STR, pulse stretching, default=2100 (10ns)
22               [    0]*4,  # TP, channels 0-6 of a NINO chip, default=0
23               [    0]*4]  # TP, channel 7 of a NINO chip, default=0
24     raw = [int.to_bytes(j, 2, byteorder = 'little') for i in config for
       j in i]
25     nino.send(b'CONFIG\n' + b''.join(raw))
26     print(f'NINO readout board configured: thr={thr}, att={att}, hyst={
      hyst}, stret={stret}.\n')
```

arguments, respectively. For the address family, an IPv4 connection is used (*AF_INET*), and a TCP socket is chosen as the socket type (*SOCK_STREAM*). Next, the `connect()`-function is called (line 6) to establish the connection by passing an address defined by the value pair (*host*, *port*). The string *host* represents a host name in internet domain notation or an IPv4 address, and the integer *port* describes the port number utilized for the connection. At MAGIX, the connection with the Z-turn board is established using port number 5001, whereas the host name depends on the network configuration and can be changed as needed. During the course of this thesis, the host name has been *Zynq3*. `NINOconnect()` then exits with returning the object *nino* (line 7).

The function `NINOdisconnect()` should be called when the data acquisition is finished.[42] The only thing it does is to terminate the connection with the Z-turn board by calling the `socket`-module's `close()`-function on the object *nino* (line 11).

[42] In retrospect, communicating with the Z-turn board should have been programmed in a more object-orientated way. The contents of the functions `NINOconnect()` and `NINOdisconnect()`, for example, could be integrated into the `__init__()` and `__del__()` methods of a class representing the connection to the Z-turn board. However, the code that has been used throughout this thesis has historically emerged into this form. In the future, a rewrite tailored to the software framework of the final MAGIX setup will prove to be advantageous.

For configuring the NINO readout board, the function `NINOconfig()` is invoked with the *control parameters* from Section 7.2, i.e. *att*, *thr*, *hyst*, and *stret*, as additional arguments. Inside the function, a list called *config* is defined (lines 15–23), whose entries are converted to byte arrays and stored in a separate list called *raw* (line 24). By merging the entries of *raw*, a binary configuration string is created, which is sent to the Z-turn board using the `send()`-function of the `socket`-module (line 25).

The definition of the list *config* needs to be explained in more detail. The entries of *config* are lists of DAC input values for each parameter that can be controlled using the Z-turn board. These include the *control parameters att*, *thr*, *hyst*, and *stret*, as well as the DAC inputs *OFS* and *OP*, which were briefly mentioned in Sections 7.2.1 and 7.2.2, respectively, and the test pulse amplitudes *TP* described in Section 5.3.1. The order of the entries is fixed and must be maintained for the configuration. It is determined by the format of the binary configuration string, which is defined on the SoC part of the Z-turn board. If necessary, the format can be changed in the future. The length of the entries depends on whether a parameter needs to be set per readout channel or per NINO chip. For example, *att* is set per readout channel, so the corresponding list has a length of 32. In contrast, *thr* is set per NINO chip, resulting in a list length of four. The DAC input values, in turn, can be freely adjusted within their 12-bit range, i.e. from 0 to 4095. In Code 7.1, however, they are uniformly set for all readout channels and NINO chips. While this is adequate for initial test measurements, the future operation of MAGIX will require precise adjustments as each readout channel will need to be individually calibrated.

7.4.2 Recording Data

After establishing the connection with the Z-turn board and configuring the NINO readout board, data can be collected. Code 7.2 shows an exemplary `Python3`-function to record data for a given amount of time.

The function `NINOtakeTime()` requires three arguments: the established connection with the Z-turn board, represented by the *nino* object, a filename, and the desired data collection duration in s. To start data recording, i.e. to tell the Z-turn board to output *hits* via the Ethernet connection, a start string must be sent to the Z-turn board using the `sendall()`-function of `Python3`'s `socket`-module (lines 5 and 6). Subsequently, several variables are initialized, such as *raw* for storing the incoming data and *event_counter* for tracking the number of events (lines 7–12). After opening the data file in binary write mode (line 14), data collection begins within the `while`-loop (line 15). The `recv()`-function of `Python3`'s `socket`-module is used with a buffer size of 4096 to receive data from the Z-turn board (lines 16 and 17). The received data is then written to the file in packages of eight bytes (lines 19–21), i.e. 64-bit words as described in Section 7.3.3. Next, the function checks for the STOP word, cf. Section 7.3.3, and if `True`, the `while`-loop is terminated, concluding the data collection process (lines 22–24). The variable *raw* is then updated by removing the data that has already been written (line 26), and metrics such as the event rate are calculated and

Code 7.2: Recording data for a given amount of time.

```
import time as t

### Collect data for a given amount of time
def NINOtakeTime(nino, filename, duration_in_s=30):
    # Start data collection
    nino.sendall(b'START\n')
    # Initialize variables
    raw = b''
    event_counter = 0
    run_time = 0.0
    rate = 0.0
    start_time = t.time()
    # Open file and collect data
    with open(filename, 'wb') as dataf:
        while True:
            # Receive data into 'raw'
            raw = raw + nino.recv(4096)
            if len(raw) >= 8:
                # Store data as packages of eight bytes (hits)
                l = 8 * (len(raw) // 8)
                dataf.write(raw[0:l])
                # Break if STOP word has been read
                if raw[l-8:l] == b'\xFF\xFF\xFF\xFF\x02\x00\x00\x00':
                    break
                # Update 'raw', calculate rate, ...
                raw = raw[l:]
                event_counter += l//8
                run_time = t.time() - start_time
                rate = event_counter/run_time
                print(f'NINO events: {event_counter}, Rate: {rate:.3f}
    Hz, Time: {run_time:.3f}s', end='\r')
                # Stop data collection after given duration
                if run_time >= duration_in_s:
                    nino.sendall(b'STOP\n')
        print(f'NINO events: {event_counter}, Rate: {rate:.3f}Hz, Time:
     {run_time:.3f}s\n')
```

Code 7.3: Reading collected *hits*.

```
from struct import unpack

### Read raw hits from file and return them for analysis
def NINOreadHits(filename, hitsToRead=2000000):
    # Initialize variables
    hits = []
    hitIndex = 0
    # Open file and read hits
    with open(filename, 'rb') as inputf:
        while len(hits) < hitsToRead:
            # Read 8 bytes, i.e. one hit, and verify length
            raw = inputf.read(8)
            if (len(raw) != 8):
                break
            # Check that file starts with START word
            if (hitIndex == 0):
                if (raw == b"\xFF\xFF\xFF\xFF\x01\x00\x00\x00"):
                    print(f"START word found at hit {hitIndex}.")
                    hitIndex += 1
                    continue
                else:
                    print("File does not start with START word.")
                    break
            # Check for STOP word
            if (raw == b"\xFF\xFF\xFF\xFF\x02\x00\x00\x00"):
                print(f"STOP word found at hit {hitIndex}.")
                break
            # Check for error words
            if (raw == b"\xFF\xFF\xFF\xFF\x08\x00\x00\x00"):
                print(f"ERROR: FIFO overrun at hit {hitIndex}.\n")
                break
            if (raw == b"\xFF\xFF\xFF\xFF\x10\x00\x00\x00"):
                print(f"ERROR: Ring buffer overrun at hit {hitIndex}.\n
    ")
                break
            # Unpack hit (64-bit word)
            # Bit 0: edge (0=leading, 1=trailing)
            # Bits 1-7: readout channel number (0-127)
            # Bits 8-55: coarse time in ns since system startup
            # Bits 56-63: fine time bin (0-255)
            hit     = unpack(format='<II', buffer=raw)
            edge    = hit[0]>>31
            channel = ((hit[0]>>24) & 0x7F)
            coarse  = (((hit[0] & 0xFFFFFF)<<24) + (hit[1]>>8))*4
            finebin = hit[1] & 0b11111111
            hits.append(HIT(edge, channel, coarse, finebin))
            print(f'{edge} {channel} {coarse} {finebin}')
            hitIndex += 1
    return hits
```

Code 7.4: Dataclass representing a *hit*.

```
1 from dataclasses import dataclass
2
3 ### Dataclass representing a hit
4 @dataclass
5 class HIT:
6     edge:    int # 0 = leading, 1 = trailing
7     channel: int # readout channel number (0-127)
8     coarse:  int # coarse time in ns since system startup
9     finebin: int # fine time bin (0-255)
```

displayed (lines 27–30). To properly stop recording data, `NINOtakeTime()` checks the elapsed time at the end of each `while`-loop iteration, and if the specified duration is exceeded, a stop string is sent to the Z-turn board (lines 31–33). During the subsequent loop iteration, the STOP word will be detected, marking the end of the data collection process.

7.4.3 Reading Data for Analysis

After collecting data and storing it in a binary data file, it must be read again for analysis. The method for doing this is demonstrated in Code 7.3.

The exemplary function `NINOreadHits()` requires the name of the data file as a mandatory argument and includes an optional argument specifying the number of *hits* to read. The function begins by declaring two variables (lines 14–16): an empty list to store the read *hits* and an index to track the number of *hits* processed. The data file is then opened in binary read mode, and the reading process starts with a `while`-loop that continues until the specified number of events has been read (lines 17–19). In each iteration, a *hit*, i.e. a 64-bit word with the length of eight bytes, is read, and its size is verified (lines 20–23). The *hit* is then compared to the reserved status words described in Section 7.3.3 (lines 24–43), beginning with the START word for the very first *hit* that is read. If the file does not begin with the START word, the data file is assumed to be empty or corrupted, and the function exits, returning an empty list of *hits*. If the STOP word or one of the two error words is encountered, the `while`-loop is terminated, and the function returns the *hits* read up to this point. When a *hit* does not match any of the reserved words, the encoded information is unpacked and appended to the list of *hits* in the format of the data class `HIT` (lines 44–54), which is defined in Code 7.4. Unpacking is done using the `unpack()`-function of `Python3`'s `struct`-module, which requires a *format* and a *buffer* as arguments. To match the data structure used by the Z-turn board, cf. Section 7.3.3, the format *"<II"* is used, where *"<"* specifies little-endian byte order, and *"II"* denotes two 32-bit unsigned integers. The buffer corresponds to the raw data that needs to be unpacked, i.e. *raw*. Once unpacked, the two 32-bit words are accessible via `hit[0]` and `hit[1]`, allowing the encoded information to be extracted according to the utilized data structure. After the desired number of *hits* has been read, the function exits and

FIGURE 7.17. Exemplary *hits* as they are used for analysis. The order of a *hit*'s entries corresponds to the data structure described in Section 7.3.3.

returns the list of read *hits*.

The *hits* are now available for analysis, which will be the topic of the coming Chapter 8. To provide a clearer understanding of the *hits* that enter the analysis process, Fig. 7.17 displays several *hits* as they appear on the console. To summarize: the first entry of a *hit* represents its edge information, while the second entry contains the number of the readout channel. The third entry corresponds to the *coarse time* in ns and the *fine time bin* is stored as the fourth entry.

CHAPTER 8

FROM DATA TO ANALYSIS

Chapter 7 outlined the readout process, concluding with collected data in form of *hits*, each of which corresponds to one edge of a logic pulse. The present chapter builds upon this data and demonstrates the key aspects of the analysis process, including the extraction of essential detector properties for the trigger detectors. To do so, data is used that has been obtained during a beam time with the MAGIX trigger detectors at MAMI in June 2024, which was conducted to test all components of the trigger layer readout as an integrated system under real experimental conditions. The key insights with respect to the design criteria for the trigger layer stated in Section 3.2 have been extracted, as will be shown.

Section 8.1 starts with a brief description of the setup used during the MAMI beam time, before Sections 8.2 and 8.3 describe the pre-processing and analysis of the data, respectively, exemplarily performed on one representative dataset. Along the way, it is demonstrated how the crucial detector properties *efficiency*, *coincidence time resolution*, and *spatial resolution* can be extracted from the data, and first values are provided for each. Section 8.4 then discusses a necessary correction, the *walk correction*, and its influence on the accuracy of the detector properties. Finally, Section 8.5 presents two significant findings for the trigger detectors: the effects of different trigger rates on the detector properties, and their stability during an overnight measurement.

Similar to Section 7.4, the individual steps of data pre-processing and analysis are performed using multiple `Python3` scripts, only excerpts of which will be included in this chapter. The complete scripts are available in the `GitLab` repository `MAGIX_DarkMESA/MXTriggerReadout`, which is accessible to all members of the MAGIX collaboration. Besides, the pre-processing and analysis steps result in the generation of one `pdf` report per dataset, summarizing all relevant information. An example of such a report can be found in Appendix F.5.

8.1 Data Collection at MAMI

MAMI, short for **MA**inz **MI**crotron, is the existing electron accelerator located at the Institute for Nuclear Physics of the Johannes Gutenberg University Mainz, Germany. Operational since 1979, MAMI has undergone continuous upgrades and expansions over the decades. Today, it incorporates four acceleration stages, the first three of which are based on the principle of the racetrack microtron (RTM), while the fourth stage utilizes a harmonic double-sided microtron (HDSM) configuration. Together, these stages enable MAMI to deliver a maximum beam energy of 1.6 GeV. Three major experimental programs are supported by MAMI: the three-spectrometer setup A1, the real photon facility A2, and X1, the applied physics site of MAMI. In the past, MAMI also hosted the parity-violation experiment A4, which has since been decommissioned. The experimental halls formerly used by A4 have now been repurposed to accommodate the new accelerator MESA. Further details on the MAMI accelerator and its configuration are omitted here, as comprehensive information is readily available elsewhere. An excellent overview can be found, for instance, in the PhD thesis by M. Christmann [27].

In June 2024, a beam time with the trigger detectors was conducted at the X1 experiment at MAMI. X1 is situated just behind MAMI´s third accelerator stage and offers a flexible and spacious environment, ideal for testing particle detectors. An impression of the measurement site can be gained from Fig. 8.1. At the X1 experiment, the MAMI electron beam can be easily decoupled, with a selectable beam energy ranging from 180 MeV to 855 MeV. Additionally, the beam current can be adjusted from approximately 0.3 fA up to 30 µA for polarized beams, and up to 100 µA for unpolarized beams.

During the beam time with the trigger detectors, an unpolarized beam with a chosen energy of 180 MeV was used, as this is the closest achievable energy at X1 to the anticipated MESA beam energy at MAGIX. The initial beam current was set to approximately 6 fA, which corresponds to an electron flux of about 35.5 kHz.[1] Later in the experiment, also higher beam currents were employed to study the effects of varying trigger rates, as will be discussed in Section 8.5.1.

As shown in Figs. 8.1 and 8.2, five trigger detectors were used during the beam time, arranged in three consecutive layers relative to the incoming electron beam, with a 65 mm spacing between the layers[2]. For the remainder of this chapter, all directions are defined with respect to the X1 experiment's beam pipe, as viewed from the perspective of an incoming beam electron. The first and third layers each consist of a single, horizontally positioned trigger detector, while the second layer comprises three vertically aligned trigger detectors placed adjacent to each other. The gaps between the three central detectors follow the design specified in Section 5.4 and measure 0.5 mm. A detailed list of the five trigger detectors used is provided in Tab. 8.1. Throughout the studies in

[1] These values for beam current and electron flux have been derived from the relationship between Wehnelt voltage and electron flux, as described in Section 8.5.1. The initial Wehnelt voltage during the beam time was $U_W = -12.15\,V$.

[2] The 65 mm distance is measured between the detector surfaces facing the beam pipe and therefore includes 26 mm of scintillator material as well as the thickness of the wrapping materials.

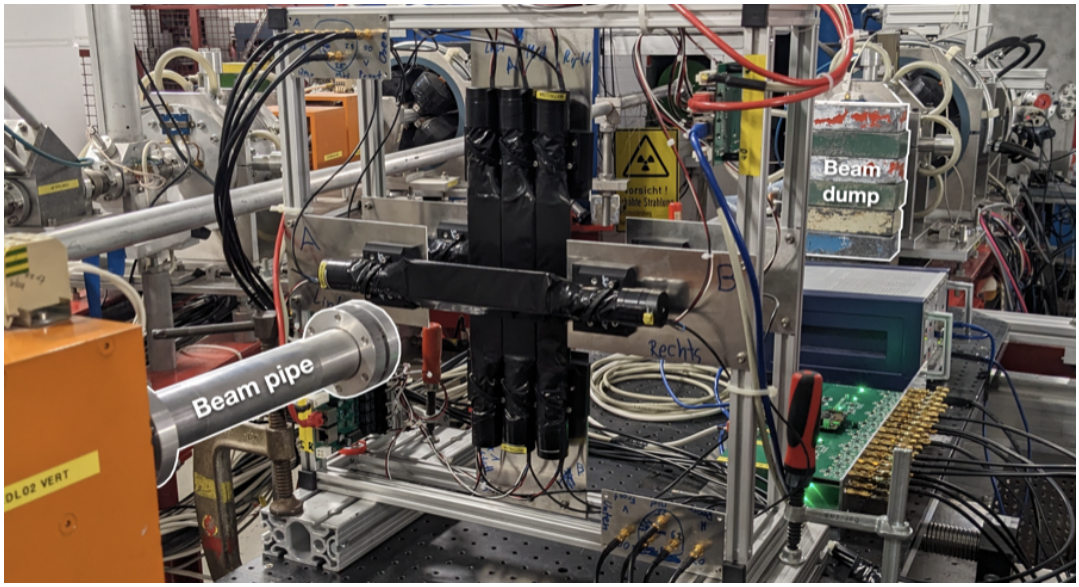

(a)

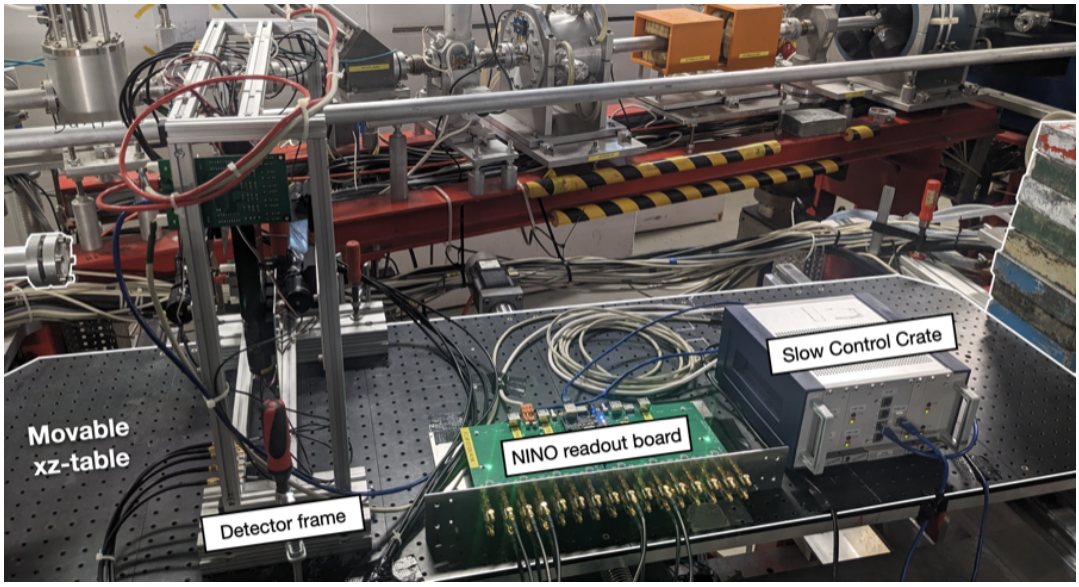

(b)

FIGURE 8.1. The setup during the MAMI beam time at X1, as viewed from the front (a) and from the side (b). Photographs taken by D. Schmitt.

this chapter, the detectors *Front* and *Rear* are used to form the trigger condition, while the three central detectors are considered test detectors.

The detectors were mounted within a MayTec frame using the 3D-printed components designed for the final MAGIX setup, cf. Section 5.4. These were screwed to aluminum sheets in a manner that avoided overlap with the scintillator regions of the detectors, thereby minimizing scattering

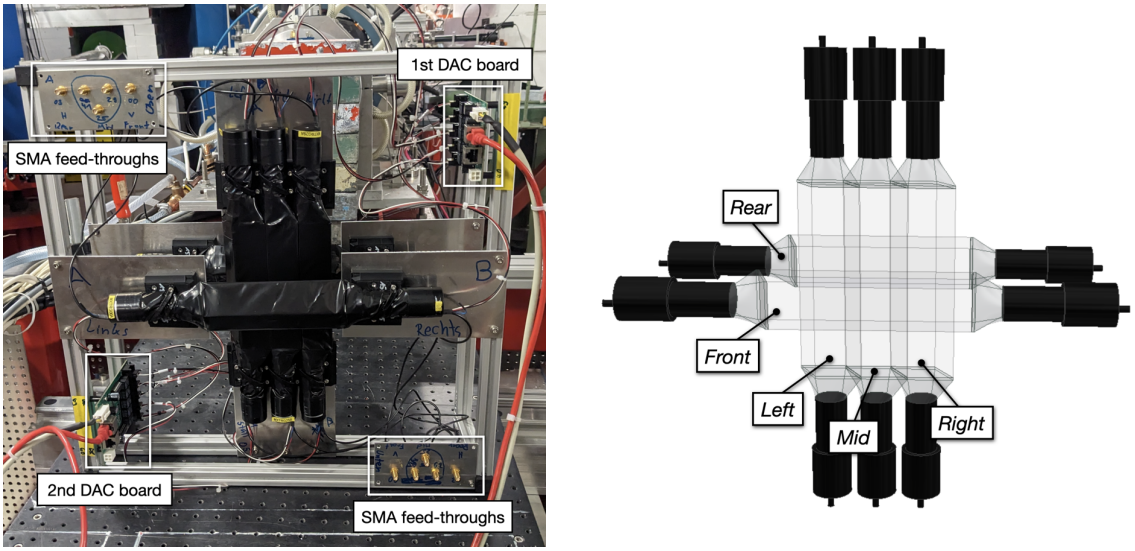

(a) (b)

FIGURE 8.2. The detector frame built for the MAMI beam time at X1 (a) and a CAD model illustrating the arrangement of the five utilized trigger detectors (b), both viewed from the perspective of the X1 beam pipe. Photograph in (a) taken by D. Schmitt.

Detector layer	**Orientation**	**Detector label**	**Identifier**	**Trigger?**
1st	horizontal	MXTRG00	*Front*	yes
2nd	vertical	MXTRG41	*Left*	no
2nd	vertical	MXTRG25	*Mid*	no
2nd	vertical	MXTRG29	*Right*	no
3rd	horizontal	MXTRG03	*Rear*	yes

TABLE 8.1. List of the trigger detectors used during the MAMI beam time at X1.

interactions of the beam electrons. The frame also incorporated two DAC boards for providing the supply and control voltages for the high-voltage sockets of the trigger detectors, as detailed in Section 5.2.1. Additionally, SMA feed-throughs were integrated into the frame, as they are also included in the mountings of the trigger layers, cf. Section 5.4.

As power supply, the half-size 19-inch slow control crate was employed, as described in Section 5.2.2, with the slow control managed via EPICS, cf. Section 5.2.3. The control voltages for the PMTs of the trigger detectors were adjusted based on a gain-matching procedure conducted prior to the beam time[3], details on which can be found in Appendix F.1. Gain-matching all PMTs allows for the definition of so-called *working points*, which correspond to specific charge values within a method-dependent charge range defined during the gain-matching procedure. Each working point

[3]Several other preparatory measurements were performed before the beam time. Further details on these can be found in the Bachelor's thesis of D. Schmitt [148].

can be viewed as representing a specific gain value and by utilizing the gain-matching results, the control voltage of each PMT can be adjusted to achieve this gain. The five working points used during the beam time were 7.0 pC, 13.5 pC, 20.0 pC, 26.5 pC, and 33.0 pC. As a default setting, working point number three was used, i.e. 20.0 pC.

For readout, the upgraded second version of the NINO readout board was employed, along with the passive 20 dB attenuators, as described in Section 7.2.1. The default settings for the control parameters across all readout channels were $att = 475$, $thr = 600$, $hyst = 0$, and $stret = 2100$.

The entire setup was mounted onto the movable xz-table of the X1 experiment, where x denotes the horizontal direction perpendiculat to the beam and z indicates the vertical direction. Using remotely controlled stepper motors[4], the table position can be accurately adjusted to the needs of the experiment. The table's default position was set to $x = 34\,\text{mm}$ and $z = 108\,\text{mm}$, referred to as *HOME*[5], which corresponded to the electron beam impinging on the centers of the detectors *Front*, *Mid*, and *Rear*. For the studies presented in this chapter, only this default setting was utilized. However, during the beam time, scans along the x- and z-directions were also conducted[6], some datasets of which have been used for the studies in Appendices F.2 and F.3. While the z-direction scans are detailed in the Bachelor's thesis of D. Schmitt [148], the final analyses of the x-direction scans are still pending.

8.2 Pre-Processing

Following Section 7.4.3, the collected *hits* of a dataset are ready to be analyzed. But before the actual analysis can be performed, a few preparatory steps are required that are condensed in this section under the term *pre-processing*. In principle, the pre-processing leads to a cleaner and tidied up dataset by filtering and cleaning the collected *hits*. Moreover, it includes the fine time calibration mentioned in Section 7.3.1.

For demonstrating the pre-processing, one representative dataset is utilized that has been obtained during the MAMI beam time presented in the last section. Specifically, the dataset `MXTriggerBeamTimeJune2024/data_posScan/meas_posScan_pos_34.0.dat` from the `GitLab` repository `MAGIX_DarkMESA/MXTriggerReadout` is used, for which the xz-table was set to the *HOME* position and all parameters were set to their default values, cf. Section 8.1. The same dataset will be used for illustrating the analysis procedure and the walk correction in Sections 8.3 and 8.4, respectively.

[4]The motor driving the x-direction has a resolution of 20 000 steps per mm, while the motor for the z-direction has a resolution of 2000 steps per mm.

[5]Additionally, a second position, termed *PARK*, was defined with coordinates $x = -80\,\text{mm}$ and $z = 18\,\text{mm}$. This position corresponded to the electron beam passing through the upper right empty quadrant of the frame setup and was used whenever optimization of the MAMI electron beam was necessary.

[6]The directions are defined such that increasing x moves the xz-table to the right from the perspective of an incoming beam electron, while decreasing x moves it to the left. Similarly, increasing z moves the table upward, and decreasing z moves it downward. Conceptually, the movement of the table can also be viewed as the electron beam moving in the opposite direction, which may be a more intuitive perspective when analyzing the corresponding data.

8.2.1 Cleaning and Sorting

Code 8.1 illustrates the individual steps of cleaning and sorting, which are performed inside the function `NINOcleanAndSort()`. The function begins with initializing several variables (lines 7–15) and starting a `for`-loop iterating over the collected *hits* (line 17). For each *hit*, the following three steps are performed:

- The first step involves cleaning the dataset to ensure that only physically reasonable *hits* proceed to the analysis stage. Several cuts are applied during this process (lines 20–29).[7] For instance, since the edge information of a *hit* can only be 0 or 1, any *hit* with a different edge value indicates a readout error and is therefore discarded. Similarly, a *hit* is removed if its *fine time bin* is below 0 or exceeds the upper limit of 222, cf. Section 7.3.1. Additionally, *hits* from irrelevant readout channels are excluded to prevent crosstalk events from these readout channels from affecting the analysis, thereby reducing the data volume. The *relevant readout channels* can be specified via the optional argument *channelsOfInterest*, whose default value is the list of channels used for the current setup, as defined in the external file `NINOglobals.py`. *Hits* that pass the above filtering criteria are added to the list of clean *hits*.

- At the time of writing this thesis, the Tapped Delay Line TDCs exhibit the phenomenon of *double counts*, which is addressed by the second step. The effect is caused by the input buffers that are implemented as part of the input stages ahead of the delay lines, cf. Section 7.3.1. The input buffers enhance the robustness of the delay lines by continuously providing a binary 1 to the delay line input from the moment an input signal occurs until the delay line is read out at the next clock cycle's rising edge. However, the input buffers introduce a delay and if an input signal occurs just before a rising clock edge, it can happen that the input signal is not read out at the rising edge, as the input buffer has not yet switched. This scenario presents two options: either accept the loss of some input signals or extend the buffer's activity into the next clock cycle to ensure the input signal is recorded. At the time of writing this thesis, the latter approach is implemented, which introduces so-called double counts, where certain input signals are recorded twice instead of only once. To address this issue, the second *hits* from these double counts are simply removed at the time of writing this thesis (lines 34–42). Future work should focus on identifying the optimal approach to addressing the phenomenon of double counts.

- The third step repositions each *hit* within the list of clean *hits* by sorting them according to their *coarse time*, which is implemented in form of a standard bubble-sort algorithm (lines 43–50). During the FIFO merging process on the Z-turn board, cf. Section 7.3.2, the final *hits* can sometimes be reordered, differing from the sequence in which the corresponding

[7] While this filtering could, in principle, already be implemented during the readout process, retaining flawed data has been valuable up to this point for diagnosing and resolving potential issues.

PMT signals occurred in the detector. Sorting the *hits* by *coarse time* ensures that they are at least in the correct order to within the accuracy of the *coarse time* measurement, i.e. to within 4 ns.

Code 8.1: Cleaning and sorting the raw *hits* as part of the pre-processing.

```
# Initialize global variables from NINOglobals.py
import NINOglobals as g
g.initialize()

### Filter hits, sort hits, and remove double counts
def NINOcleanAndSort(hits, channelsOfInterest=g.channels):
    # Initialize variables
    cleanHits = []
    hitHist = [0]*32
    hitHistFiltered = [0]*32
    hitHistClean = [0]*32
    edgeCutCounter = 0
    finebinCutCounter = 0
    channelCutCounter = 0
    doubleCountCounter = 0
    # Iterate over hits
    for hit in hits:
        # Count hits per readout channel
        hitHist[hit.channel] += 1
        # Check whether hit data is physically reasonable
        if (hit.edge not in (0,1)):
            edgeCutCounter += 1
            continue
        if (hit.finebin > 222) or (hit.finebin < 0):
            finebinCutCounter += 1
            continue
        if (hit.channel not in channelsOfInterest):
            channelCutCounter += 1
            continue
        # Add hit to list of clean hits
        cleanHits.append(hit)
        hitHistFiltered[hit.channel] += 1
        hitHistClean[hit.channel] += 1
        # Remove double counts
        for i in range(8):
            if (len(cleanHits)-i > 1) and \
            (cleanHits[-2-i].channel == cleanHits[-1].channel) and \
```

```
38              (cleanHits[-1].coarse - cleanHits[-2-i].coarse == int(g.
    clockPeriod)):
39                  doubleCountCounter += 1
40                  hitHistClean[cleanHits[-2-i].channel] -= 1
41                  del cleanHits[-2-i]
42                  break
43          # Move hit to correct position in list of clean hits (bubble
    sort by coarse time)
44          j = len(cleanHits)-1
45          while (j > 1) and \
46          (cleanHits[j].coarse < cleanHits[j-1].coarse) and \
47          (cleanHits[j].channel != 0x7F) and \
48          (cleanHits[j-1].channel != 0x7F):
49              cleanHits[j-1], cleanHits[j] = cleanHits[j], cleanHits[j-1]
50              j -= 1
51      # Display hit information
52      print(f"\n{len(hits)} hits to be analyzed (clean: {len(cleanHits)},
        edge cut: {edgeCutCounter}, finebin cut: {finebinCutCounter},
    channel cut: {channelCutCounter}, double counts: {
    doubleCountCounter}).")
53      print("Hits per readout channel:")
54      print(hitHist[0:8], hitHist[8:16])
55      print(hitHist[16:24], hitHist[24:32])
56      print("Filtered hits per readout channel (cuts applied):")
57      print(hitHistFiltered[0:8], hitHistFiltered[8:16])
58      print(hitHistFiltered[16:24], hitHistFiltered[24:32])
59      print("Clean hits per readout channel (double counts removed):")
60      print(hitHistClean[0:8], hitHistClean[8:16])
61      print(hitHistClean[16:24], hitHistClean[24:32])
62      return cleanHits
```

Following the above three steps, the collected *hits* have been cleaned, sorted, and are ready for analysis. The function `NINOcleanAndSort()` concludes by displaying information on the collected *hits*, along with the numbers discarded due to cuts or double count removal (lines 51–61). Finally, the function exits, returning the list of clean *hits*.

Fig. 8.3 illustrates the output of the `NINOcleanAndSort()`-function for the first 2000000 *hits* from the aforementioned dataset. As shown, 146646 *hits*, which corresponds to more than 3 % of the read *hits*, are identified as double counts and subsequently discarded. The cause of this significant percentage remains unclear at the time of writing this thesis and will be an important aspect to investigate in future studies. In addition, 720 *hits* are excluded by applying the cut on the *fine time bin*, corresponding to 0.036 % of the read *hits*. When the cleaning and sorting process is performed without this cut, 715 of these *hits* are identified as double counts and discarded,

```
2000000 hits to be analyzed (clean: 1852634, edge cut: 0, finebin cut: 720, channel cut: 0, double counts: 146646).
Hits per readout channel:
[0, 2083, 327050, 6036, 0, 0, 0, 0] [329914, 0, 327588, 0, 0, 0, 0, 0]
[0, 2458, 333070, 6011, 0, 0, 0, 0] [334375, 0, 331415, 0, 0, 0, 0, 0]
Filtered hits per readout channel (cuts applied):
[0, 2083, 327043, 6035, 0, 0, 0, 0] [329901, 0, 326903, 0, 0, 0, 0, 0]
[0, 2458, 333067, 6010, 0, 0, 0, 0] [334371, 0, 331409, 0, 0, 0, 0, 0]
Clean hits per readout channel (double counts removed):
[0, 1927, 305846, 5626, 0, 0, 0, 0] [306196, 0, 304273, 0, 0, 0, 0, 0]
[0, 2256, 307367, 5612, 0, 0, 0, 0] [307419, 0, 306112, 0, 0, 0, 0, 0]
1852634 clean hits to be analyzed.
```

FIGURE 8.3. Information on the collected *hits* displayed by the function `NINOcleanAndSort()`. At the time of writing this thesis, more than 3 % of the recorded *hits* are identified as double counts and thus discarded.

indicating that five *hits* are erroneously removed by the *fine time bin* cut. Although this will have a negligible impact on the obtained efficiency, affecting only 0.000 25 % of the read *hits*, it shows that the cut implementations and the double count removal process should be carefully reviewed at some point. Such refinements will be crucial for ensuring the highest level of accuracy in future experiments.

8.2.2 Fine Time Calibration

The second part of the pre-processing is the already mentioned fine time calibration, i.e. the conversion from *fine time bin* to the actual *fine time* in ns. Combined with the measured *coarse time*, this calibration then allows for the calculation of a precise timestamp for each edge of a logic pulse, cf. Fig. 7.13.

As noted in Section 7.3.1, each delay line cell of a Tapped Delay Line introduces a specific delay time, which, while consistent within a certain accuracy, can vary slightly from cell to cell. Furthermore, the cumulative delay of 256 delay line cells, each contributing approximately 18 ps, exceeds the clock period of 4 ns. As a result, the delay line is always read out before the propagating signal can reach the end of the delay line. Both of these factors must be considered when calibrating the conversion from *fine time bin* to *fine time* in ns.

The idea of the fine time calibration is as follows: Detector signals are generally expected to occur uniformly within the clock period. Therefore, if sufficient statistics are collected, the frequencies of all *fine time* values should be approximately equal. The fine time calibration can thus be performed by histogramming the *fine time bins* of a dataset and smoothing the distribution by adjusting the widths of the individual bins. The resulting bin sizes then correspond to the delay times of the individual delay line cells, with each cell having an associated cumulative delay, which indicates the *fine time* of a *hit* that has travelled through the delay line down to that specific cell. Using this approach, the variations in delay time among the cells that cumulatively contribute to the 4 ns clock period can be compensated for, and the cells that cannot be reached within the clock period end up having very narrow bin widths.

Code 8.2: Fine time calibration.

```
1  ### Perform fine time calibration
2  def NINOfineTimeCalibration(cleanHits):
3      # Initialize variables
4      fineTimeCalib = [[] for i in range(32)]
5      fineHist = [[0]*256 for i in range(32)]
6      # Make histogram of fine time bins
7      for hit in cleanHits:
8          fineHist[hit.channel][hit.finebin] += 1
9      # Iterate over readout channels
10     for ch in range(32):
11             # Cumulatively add up the entries of the fine time bin
    histogram (this corresponds to the run time through the delay line)
12             entries = 0
13             for j in range(256):
14                 entries += finehist[ch][j]
15                 fineTimeCalib[ch].append(entries)
16             # Normalize to the total number of hits and convert to fine
     time using the clock period
17             if fineTimeCalib[ch][-1] > 0:
18                 for j in range(256):
19                     fineTimeCalib[ch][j] /= fineTimeCalib[ch][-1]/4.0
20     return fineTimeCalib
```

Code 8.2 guides through the fine time calibration using the Python3-function `NINOfineTimeCalibration()`, which takes the clean *hits* from the previous section as its argument. The function begins by initializing the empty list *fineTimeCalib* that will be filled with the cumulative delays of the delay line cells, as well as the empty histogram *fineHist* for histogramming the *fine time bins* of the dataset (lines 3–5). It then iterates over the clean *hits*, populating the histogram with the corresponding *fine time bin* for each *hit* (lines 6–8). Next, for each readout channel (lines 9 and 10), the function then cumulatively sums the histogram entries and appends the results to *fineTimeCalib* (lines 11–15). The entries of *fineTimeCalib* are then normalized to the total number of *hits* for the individual readout channel and converted to the corresponding *fine times* using the clock period (lines 16–19). Consequently, each entry indicates a calibrated *fine time* in ns, corresponding to a specific *fine time bin* of the individual readout channel's delay line. Finally, the function exits and returns the list of calibrated *fine times*.

The impact of the fine time calibration is illustrated in Fig. 8.4, where Fig. 8.4a shows the histogram of *fine time bins* for the first 2 000 000 raw *hits* from the above mentioned dataset, recorded with the trigger detector *FrontA*. As shown, the distribution abruptly terminates at bin values near 222, which corresponds to the point where the cumulative delay of the delay line

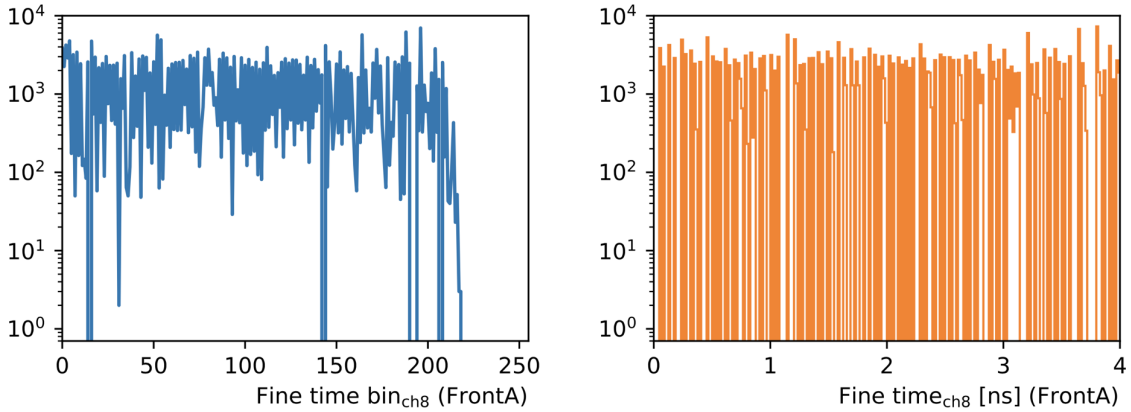

FIGURE 8.4. Impact of the fine time calibration. The calibration ensures that the frequencies of the individual *fine time* values are approximately equal across the entire 4 ns clock period.

cells reaches the clock period of 4 ns[8]. Beyond that, the distribution appears relatively flat.[9] In contrast, Fig. 8.4b illustrates the calibrated *fine times* in ns, where, as anticipated, the resulting distribution is uniformly flat across the entire clock period of 4 ns.

8.3 Analysis

After the pre-processing, the dataset is prepared for analysis, which is carried out in two main steps using the Python3-functions `interpretHits()` and `analyze_event()`. The `interpretHits()`-function calculates and collects the timestamps of all *hits* occurring within a specific coincidence window and passes them to the `analyze_event()`-function. This function then examines the collected timestamps for valid *events*, which represent the recorded logic pulses. The events can then be assigned to different event categories based on the event pattern observed across the relevant readout channels. Subsequently, the event categories can be analyzed in terms of the detector properties outlined in Section 8.3.3.

Please note that while the first step of the analysis is entirely independent of the used setup, this is not the case for the second part. For example, the results for the detector property efficiency will vary depending on which detectors are used to form the trigger condition. In the final MAGIX setup, there will be a single, fixed configuration, with the detector properties defined accordingly. However, at the time of writing this thesis - during the time of preparatory lab measurements and test beam runs -, the setup can change frequently, necessitating adjustments

[8]When generating the plots for Fig. 8.4, no cut on the *fine time bin* has been applied during the cleaning and sorting process.

[9]Some *fine time bins* remain empty. However, the corresponding *hits* are not lost, but instead appear in the adjacent *fine time bins*. This behaviour is under investigation at the time of writing this thesis.

to the `analyze_event()`-function. For the studies in this chapter, the `analyze_event()`-function has been tailored to the setup presented in Section 8.1, where the detectors *Front* and *Rear* are used to establish the trigger condition, and the three central detectors *Left*, *Mid*, and *Right* are considered test detectors.

8.3.1 Interpreting Hits

The first part of the analysis is encapsulated in the function `interpretHits()`, as shown in Code 8.3. The function requires three inputs: the cleaned *hits*, the list of calibrated *fine times* from the previous section, and the coincidence window in ns. The function begins by initializing several variables (lines 7–9) and then iterates over the cleaned *hits* (lines 10 and 11). For each *hit*, the *fine time bin* is converted to the actual *fine time* using the list of calibrated *fine times* (lines 12 and 13), enabling the calculation of the *hit's* precise timestamp according to the method illustrated in Fig. 7.13 (lines 14 and 15). Next, the function checks the time difference between the current *hit* and the *hit* from the previous iteration, and compares it to the specified coincidence window (lines 16 and 17). If the time difference is smaller than the coincidence window, the timestamp of the current *hit* is added to one of two lists, based on the *hit's* edge (lines 26–30), and the function continues to the next iteration. If the time difference exceeds the coincidence window, an *offset correction* is applied to account for different signal propagation delays across the readout channels, and the two lists of collected timestamps are passed to the `analyze_event()`-function (lines 18–25), from now on termed a *collection of timestamps*.

In principle, the coincidence window can be freely selected. However, it should be adjusted to align with the expected input rate and the time resolution of the used detector. For the analysis presented in this chapter, a coincidence window of 50 ns has been chosen. Details on the offset correction are provided in Appendix F.2

8.3.2 Analyzing Events

The second part of the analysis is realized in form of the function `analyze_event()`, which is triggered by the `interpretHits()`-function when the time difference between two *hits* exceeds the specified coincidence window, as described in the previous paragraph. Given its length, the `analyze_event()`-function has been moved to Code F.3 in Appendix F.4, with only the main concept summarized here. The collection of timestamps is processed channel-by-channel to create objects using the two classes shown in Code 8.4.

The class `NINOchannel` models a readout channel of a NINO readout board, while the class `Bar` aggregates data from two partner channels to represent a connected trigger detector. For each `NINOchannel` object, the ToT of a recorded logic pulse is calculated by subtracting the timestamp of its leading edge from that of its trailing edge. If no valid ToT is obtained, the function returns zero. At this point, a ToT cut is applied to account for the pulse stretching of the NINO chip, cf.

Code 8.3: Collecting the timestamps of all hits occurring within a specific coincidence window.

```
# Initialize global variables from NINOglobals.py
import NINOglobals as g
g.initialize()

### Collect hits during a coincidence window
def interpretHits(hits, fineTimeCalib, coincidenceWindow = 50):
    # Initialize variables
    timestamp0 = 0
    le, tr = resetEdgeLists()
    # Iterate over hits
    for i, hit in enumerate(hits):
        # Use fine time calibration to get fine time
        fine = fineTimeCalib[hit.channel][hit.finebin]
        # Calculate hit timestamp
        timestamp = hit.coarse - fine
        # Analyze collected timestamps if the coincidence window (in ns) has passed since the last hit
        if (timestamp - timestamp0 > coincidenceWindow) and (i > 0):
            # Offset correction
            for j in range(32):
                le[j] -= g.offsetCalib[j]
                tr[j] -= g.offsetCalib[j]
            # Analyze the collected timestamps
            analyze_event(le, tr)
            timestamp0 = timestamp
            le, tr = resetEdgeLists()
        # Collect timestamps in corresponding edge lists (do not overwrite if second hit occurs during coincidence window)
        if (hit.edge == 0) and (le[hit.channel] < 0):
            le[hit.channel] = timestamp
        if (hit.edge == 1) and (tr[hit.channel] < 0):
            tr[hit.channel] = timestamp

# Create lists to store hit timestamps of leading and trailing edges
def resetEdgeLists():
    # leading edges
    le = [-100.0*(i+1) for i in range(32)]
    # trailing edges
    tr = [-100.0*(i+33) for i in range(32)]
    return le, tr
```

Code 8.4: Classes used during the event analysis.

```
### Class representing a readout channel
class NINOchannel:
    def __init__(self, leading, trailing, channel):
        self.time = leading # channel time (or PMT time)
        self.trailing = trailing
        self.channel = channel
        self.tot = self.tot(leading, trailing)
        self.charge = totToCharge(self.tot, channel)
    # Calculate ToT
    def tot(self, leading, trailing):
        return trailing - leading if (trailing - leading > 8.0) else
   0.0

### Class representing a trigger detector
class Bar:
    def __init__(self, leading, trailing, channel):
        self.time = leading # channel times (or PMT times)
        self.trailing = trailing
        self.channel = channel
        self.tot = self.tot(leading, trailing, channel)
        self.charge = [totToCharge(self.tot[0], channel[0]),
                       totToCharge(self.tot[1], channel[1])]
        self.diff = self.time[0] - self.time[1] # channel time
   difference (or PMT time difference)
        self.mean = (self.time[0] + self.time[1])/2 # detector time
    # Calculate ToT
    def tot(self, leading, trailing, channel):
        return [trailing[0] - leading[0] if (trailing[0] - leading[0] >
    8.0) else 0.0, trailing[1] - leading[1] if (trailing[1] - leading
   [1] > 8.0) else 0.0]
```

Section 7.2, which has been conservatively set to 8.0 ns for the studies presented in this chapter. The resulting ToT can then be converted into the corresponding charge of the analog PMT pulse, provided that their relationship has been measured in advance, as outlined in Section 7.2.3. In Code 8.4, the conversion is implemented as the function `totToCharge()`, which accesses a list called `totCalib` that contains the fit parameters of the previously measured relation. The complete `totToCharge()`-function can be found in Code F.4 in Appendix F.4. A charge cut is also implemented at this stage, although it has been set to 0 pC throughout the studies in this thesis. This is because the charge has not been essential yet, as no energy-loss measurements have been performed so far. Instead, the focus has been on extracting the detector properties described in Section 8.3.3, which can be derived solely from the timing information of the logic pulses.

For a `NINOchannel` object, this timing information is characterized by the parameter *channel time* (or *PMT time*), which is the time assigned to a logic pulse occurring in a specific readout channel and is defined as the timestamp of the logic pulse's leading edge. This choice is based on

the fact that the leading edge is closest in time to the original analog PMT pulse. Additionally, the rise time of a PMT pulse is the fastest component of the signal and is least affected by the signal's amplitude or charge.

For each `Bar` object, both corresponding readout channels are treated in the same manner as a `NINOchannel` object. Besides, two additional timing parameters are defined for a trigger detector: the *detector time*, which is defined as the mean of the two channel times, and the *channel time difference* (or *PMT time difference*) that represents the time difference between the channel times of the two readout channels of a trigger detector.

For each `NINOchannel` object, as well as for each channel of a `Bar` object, it can now be checked, whether the collection of timestamps exhibits a valid event, indicating a recorded logic pulse. A valid event in a specific readout channel is defined by the following three criteria:

1. Two timestamps have been collected, corresponding to the leading and trailing edges of a logic pulse.
2. The calculated ToT exceeds the implemented ToT cut.
3. The corresponding charge is larger than the chosen charge cut.

Next, based on the identified events, each collection of timestamps can be assigned, channel-by-channel, to one or more of the following event categories:

- **all**: This category contains all events of a readout channel.
- **coinc**: This category holds the events of a readout channel, whose partner channel has also recorded an event, i.e. the coincidence events of the trigger detector associated with the readout channel.
- **trigger**: For the readout channels that contribute to the trigger condition, i.e. the readout channels associated with the two trigger detectors *Front* and *Rear*, this category includes the events where all other three associated readout channels have also recorded an event. Thus, this category contains the double-coincidence events between the two detectors *Front* and *Rear*. At this stage, a cut on the absolute value of the channel time difference is applied for each detector in this category, which has been conservatively set to 4 ns for the studies in this chapter. For context, the theoretical direct light propagation time across the length of a scintillator is approximately 0.79 ns[10]. Additionally, a second cut is applied to the absolute value of the time difference between the detector times of the two detectors *Front* and *Rear*, also termed *detector time difference*, which can be considered a cut on the time-of-flight between the two detectors. For the studies in this chapter, the cut value has been conservatively chosen to be 4 ns. For reference, the detectors *Front* and *Rear* were

[10] With a length of 150 mm and a refractive index of 1.58, cf. Section 5.1.2, the light propagation time across the length of a scintillator amounts to $150\,\text{mm} \times 1.58/c_0 = 0.79\,\text{ns}$.

positioned 130 mm apart, cf. Section 8.1, which, for electrons close to the speed of light, corresponds to a time-of-flight of approximately 0.43 ns.

- **eff**: This category is a subset of the previous category *trigger*. When the trigger condition is met, this category includes the coincidence events from the readout channels associated with the three test detectors *Left*, *Mid*, and *Right*. In other words, this category captures the triple-coincidence events between the detectors *Front* and *Rear*, as well as one of the test detectors. A distinct cut value for the cut on the absolute value of the channel time difference can be applied for this category. Additionally, a cut on the detector time difference between the respective test detector and the detector *Front* can be applied. As before, both values have been conservatively set to 4 ns for the studies in this chapter.

- **lost**: This category serves as the complementary set to the above category *eff*. When the trigger condition is met, but a readout channel associated with one of the test detectors has not recorded an event, the corresponding timestamps are assigned to this category. The total number of events in the categories *eff* and *lost* must always match the number of events in the category *trigger*.

The loss or absence of an event in one of the readout channels of the test detectors can arise from various factors. Consequently, the category *lost* is further divided into subcategories:

- **lostCut**: This category encompasses the coincidence events of a test detector that are filtered out by the applied cuts.

- **lostA**: In this category, events are recorded for PMT "B" of a test detector, but not for PMT "A". The absence of these events may result from several factors. One possibility is that one of the two *hits* for PMT "A" is missing, which could indicate a potential software failure on the Z-turn board or data transmission issues, such as network problems. Another scenario is that the calculated ToT is greater than zero but below the 8 ns cut, suggesting issues with the *hit* collection procedure within the `interpretHits()`-function described in Section 8.3.1. Lastly, it may be that there hasn't been a signal for PMT "A", or that the signal has been too weak to exceed the effective signal threshold of the readout channel. In both cases, potential explanations include insufficient gain for PMT "A" or an inherent inefficiency on this specific side of the detector.

- **lostB**: This category is analogous to *lostA*, but the other way round. In this category, events are recorded for PMT "A" of a test detector, but not for PMT "B".

- **lostBoth**: This category includes the collections of timestamps for the test detectors in which no event is recorded for either PMT "A" or PMT "B". This absence may be due to simultaneous issues affecting both PMTs, as outlined in the category *lostA*, or from an

actual inefficiency of the detector. Alternatively, it may indicate that the detector has not been hit by a particle, which is typically related to the geometry of the used setup.

For each category and subcategory, dedicated lists for the individual parameters are utilized, which are filled during the analysis procedure.[11] These lists can then be plotted as histograms, as exemplified in Fig. 8.5 for the first 2 000 000 raw *hits* of the aforementioned dataset.

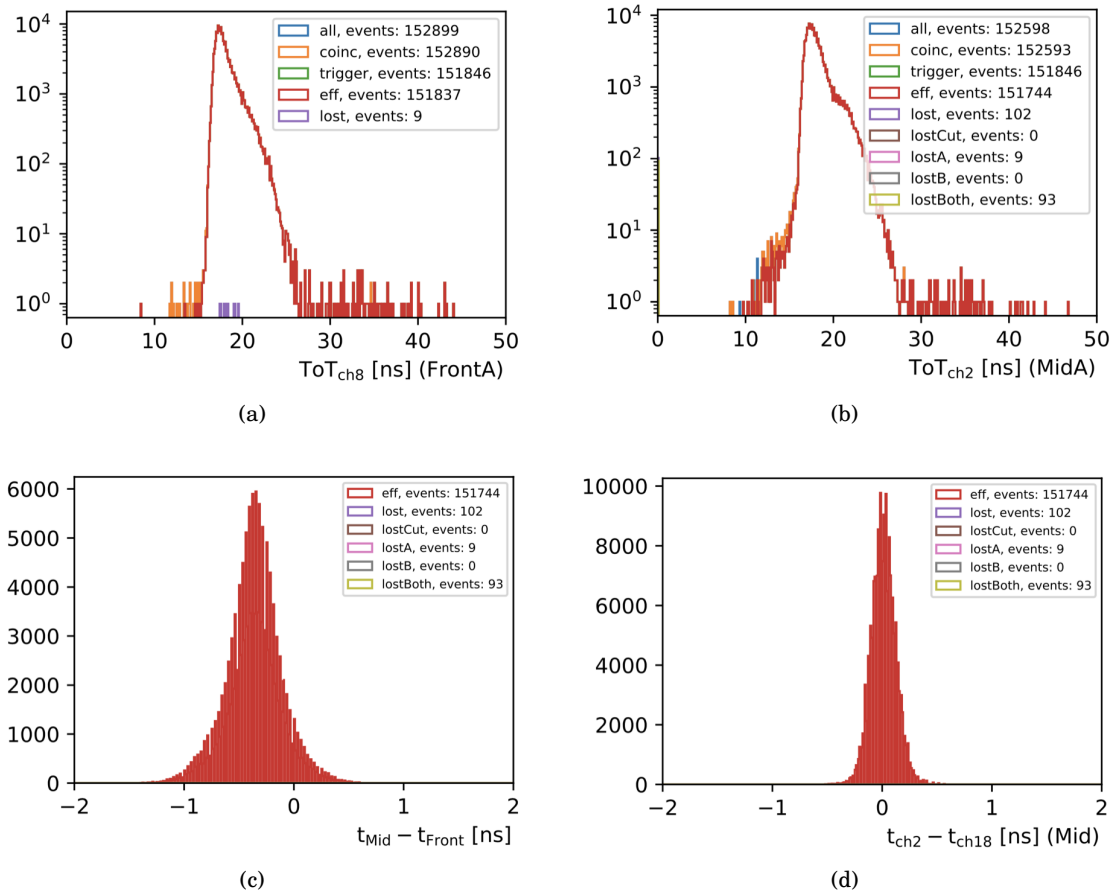

FIGURE 8.5. Exemplary ToT histograms are presented for one of the readout channels contributing to the trigger condition (a) and for one readout channel of the test detector *Mid* (b), each with a bin width of 100 ps. In addition, example histograms of the detector time difference (c) and the channel time difference (d) are shown for the test detector *Mid*, both with a bin width of 10 ps.

[11] Similar to Section 7.4.1, the code historically emerged this way. In the future, a more efficient and object-orientated rewrite will probably prove advantageous.

```
EFFICIENCY:
Per test detector [%]: [0.5769002805473966, 99.93282667966228, 1.6253309273869576] # (Left, Mid, Right)
Total efficiency: 99.99407294232314%

COINCIDENCE TIME RESOLUTIONS:
Raw [ps]: [390.0000000000001, 0.0, 390.0000000000001, 0.0] # (Rear, Left, Mid, Right)
Walk-corrected [ps]: [189.99999999999972, 0.0, 179.99999999999972, 0.0] # (Rear, Left, Mid, Right)

SPATIAL RESOLUTIONS (underlying timing resolutions):
Raw [ps]: [219.99999999999974, 259.9999999999998, 0.0, 239.99999999999977, 0.0] # (Front, Rear, Left, Mid, Right)
Walk-corrected [ps]: [250.0, 259.9999999999998, 0.0, 240.0, 0.0] # (Front, Rear, Left, Mid, Right)
```

FIGURE 8.6. Console output during analysis, presenting the results for the detector properties.

8.3.3 Extracting the Detector Properties Efficiency, Coincidence Time Resolution, and Spatial Resolution

With the recorded events now assigned to distinct categories, three key detector properties can be extracted: *efficiency*, *coincidence time resolution*, and *spatial resolution*. While efficiency and coincidence time resolution are part of the trigger layer criteria outlined in Section 3.2, the spatial resolution has not been addressed so far. The following paragraphs describe the methods used to extract the detector properties from the data.

Efficiency To evaluate the efficiency of a test detector, only the event counts in specific categories are needed. For a given dataset, the efficiency of a test detector is defined as the ratio of the number of events for the detector in the category *eff* to the total number of events in the category *trigger*. Applied to Fig. 8.5b, the efficiency amounts to $\frac{151\,744}{151\,846} \sim 99.93\,\%$. The stated goal of a detection efficiency very close to 100 % is therefore achieved.[12]

During the analysis of a data file, a console output is generated that summarizes all relevant information on the extracted detector properties. Additionally, this information is included in the `pdf` report generated for each analyzed data file, cf. Appendix F.5. The output for the aforementioned dataset is shown in Fig. 8.6. As can be seen, a *total efficiency* for all three test detectors is defined as well, which is the sum of the individual detector efficiencies, corrected for random coincidences and particles that hit the overlapping regions of two detectors, which would otherwise be counted multiple times. Specifically, the number of events occurring in two of the three test detectors - encompassing events in the overlapping regions as well as random coincidences - must be subtracted once from the sum of the individual efficiencies to avoid double counting. Similarly, events occurring in all three detectors, which arise solely by random coincidences, must

[12] Towards the end of writing this thesis, the analysis of the remaining beam time data was started. Among the conducted measurements were parameter scans of the *control parameters* *cv*, *att*, and *thr*. Preliminary results indicate that the default settings used for the analysis in this chapter do not achieve optimal efficiency. By increasing the control voltages for the PMTs of the trigger detectors, i.e. by raising *cv*, and/or by reducing the effective signal threshold of the involved readout channels, determined by the combination of *att* and *thr*, the efficiency can be enhanced to approximately 99.98 %. However, further investigation is required to fully understand and confirm this behavior.

be subtracted twice to prevent triple counting. For a better understanding, the total efficiency can also be understood as the logical OR of the individual efficiencies of the three test detectors.

For the aforementioned dataset, the total efficiency is $\sim 99.99\,\%$. However, for the studies in this chapter, the total efficiency is better ignored, as it artificially inflates the extracted efficiency by including additional background events such as random coincidences. Nevertheless, when analyzing the conducted scans along the x-direction, cf. Section 8.1, the total efficiency will become relevant, as the focus will shift to investigating the overlapping regions of the test detectors.

Coincidence Time Resolution As noted in the previous section, the detector time is defined as the mean of the two channel times of a detector. The coincidence time resolution, σ_{CTR}, of a detector now quantifies the accuracy with which the detector time can be resolved relative to the signal from a second detector. For the studies in this chapter, the coincidence time resolution of a test detector is therefore contained in its detector time difference distribution, which represents its detector time relative to that of the trigger detector *Front*. Specifically, the width of the detector time difference distribution serves as a measure of the coincidence time resolution σ_{CTR}.

In practice, the width of a distribution is typically characterized by its FWHM, as it is independent of the specific shape of the distribution and thus provides a more general measure. If the distribution is Gaussian, the standard deviation, σ, can also be employed, in which case σ and FWHM are related by the fixed equation $\mathrm{FWHM} = 2.35 \cdot \sigma$ [101]. For the studies in this chapter, however, the FWHM is used since the resulting detector time difference distributions are not perfectly Gaussian-shaped.

Fig. 8.7a illustrates the extraction of the FWHM from the detector time difference histogram for the test detector *Mid*. The FWHM, and consequently the σ_{CTR}, amounts to $(390 \pm 30)\,\mathrm{ps}$[13], which already fulfills the trigger layer criterion of $\leq 1\,\mathrm{ns}$ for the coincidence time resolution stated in Section 3.2. Nevertheless, this result will be further improved through the application of the walk correction in Section 8.4. The error of the FWHM has been estimated as three times the bin width, i.e. 30 ps, to account for the minor binning structure within the distribution. This structure occurs due to the walk effect, cf. Section 8.4, and will be eliminated once the walk correction has been applied.

Spatial Resolution Following the offset correction applied as part of the `interpretHits()`-function, the channel time difference distribution of a detector is symmetrically centered around 0 ns for particles striking the middle position along its scintillator.[14] For particles hitting a detector at other positions along its scintillator, e.g. due to a changed beam position, the distribution shifts accordingly. This means that the hit or beam position x along the scintillator can be

[13] This corresponds to a Gaussian σ of $(166 \pm 30)\,\mathrm{ps}$.

[14] Without the offset correction, the zero point of the channel time difference distribution would effectively shift along the scintillator, reflecting the difference in signal propagation delays between the two readout channels of the detector.

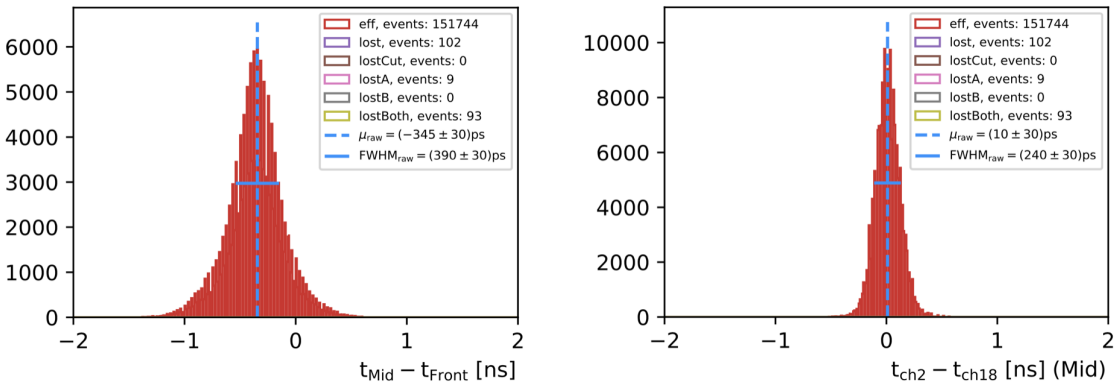

(a) (b)

FIGURE 8.7. The FWHM of the detector time difference distribution for the test detector *Mid* (a) is used to determine the coincidence time resolution σ_{CTR}. Similarly, the spatial resolution σ_{spat} is obtained by extracting the FWHM from the detector's channel time difference distribution (b).

determined from the center position μ of the channel time difference distribution. Specifically, x can be calculated following $x = \frac{\mu}{2} \cdot v_{eff}$, where v_{eff} is the effective speed of light inside the scintillator. [127] For this section, v_{eff} amounts to $(105.54 \pm 1.67)\,\mathrm{mm\,ns^{-1}}$, or about $\frac{c_0}{3}$.[15] Details on its determination can be found in Appendix F.3.

The width of the channel time difference distribution in turn provides a measure for the accuracy with which the hit or beam position can be resolved, i.e. the spatial resolution, σ_{spat}, along the detector. With respect to the later MAGIX setup, σ_{spat} translates directly to the spatial resolution of the trigger layer along the non-dispersive direction of the spectrometer. Analogously to the previous paragraph, the FWHM of the distribution is used to characterize its width. Fig. 8.7b illustrates the extraction of the FWHM for the channel time difference distribution of the test detector *Mid*, which yields $(240 \pm 30)\,\mathrm{ps}$[16]. This value can now be converted into the spatial resolution σ_{spat} using the relation $\sigma_{spat} = \mathrm{FWHM} \cdot v_{eff}$, resulting in $(25.33 \pm 3.19)\,\mathrm{mm}$, where the error has been calculated using Gaussian error propagation.[17] Similar to the previous paragraph, the error of the FWHM has been estimated as three times the bin width of the distribution, i.e. 30 ps. As with the coincidence time resolution, this result will be improved by the walk correction described in Section 8.4.

Worth noting at this point is that the spatial resolution along a detector can also be derived from the signal or charge asymmetry distribution between its PMTs. When the two PMTs are

[15] In an ideal scenario, the effective speed of light would match the speed of light inside the scintillator material, i.e. $\frac{c_0}{n} = \frac{c_0}{1.58} \sim 189.87\,\mathrm{mm\,ns^{-1}}$. However, in practice, the obtained value is lower because the effective speed of light represents an average velocity along the scintillator, which is substantially influenced by the scintillator's geometry, its reflective wrapping, and the quality of its optical coupling.

[16] The corresponding Gaussian σ is $(102 \pm 30)\,\mathrm{ps}$.

[17] When using the Gaussian σ, the obtained spatial resolution is $(10.77 \pm 3.17)\,\mathrm{mm}$.

gain-matched, a signal asymmetry distribution centered around zero corresponds to particles hitting the middle of the scintillator, while deviations from zero indicate hit or beam positions elsewhere along the scintillator. Although this method has not been employed up to the writing of this thesis due to time constraints, it should be implemented in the future as a cross-check for the spatial resolution results of the MAGIX trigger detectors.

8.4 Walk Correction

The final step along the way from data to analysis involves applying a correction that is crucial for achieving precise results, known as the *walk correction*. It addresses the underlying *walk effect*, a phenomenon commonly observed in analog signals when using the leading-edge triggering technique for discrimination. A detailed explanation of the walk effect is not provided at this point, as it has been extensively covered in the literature. An excellent explanation can be found, for instance, in Chapter 17 of Ref. [101].

In brief, when two analog input signals A and B with identical shapes and approximately equal rise times but different amplitudes occur simultaneously, the fixed threshold of the leading-edge discriminator causes the signal with the higher amplitude to trigger earlier. This results in two logic pulses that are shifted in time relative to each other, as illustrated in Fig. 8.8. This artificial time shift between the logic pulses is referred to as *walk*, and it must be corrected for to accurately reconstruct the timestamp of an analog input signal.

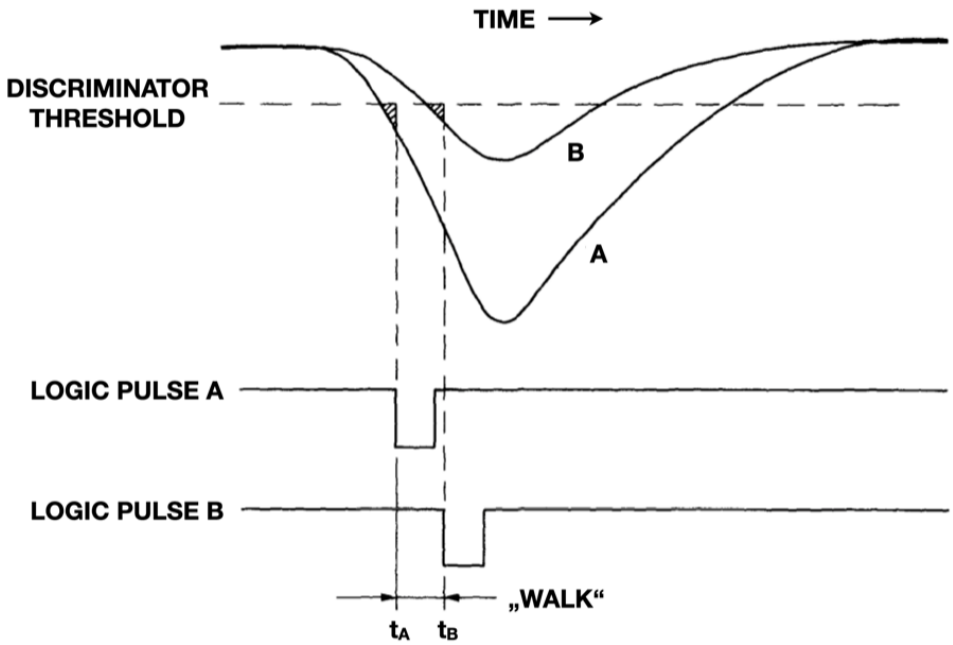

FIGURE 8.8. Illustration of the walk effect. Figure adapted from [101].

In the context of the MAGIX trigger veto system, the walk effect arises when the analog PMT signals from the trigger detectors[18] are processed by the leading-edge discriminator of the NINO chips on the NINO readout board. Each NINO chip is configured with a fixed discriminator threshold, and all PMT signals share the same signal shape with a pulse rise time of 1.5 ns, cf. Section 5.1.1. The resulting walk sensitively influences both the coincidence time resolution σ_{CTR} and the spatial resolution σ_{spat} by introducing a dependency between the time difference distributions used to extract these detector properties and the ToT distributions of the involved readout channels, see Figs. 8.9a and 8.11a.

In practice, two methods can be used to implement the walk correction in the analysis procedure. First, it can be performed once for a given setup, extracting correction parameters for each readout channel, which can then be applied within the `interpretHits()`-function, similar to the offset correction. The second method, which has been adopted for the studies in this thesis, applies the walk correction as the final step of the analysis, performed separately for each dataset. This requires distinct corrections for both the coincidence time resolution and the spatial resolution, as will be shown in the upcoming Sections 8.4.1 and 8.4.2. Importantly, the efficiency remains unaffected, since the walk correction is applied after the recorded events have been assigned to their respective event categories.

The first approach was tested, but no satisfying results could be obtained due to excessive interference between the correction parameters of the individual readout channels, preventing the correction process from converging. Nevertheless, future work could benefit from a more rigorous investigation of this approach, as it has the potential to significantly reduce computational demands when analyzing data from the MAGIX trigger veto system.

8.4.1 Impact on the Coincidence Time Resolution

With respect to the coincidence time resolution, the walk correction for a detector is performed using its detector time difference distribution and the ToT sum of its readout channels[19], as exemplified in Fig. 8.9 for the readout channel connected to PMT "A" of the test detector *Mid*, termed *MidA*. As mentioned above, the walk effect introduces a dependency between these two parameters, see Fig. 8.9a, that has to be corrected for. In an iterative process looping over all relevant readout channels, see Figs. 8.9b–8.9d, the corresponding detector time difference distributions are plotted against the ToT sum distribution of the detector, the found dependencies are fitted with a quadratic function, and the fit results are subtracted from the data. This results in the data points being uniformly distributed around 0 ns. By this, a corrected timing distribution is obtained for each detector time difference distribution. For the studies in this chapter, three

[18] The walk effect also needs to be considered and corrected for the SiPM signals from the veto detectors.

[19] The ToT sum is used instead of the individual ToT of a readout channel to include as much information into the correction process as possible. The ToT sum of a detector is a measure for its total light yield and therefore contains more information than the ToT of a single readout channel. Using the individual ToT distributions was tested, but resulted in a similar interference problem as described above for the first method of implementing the walk correction.

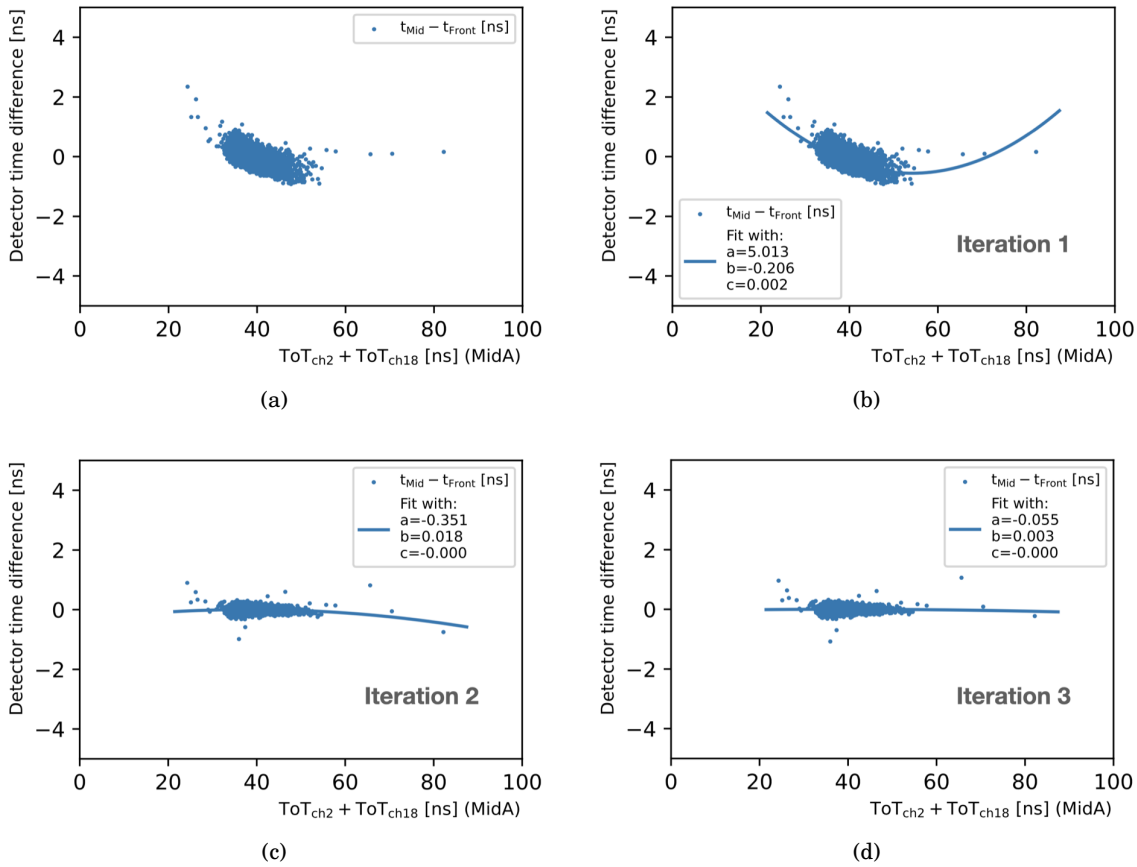

FIGURE 8.9. The iterative walk-correction process applied to the detector time difference distributions, exemplified for the readout channel connected to PMT "A" of the test detector *Mid*, termed *MidA*.

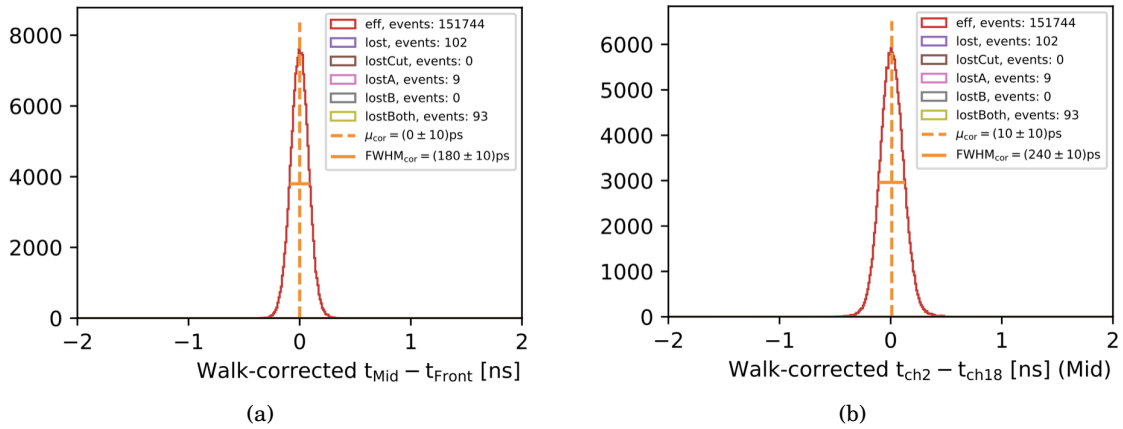

FIGURE 8.10. The walk-corrected detector time difference distribution for the test detector *Mid* (a), as well as its walk-corrected channel time difference distribution (b).

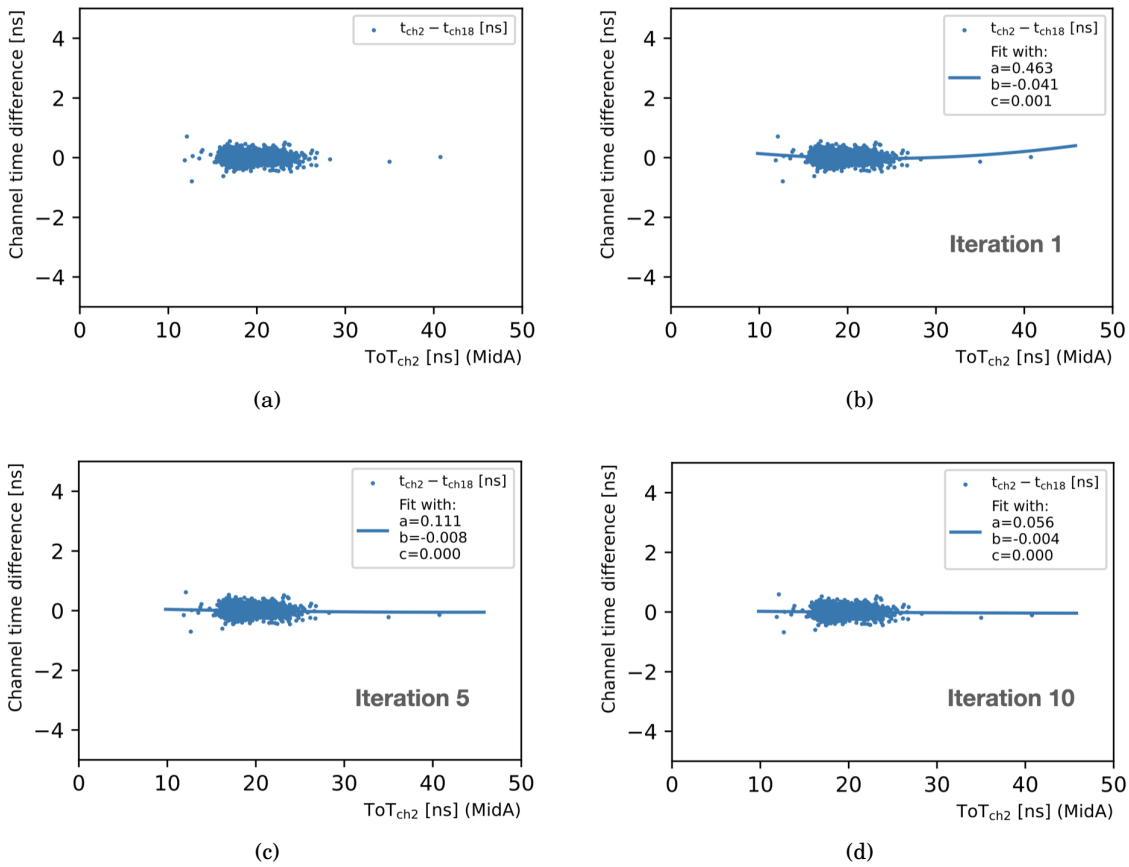

FIGURE 8.11. The iterative walk-correction process applied to the channel time difference distributions, exemplified for the readout channel *MidA*.

iterations of the walk correction have been applied.

The impact of the walk correction is illustrated in Fig. 8.10a, applied to the detector time difference histogram for the test detector *Mid*. As before, the chosen bin width is 10 ps. The extracted FWHM, and thus the walk-corrected σ_{CTR}, amounts to (180 ± 10) ps[20], representing a significant improvement over the previous value of (390 ± 30) ps obtained without the walk correction. Furthermore, the binning structure present in Fig. 8.7a has been eliminated during the walk correction process, resulting in a noticeably smoother distribution. Consequently, the timing errors are now estimated as just one times the bin width, i.e. 10 ps.

8.4.2 Impact on the Spatial Resolution

The walk correction for the spatial resolution of a detector follows a similar procedure as that for the coincidence time resolution described in the previous section. However, it relies on the detector's channel time difference distribution and the ToT distributions of its two readout

[20]The corresponding Gaussian σ is (77 ± 10) ps.

channels, see Fig. 8.11. Moreover, ten iterations of the walk correction have been performed instead of three, as the convergence process required more time.

The impact of the walk correction is shown in Fig. 8.10b, where the FWHM results in $(240 \pm 10)\,\mathrm{ps}$[21]. Again, the chosen bin width is 10 ps. While no immediate improvement is observed compared to the extraction in Fig. 8.7b, the walk-corrected distribution is smoother and the binning structure has been eliminated, motivating the reduced timing error similar to that in the previous section. Using the value for the effective speed of light obtained after the walk-correction, cf. Appendix F.3, which is $v_{\mathrm{eff}} = (104.44 \pm 0.55)\,\mathrm{mm\,ns^{-1}}$, the resulting σ_{spat} is calculated to be $(25.07 \pm 1.05)\,\mathrm{mm}$.[22] This is a slight improvement compared to the previous value of $(25.33 \pm 3.19)\,\mathrm{mm}$ obtained before applying the walk correction. Yet, the improvement is solely attributed to the improved timing error, as the width of the underlying channel time distribution remains unchanged.

8.5 Further Studies

After the extraction of the detector properties efficiency, coincidence time resolution, and spatial resolution during the previous sections, as well as the dead time estimation in Section 7.1, two criteria from Section 3.2 remain to be examined: trigger rate tolerance and long-term stability. During the MAMI beam time described in Section 8.1, dedicated measurements were conducted to investigate these two criteria. The results are presented in the following sections.

8.5.1 Trigger Rate Tolerance

For testing the trigger rate tolerance of the trigger layer, data for different beam currents or electron fluxes was collected. The beam current of MAMI is controlled by the so-called Wehnelt voltage, U_{W}, which adjusts the voltage of the Wehnelt cylinder of the unpolarized electron source of MAMI. The negative Wehnelt voltage defines the amount of extracted electrons per time from the source, where a higher value for U_{W} leads to more electrons extracted from the source, resulting in higher electron fluxes and beam currents. At MAMI, its minimum value is $U_{\mathrm{W}} = -25.00\,\mathrm{V}$, which corresponds to an electron flux of approximately 2 kHz and correspondingly a beam current of about 0.3 fA.

The relation between Wehnelt voltage and electron flux is illustrated in Fig. 8.12. The underlying data, originally gathered by M. Biroth and A. Wilczek during the MAMI beam time with the MAGIX silicon strip detector in February 2024, has been fitted during the preparation for the beam time described in Section 8.1, using a model based on the sum of two exponential functions. For Wehnelt voltages between $-25.00\,\mathrm{V}$ and approximately $-13.00\,\mathrm{V}$, the increase in electron flux is relatively modest. At higher U_{W} values, however, the electron flux rises sharply, where

[21] This corresponds to a Gaussian σ of $(102 \pm 10)\,\mathrm{ps}$.

[22] When using the Gaussian σ, the walk-corrected spatial resolution results in $(10.67 \pm 1.05)\,\mathrm{mm}$.

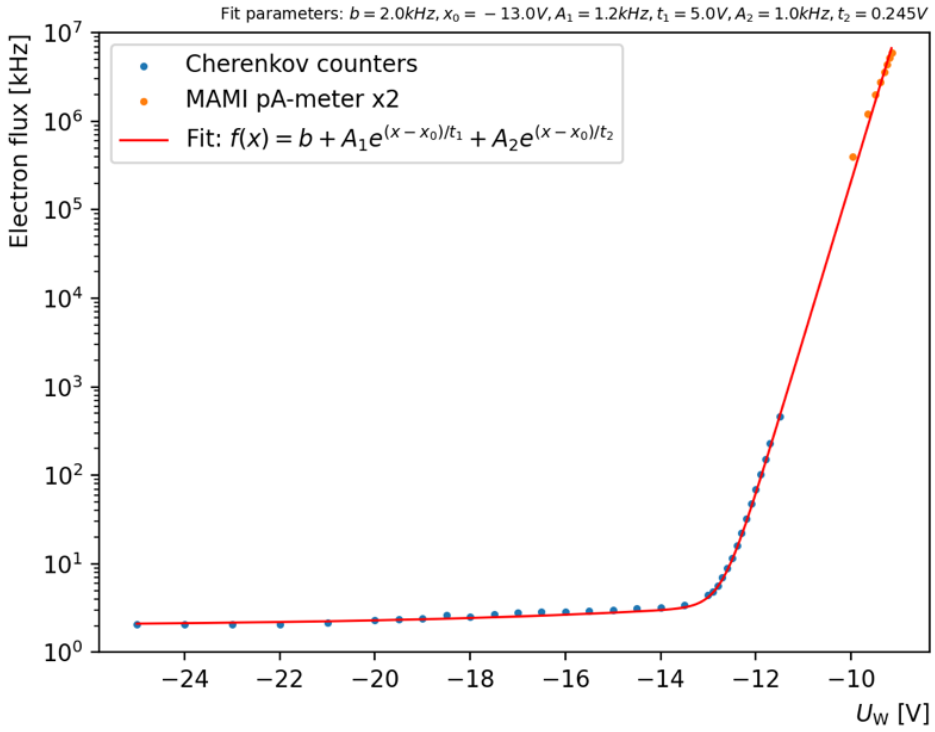

FIGURE 8.12. Relationship between the Wehnelt voltage U_W and the resulting electron flux at MAMI, based on data obtained by M. Biroth and A. Wilczek.

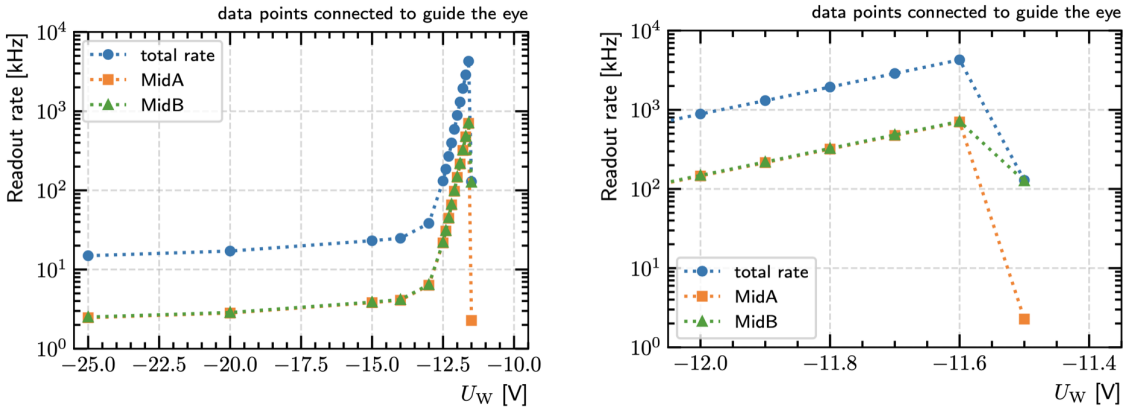

FIGURE 8.13. The total readout rate, along with the individual rates for the readout channels *MidA* and *MidB*, as a function of the Wehnelt voltage U_W: across the entire scanned Wehnelt voltage range (a) and with a close-up view for $U_W > -12.00\,V$ (b). Only the detectors *Front*, *Rear*, and *Mid* have been used.

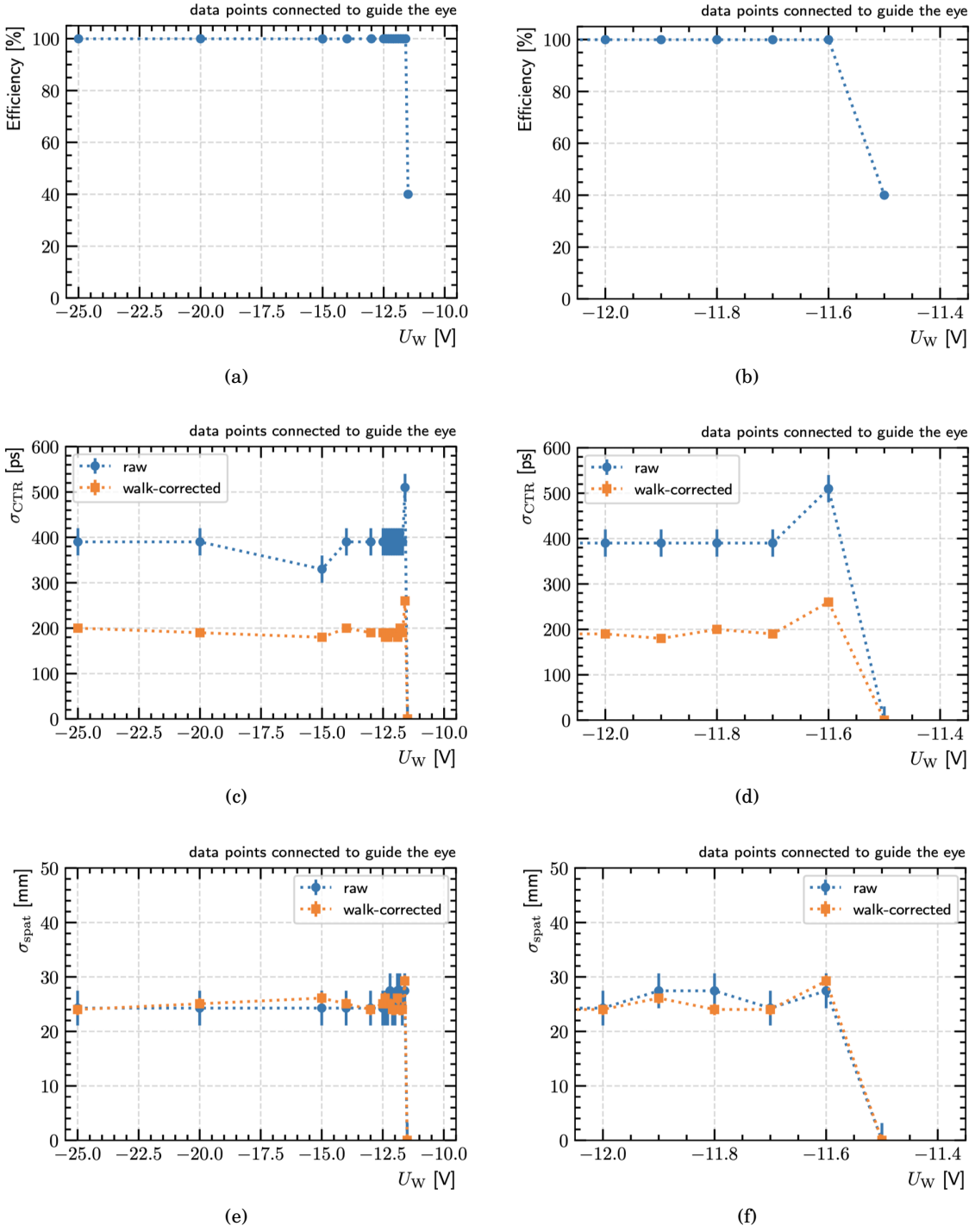

FIGURE 8.14. The detector properties efficiency, coincidence time resolution, and spatial resolution as a function of the Wehnelt voltage U_W: across the entire scanned Wehnelt voltage range (left) and with a close-up view for $U_W > -12.00\,V$ (right). Only the detectors *Front*, *Rear*, and *Mid* have been used.

even minor adjustments in U_W result in significant changes in flux.

For the study in this section, data was collected for Wehnelt voltages ranging from −25.00 V to −11.50 V, with each dataset recorded over a period of 20 s. The corresponding electron fluxes range from approximately 2 kHz to 460 kHz, and the resulting beam currents range from 0.3 fA to 78 fA. Only the detectors *Front*, *Rear*, and *Mid* were used, thereby excluding background events from the detectors *Left* and *Right*, which would otherwise artificially inflate the readout rate.

Fig. 8.13 depicts the total readout rate of the NINO readout board, i.e. the sum of the readout rates in all connected readout channels, along with the individual rates for the two readout channels *MidA* and *MidB*, as a function of the Wehnelt voltage U_W. As shown, the readout rates increase with U_W, following the same exponential trend shown in Fig. 8.12. At $U_W = -11.60$ V, the total readout rate reaches 4.27 MHz, with the readout channels *MidA* and *MidB* achieving rates of around 700 kHz, before, at $U_W = -11.50$ V, the readout rates collapse, indicating that the system can no longer process all input signals. This behavior also impacts the extracted detector properties, see Fig. 8.14. Up to $U_W = -11.60$ V, the detector properties remain stable and consistent with the values obtained in Sections 8.3.3 and 8.4. Yet, at $U_W = -11.50$ V, the efficiency drops to around 40 % and a determination of σ_{CTR} and σ_{spat} is no longer possible.

To identify the limiting factor - whether it is the total readout rate of the system or the readout rate of the individual readout channel -, an additional study was performed. For this, only the test detector *Mid* was utilized, ensuring that the total readout rate equaled the sum of the rates in the two readout channels *MidA* and *MidB*. The Wehnelt voltage range from −12.00 V to −11.50 V was investigated in more detail, with a data acquisition period of 20 s for each dataset.

The results are presented in Fig. 8.15. As previously observed, the readout system fails between the Wehnelt voltages of −11.60 V and −11.50 V. However, this time, the system does not exceed a total readout rate of 4 MHz, but reaches only about 2/6 of the previously achieved rate using 6 readout channels, namely 1.67 MHz. In contrast, the individual readout channels achieve rates exceeding 800 kHz, with readout channel *MidB* even surpassing 900 kHz. Moreover, readout channel *MidB* continues to function longer than *MidA*. Specifically, *MidA* starts failing at a Wehnelt voltage of $U_W = -11.54$ V, while *MidB* remains operational until $U_W = -11.52$ V.

These observations suggest that the primary limiting factor for the system are the readout rates of the individual readout channels. In fact, the achievable readout rates appear to be highly dependent on the specific channel, as can be seen from Fig. 8.15b. However, the data processing of the readout system - presumably the *hit* merging on the Z-turn board as described in Section 7.3.2 - also contributes to limiting the achievable readout rates. Notably, the total readout rate achieved in Fig. 8.15 is higher than in Fig. 8.13.

Nonetheless, the readout system of the MAGIX trigger veto system demonstrates a trigger rate tolerance well into the MHz region, while the individual readout channels appear to be limited to somewhat between 700 kHz and 1 MHz. The exact reason for this limitation remains unclear at the time of writing this thesis and warrants further investigation in the future. Nevertheless,

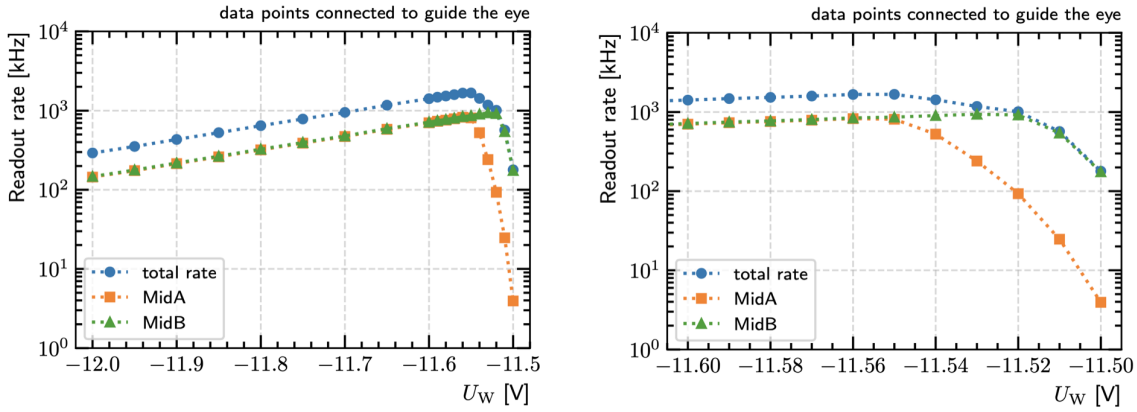

(a) (b)

FIGURE 8.15. The total readout rate, along with the individual rates for the readout channels *MidA* and *MidB*, as a function of the Wehnelt voltage U_W: across the detailed examined Wehnelt voltage range between −12.00 V and −11.50 V (a) and with a close-up view for $U_W > -11.60$ V (b). Only the test detector *Mid* has been employed.

even a readout rate limit of 700 kHz per readout channel significantly exceeds the expected count rates in the final MAGIX setup. This is particularly evident when compared to the expected count rates for the proposed visible dark photon search, which includes multiple background channels from QED and is anticipated to be the highest-rate experiment at MAGIX. Fortunately, a comparable measurement was previously performed by the A1 collaboration at MAMI [158], whose results provide valuable insights for estimating the expected count rates in the MAGIX setup. During the A1 experiment, the maximum count rates observed reached several hundred kHz, distributed across an entire trigger layer [154]. Therefore, the current readout capabilities of the MAGIX trigger veto system are more than sufficient to ensure its effective operation, even under the most demanding experimental conditions.

8.5.2 Long-Term Stability

As a test of the long-term stability of the readout system of the MAGIX trigger veto system, an overnight measurement was conducted involving all five detectors. For this test, the Wehnelt voltage was set to $U_W = -25.00$ V to keep the recorded data at a manageable level. Data was collected in 1 h intervals, generating datasets with more than 40,000,000 raw *hits*. At the time of writing this thesis, the analysis procedure cannot readily handle such high numbers of *hits* due to the current implementation of the walk correction, cf. Section 8.4. Additionally, a slight increase in the MAMI beam current occurred overnight[23], which further elevated the amount of recorded data. To address this issue, the analysis has been limited to 40,000,000 raw *hits* per dataset

[23] Fluctuations like these can arise due to factors such as temperature drifts or voltage shifts, but they are generally inconsequential and do not pose significant issues.

when extracting the detector properties, i.e. when the walk correction needed to be applied. The readout rates have been calculated based on the entire datasets.

The results of the stability test are illustrated in Fig. 8.16. In Fig. 8.16a, the readout rates over the course of the night are shown, with both the total readout rate of the NINO readout board and the individual rates for channels *MidA* and *MidB*. The empty dataset with the timestamp "01:58:20" resulted from an unintended switch-off of the MAMI beam. The increase in MAMI beam current during the night is evident, while the readout rates remain generally stable, showing no significant deviations. Similarly, the extracted detector properties efficiency, coincidence time resolution, and spatial resolution, see Figs. 8.16b–8.16d, respectively, are stable and align with the values extracted in Sections 8.3.3 and 8.4[24].

The readout system of the NINO readout board therefore successfully passes this initial overnight stability test. For a more rigorous validation, however, a significantly extended stability test should be performed in the future.

[24] An exception to this can be observed in the spatial resolutions σ_{spat}. Four of the seven datasets show a better spatial resolution for the raw data than for the walk-corrected data. This discrepancy is attributed to the binning structure mentioned in Section 8.3.3, suggesting that the estimated error for the FWHM values extracted from the raw data should ideally be larger than three times the bin width, i.e. 30 ps.

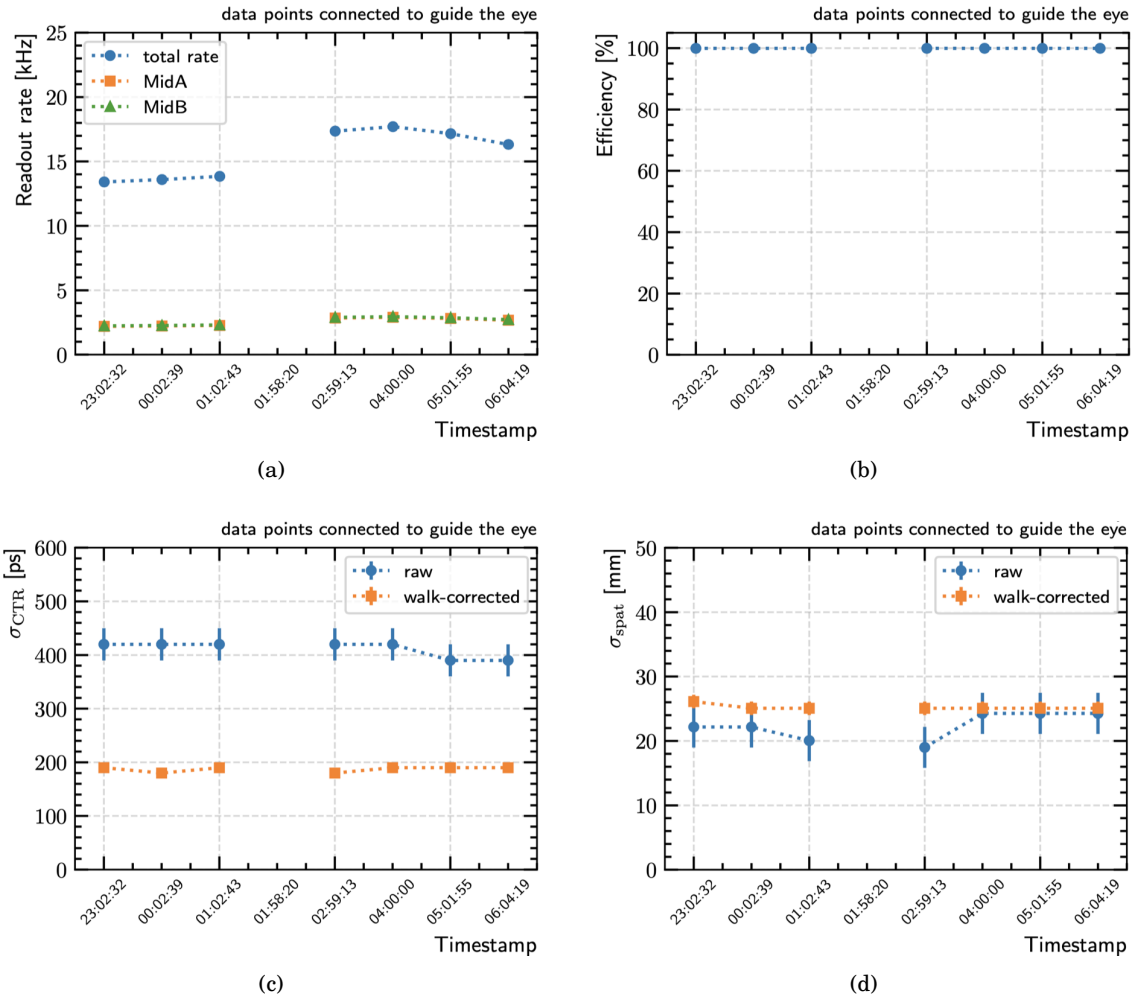

FIGURE 8.16. Readout rates (a), as well as the detector properties efficiency (b), coincidence time resolution (c), and spatial resolution (d), during the overnight stability test.

CHAPTER 9

SUMMARY & OUTLOOK

The present work detailed the design and development of the MAGIX trigger veto system, progressing from the initial concept through design and development phases, alongside the determination of key detector properties. The final detector design was optimized and is now ready to be installed at the MAGIX experiment at MESA.

Chapter 1 opened with highlighting the scientific motivation behind the planned measurements at MAGIX, a versatile multi-purpose experiment poised to make significant contributions across various fields of nuclear, hadron, and particle physics. Among the highly anticipated studies are precise measurements of the astrophysical S-factor of the reaction $^{12}\mathrm{C}(\alpha,\gamma)^{16}\mathrm{O}$ and the electromagnetic form factors of the proton. Additionally, MAGIX is well-positioned to advance ongoing dark sector searches by investigating both visible and invisible decay modes of the hypothetical dark photon, and to address the complexities of few-body physics through highly accurate nuclear transition measurements. Its fully window-less design enables an unprecedented level of precision in these studies.

As described in Chapter 2, the MAGIX experiment is located at the new electron accelerator MESA in Mainz, Germany. MESA will offer two distinct operation modes: an extracted beam (EB) mode and an energy-recovery linac (ERL) mode. In EB mode, the electron beam will be operated with energies between somewhere below 30 MeV and 155 MeV, a maximum beam current of 0.15 mA, and beam polarization levels above 85 %, serving the external experiment P2 and, concurrently, DarkMESA. Conversely, the ERL mode will provide an unpolarized electron beam with beam energies ranging from 30 MeV up to 105 MeV and beam currents exceeding 1 mA. MESA will be the first accelerator to combine the concept of energy-recovery with an experimental program in nuclear, hadron, and particle physics. The MAGIX experiment features a window-less scattering chamber housing a versatile cluster-jet target that can be operated with

a variety of different gases, two high-precision magnetic spectrometers, as well as sophisticated detector systems positioned at the spectrometers' focal planes. This setup, combining the gas jet target, MESA's high-intensity electron beam, and the fully window-less design, allows for an exceptionally clean experimental environment by drastically reducing background effects like multiple scattering and energy straggling. The focal plane detectors include a tracking detector realized by a time projection chamber, as well as the MAGIX trigger veto system.

The conceptual design and working principle of the trigger veto system were presented in Chapter 3. It is designed to address four main objectives: delivering a fast and reliable trigger decision signal that is (1) used to start the DAQ and which (2) defines the inter-detector timing of the overall experiment; (3) serving as the timing reference for the MAGIX TPC; and (4) distinguishing between signal and background events by raising specific response patterns for different incoming particles. These four tasks are achieved through the system's two main components: the trigger layer and the veto system. Whereas the trigger layer addresses the first three tasks, the veto system focuses on the fourth. The trigger layer is composed of plastic scintillation detectors with a rhombic profile, read out by PMTs. In contrast, the veto system includes three veto layers, made from rhombic-shaped plastic scintillation detectors read out by SiPMs, and several lead absorber layers. For the trigger layer, concrete design criteria were stated, namely a detection efficiency very close to 100 %, an intrinsic timing resolution sufficient to achieve a coincidence time resolution of $\leq 1\,\mathrm{ns}$, a trigger rate tolerance up into the MHz region, an almost dead time free readout, as well as long-term stability.

Chapter 4 then presented the simulation studies conducted using `Geant4`, during which multiple design parameters for the trigger veto system were defined and subsequently optimized. The design parameters encompassed global detector characteristics, such as the number of detectors within the trigger layer and the areal dimensions of the veto layers. The optimization was performed based on the trigger and veto response probabilities of the individual detector layers, which served as figures of merit. As a result of these studies, final values for the design parameters were determined and agreed upon.

Chapters 5 and 6 detailed the development of the trigger layer and the veto system, respectively. For the detectors of the trigger layer, extensive component tests led to a finalized and ready-to-build design, culminating in the production of 51 trigger detectors. Besides, a dedicated power supply was developed for the trigger layer, alongside the implementation of a slow control driver to ensure reliable monitoring and control. The technical design for assembling and mounting the trigger layer was also presented. Similarly, comprehensive technical designs were established for the assembly and future installation of the veto system. Regarding the veto detectors, multiple preparatory studies enabled the finalization of the design of the corresponding power supply and readout electronics. The signals from both the trigger layer and the veto layers will be read out by a custom, in-house developed readout board based on the NINO chip, originally designed for the ALICE experiment at CERN. This so-called NINO readout board was rigorously tested and

verified to ensure it meets the stringent requirements of the trigger veto system.

An in-depth description of the readout system for the trigger veto system was provided in Chapter 7, outlining the full pathway from signal to data, exemplified for the PMT pulses of the trigger layer. In this context, the initial version of the data acquisition software stack for the NINO readout board was also presented. A first estimate of the trigger layer's dead time could be extracted from the sharp peaks of the trigger PMTs, which show pulse widths (FWHM) of only a few ns.

Chapter 8 showcased the analysis of trigger layer signals using data collected during a beam time at MAMI, employing an initial version of the analysis software stack developed for the NINO readout board. This preliminary system demonstrated functionality, although refinements and optimizations will be necessary, with a more efficient rewrite expected to benefit the final software framework at MAGIX. The analysis detailed the extraction of crucial detector properties, including efficiency, coincidence time resolution, and spatial resolution, with promising results. An efficiency of approximately 99.93 % was achieved, the coincidence time resolution reached values around 180 ps (FWHM), and the spatial resolution along a trigger scintillator was extracted to be about 25 mm. The readout system's trigger rate tolerance was also evaluated, along with a preliminary assessment of its long-term stability. The entire system successfully withstood readout rates exceeding 4 MHz, while the individual channels operated at rates above 700 kHz. All the design criteria for the trigger layer, outlined in Section 3.2, are thus met, validating the trigger layer's readiness for a precise and robust operation in the later experimental conditions at MAGIX.

The completion of this thesis marks a significant milestone, yet the work on the MAGIX trigger veto system is far from finished. Exciting next steps lie just ahead, outlined briefly below:

- **Data Analysis of the MAMI Beam Time**: The analysis of the beam time data obtained at MAMI is ongoing. Particular focus is placed on the dependencies of the detector properties efficiency, coincidence time resolution, and spatial resolution on the control parameters introduced in Chapter 7, namely *cv*, *att*, and *thr*. These findings are highly anticipated, as they will offer deeper insights into the performance of the trigger layer. Furthermore, the results from the conducted scans along the x-direction will be crucial for evaluating the trigger layer's efficiency in the overlapping regions of the individual trigger detectors and therefore the consistency of the detection efficiency across the entire layer.

- **Testing of the Trigger Layer**: Towards the end of writing this thesis, a complete trigger layer has been assembled for calibrating and commissioning the detector system, as well as for refining the mechanical setup, especially with respect to its assembly with the MAGIX TPC. A photograph of the completed assembly is shown in Fig. 9.1. Multiple refinements have been implemented[1], the most important of which has been relocating the SMA feed-

[1]Not all upgrades are detailed here, however, the implemented changes are documented in Tab. C.2 in Ap-

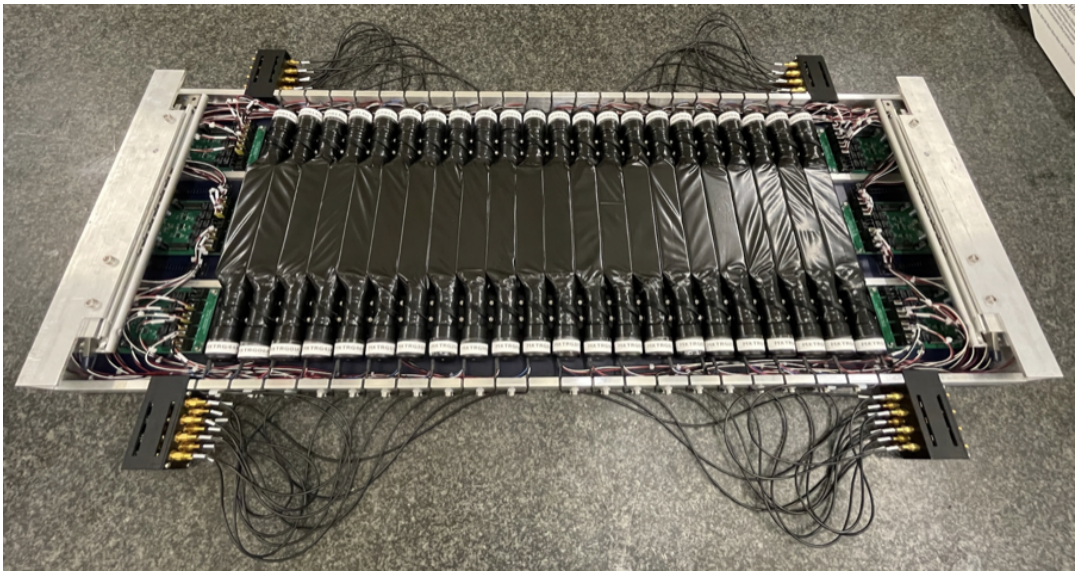

FIGURE 9.1. A completely assembled trigger layer. Shortly, testing will begin in conjunction with the MAGIX TPC.

throughs from their previous position embedded within the long side profiles of the trigger layer mounting to newly designed 3D-printed boxes attached externally. These boxes also contain the passive 20 dB attenuators for the trigger layer signals, significantly easing the cable management at the inputs of the NINO readout boards. Additionally, this redesign drastically simplifies the cable routing inside the trigger layer mounting, as only the power supply cables have to be guided beneath the high-voltage sockets. Besides, the two full-size 19-inch crates, which house the power supplies for the trigger detectors and the NINO readout boards, cf. Section 5.2.4, have been finalized and produced, and are now ready for testing. As a result, testing of the complete trigger layer in conjunction with the MAGIX TPC, thus simulating the operational conditions of the future MAGIX setup, is set to begin shortly.

- **Further Development of the Veto System**: The first iteration of the readout and power supply electronics for the veto layers is expected to be completed soon, enabling further advancement in the development of the veto layers. Meanwhile, the MAGIX setup is rapidly taking shape, with the ring rails and kingpin already ingrained in their final position. Soon, the assembly of the spectrometer arms will begin, including the installation of the veto system cradles and drawers.

These are truly exciting times for the MAGIX experiment and for everyone involved in its development. It is rare to have the opportunity to contribute to the setup of an experiment

pendix C.3.

from the ground up, and even rarer to do so within a close-knit team that allows for hands-on experience across all facets of experimental particle physics. Walking through the experimental halls of MESA and MAGIX, it is inspiring to see the spaces gradually come to life, filling up with carefully designed and assembled instrumentation that will soon push the boundaries of discovery. The anticipation is palpable, and I can hardly wait for MAGIX to begin operations, where the trigger veto system will finally take its place within a larger scientific endeavor, contributing to groundbreaking research.

APPENDIX A

APPENDIX TO CHAPTER 2

A.1 The DarkMESA Veto System and Overlaps with MAGIX

Fig. A.1 shows the concept of the DarkMESA veto system. The calorimeter is hermetically enclosed by two veto layers in the form of plastic scintillation detectors and a 10 mm lead absorber layer in between, made from the antimonial lead alloy PbSb4. Depending on their energy, electrons and photons will with a high probability only leave signals in the outer veto layer and will then be stopped inside the lead absorber layer. Cosmogenic muons will pass the whole setup and leave signals in the veto layers on both sides of the calorimeter, as well as in the calorimeter crystals themselves. The hypothetical DM particles will only interact with one of the calorimeter crystals due to their very low interaction probability with SM particles. [27]

The design of the veto system for DarkMESA Phase A has already been finalized and at the time of writing this thesis, it is in the final stages of development. In the following, the focus will therefore lie on the veto system for Phase A. If you are interested in the design of the DarkMESA veto system for the subsequent phases, please refer to the PhD thesis of M. Christmann [27].

The plastic scintillation detectors of the Phase A veto system are made from 20 mm thick sheets of the plastic scintillator EJ-200 by Eljen Technology [103]. Since each veto layer forms a cuboid around the calorimeter, scintillator sheets of different sizes are needed per veto layer. The inner layer is made from four sheets with areal dimensions 500 mm × 250 mm and two sheets of size 250 mm × 250 mm. The outer layer is composed of two sheets with areal dimensions 500 mm × 361 mm, two sheets of size 500 mm × 323 mm, and two sheets with dimensions 314 mm × 314 mm. The short sides of the sheets are each read out by SiPMs and a lot of effort has already been invested in the development of the corresponding readout boards and dedicated electronics. The in-house developed "carrier boards", see Fig. A.2a, are directly coupled to the scintillator

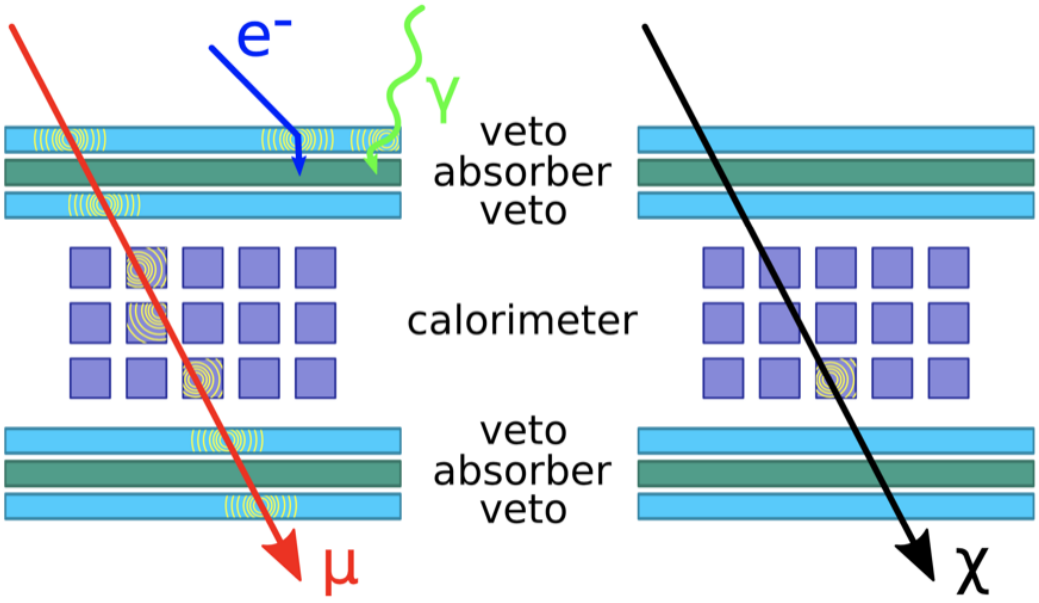

FIGURE A.1. The concept of the DarkMESA veto system. The incident particles leave characteristic signal patterns inside the calorimeter and the veto layers, and can thus be identified. Figure from [27].

faces. The boards have a size of 10 mm × 250 mm and each carries nine SiPMs[1] of the model MicroFJ-60035-TSV by onsemi [137], a first amplifier stage, and temperature sensors. The nine SiPMs are operated as three groups of three, see Fig. A.2b, where the individual SiPMs of a group are run in parallel with the same bias voltage. Per group, only the sum signal of the three SiPMs is used, in order to reduce the overall number of readout channels. The signals of up to six carrier boards are then routed to a so-called "collector board", also developed in-house, comprising a second amplification stage and discrimination, but also voltage supply and the corresponding DACs[2]. In addition, both analog and digital outputs are available for further signal processing and the data transfer to a computer.

At MAGIX, the trigger veto system also uses plastic scintillator sheets that are read out by SiPMs for its veto layers. To avoid a complete redesign of the corresponding readout electronics, it seems apparent to adopt the above DarkMESA concept and reuse it with as few changes as possible. The only obvious modifications that would have to be made are the division of the carrier board into several smaller boards due to the required segmentation of the MAGIX veto layer and the customization of the boards to the rhombic profiles of the veto scintillators. The division according to the three SiPM groups seems natural, see Fig. A.2c, which explains the segmentation of the

[1] This decision is based on extensive experimental studies [54, 57]. The initial idea was to use only four SiPMs per scintillator face and increase the light yield by embedding optical fibers into the scintillator sheets. But unfortunately, this design showed decreased uniformity at the scintillator faces, while drastically increasing the complexity of the veto system construction. Therefore, the route using nine SiPMs was chosen instead.

[2] **D**igital to **A**nalog **C**onverter

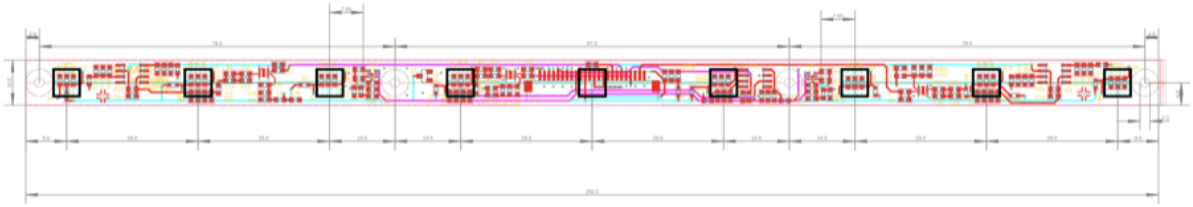

(a) The layout of the DarkMESA carrier board. Nine SiPMs are evenly distributed over a length of 250 mm.

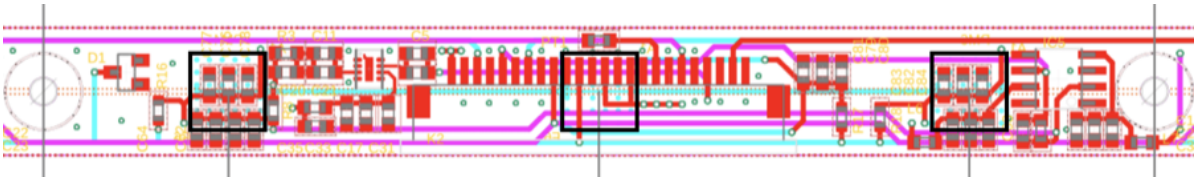

(b) Three SiPMs are operated as a group. They are run in parallel and therefore share the same bias voltage. To reduce the overall number of readout channels, only their sum signal is used.

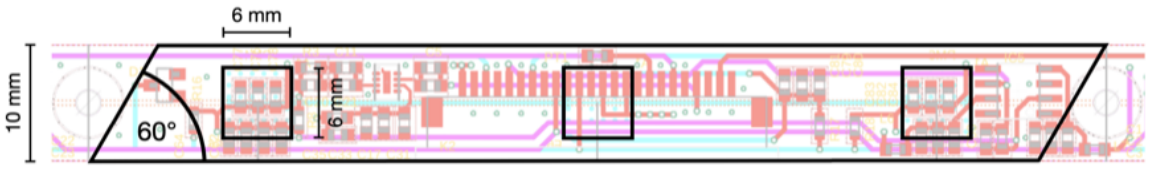

(c) At MAGIX, one SiPM group of three could be used to read out the scintillator face of a veto layer segment.

FIGURE A.2.

MAGIX veto layers into three individual veto detectors. In the end, several more changes were made when designing the readout for the veto layers of MAGIX, all of which are described in Section 6.2.

A.2 The Vacuum System of MAGIX

Section 2.3 mentioned that MAGIX needs a lot of pumping power to provide the intended vacuum conditions inside the scattering chamber. When the gas target is not operated, a vacuum in the order of 10^{-6} mbar is aimed for, and with target operation, $\sim 10^{-2}$ mbar is the strived for value. Besides, the vacuum conditions close to the MESA cavities must be on a level of $\sim 10^{-8}$ mbar in any case. To give an idea of the effort required, Fig. A.3 shows a schematic sketch of the vacuum system at MAGIX, including the installed turbo(molecular) pumps, their frequency converters, and the corresponding roughing pumps. In addition to the eight turbo pumps mounted directly to the scattering chamber (SC) and the powerful pumping station (RUTA) connected to the target's

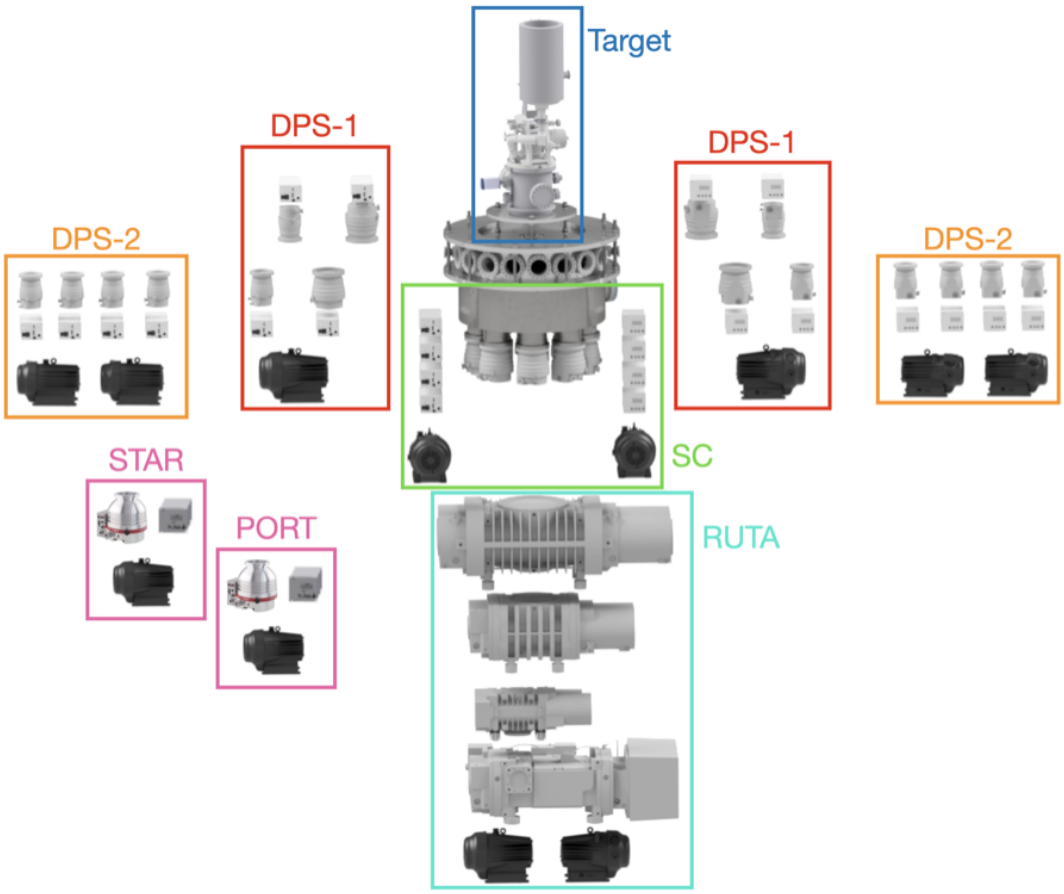

FIGURE A.3. A schematic sketch of the MAGIX vacuum system. Dedicated pumping systems are connected to the scattering chamber (SC), the target's catcher (RUTA), and the spectrometers (STAR and PORT). Additionally, two differential pumping systems (DPS-1 and DPS-2) are installed along the MESA beam line.

catcher, two differential pumping systems (DPS-1 and DPS-2) are installed both upstream and downstream along the MESA beam lines. While the DPS-1 is implemented in the direct vicinity of the MAGIX setup, the pumps of the DPS-2 are distributed over the recirculation arc of MAGIX. Furthermore, additional pumping sections are mounted to the magnetic spectrometers STAR and PORT. A list of all the pumps composing the vacuum system of MAGIX is given in Tab. A.1. Note that in the case of the differential pumping systems and the spectrometers, the listed quantities are for the double versions.

Scattering chamber SC				
Quantity	**Manufacturer**	**Pump model**	**Pump type**	**Rated pumping speed**
8x	Pfeiffer Vacuum	HiPace 700	turbo pump	685 L/s
2x	Pfeiffer Vacuum	HiScroll 18	scroll pump	18.1 m^3/h
Catcher pumping cascade RUTA				
Quantity	**Manufacturer**	**Pump model**	**Pump type**	**Rated pumping speed**
1x	Leybold	RUVAC WH7000FU	roots pump	7000 m^3/h
1x	Leybold	RUVAC WH2500FU	roots pump	2500 m^3/h
1x	Leybold	RUVAC WH700FU	roots pump	710 m^3/h
1x	Leybold	DRYVAC DV650C	screw pump	650 m^3/h
2x	Pfeiffer Vacuum	HiScroll 18	scroll pump	18.1 m^3/h
Differential pumping system DPS-1				
Quantity	**Manufacturer**	**Pump model**	**Pump type**	**Rated pumping speed**
4x	Pfeiffer Vacuum	HiPace 700	turbo pump	685 L/s
4x	Pfeiffer Vacuum	HiPace 300	turbo pump	260 L/s
2x	Pfeiffer Vacuum	HiScroll 18	scroll pump	18.1 m^3/h
Differential pumping system DPS-2				
Quantity	**Manufacturer**	**Pump model**	**Pump type**	**Rated pumping speed**
6x	Pfeiffer Vacuum	HiPace 300	turbo pump	260 L/s
2x	Pfeiffer Vacuum	HiPace 300H	turbo pump	260 L/s
4x	Pfeiffer Vacuum	HiScroll 6	scroll pump	6.1 m^3/h
Spectrometers STAR and PORT				
Quantity	**Manufacturer**	**Pump model**	**Pump type**	**Rated pumping speed**
2x	Pfeiffer Vacuum	HiPace 400	turbo pump	350 L/s
2x	Pfeiffer Vacuum	HiScroll 18	scroll pump	18.1 m^3/h

TABLE A.1. Pumps included in the vacuum system of MAGIX. The rated pumping speed is given for single pumps.

APPENDIX B

APPENDIX TO CHAPTER 4

B.1 Introduction to the Geant4 Framework

As the successor of GEANT3, Geant4 is the successful re-design of CERNs major software toolkit for the simulation of particles passaging through matter. It is the simulation engine of choice for high energy physics experiments at the LHC, but is also used in heavy ion physics, CP violation physics, cosmic ray physics, biochemistry, material science, as well as medical physics and space science applications. After GEANT3 started facing critical difficulties in the early 1990's, such as an overly complex structure and manpower shortage, a new R&D project was launched in 1994 [159] to rewrite GEANT3 using the most recent software engineering methodologies based on object-orientation and C++. This project resulted in the first production release of Geant4 in 1998 and the associated Geant4 collaboration, that continues to develop and maintain the Geant4 code to this day. Usually, there are several releases per year that upgrade the functionalities and further expand the documentation, with the latest version being 11.2.2 at the time of writing this thesis. In addition to numerous user guides [160, 161, 162, 163, 164, 165], the user is provided with lots of helpful examples [166] that can serve as a base for individual applications. [167, 168]

As the name *Geant* suggests, which stands for ***Ge**ometry **an**d **t**racking*, Geant4 enables the user to create any number of any *primary particles* inside a previously defined geometry, and track the primary particles and their *secondaries* during their interaction with the implemented materials. The user can choose from leptons, mesons, baryons, ions, quarks, and messenger particles, but is also allowed to define new particles. Primary particles can be placed anywhere inside the *world volume* of the user-defined geometry and can have initial parameters in a wide energy and momentum range. The allowed interaction channels for the particles are defined in a so-called *physics list*, which can be predefined or individually created by the user as well. After creation,

the *track* of a particle is traced through the entire world volume and the influence on sensitive detector parts can be stored in the file format of choice. In short, Geant4 gives the user complete freedom in simulating particles for the application at hand. [167, 27]

The basic structure of a Geant4 application is always the same. There are several mandatory methods and classes that have to be provided by the user, in addition to some optional classes that can be implemented as needed. In the mandatory main() method, the user has to construct G4RunManager or its derived class, which defines the main interaction with the user, and has to set the three mandatory classes G4UserDetectorConstruction, G4UserPhysicsList, and G4UserPrimaryGeneratorAction. The user can also define things like a vis(ualization) manager, a (G)UI session, or multithreading inside the main() method. In G4UserDetectorConstruction, the user constructs all the necessary materials, volumes, and sensitive detector classes for the individual application; in G4UserPhysicsList, all necessary particles and processes are declared and must be assigned to each other, together with corresponding cut-off values; and in G4UserPrimaryGeneratorAction, the concrete generator is defined that generates the primary particles and vertices. These four files already allow for the basic scenario how Geant4 runs. [167]

The execution of a Geant4 application can be divided into two phases, *initialization* and *run*, which are illustrated in Fig. B.1. The initialization phase is triggered by the Initialize() method of G4RunManager, followed by the construction of the world volume according to the geometry and materials definitions in G4UserDetectorConstruction, as well as the construction of particles and physics processes according to G4UserPhysicsList. The run phase begins with the BeamOn() method of G4RunManager, after which the geometry is closed and the *event loop* starts generating and processing *events*. After all events have been processed, the geometry is opened again and a new *run* can be initialized. This means that Geant4 conceptually adapts the procedure of a real experiment, namely taking data in runs, which in turn are collections of events sharing the same detector conditions. In analogy to a typical real experiment, the setup cannot be changed during a run, which is why the geometry gets closed during the run phase. [167]

The event loop is illustrated in Fig. B.2. At the beginning of processing one event, the event contains primary particles that are pushed into a *stack*. One by one, the particles are then popped from the stack and their tracks are processed. A track is divided into *steps*, and for each step, quantities like the particle's current energy, momentum, or position are calculated based on the implemented physics list. If secondary particles are created, they are added to the stack, and if a sensitive detector volume is hit, the corresponding information is stored. The tracks are traced down to zero kinetic energy, until they go out of the world volume, or until the corresponding particle decays. Once the stack is empty, the event loop ends and the run is over. [167]

Geant4 enables the user to intervene at any point in the event loop. With the optional classes G4UserRunAction, G4UserEventAction, G4UserStackingAction, G4UserTrackingAction, and G4UserSteppingAction, which can be defined in the main() method, the user can sensitively

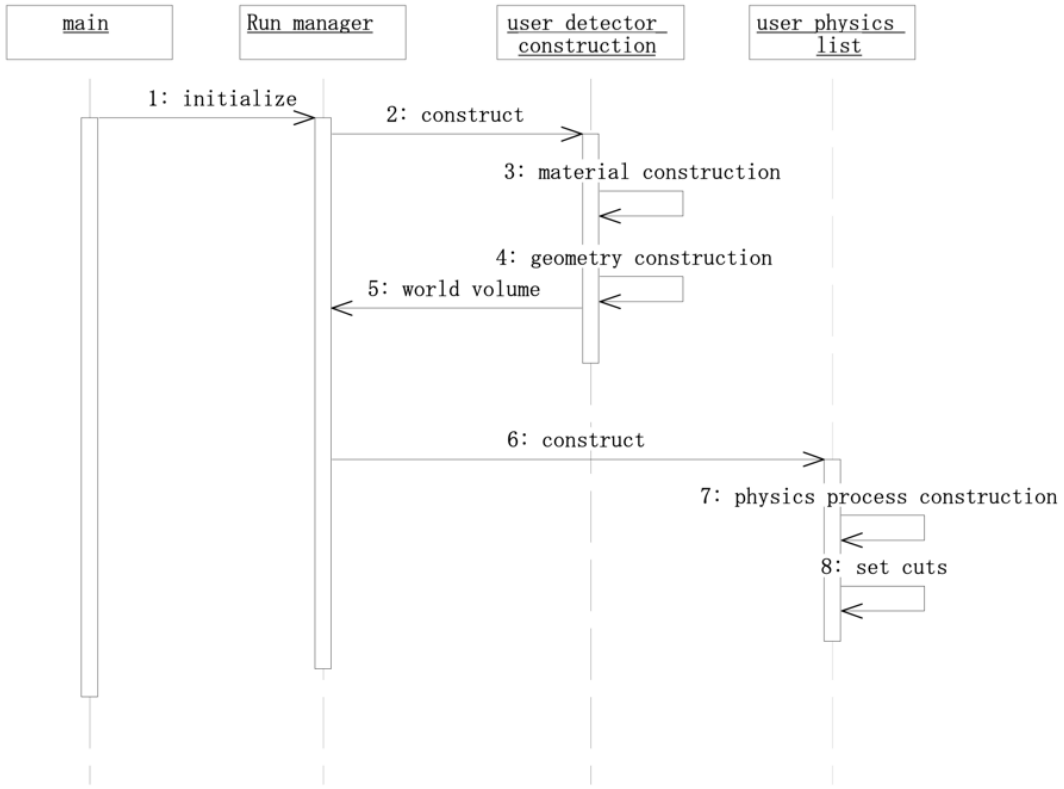

(a) Scenario diagram for the initialization phase. Figure from [167].

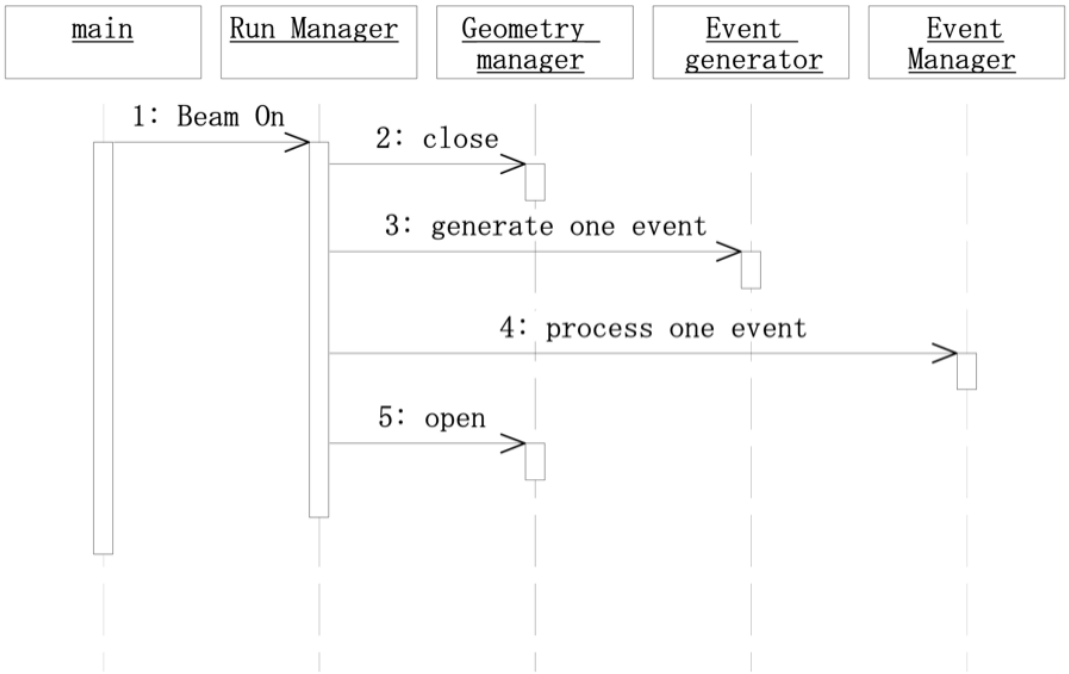

(b) Scenario diagram for the run phase. Steps 3 and 4 are repeated within the event loop. Figure adapted from [167].

FIGURE B.1. The two program phases of `Geant4`: *initialization* (top) and *run* (bottom).

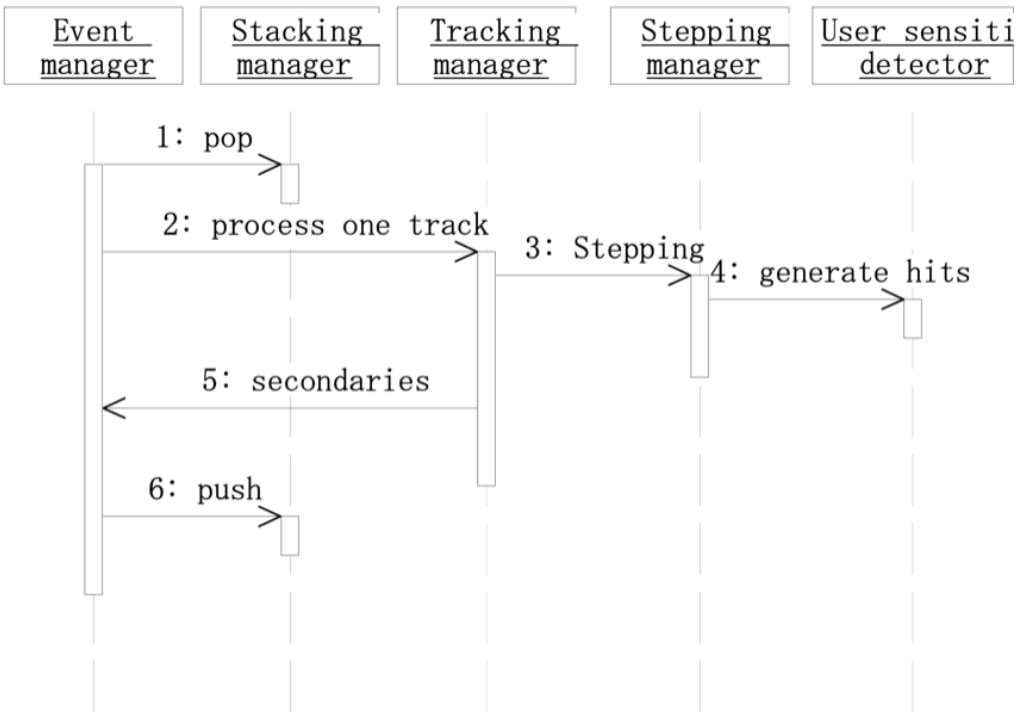

FIGURE B.2. The event loop of Geant4. Figure from [167].

influence the behaviour of the Geant4 kernel dependent on the individual application. [167]

B.2 Instruction Manual to the GitLab Repository *MXTriggerVetoSimulation*

The Geant4 simulation of the MAGIX trigger veto system can be found in the GitLab repository MXTriggerVetoSimulation, that can be made available to all members of the MAGIX collaboration. For the scope of this thesis, a new branch was created, termed *SebNew*. To facilitate the first use, the corresponding folder contains a README file and a guide for installing Geant4 on Linux or MAC. Please make sure, that ROOT and a C++ compiler are installed as well, since Geant4 needs these to run properly. The used versions for the studies in this thesis are Geant4 10.4.3, ROOT 6.22.00, and the C++ standard C++11. If any other combination of versions is used, errors are likely to occur.

Since Geant4 and its applications are written in C++, it is common to use CMake and GNUmake for building and testing the software. The content of the GitLab repository should therefore be stored as the so-called *source folder*, from which the Geant4 application is built into a user-defined *build folder* using CMake. This process also includes the creation of a Makefile, which is then used by GNUmake to create executables inside the build folder. Further information on these steps can be found in the above mentioned installation guide. The code modules that shall be included in the build process must be declared in CMakeLists.txt and details on how the Makefile is created can be defined in the file GNUmakefile. As usual for C++, the code modules are separated into *header files* (*.hh) and *source files* (*.cc), which are stored in the folders include/ and src/, respectively. The only exception to this rule is the file main.cc, that is stored directly inside the source folder.

As can be seen in Appendix B.1, there are several mandatory methods and classes that have to be defined in Geant4, in addition to some optional classes. For a better readability of the application, these methods and classes are normally distributed to individual header files and the corresponding source files, which was also done for the MAGIX trigger veto simulation. The assignment of the Geant4 methods and classes from Appendix B.1 to the header and source files found in the GitLab repository is shown in Tab. B.1. Additionally, there are some more header and source files inside the GitLab repository, which have not been mentioned yet, and which are only used for a more convenient usage of the simulation: MAGIXExceptionHandler, MAGIXPhysicsListMessenger, MAGIXActionInitialization, and MAGIXSteering. The MAGIXExceptionHandler class is constructed inside the mainMAGIX.cc file, right after constructing the G4RunManager, and is responsible for raising error messages if necessary. MAGIXPhysicsMessengerList is derived from the G4UIMessenger class and enables the user to define commands for interacting with MAGIXPhysicsList. MAGIXActionInitialization comprises all the classes influencing the run phase of Geant4 and is used to keep mainMAGIX.cc more readable. Finally, MAGIXSteering is used to give the user the possibility to change parameters of the application without having to recompile the code. The design parameters of the MAGIX trigger veto system as well as other important parameters

Geant4 method or class	**Filename(s) in GitLab repository**
main()	mainMAGIX.cc
G4UserDetectorConstruction	MAGIXConstruction.hh/.cc
G4UserPhysicsList	MAGIXPhysicsList.hh/.cc
G4UserPrimaryGeneratorAction	MAGIXPrimaryGeneratorAction.hh/.cc
G4UserRunAction	MAGIXRunAction.hh/.cc
G4UserEventAction	MAGIXEventAction.hh/.cc
G4UserStackingAction	/
G4UserTrackingAction	/
G4UserSteppingAction	MAGIXSteppingAction.hh/.cc

TABLE B.1. The mandatory (upper panel) and optional (lower panel) Geant4 methods and classes and their corresponding files inside the GitLab repository.

of the simulation are defined in a so-called *steering file*, found in the folder steering/, and loaded into the application by MAGIXSteering at the beginning of mainMAGIX.cc. Further details on the practice of using steering files can be found in the PhD thesis of M. Christmann [27].

After building the Geant4 application with CMake and creating the executables with GNUmake, a simulation can be started from the build folder in one of two modes, *vis* or *bash*. In the vis mode, a vis(ualization) manager is opened using the command ./mainMAGIX vis steeringX, where steering/steeringX.xml is the steering file of choice. Inside the vis manager, the simulation of a run with an individual number of events N can be started using the command /run/beamOn N. The vis manager is a great tool for visualizing the implemented detector geometries and is indispensable for debugging. In the files init_vis.mac, vis.mac, and gui.mac, all sorts of adjustments to the vis manager can be implemented. In contrast to the vis mode, the bash mode runs only inside the terminal and a simulation is started via the command ./mainMAGIX bash steeringX, where steering/steeringX.xml is again the chosen steering file. Inside the subsequent Geant4 environment, a run can be simulated analogously to the vis mode using the command /run/beamOn N.

Unfortunately, simulating more than one event at the same time is not suitable for the studies in this thesis. The quantities of interest when simulating the MAGIX trigger veto system are the numbers of produced optical photons inside the scintillator segments of the trigger and veto layers, whose calculation happens runwise. Therefore, additional bash scripts were written to repeat the /run/beamOn 1 command M times, making the numbers of produced optical photons available for each event. These *beamOn scripts* can be used via the command bash beamOnM.sh. Furthermore, if several simulations shall be run in parallel, the script runSim.sh can be used, which loops over several of the beamOn scripts.

Running a simulation results in the creation of two files. In log/*_steering.dat, a copy of the used steering file is stored so that, even at a later time, it can be traced which parameters were used for the simulation. Like mentioned above, the quantities of interest are the numbers of

produced optical photons inside the scintillator segments of the trigger and veto layers. This is the actual data that is stored, together with the most important input parameters, inside the second file, `log/*.dat`, where each line contains the data of one event. The exact filenames contain the most important input parameters as well, enabling the matching of a given datafile to a specific simulation run.

For finally analyzing and plotting the simulation data, the scripts `runAnalysis.py`, `runMultiAnalysis.sh`, and `runPlots.py` are used. `runAnalysis.py` scans a given datafile line by line and increases a counter for each of the trigger configurations and veto patterns defined in Section 4.1.3, if the number of produced optical photons inside the corresponding scintillator segments exceed a certain threshold, the before defined variable *Photon cut*. The trigger and veto response probabilities as well as their errors are then calculated and stored inside a separate file. Using the script `runMultiAnalysis.sh`, this process can be repeated for several datafiles, for which a certain parameter of the simulation has been varied. Afterwards, the response probabilities are plotted against the varied design parameter using the script `runPlots.py`.

B.3 Study to distinguish between Electrons and Low-Energy Muons

As can be seen in Fig. B.3, muons with different energies leave different signals inside the MAGIX trigger veto system. While the distributions of the produced optical photons inside the individual veto layers V1, V2, and V3 all peak at the same position for higher-energy muons, the peak positions of the distributions differ for lower-energy muons with energies of 300 MeV and 100 MeV. For 300 MeV muons, the peaks for V2 and V3 lie slightly higher than the peak for V1. This can be explained by the fact that the energy loss by ionization increases as the energy of the muons decrease. After passing the eleven lead absorber layers between V1 and V2, the 300 MeV muons have already lost a considerable amount of their energy, bringing their energy loss in the veto layers V2 and V3 closer to the Bragg peak. In addition, if one compares the optical photon distributions of the 300 MeV muons with those of the higher-energy muons, it can be seen that many of the 300 MeV muons do not reach the veto layers V2 and V3 at all. For 100 MeV muons, the effect is even larger. Since the muons have that less energy, even the peaks in the distributions of the trigger layer T and the veto layer V1 are slightly shifted to higher optical photon numbers. Furthermore, almost no muons are detected in layers V2 and V3 anymore, which raises the problem that 100 MeV muons cannot longer be separated from the electrons originating from the interaction point. This can be seen in Fig. B.3 as well, where the distributions for 105 MeV electrons are hardly distinguishable from the distributions for the 100 MeV muons.

This means that the purpose of the trigger veto system fails for low-energy muons, increasing the number of muons falsely identified as electrons, as well as the number of electrons falsely identified as muons. In the following, it shall be investigated, whether this situation can be improved.

In theory, it should be possible to improve the distinction between electrons and low-energy muons, at least to a certain extent. The CSDA ranges[1] for 100 MeV and 300 MeV muons in lead are $5.943 \times 10^1\,\mathrm{g/cm^2}$ and $2.352 \times 10^2\,\mathrm{g/cm^2}$, respectively [104]. Or alternatively, 5.24 cm and 20.72 cm, if the density of lead, i.e. $\rho_{\mathrm{Pb}} = 11.35\,\mathrm{g/cm^2}$ [104], is used as a conversion factor. This means that, on average, 300 MeV muons will pass the 11 cm of lead absorbers between the veto layers V1 and V2, while 100 MeV muons will be stopped inside the lead absorber layers, which is exactly the behaviour visible in Fig. B.3. However, the CSDA range of 100 MeV muons is approximately ten times the radiation length in lead, i.e. $6.37\,\mathrm{g/cm^2}$ or 0.5612 cm [104]. So on average, electrons will be stopped much earlier in the trigger veto system than 100 MeV muons. Therefore, by changing the placement of the veto layer V2 closer to V1, it should be possible to improve the distinction between the two particle types.

[1] The **C**ontinuous **S**lowing **D**own **A**pproximation range gives a very close approximation to the average path length traveled by a charged particle as it slows down to rest, calculated in the continuous-slowing-down approximation. [169]

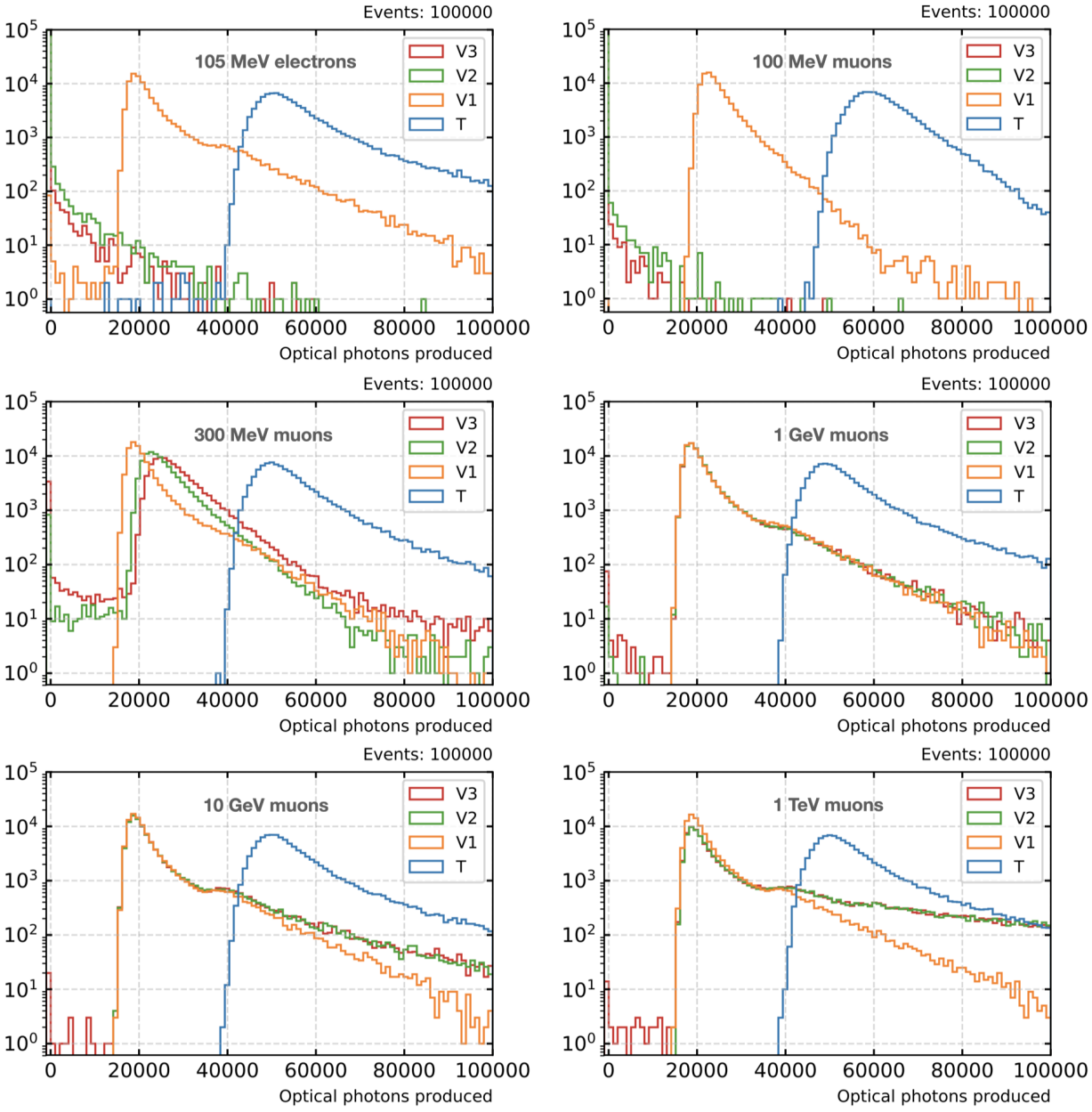

FIGURE B.3. Distributions of the produced optical photons inside the individual scintillator layers of the trigger veto system for 105 MeV electrons and muons of different energy.

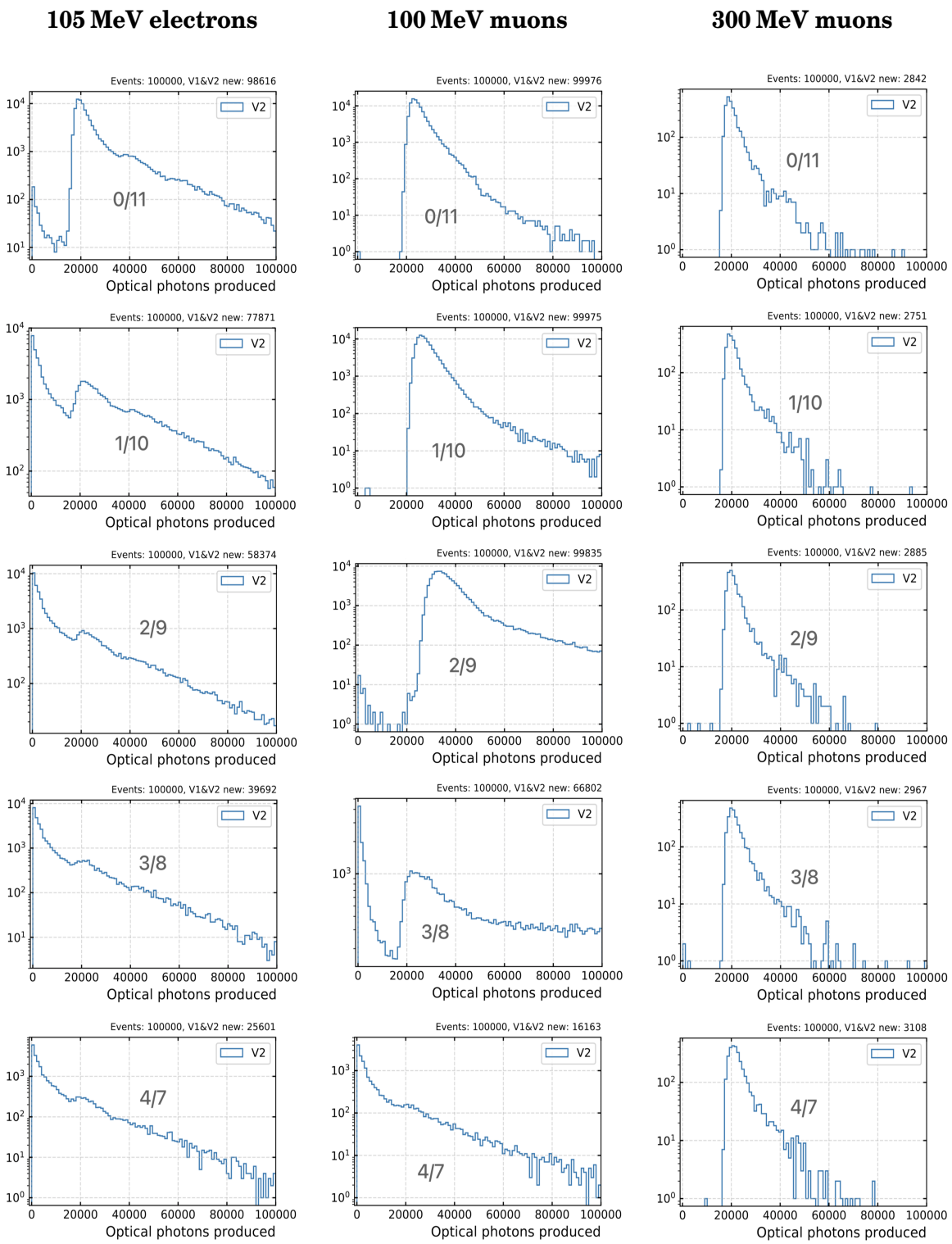

FIGURE B.4. Distribution of the produced optical photons inside veto layer V2 for different particle types and different placements of V2. The notation "2/9", for example, means that two lead absorber layers are placed between veto layers V1 and V2 and nine are placed between V2 and V3.

To quantify this, an additional veto pattern has been defined, termed `V1&V2 new`, which requires the logical OR of the veto patterns `all V` and `only V1 and V2`, where the variable *Photon cut* can be set individually for each scintillator layer in both of these patterns. With this, the principle of the trigger veto system stays unchanged for electrons and high-energy muons, but is modified for low-energy muons. Electrons will, on average, still leave a signal in the first veto layer before they are stopped inside the lead absorber layers between V1 and V2, and high-energy muons will keep on leaving signals in all three veto layers. Low-energy muons on the other hand, will now leave signals in veto layers V1 and V2 before they are stopped inside the lead absorber layers between V2 and V3. If the *Photon cut* values for the individual scintillator layers are set properly, this modification in the veto pattern should enable improving the separation of electrons and low-energy muons.

That this works can be seen in Fig. B.4, where the optical photon distribution of the veto layer V2 is shown for 105 MeV electrons, 100 MeV muons, and 300 MeV muons, as well as for different placements of V2. As an example, the placement "2/9" refers to the lead absorber configuration where two lead absorber layers are placed between veto layers V1 and V2 and nine are placed between V2 and V3. For this study, the variable *Photon cut* has been set to 10,000 for all three veto layers in the veto pattern `all V`, as well as for layer V1 in the pattern `only V1 and V2`. For the layer V2 in `only V1 and V2`, *Photon cut* has been set to 0 so that the complete optical photon distribution of V2 can be investigated. The design parameters of the trigger veto system have been set to the values concluded in Section 4.3.4.
For the electrons, the shape of the distribution changes rather fast as more and more lead absorber layers are placed between V1 and V2. Starting with a peak at around 19,000 produced optical photons for the placement "0/11", this peak is almost gone for the placement "3/8". The 100 MeV muons behave similarly but the vanishing of the peak happens more slowly. For the placement "3/8", the peak is drastically reduced but still clearly visible, before it can only be guessed for the placement "4/7". In contrast, the 300 MeV muons show a clear peak for all V2 placements. All of this fits in quite nicely with the expectations, but the important part here is that changing the placement of V2 can obviously be used to better distinguish between electrons and 100 MeV muons. From the distributions for the placements "1/10", "2/9", and "3/8", it is clear that the right choice of the *Photon cut* value for V2 in the pattern `only V1 and V2` will help to resolve the problem.

Exactly that is shown in Fig. B.5a, where the individual veto response probabilities $\epsilon_{\mathrm{V,P}}$ are plotted against the placement of the veto layer V2 for 100 MeV muons. In addition, Fig. B.5b shows the differences $1-\epsilon_{\mathrm{V,P}}$ and the corresponding numbers can be found in Tab, B.2. As a reminder, for the trigger veto system to work as intended, a certain veto response probability has to be maximized for muons, or alternatively, the corresponding difference has to be minimized. For electrons, it is the other way around. It can be seen that the veto pattern `V1&V2 new` outperforms the pattern `all V` for every single V2 placement. Especially for the placements close to V1, i.e.

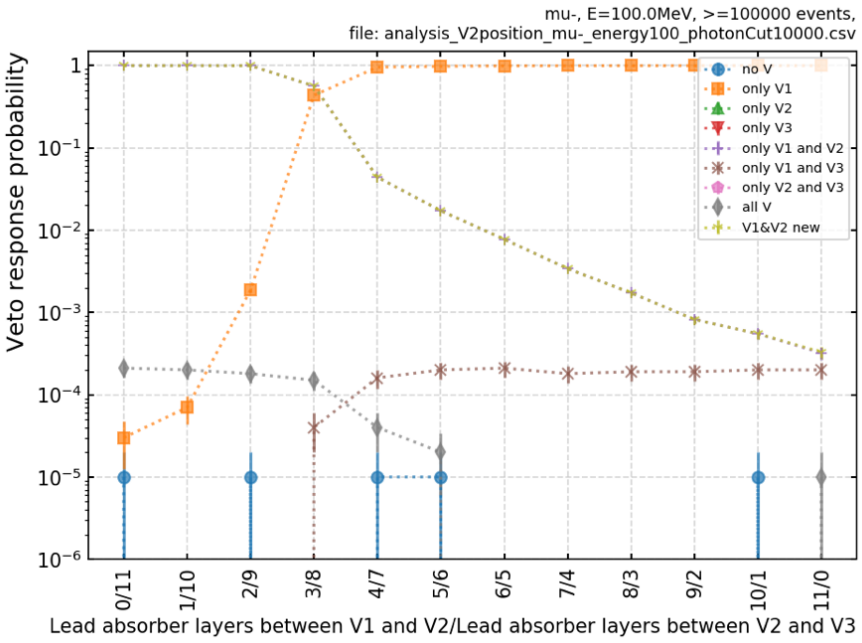

(a)

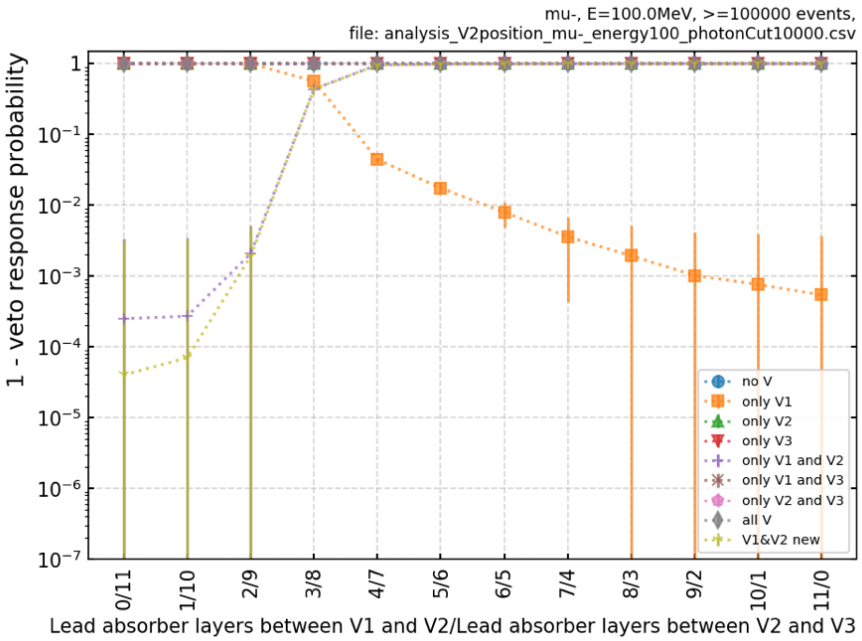

(b)

FIGURE B.5. The individual veto response probabilities v_R for the different placements of V2 (top), and the corresponding differences $1-\epsilon_{V,P}$ (bottom) for 100 MeV muons. The pattern `V1&V2 new` clearly outperforms the pattern `all V`.

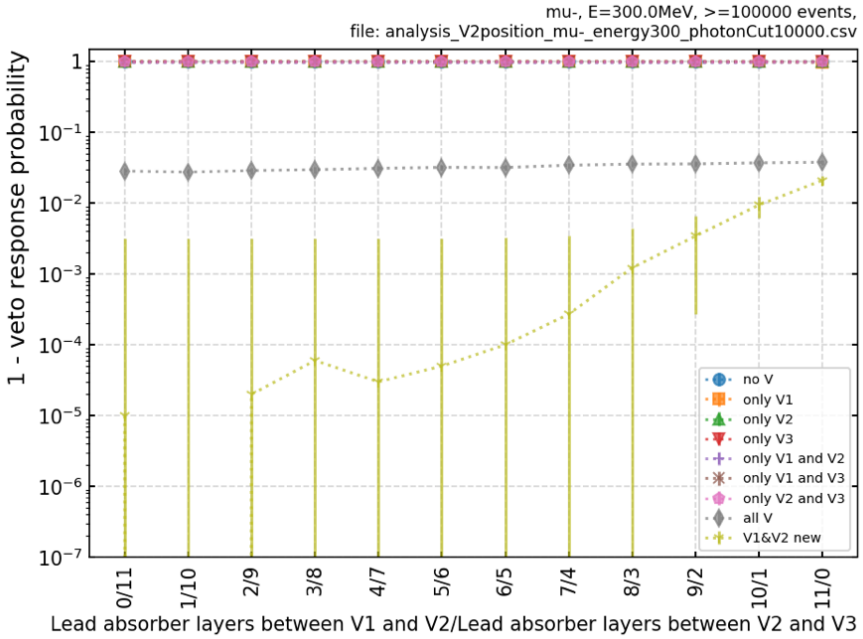

FIGURE B.6. The individual differences $1 - \epsilon_{V,P}$ for the different placements of V2 and 300 MeV muons. Obviously, the pattern `V1&V2 new` outperforms the pattern `all V`.

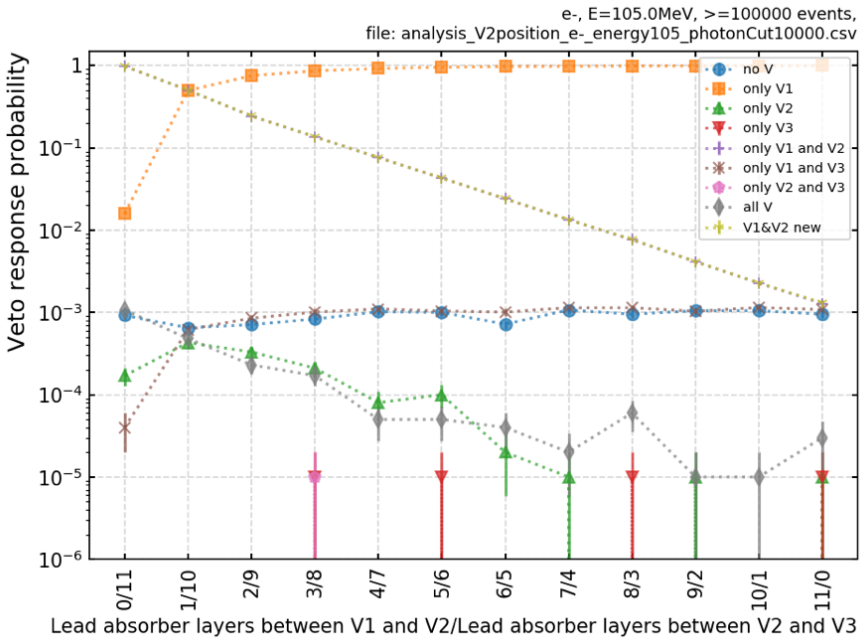

FIGURE B.7. The individual veto response probabilities for different V2 placements and 105 MeV electrons. The pattern `all V` works as intended, while the pattern `V1&V2 new` rejects considerable amounts of electrons.

"0/11", "1/10", and "2/9", the difference $1-\epsilon_{\mathrm{V,V1\&V2\,new}}$ can be brought down into the 10^{-4} region, whereas the pattern `all V` reaches the same order of magnitude, but with the veto response probability $\epsilon_{\mathrm{V,all\,V}}$. From this it can be concluded that placing the veto layer V2 closer to V1 can be used for effectively identifying and rejecting 100 MeV muons.
Fig. B.6 shows the individual differences $1-\epsilon_{\mathrm{V,P}}$ for 300 MeV muons. Also here, the pattern `V1&V2 new` outperforms the pattern `all V` for every single V2 placement, even coming down into the 10^{-5} region for the V2 placements close to V1. Thus, the pattern `V1&V2 new` improves the veto efficiency for 300 MeV muons as well. The corresponding numbers to Fig. B.6 are listed in Tab. B.3.
Finally, Fig. B.7 shows the individual veto response probabilities for 105 MeV electrons. Unfortunately, the performance of the pattern `V1&V2 new` reaches its limit here, which can be seen from the pattern `all V` outperforming the pattern `V1&V2 new` for all V2 placements. Whereas the pattern `all V` gives a veto response probability of 10^{-3} or better for every V2 placement, $\epsilon_{\mathrm{V,V1\&V2\,new}}$ slowly decreases as V2 is moved away from V1, without reaching 10^{-3} at all. For the placements close to V1, one can see that `V1&V2 new` rejects considerable amounts of the electrons. For the placement "2/9" for example, more than 24 % of electrons are rejected, and for the placement "1/10", this number even increases to around 50 %. The exact numbers can be found in Tab. B.4.

Unfortunately, this means that the pattern `V1&V2 new` cannot be used as intended, since the electron veto efficiency of the trigger veto system has to be as small as possible for the experiments proposed at MAGIX. For the determination of the electromagnetic form factors of the proton for example, see Section 1.2, the electron veto efficiency directly influences the accuracy of the results. However, should electron data with a very high purity be needed in the future, where it does not matter that a considerable amount of electrons has been rejected, the results from this study can be put into practice.

V2 placement	$\epsilon_{\text{V,all V}}$	$1-\epsilon_{\text{V,all V}}$	$\Delta\epsilon_{\text{V,all V}}$	$\epsilon_{\text{V,V1\&V2 new}}$	$1-\epsilon_{\text{V,V1\&V2 new}}$	$\Delta\epsilon_{\text{V,V1\&V2 new}}$
0/11	0.00021	0.99979	0.00005	0.99996	0.00004	0.00316
1/10	0.00020	0.99980	0.00004	0.99993	0.00007	0.00316
2/9	0.00018	0.99982	0.00004	0.99812	0.00188	0.00316
3/8	0.00015	0.99985	0.00004	0.56476	0.43524	0.00238
4/7	0.00004	0.99996	0.00002	0.04404	0.95596	0.00066
5/6	0.00002	0.99998	0.00001	0.01723	0.98277	0.00042
6/5	0.00000	1.00000	0.00000	0.00774	0.99226	0.00028
7/4	0.00000	1.00000	0.00000	0.00341	0.99659	0.00018
8/3	0.00000	1.00000	0.00000	0.00173	0.99827	0.00013
9/2	0.00000	1.00000	0.00000	0.00082	0.99918	0.00009
10/1	0.00000	1.00000	0.00000	0.00055	0.99945	0.00007
11/0	0.00001	0.99999	0.00001	0.00033	0.99967	0.00006

TABLE B.2. The exact numbers to Fig. B.5. The placement of V2 is varied and $\epsilon_{\text{V,all V}}$ and $\epsilon_{\text{V,V1\&V2 new}}$ are compared for 100 MeV muons.

V2 placement	$\epsilon_{\text{V,all V}}$	$1-\epsilon_{\text{V,all V}}$	$\Delta\epsilon_{\text{V,all V}}$	$\epsilon_{\text{V,V1\&V2 new}}$	$1-\epsilon_{\text{V,V1\&V2 new}}$	$\Delta\epsilon_{\text{V,V1\&V2 new}}$
0/11	0.97157	0.02843	0.00312	0.99999	0.00001	0.00316
1/10	0.97249	0.02751	0.00312	1.00000	0.00000	0.00316
2/9	0.97115	0.02885	0.00312	0.99998	0.00002	0.00316
3/8	0.97030	0.02970	0.00311	0.99994	0.00006	0.00316
4/7	0.96890	0.03110	0.00311	0.99997	0.00003	0.00316
5/6	0.96794	0.03206	0.00311	0.99995	0.00005	0.00316
6/5	0.96808	0.03192	0.00311	0.99990	0.00010	0.00316
7/4	0.96566	0.03434	0.00311	0.99973	0.00027	0.00316
8/3	0.96439	0.03561	0.00311	0.99878	0.00122	0.00316
9/2	0.96414	0.03586	0.00311	0.99657	0.00343	0.00316
10/1	0.96289	0.03711	0.00310	0.99058	0.00942	0.00315
11/0	0.96219	0.03781	0.00310	0.97897	0.02103	0.00313

TABLE B.3. The exact numbers to Fig. B.6. The placement of V2 is varied and $\epsilon_{\text{V,all V}}$ and $\epsilon_{\text{V,V1\&V2 new}}$ are compared for 300 MeV muons.

V2 placement	$\epsilon_{\mathrm{V,all\,V}}$	$1-\epsilon_{\mathrm{V,all\,V}}$	$\Delta\epsilon_{\mathrm{V,all\,V}}$	$\epsilon_{\mathrm{V,V1\&V2\,new}}$	$1-\epsilon_{\mathrm{V,V1\&V2\,new}}$	$\Delta\epsilon_{\mathrm{V,V1\&V2\,new}}$
0/11	0.00107	0.99893	0.00010	0.98296	0.01704	0.00314
1/10	0.00048	0.99952	0.00007	0.50126	0.49874	0.00224
2/9	0.00023	0.99977	0.00005	0.24377	0.75623	0.00156
3/8	0.00017	0.99983	0.00004	0.13645	0.86355	0.00117
4/7	0.00005	0.99995	0.00002	0.07625	0.92375	0.00087
5/6	0.00005	0.99995	0.00002	0.04291	0.95709	0.00066
6/5	0.00004	0.99996	0.00002	0.02411	0.97589	0.00049
7/4	0.00002	0.99998	0.00001	0.01340	0.98660	0.00037
8/3	0.00006	0.99994	0.00002	0.00770	0.99230	0.00028
9/2	0.00001	0.99999	0.00001	0.00415	0.99585	0.00020
10/1	0.00001	0.99999	0.00001	0.00228	0.99772	0.00015
11/0	0.00003	0.99997	0.00002	0.00131	0.99869	0.00011

TABLE B.4. The exact numbers to Fig. B.7. The placement of V2 is varied and $\epsilon_{\mathrm{V,all\,V}}$ and $\epsilon_{\mathrm{V,V1\&V2\,new}}$ are compared for 105 MeV electrons.

B.4 Additional Tables and Plots to the Simulation Studies

Chapter 4 shows the idea, the realization, and the results of the simulation studies performed for the MAGIX trigger veto system using `Geant4`. For a better readability of the chapter, additional information has been moved to this appendix. In the following sections, additional tables and plots to the preparatory studies and the optimization studies of the design parameters of the trigger veto system are given.

B.4.1 Preparatory Studies

Photon cut	$1-\epsilon_{\mathrm{V,all\,V}}$	$\epsilon_{\mathrm{V,all\,V}}$	$\Delta\epsilon_{\mathrm{V,all\,V}}$
100	0.999730	0.000270	0.000052
500	0.999780	0.000220	0.000047
1000	0.999810	0.000190	0.000044
2000	0.999880	0.000120	0.000035
3000	0.999900	0.000100	0.000032
4000	0.999910	0.000090	0.000030
5000	0.999940	0.000060	0.000024
6000	0.999940	0.000060	0.000024
7000	0.999950	0.000050	0.000022
8000	0.999980	0.000020	0.000014
9000	0.999980	0.000020	0.000014
10000	0.999990	0.000010	0.000010
11000	0.999990	0.000010	0.000010
12000	0.999990	0.000010	0.000010
13000	0.999990	0.000010	0.000010
14000	0.999990	0.000010	0.000010
15000	0.999990	0.000010	0.000010
16000	0.999990	0.000010	0.000010
17000	0.999990	0.000010	0.000010
18000	0.999990	0.000010	0.000010
19000	1.0	0.0	0.0
20000	1.0	0.0	0.0

TABLE B.5. The exact numbers to Fig. 4.5. The variable *Photon cut* is varied and $\epsilon_{\mathrm{V,all\,V}}$ is the chosen figure of merit.

Lead absorber layers between V1 and V2	$1-\epsilon_{\mathrm{V,all\,V}}$	$\epsilon_{\mathrm{V,all\,V}}$	$\Delta\epsilon_{\mathrm{V,all\,V}}$
0	0.00374	0.99626	0.00316
1	0.32421	0.67579	0.00260
2	0.63098	0.36902	0.00192
3	0.77397	0.22603	0.00150
4	0.86473	0.13527	0.00116
5	0.92243	0.07757	0.00088
6	0.95489	0.04511	0.00067
7	0.97321	0.02679	0.00052
8	0.98481	0.01519	0.00039
9	0.99073	0.00927	0.00030
10	0.99457	0.00543	0.00023
11	0.99684	0.00316	0.00018
12	0.99806	0.00194	0.00014
13	0.99868	0.00132	0.00011
14	0.99924	0.00076	0.00009
15	0.99945	0.00055	0.00007

TABLE B.6. The exact numbers to Fig. 4.6, where the amount of lead absorber layers between V1 and V2 is varied and $\epsilon_{\mathrm{V,all\,V}}$ is the chosen figure of merit. No steel sheets are used.

Lead absorber layers between V1 and V2	$1-\epsilon_{\mathrm{V,all\,V}}$	$\epsilon_{\mathrm{V,all\,V}}$	$\Delta\epsilon_{\mathrm{V,all\,V}}$
0	0.05196	0.94804	0.00308
1	0.52300	0.47700	0.00218
2	0.76079	0.23921	0.00155
3	0.88038	0.11962	0.00109
4	0.94385	0.05615	0.00075
5	0.97310	0.02690	0.00052
6	0.98728	0.01272	0.00036
7	0.99404	0.00596	0.00024
8	0.99727	0.00273	0.00017
9	0.99829	0.00171	0.00013
10	0.99921	0.00079	0.00009
11	0.99953	0.00047	0.00007
12	0.99981	0.00019	0.00004
13	0.99991	0.00009	0.00003
14	0.99996	0.00004	0.00002
15	0.99997	0.00003	0.00002

TABLE B.7. The exact numbers to Fig. 4.7. $\epsilon_{\mathrm{V,all\,V}}$ is the chosen figure of merit and the amount of lead absorber layers between V1 and V2 is varied. The steel sheets are included.

B.4.2 Optimization for the Trigger Layer

Number of trigger scintillators	$1-\epsilon_{T,T}$	$\epsilon_{T,T}$	$\Delta\epsilon_{T,T}$
15	0.26095	0.73905	0.00272
16	0.21323	0.78677	0.00280
17	0.16408	0.83592	0.00289
18	0.11531	0.88469	0.00297
19	0.06854	0.93146	0.00305
20	0.01957	0.98043	0.00313
21	0.00000	1.00000	0.00316
22	0.00001	0.99999	0.00316
23	0.00000	1.00000	0.00316
24	0.00001	0.99999	0.00316

TABLE B.8. The exact numbers to Fig. 4.9. $(1-\epsilon_{T,T})$ is the chosen figure of merit and the number of trigger scintillators is varied.

Length of the trigger scintillators	$1-\epsilon_{T,T}$	$\epsilon_{T,T}$	$\Delta\epsilon_{T,T}$
100 mm	0.21895	0.78105	0.00279
110 mm	0.14512	0.85488	0.00292
120 mm	0.06763	0.93237	0.00305
130 mm	0.00105	0.99895	0.00316
140 mm	0.00000	1.00000	0.00316
145 mm	0.00000	1.00000	0.00316
150 mm	0.00000	1.00000	0.00316
155 mm	0.00000	1.00000	0.00316
160 mm	0.00001	0.99999	0.00316
170 mm	0.00001	0.99999	0.00316
180 mm	0.00000	1.00000	0.00316
190 mm	0.00000	1.00000	0.00316
200 mm	0.00001	0.99999	0.00316
250 mm	0.00000	1.00000	0.00316
300 mm	0.00001	0.99999	0.00316

TABLE B.9. The exact numbers to Fig. 4.10, where the length of the trigger scintillators is varied and $1-\epsilon_{T,T}$ is the chosen figure of merit.

B.4.3 Optimization for the Veto Layers

Veto layer length	$\mathbf{1-\epsilon_{T,V3}}$	$\boldsymbol{\epsilon_{T,V3}}$	$\boldsymbol{\Delta\epsilon_{T,V3}}$
600 mm	0.26516	0.73484	0.00271
625 mm	0.23034	0.76966	0.00277
650 mm	0.19891	0.80109	0.00283
675 mm	0.16626	0.83374	0.00289
700 mm	0.13391	0.86609	0.00294
725 mm	0.10027	0.89973	0.00300
750 mm	0.07146	0.92854	0.00305
775 mm	0.04876	0.95124	0.00308
800 mm	0.03464	0.96536	0.00311
825 mm	0.02354	0.97646	0.00312
850 mm	0.01504	0.98496	0.00314
875 mm	0.00924	0.99076	0.00315
900 mm	0.00499	0.99501	0.00315
925 mm	0.00261	0.99739	0.00316
950 mm	0.00076	0.99924	0.00316
975 mm	0.00025	0.99975	0.00316
1000 mm	0.00006	0.99994	0.00316

TABLE B.10. The exact numbers to Fig. 4.12. $\left(1-\epsilon_{T,V3}\right)$ is chosen as figure of merit and the length of the veto layers is varied.

Veto layer width	$\mathbf{1-\epsilon_{T,V3}}$	$\boldsymbol{\epsilon_{T,V3}}$	$\boldsymbol{\Delta\epsilon_{T,V3}}$
140 mm	0.03238	0.96762	0.00311
150 mm	0.01654	0.98346	0.00314
160 mm	0.00690	0.99310	0.00315
170 mm	0.00300	0.99700	0.00316
180 mm	0.00122	0.99878	0.00316
190 mm	0.00038	0.99962	0.00316
200 mm	0.00018	0.99982	0.00316
210 mm	0.00010	0.99990	0.00316
220 mm	0.00008	0.99992	0.00316
230 mm	0.00002	0.99998	0.00316
240 mm	0.00002	0.99998	0.00316
250 mm	0.00007	0.99993	0.00316
260 mm	0.00000	1.00000	0.00316
270 mm	0.00007	0.99993	0.00316
280 mm	0.00002	0.99998	0.00316
290 mm	0.00005	0.99995	0.00316
300 mm	0.00004	0.99996	0.00316

TABLE B.11. The exact numbers to Fig. 4.14. The width of the veto layers is varied and $1-\epsilon_{T,V3}$ is the chosen figure of merit.

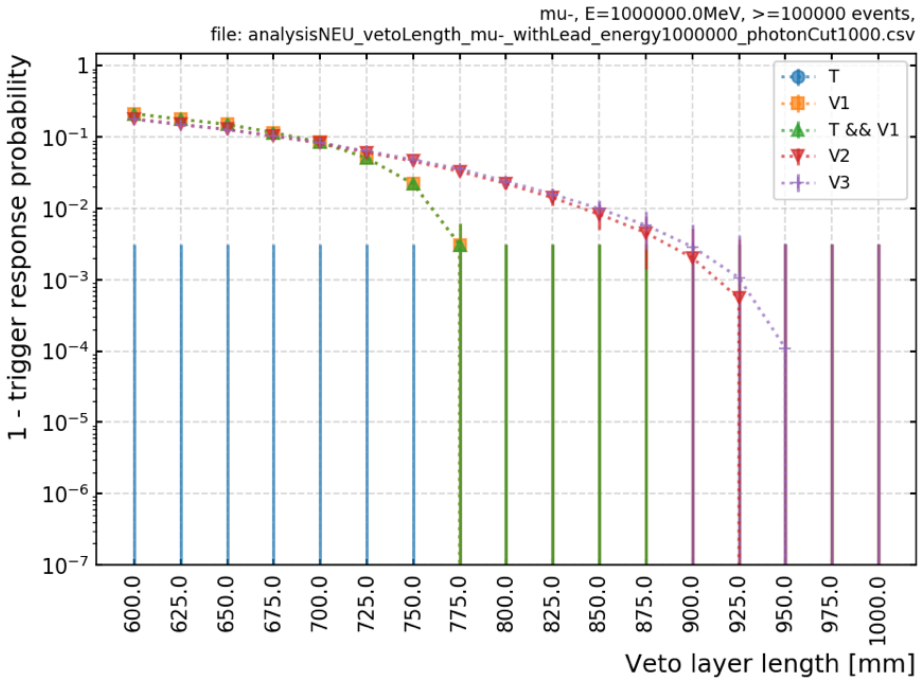

FIGURE B.8. The veto layer length is varied and $1-\epsilon_{\mathrm{T,V3}}$ is the chosen figure of merit. 1 TeV muons are used. For a length of 950 mm, $1-\epsilon_{\mathrm{T,V3}}$ falls below 10^{-3}.

Veto layer length	$\mathbf{1-\epsilon_{T,V3}}$	$\boldsymbol{\epsilon_{T,V3}}$	$\boldsymbol{\Delta\epsilon_{T,V3}}$
600 mm	0.25189	0.74811	0.00274
625 mm	0.21677	0.78323	0.00280
650 mm	0.18867	0.81133	0.00285
675 mm	0.15447	0.84553	0.00291
700 mm	0.12198	0.87802	0.00296
725 mm	0.08796	0.91204	0.00302
750 mm	0.05884	0.94116	0.00307
775 mm	0.03945	0.96055	0.00310
800 mm	0.02633	0.97367	0.00312
825 mm	0.01771	0.98229	0.00313
850 mm	0.01092	0.98908	0.00314
875 mm	0.00640	0.99360	0.00315
900 mm	0.00313	0.99687	0.00316
925 mm	0.00110	0.99890	0.00316
950 mm	0.00011	0.99989	0.00316
975 mm	0.00000	1.00000	0.00316
1000 mm	0.00000	1.00000	0.00316

TABLE B.12. The exact numbers to Fig. B.8, see above.

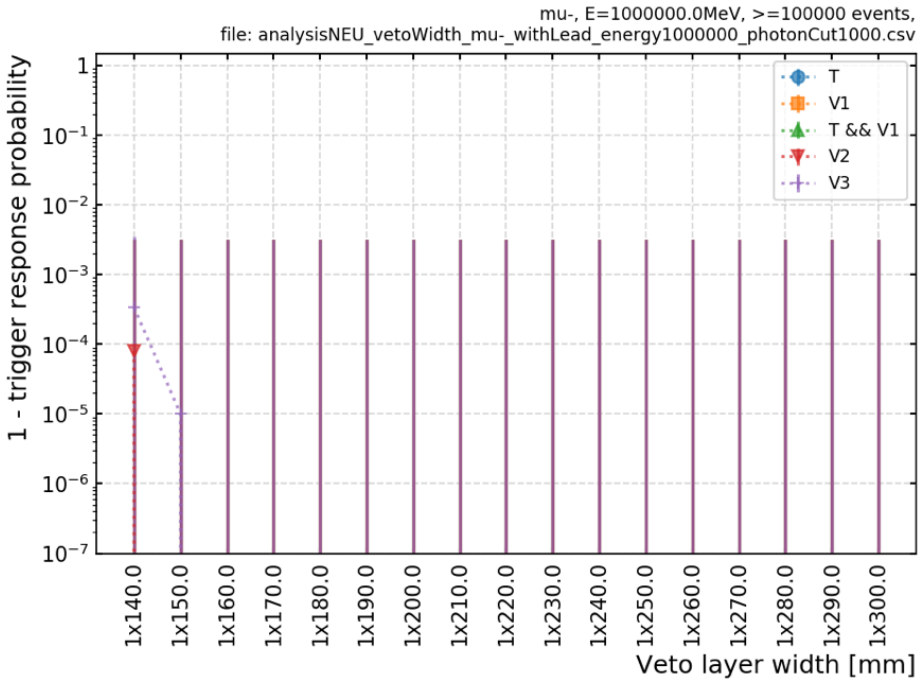

FIGURE B.9. The width of the veto layers is varied for 1 TeV muons. $1-\epsilon_{\mathrm{T,V3}}$ is the chosen figure of merit, which lies below 10^{-3} for all veto layer width values.

Veto layer width	$1-\epsilon_{\mathrm{T,V3}}$	$\epsilon_{\mathrm{T,V3}}$	$\Delta\epsilon_{\mathrm{T,V3}}$
140 mm	0.00035	0.99965	0.00316
150 mm	0.00001	0.99999	0.00316
160 mm	0.00000	1.00000	0.00316
170 mm	0.00000	1.00000	0.00316
180 mm	0.00000	1.00000	0.00316
190 mm	0.00000	1.00000	0.00316
200 mm	0.00000	1.00000	0.00316
210 mm	0.00000	1.00000	0.00316
220 mm	0.00000	1.00000	0.00316
230 mm	0.00000	1.00000	0.00316
240 mm	0.00000	1.00000	0.00316
250 mm	0.00000	1.00000	0.00316
260 mm	0.00000	1.00000	0.00316
270 mm	0.00000	1.00000	0.00316
280 mm	0.00000	1.00000	0.00316
290 mm	0.00000	1.00000	0.00316
300 mm	0.00000	1.00000	0.00316

TABLE B.13. The exact numbers to Fig. B.9, see above.

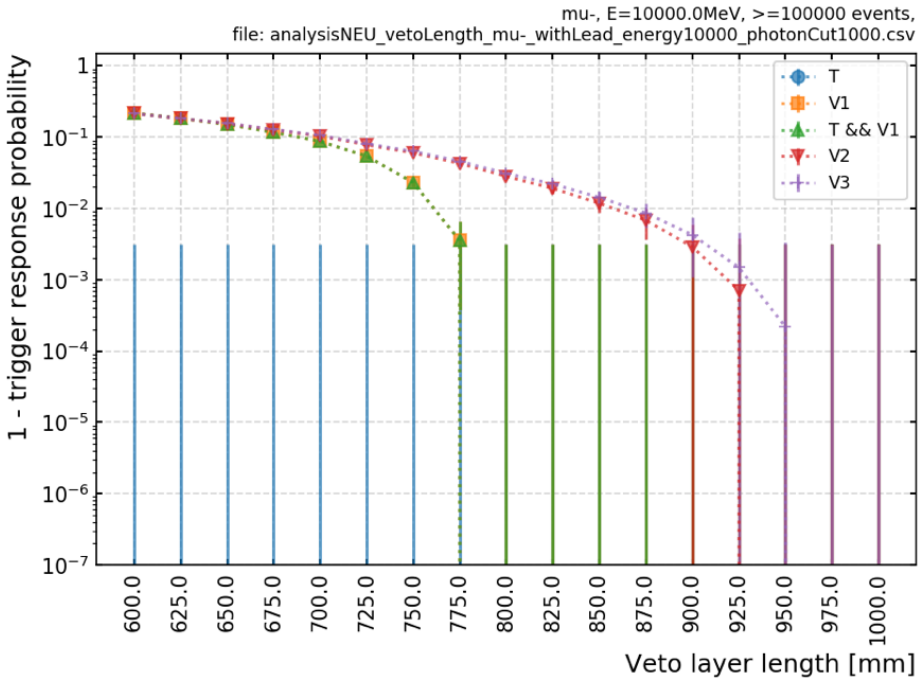

FIGURE B.10. The veto layer length is varied and $1-\epsilon_{T,V3}$ is the chosen figure of merit. 10 GeV muons are used. For a length of 950 mm, $1-\epsilon_{T,V3}$ falls below 10^{-3}.

Veto layer length	$1-\epsilon_{T,V3}$	$\epsilon_{T,V3}$	$\Delta\epsilon_{T,V3}$
600 mm	0.26265	0.73735	0.00272
625 mm	0.22893	0.77107	0.00278
650 mm	0.19649	0.80351	0.00283
675 mm	0.16276	0.83724	0.00289
700 mm	0.13302	0.86698	0.00294
725 mm	0.09874	0.90126	0.00300
750 mm	0.06833	0.93167	0.00305
775 mm	0.04702	0.95298	0.00309
800 mm	0.03191	0.96809	0.00311
825 mm	0.02261	0.97739	0.00313
850 mm	0.01455	0.98545	0.00314
875 mm	0.00890	0.99110	0.00315
900 mm	0.00433	0.99567	0.00316
925 mm	0.00150	0.99850	0.00316
950 mm	0.00022	0.99978	0.00316
975 mm	0.00000	1.00000	0.00316
1000 mm	0.00000	1.00000	0.00316

TABLE B.14. The exact numbers to Fig. B.10, see above.

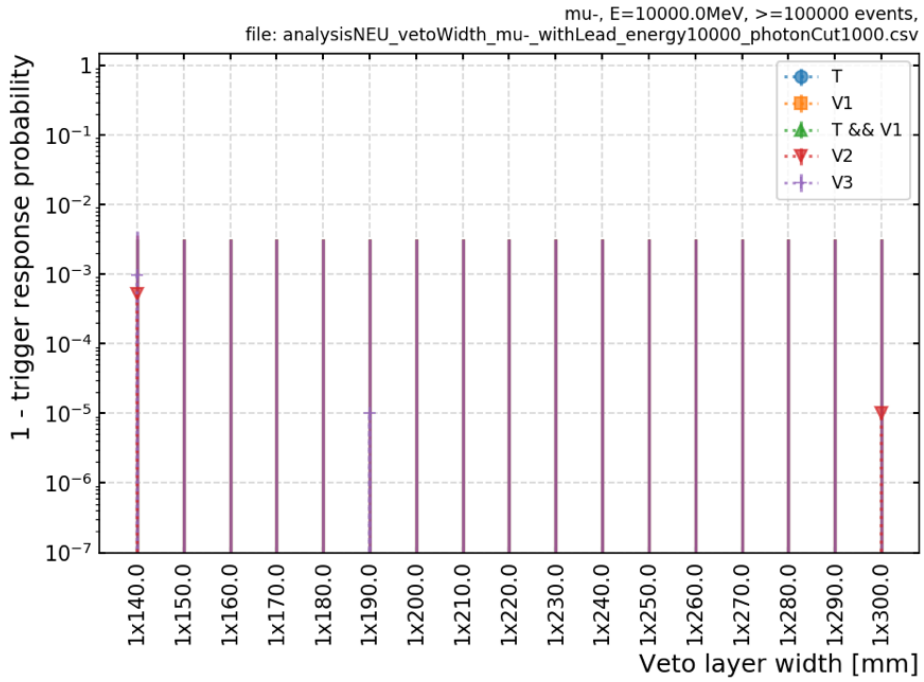

FIGURE B.11. The veto layer width is varied and $1-\epsilon_{T,V3}$ is the chosen figure of merit. 10 GeV muons are used. For a width of 150 mm, $1-\epsilon_{T,V3}$ falls below 10^{-3}.

Veto layer width	$1-\epsilon_{T,V3}$	$\epsilon_{T,V3}$	$\Delta\epsilon_{T,V3}$
140 mm	0.00100	0.99900	0.00316
150 mm	0.00000	1.00000	0.00316
160 mm	0.00000	1.00000	0.00316
170 mm	0.00000	1.00000	0.00316
180 mm	0.00000	1.00000	0.00316
190 mm	0.00001	0.99999	0.00316
200 mm	0.00000	1.00000	0.00316
210 mm	0.00000	1.00000	0.00316
220 mm	0.00000	1.00000	0.00316
230 mm	0.00000	1.00000	0.00316
240 mm	0.00000	1.00000	0.00316
250 mm	0.00000	1.00000	0.00316
260 mm	0.00000	1.00000	0.00316
270 mm	0.00000	1.00000	0.00316
280 mm	0.00000	1.00000	0.00316
290 mm	0.00000	1.00000	0.00316
300 mm	0.00000	1.00000	0.00316

TABLE B.15. The exact numbers to Fig. B.11, see above.

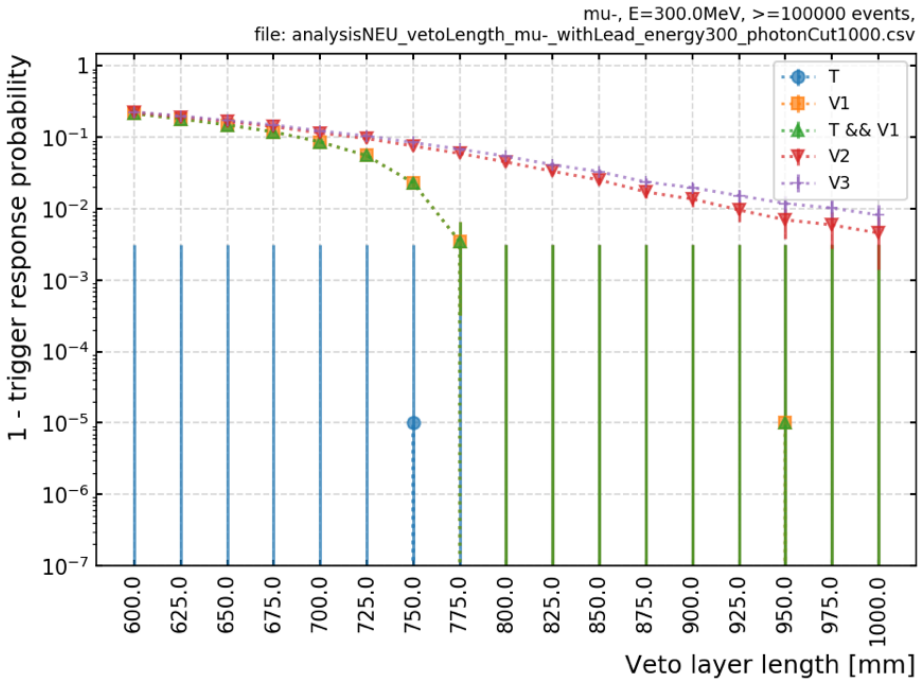

FIGURE B.12. The veto layer length is varied and $1-\epsilon_{T,V3}$ is the chosen figure of merit. 300 MeV muons are used. Here, the aim of 10^{-3} cannot be achieved. Too many of the muons are stopped inside the lead absorber layers between V1 and V2.

Veto layer length	$\mathbf{1-\epsilon_{T,V3}}$	$\boldsymbol{\epsilon_{T,V3}}$	$\boldsymbol{\Delta\epsilon_{T,V3}}$
600 mm	0.28362	0.71638	0.00268
625 mm	0.24923	0.75077	0.00274
650 mm	0.21781	0.78219	0.00280
675 mm	0.18765	0.81235	0.00285
700 mm	0.15310	0.84690	0.00291
725 mm	0.12387	0.87613	0.00296
750 mm	0.09182	0.90818	0.00301
775 mm	0.06966	0.93034	0.00305
800 mm	0.05502	0.94498	0.00307
825 mm	0.04195	0.95805	0.00310
850 mm	0.03349	0.96651	0.00311
875 mm	0.02411	0.97589	0.00312
900 mm	0.02016	0.97984	0.00313
925 mm	0.01557	0.98443	0.00314
950 mm	0.01221	0.98779	0.00314
975 mm	0.01050	0.98950	0.00315
1000 mm	0.00848	0.99152	0.00315

TABLE B.16. The exact numbers to Fig. B.12, see above.

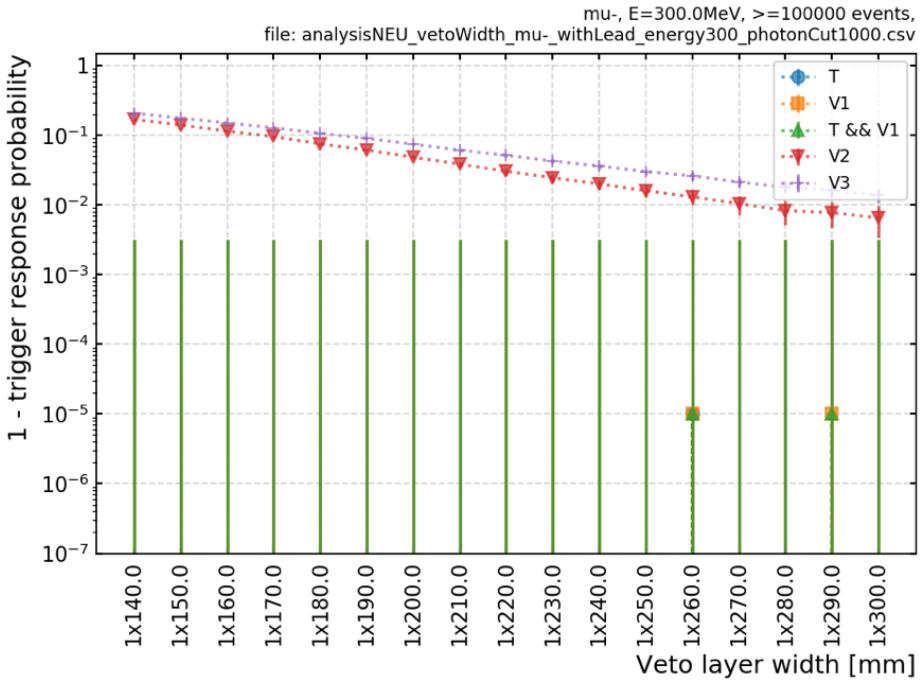

FIGURE B.13. The veto layer width is varied and $1-\epsilon_{\mathrm{T,V3}}$ is chosen as the figure of merit. 300 MeV muons are used. The aim of 10^{-3} cannot be achieved, since too many of the muons are stopped inside the lead absorber layers between V1 and V2.

Veto layer width	$1-\epsilon_{\mathrm{VT,3}}$	$\epsilon_{\mathrm{VT,3}}$	$\Delta\epsilon_{\mathrm{VT,3}}$
140 mm	0.21075	0.78925	0.00281
150 mm	0.17919	0.82081	0.00286
160 mm	0.15241	0.84750	0.00291
170 mm	0.12957	0.87043	0.00295
180 mm	0.10769	0.89231	0.00299
190 mm	0.09076	0.90924	0.00302
200 mm	0.07528	0.92472	0.00304
210 mm	0.06174	0.93826	0.00306
220 mm	0.05209	0.94791	0.00308
230 mm	0.04310	0.95690	0.00309
240 mm	0.03659	0.96341	0.00310
250 mm	0.03048	0.96952	0.00311
260 mm	0.02648	0.97352	0.00312
270 mm	0.02168	0.97832	0.00313
280 mm	0.01820	0.98180	0.00313
290 mm	0.01654	0.08346	0.00314
300 mm	0.01422	0.98578	0.00314

TABLE B.17. The exact numbers to Fig. B.13, see above.

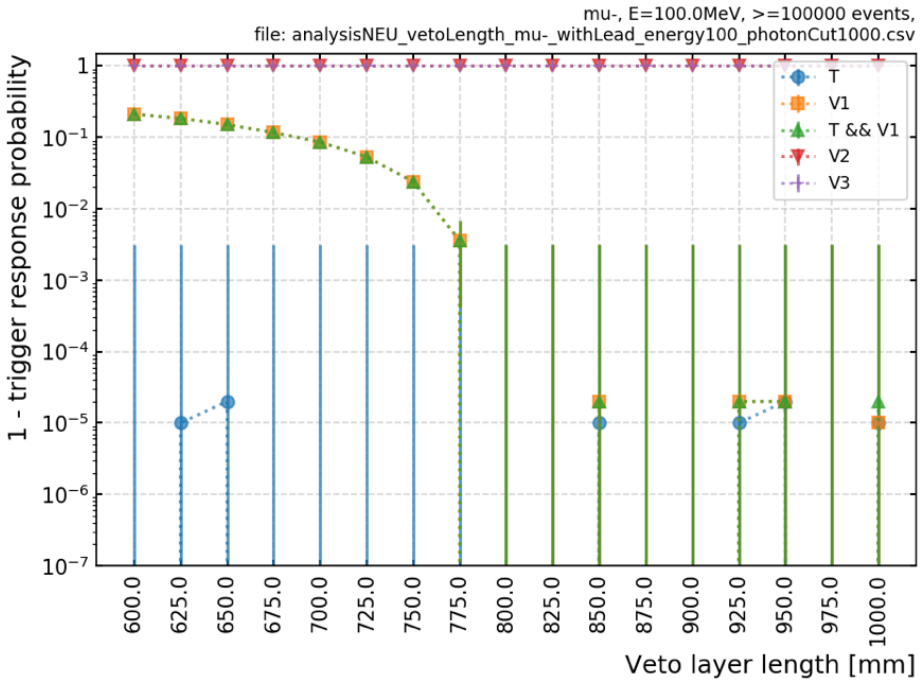

FIGURE B.14. The veto layer length is varied and $1-\epsilon_{T,V3}$ is the chosen figure of merit. 100 MeV muons are used. The aim of 10^{-3} cannot be achieved. Almost all of the muons are stopped inside the lead absorber layers between V1 and V2, since they behave too much like the 105 MeV electrons, which the lead absorber layers are supposed to stop.

Veto layer length	$\mathbf{1-\epsilon_{VT,3}}$	$\boldsymbol{\epsilon_{VT,3}}$	$\boldsymbol{\Delta\epsilon_{VT,3}}$
600 mm	0.999 890	0.000 110	0.000 033
625 mm	0.999 920	0.000 080	0.000 028
650 mm	0.999 910	0.000 090	0.000 030
675 mm	0.999 930	0.000 070	0.000 026
700 mm	0.999 920	0.000 080	0.000 028
725 mm	0.999 850	0.000 150	0.000 039
750 mm	0.999 920	0.000 080	0.000 028
775 mm	0.999 910	0.000 090	0.000 030
800 mm	0.999 940	0.000 060	0.000 024
825 mm	0.999 910	0.000 090	0.000 030
850 mm	0.999 950	0.000 050	0.000 022
875 mm	0.999 930	0.000 070	0.000 026
900 mm	0.999 870	0.000 130	0.000 036
925 mm	0.999 890	0.000 110	0.000 033
950 mm	0.999 940	0.000 060	0.000 024
975 mm	0.999 910	0.000 090	0.000 030
1000 mm	0.999 960	0.000 040	0.000 020

TABLE B.18. The exact numbers to Fig. B.14, see above.

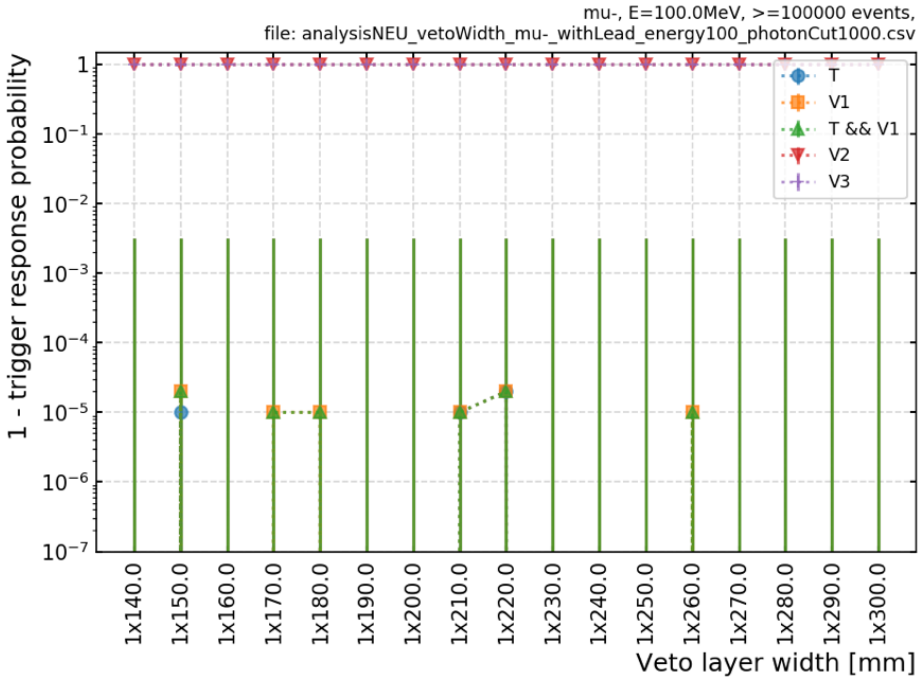

FIGURE B.15. The veto layer width is varied and $1-\epsilon_{T,V3}$ is chosen as the figure of merit. 100 MeV muons are used. Almost all of the muons are stopped inside the lead absorber layers between V1 and V2, as already seen in Fig. B.14. The goal of 10^{-3} cannot be achieved for 100 MeV muons.

Veto layer width	$\mathbf{1-\epsilon_{VT,3}}$	$\boldsymbol{\epsilon_{VT,3}}$	$\boldsymbol{\Delta\epsilon_{VT,3}}$
140 mm	0.999960	0.000040	0.000020
150 mm	0.999960	0.000040	0.000020
160 mm	1.000000	0.000000	0.000000
170 mm	0.999980	0.000020	0.000014
180 mm	0.999950	0.000050	0.000022
190 mm	0.999950	0.000050	0.000022
200 mm	0.999960	0.000040	0.000020
210 mm	0.999950	0.000050	0.000022
220 mm	0.999960	0.000040	0.000020
230 mm	0.999940	0.000060	0.000024
240 mm	0.999930	0.000070	0.000026
250 mm	0.999950	0.000050	0.000022
260 mm	0.999910	0.000090	0.000030
270 mm	0.999990	0.000010	0.000010
280 mm	0.999930	0.000070	0.000026
290 mm	0.999930	0.000070	0.000026
300 mm	0.999880	0.000120	0.000035

TABLE B.19. The exact numbers to Fig. B.15, see above.

B.4.4 Optimization for the Lead Absorber Layers

Lead absorber layer length	$\epsilon_{V,all\,V}$	$\Delta\epsilon_{V,all\,V}$
1000 mm	0.00030	0.00005
975 mm	0.00030	0.00005
950 mm	0.00029	0.00005
925 mm	0.00029	0.00005
900 mm	0.00038	0.00006
875 mm	0.00029	0.00005
850 mm	0.00042	0.00006
825 mm	0.00042	0.00006
800 mm	0.00060	0.00008
775 mm	0.00134	0.00012
750 mm	0.00348	0.00019
725 mm	0.00685	0.00026
700 mm	0.01106	0.00033
675 mm	0.01510	0.00039
650 mm	0.01956	0.00044
625 mm	0.02560	0.00051
600 mm	0.03004	0.00055

TABLE B.20. The exact numbers to Fig. 4.16. The length of the lead absorber layers is varied and $\epsilon_{V,all\,V}$ is the chosen figure of merit.

Lead absorber layer width	$\epsilon_{V,all\,V}$	$\Delta\epsilon_{V,all\,V}$
300 mm	0.00041	0.00006
290 mm	0.00035	0.00006
280 mm	0.00030	0.00005
270 mm	0.00040	0.00006
260 mm	0.00022	0.00005
250 mm	0.00036	0.00006
240 mm	0.00031	0.00006
230 mm	0.00033	0.00006
220 mm	0.00040	0.00006
210 mm	0.00038	0.00006
200 mm	0.00042	0.00006
190 mm	0.00039	0.00006
180 mm	0.00036	0.00006
170 mm	0.00037	0.00007
160 mm	0.00045	0.00009
150 mm	0.00076	0.00006

TABLE B.21. The exact numbers to Fig. 4.17. The width of the lead absorber layers is varied and $\epsilon_{V,all\,V}$ is chosen as the figure of merit.

B.4.5 Performance of the Veto System for different Electron Energies

Electron energy	$\epsilon_{\mathrm{V,all\,V}}$	$\Delta\epsilon_{\mathrm{V,all\,V}}$
20 MeV	0.00002	0.00001
30 MeV	0.00001	0.00001
40 MeV	0.00006	0.00002
50 MeV	0.00004	0.00002
55 MeV	0.00009	0.00003
60 MeV	0.00011	0.00003
70 MeV	0.00020	0.00004
80 MeV	0.00018	0.00004
90 MeV	0.00032	0.00006
100 MeV	0.00037	0.00006
105 MeV	0.00030	0.00005

TABLE B.22. The exact numbers to Fig. 4.18. The electron energy is varied and $\epsilon_{\mathrm{V,all\,V}}$ is the chosen figure of merit.

APPENDIX C

APPENDIX TO CHAPTER 5

C.1 More on the Trigger Detectors

C.1.1 Tested Coupling Materials

The final MAGIX trigger detectors have been coupled using the optically transparent epoxy EPO-TEK 301-2 by Epoxy Technology [118]. This choice is the result of previous studies, where also two other materials have been used and tested: The optical cement EJ-500 by Eljen Technology [170] and the optical silicone Elastosil RT 601 by Wacker Chemie AG [171]. Since all three have their advantages and disadvantages, Tab. C.1 gives an overview on their most important parameters. More details can be found in the respective data sheets.

Note that all three are two-component materials that have to be mixed before using them. This results in the mixture containing air bubbles, which must be removed. For the trigger detectors,

	EPO-TEK 301-2	**EJ-500**	**Elastosil RT 601**
Mixing ratio A:B by volume	1:0.42	3:1	9:1
Pot life at 20 °C	8 h	60 min	90 min
Curing time at 20 °C	48 h	24 h	24 h
Refractive index n	1.53	1.57	1.41 [172]
Comments	less viscous, durable, hardly removable	viscous, durable, hardly removable	viscous, can be removed easily

TABLE C.1. Overview on the coupling materials that have been tested for the MAGIX trigger detectors. All of them consist of two components A and B that have to be mixed in a certain volumetric ratio. Data taken from [118, 170, 171] if not stated otherwise.

this has been done using a vacuum bell.

All first coupling tests and applications used Elastosil RT 601 since it can be easily removed mechanically or by using coolant spray. Unfortunately, it is not durable enough to be used for a long-term experiment. As an example, it happened several times that the coupling had to be redone since it did not survive the wrapping process.

To ensure a more durable coupling, EJ-500 was tested. As an optical cement, it definitely meets this requirement. But during testing, it was found that the geometry of the scintillators and light guides requires a less viscous coupling material to accurately couple the sharp corners of the rhombic profile. When using the viscous EJ-500, these corners could either not completely be filled or a drop protruded to the outside.

EPO-TEK 301-2 solves this issue. It is less viscous and can be used in the sharp corners without any problems. It is even soaked into the gap between scintillator and light guide. This results in a clean and uniform coupling. Additionally, as an epoxy, it is as durable as EJ-500. Therefore, it has been chosen as the coupling material for the final MAGIX trigger detectors.

Besides, with EPO-TEK 301-2 as the coupling material of choice, the refractive indexes of the individual components of a trigger detector are very similar to each other. By this, the amount of reflected light at each material transition is minimized and an effective transmission of the scintillation light from scintillator to PMT is assured. Following its production inside the scintillator with a refractive index of $n = 1.58$, the scintillation light passes the first layer of EPO-TEK 301-2 with $n = 1.53$, the light guide with $n = 1.51$, and the second epoxy layer with $n = 1.53$, before it enters the PMT entry window with $n \sim 1.5$.

C.1.2 Coupling Guide

This guide is meant to give an overview on the coupling procedure of the MAGIX trigger detectors. The necessary steps are shown along with useful tips so that additional trigger detectors can be coupled easily if needed in the future.

Coupling Preparation Make sure to have the following things available: One scintillator bar (still covered by the manufacturer's protective foil), two polished mirror-inverted acrylic glass light guides, two PMTs and the corresponding high-voltage sockets, optical epoxy EPO-TEK 301-2, a vacuum bell for air bubble removal, a glass container which will be placed underneath the vacuum bell, and the two coupling stations with its 3D-printed molds, see Figs. C.2a and C.3a. It is also recommended to have a lamp available so that the coupling area can be completely illuminated and precisely inspected.

Several disposable items are needed as well. For mixing the two components of EPO-TEK 301-2, keep ready 2 ml and 5 ml syringes, two suitable blunt needles with a bevel angle of 90° (better for viscous liquids, see Fig. C.1a), a plastic swizzle stick, lint-free paper (as soft as possible), and

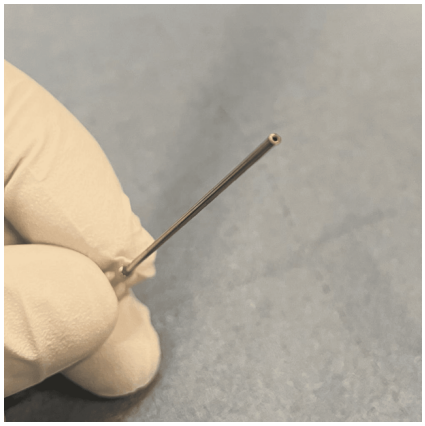

(a) Blunt needle.

(b) Component A inside oven for decrystallization.

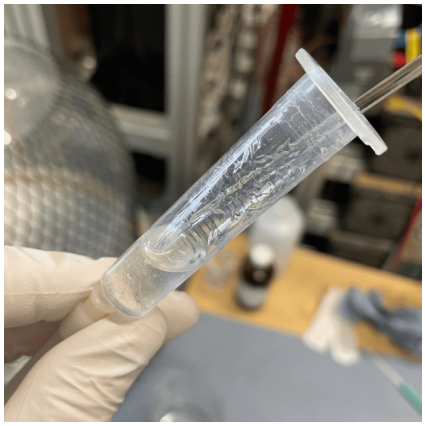

(c) Mixing the two components.

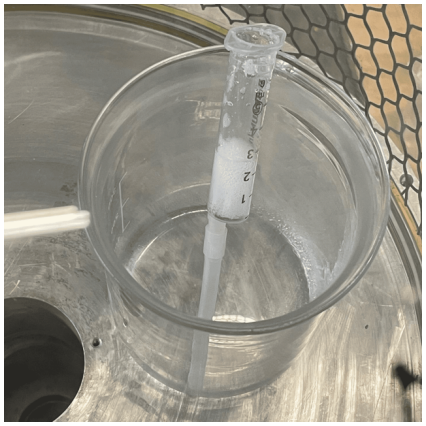

(d) Removing air bubbles from the mixture.

FIGURE C.1. Mixing EPO-TEK 301-2.

plastic gloves. If no blunt needles are available, use any other needles and grind them using a grinding machine or sandpaper. For coupling, ethanol, a lint-free cloth, lint-free cotton buds, some tape, and additional lint-free paper are necessary.

Mixing EPO-TEK 301-2 Before mixing the epoxy, make sure that component A has not crystallized during storage. If this should be the case, crystallization can be reversed by placing the container of component A in a water bath inside an oven, see Fig. C.1b, at 40 °C to 50 °C [118]. 45 °C over night proved to be effective.

The two components must be mixed in the volumetric ratio 1:0.42 (A:B). As a reference, roughly 0.1 ml epoxy per coupling is required. With the light guide and PMT coupling areas being 9.36 cm^2 and 5.07 cm^2, respectively, this corresponds to an epoxy layer thickness of 0.1 mm to 0.2 mm. It is recommended to wear the plastic gloves throughout the mixing process. The 5 ml syringe

from which the plunger has been removed is put on one of the needles and placed inside the glass container. Component A is now filled into the syringe directly from its container followed by component B using the 2 ml syringe and the second needle. The components are then mixed using the plastic swizzling stick, see Fig. C.1c, until no streaks are left (approximately 1 min).

The glass container with the 5 ml syringe and the mixture in it is then placed underneath the vacuum bell and the vacuum pump is turned on until all air bubbles have escaped (about 10 min), see Fig. C.1d. After that, the plunger is carefully put back inside the syringe and all new air bubbles are removed by gently pressing them out into lint-free paper. The epoxy-filled syringe is now ready for coupling.

Coupling Scintillator and Light Guides The station for coupling scintillator and light guides, see Fig. C.2a, can be used for four couplings simultaneously. Thus, do the following steps in parallel for the number of couplings to make. Again, it is recommended to wear plastic gloves throughout the coupling process.

First, remove the protective foil from the scintillator on the side to be coupled. The easiest way to do this is to just pull the foil over the scintillator and leave it that way until wrapping. Next, clean the coupling area and the surrounding edges with ethanol and a lint-free cloth. Do the same with the light guide.

After that, lay the light guide inside the respective 3D-printed mold and put it, together with the scintillator, into the coupling station. Now the light guide can be adjusted inside the mold. Therefore, put scintillator and light guide gently onto each other and fixate the light guide using the plastic screws of the mold. Be careful and do not fasten the screws too much. Otherwise, the light guide will escape upwards or could be scratched. Make sure that this adjustment is done with highest precision since this step is crucial for the final coupling result.

Now, lift the scintillator again and put epoxy diagonally from sharp corner to sharp corner onto the coupling area of the light guide, see Fig. C.2b. Again, roughly 0.1 ml should be used. The scintillator can now be lowered again until it touches the epoxy. Do this very gently and make sure you do not capture any air bubbles while doing so. The scintillator can then be slowly lowered further until it rests on the epoxy layer. The epoxy can now be watched flowing to the edges and filling the gap between scintillator and light guide. If enough epoxy has been used, the epoxy fills the complete coupling area. If not, some corners can stay epoxy-free. If this happens, gently press on top of the scintillator until the corners are filled with epoxy. If this is still not enough, additional epoxy can be filled into the gap. Do this slowly so that the epoxy is soaked in and the air can remove.

Any excess epoxy leaking from the gap should be removed using a cotton bud. The coupling should now look like in Fig. C.2c. As a last step, any excess epoxy that leaked into the gap between light guide and mold should be removed using small lint-free paper cuts, see Fig. C.2d. Otherwise, the light guide will stick to the mold and will be hard to remove. Also, the transition from light guide

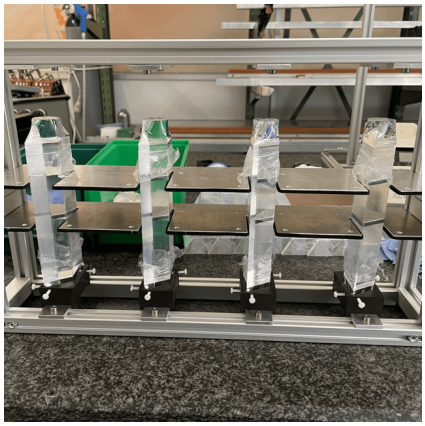

(a) Scintillator/light guide coupling station.

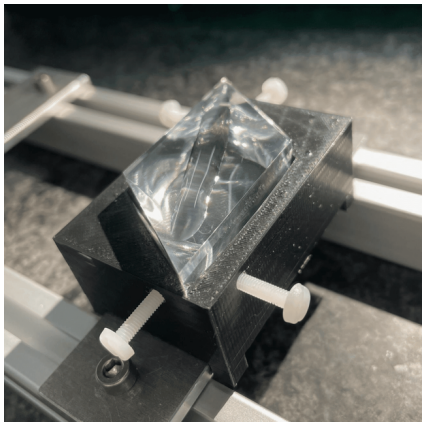

(b) Diagonally applied epoxy.

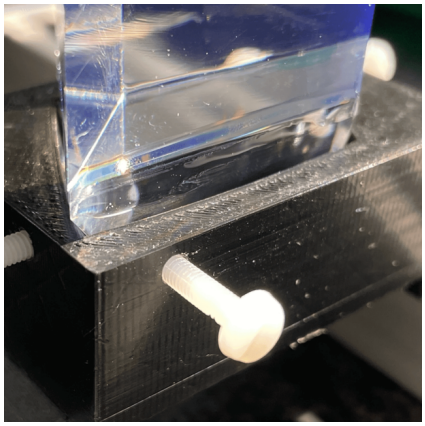

(c) Excess epoxy has been removed using cotton buds.

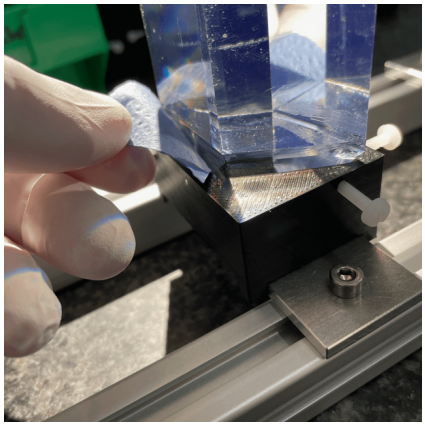

(d) Cleaning gaps with lint-free paper cuts.

FIGURE C.2. Coupling scintillator and light guides.

to scintillator should be cleaned in the same manner.

The epoxy should now harden for 48 h. After that, flip the coupling station and couple the second light guide. The mixed but unused epoxy has to be dumped after 8 h.

Coupling Light Guides and PMTs The station for coupling light guides and PMTs, see Fig. C.3a, can be used for four couplings simultaneously as well. So do the following steps in parallel as for coupling scintillator and light guides, and wear plastic gloves throughout the process. Note that when using the term "scintillator" in this paragraph, the already coupled combination of scintillator and light guides is meant.

First, plug the PMT onto a high-voltage socket, remove the rubber cap from the PMT, and clean the PMT window using ethanol and a lint-free cloth. Also, clean the coupling area of the light guide and the surrounding edges. It is also recommended to put a ring of paper around the PMT,

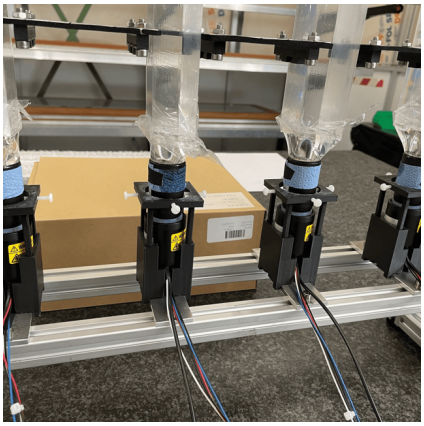

(a) Light guide/PMT coupling station.

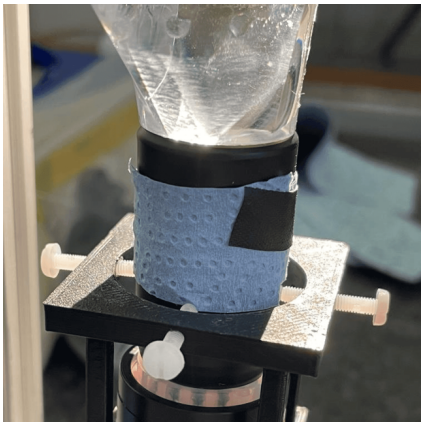

(b) PMT adjusted to light guide.

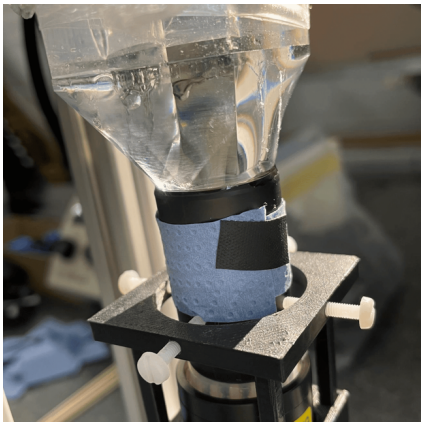

(c) Epoxy layer between light guide and PMT.

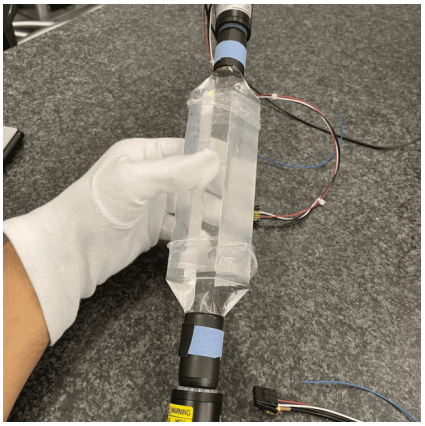

(d) Scintillation detector ready for wrapping.

FIGURE C.3. Coupling light guides and PMTs.

see Fig. C.3b, to prevent excess epoxy from flowing into the connection between PMT and socket.

Next, place the PMT inside the respective 3D-printed mold and centrally fixate it using the four plastic screws. Now, put it into the coupling station and do the same with the scintillator. Gently lower the scintillator onto the PMT and adjust the PMT position using the plastic screws, see Fig. C.3b. Be careful so that the components do not get scratched and do this step with highest precision since it is crucial for the final coupling result.

Lift the scintillator again and put a drop of epoxy in the middle of the PMT window. Again, about 0.1 ml should be used. Lower the scintillator until it touches the epoxy. Do this gently and make sure you do not capture any air bubbles. Lower the scintillator further so that it rests on the epoxy layer. The epoxy should fill the complete gap between light guide and PMT, see Fig. C.3c. If not, slowly fill the gap with additional epoxy and make sure you do not trap air within the gap. Finally, remove any excess epoxy with a cotton bud.

The epoxy should now harden for 48 h before flipping the coupling station and coupling the second PMT. After that, the scintillation detector is completely coupled and ready for wrapping, see Fig. C.3d.

C.1.3 Wrapping Guide

In addition to the coupling guide in Appendix C.1.2, this section guides through the wrapping procedure used for the MAGIX trigger detectors. PTFE is used as a reflective layer around scintillator and light guides. Light-tightness is achieved by wrapping the whole detector in black polyethylene (PE) foil.

Wrapping Preparation Before wrapping, make sure you have the following things available: A completely coupled scintillation detector; PTFE tape; black PE foil; black, light-tight sealing tape; tesafilm invisible®; scissors; lint-free cotton gloves; ethanol; a lint-free cloth; two hair clips, and the wrapping station with its 3D-printed molds, see Fig. C.4a. For the final trigger detectors, PTFE tape with a thickness of 75 µm and a width of 19 mm made by Silverline Tools has been used. As sealing tape, the 25 mm wide and 250 µm thick Scotchrap 50 corrosion tape by 3M has been utilized.

First, remove the paper rings from the PMTs if some were used for coupling. Also, document the serial numbers of the components so that the matching with data from previous measurements, e.g. the final test sheet by Hamamatsu, is still possible after wrapping. Next, put on the lint-free cotton gloves, place the trigger detector inside the molds, and clamp it into the wrapping station. It is helpful to fixate the cables using the hair clips, see Fig. C.4a. Now, remove the protective foil from the scintillator and clean the scintillator and the light guides using ethanol and the lint-free cloth, see Fig. C.4b.

Additionally, a PE foil cut measuring 23.5 cm × 27.5 cm needs to be prepared, see Fig. C.4c. The best way to do this has proven to be using a paper cutting machine, see Fig. C.4d. To ensure a clean cut, it is best to place the PE foil between two sheets of DIN A4 paper.

PTFE Wrapping As a starting point, use one of the sharp corners of the scintillator at the transition to the upper light guide to fixate the PTFE tape with your finger (wear cotton gloves!). After one winding, the PTFE tape will hold by itself if you make it overlap, see Fig. C.5a. After that, wrap the scintillator one winding after another, always overlapping with the previous winding, until you reach the lower light guide, see Fig. C.5b. Approximately half a tape width overlap has proven to be effective.

For the upper light guide, start again at one of the sharp corners of the scintillator. The PTFE tape can be fixated around the scintillator by doing one overlapping winding and using the corner as an attachment point, see Fig. C.5c. Make sure that for the first winding, half a tape width or more does cover the light guide. Now, the PTFE tape can be wrapped around the light guide.

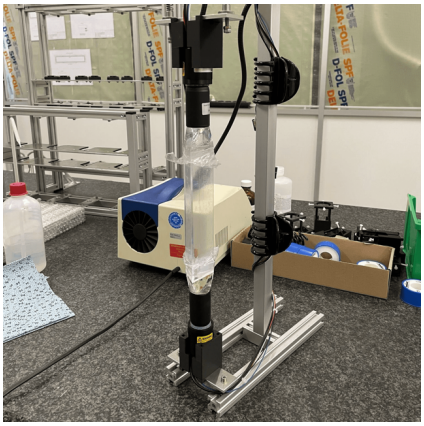

(a) Scintillation detector inside wrapping station.

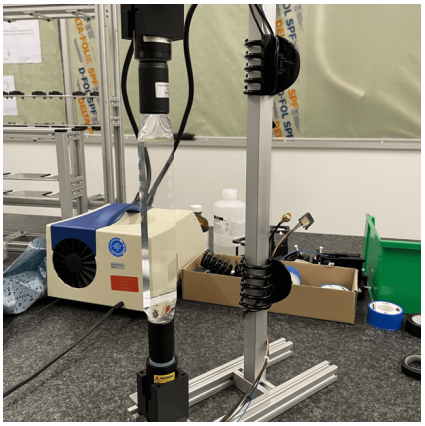

(b) Foil has been removed, surfaces have been cleaned.

(c) PTFE tape, sealing tape, tesafilm invisible®, and PE foil cut.

(d) Paper cutting machine for PE foil preparation.

FIGURE C.4. Wrapping preparation.

It is helpful to cut off about 20 cm of tape from the attachment point to get rid of the tape roll. While wrapping the light guide, use the fingers to fixate the PTFE tape at some points since it easily slides down the light guide if stretched too hard. Make sure that the light guide is fully covered. The result then looks like in Fig. C.5d. It does not matter if the PTFE tape covers the PMT in some spots. Finally, turn the wrapping station on its side and wrap the second light guide repeating the above steps.

Light-tight Wrapping Wrapping the detector with the light-tight, black PE foil happens in several steps. First, the scintillator, the light guides, and the transitions to the PMTs are wrapped with the 23.5 cm × 27.5 cm PE foil cut. After that, the PMTs and the transitions to the high-voltage sockets are completely covered with black, light-tight sealing tape. Please note that the transitions to the high-voltage sockets must be wrapped particularly carefully. If this is not

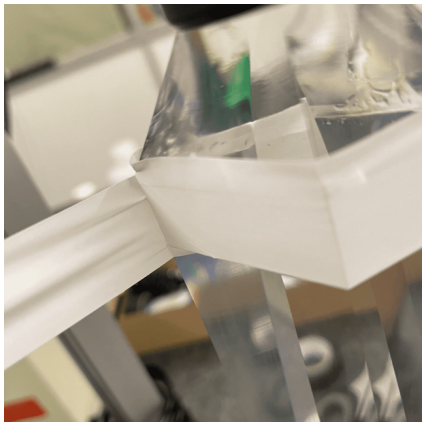

(a) Use overlap to fixate PTFE tape.

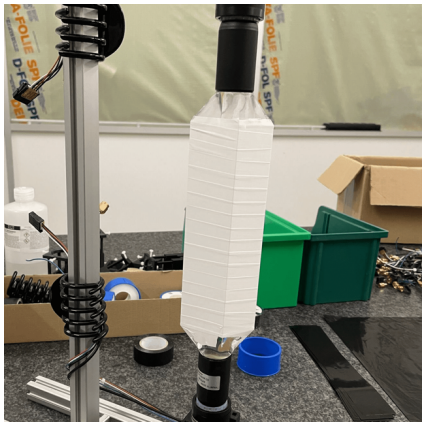

(b) PTFE wrapped scintillator.

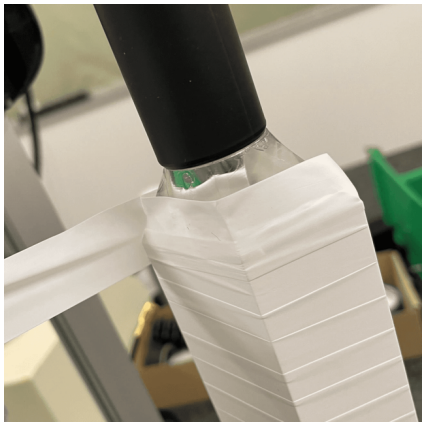

(c) Use scintillator edge as attachment point.

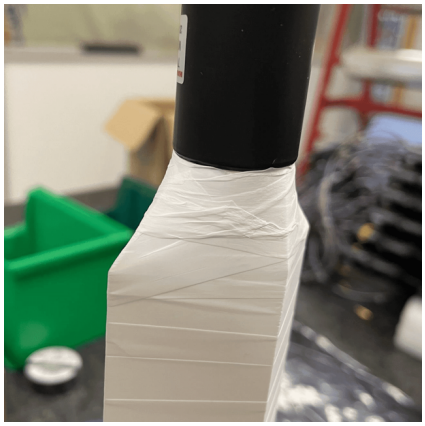

(d) PTFE wrapped light guide.

FIGURE C.5. PTFE wrapping.

taken into account, PMT noise will be significantly increased.

For wrapping the scintillator, the light guides, and the transitions to the PMTs, start with fixating the short 23.5 cm side of the PE foil cut with three pieces of tesafilm invisible® on one of the large scintillator surfaces, see Fig. C.6a. Wrap the cut around the scintillator (the 27.5 cm are enough for almost exactly two windings), stretch it so that it fits as tightly as possible, and fixate it with three pieces of tesafilm invisible®, see Fig. C.6b. Make sure that both PMTs are equally covered and that the resulting foil seam runs along the midline of the large scintillator surface as the seam will later be covered with sealing tape, which is too thick to fit inside the gap between two trigger detectors. Now, take the protruding PE foil at one side of one PMT, see Fig. C.6c, create a flap, fold it over the ridge of the light guide, and fixate it with tesafilm invisible®, see Fig. C.6d. Do the same on the other side of the PMT. Then, flip the wrapping station and do the same with the protruding PE foil at the second PMT.

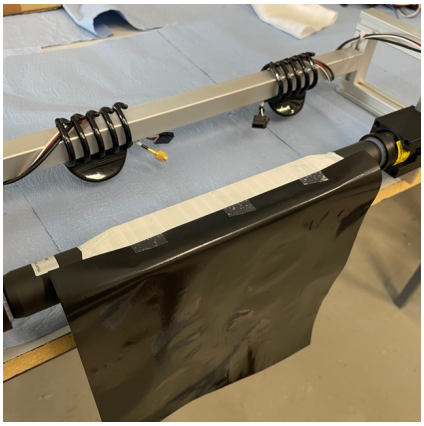

(a) Large scintillator surface as starting point for PE foil cut.

(b) PE foil cut fully wrapped.

(c) Protruding PE foil.

(d) Create flap and fixate with tesafilm invisible®.

FIGURE C.6. Light-tight wrapping.

After the foil flaps have been fixated, remove the detector from the wrapping station and cover the foil seam with a long strip of sealing tape, see Fig. C.7a. Now, only the surfaces of the PMTs, which have not yet been wrapped, and the transitions to the high-voltage sockets remain, which will now be completely wrapped with sealing tape. Start at the transition from light guide to PMT, ensuring that the fixated foil flaps are completely covered, and proceed towards the transition from PMT to high-voltage socket, see Fig. C.7b. Next, wrap the transition from PMT to high-voltage socket, starting with a tape winding around the high-voltage socket and proceeding upwards towards the PMT, see Fig. C.7c. Apply the tape up to about the middle of the PMT and ensure that the exposed end of the tape is not too tight. Otherwise, it will eventually come loose over time. Repeat the above steps for both detector sides and the wrapping procedure is finished, see Fig. C.7d.

After the wrapping process, the trigger detector should be tested for light-tightness. For that,

(a) Foil seam covered with sealing tape.

(b) PMT covered with sealing tape.

(c) Transition from PMT to high-voltage socket fully wrapped.

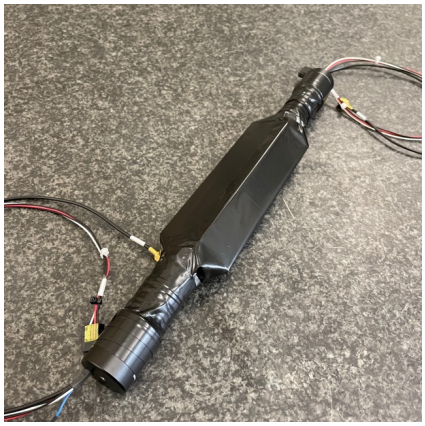

(d) Ready wrapped scintillator.

FIGURE C.7. Light-tight wrapping (cont.).

check the PMT signals with an oscilloscope, where the trigger threshold is set to a relatively low level, i.e. a few mV. Use a flash light as artificial light source and illuminate the entire surface of the detector, while paying attention to whether the signal rate is influenced. If any spot of the detector is not light-tightly wrapped, a high rate of small signals with amplitudes of a few mV will be observable.

C.2 EPICS Driver for the Slow Control of the Trigger Layer

The EPICS driver for the trigger layer power supply consists of several parts: A section inside the EPICS command file (`*.cmd`), two database files (`*.db`), and a protocol file (`*.proto`). Inside the EPICS command file, the TCP/IP connection with the Z-turn board of the slow control crate is configured and the required EPICS PVs are loaded from the database files. The database files define the individual EPICS PVs using so-called *records*, where each record provides exactly one

EPICS PV. The TCP/IP communication with the Z-turn board of the slow control crate is stored inside the protocol file.

C.2.1 Section of the Command File

Code C.1 shows an example for the section that has to be included inside the EPICS command file. The TCP/IP connection with the Z-turn board is configured in lines 2, 3, and 4, where <port_name> is the freely selectable name of the IP port, <ip_address> is the network-dependent IP address of the Z-turn board, and the communication port to be used is "5000" [121]. In lines 7, 8, and 9, the database files are exemplarily loaded with different configurations, using the standard EPICS-module `dbLoadRecords` and the module `dbLoadMultiRecords` written by S. Lunkenheimer [7]. In addition to the names of the database files, the parameters "P", "PORT", and "BASE" are passed. The parameter "P" stands for the freely selectable device code that will reappear as the prefix of all created EPICS PVs, "PORT" is again the name of the IP port, and "BASE" determines the 4-pin jack addresses on the DAC boards that are to be loaded (0-79).

Code C.1: The section to include in the command file of the EPICS driver.

```
1    ## configure the TCP/IP connection to the slow control crate
2    drvAsynIPPortConfigure("<port_name>", "<ip_address>:5000 TCP", 0,
     1, 0)
3    asynSetTraceIOMask("<port_name>", -1, 0x2)
4    asynSetTraceMask("<port_name>", -1, 0x1)
5
6    ## load record instances from database files
7    dbLoadRecords("$(TOP)/db/devTriggerPS_crate.db","P=<device_name>,
     PORT=<port_name>")
8    dbLoadMultiRecords("$(TOP)/db/devTriggerPS_dacBoards.db", "P={<
     device_name>}, PORT={<port_name>}, BASE={30;31;38;39}")
9    dbLoadMultiRecords("$(TOP)/db/devTriggerPS_dacBoards.db", "P={<
     device_name>}, PORT={<port_name>}, BASE=60..69")
```

C.2.2 Database Files

Codes C.2 and C.3 show the database files of the EPICS driver. For details on the individual record fields, please refer to the EPICS documentation [94, 95, 96].

Code C.2: The EPICS driver's database file for the slow control crate (`devTriggerPS_crate.db`).

```
1    record(stringin, "$(P):getID") {
2        field(DESC, "Currently running application")
3        field(DTYP, "stream")
4        field(INP,  "@devTriggerPS.proto getID($(P)) $(PORT)")
5        field(PINI, "YES")
```

```
6     }
7
8     record(stringin, "$(P):getVER") {
9         field(DESC, "Version of currently running application")
10        field(DTYP, "stream")
11        field(INP,  "@devTriggerPS.proto getVER($(P)) $(PORT)")
12        field(PINI, "YES")
13    }
14
15    record(stringin, "$(P):reset") {
16        field(DESC, "Reset I2C bus and DACs")
17        field(DTYP, "stream")
18        field(INP,  "@devTriggerPS.proto reset($(P)) $(PORT)")
19        field(PINI, "YES")
20    }
21
22    record(stringin, "$(P):reinit") {
23        field(DESC, "Reinitializes currently running appl")
24        field(DTYP, "stream")
25        field(INP,  "@devTriggerPS.proto appReinit($(P)) $(PORT)")
26        field(PINI, "YES")
27    }
28
29    record(stringin, "$(P):errCount") {
30        field(DESC, "Number of stored errors in history")
31        field(DTYP, "stream")
32        field(INP,  "@devTriggerPS.proto errCount($(P)) $(PORT)")
33        field(PINI, "YES")
34    }
35
36    record(stringin, "$(P):errOldest") {
37        field(DESC, "Show oldest error and delete")
38        field(DTYP, "stream")
39        field(INP,  "@devTriggerPS.proto err?($(P)) $(PORT)")
40        field(PINI, "YES")
41    }
42
43    record(stringin, "$(P):errClear") {
44        field(DESC, "Clear error history")
45        field(DTYP, "stream")
46        field(INP,  "@devTriggerPS.proto errClear($(P)) $(PORT)")
47        field(PINI, "YES")
48    }
```

```
49
50      record(bo, "$(P):15VOnOff") {
51          field(DESC, "Turn on/off global 15V supply")
52          field(DTYP, "stream")
53          field(OUT,  "@devTriggerPS.proto setPS($(P)) $(PORT)")
54          field(ZNAM, "OFF")
55          field(ONAM, "ON")
56      }
57
58      record(bi, "$(P):get15VOnOff") {
59          field(DESC, "Is global 15V supply on or off?")
60          field(DTYP, "stream")
61          field(INP,  "@devTriggerPS.proto getPS($(P)) $(PORT)")
62          field(SCAN, "1 second")
63          field(PINI, "YES")
64          field(ZNAM, "OFF")
65          field(ONAM, "ON")
66      }
67
68      record(bo, "$(P):DAQOnOff") {
69          field(DESC, "Turn on/off DAQ voltage supply")
70          field(DTYP, "stream")
71          field(OUT,  "@devTriggerPS.proto setDAQ($(P)) $(PORT)")
72          field(ONAM, "OFF")
73          field(ZNAM, "ON")
74      }
75
76      record(bi, "$(P):getDAQOnOff") {
77          field(DESC, "Is DAQ voltage supply on or off?")
78          field(DTYP, "stream")
79          field(INP,  "@devTriggerPS.proto getDAQ($(P)) $(PORT)")
80          field(SCAN, "1 second")
81          field(PINI, "YES")
82          field(ONAM, "OFF")
83          field(ZNAM, "ON")
84      }
85
86      record(bo, "$(P):resetDAQ") {
87          field(DESC, "Reset DAQ voltage supply")
88          field(DTYP, "stream")
89          field(OUT,  "@devTriggerPS.proto setDAQ($(P)) $(PORT)")
90          field(ONAM, "RESET")
91          field(HIGH, 10)
```

```
92      }
```

Code C.3: The EPICS driver's database file for the DAC boards (`devTriggerPS_dacBoards.db`).

```
    record(ao, "$(P):$(BASE):setVoltage") {
        field(DESC, "Set voltage in mV")
        field(EGU, "mV")
        field(HOPR, "5000")
        field(LOPR, "0")
        field(PREC, 1)
        field(FLNK, "$(P):$(BASE):setVoltageRaw")
    }

    record(calcout, "$(P):$(BASE):setVoltageRaw") {
        field(DESC, "Set voltage as ADC value")
        field(DTYP, "stream")
        field(HOPR, "65535")
        field(LOPR, "0")
        field(PREC, 1)
        field(INPA, "$(P):$(BASE):setVoltage")
        field(CALC, "FLOOR(0.5 + A/5000*65535)")
        field(OUT,  "@devTriggerPS.proto setHV($(P),$(BASE)) $(PORT)")
    }

    record(ai, "$(P):$(BASE):getVoltageRaw") {
        field(DESC, "Get voltage as ADC value")
        field(DTYP, "stream")
        field(INP,  "@devTriggerPS.proto getHV($(P),$(BASE)) $(PORT)")
        field(SCAN, "1 second")
        field(FLNK, "$(P):$(BASE):getVoltage")
    }

    record(calc, "$(P):$(BASE):getVoltage") {
        field(DESC, "Get voltage in mV")
        field(EGU, "mV")
        field(PREC, "5")
        field(INPA,  "$(P):$(BASE):getVoltageRaw")
        field(CALC, "A/65535*5000")
        field(SCAN, "Passive")
        field(HOPR, "5000")
        field(LOPR, "0")
        field(FLNK, "$(P):$(BASE):getVoltageV")
        field(PINI, "YES")
    }

    record(calc, "$(P):$(BASE):getVoltageV") {
```

```
43          field(DESC, "Get voltage in V")
44          field(EGU, "V")
45          field(PREC, "5")
46          field(INPA,  "$(P):$(BASE):getVoltage")
47          field(CALC, "A/1000")
48          field(SCAN, "Passive")
49          field(HOPR, "5")
50          field(LOPR, "0")
51      }
52
53      record(bo, "$(P):$(BASE):15VOnOff") {
54          field(DESC, "Turn on/off 15V supply for base")
55          field(DTYP, "stream")
56          field(OUT,  "@devTriggerPS.proto setSW($(P),$(BASE)) $(PORT)")
57          field(ZNAM, "OFF")
58          field(ONAM, "ON")
59      }
60
61      record(bi, "$(P):$(BASE):get15VOnOff") {
62          field(DESC, "15V supply for base on or off?")
63          field(DTYP, "stream")
64          field(INP,  "@devTriggerPS.proto getSW($(P),$(BASE)) $(PORT)")
65          field(SCAN, "1 second")
66          field(PINI, "YES")
67          field(ZNAM, "OFF")
68          field(ONAM, "ON")
69      }
```

C.2.3 Protocol File

The protocol file of the EPICS driver is shown in Code C.4, where all available TCP/IP commands for the slow control crate and the DAC boards to be used by EPICS are implemented.

Code C.4: The protocol file of the EPICS driver (`devTriggerPS.proto`).

```
1       getID {
2         out "id\r\n";
3         in "%s\r\n";
4         ExtraInput = Ignore;
5       }
6
7       getVER {
8         out "ver\r\n";
9         in "%s\r\n";
```

```
10        ExtraInput = Ignore;
11      }
12
13      reset {
14        out "reset\r\n";
15        in "%s\r\n";
16        ExtraInput = Ignore;
17      }
18
19      appReinit {
20        out "app reinit\r\n";
21        in "%s\r\n";
22        ExtraInput = Ignore;
23      }
24
25      errCount {
26        out "err count\r\n";
27        in "%s\r\n";
28        ExtraInput = Ignore;
29      }
30
31      err? {
32        out "err ?\r\n";
33        in "%s\r\n";
34        ExtraInput = Ignore;
35      }
36
37      errClear {
38        out "err clear\r\n";
39        in "%s\r\n";
40        ExtraInput = Ignore;
41      }
42
43      getHV { # $1=$(P); $2={Base}
44        out "hv \$2 ?\r\n";
45        in "%d";
46        ExtraInput = Ignore;
47      }
48
49      setHV { # $1=$(P); $2=${Base}
50        out "hv \$2 %d\r\n";
51        in "ok\r\n";
52        ExtraInput = Ignore;
```

```
53      @init {
54        getHV;
55      }
56    }
57
58    getSW { # $1=$(P); $2={Base}
59      out "sw \$2 ?\r\n";
60      in "%b";
61      ExtraInput = Ignore;
62    }
63
64    setSW { # $1=$(P); $2=${Base}
65      out "sw \$2 %b\r\n";
66      in "ok\r\n";
67      ExtraInput = Ignore;
68      @init {
69        getSW;
70      }
71    }
72
73    getPS { # $1=$(P)
74      out "ps ?\r\n";
75      in "%b";
76      ExtraInput = Ignore;
77    }
78
79    setPS { # $1=$(P)
80      out "ps %b\r\n";
81      in "ok\r\n";
82      ExtraInput = Ignore;
83      @init {
84        getPS;
85      }
86    }
87
88    getDAQ{ # $1=$(P)
89      out "daq ?\r\n";
90      in "%b";
91      ExtraInput = Ignore;
92    }
93
94    setDAQ{ # $1=$(P)
95      out "daq %b\r\n";
```

```
96        in "ok\r\n";
97        ExtraInput = Ignore;
98        @init {
99          getDAQ;
100       }
101     }
```

C.3 More on the Mounting of the Trigger Layer

This appendix provides further information on the mounting of the MAGIX trigger layer. A short overview completes the description from Section 5.4 and the detailed assembly guide can be used if additional specimens are needed or individual instances need to be repaired.

Overview The trigger layer mounting is built in the form of a drawer that is directly attached to the lower flange of the TPC frame using a pair of horizontally mounted telescopic rails. It is composed of a 4 mm steel sheet and a frame of different aluminum profiles. The short sides of the frame are made from L-shaped profiles, incorporating cut-outs for the power supply and control cables of the DAC boards. The long sides of the frame are made from rectangular profiles and provide SMA feed-throughs for connecting the readout cables. The steel sheet includes a large rectangular cut-out for minimizing the material budget between the trigger layer and the first veto layer. Two quadratic aluminum profiles are mounted along the edges of the rectangular cut-out to prevent the mounting from too much sagging. The trigger detectors are positioned using 3D-printed molds that are plugged onto steel spacers, which are screwed into the steel sheet. Additional 3D-printed clamps are used for fixation. The DAC boards are mounted using steel spacers as well.

A CAD model of the trigger layer mounting is shown in Fig. C.8. The outer dimensions of the mounting are a width of 1098 mm, a height of 80 mm, and a depth of 420 mm. The empty mounting has a weight of 15.1 kg. If the trigger detectors, DAC boards, and 3D-printed parts are added, the weight increases to 27.2 kg.

The employed telescopic rails are from the model D5VF by Chambrelan [173], formerly Profilscope. When mounted horizontally, their maximal payload is 27 kg per pair, which unfortunately had to be exceeded by 0.2 kg. However, this corresponds to an exceeding of only 0.74 % and should fall within the safety margin. For more details on the telescopic rails, please refer to the respective data sheet.

All technical drawings are stored on the internal Autodesk Vault server of the MAGIX collaboration (pdf and dwg formats). Tab. C.2 shows the corresponding file names and the necessary parts for assembly.

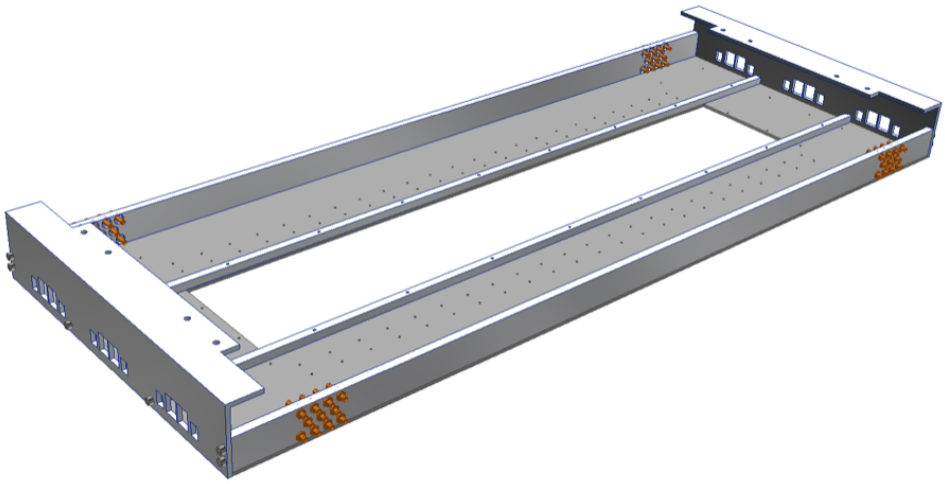

FIGURE C.8. CAD model of a fully assembled trigger layer mounting. The DAC boards and the 3D-printed molds are not shown.

Part(s)	**Name of drawing(s)**	**Necessary screws**
L-shaped profiles	*LProfileL, LProfileR*	6× M6×12 (ISO 4762)
Steel sheet	*SteelSheet*	36× M4×10 (ISO 10642)
Quadratic profiles	*MidProfileV2*	4× M5×20 (ISO 4762)
Rectangular profiles	*SideProfileV2*	8× M5×20 (ISO 4762)
SMA feed-throughs	/	44× DELOCK 8879
DAC boards	/	24× steel spacer M3×5.0, 24× M3×4 (ISO 4762)
3D-printed molds and clamps	*Scintifixer_reduced_v2*, *ScintifixerBogen*	92× steel spacer M3×15.0, 92× M3×10 (ISO 4762)
Rectangular profiles	*SideProfileV3*	8× M5×20 (ISO 4762)
3D-printed molds and clamps	*Scintifixer_reduced_v3*, *ScintifixerBogen_v2*	92× steel spacer M3×15.0, 92× M3×10 (ISO 4762)
3D-printed boxes for passive 20 dB attenuators	*SMA_Holder_CapAtFront*, *SMA_Holder_FeedthroughPlate2*	16× M4×10 (ISO 4762), 4× M3×16 (ISO 4762)

TABLE C.2. Overview on the individual parts of the trigger layer mounting. The names of the corresponding technical drawings are given together with the necessary screws for assembly. The lower part of the table lists the upgrades mentioned in Chapter 9.

(a) The nuts of the feed-throughs should be on the side without the countersinks.

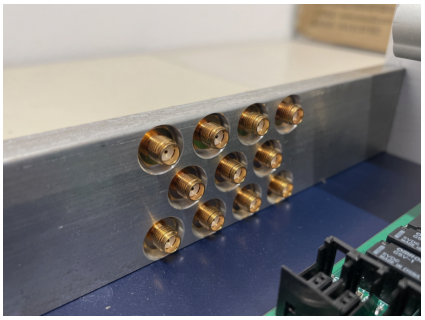

(b) The countersinks should be on the inner side of the mounting.

FIGURE C.9. Assembling the SMA feed-throughs.

Assembly Guide Before starting, make sure you have all the parts and screws available that are listed in Tab. C.2. All the screws, spacers, and SMA feed-throughs can be bought off the shelf. Start with screwing the SMA feed-throughs to the rectangular aluminum profiles using the countersunk holes, where the nuts should be on the side without the countersinks, see Fig. C.9a. The rectangular profiles can then be screwed to the L-shaped profiles using eight of the M5×20 ISO 4762 screws. Note that the countersinks should be on the inner side of the mounting as shown in Fig. C.9b. Continue with adding the quadratic aluminum profiles using the remaining four M5×20 ISO 4762 screws. Then, turn everything upside down and mount the steel sheet using the 36 M4×10 ISO 10642 screws. Flipping the mounting again, the steel spacers can be screwed to the M3 threads inside the steel sheet. Use the M3×5.0 spacers with the M3×4 ISO 4762 screws to attach the DAC boards. The M3×15.0 spacers are used for plugging the 3D-printed molds. Finally, use the six M6×12 ISO 4762 screws to connect the mounting to the telescopic rails.

APPENDIX D

APPENDIX TO CHAPTER 6

D.1 More on the Veto System Drawers

This appendix provides further information on the veto system drawers of the MAGIX trigger veto system. A short overview completes their description from Section 6.1.1 and the detailed assembly guide can be used if additional specimens are needed or individual instances need to be repaired.

Overview Each drawer consists of two levels, each of which provides space for one veto layer or one lead absorber layer. Each level is composed of a 4 mm steel sheet and a frame of aluminum profiles, of which the side and rear profiles are permanently screwed to the steel sheets and the front profiles can be mounted as required - the lead absorber layers need the front profiles for stability, the veto layers do not. The side profiles are mounted to a pair of telescopic rails using an adapter profile in between that is needed to enable the screw connection and is also used for mounting handles and lifting brackets. The placement of the veto and lead absorber layers inside the drawer can be fixed using the threaded holes in the front and rear profiles. The CAD model of a fully assembled drawer can be seen in Fig. 6.2a.

The outer dimensions of a drawer, including the telescopic rails, are a width of 1098 mm, a height of 32 mm, and a depth of 300 mm. Its weight, excluding veto or lead absorber layers, is 23.9 kg. If the rails are excluded, width and weight reduce to 1064 mm and 22.0 kg, respectively.

As telescopic rails, the model MX-DTP30.030 by Miluxor [174] is used[1], which exhibit a maximal

[1] Unfortunately, Miluxor stopped the production of the model MX-DTP30.030 at some point. Thus, two of the 18 assembled drawers employ telescopic rails of the model E1400 by Chambrelan [175], formerly Profilscope, instead. The parameters of the E1400 rails are comparable to those of the MX-DTP30.030, ensuring no anticipated drawbacks. The only notable difference is that the E1400's outer dimensions are slightly smaller than those of the MX-DTP30.030.

Part(s)	**Name of drawing**	**Necessary screws**
Left adapter profile	*AdapterLinks*	4× M5×10 (ISO 4762)
Right adapter profile	*AdapterRechts*	4× M5×10 (ISO 4762)
Left lower profile	*ProfilLinksUnten*	5× M4×12 (ISO 4762)
Left upper profile	*ProfilLinksOben*	5× M4×12 (ISO 4762)
Right lower profile	*ProfilRechtsUnten*	5× M4×12 (ISO 4762)
Right upper profile	*ProfilRechtsOben*	5× M4×12 (ISO 4762)
Lower steel sheet	*StahlblechUnten*	19× M3×30, 2× M3×32 (ISO 14581)
Lower rear profile	*ProfilHintenUnten*	/
Upper steel sheet	*StahlblechOben*	/
Upper rear profile	*ProfilHintenOben*	/
Lower front profile	*VorderwandUnten*	11× M3×12 (ISO 14581)
Upper front profile	*VorderwandOben*	11× M3×10 (ISO 14579)
Handles	/	2× M3×10, 2× M4×10 (DIN 464)
Lifting brackets	/	4× M4×10 (ISO 3266)

TABLE D.1. Overview on the individual drawer parts. The names of the corresponding technical drawings are given together with the necessary screws for assembly.

load per pair of 120 kg. More details can be found in the respective data sheet.

The technical drawings of the individual drawer parts can be found on the internal Autodesk Vault server of the MAGIX collaboration (pdf and dwg formats). Tab. D.1 shows the corresponding file names as well as the necessary screws for assembly.

Stability Analysis The results of the stability analysis for the veto system drawers using Autodesk Inventor 2019 are shown in Fig. D.1, once for a closed drawer and once for an open drawer. The study is performed modeling the weight of two lead absorber layers placed inside the drawer, since this will be the maximal load a drawer will encounter. Each of the two lead absorber layers has a weight of 26.62 kg but is modeled as a pressure of 1 kPa on the respective steel sheet, which corresponds to a modeled weight of 31.90 kg. Thus, a safety margin of roughly 20 % is considered. In addition to the two lead absorber layers, the influence of the drawers' own weight is accounted for by using Inventor's option to include gravity. For the closed drawer, a maximal sagging of 0.7616 mm is observed within the red areas, see Fig. D.1a. For the open drawer, the maximal sagging slightly increases to 1.2660 mm, see Fig. D.1b.

Assembly Guide Before starting the assembly, make sure you have all the parts and screws available listed in Tab. D.1. The two M3×32 ISO 14581 screws probably can not be bought off the shelf. Instead, use two screws of length 35 mm and shorten them using a jab saw or belt sander. In addition, it has proven helpful to fix the telescopic rails with tape so that they stay closed during the assembly.

However, this is inconsequential as the positions of the screw connections are identical.

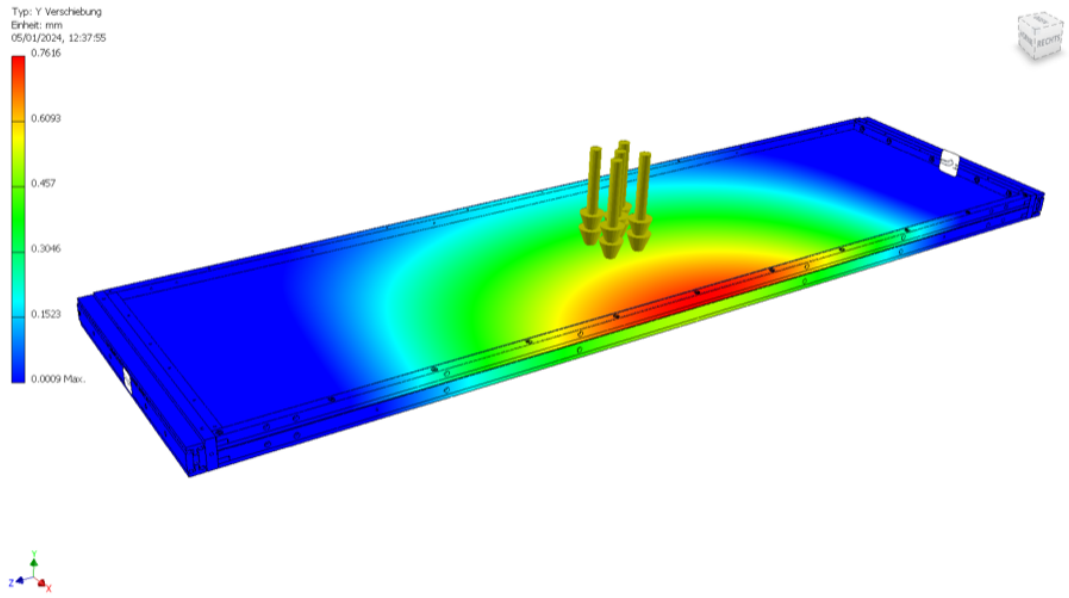

(a)

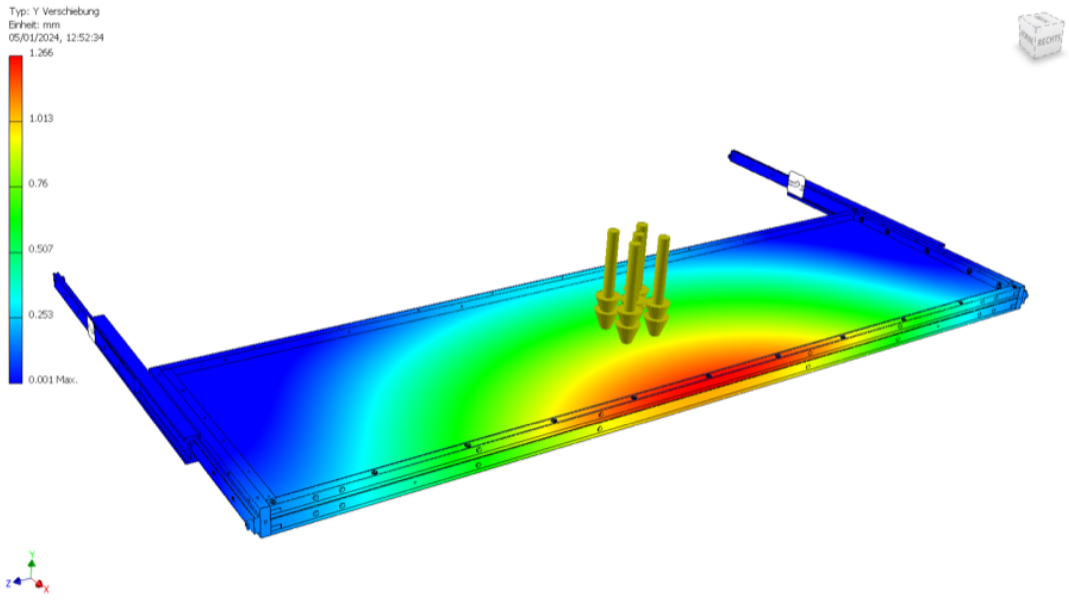

(b)

FIGURE D.1. Stability analysis for the veto system drawers using Autodesk Inventor 2019. The two pressures representing the lead absorber layers are each illustrated by four arrows arranged in a square. The additional arrow at the center of the squares indicates the direction of gravity. Within the red areas, the closed (a) and the open (b) drawer show a maximal sagging of 0.7616 mm and 1.2660 mm, respectively.

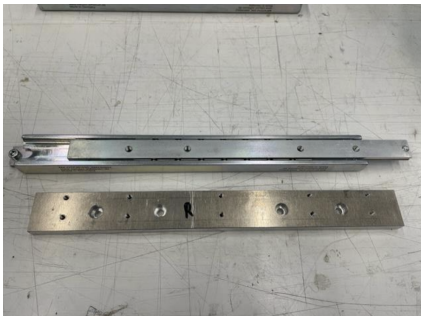

(a) Right adapter profile and telescopic rail.

(b) Screw right adapter profile to telescopic rail.

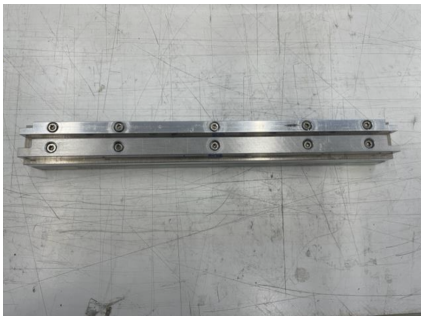

(c) Screw right lower and upper profiles to right adapter profile.

FIGURE D.2. Assembling the drawer side parts, exemplarily shown for the right side part.

Start with mounting the drawer side parts consisting of the telescopic rails, the adapter profiles, and the side profiles. Fig. D.2 shows this exemplarily for the right side part. Make sure that the telescopic rail and the adapter profile are oriented correctly, see Fig. D.2a. The face of the adapter profile with the single threaded hole will be the front side of the drawer, the face with the two threaded holes will be the top side. The single threaded hole can be used to mount an M4×10 DIN 464 screw as a handle, the two threaded holes on the top side can be used for mounting two M4×10 ISO 3266 screws as lifting brackets. Now, screw the adapter profile to the telescopic rail using the four M5×10 ISO 4762 screws, see Fig. D.2b, and make sure that the two bottom sides are in the same plane. After that, mount the upper and lower side profiles to the adapter profile using the M4×12 ISO 4762 screws. Leave both profiles slightly loose so that the upper steel sheet will have some clearance to fit in between, see Fig. D.2c. Repeat the previous steps for the left side part.

Next, the side parts will be joined with the steel sheets and rear profiles. Therefore, place the side parts upside down and clamp the upper rear profile and the upper steel sheet in between the side parts, see Fig. D.3a. The side of the steel sheets and side profiles where the two closely placed holes are located, will be the front side of the drawer. Make sure that all holes align perfectly. Now,

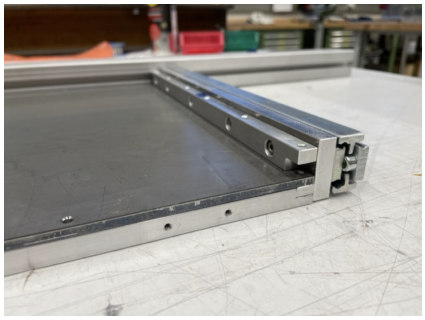

(a) Clamp upper rear profile and upper steel sheet in between the side parts.

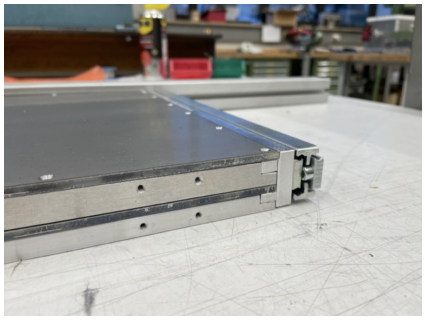

(b) Add lower rear profile and lower steel sheet.

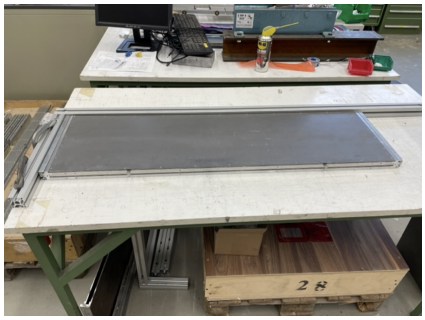

(c) Screw everything together.

(d) Mount front profiles as required.

FIGURE D.3. Connecting the side parts with the steel sheets, rear profiles, and front profiles.

pull the M4×12 ISO 4762 screws of the lower side profiles tight since they will not be accessible anymore once the lower steel sheet has been added. Then go on with adding the lower rear profile and the lower steel sheet, see Fig. D.3b. Again, make sure that all holes align perfectly. The parts can now be screwed together by using the M3 ISO 14581 screws, see Fig. D.3c. The two screws of length 32 mm are used for the rear corner holes and the screws of length 30 mm for all other holes except the holes along the front side of the drawer as these will be used for screwing the front profiles. If you do the assembly alone, it can be helpful to use a frame for clamping the parts like seen in Fig. D.3c. Finally, do not forget to tighten the M4×12 ISO 4762 screws of the upper side profiles that have been left loose when mounting the side parts.

If the drawer will be used for holding one or two lead absorber layers, it is necessary to mount the respective front profile(s), see Fig. D.3d. The lower front profile gets screwed from the bottom using the M3×12 ISO 14581 screws. For the upper front profile, screw from above using the M3×10 ISO 14579 screws. The lower front profile should be provided with the two M3×10 DIN 464 screws serving as handles. Use two of the threaded holes on the side for this.

Cradle part(s)	**Name of drawing**	**Necessary screws**
Lower steel beams	*QuertraegerVierkant*	8× M8×18 (ISO 4762)
Lower adapter pieces	*GegenstueckVierkant*	2× M8×65 (ISO 4762), 4× M8 washer (ISO 7092), 2× M8 nut (ISO 4032), 8× M8×18 (ISO 4762)
L-shaped profiles	*LProfil2*	4× SKF SM12 E-SS, 4× SKF SMSW 16 LPAST, 4× M16×140 (ISO 4762), 4× M16 nut (ISO 4032), 8× M16 washer (ISO 7092)
Hole plates	*LochplatteFlexibel*	8× M8×12 (ISO 4762), 72× M5×14 (ISO 4762)
Upper steel beam left	*QuertraegerVierkant-KurzLinks*	4× M8×18 (ISO 4762), 4× M8 washer (ISO 7092)
Upper steel beam right	*QuertraegerVierkant-KurzRechts*	4× M8×18 (ISO 4762), 4× M8 washer (ISO 7092)
Upper adapter pieces	*GegenstueckVierkant-Oben*	2× M8×65 (ISO 4762), 12× M8 washer (ISO 7092), 2× M8 nut (ISO 4032), 8× M8×12 (ISO 4762)

TABLE D.2. Overview on the individual parts of a veto system cradle. The names of the corresponding technical drawings are given together with the necessary screws for assembly.

D.2 More on the Veto System Cradle

This appendix provides additional information on the veto system cradle in case some parts need to be replaced or repaired.

The CAD model of the veto system cradle is shown in Fig. 6.3 and all corresponding technical drawings can be found on the internal Autodesk Vault server of the MAGIX collaboration (pdf and dwg formats). The corresponding file names as well as the necessary screws for assembly are listed in Tab. D.2.

The cradle is based on two steel beams (lower steel beams) with a rectangular profile ($70 \times 50 \times 4.0\,\text{mm}$) that are directly mounted to the walls of the shielding house. In order to be able to install the beams, they are realized as "telescopic beams", where short steel beams (lower adapter pieces) with a smaller rectangular profile ($60 \times 40 \times 5.0\,\text{mm}$) are used that can be inserted into the larger steel beams. The smaller and larger steel beams are connected using elongated holes so that the overall length of the telescopic beam can be adjusted to the exact distance between the shielding house walls.

The drawers are mounted to two aluminum plates with a precisely produced hole pattern (hole plates), ensuring the concise positioning of the veto system drawers with respect to each other. The hole plates are attached to the lower steel beams using L-shaped profiles and adjustable chocks[2] with spherical washers[3], where elongated holes ensure the adjustability of the hole plates in the two directions not covered by the adjustable chocks. At the upper edges of the hole plates,

[2] SKF Vibracon SM 12 E-SS
[3] SKF SMSW 16LPAST

two shorter telescopic beams are introduced as additional struts (upper steel beam left, upper steel beam right, upper adapter pieces).

The weight of a veto system cradle, without any drawers attached, amounts to 32.5 kg. The weight of a complete veto system, including nine drawers with 15 lead absorber layers and three veto layers, adds up to roughly 667.2 kg.

APPENDIX E

APPENDIX TO CHAPTER 7

E.1 Plots for the Impact of the Effective Signal Threshold - Alternative Presentation

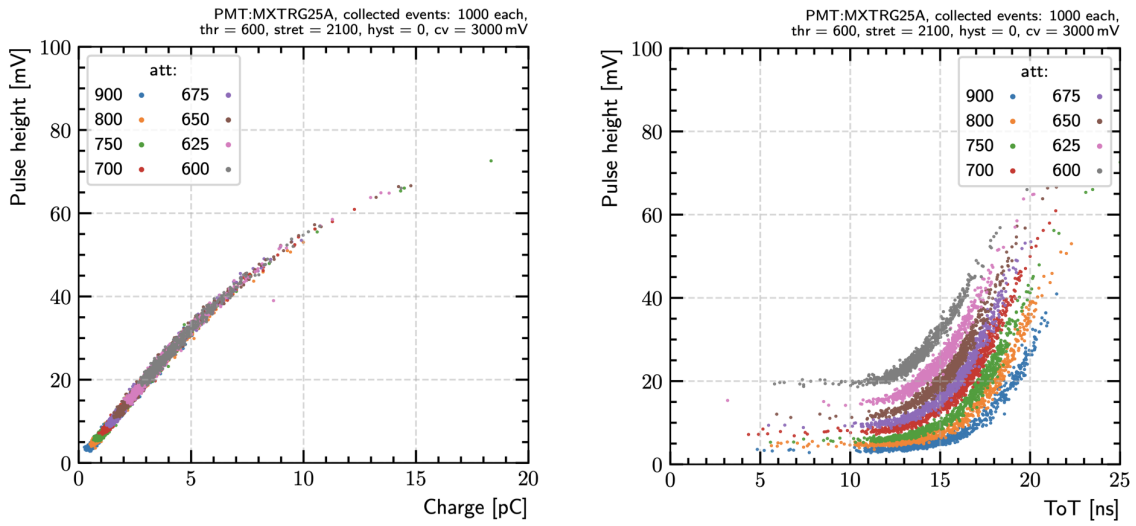

(a) (b)

FIGURE E.1. Alternative plots illustrating the impact of the effective signal threshold on the PMT pulses' characteristic variables charge and pulse height, as well as on the ToT of the output logic pulses. Compared to the plots in Section 7.2.3, the pulse height has been plotted using a linear scale. A fixed *thr* value of 600 has been used and *att* has been varied.

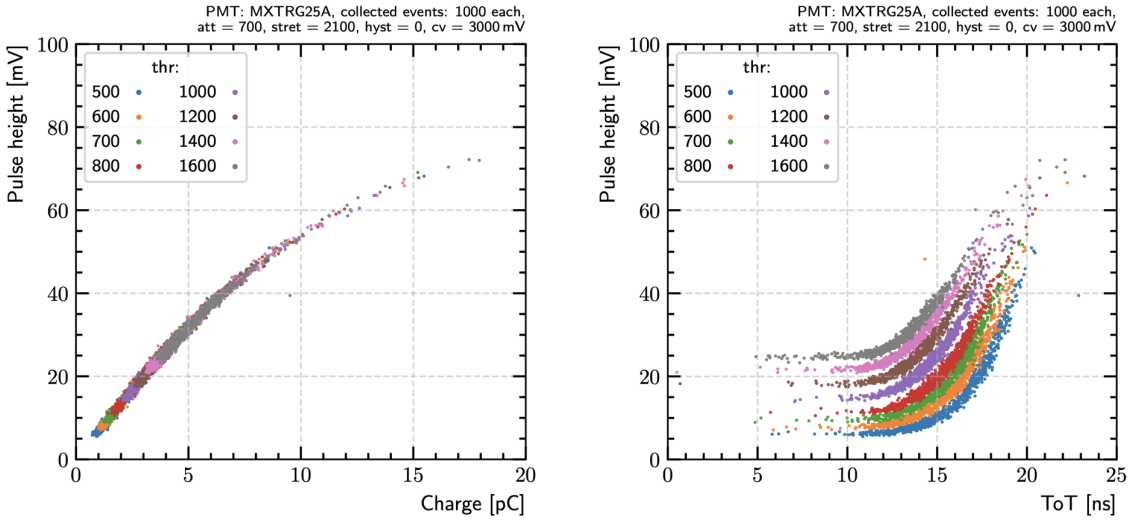

(a) (b)

FIGURE E.2. Alternative plots illustrating the impact of the effective signal threshold on the PMT pulses' characteristic variables charge and pulse height, as well as on the ToT of the output logic pulses. Compared to the plots in Section 7.2.3, the pulse height has been plotted using a linear scale. A fixed *att* value of 700 has been used and *thr* has been varied.

APPENDIX F

APPENDIX TO CHAPTER 8

F.1 Gain-Matching of the Trigger Detectors

For the future experimental operations of MAGIX, it is desirable that all PMTs of a trigger layer can be matched to the same gain. This is important for two reasons:

1. If the gains of the two PMTs of a trigger detector are identical, an incoming charged particle passing precisely through the center of its scintillator will produce equally large signals in both PMTs[1]. Conversely, a measured signal asymmetry between the two gain-matched PMTs of a trigger detector can be used to infer the impact location of an incoming particle, thereby providing additional spatial resolution along its scintillator, i.e. the non-dispersive direction of the MAGIX spectrometers.[2]

2. Particles impinging on the trigger layer should, regardless of which specific trigger detector is hit, leave a signal that depends solely on their particle type and energy. This ensures comparable signals, as well as an uniform efficiency across the entire trigger layer.

As a result, the gain-matching of the trigger detectors has been dedicated its own measurement series, which has been initiated within the scope of the Bachelor's thesis of K. Bent [120] and has been concluded as part of this thesis. Please note that the passive 20 dB attenuators, which will be used for the trigger layer signals in the final setup of MAGIX, cf. Section 7.2.1, have not been used for the initial study. All further details on the used setup and the analysis procedure can be

[1] Provided, the effects of guiding the scintillation light from its origin to the PMTs' photocathodes are identical for both PMTs.

[2] The impact location of an incoming particle can also be extracted from the time difference between the two PMT signals of a trigger detector, cf. Section 8.3.3. Nonetheless, the signal asymmetry provides additional information and can therefore further improve the spatial resolution or simply serve as a cross-check.

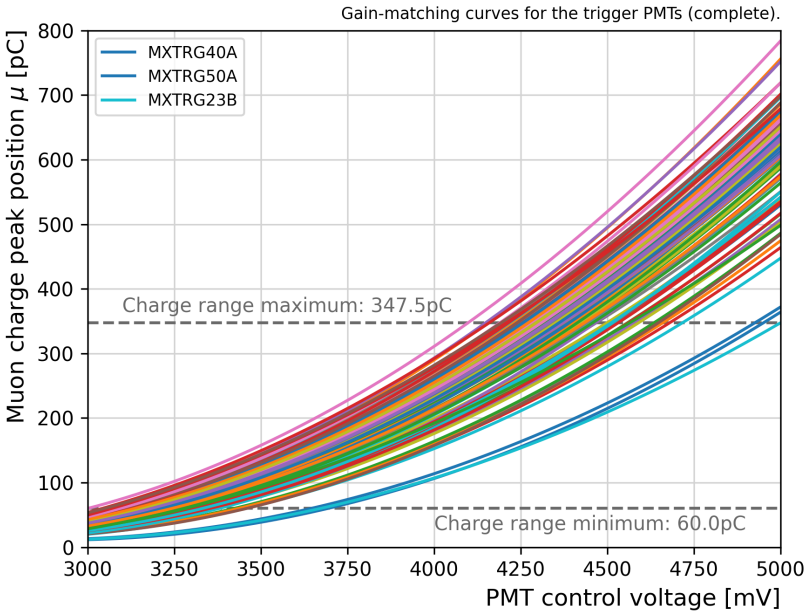

(a)

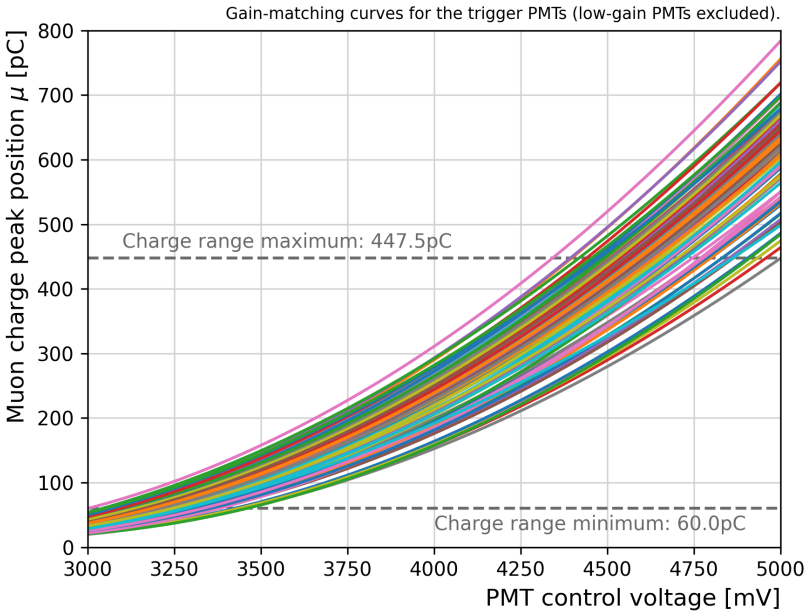

(b)

FIGURE F.1. Gain-matching of the trigger detectors without making use of the 20 dB attenuators. The relations between control voltage and position of the muon charge peak are shown for all trigger detectors (a) and with the three low-gain PMTs excluded (b). A method-dependent charge range can be defined, within which several operating points can be chosen. The PMT control voltages can then be adjusted accordingly.

found in the above mentioned Bachelor's thesis. Here, only the basic principle shall be briefly explained.

When signals are uniformly generated across the surface of a trigger detector, e.g. by using cosmogenic muons, this corresponds, on average, to generating signals exactly in the center of the detector's scintillator. Consequently, if the two PMTs of the detector are properly gain-matched, their resulting muon charge peaks, regardless of the specific gain value, should be distributed around the same mean value. Conversely, if the two muon charge peaks are at different positions, the two PMTs can be gain-matched by adjusting the PMTs' gain, i.e. their control voltages, so that the muon charge peaks end up around a chosen, identical mean value. This concept can be extended to an entire trigger layer. By measuring the relation between control voltage and position of the muon charge peak for each PMT, a method-dependent charge range can be defined that is accessible to each PMT. Within this range, an operating point can be chosen, and the control voltages for all PMTs can be adjusted accordingly.

Fig. F.1a shows the relations between control voltage and position of the muon charge peak for the PMTs of all 51 trigger detectors, as well as for the two shorter trigger detectors "MXTRGEFF0" and "MXTRGEFF1", which have been produced as supplementary detectors for the laboratory. The relationships are represented by quadratic functions that have been fitted to the collected data. The corresponding fit parameters and their errors are provided in Code F.1. Within the indicated charge range from 60.0 pC to 347.5 pC, several working points can now be defined and per PMT, the inverse of the fit function can be used to obtain the corresponding control voltages. However, as can be clearly seen, three PMTs exhibit a significantly lower gain - "MXTRG23B", "MXTRG40A", and "MXTRG50A" -, which is why they have been excluded for determining the accessible charge range, see Fig. F.1b. The indicated charge range from 60.0 pC to 447.5 pC therefore provides more flexibility for choosing working points compared to the charge range including the three low-gain PMTs.

Up to the point of writing this thesis, the exact cause of the low gain observed in these PMTs has not been fully investigated. Before these detectors are integrated into the final MAGIX setup, this issue should be addressed. Potential explanations include a factory-set low gain or production defects that occurred during coupling and wrapping the respective trigger detectors, leading to less scintillation light reaching the PMT cathodes. A review of the test sheets provided by Hamamatsu [176, 177, 178] shows that these three PMTs have indeed comparably lower anode luminous sensitivities, which naturally results in a reduced gain.[3] However, several PMTs with similarly low anode luminous sensitivities do not show such poor performance during the gain-matching procedure. Therefore, the low gain must be caused by a combination of the factory-set low gain and potential production defects.

[3]The PMTs "MXTRG23B", "MXTRG40A", and "MXTRG50A" correspond to the Hamamatsu serial numbers "AP9240", "AP4447", and "AM6522", respectively. [120]

Code F.1: Gain-matching fit parameters for the trigger detectors without making use of the passive 20 dB attenuators. As fit function, $f(x) = ax^2 + bx + c$ has been employed.

```
PMT a aError  b bError  c cError
MXTRG00A  1.03E-04  2.91E-06  -5.25E-01 2.20E-02  6.81E+02  3.98E+01
MXTRG00B  1.14E-04  2.36E-06  -5.60E-01 1.75E-02  7.06E+02  3.19E+01
MXTRG01A  8.74E-05  1.46E-06  -4.54E-01 1.06E-02  6.01E+02  1.88E+01
MXTRG01B  8.46E-05  1.66E-06  -4.55E-01 1.23E-02  6.24E+02  2.19E+01
MXTRG02A  1.08E-04  2.57E-06  -5.13E-01 1.88E-02  6.17E+02  3.38E+01
MXTRG02B  9.66E-05  2.63E-06  -4.57E-01 1.95E-02  5.41E+02  3.54E+01
MXTRG03A  1.11E-04  2.91E-06  -5.26E-01 2.16E-02  6.39E+02  3.88E+01
MXTRG03B  9.77E-05  2.62E-06  -4.56E-01 1.95E-02  5.37E+02  3.54E+01
MXTRG04A  8.96E-05  2.78E-06  -4.37E-01 2.03E-02  5.39E+02  3.62E+01
MXTRG04B  1.02E-04  2.03E-06  -5.15E-01 1.50E-02  6.63E+02  2.69E+01
MXTRG05A  8.62E-05  2.42E-06  -4.37E-01 1.74E-02  5.60E+02  3.07E+01
MXTRG05B  9.86E-05  1.54E-06  -4.85E-01 1.13E-02  6.04E+02  2.04E+01
MXTRG06A  9.70E-05  2.47E-06  -4.69E-01 1.81E-02  5.74E+02  3.23E+01
MXTRG06B  8.88E-05  2.53E-06  -4.53E-01 1.82E-02  5.87E+02  3.19E+01
MXTRG07A  8.79E-05  2.29E-06  -4.63E-01 1.73E-02  6.25E+02  3.13E+01
MXTRG07B  9.90E-05  2.17E-06  -4.78E-01 1.60E-02  5.87E+02  2.93E+01
MXTRG08A  9.80E-05  2.65E-06  -4.62E-01 1.95E-02  5.48E+02  3.50E+01
MXTRG08B  8.71E-05  2.24E-06  -4.27E-01 1.70E-02  5.29E+02  3.09E+01
MXTRG09A  1.03E-04  2.27E-06  -5.00E-01 1.69E-02  6.13E+02  3.05E+01
MXTRG09B  8.95E-05  1.60E-06  -4.63E-01 1.22E-02  6.13E+02  2.23E+01
MXTRG10A  9.27E-05  2.91E-06  -4.56E-01 2.19E-02  5.67E+02  3.97E+01
MXTRG10B  9.21E-05  1.57E-06  -4.83E-01 1.15E-02  6.45E+02  2.08E+01
MXTRG11A  1.06E-04  2.50E-06  -5.72E-01 1.84E-02  7.88E+02  3.27E+01
MXTRG11B  9.85E-05  2.45E-06  -4.80E-01 1.74E-02  5.94E+02  3.07E+01
MXTRG12A  9.91E-05  2.74E-06  -4.75E-01 1.99E-02  5.75E+02  3.52E+01
MXTRG12B  9.50E-05  2.65E-06  -4.56E-01 1.95E-02  5.53E+02  3.51E+01
MXTRG13A  1.08E-04  2.34E-06  -5.50E-01 1.72E-02  7.14E+02  3.09E+01
MXTRG13B  9.91E-05  2.52E-06  -4.83E-01 1.86E-02  5.98E+02  3.33E+01
MXTRG14A  9.11E-05  2.73E-06  -4.45E-01 1.96E-02  5.50E+02  3.44E+01
MXTRG14B  9.22E-05  2.82E-06  -4.59E-01 2.05E-02  5.81E+02  3.69E+01
MXTRG15A  9.00E-05  2.23E-06  -4.88E-01 1.61E-02  6.76E+02  2.82E+01
MXTRG15B  9.89E-05  1.95E-06  -4.77E-01 1.43E-02  5.85E+02  2.58E+01
MXTRG16A  9.26E-05  2.75E-06  -4.34E-01 1.99E-02  5.13E+02  3.52E+01
MXTRG16B  9.76E-05  2.24E-06  -4.64E-01 1.61E-02  5.55E+02  2.83E+01
MXTRG17A  9.59E-05  3.30E-06  -4.74E-01 2.41E-02  5.95E+02  4.29E+01
MXTRG17B  9.23E-05  3.35E-06  -4.34E-01 2.49E-02  5.10E+02  4.48E+01
MXTRG18A  9.98E-05  1.49E-06  -5.17E-01 1.08E-02  6.84E+02  1.91E+01
MXTRG18B  8.11E-05  3.00E-06  -4.35E-01 2.19E-02  5.95E+02  3.89E+01
MXTRG19A  9.96E-05  2.62E-06  -5.08E-01 1.93E-02  6.58E+02  3.47E+01
MXTRG19B  9.60E-05  3.64E-06  -4.49E-01 2.65E-02  5.31E+02  4.71E+01
```

MXTRG20A	9.82E-05	2.34E-06	-5.08E-01	1.74E-02	6.72E+02	3.14E+01
MXTRG20B	9.37E-05	1.75E-06	-4.76E-01	1.26E-02	6.14E+02	2.23E+01
MXTRG21A	9.30E-05	3.31E-06	-4.53E-01	2.47E-02	5.58E+02	4.46E+01
MXTRG21B	9.45E-05	2.61E-06	-4.47E-01	1.88E-02	5.31E+02	3.31E+01
MXTRG22A	1.01E-04	2.81E-06	-4.97E-01	2.08E-02	6.21E+02	3.80E+01
MXTRG22B	1.01E-04	3.02E-06	-4.94E-01	2.19E-02	6.14E+02	3.90E+01
MXTRG23A	9.88E-05	1.56E-06	-5.11E-01	1.16E-02	6.75E+02	2.10E+01
MXTRG23B	7.27E-05	1.17E-06	-4.14E-01	8.34E-03	6.00E+02	1.47E+01
MXTRG24A	8.94E-05	2.25E-06	-4.26E-01	1.64E-02	5.10E+02	2.95E+01
MXTRG24B	8.89E-05	2.27E-06	-4.85E-01	1.73E-02	6.77E+02	3.17E+01
MXTRG25A	9.72E-05	2.56E-06	-4.76E-01	1.89E-02	5.89E+02	3.37E+01
MXTRG25B	8.72E-05	1.42E-06	-4.44E-01	1.04E-02	5.75E+02	1.87E+01
MXTRG26A	9.31E-05	3.56E-06	-4.53E-01	2.59E-02	5.56E+02	4.62E+01
MXTRG26B	1.07E-04	2.60E-06	-5.28E-01	1.89E-02	6.63E+02	3.37E+01
MXTRG27A	1.03E-04	2.27E-06	-5.10E-01	1.77E-02	6.42E+02	3.38E+01
MXTRG27B	9.84E-05	2.41E-06	-4.87E-01	1.79E-02	6.12E+02	3.22E+01
MXTRG28A	9.91E-05	5.12E-06	-4.99E-01	3.68E-02	6.43E+02	6.45E+01
MXTRG28B	9.85E-05	4.72E-06	-4.62E-01	3.53E-02	5.44E+02	6.37E+01
MXTRG29A	9.75E-05	3.45E-06	-4.64E-01	2.55E-02	5.56E+02	4.57E+01
MXTRG29B	9.04E-05	3.11E-06	-4.38E-01	2.27E-02	5.34E+02	4.04E+01
MXTRG30A	9.99E-05	3.59E-06	-5.16E-01	2.61E-02	6.79E+02	4.62E+01
MXTRG30B	9.97E-05	2.25E-06	-4.68E-01	1.71E-02	5.49E+02	3.18E+01
MXTRG31A	9.19E-05	2.54E-06	-4.49E-01	1.80E-02	5.54E+02	3.13E+01
MXTRG31B	9.51E-05	1.60E-06	-5.29E-01	1.13E-02	7.52E+02	1.96E+01
MXTRG32A	9.70E-05	2.95E-06	-4.72E-01	2.12E-02	5.80E+02	3.74E+01
MXTRG32B	9.63E-05	2.74E-06	-4.73E-01	2.00E-02	5.88E+02	3.56E+01
MXTRG33A	8.75E-05	1.61E-06	-4.61E-01	1.21E-02	6.20E+02	2.20E+01
MXTRG33B	1.01E-04	1.81E-06	-5.44E-01	1.32E-02	7.45E+02	2.33E+01
MXTRG34A	1.02E-04	3.16E-06	-5.17E-01	2.35E-02	6.74E+02	4.28E+01
MXTRG34B	1.01E-04	2.58E-06	-4.95E-01	1.87E-02	6.19E+02	3.33E+01
MXTRG35A	9.00E-05	2.67E-06	-4.52E-01	1.97E-02	5.74E+02	3.51E+01
MXTRG35B	8.96E-05	2.42E-06	-4.71E-01	1.72E-02	6.32E+02	3.01E+01
MXTRG36A	9.58E-05	2.72E-06	-4.67E-01	1.97E-02	5.74E+02	3.53E+01
MXTRG36B	1.03E-04	3.07E-06	-5.04E-01	2.28E-02	6.33E+02	4.10E+01
MXTRG37A	1.03E-04	2.90E-06	-4.88E-01	2.18E-02	5.84E+02	3.94E+01
MXTRG37B	9.19E-05	1.78E-06	-4.67E-01	1.38E-02	6.09E+02	2.54E+01
MXTRG38A	9.54E-05	2.53E-06	-4.57E-01	1.90E-02	5.51E+02	3.46E+01
MXTRG38B	9.24E-05	2.03E-06	-4.81E-01	1.53E-02	6.37E+02	2.79E+01
MXTRG39A	9.79E-05	2.31E-06	-4.91E-01	1.70E-02	6.27E+02	3.05E+01
MXTRG39B	9.02E-05	2.95E-06	-4.51E-01	2.12E-02	5.74E+02	3.72E+01
MXTRG40A	8.14E-05	1.52E-06	-4.75E-01	1.12E-02	7.04E+02	2.02E+01
MXTRG40B	1.05E-04	1.38E-06	-5.27E-01	1.00E-02	6.74E+02	1.77E+01
MXTRG41A	1.03E-04	2.34E-06	-5.28E-01	1.69E-02	6.86E+02	3.00E+01

```
MXTRG41B   1.07E-04   1.94E-06   -5.46E-01 1.42E-02   7.10E+02   2.55E+01
MXTRG42A   1.11E-04   1.68E-06   -5.75E-01 1.25E-02   7.62E+02   2.26E+01
MXTRG42B   9.82E-05   2.28E-06   -4.83E-01 1.67E-02   5.98E+02   2.98E+01
MXTRG43A   9.77E-05   1.92E-06   -4.65E-01 1.35E-02   5.58E+02   2.36E+01
MXTRG43B   9.08E-05   2.07E-06   -4.94E-01 1.54E-02   6.86E+02   2.76E+01
MXTRG44A   8.34E-05   2.21E-06   -4.12E-01 1.62E-02   5.13E+02   2.88E+01
MXTRG44B   9.43E-05   2.33E-06   -4.47E-01 1.71E-02   5.32E+02   3.06E+01
MXTRG45A   1.00E-04   2.20E-06   -4.93E-01 1.67E-02   6.14E+02   3.04E+01
MXTRG45B   9.42E-05   2.79E-06   -4.50E-01 2.06E-02   5.46E+02   3.70E+01
MXTRG46A   9.80E-05   2.21E-06   -4.92E-01 1.69E-02   6.27E+02   3.13E+01
MXTRG46B   9.42E-05   3.00E-06   -4.21E-01 2.21E-02   4.69E+02   4.00E+01
MXTRG47A   9.45E-05   2.62E-06   -4.67E-01 1.92E-02   5.84E+02   3.45E+01
MXTRG47B   8.34E-05   2.70E-06   -3.84E-01 2.00E-02   4.39E+02   3.62E+01
MXTRG48A   9.49E-05   1.88E-06   -4.65E-01 1.41E-02   5.78E+02   2.59E+01
MXTRG48B   8.33E-05   2.84E-06   -4.07E-01 2.04E-02   5.03E+02   3.59E+01
MXTRG49A   1.08E-04   2.05E-06   -5.58E-01 1.53E-02   7.39E+02   2.79E+01
MXTRG49B   9.38E-05   2.36E-06   -4.78E-01 1.73E-02   6.16E+02   3.15E+01
MXTRG50A   7.88E-05   1.44E-06   -4.51E-01 1.07E-02   6.57E+02   1.92E+01
MXTRG50B   8.77E-05   2.27E-06   -4.31E-01 1.60E-02   5.35E+02   2.79E+01
MXTRGEFF0A   7.15E-05   2.08E-06   -3.37E-01 1.51E-02   3.96E+02   2.67E+01
MXTRGEFF0B   8.62E-05   1.88E-06   -3.75E-01 1.42E-02   3.99E+02   2.58E+01
MXTRGEFF1A   9.48E-05   2.16E-06   -4.62E-01 1.62E-02   5.70E+02   2.94E+01
MXTRGEFF1B   9.38E-05   1.95E-06   -4.28E-01 1.50E-02   4.93E+02   2.79E+01
```

Gain-Matching Including the Passive 20 dB Attenuators

Towards the end of this thesis, the gain-matching study has been repeated including the passive 20 dB attenuators that will be used for the trigger layer signals in the final setup of MAGIX, cf. Section 7.2.1. The corresponding relations and the resulting charge ranges are shown in Fig. F.2. The fit parameters and their errors can be found in Code F.2. Whereas Fig. F.2a includes all 51 produced trigger detectors, as well as the two shorter trigger detectors "MXTRGEFF0" and "MXTRGEFF1", Fig. F.2b again excludes the three lower gain PMTs "MXTRG23B", "MXTRG40A", and "MXTRG50A". For the MAMI beam time at X1, cf. Section 8.1, the even larger charge range from 0.0 pC to 40.0 pC was used to define the five working points 7.0 pC, 13.5 pC, 20.0 pC, 26.5 pC, and 33.0 pC. This approach was chosen because, at that time, the gain-matching procedure including the passive 20 dB attenuators had been conducted solely for the five trigger detectors used during the beam time and the final charge range had not yet been determined.

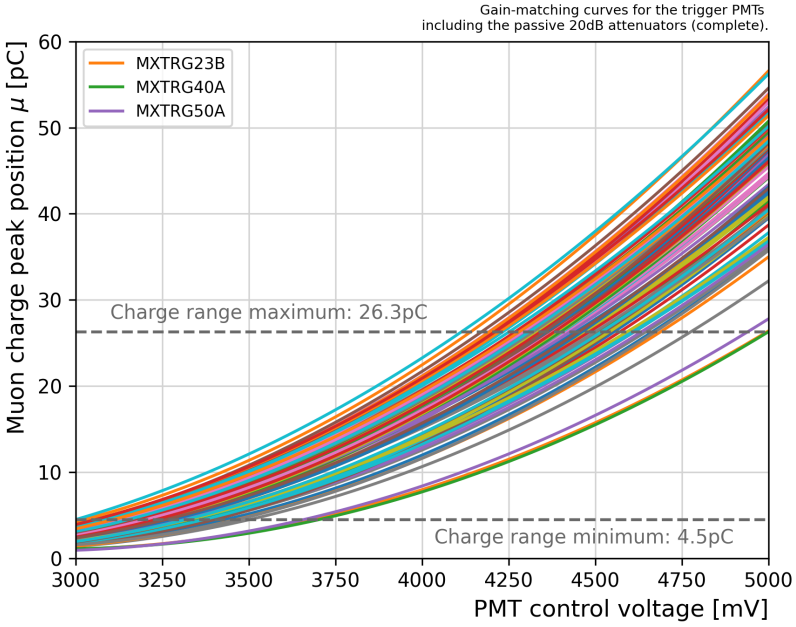

(a)

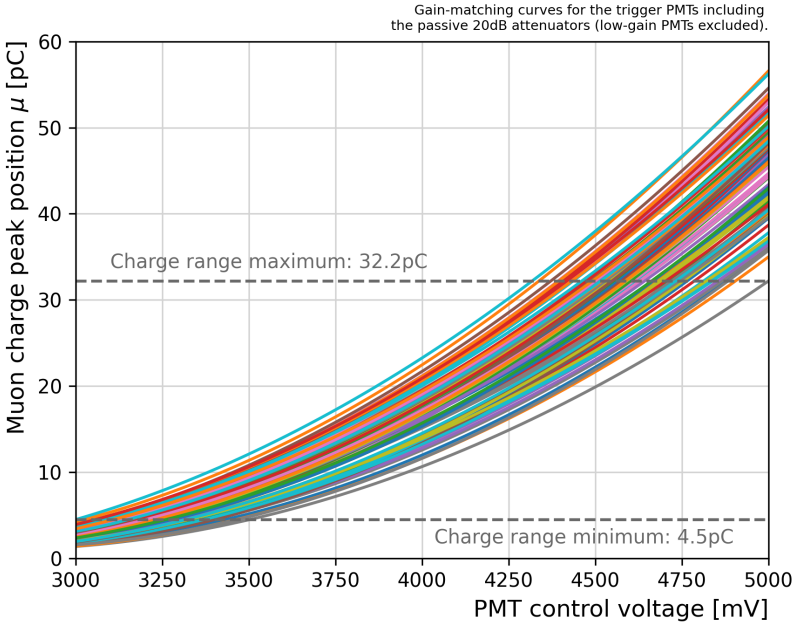

(b)

FIGURE F.2. Gain-matching of the trigger detectors including the 20 dB attenuators. The relations between control voltage and position of the muon charge peak are shown for all trigger detectors (a) and with the three low-gain PMTs excluded (b).

Code F.2: Gain-matching fit parameters for the trigger detectors including the passive 20 dB attenuators. As fit function, $f(x) = ax^2 + bx + c$ has been employed.

```
PMT a aError  b bError  c cError
MXTRG00A  7.08E-06  1.98E-07  -3.48E-02 1.43E-03  4.33E+01  2.52E+00
MXTRG00B  7.96E-06  3.52E-07  -3.75E-02 2.59E-03  4.51E+01  4.65E+00
MXTRG01A  6.94E-06  2.14E-07  -3.46E-02 1.56E-03  4.37E+01  2.79E+00
MXTRG01B  6.72E-06  2.45E-07  -3.54E-02 1.74E-03  4.77E+01  3.02E+00
MXTRG02A  6.94E-06  2.49E-07  -3.12E-02 1.85E-03  3.49E+01  3.32E+00
MXTRG02B  7.46E-06  2.55E-07  -3.60E-02 1.81E-03  4.40E+01  3.15E+00
MXTRG03A  7.75E-06  2.57E-07  -3.70E-02 1.90E-03  4.52E+01  3.42E+00
MXTRG03B  6.35E-06  2.53E-07  -2.80E-02 1.81E-03  3.00E+01  3.17E+00
MXTRG04A  6.57E-06  3.58E-07  -3.25E-02 2.56E-03  4.06E+01  4.48E+00
MXTRG04B  7.20E-06  2.36E-07  -3.56E-02 1.67E-03  4.49E+01  2.91E+00
MXTRG05A  6.94E-06  1.64E-07  -3.67E-02 1.19E-03  4.95E+01  2.11E+00
MXTRG05B  7.55E-06  2.49E-07  -3.80E-02 1.83E-03  4.89E+01  3.28E+00
MXTRG06A  7.53E-06  3.09E-07  -3.78E-02 2.23E-03  4.85E+01  3.92E+00
MXTRG06B  7.18E-06  1.80E-07  -3.82E-02 1.27E-03  5.21E+01  2.21E+00
MXTRG07A  6.39E-06  2.08E-07  -3.36E-02 1.51E-03  4.53E+01  2.67E+00
MXTRG07B  7.40E-06  2.37E-07  -3.37E-02 1.78E-03  3.81E+01  3.21E+00
MXTRG08A  7.32E-06  2.70E-07  -3.56E-02 1.92E-03  4.40E+01  3.36E+00
MXTRG08B  6.88E-06  2.26E-07  -3.53E-02 1.68E-03  4.64E+01  3.01E+00
MXTRG09A  7.32E-06  3.00E-07  -3.53E-02 2.12E-03  4.30E+01  3.67E+00
MXTRG09B  5.94E-06  1.51E-07  -2.99E-02 1.09E-03  3.82E+01  1.93E+00
MXTRG10A  7.50E-06  2.65E-07  -3.84E-02 1.91E-03  5.01E+01  3.36E+00
MXTRG10B  6.69E-06  1.61E-07  -3.45E-02 1.12E-03  4.54E+01  1.91E+00
MXTRG11A  7.37E-06  2.00E-07  -3.91E-02 1.45E-03  5.27E+01  2.59E+00
MXTRG11B  7.07E-06  2.22E-07  -3.38E-02 1.62E-03  4.09E+01  2.88E+00
MXTRG12A  7.18E-06  2.93E-07  -3.48E-02 2.13E-03  4.28E+01  3.80E+00
MXTRG12B  6.89E-06  2.74E-07  -3.25E-02 2.00E-03  3.86E+01  3.56E+00
MXTRG13A  6.98E-06  2.44E-07  -3.41E-02 1.81E-03  4.22E+01  3.25E+00
MXTRG13B  7.76E-06  2.54E-07  -3.89E-02 1.87E-03  4.99E+01  3.33E+00
MXTRG14A  6.89E-06  2.46E-07  -3.42E-02 1.74E-03  4.31E+01  3.02E+00
MXTRG14B  7.33E-06  1.98E-07  -3.76E-02 1.44E-03  4.94E+01  2.56E+00
MXTRG15A  6.78E-06  1.46E-07  -3.72E-02 1.04E-03  5.23E+01  1.83E+00
MXTRG15B  7.24E-06  2.22E-07  -3.50E-02 1.62E-03  4.30E+01  2.87E+00
MXTRG16A  7.81E-06  2.73E-07  -3.87E-02 2.00E-03  4.90E+01  3.56E+00
MXTRG16B  7.05E-06  2.49E-07  -3.30E-02 1.81E-03  3.87E+01  3.21E+00
MXTRG17A  7.11E-06  2.78E-07  -3.52E-02 1.97E-03  4.42E+01  3.40E+00
MXTRG17B  7.35E-06  3.22E-07  -3.62E-02 2.28E-03  4.55E+01  3.96E+00
MXTRG18A  7.75E-06  3.13E-07  -3.93E-02 2.23E-03  5.11E+01  3.89E+00
MXTRG18B  6.14E-06  1.26E-07  -3.37E-02 8.55E-04  4.72E+01  1.44E+00
MXTRG19A  7.58E-06  2.67E-07  -3.90E-02 1.85E-03  5.11E+01  3.16E+00
MXTRG19B  7.11E-06  2.22E-07  -3.10E-02 1.69E-03  3.35E+01  3.10E+00
```

MXTRG20A	7.02E-06	1.52E-07	-3.60E-02	1.10E-03	4.71E+01	1.93E+00
MXTRG20B	6.76E-06	1.99E-07	-3.40E-02	1.46E-03	4.33E+01	2.59E+00
MXTRG21A	7.17E-06	2.38E-07	-3.50E-02	1.70E-03	4.32E+01	2.98E+00
MXTRG21B	7.58E-06	2.82E-07	-3.57E-02	2.10E-03	4.23E+01	3.78E+00
MXTRG22A	7.30E-06	1.96E-07	-3.52E-02	1.43E-03	4.29E+01	2.54E+00
MXTRG22B	7.26E-06	2.31E-07	-3.52E-02	1.66E-03	4.35E+01	2.92E+00
MXTRG23A	7.42E-06	1.83E-07	-3.90E-02	1.27E-03	5.26E+01	2.17E+00
MXTRG23B	5.76E-06	9.50E-08	-3.34E-02	6.78E-04	4.94E+01	1.19E+00
MXTRG24A	6.80E-06	2.93E-07	-3.33E-02	2.08E-03	4.12E+01	3.63E+00
MXTRG24B	6.31E-06	2.55E-07	-3.33E-02	1.80E-03	4.48E+01	3.12E+00
MXTRG25A	7.38E-06	2.55E-07	-3.64E-02	1.83E-03	4.55E+01	3.23E+00
MXTRG25B	6.02E-06	1.54E-07	-3.08E-02	1.15E-03	4.03E+01	2.08E+00
MXTRG26A	7.39E-06	2.08E-07	-3.72E-02	1.49E-03	4.77E+01	2.64E+00
MXTRG26B	7.64E-06	2.85E-07	-3.61E-02	2.03E-03	4.33E+01	3.56E+00
MXTRG27A	7.35E-06	2.71E-07	-3.61E-02	1.95E-03	4.52E+01	3.41E+00
MXTRG27B	7.15E-06	2.11E-07	-3.40E-02	1.51E-03	4.07E+01	2.64E+00
MXTRG28A	7.32E-06	2.44E-07	-3.67E-02	1.75E-03	4.70E+01	3.06E+00
MXTRG28B	7.12E-06	1.79E-07	-3.29E-02	1.33E-03	3.82E+01	2.41E+00
MXTRG29A	8.01E-06	2.73E-07	-3.93E-02	2.06E-03	4.92E+01	3.73E+00
MXTRG29B	6.85E-06	2.11E-07	-3.34E-02	1.58E-03	4.13E+01	2.84E+00
MXTRG30A	6.88E-06	2.29E-07	-3.50E-02	1.67E-03	4.52E+01	2.95E+00
MXTRG30B	7.36E-06	1.87E-07	-3.47E-02	1.39E-03	4.13E+01	2.51E+00
MXTRG31A	7.54E-06	2.88E-07	-3.87E-02	2.06E-03	5.07E+01	3.60E+00
MXTRG31B	6.60E-06	1.11E-07	-3.60E-02	8.00E-04	5.00E+01	1.41E+00
MXTRG32A	7.20E-06	1.83E-07	-3.55E-02	1.35E-03	4.45E+01	2.41E+00
MXTRG32B	7.21E-06	1.84E-07	-3.55E-02	1.34E-03	4.45E+01	2.38E+00
MXTRG33A	6.33E-06	1.59E-07	-3.33E-02	1.16E-03	4.47E+01	2.06E+00
MXTRG33B	7.83E-06	1.82E-07	-4.31E-02	1.35E-03	6.05E+01	2.42E+00
MXTRG34A	7.44E-06	2.67E-07	-3.77E-02	1.97E-03	4.88E+01	3.53E+00
MXTRG34B	6.97E-06	3.06E-07	-3.34E-02	2.20E-03	4.05E+01	3.85E+00
MXTRG35A	6.76E-06	1.70E-07	-3.43E-02	1.25E-03	4.43E+01	2.23E+00
MXTRG35B	6.54E-06	2.54E-07	-3.43E-02	1.76E-03	4.58E+01	3.00E+00
MXTRG36A	7.72E-06	2.23E-07	-3.95E-02	1.64E-03	5.16E+01	2.93E+00
MXTRG36B	6.92E-06	1.70E-07	-3.30E-02	1.27E-03	4.00E+01	2.28E+00
MXTRG37A	7.05E-06	2.43E-07	-3.32E-02	1.72E-03	3.91E+01	2.99E+00
MXTRG37B	6.30E-06	2.59E-07	-3.11E-02	1.91E-03	3.91E+01	3.41E+00
MXTRG38A	7.27E-06	2.13E-07	-3.52E-02	1.50E-03	4.33E+01	2.60E+00
MXTRG38B	6.55E-06	2.27E-07	-3.34E-02	1.64E-03	4.31E+01	2.89E+00
MXTRG39A	7.14E-06	2.61E-07	-3.62E-02	1.84E-03	4.68E+01	3.19E+00
MXTRG39B	6.27E-06	1.99E-07	-3.11E-02	1.43E-03	3.93E+01	2.52E+00
MXTRG40A	6.00E-06	8.72E-08	-3.54E-02	5.88E-04	5.33E+01	9.88E-01
MXTRG40B	7.35E-06	2.01E-07	-3.70E-02	1.48E-03	4.73E+01	2.62E+00
MXTRG41A	7.67E-06	2.46E-07	-3.97E-02	1.82E-03	5.25E+01	3.27E+00

```
MXTRG41B   7.88E-06   1.94E-07   -4.07E-02 1.45E-03   5.34E+01   2.61E+00
MXTRG42A   8.49E-06   2.00E-07   -4.56E-02 1.46E-03   6.26E+01   2.59E+00
MXTRG42B   8.10E-06   2.90E-07   -4.19E-02 2.11E-03   5.52E+01   3.75E+00
MXTRG43A   6.86E-06   1.78E-07   -3.20E-02 1.31E-03   3.73E+01   2.35E+00
MXTRG43B   7.05E-06   1.99E-07   -3.93E-02 1.37E-03   5.60E+01   2.34E+00
MXTRG44A   6.77E-06   1.95E-07   -3.53E-02 1.43E-03   4.70E+01   2.54E+00
MXTRG44B   7.15E-06   1.71E-07   -3.45E-02 1.22E-03   4.22E+01   2.12E+00
MXTRG45A   7.68E-06   2.13E-07   -3.94E-02 1.50E-03   5.15E+01   2.60E+00
MXTRG45B   6.78E-06   2.31E-07   -3.15E-02 1.68E-03   3.69E+01   2.97E+00
MXTRG46A   7.47E-06   2.46E-07   -3.82E-02 1.80E-03   4.98E+01   3.21E+00
MXTRG46B   7.10E-06   2.78E-07   -3.27E-02 2.09E-03   3.81E+01   3.78E+00
MXTRG47A   6.64E-06   2.63E-07   -3.27E-02 1.84E-03   4.09E+01   3.18E+00
MXTRG47B   7.22E-06   3.15E-07   -3.61E-02 2.38E-03   4.61E+01   4.32E+00
MXTRG48A   6.85E-06   2.10E-07   -3.34E-02 1.51E-03   4.12E+01   2.66E+00
MXTRG48B   5.82E-06   2.18E-07   -2.79E-02 1.55E-03   3.36E+01   2.69E+00
MXTRG49A   7.41E-06   3.03E-07   -3.75E-02 2.12E-03   4.82E+01   3.65E+00
MXTRG49B   6.67E-06   1.79E-07   -3.41E-02 1.28E-03   4.42E+01   2.24E+00
MXTRG50A   5.98E-06   1.15E-07   -3.44E-02 8.11E-04   5.03E+01   1.42E+00
MXTRG50B   6.95E-06   2.12E-07   -3.53E-02 1.53E-03   4.57E+01   2.70E+00
MXTRGEFF0A   5.83E-06   1.59E-07   -2.91E-02 1.11E-03   3.70E+01   1.90E+00
MXTRGEFF0B   6.87E-06   2.09E-07   -3.17E-02 1.56E-03   3.69E+01   2.82E+00
MXTRGEFF1A   6.24E-06   1.92E-07   -3.00E-02 1.34E-03   3.64E+01   2.31E+00
MXTRGEFF1B   7.04E-06   2.26E-07   -3.26E-02 1.64E-03   3.84E+01   2.89E+00
```

F.2 Offset Correction

This correction has been briefly mentioned in Section 8.3.1, where it is applied as part of the `interpretHits()` function. It addresses the offsets introduced due to different signal propagation delays along the individual readout channels of a NINO readout board, which can result from different cable lengths or varying processing times within the readout electronics. If the propagation delay differences would be too large, this would result in a faulty merging or collection of the individual *hits* as the timestamps are shifted with respect to the applied coincidence window. Additionally, the cuts applied to the absolute values of the channel time differences and the detector time differences would be compromised, negatively affecting the detector parameters efficiency, coincidence time resolution, and spatial resolution. To prevent these issues, the timestamps of the collected *hits* must be corrected for the introduced timing offsets.

In practice, the correction is applied using the channel time difference distributions of the individual detectors, as exemplified in Fig. F.3 for the test detector *Mid*, where the same data file is used as in Sections 8.2, 8.3, and 8.4. Fig. F.3a shows the channel time difference distribution for 2 000 000 collected *hits* after pre-processing and analysis, but without the offset correction applied. Ideally, the channel time distribution would be centered around zero, given that the

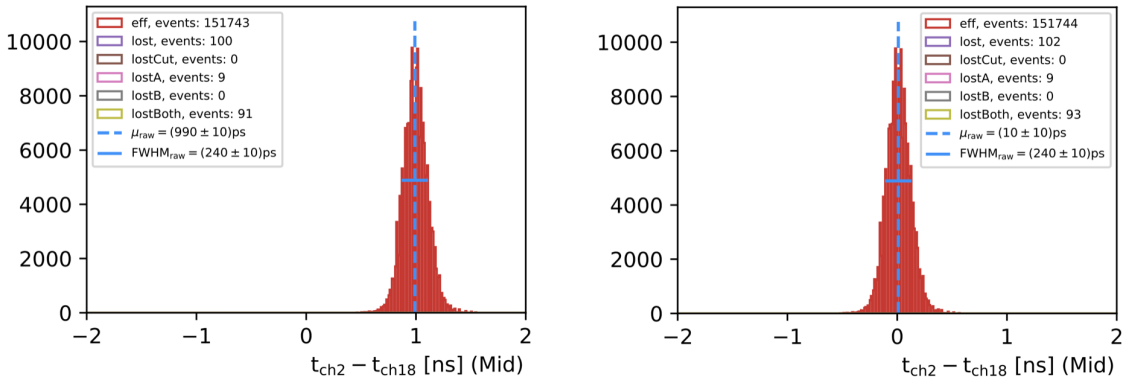

(a) (b)

FIGURE F.3. Effect of the applied offset correction, exemplified for the test detector *Mid*. The distribution of the detector's channel time difference exhibits an offset introduced due to different signal propagation delays along the readout channels (a), which is eliminated after the iterative correction process (b).

dataset has been obtained with the electron beam hitting the center of the detector's scintillator. But clearly, this is not the case. Instead, the distribution is centered at around 1 ns, indicating a longer signal propagation delay in channel 2 compared to channel 18.

In an effective way, this offset can be eliminated by fitting the channel time difference distribution with a Subbotin distribution[4] and correcting each *hit* by the obtained mean value of the fit. When repeating this fitting procedure over several iterations — three iterations have been used during the studies of this chapter —, the result can be further refined. The cumulative correction from this iterative process is then stored in a list called `offsetCalib`, which can be loaded from the external file `NINOglobals.py`. Fig. F.3b demonstrates the effect of the offset correction, where the channel time difference distribution is well-centered around zero after applying the correction as part of the `interpretHits()` function.

Please note that the offset correction must be performed separately for each setup. Fortunately, it only needs to be done once and can then be applied to all datasets recorded with the corresponding setup. For the studies in Chapter 8, the offset correction has been part of the preparation for the beam time presented in Section 8.1. For the offset correction of the detectors *Front*, *Rear*, and *Mid*, the same dataset as above has been used. For the test detector *Left*, the offset corrections from the two datasets `MAGIXTriggerBeamTimeJune2024/data_posScan/meas_posScan_pos_70.0.dat` and `MAGIXTriggerBeamTimeJune2024/data_posScan/meas_posScan_pos_71.0.dat` have been averaged to simulate the result at the motor position 70.5 mm along the x-direction, which

[4]The Subbotin distribution, or Generalized Gaussian distribution, extends the standard Gaussian distribution by adding a shape parameter. Its probability density function is given by $f(x) = \frac{\beta}{2\sigma\Gamma(1/\beta)} \exp\left(-\left(\frac{|x-\mu|}{\sigma}\right)^{\beta}\right)$, where μ is the mean, σ is the standard deviation, β is the shape parameter, and Γ is the gamma function, defined as $\Gamma(x) = \int_0^{\infty} t^{x-1} e^{-t} dt$. [179]

wasn't recorded during the beam time.[5] Similarly, for the test detector *Right*, the offset corrections from the datasets `MAGIXTriggerBeamTimeJune2024/data_posScan/meas_posScan_pos_-2.0.dat` and `MAGIXTriggerBeamTimeJune2024/data_posScan/meas_posScan_pos_-3.0.dat` have been averaged to obtain the result for the motor position −2.5 mm.

F.3 Extraction of the Effective Speed of Light inside a Trigger Detector

As described in Section 8.3.3, the effective speed of light v_{eff} is required to determine the hit or beam position x along the scintillator of a MAGIX trigger detector. It can be calculated using the relation $x = \frac{\mu}{2} \cdot v_{\text{eff}}$, where μ represents the center position of the corresponding channel time difference distribution. Naturally, this only makes sense if the offset correction, cf. Appendix F.2, has been applied beforehand. Vice versa, if the position x is known, v_{eff} can be determined following $v_{\text{eff}} = \frac{2}{\mu} \cdot x$. So, in principle, for any dataset with a hit or beam position different from zero, a corresponding value for v_{eff} can be extracted. Averaging these values will then improve the overall accuracy of the result.

Alternatively, one can examine the position difference between two datasets by observing the corresponding shift in μ, where, to maximize accuracy, the position difference should be as large as possible, approximating an average over multiple datasets. For the studies in Chapter 8, v_{eff} has been extracted using the trigger detector *Front*, where two datasets from the conducted x-direction scan have been used, namely those for the motor positions 84 mm and −16 mm, see Fig. F.4.[6] The position difference between the two datasets therefore is 100 mm. The next step is to calculate the shift in the center position μ between the two datasets. With the two distributions located at (-0.975 ± 0.030) ns and (0.920 ± 0.030) ns, respectively, the shift amounts to (1.895 ± 0.030) ns. Thus, the effective speed of light results in $v_{\text{eff}} = \frac{2}{1.895\,\text{ns}} \cdot 100\,\text{mm} = (105.54 \pm 1.67)\,\text{mm}\,\text{ns}^{-1}$, where the error has been calculated using Gaussian error propagation[7].

The same procedure can be performed using the walk-corrected channel time distributions, cf. Section 8.4.2. As illustrated in Fig. F.5, this adjustment changes the center positions μ to (-0.980 ± 0.010) ns and (0.935 ± 0.010) ns, respectively, resulting in an increased shift of (1.915 ± 0.010) ns.

[5] The *HOME* position at $x = 34$ mm corresponds to the center of the test detector *Mid*, with the other two test detectors positioned at a distance of ±36.5 mm along the x-direction, cf. Section 8.1. Accordingly, the motor position of 70.5 mm corresponds to the test detector *Left*, while the motor position of −2.5 mm corresponds to the test detector *Right*.

[6] The choice for these two datasets has been made because they are symmetric around the *HOME* position at $x = 34$ mm and are relatively far apart. Even farther apart positions could have been chosen, but for those, there wouldn't have been enough events in the category *eff* to precisely determine the mean and width of the channel time difference distributions. While the *trigger* category could have been used for the detector *Front*, doing so would have required modifications to the code base without significantly altering the result. Fig. F.4 also shows that the *HOME* position at $x = 34$ mm does not correspond to the perfect center of the three test detectors, as the dataset for the motor position −16 mm exhibits significantly more lost events than that for position 84 mm.

[7] The error for the position difference has been estimated as the displacement per step of the stepper motor driving the x-direction, i.e. 1/(20000 mm).

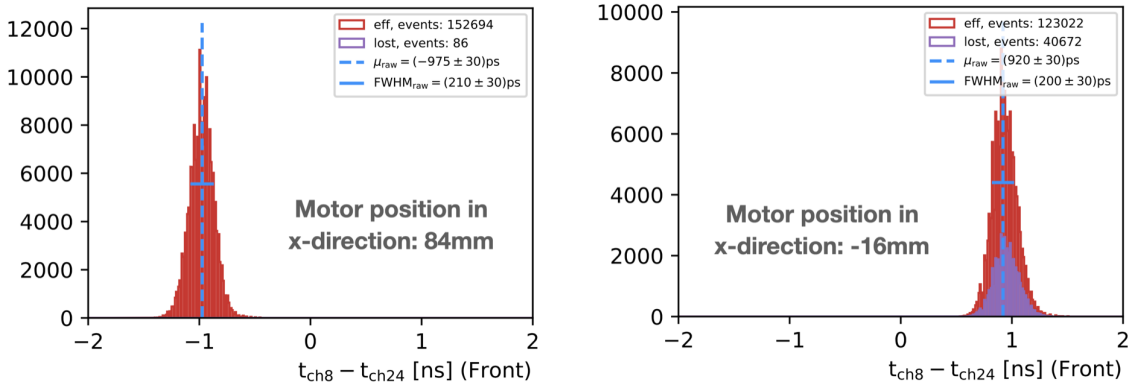

(a) (b)

FIGURE F.4. The channel time difference distributions of the detector *Front* for the two motor positions 84 mm (a) and −16 mm (b). The effective speed of light v_{eff} is determined by relating the position difference to the shift in the center position μ between the two datasets.

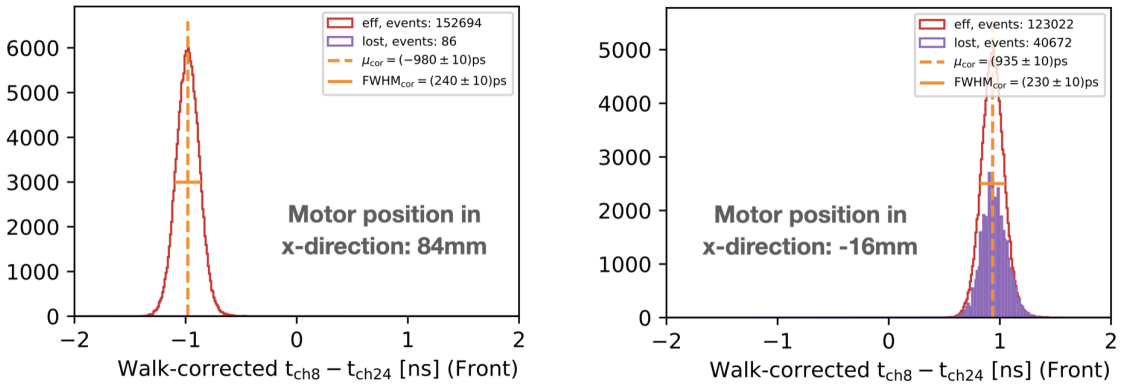

(a) (b)

FIGURE F.5. The walk-corrected channel time difference distributions of the detector *Front* for the two motor positions 84 mm (a) and −16 mm (b).

Consequently, the effective speed of light amounts to $(104.44 \pm 0.55)\,\text{mm}\,\text{ns}^{-1}$, where the error has again been calculated using Gaussian error propagation.

F.4 The Python3-Functions *analyze_event()* and *totToCharge()*

Code F.3: The function analyze_event().

```
# Initialize global variables from NINOglobals.py
import NINOglobals as g
g.initialize()
import NINOfunctions as f

def analyze_event(lea, tra):
  global triggerCounter, effSingleCounter, effDoubleCounter,
   effTripleCounter, loseCounter, effCounter
  # create bar instance
  bars = f.getBarsFromEdgeLists(lea, tra, g.scintiNames)
  NINOchannels = [f.NINOchannel(lea[i], tra[i], i) for i in range(g.
   NINOchannelsInUse)]
  lost = 0

  # get tot for each channel (the events with t < 10ns but > 0ns get
   lost in tot function; these events shouldn't even exist; problem
   should disappear when readout and sorting work better/perfectly)
  t = []
  q = []
  for i in range(g.NINOchannelsInUse):
    t.append(NINOchannels[i].tot)
    q.append(NINOchannels[i].charge)

  # all events
  for i in range(g.NINOchannelsInUse):
    if (lea[i] > 0) and (tra[i] > 0) and (t[i] > 0) and (q[i] > 0):
      tot[i].append(t[i])
      charge[i].append(q[i])

  # single bar coincidences
  for i, scintiName in enumerate(g.scintiNames):
    channelA = g.nameToChannel[scintiName+"A"]
    channelB = g.nameToChannel[scintiName+"B"]
    if (lea[channelA] > 0) and (tra[channelA] > 0) and (t[channelA] >
   0) and (q[channelA] > 0) and \
       (lea[channelB] > 0) and (tra[channelB] > 0) and (t[channelB] >
   0) and (q[channelB] > 0):
      totC[channelA].append(t[channelA])
      chargeC[channelA].append(q[channelA])
      totC[channelB].append(t[channelB])
```

```
35      chargeC[channelB].append(q[channelB])
36      channelDiffsC[i].append(bars[i].diff)
37      channelDiffsC_cor[i].append(bars[i].diffcor)
38
39  # coincidences for efficiency
40  frontChannelA = g.nameToChannel[g.scintiNames[0]+"A"]
41  frontChannelB = g.nameToChannel[g.scintiNames[0]+"B"]
42  rearChannelA = g.nameToChannel[g.scintiNames[1]+"A"]
43  rearChannelB = g.nameToChannel[g.scintiNames[1]+"B"]
44  if ((lea[frontChannelA] > 0) and (tra[frontChannelA] > 0) and (t[
     frontChannelA] > 0) and (q[frontChannelA] > 0)) and \
45    ((lea[frontChannelB] > 0) and (tra[frontChannelB] > 0) and (t[
     frontChannelB] > 0) and (q[frontChannelB] > 0)) and \
46    ((lea[rearChannelA] > 0) and (tra[rearChannelA] > 0) and (t[
     rearChannelA] > 0) and (q[rearChannelA] > 0)) and \
47    ((lea[rearChannelB] > 0) and (tra[rearChannelB] > 0) and (t[
     rearChannelB] > 0) and (q[rearChannelB] > 0)) and \
48    (abs(bars[0].diff) < singleTimeCut_trg) and \
49    (abs(bars[1].diff) < singleTimeCut_trg) and \
50    (abs(bars[1].mean - bars[0].mean) < timeOfFlightCut_trg):
51     totCC[frontChannelA].append(t[frontChannelA])
52     chargeCC[frontChannelA].append(q[frontChannelA])
53     totCC[frontChannelB].append(t[frontChannelB])
54     chargeCC[frontChannelB].append(q[frontChannelB])
55     totCC[rearChannelA].append(t[rearChannelA])
56     chargeCC[rearChannelA].append(q[rearChannelA])
57     totCC[rearChannelB].append(t[rearChannelB])
58     chargeCC[rearChannelB].append(q[rearChannelB])
59     channelDiffsCC[0].append(bars[0].diff)
60     channelDiffsCC_cor[0].append(bars[0].diffcor)
61     channelDiffsCC[1].append(bars[1].diff)
62     channelDiffsCC_cor[1].append(bars[1].diffcor)
63     totCC_channelWalk[0][frontChannelA].append(t[frontChannelA])
64     totCC_channelWalk[0][frontChannelB].append(t[frontChannelB])
65     totCC_channelWalk[1][rearChannelA].append(t[rearChannelA])
66     totCC_channelWalk[1][rearChannelB].append(t[rearChannelB])
67     triggerDiffsCC[0].append(bars[1].mean - bars[0].mean)
68     triggerDiffsCC_cor[0].append(bars[1].meancor - bars[0].meancor)
69     totCC_detectorWalk[0][frontChannelA].append(t[frontChannelA])
70     totCC_detectorWalk[0][frontChannelB].append(t[frontChannelB])
71     totCC_detectorWalk[0][rearChannelA].append(t[rearChannelA])
72     totCC_detectorWalk[0][rearChannelB].append(t[rearChannelB])
73     triggerCounter += 1
```

```
74
75      # coincidences with central detectors
76      for i, scintiName in enumerate(g.scintiNames[2:]): # i starts at 0
    -> consider this for index of g.scintiNames!
77        channelA = g.nameToChannel[scintiName+"A"]
78        channelB = g.nameToChannel[scintiName+"B"]
79        totCC[channelA].append(t[channelA])
80        chargeCC[channelA].append(q[channelA])
81        totCC[channelB].append(t[channelB])
82        chargeCC[channelB].append(q[channelB])
83        channelDiffsCC[i+2].append(bars[i+2].diff)
84        channelDiffsCC_cor[i+2].append(bars[i+2].diffcor)
85        triggerDiffsCC[i+1].append(bars[i+2].mean - bars[0].mean)
86        triggerDiffsCC_cor[i+1].append(bars[i+2].meancor - bars[0].
    meancor)
87
88        # define channels of neighbouring detector only for second and
    third central detector
89        if (i > 0):
90          neighbourChannelA = g.nameToChannel[g.scintiNames[i+1]+"A"]
91          neighbourChannelB = g.nameToChannel[g.scintiNames[i+1]+"B"]
92        if (i > 1):
93          neighbourChannelA2 = g.nameToChannel[g.scintiNames[i]+"A"]
94          neighbourChannelB2 = g.nameToChannel[g.scintiNames[i]+"B"]
95
96        # check coincidence
97        if ((lea[channelA] > 0) and (tra[channelA] > 0) and (t[channelA]
    > 0) and (q[channelA] > 0)) and \
98            ((lea[channelB] > 0) and (tra[channelB] > 0) and (t[channelB]
    > 0) and (q[channelB] > 0)) and \
99            (abs(bars[i+2].diff) < singleTimeCut_mid) and \
100           (abs(bars[i+2].mean - bars[0].mean) < timeOfFlightCut_mid):
101         totCCC[channelA].append(t[channelA])
102         chargeCCC[channelA].append(q[channelA])
103         totCCC[channelB].append(t[channelB])
104         chargeCCC[channelB].append(q[channelB])
105         channelDiffsCCC[i+2].append(bars[i+2].diff)
106         channelDiffsCCC_cor[i+2].append(bars[i+2].diffcor)
107         totCCC_channelWalk[i+2][channelA].append(t[channelA])
108         totCCC_channelWalk[i+2][channelB].append(t[channelB])
109         triggerDiffsCCC[i+1].append(bars[i+2].mean - bars[0].mean)
110         triggerDiffsCCC_cor[i+1].append(bars[i+2].meancor - bars[0].
    meancor)
```

```
111         totCCC_detectorWalk[i+1][channelA].append(t[channelA])
112         totCCC_detectorWalk[i+1][channelB].append(t[channelB])
113         totCCC_detectorWalk[i+1][frontChannelA].append(t[frontChannelA
    ])
114         totCCC_detectorWalk[i+1][frontChannelB].append(t[frontChannelB
    ])
115         effSingleCounter[i] += 1
116 
117         # look at overlap area to neighbouring detector (this also
    includes random coincidences)
118         if (i > 0) and \
119            ((lea[neighbourChannelA] > 0) and (tra[neighbourChannelA] >
    0) and (t[neighbourChannelA] > 0) and (q[neighbourChannelA] > 0))
    and \
120            ((lea[neighbourChannelB] > 0) and (tra[neighbourChannelB] >
    0) and (t[neighbourChannelB] > 0) and (q[neighbourChannelB] > 0))
    and \
121            (abs(bars[i+1].diff) < singleTimeCut_mid) and \
122            (abs(bars[i+1].mean - bars[0].mean) < timeOfFlightCut_mid):
123           effDoubleCounter[i-1] += 1
124         # look at random coincidences between the two outer central
    detectors and all three detectors
125         if (i > 1) and \
126            ((lea[neighbourChannelA2] > 0) and (tra[neighbourChannelA2]
    > 0) and (t[neighbourChannelA2] > 0) and (q[neighbourChannelA2] >
    0)) and \
127            ((lea[neighbourChannelB2] > 0) and (tra[neighbourChannelB2]
    > 0) and (t[neighbourChannelB2] > 0) and (q[neighbourChannelB2] >
    0)) and \
128            (abs(bars[i].diff) < singleTimeCut_mid) and \
129            (abs(bars[i].mean - bars[0].mean) < timeOfFlightCut_mid):
130          # look at random coincidences between all three central
    detectors (and correct double counts in this case)
131          if ((lea[neighbourChannelA] > 0) and (tra[neighbourChannelA]
    > 0) and (t[neighbourChannelA] > 0) and (q[neighbourChannelA] > 0))
     and \
132             ((lea[neighbourChannelB] > 0) and (tra[neighbourChannelB]
    > 0) and (t[neighbourChannelB] > 0) and (q[neighbourChannelB] > 0))
     and \
133             (abs(bars[i+1].diff) < singleTimeCut_mid) and \
134             (abs(bars[i+1].mean - bars[0].mean) < timeOfFlightCut_mid)
    :
135            effTripleCounter[i-2] += 1
```

```
136             effDoubleCounter[i-1] -= 1
137             effDoubleCounter[i-2] -= 1
138           else:
139             effDoubleCounter[i] += 1
140
141       else:
142         totLose[channelA].append(t[channelA])
143         chargeLose[channelA].append(q[channelA])
144         totLose[channelB].append(t[channelB])
145         chargeLose[channelB].append(q[channelB])
146         channelDiffsLose[i+2].append(bars[i+2].diff)
147         channelDiffsLose_cor[i+2].append(bars[i+2].diffcor)
148         triggerDiffsLose[i+1].append(bars[i+2].mean - bars[0].mean)
149         triggerDiffsLose_cor[i+1].append(bars[i+2].meancor - bars[0].
    meancor)
150         lost += 1
151
152     # detailed look at lost events in central detectors
153     for i, scintiName in enumerate(g.scintiNames[2:]):
154       channelA = g.nameToChannel[scintiName+"A"]
155       channelB = g.nameToChannel[scintiName+"B"]
156       if ((lea[channelA] <= 0) or (tra[channelA] <= 0) or (t[channelA]
    <= 0) or (q[channelA] <= 0)) and \
157           ((lea[channelB] > 0) and (tra[channelB] > 0) and (t[channelB]
    > 0) and (q[channelB] > 0)):
158         totLoseA[channelA].append(t[channelA])
159         chargeLoseA[channelA].append(q[channelA])
160         totLoseA[channelB].append(t[channelB])
161         chargeLoseA[channelB].append(q[channelB])
162         channelDiffsLoseA[i+2].append(bars[i+2].diff)
163         channelDiffsLoseA_cor[i+2].append(bars[i+2].diffcor)
164         triggerDiffsLoseA[i+1].append(bars[i+2].mean - bars[0].mean)
165         triggerDiffsLoseA_cor[i+1].append(bars[i+2].meancor - bars[0].
    meancor)
166       elif ((lea[channelA] > 0) and (tra[channelA] > 0) and (t[channelA
    ] > 0) and (q[channelA] > 0)) and \
167           ((lea[channelB] <= 0) or (tra[channelB] <= 0) or (t[channelB
    ] <= 0) or (q[channelB] <= 0)):
168         totLoseB[channelA].append(t[channelA])
169         chargeLoseB[channelA].append(q[channelA])
170         totLoseB[channelB].append(t[channelB])
171         chargeLoseB[channelB].append(q[channelB])
172         channelDiffsLoseB[i+2].append(bars[i+2].diff)
```

```
173         channelDiffsLoseB_cor[i+2].append(bars[i+2].diffcor)
174         triggerDiffsLoseB[i+1].append(bars[i+2].mean - bars[0].mean)
175         triggerDiffsLoseB_cor[i+1].append(bars[i+2].meancor - bars[0].
    meancor)
176       elif ((lea[channelA] <= 0) or (tra[channelA] <= 0) or (t[channelA
    ] <= 0) or (q[channelA] <= 0)) and \
177           ((lea[channelB] <= 0) or (tra[channelB] <= 0) or (t[channelB
    ] <= 0) or (q[channelB] <= 0)):
178         totLoseBoth[channelA].append(t[channelA])
179         chargeLoseBoth[channelA].append(q[channelA])
180         totLoseBoth[channelB].append(t[channelB])
181         chargeLoseBoth[channelB].append(q[channelB])
182         channelDiffsLoseBoth[i+2].append(bars[i+2].diff)
183         channelDiffsLoseBoth_cor[i+2].append(bars[i+2].diffcor)
184         triggerDiffsLoseBoth[i+1].append(bars[i+2].mean - bars[0].mean)
185         triggerDiffsLoseBoth_cor[i+1].append(bars[i+2].meancor - bars
    [0].meancor)
186       elif ((lea[channelA] > 0) and (tra[channelA] > 0) and (t[channelA
    ] > 0) and (q[channelA] > 0)) and \
187           ((lea[channelB] > 0) and (tra[channelB] > 0) and (t[channelB
    ] > 0) and (q[channelB] > 0)) and \
188           ((abs(bars[i+2].diff) >= singleTimeCut_mid) or (abs(bars[i
    +2].mean - bars[0].mean) >= timeOfFlightCut_mid)):
189         totLoseCut[channelA].append(t[channelA])
190         chargeLoseCut[channelA].append(q[channelA])
191         totLoseCut[channelB].append(t[channelB])
192         chargeLoseCut[channelB].append(q[channelB])
193         channelDiffsLoseCut[i+2].append(bars[i+2].diff)
194         channelDiffsLoseCut_cor[i+2].append(bars[i+2].diffcor)
195         triggerDiffsLoseCut[i+1].append(bars[i+2].mean - bars[0].mean)
196         triggerDiffsLoseCut_cor[i+1].append(bars[i+2].meancor - bars
    [0].meancor)
197       else:
198         pass
199
200     if (lost == 3):
201       totLose[frontChannelA].append(t[frontChannelA])
202       chargeLose[frontChannelA].append(q[frontChannelA])
203       totLose[frontChannelB].append(t[frontChannelB])
204       chargeLose[frontChannelB].append(q[frontChannelB])
205       totLose[rearChannelA].append(t[rearChannelA])
206       chargeLose[rearChannelA].append(q[rearChannelA])
207       totLose[rearChannelB].append(t[rearChannelB])
```

```
208         chargeLose[rearChannelB].append(q[rearChannelB])
209         channelDiffsLose[0].append(bars[0].diff)
210         channelDiffsLose_cor[0].append(bars[0].diffcor)
211         channelDiffsLose[1].append(bars[1].diff)
212         channelDiffsLose_cor[1].append(bars[1].diffcor)
213         triggerDiffsLose[0].append(bars[1].mean - bars[0].mean)
214         triggerDiffsLose_cor[0].append(bars[1].meancor - bars[0].meancor)
215         loseCounter += 1
216       else:
217         totCCC[frontChannelA].append(t[frontChannelA])
218         chargeCCC[frontChannelA].append(q[frontChannelA])
219         totCCC[frontChannelB].append(t[frontChannelB])
220         chargeCCC[frontChannelB].append(q[frontChannelB])
221         totCCC[rearChannelA].append(t[rearChannelA])
222         chargeCCC[rearChannelA].append(q[rearChannelA])
223         totCCC[rearChannelB].append(t[rearChannelB])
224         chargeCCC[rearChannelB].append(q[rearChannelB])
225         channelDiffsCCC[0].append(bars[0].diff)
226         channelDiffsCCC_cor[0].append(bars[0].diffcor)
227         channelDiffsCCC[1].append(bars[1].diff)
228         channelDiffsCCC_cor[1].append(bars[1].diffcor)
229         totCCC_channelWalk[0][frontChannelA].append(t[frontChannelA])
230         totCCC_channelWalk[0][frontChannelB].append(t[frontChannelB])
231         totCCC_channelWalk[1][rearChannelA].append(t[rearChannelA])
232         totCCC_channelWalk[1][rearChannelB].append(t[rearChannelB])
233         triggerDiffsCCC[0].append(bars[1].mean - bars[0].mean)
234         triggerDiffsCCC_cor[0].append(bars[1].meancor - bars[0].meancor)
235         totCCC_detectorWalk[0][frontChannelA].append(t[frontChannelA])
236         totCCC_detectorWalk[0][frontChannelB].append(t[frontChannelB])
237         totCCC_detectorWalk[0][rearChannelA].append(t[rearChannelA])
238         totCCC_detectorWalk[0][rearChannelB].append(t[rearChannelB])
239         effCounter += 1
```

Code F.4: The function `totToCharge()`.

```
import math as m
# Initialize global variables from NINOglobals.py
import NINOglobals as g
g.initialize()

def totToCharge(tot, channel):
    if tot > 0:
        charge = (-g.totCalib[channel][0] + 2*g.totCalib[channel][1]*g.totCalib[channel][2] + tot + m.sqrt(g.totCalib[channel][0]**2 + 4*g.totCalib[channel][1]*g.totCalib[channel][3] - 2*g.totCalib[channel][0]*tot + tot**2))/2/g.totCalib[channel][1]
    else:
        return 0.0
    if charge > g.chargeCut[channel]:
        return charge
    else:
        return 0.0
```

F.5 Exemplary Analysis Report

During data analysis, a `pdf` report is generated for each dataset, providing a comprehensive summary of all relevant information. The following pages contain the `pdf` report for the dataset `MXTriggerBeamTimeJune2024/data_posScan/meas_posScan_pos_34.0.dat` from the `GitLab` repository `MAGIX_DarkMESA/MXTriggerReadout`, which served as the representative example throughout Chapter 8. Please note that many plots display the label "Channel not connected.", as only ten readout channels were active during the MAMI beam time described in Section **??**. In setups with a different channel configuration, the corresponding plots would automatically populate with data.

Fine time calibrations per channel

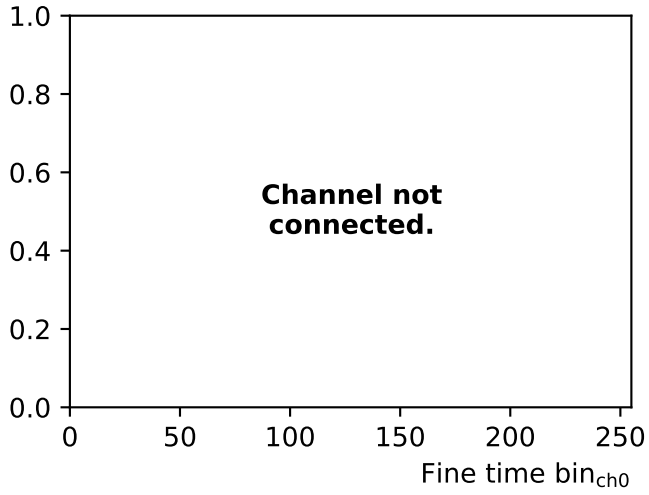
Channel not connected.
Fine time bin$_{ch0}$

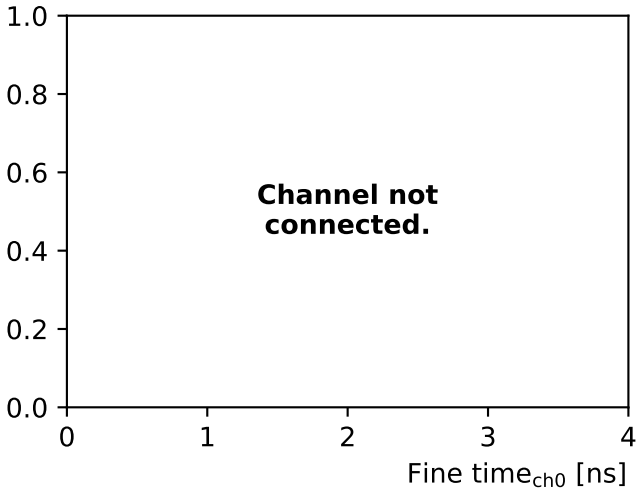
Channel not connected.
Fine time$_{ch0}$ [ns]

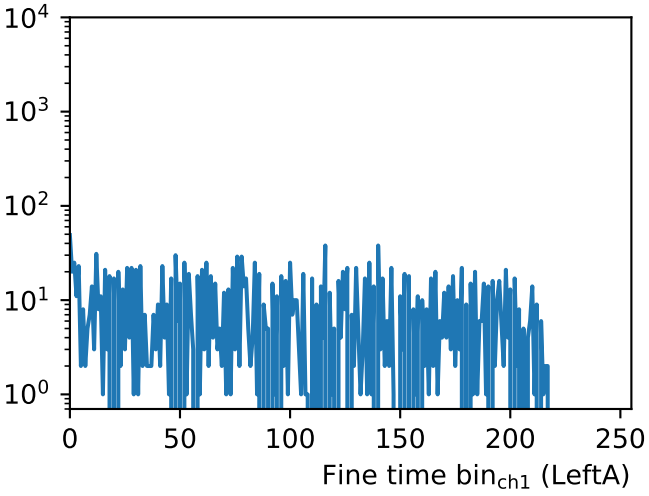
Fine time bin$_{ch1}$ (LeftA)

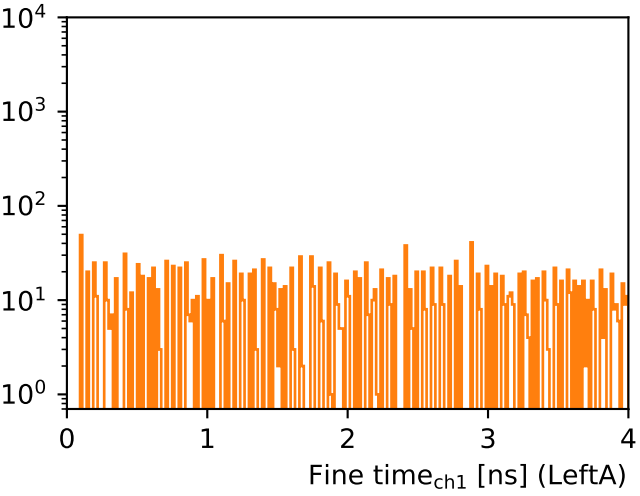
Fine time$_{ch1}$ [ns] (LeftA)

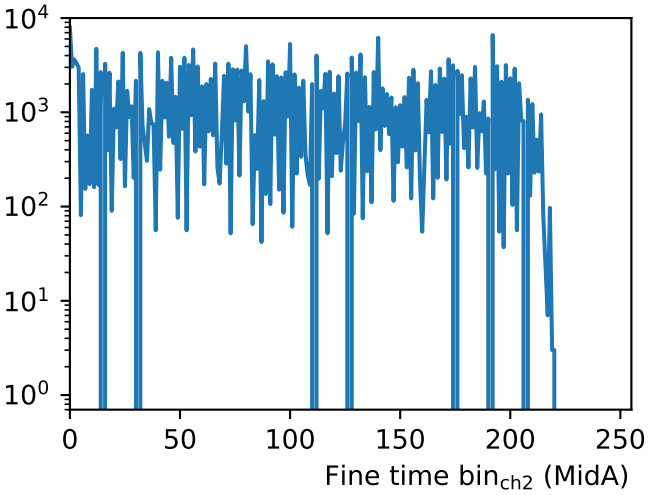
Fine time bin$_{ch2}$ (MidA)

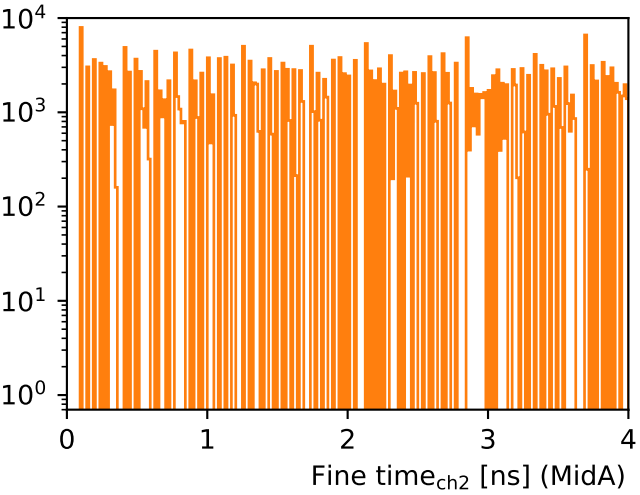
Fine time$_{ch2}$ [ns] (MidA)

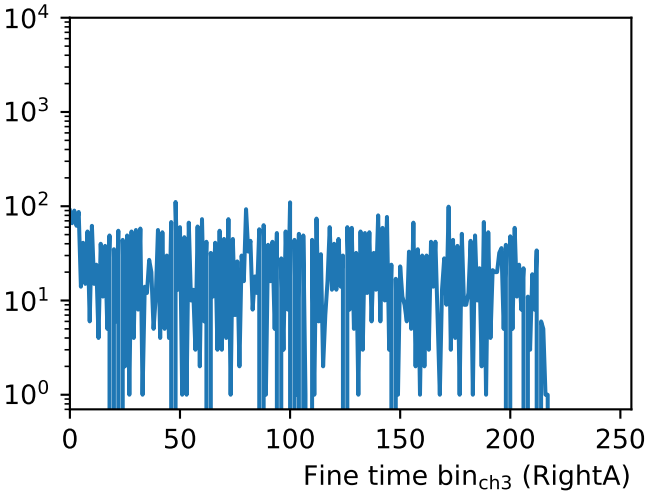
Fine time bin$_{ch3}$ (RightA)

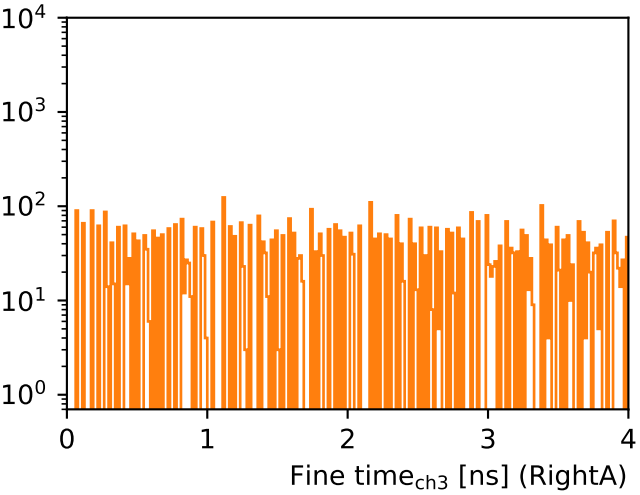
Fine time$_{ch3}$ [ns] (RightA)

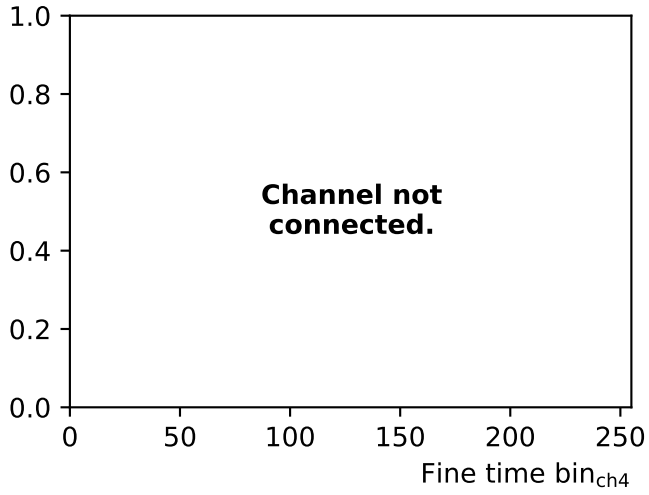
Channel not connected.
Fine time bin$_{ch4}$

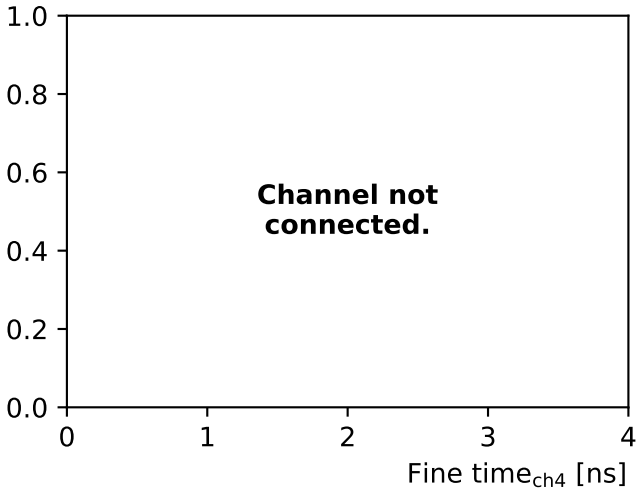
Channel not connected.
Fine time$_{ch4}$ [ns]

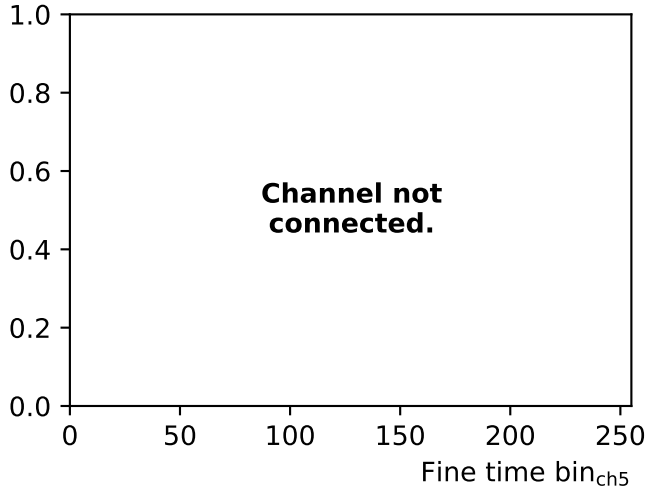
Channel not connected.
Fine time bin$_{ch5}$

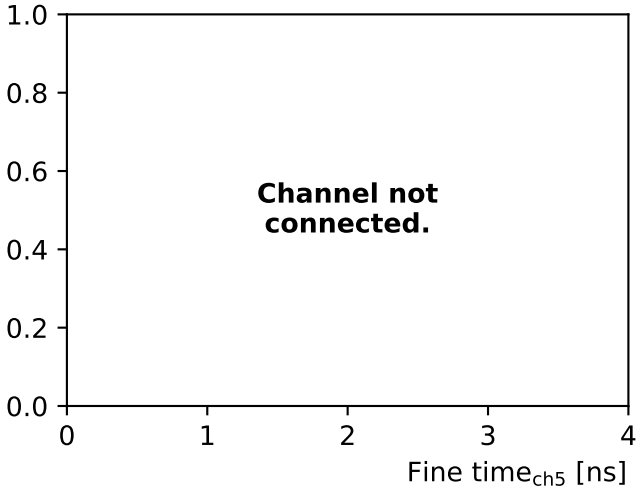
Channel not connected.
Fine time$_{ch5}$ [ns]

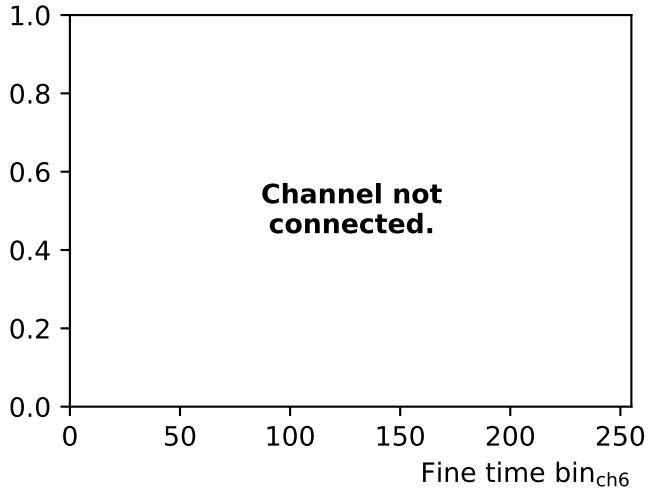
Channel not connected.
Fine time bin$_{ch6}$

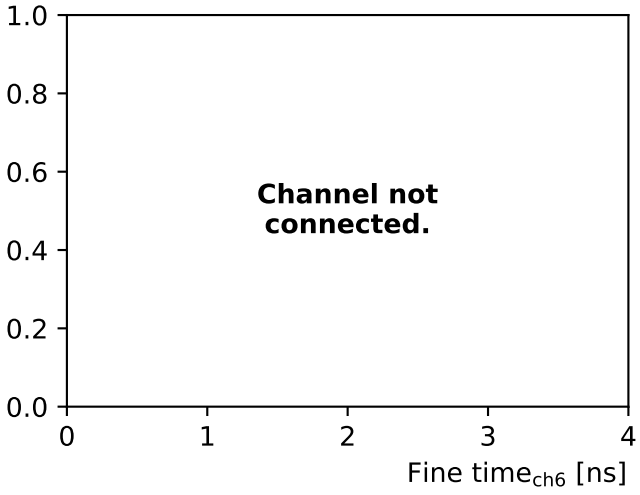
Channel not connected.
Fine time$_{ch6}$ [ns]

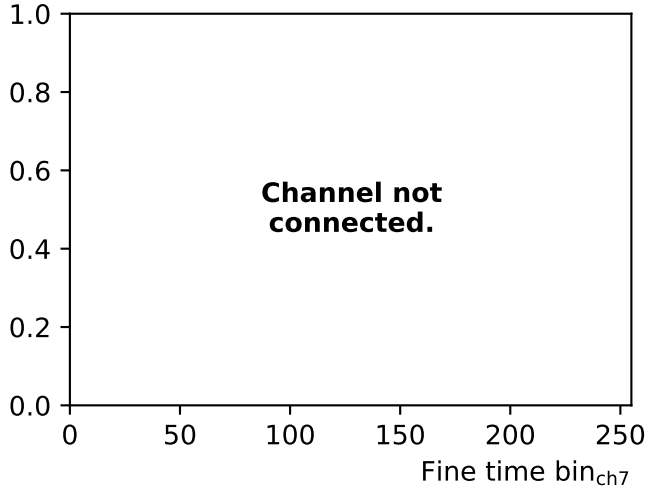
Channel not connected.
Fine time bin$_{ch7}$

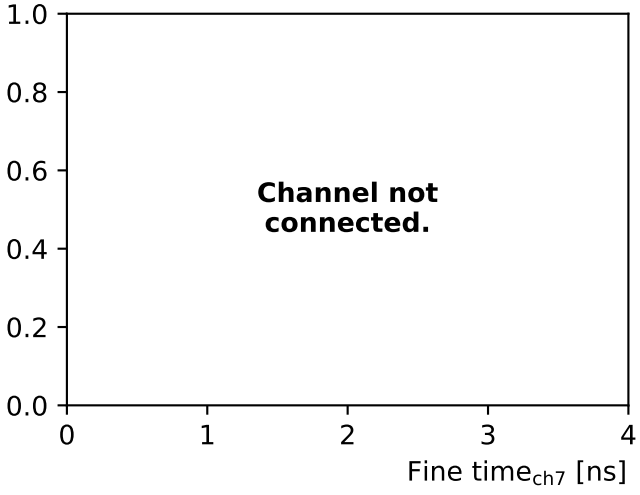
Channel not connected.
Fine time$_{ch7}$ [ns]

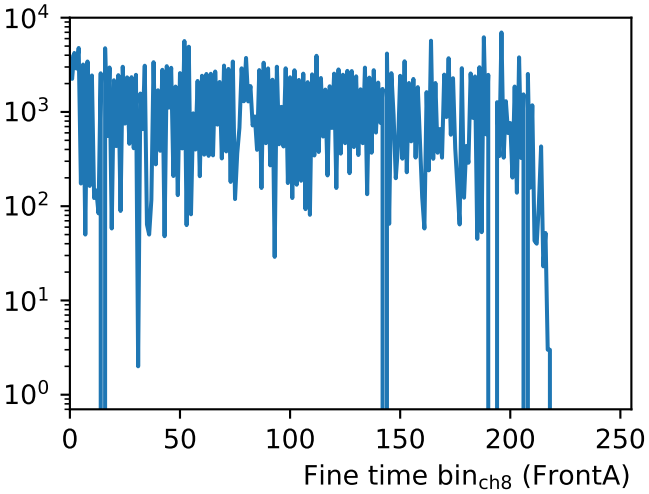
Fine time bin$_{ch8}$ (FrontA)

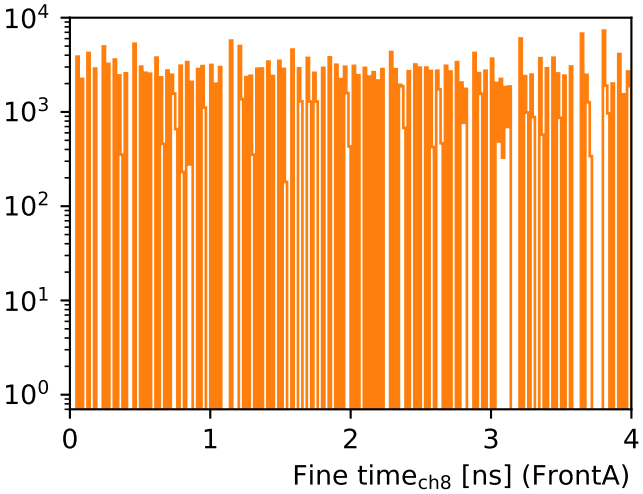
Fine time$_{ch8}$ [ns] (FrontA)

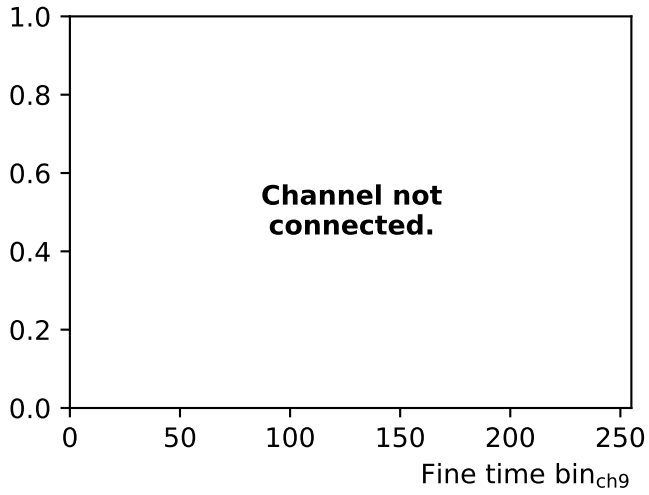
Channel not connected.
Fine time bin$_{ch9}$

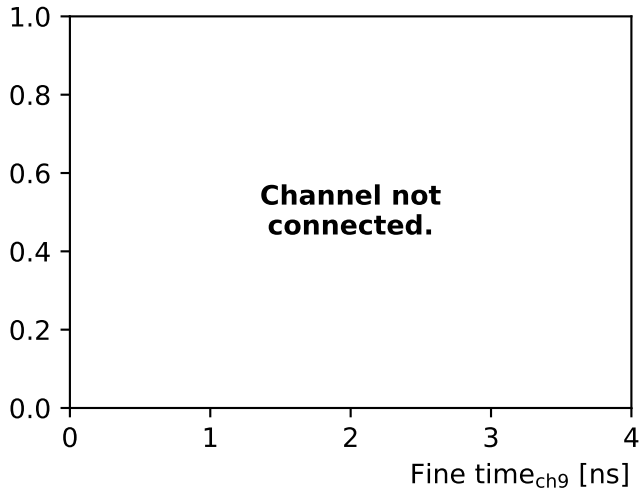
Channel not connected.
Fine time$_{ch9}$ [ns]

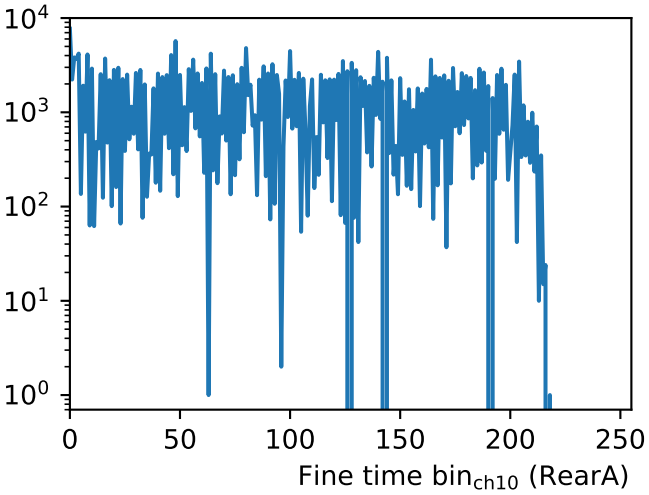
Fine time bin$_{ch10}$ (RearA)

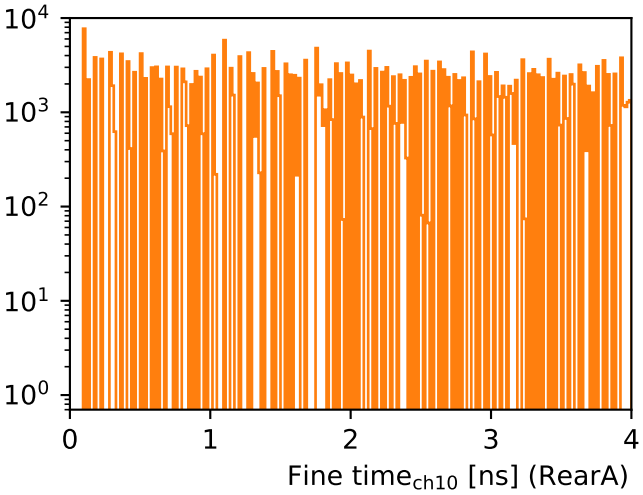
Fine time$_{ch10}$ [ns] (RearA)

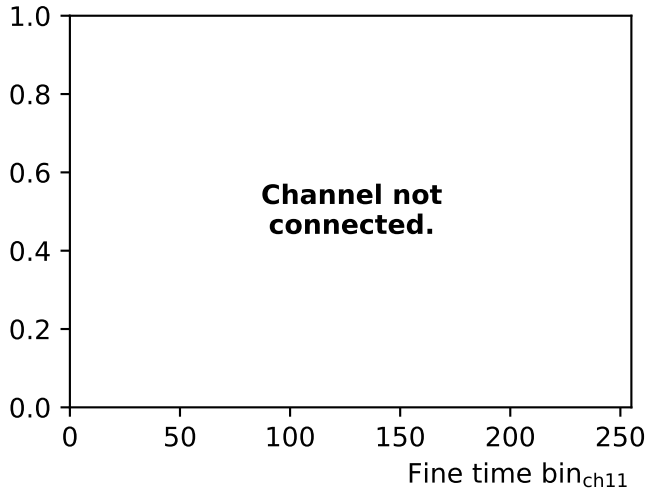
Channel not connected.
Fine time bin$_{ch11}$

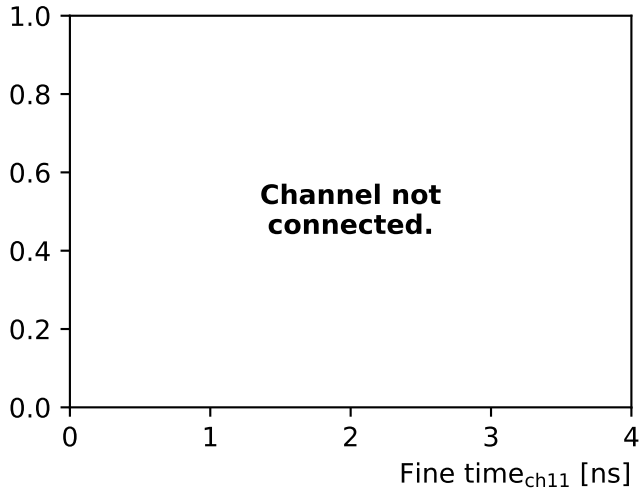
Channel not connected.
Fine time$_{ch11}$ [ns]

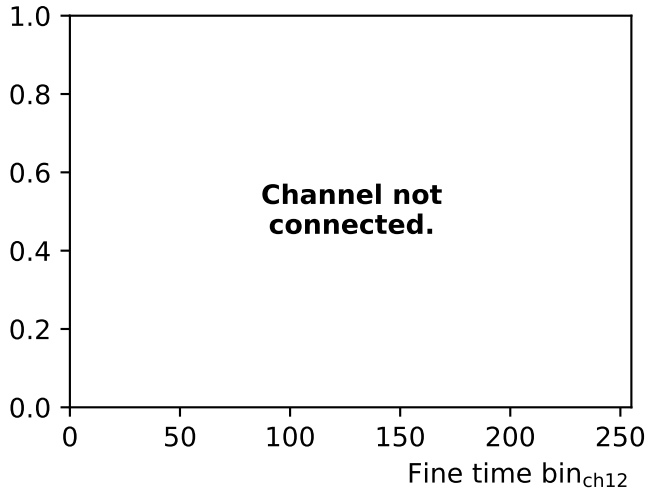
Channel not connected.
Fine time bin$_{ch12}$

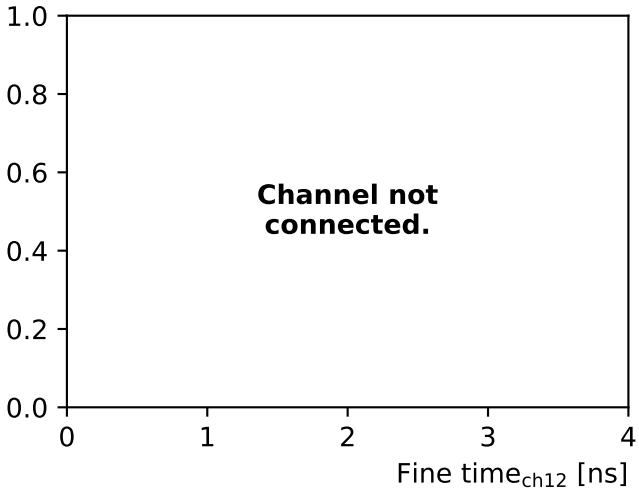
Channel not connected.
Fine time$_{ch12}$ [ns]

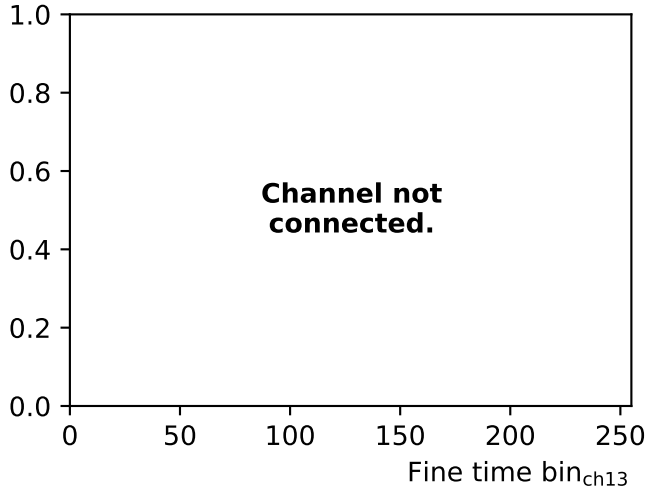
Channel not connected.
Fine time bin$_{ch13}$

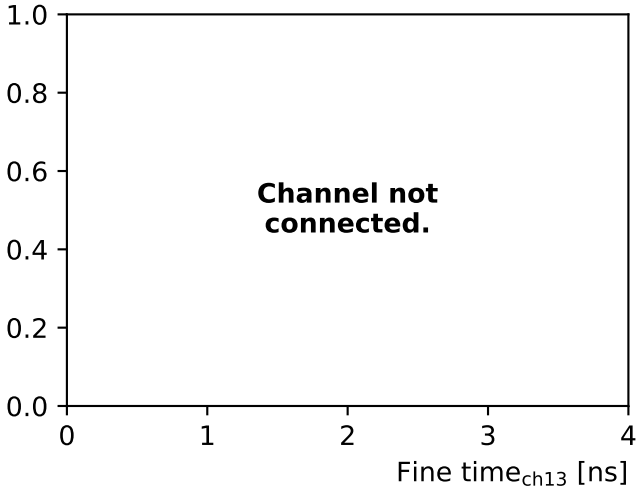
Channel not connected.
Fine time$_{ch13}$ [ns]

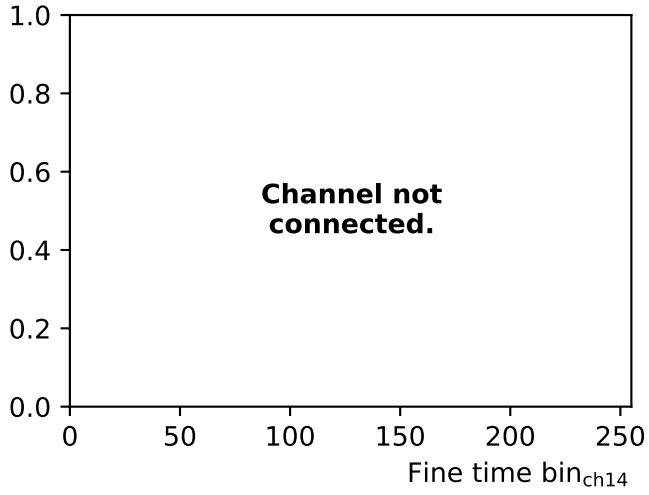
Channel not connected.
Fine time bin$_{ch14}$

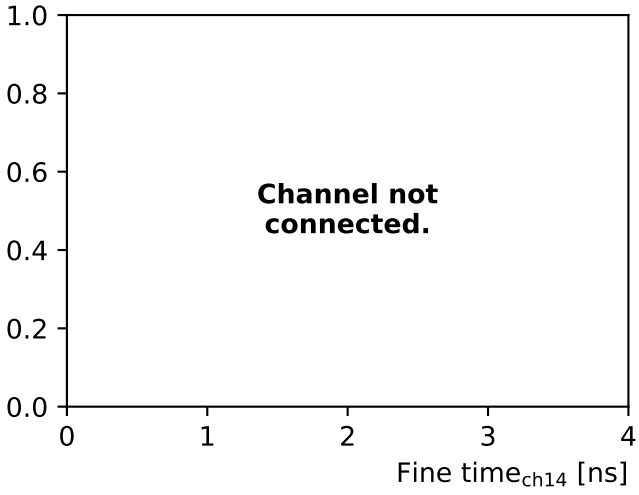
Channel not connected.
Fine time$_{ch14}$ [ns]

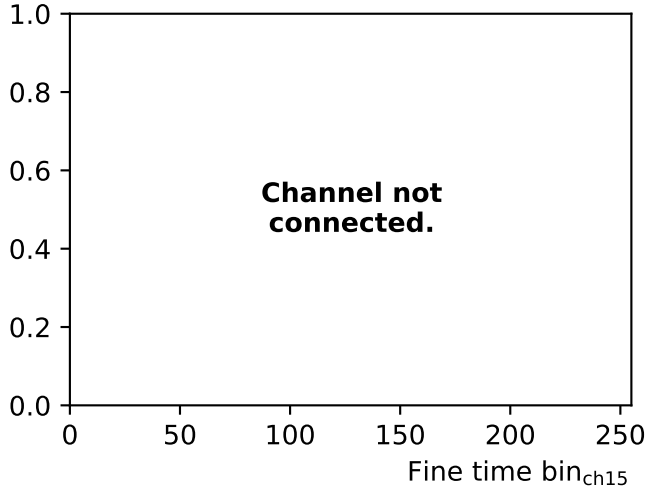
Channel not connected.
Fine time bin$_{ch15}$

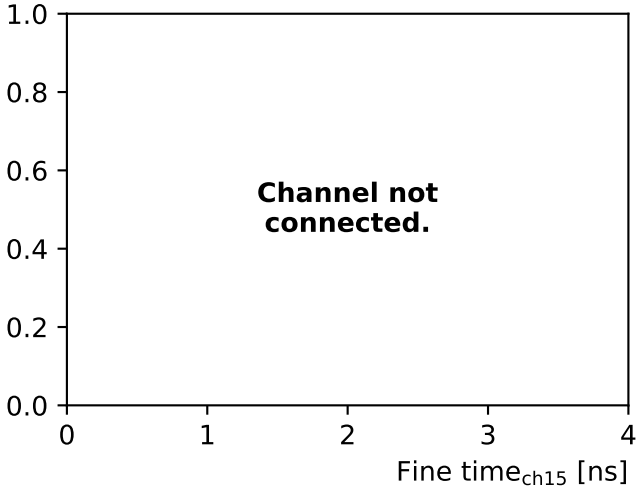
Channel not connected.
Fine time$_{ch15}$ [ns]

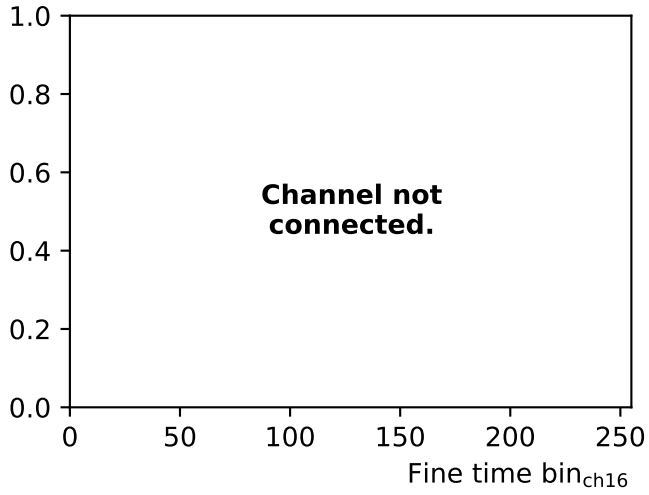
Channel not connected.
Fine time bin$_{ch16}$

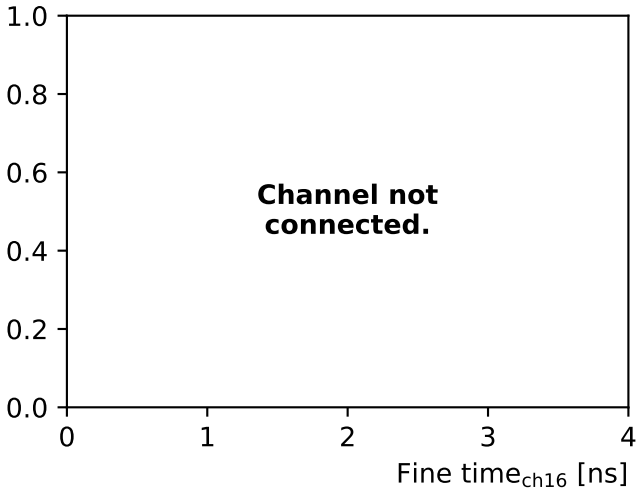
Channel not connected.
Fine time$_{ch16}$ [ns]

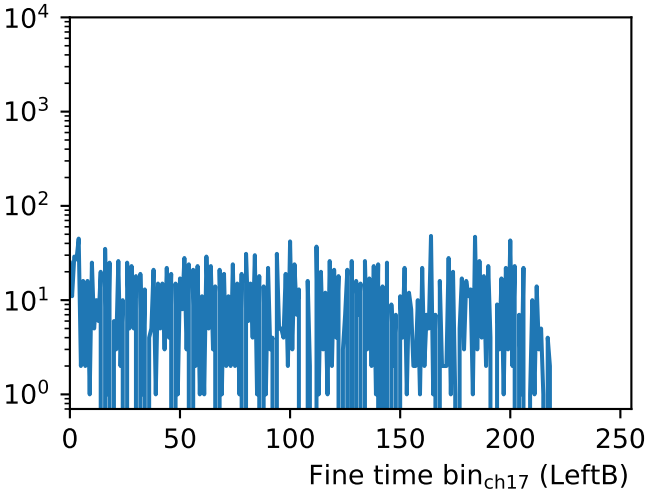
Fine time bin$_{ch17}$ (LeftB)

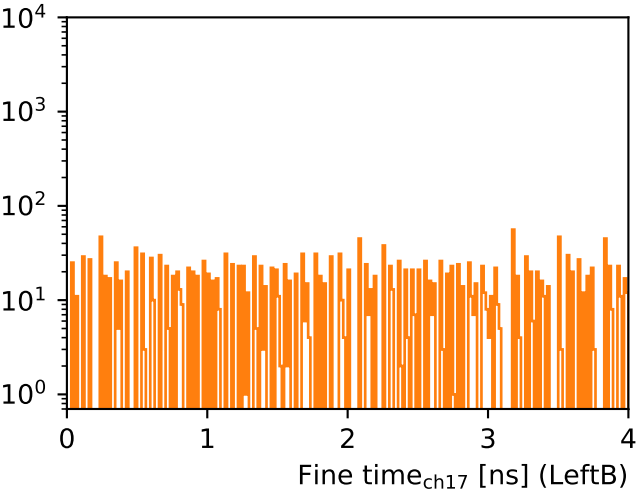
Fine time$_{ch17}$ [ns] (LeftB)

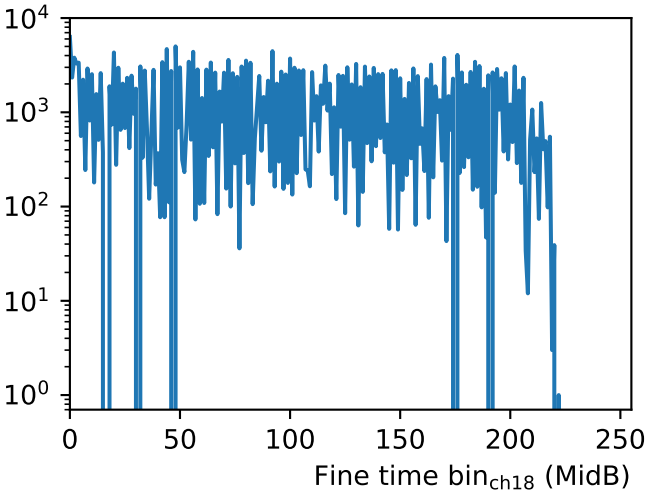
Fine time bin$_{ch18}$ (MidB)

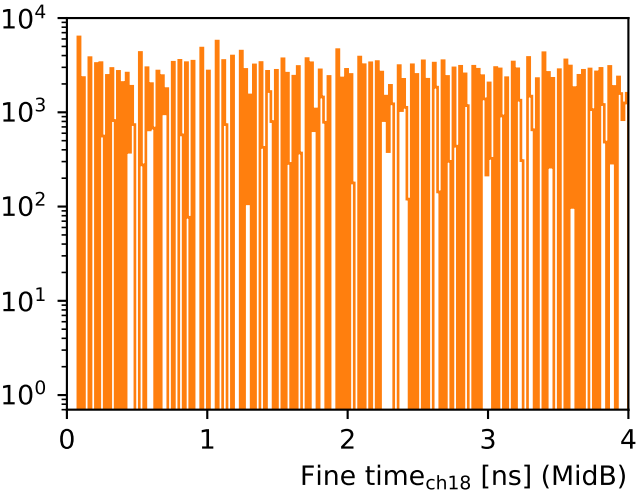
Fine time$_{ch18}$ [ns] (MidB)

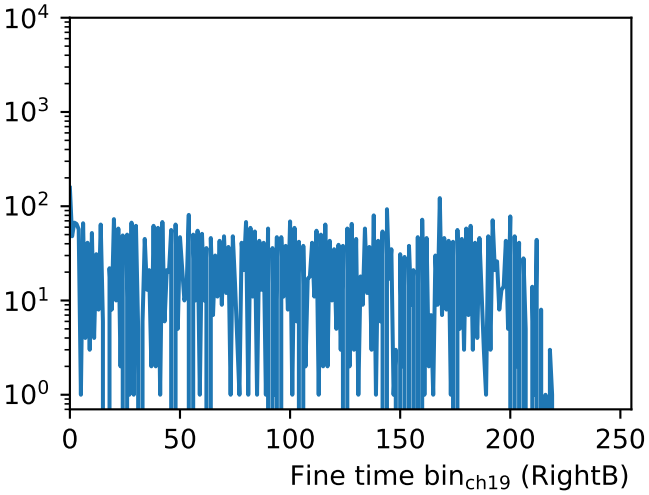
Fine time bin$_{ch19}$ (RightB)

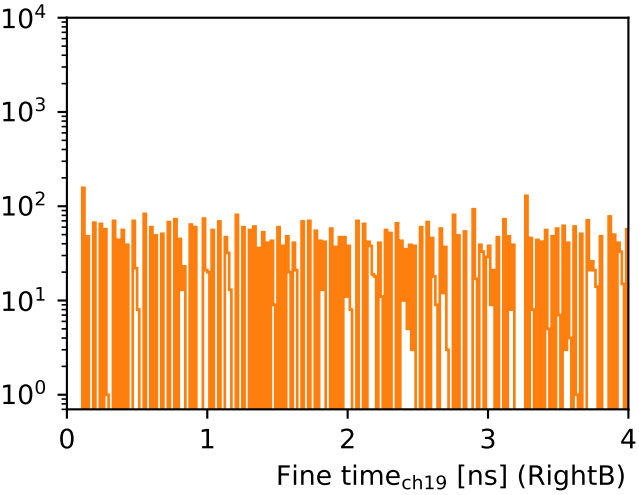
Fine time$_{ch19}$ [ns] (RightB)

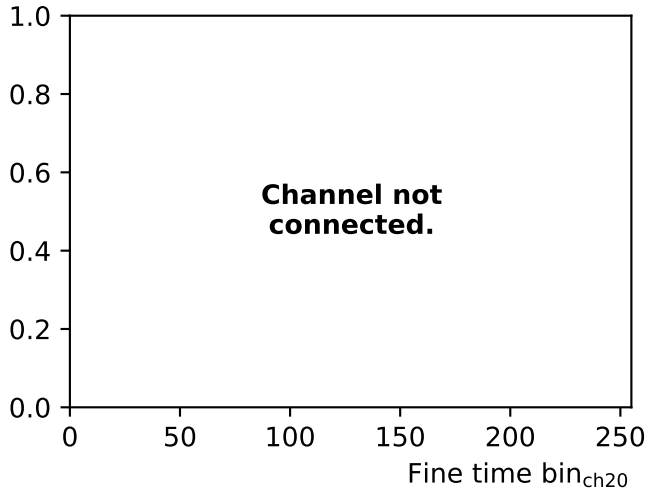
Channel not connected.
Fine time bin$_{ch20}$

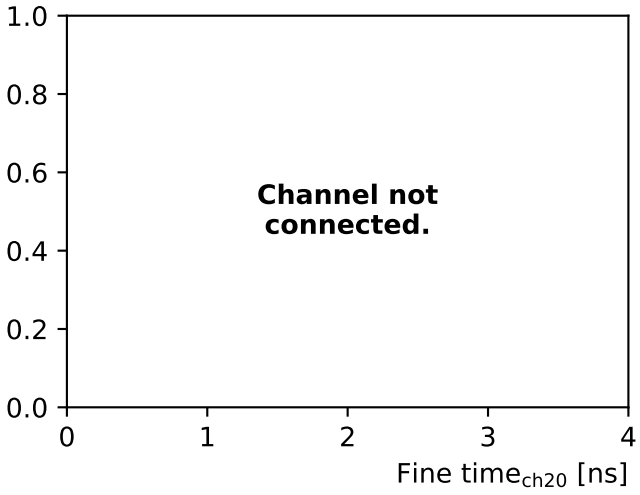
Channel not connected.
Fine time$_{ch20}$ [ns]

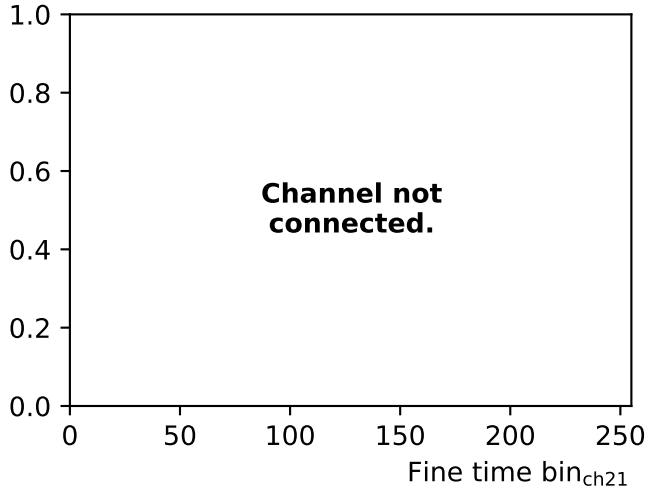
Channel not connected.
Fine time bin$_{ch21}$

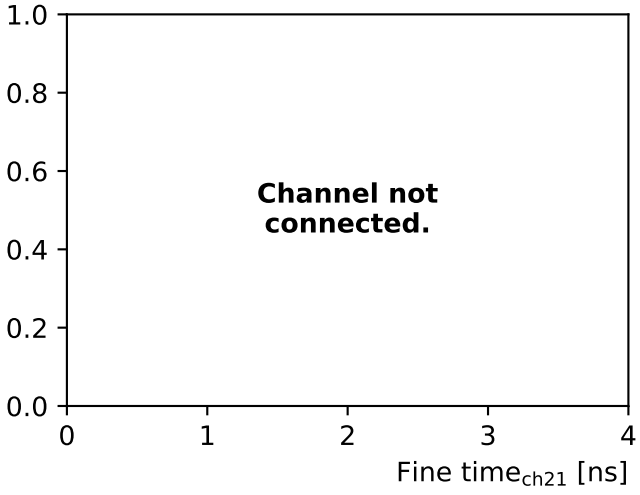
Channel not connected.
Fine time$_{ch21}$ [ns]

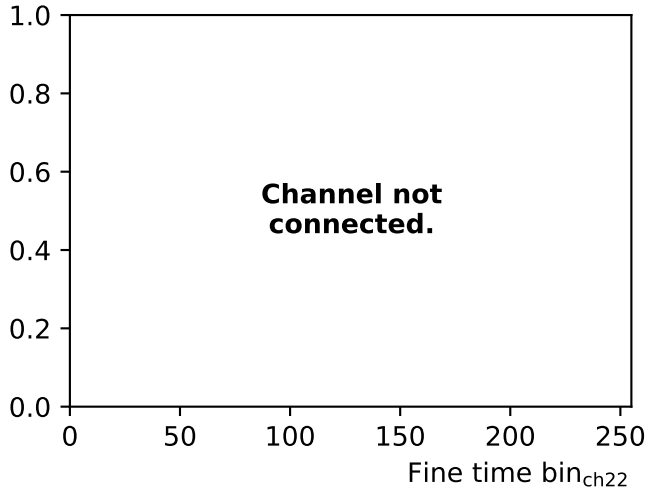
Channel not connected.
Fine time bin$_{ch22}$

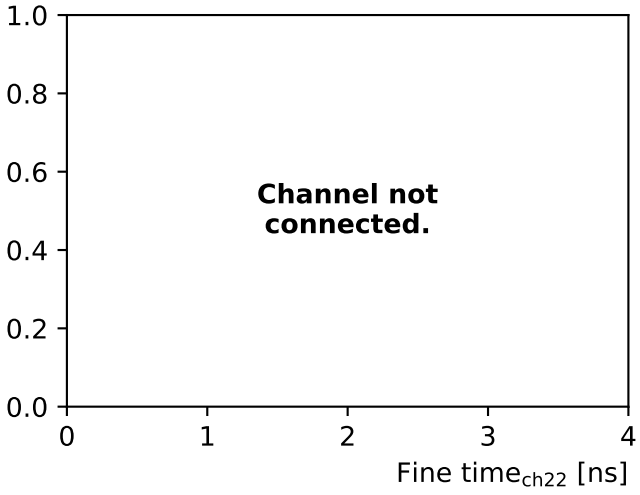
Channel not connected.
Fine time$_{ch22}$ [ns]

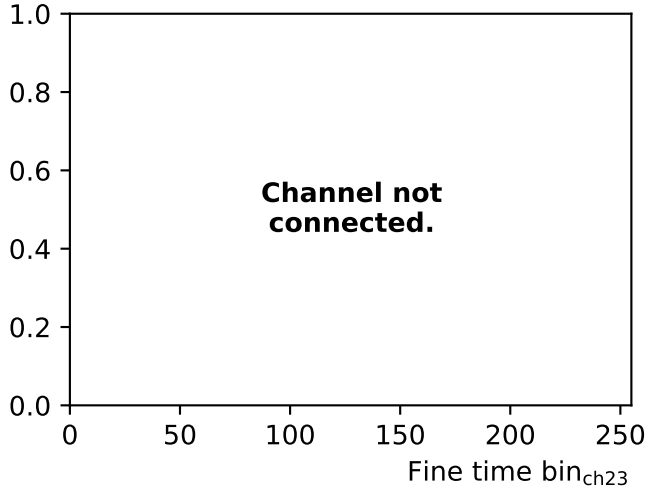
Channel not connected.
Fine time bin$_{ch23}$

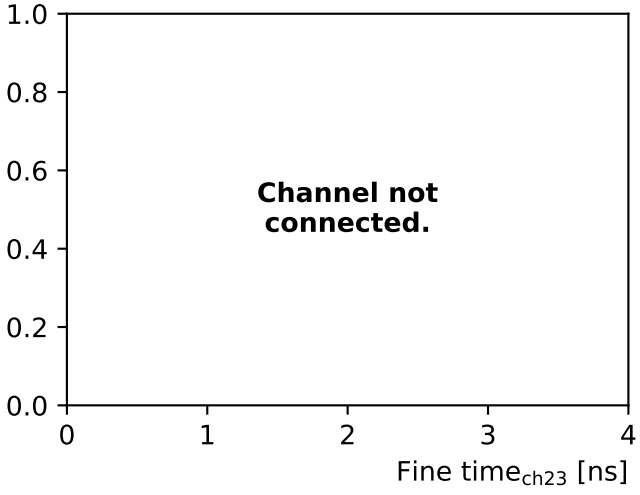
Channel not connected.
Fine time$_{ch23}$ [ns]

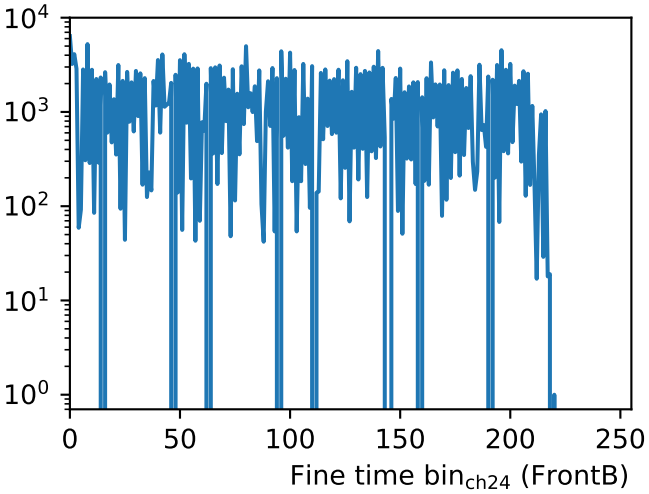
Fine time bin$_{ch24}$ (FrontB)

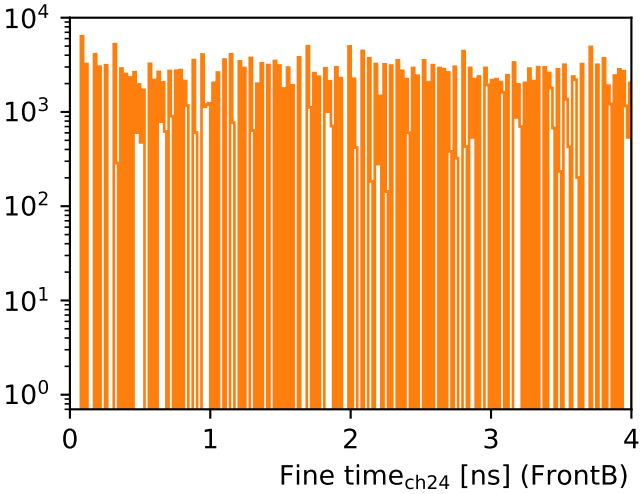
Fine time$_{ch24}$ [ns] (FrontB)

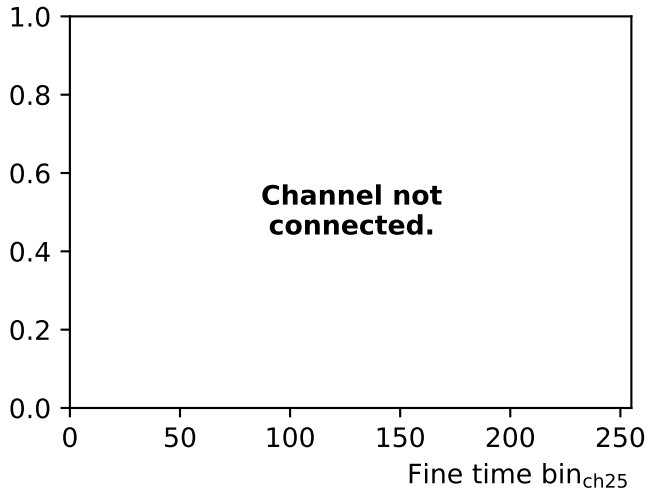
Channel not connected.
Fine time bin$_{ch25}$

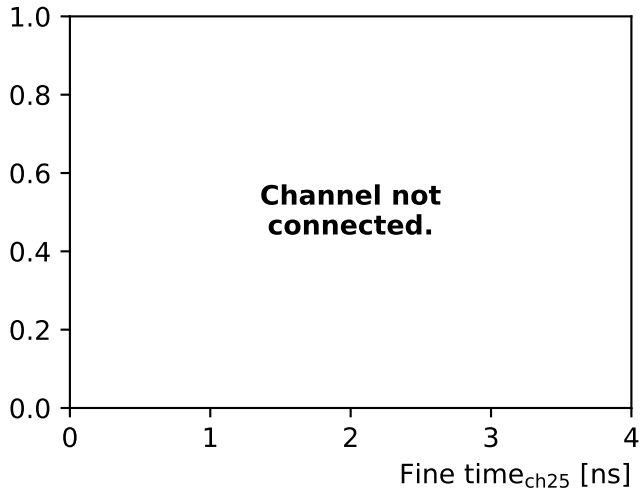
Channel not connected.
Fine time$_{ch25}$ [ns]

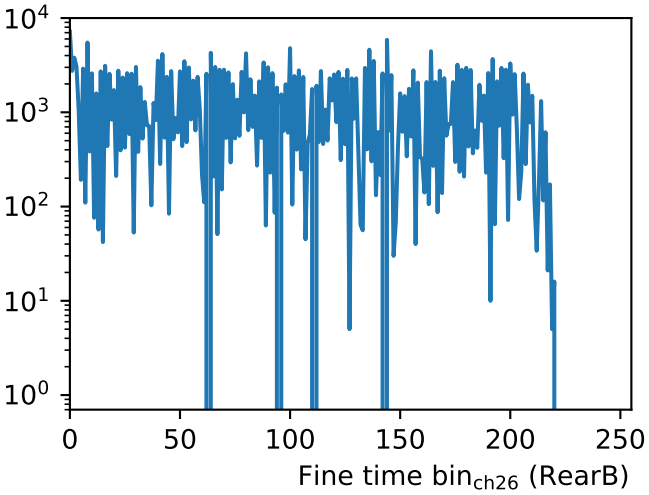
Fine time bin$_{ch26}$ (RearB)

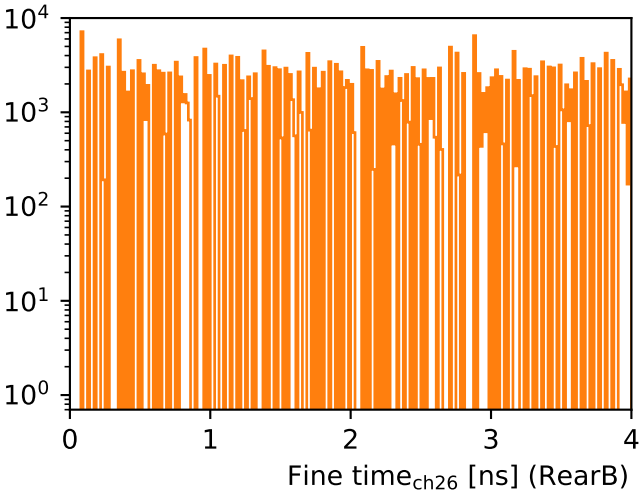
Fine time$_{ch26}$ [ns] (RearB)

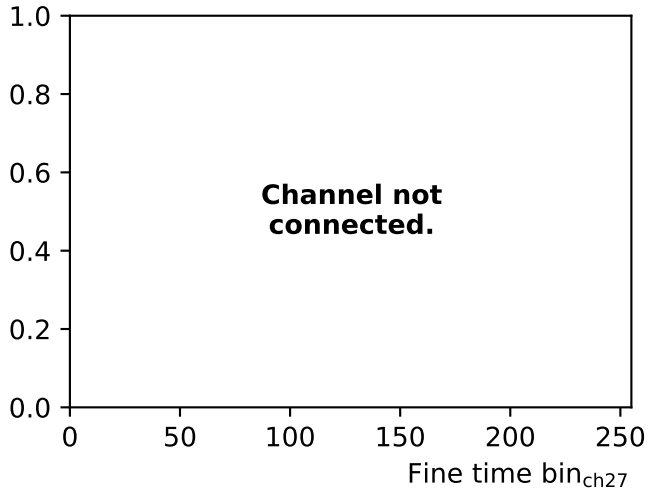
Channel not connected.
Fine time bin$_{ch27}$

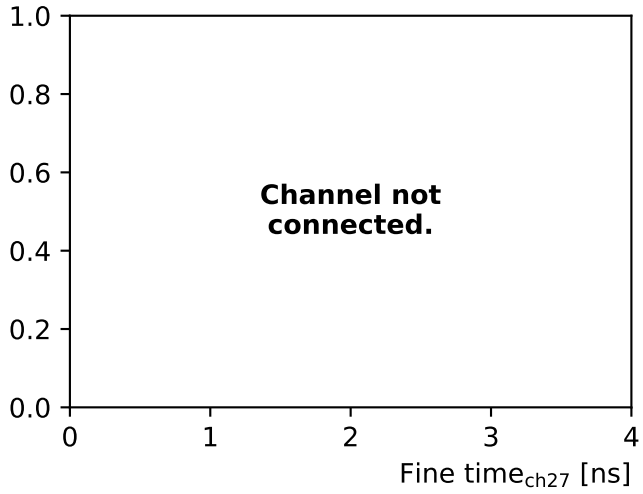
Channel not connected.
Fine time$_{ch27}$ [ns]

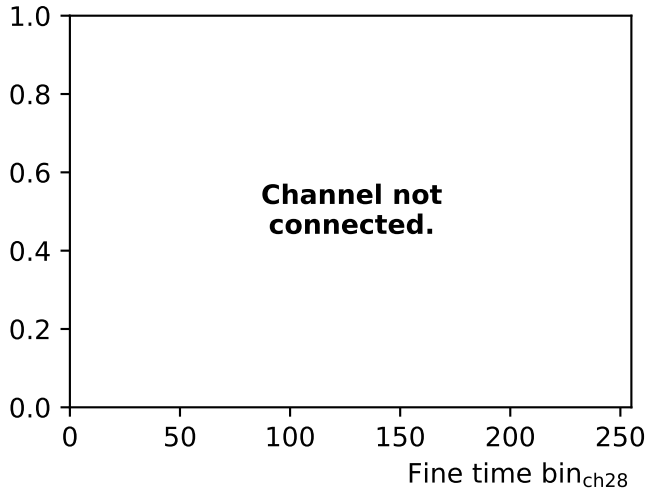
Channel not connected.
Fine time bin$_{ch28}$

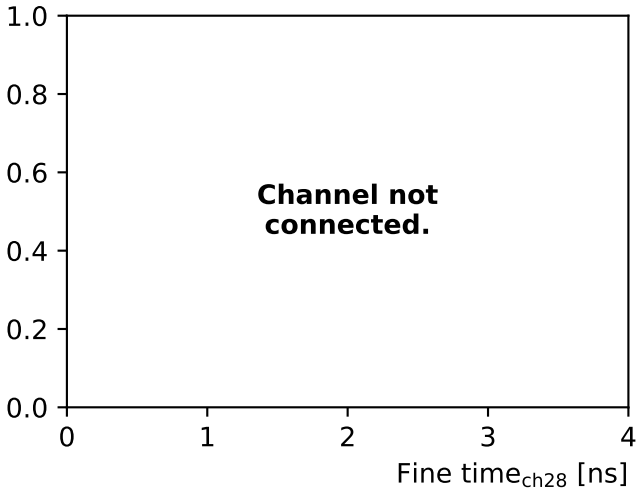
Channel not connected.
Fine time$_{ch28}$ [ns]

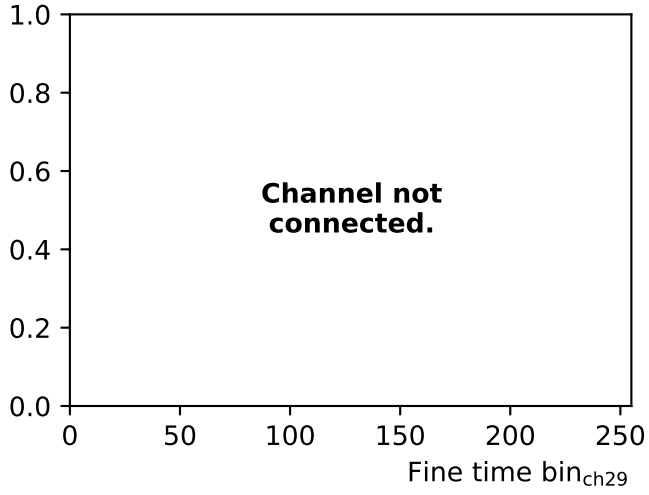
Channel not connected.
Fine time bin$_{ch29}$

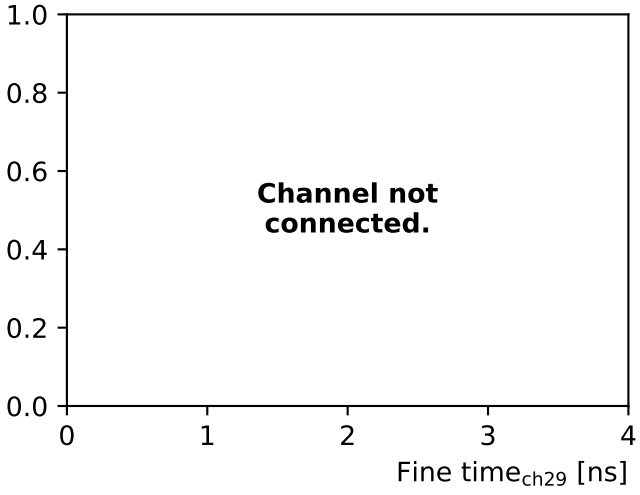
Channel not connected.
Fine time$_{ch29}$ [ns]

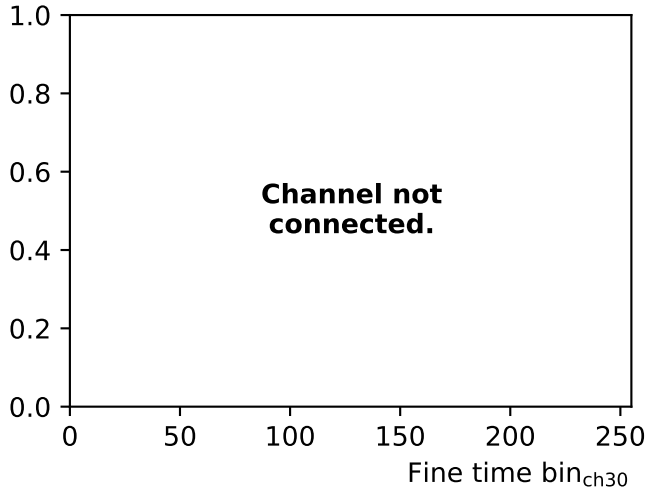
Channel not connected.
Fine time bin$_{ch30}$

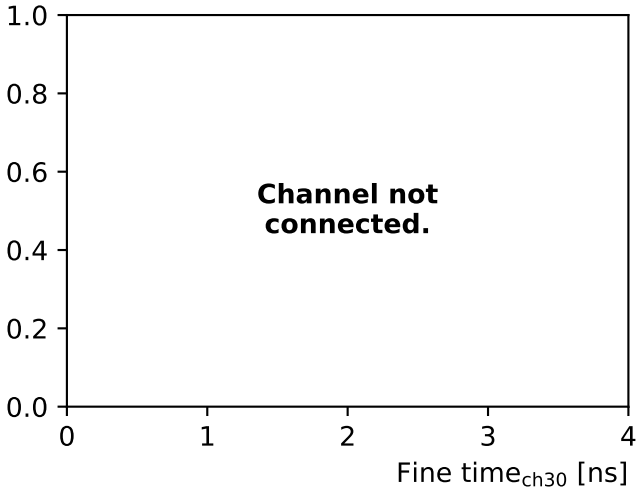
Channel not connected.
Fine time$_{ch30}$ [ns]

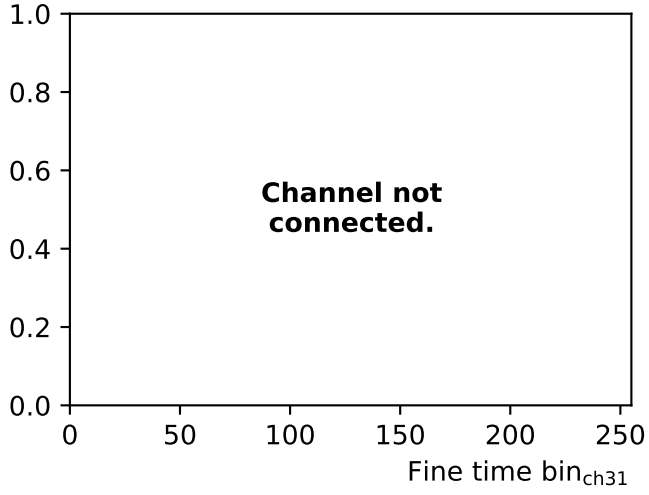
Channel not connected.
Fine time bin$_{ch31}$

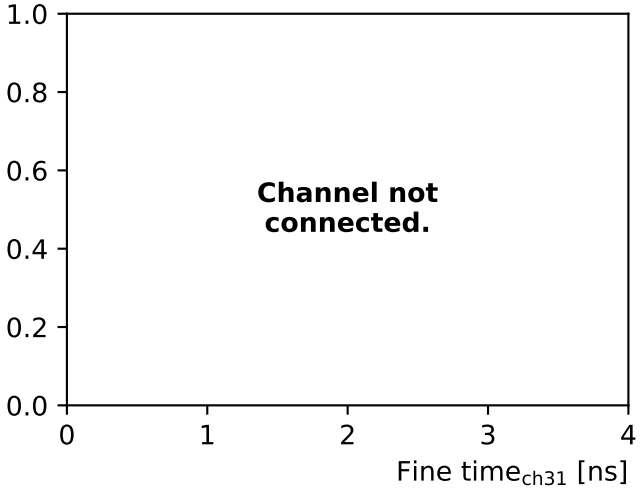
Channel not connected.
Fine time$_{ch31}$ [ns]

ToT
histograms
per channel

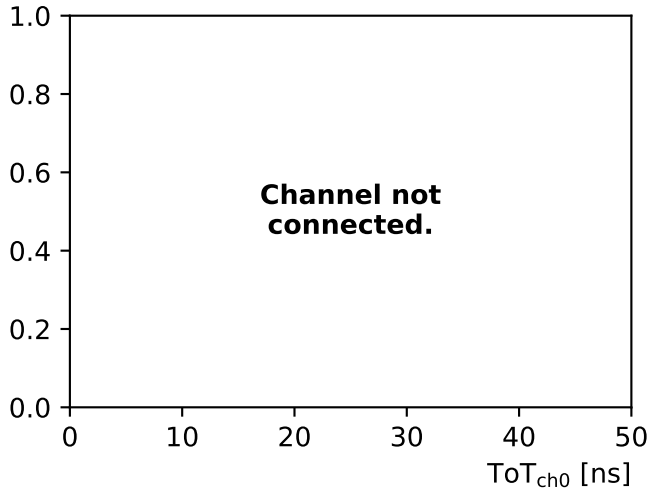
Channel not connected.
ToT$_{ch0}$ [ns]

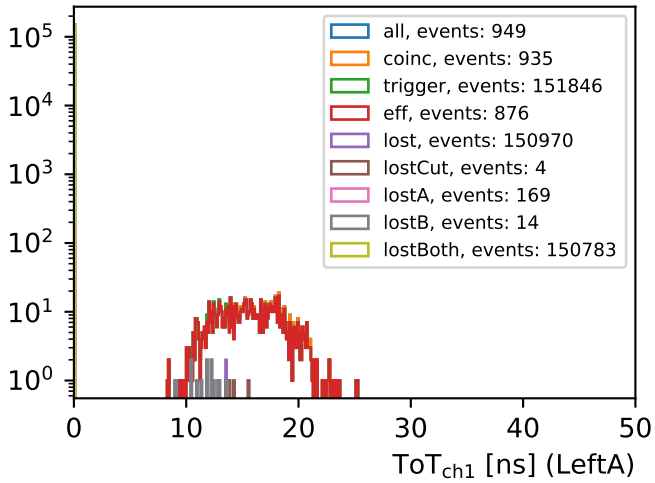
all, events: 949
coinc, events: 935
trigger, events: 151846
eff, events: 876
lost, events: 150970
lostCut, events: 4
lostA, events: 169
lostB, events: 14
lostBoth, events: 150783
ToT$_{ch1}$ [ns] (LeftA)

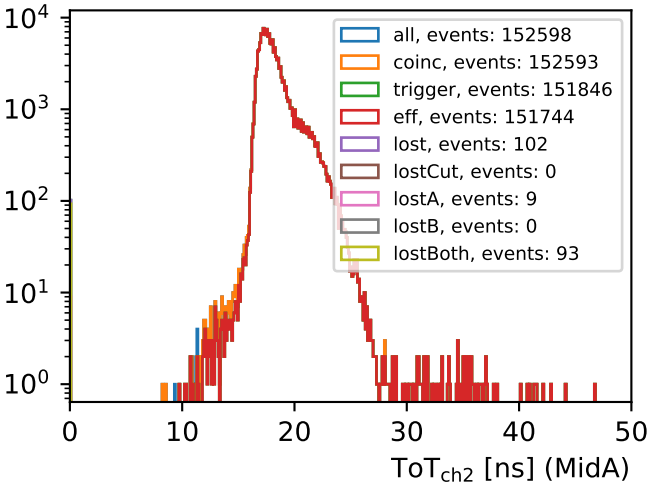
all, events: 152598
coinc, events: 152593
trigger, events: 151846
eff, events: 151744
lost, events: 102
lostCut, events: 0
lostA, events: 9
lostB, events: 0
lostBoth, events: 93
ToT$_{ch2}$ [ns] (MidA)

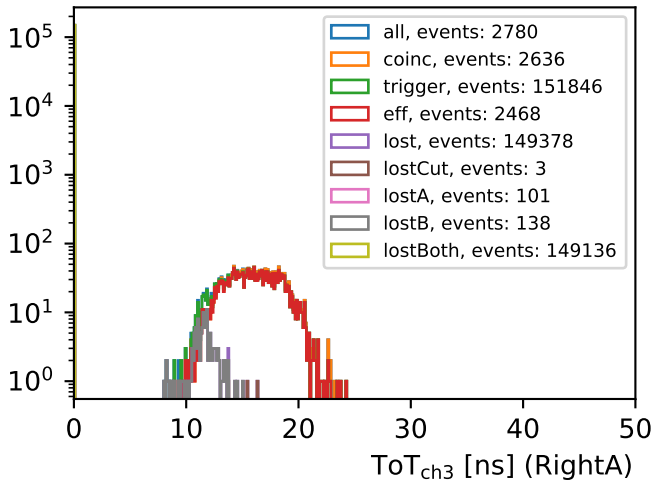
all, events: 2780
coinc, events: 2636
trigger, events: 151846
eff, events: 2468
lost, events: 149378
lostCut, events: 3
lostA, events: 101
lostB, events: 138
lostBoth, events: 149136
ToT$_{ch3}$ [ns] (RightA)

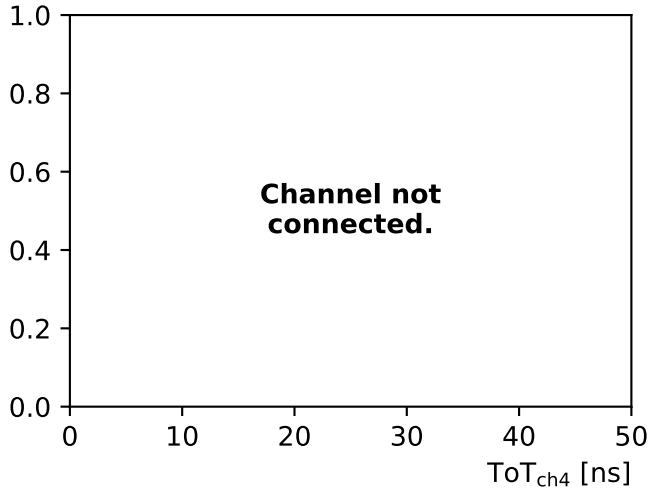
Channel not connected.
ToT$_{ch4}$ [ns]

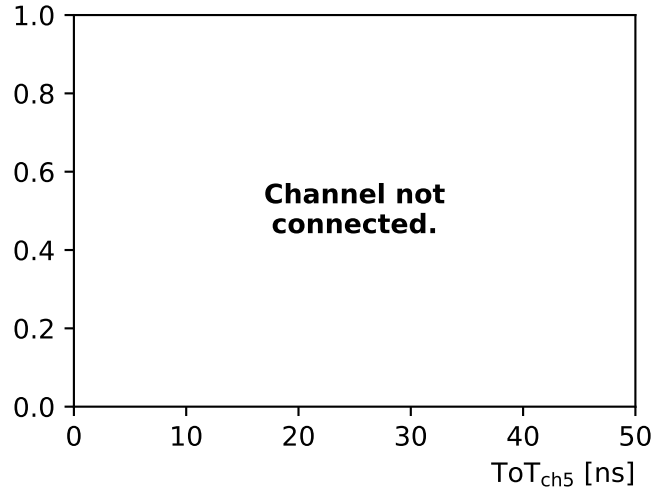
Channel not connected.
ToT$_{ch5}$ [ns]

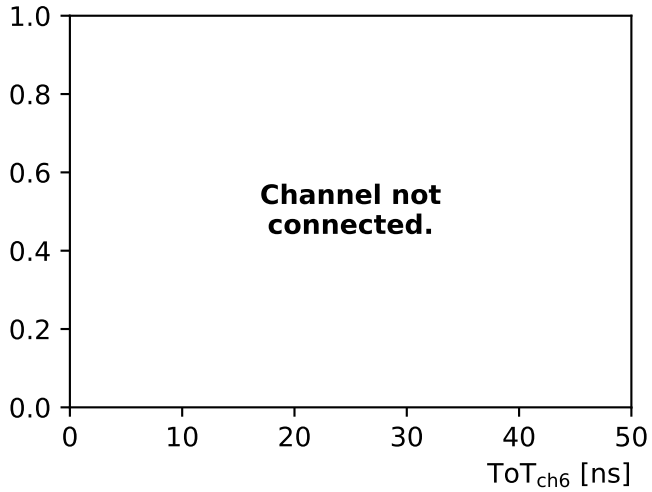
Channel not connected.
ToT$_{ch6}$ [ns]

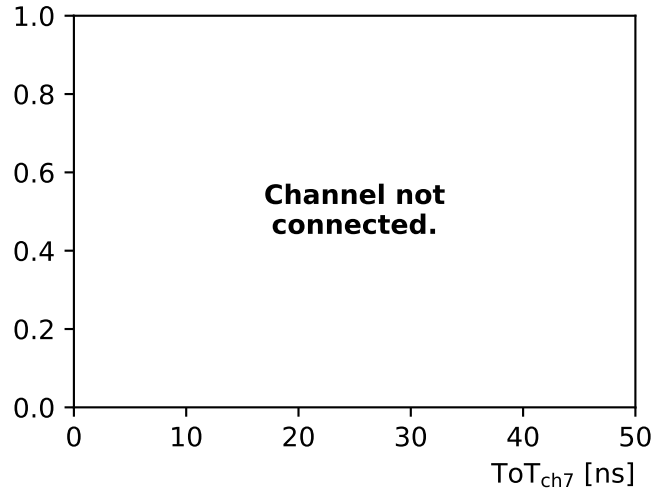
Channel not connected.
ToT$_{ch7}$ [ns]

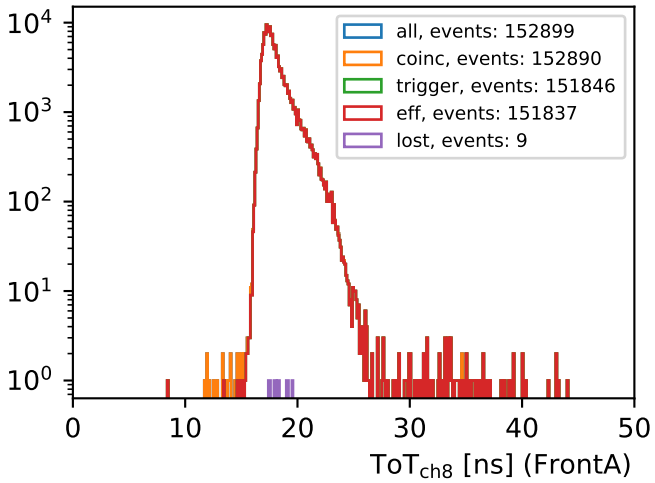
all, events: 152899
coinc, events: 152890
trigger, events: 151846
eff, events: 151837
lost, events: 9
ToT$_{ch8}$ [ns] (FrontA)

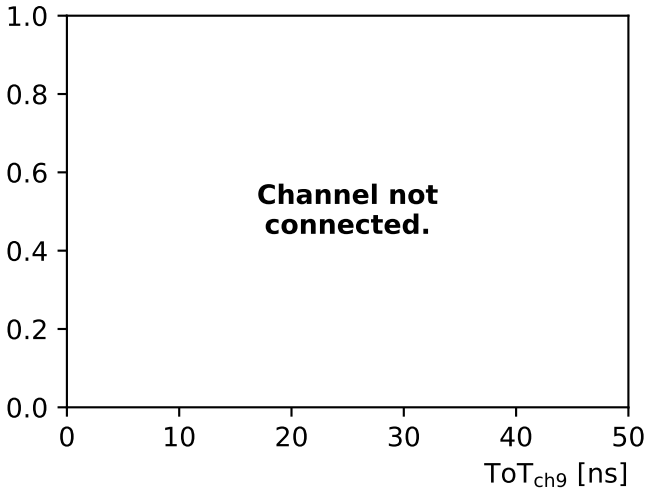
Channel not connected.
ToT$_{ch9}$ [ns]

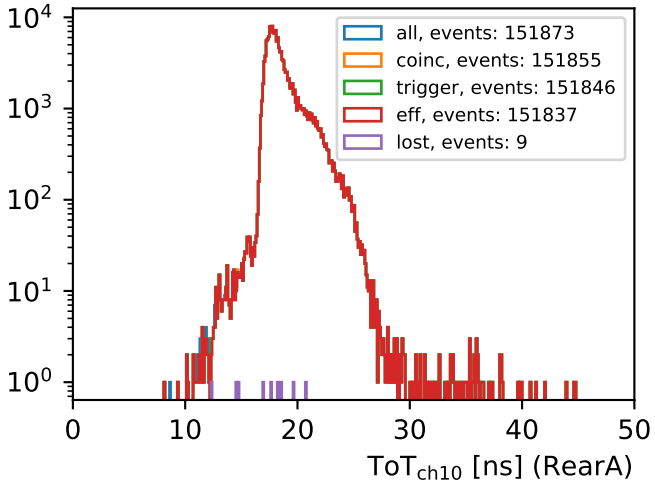
all, events: 151873
coinc, events: 151855
trigger, events: 151846
eff, events: 151837
lost, events: 9
ToT$_{ch10}$ [ns] (RearA)

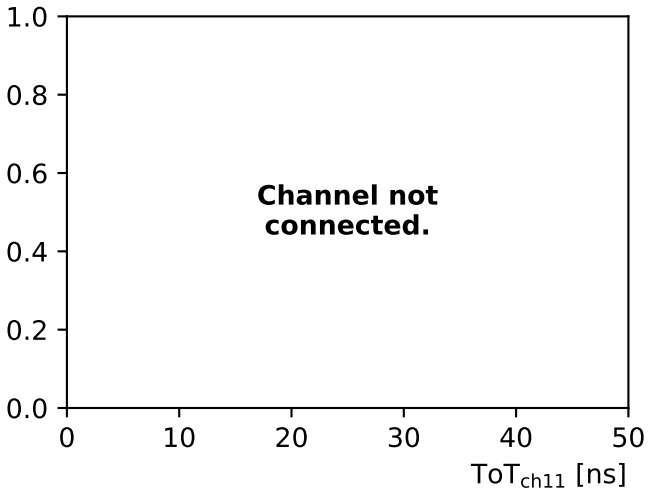
Channel not connected.
ToT$_{ch11}$ [ns]

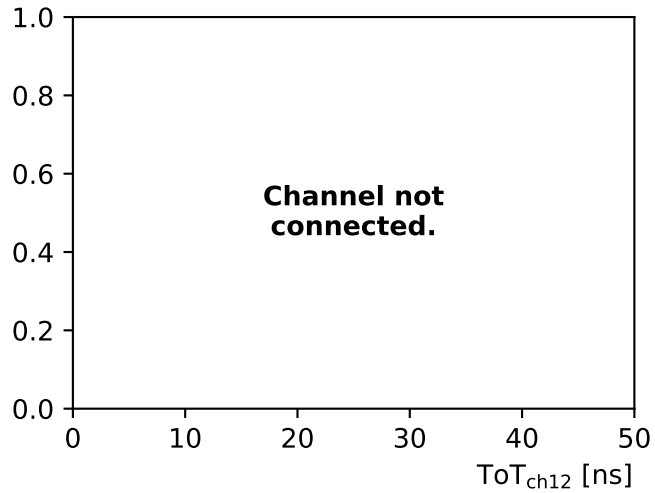
Channel not connected.
ToT$_{ch12}$ [ns]

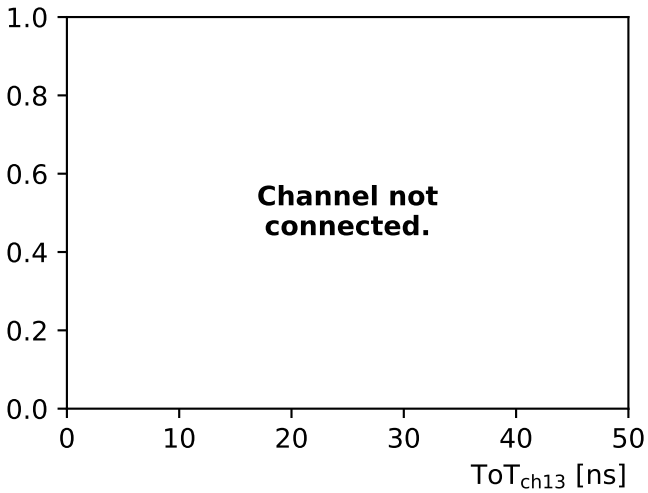
Channel not connected.
ToT$_{ch13}$ [ns]

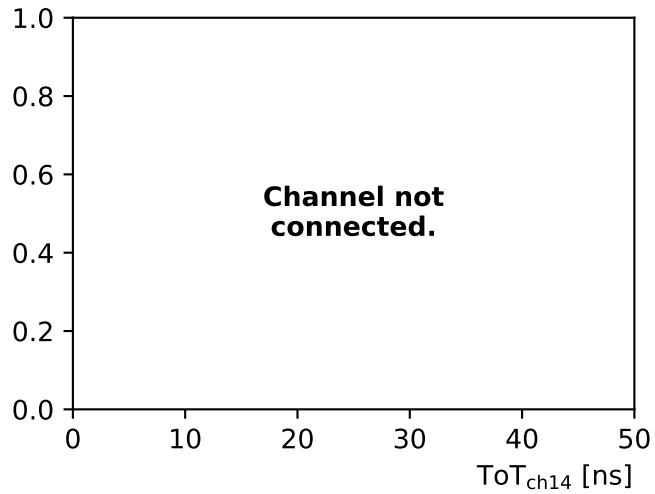
Channel not connected.
ToT$_{ch14}$ [ns]

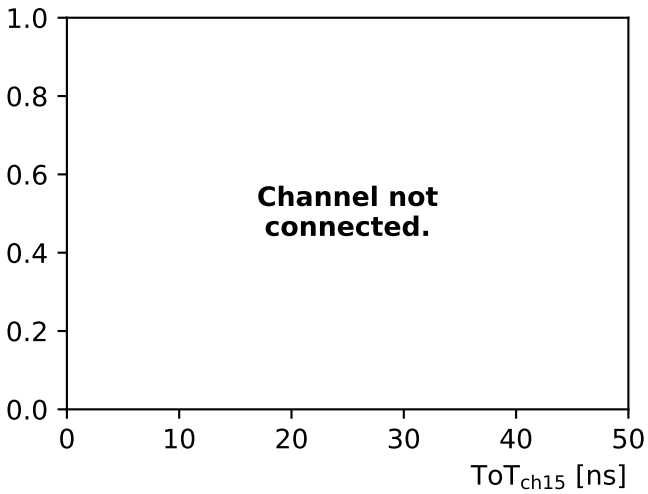
Channel not connected.
ToT$_{ch15}$ [ns]

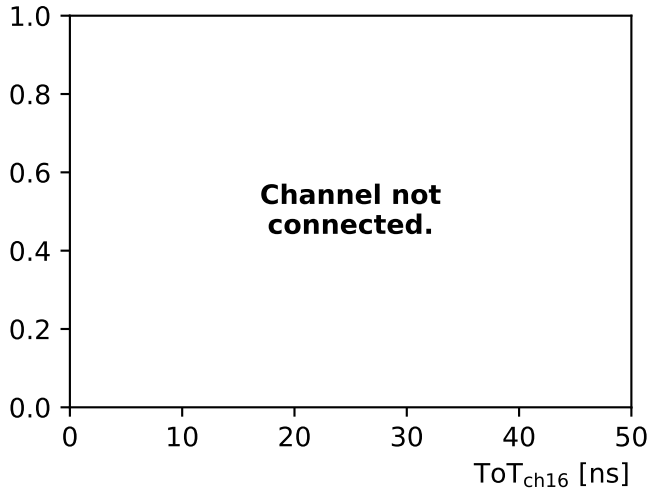
Channel not connected.
ToT$_{ch16}$ [ns]

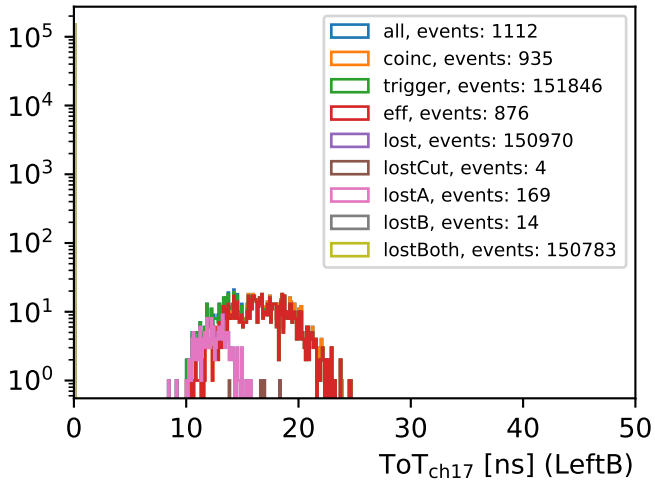
all, events: 1112
coinc, events: 935
trigger, events: 151846
eff, events: 876
lost, events: 150970
lostCut, events: 4
lostA, events: 169
lostB, events: 14
lostBoth, events: 150783
ToT$_{ch17}$ [ns] (LeftB)

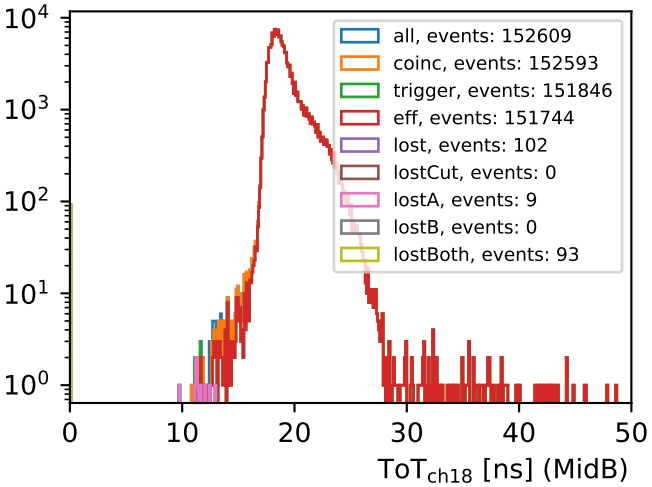
all, events: 152609
coinc, events: 152593
trigger, events: 151846
eff, events: 151744
lost, events: 102
lostCut, events: 0
lostA, events: 9
lostB, events: 0
lostBoth, events: 93
ToT$_{ch18}$ [ns] (MidB)

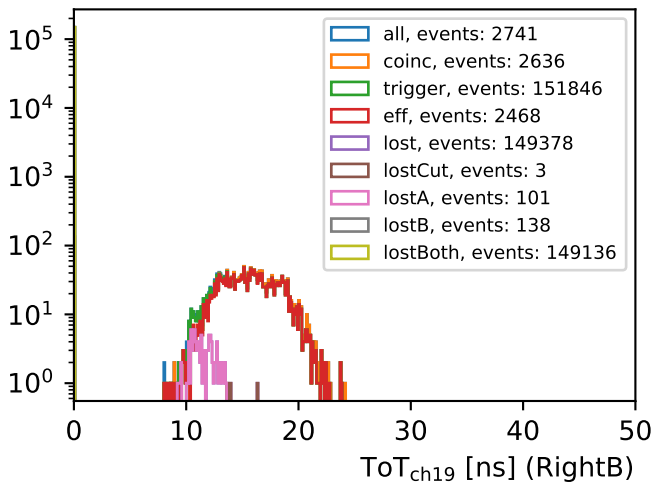
all, events: 2741
coinc, events: 2636
trigger, events: 151846
eff, events: 2468
lost, events: 149378
lostCut, events: 3
lostA, events: 101
lostB, events: 138
lostBoth, events: 149136
ToT$_{ch19}$ [ns] (RightB)

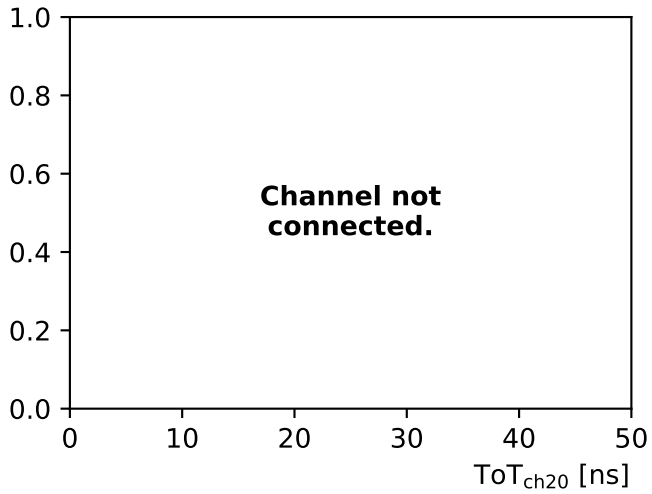
Channel not connected.
ToT$_{ch20}$ [ns]

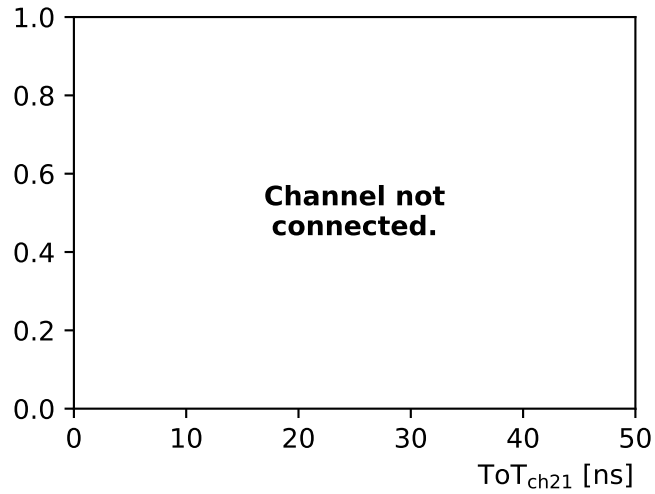
Channel not connected.
ToT$_{ch21}$ [ns]

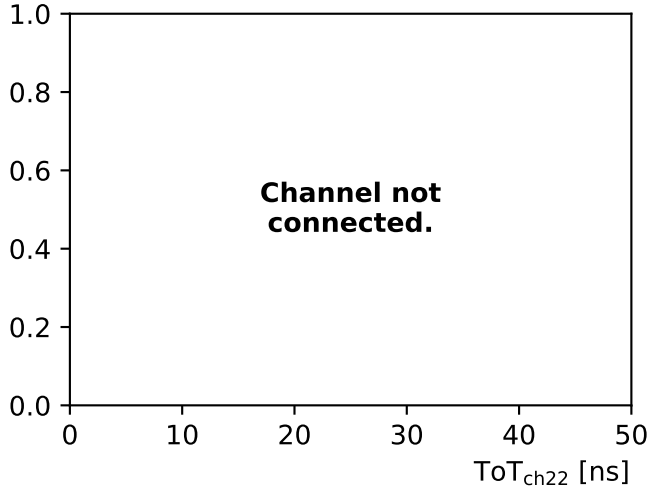
Channel not connected.
ToT$_{ch22}$ [ns]

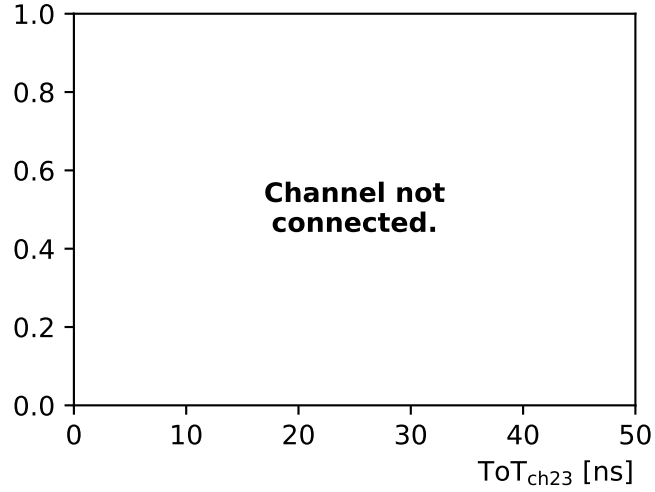
Channel not connected.
ToT$_{ch23}$ [ns]

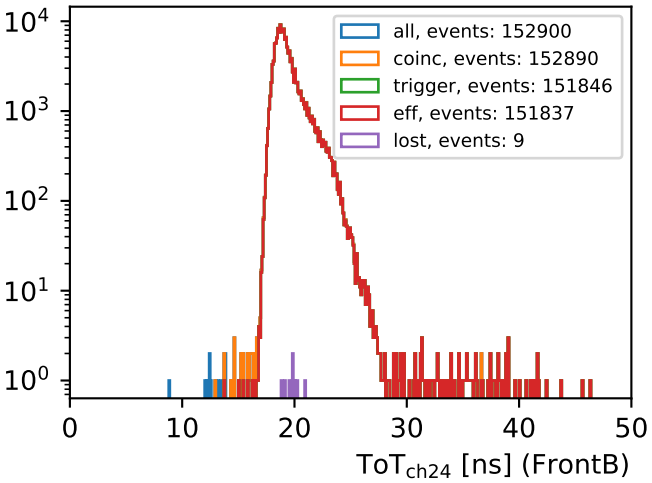
all, events: 152900
coinc, events: 152890
trigger, events: 151846
eff, events: 151837
lost, events: 9
ToT$_{ch24}$ [ns] (FrontB)

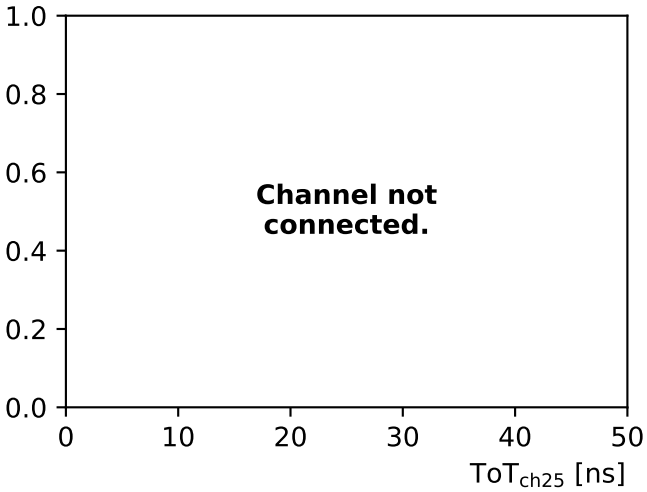
Channel not connected.
ToT$_{ch25}$ [ns]

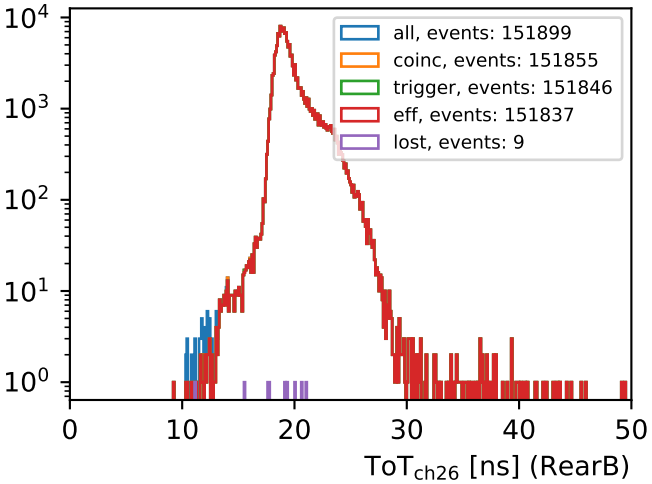
all, events: 151899
coinc, events: 151855
trigger, events: 151846
eff, events: 151837
lost, events: 9
ToT$_{ch26}$ [ns] (RearB)

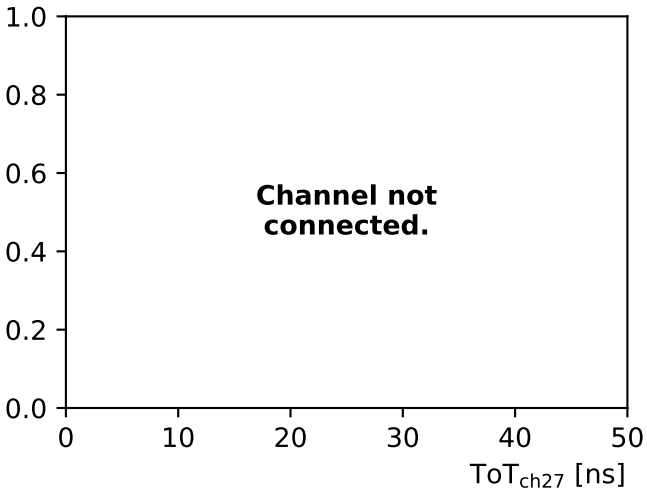
Channel not connected.
ToT$_{ch27}$ [ns]

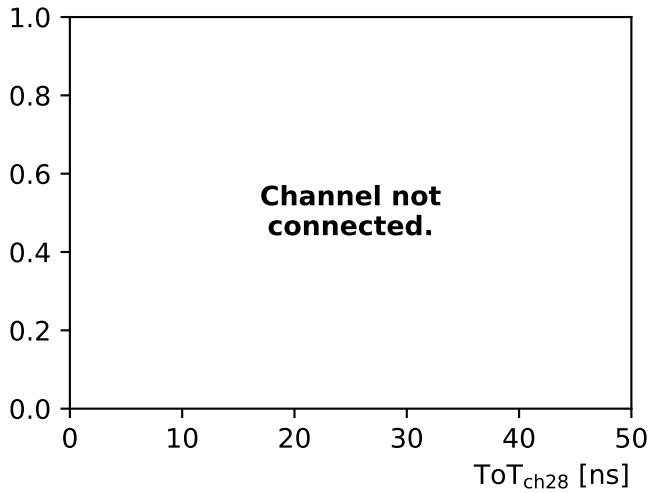
Channel not connected.
ToT$_{ch28}$ [ns]

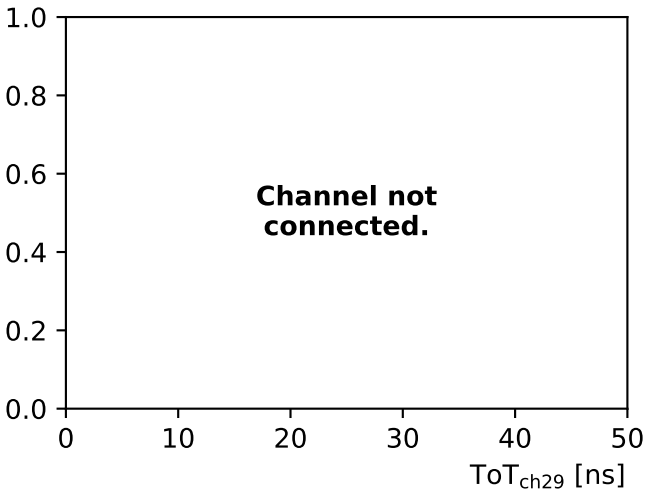
Channel not connected.
ToT$_{ch29}$ [ns]

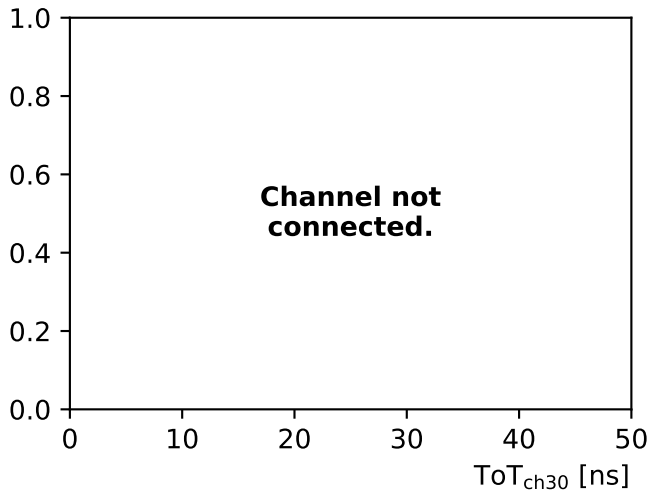
Channel not connected.
ToT$_{ch30}$ [ns]

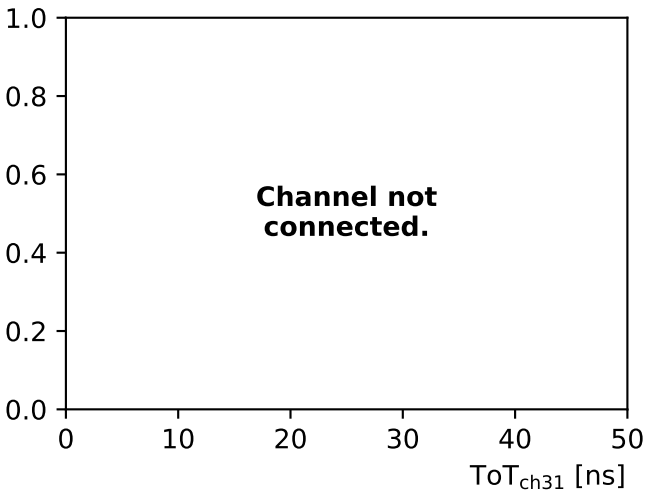
Channel not connected.
ToT$_{ch31}$ [ns]

ToT sum histograms per detector

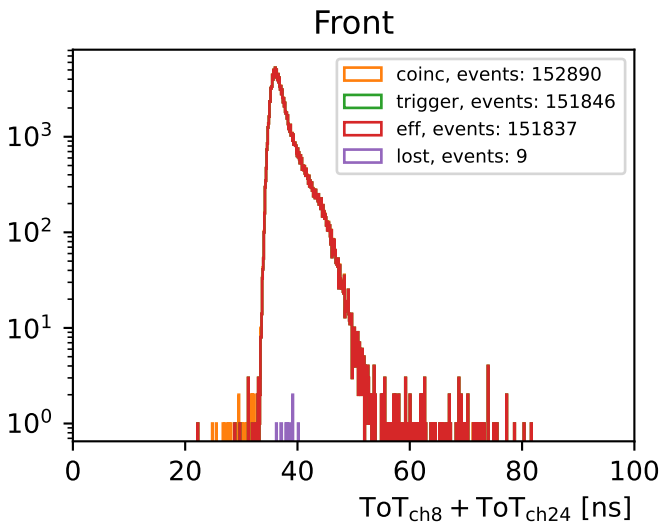
Front
coinc, events: 152890
trigger, events: 151846
eff, events: 151837
lost, events: 9
10^3
10^2
10^1
10^0
0
20
40
60
80
100
$\mathrm{ToT}_{\mathrm{ch8}} + \mathrm{ToT}_{\mathrm{ch24}}$ [ns]

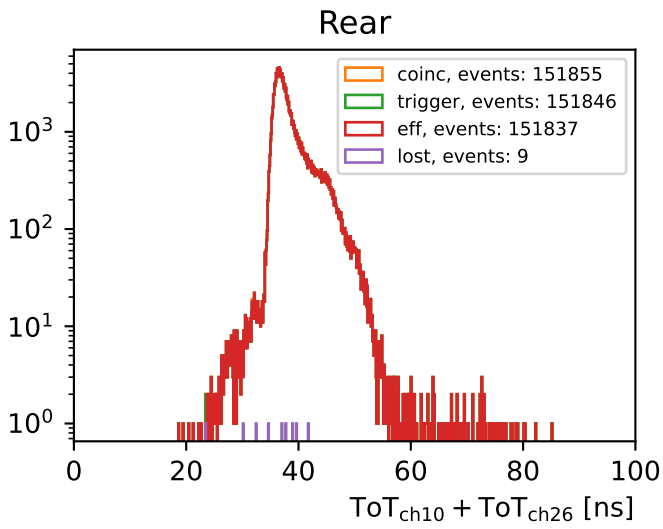
Rear
coinc, events: 151855
trigger, events: 151846
eff, events: 151837
lost, events: 9
10^3
10^2
10^1
10^0
0
20
40
60
80
100
$\mathrm{ToT}_{\mathrm{ch10}} + \mathrm{ToT}_{\mathrm{ch26}}$ [ns]

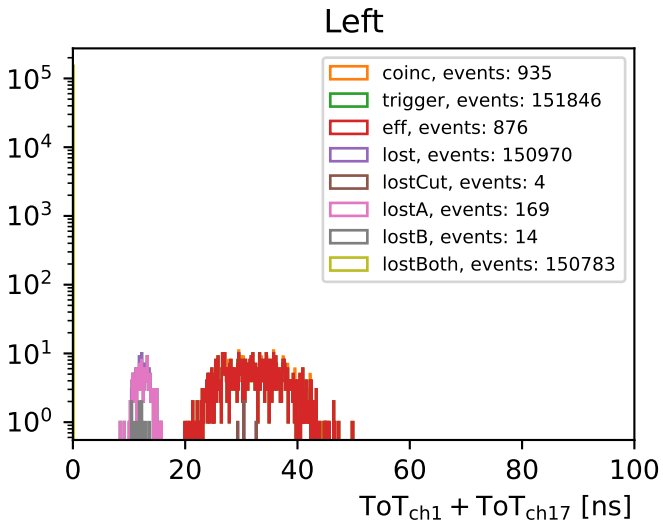
Left
coinc, events: 935
trigger, events: 151846
eff, events: 876
lost, events: 150970
lostCut, events: 4
lostA, events: 169
lostB, events: 14
lostBoth, events: 150783
10^5
10^4
10^3
10^2
10^1
10^0
0
20
40
60
80
100
$\mathrm{ToT}_{\mathrm{ch1}} + \mathrm{ToT}_{\mathrm{ch17}}$ [ns]

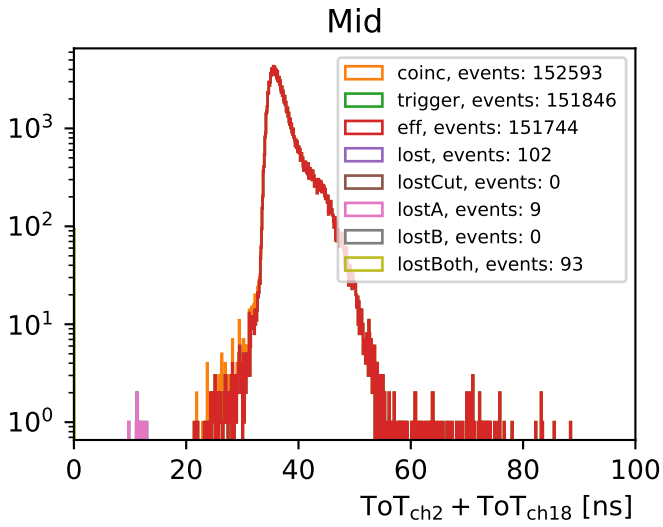
Mid
coinc, events: 152593
trigger, events: 151846
eff, events: 151744
lost, events: 102
lostCut, events: 0
lostA, events: 9
lostB, events: 0
lostBoth, events: 93
10^3
10^2
10^1
10^0
0
20
40
60
80
100
$\mathrm{ToT}_{\mathrm{ch2}} + \mathrm{ToT}_{\mathrm{ch18}}$ [ns]

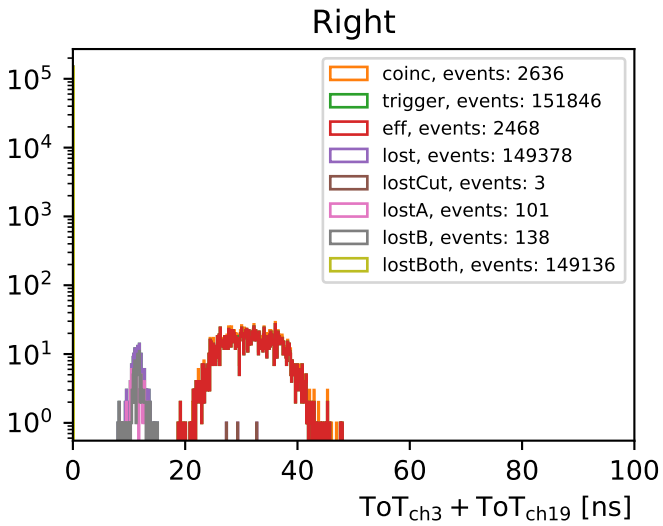
Right
coinc, events: 2636
trigger, events: 151846
eff, events: 2468
lost, events: 149378
lostCut, events: 3
lostA, events: 101
lostB, events: 138
lostBoth, events: 149136
10^5
10^4
10^3
10^2
10^1
10^0
0
20
40
60
80
100
$\mathrm{ToT}_{\mathrm{ch3}} + \mathrm{ToT}_{\mathrm{ch19}}$ [ns]

Charge histograms per channel

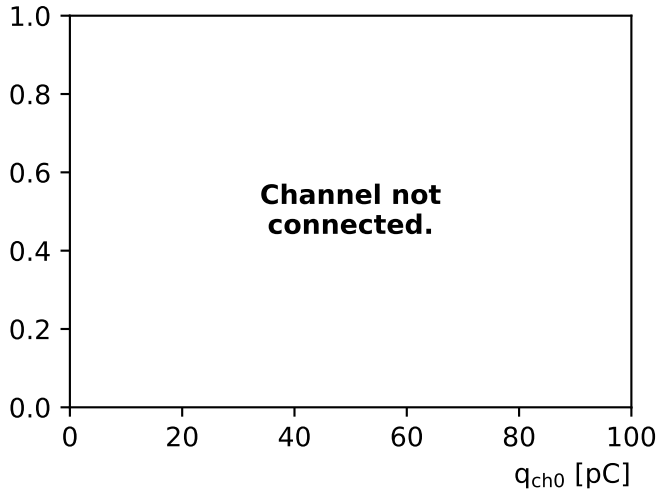
Channel not connected.
q_{ch0} [pC]

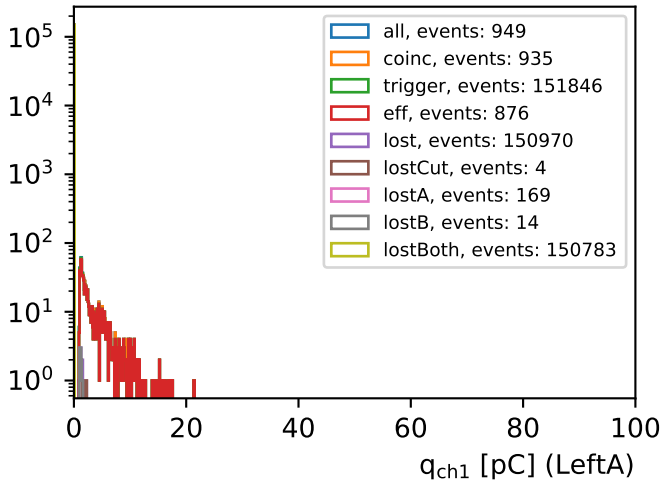
all, events: 949
coinc, events: 935
trigger, events: 151846
eff, events: 876
lost, events: 150970
lostCut, events: 4
lostA, events: 169
lostB, events: 14
lostBoth, events: 150783
q_{ch1} [pC] (LeftA)

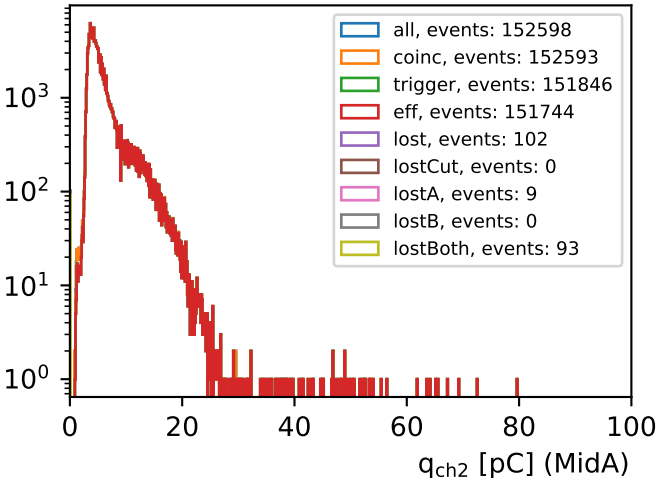
all, events: 152598
coinc, events: 152593
trigger, events: 151846
eff, events: 151744
lost, events: 102
lostCut, events: 0
lostA, events: 9
lostB, events: 0
lostBoth, events: 93
q_{ch2} [pC] (MidA)

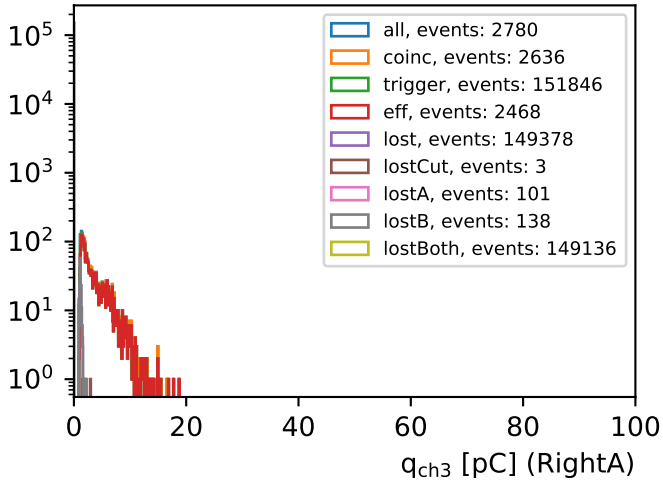
all, events: 2780
coinc, events: 2636
trigger, events: 151846
eff, events: 2468
lost, events: 149378
lostCut, events: 3
lostA, events: 101
lostB, events: 138
lostBoth, events: 149136
q_{ch3} [pC] (RightA)

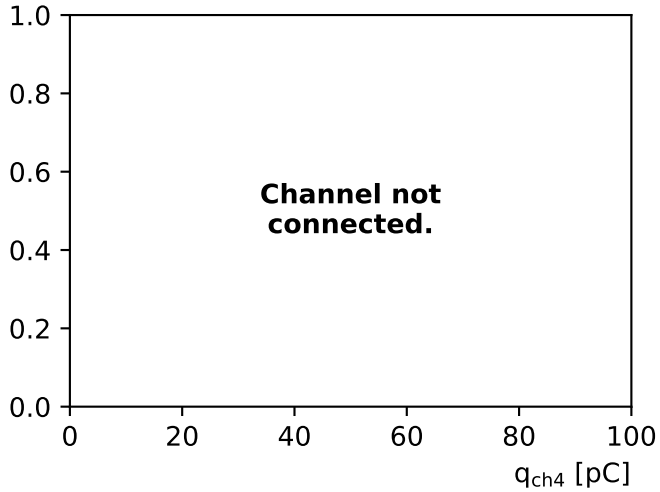
Channel not connected.
q_{ch4} [pC]

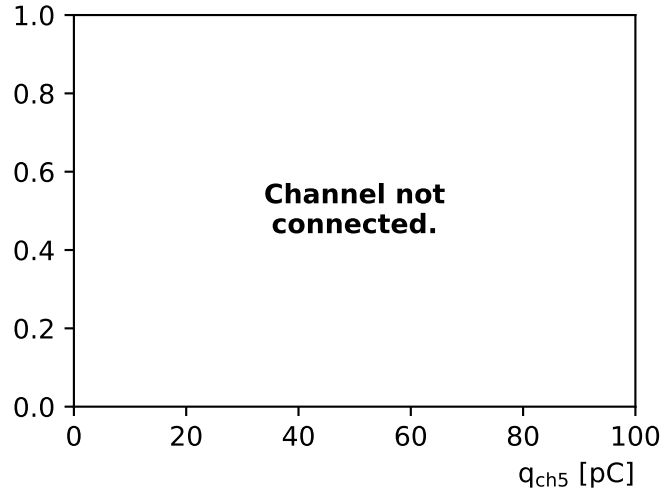
Channel not connected.
q_{ch5} [pC]

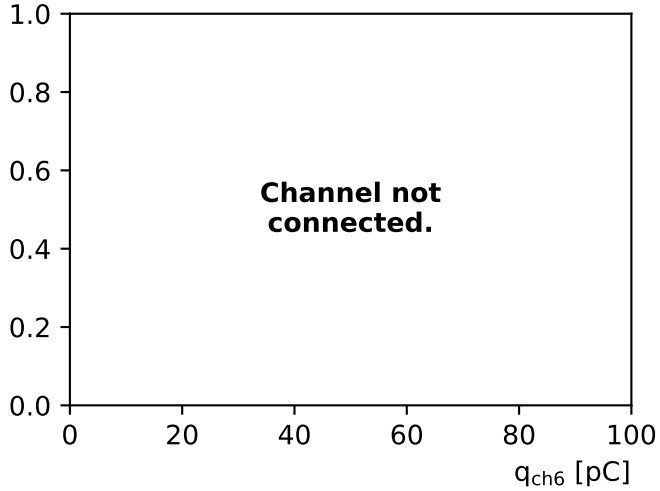
Channel not connected.
q_{ch6} [pC]

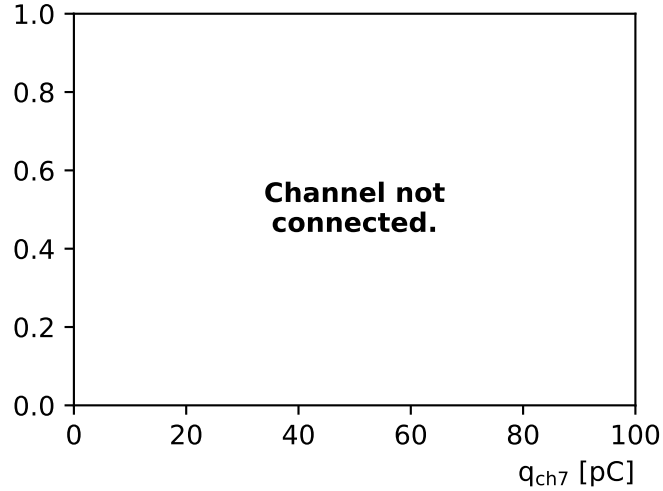
Channel not connected.
q_{ch7} [pC]

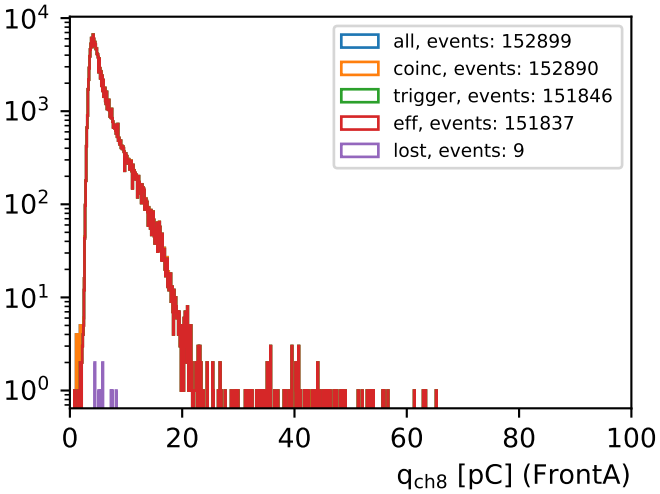
all, events: 152899
coinc, events: 152890
trigger, events: 151846
eff, events: 151837
lost, events: 9
q_{ch8} [pC] (FrontA)

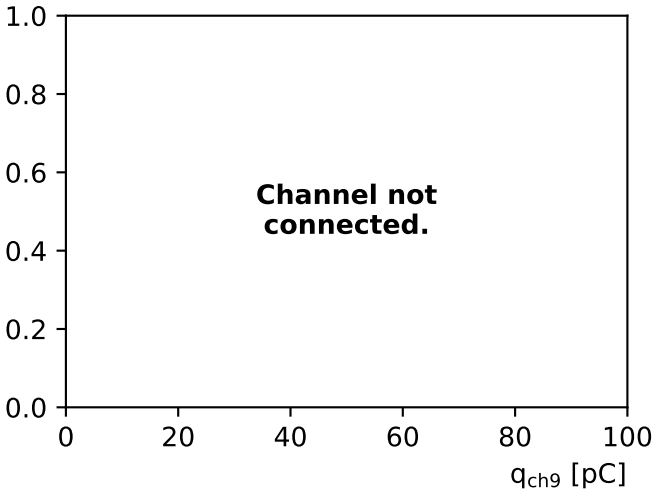
Channel not connected.
q_{ch9} [pC]

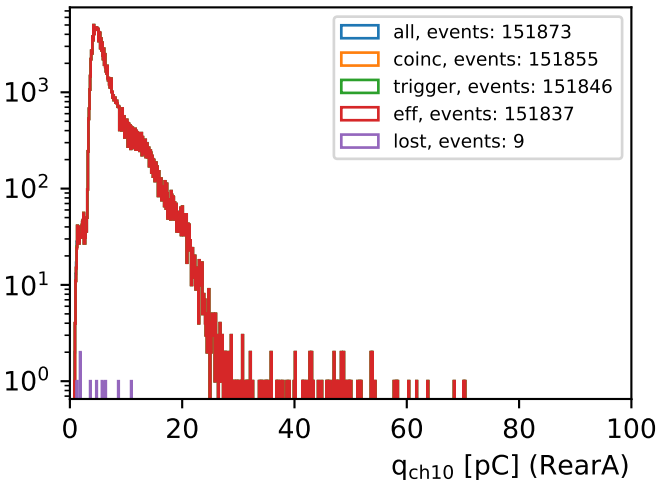
all, events: 151873
coinc, events: 151855
trigger, events: 151846
eff, events: 151837
lost, events: 9
q_{ch10} [pC] (RearA)

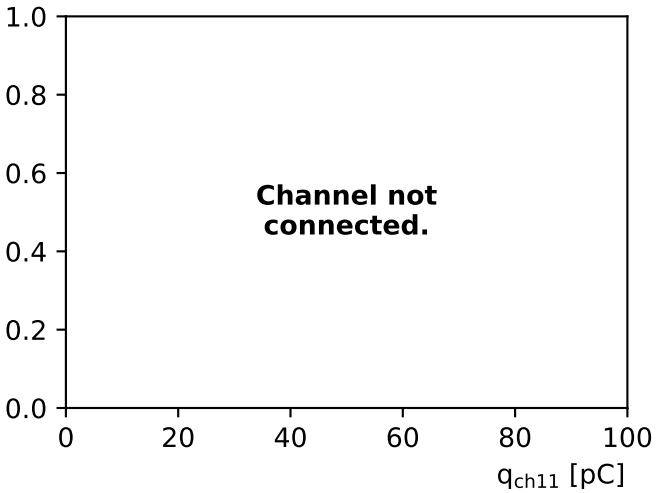
Channel not connected.
q_{ch11} [pC]

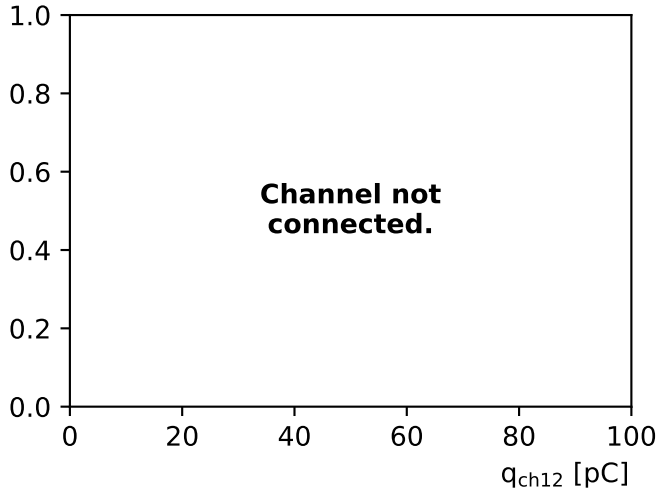
Channel not connected.
q_{ch12} [pC]

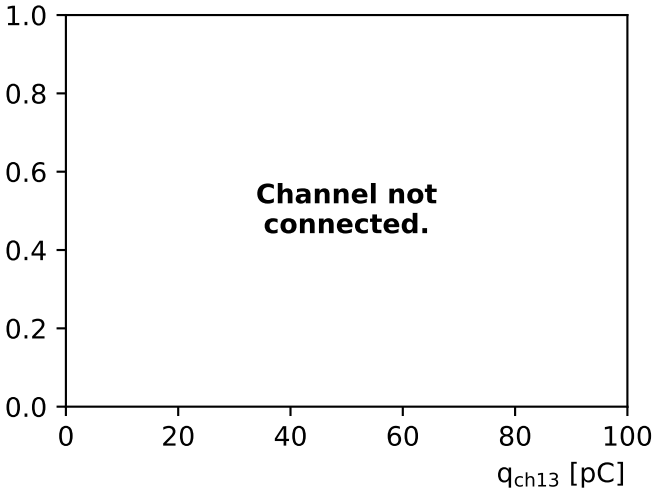
Channel not connected.
q_{ch13} [pC]

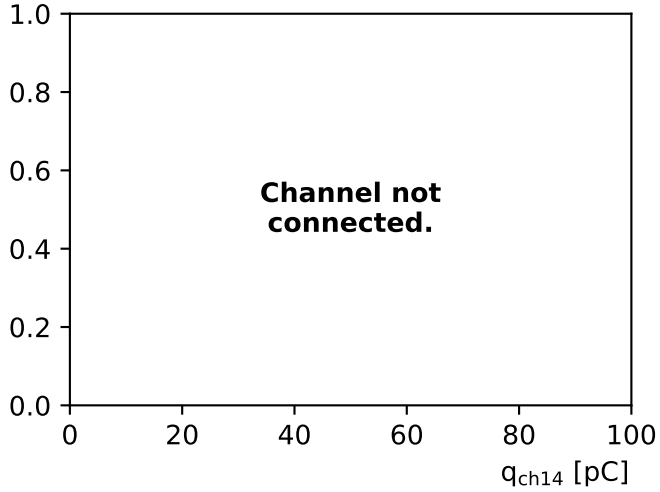
Channel not connected.
q_{ch14} [pC]

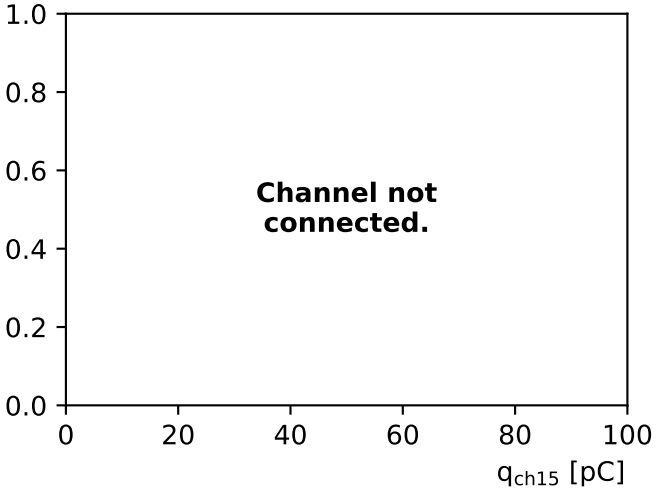
Channel not connected.
q_{ch15} [pC]

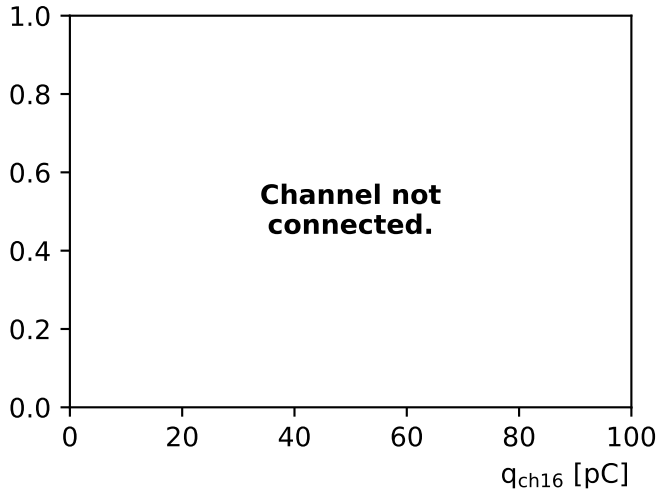
Channel not connected.
q_{ch16} [pC]

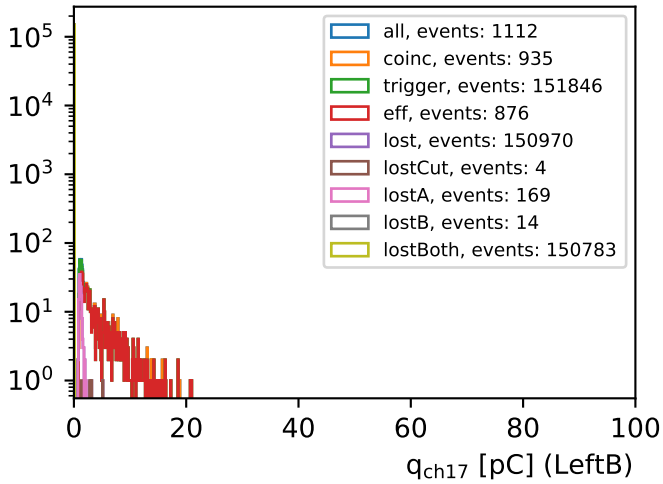
all, events: 1112
coinc, events: 935
trigger, events: 151846
eff, events: 876
lost, events: 150970
lostCut, events: 4
lostA, events: 169
lostB, events: 14
lostBoth, events: 150783
q_{ch17} [pC] (LeftB)

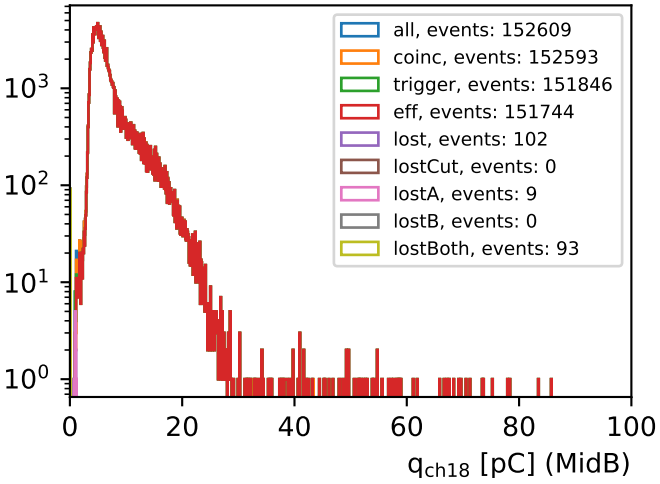
all, events: 152609
coinc, events: 152593
trigger, events: 151846
eff, events: 151744
lost, events: 102
lostCut, events: 0
lostA, events: 9
lostB, events: 0
lostBoth, events: 93
q_{ch18} [pC] (MidB)

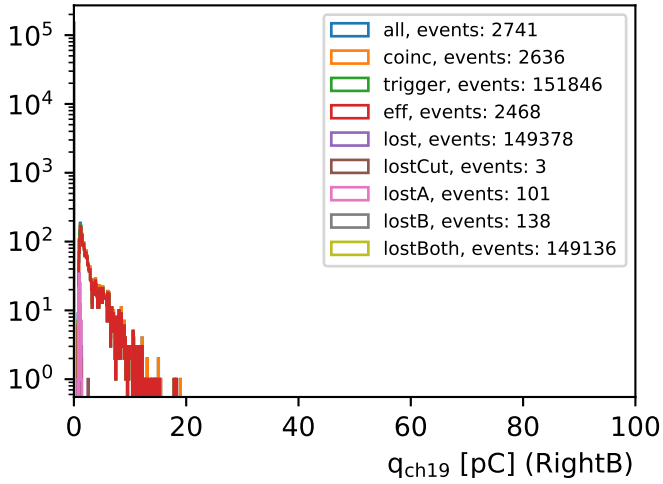
all, events: 2741
coinc, events: 2636
trigger, events: 151846
eff, events: 2468
lost, events: 149378
lostCut, events: 3
lostA, events: 101
lostB, events: 138
lostBoth, events: 149136
q_{ch19} [pC] (RightB)

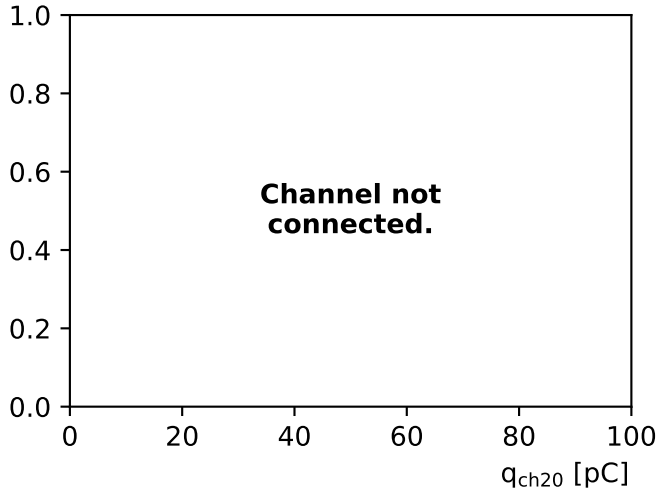
Channel not connected.
q_{ch20} [pC]

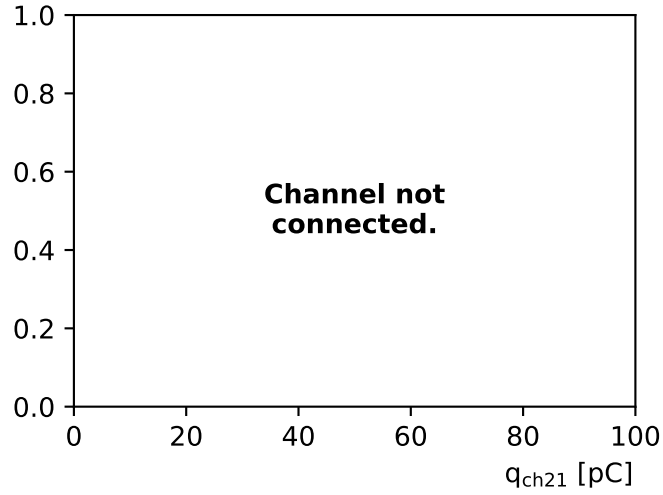
Channel not connected.
q_{ch21} [pC]

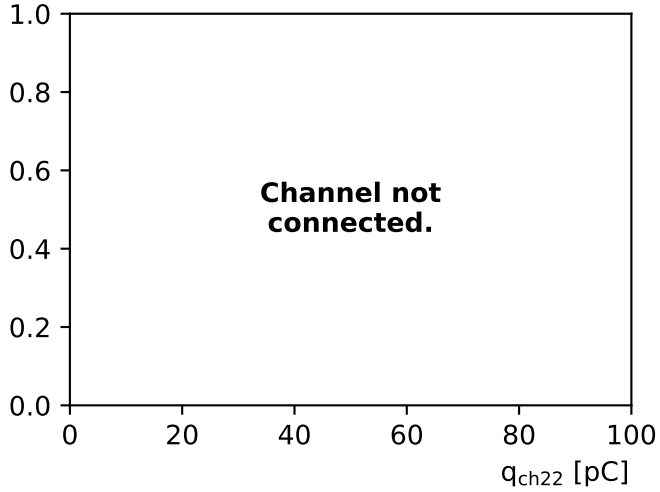
Channel not connected.
q_{ch22} [pC]

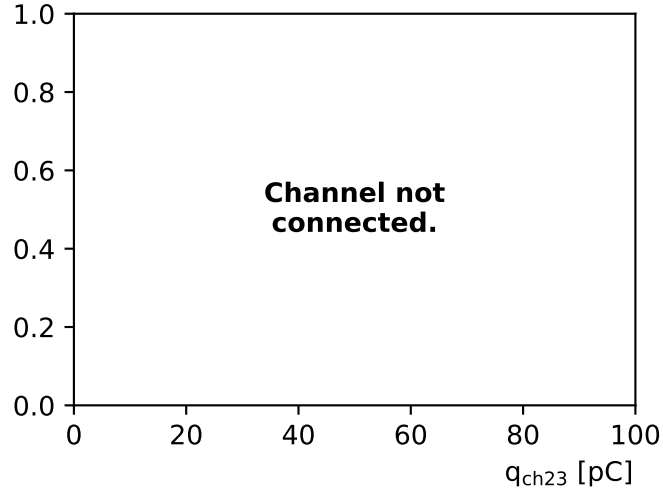
Channel not connected.
q_{ch23} [pC]

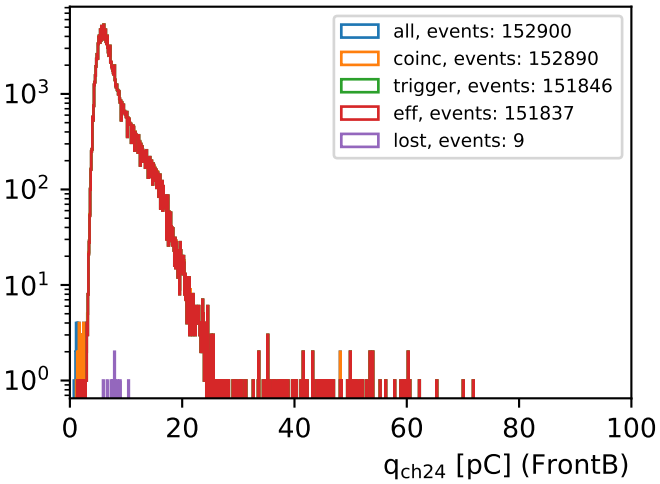
all, events: 152900
coinc, events: 152890
trigger, events: 151846
eff, events: 151837
lost, events: 9
10^3
10^2
10^1
10^0
0
20
40
60
80
100
q_{ch24} [pC] (FrontB)

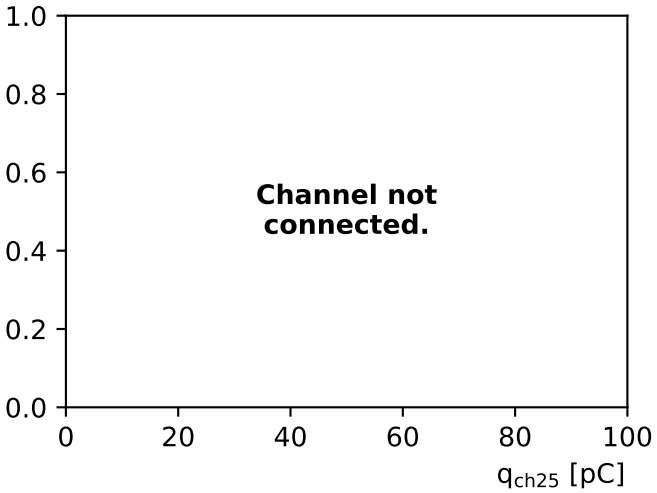
1.0
0.8
0.6
0.4
0.2
0.0
Channel not connected.
0
20
40
60
80
100
q_{ch25} [pC]

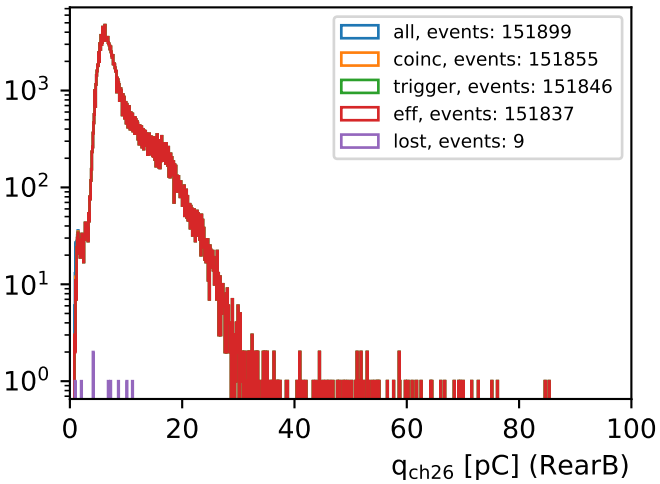
all, events: 151899
coinc, events: 151855
trigger, events: 151846
eff, events: 151837
lost, events: 9
10^3
10^2
10^1
10^0
0
20
40
60
80
100
q_{ch26} [pC] (RearB)

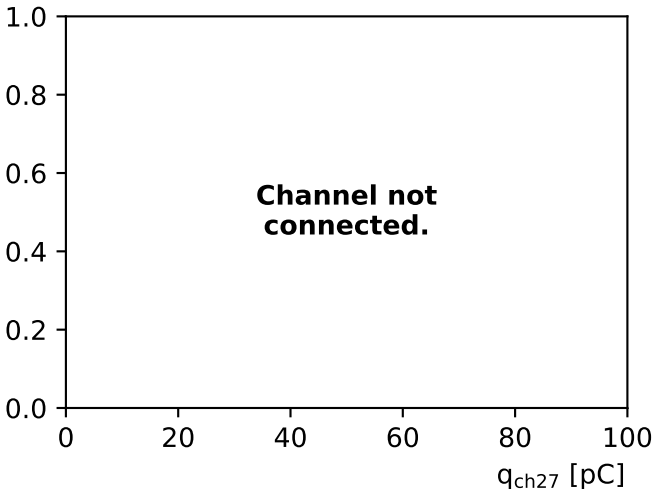
1.0
0.8
0.6
0.4
0.2
0.0
Channel not connected.
0
20
40
60
80
100
q_{ch27} [pC]

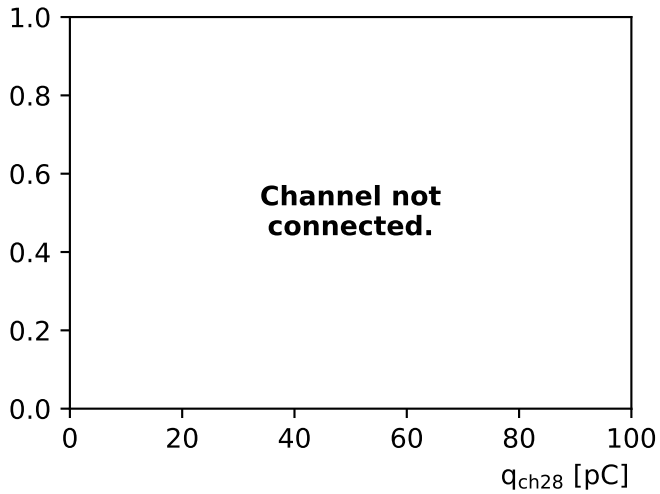
1.0
0.8
0.6
0.4
0.2
0.0
Channel not connected.
0
20
40
60
80
100
q_{ch28} [pC]

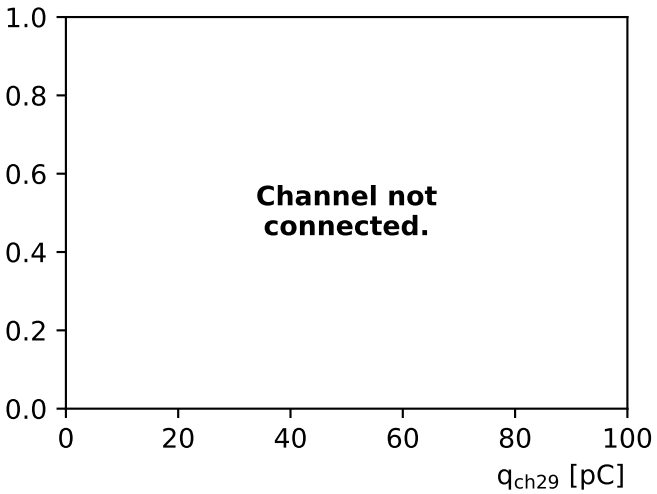
1.0
0.8
0.6
0.4
0.2
0.0
Channel not connected.
0
20
40
60
80
100
q_{ch29} [pC]

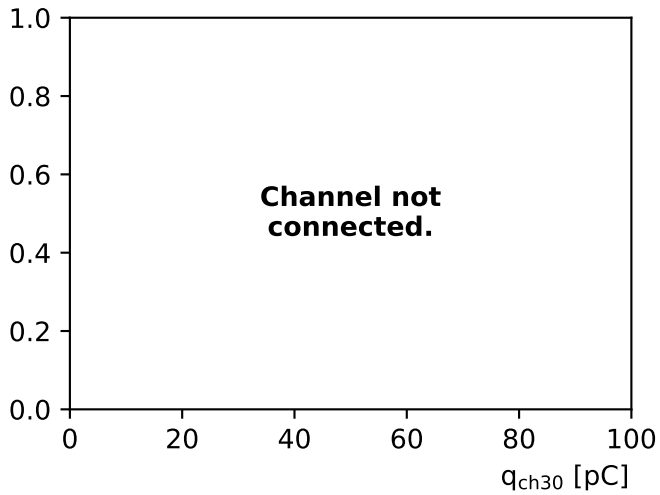
1.0
0.8
0.6
0.4
0.2
0.0
Channel not connected.
0
20
40
60
80
100
q_{ch30} [pC]

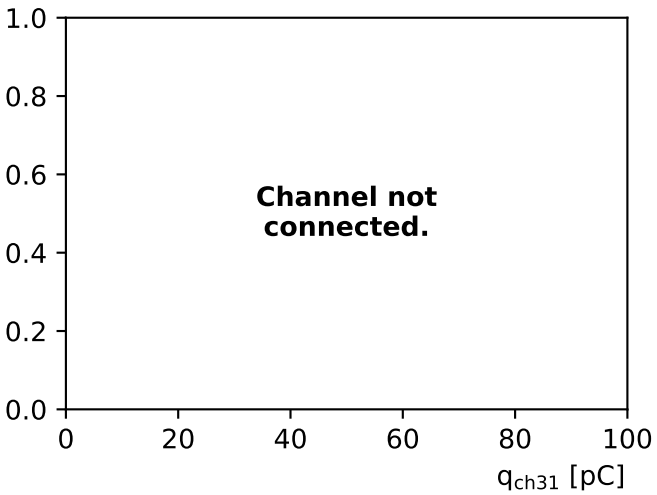
1.0
0.8
0.6
0.4
0.2
0.0
Channel not connected.
0
20
40
60
80
100
q_{ch31} [pC]

Charge sum histograms per channel

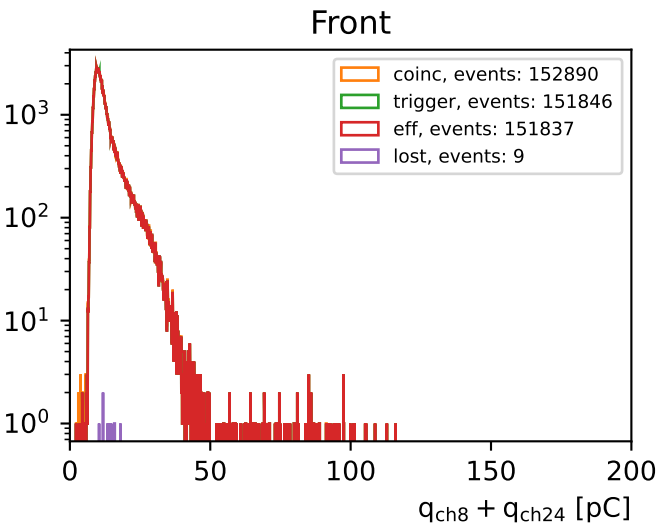
Front
coinc, events: 152890
trigger, events: 151846
eff, events: 151837
lost, events: 9
10^3
10^2
10^1
10^0
0
50
100
150
200
$q_{ch8} + q_{ch24}$ [pC]

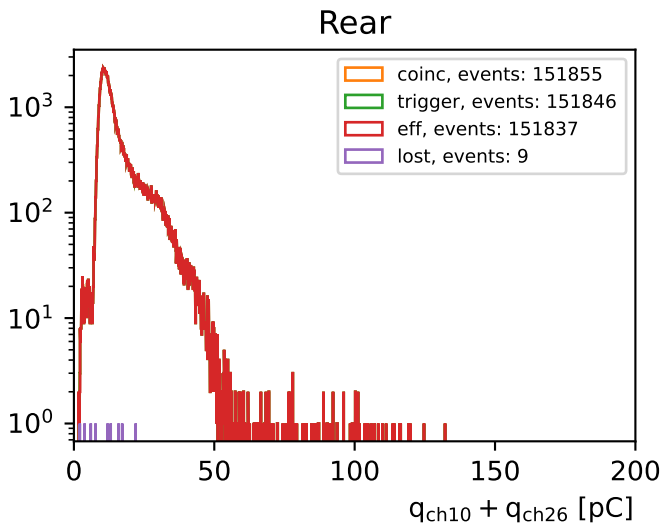
Rear
coinc, events: 151855
trigger, events: 151846
eff, events: 151837
lost, events: 9
10^3
10^2
10^1
10^0
0
50
100
150
200
$q_{ch10} + q_{ch26}$ [pC]

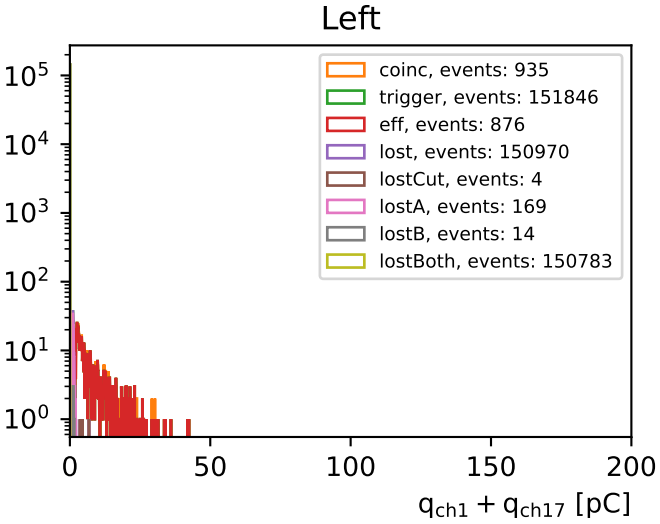
Left
coinc, events: 935
trigger, events: 151846
eff, events: 876
lost, events: 150970
lostCut, events: 4
lostA, events: 169
lostB, events: 14
lostBoth, events: 150783
10^5
10^4
10^3
10^2
10^1
10^0
0
50
100
150
200
$q_{ch1} + q_{ch17}$ [pC]

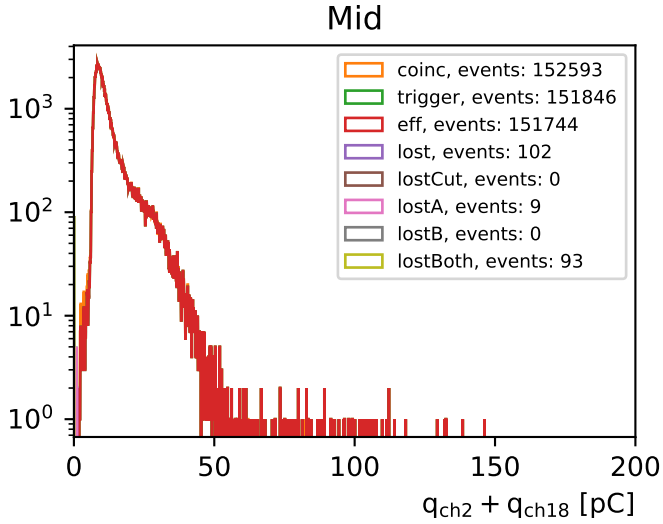
Mid
coinc, events: 152593
trigger, events: 151846
eff, events: 151744
lost, events: 102
lostCut, events: 0
lostA, events: 9
lostB, events: 0
lostBoth, events: 93
10^3
10^2
10^1
10^0
0
50
100
150
200
$q_{ch2} + q_{ch18}$ [pC]

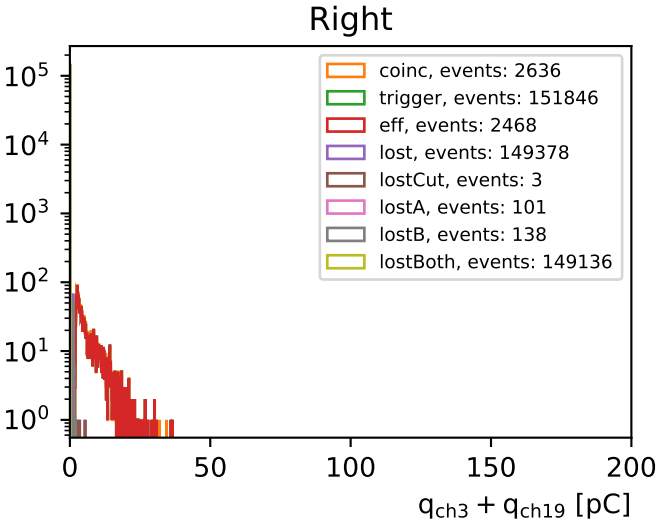
Right
coinc, events: 2636
trigger, events: 151846
eff, events: 2468
lost, events: 149378
lostCut, events: 3
lostA, events: 101
lostB, events: 138
lostBoth, events: 149136
10^5
10^4
10^3
10^2
10^1
10^0
0
50
100
150
200
$q_{ch3} + q_{ch19}$ [pC]

Detector
time differences

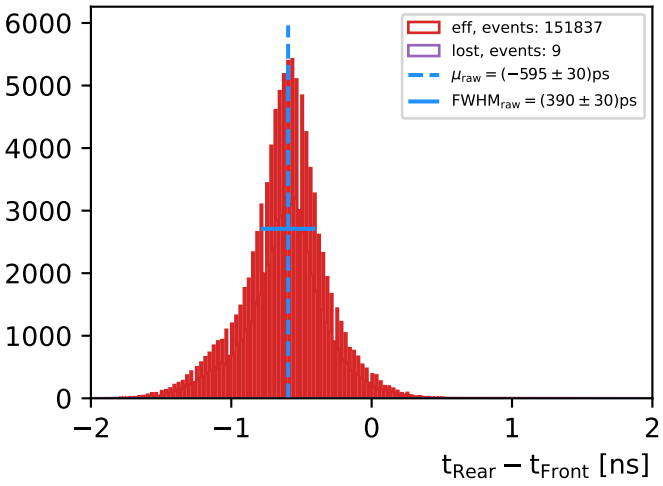
eff, events: 151837
lost, events: 9
$\mu_{raw} = (-595 \pm 30)$ps
$FWHM_{raw} = (390 \pm 30)$ps
$t_{Rear} - t_{Front}$ [ns]

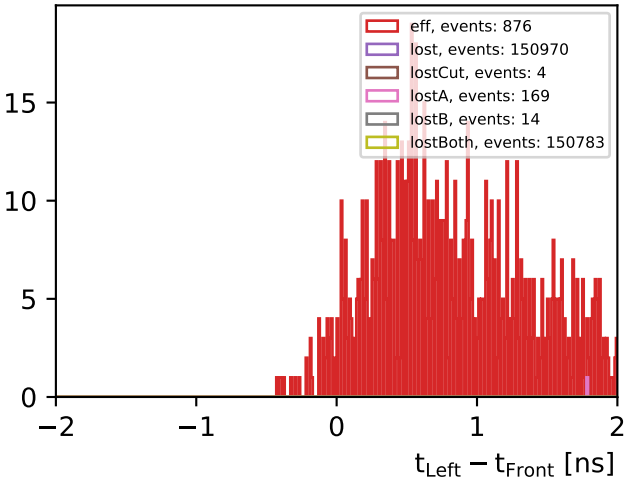
eff, events: 876
lost, events: 150970
lostCut, events: 4
lostA, events: 169
lostB, events: 14
lostBoth, events: 150783
$t_{Left} - t_{Front}$ [ns]

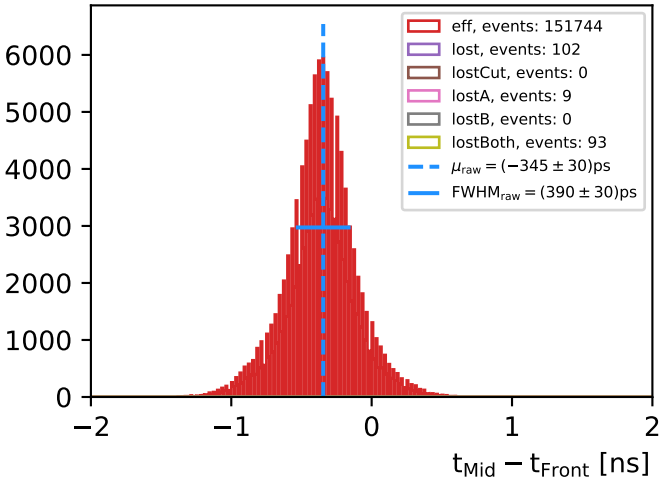
eff, events: 151744
lost, events: 102
lostCut, events: 0
lostA, events: 9
lostB, events: 0
lostBoth, events: 93
$\mu_{raw} = (-345 \pm 30)$ps
$FWHM_{raw} = (390 \pm 30)$ps
$t_{Mid} - t_{Front}$ [ns]

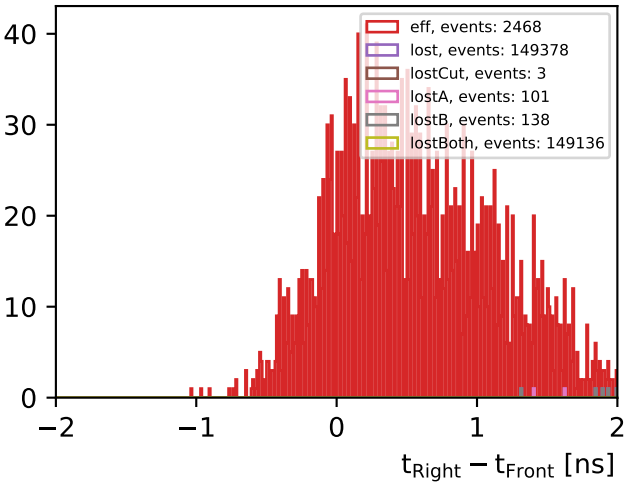
eff, events: 2468
lost, events: 149378
lostCut, events: 3
lostA, events: 101
lostB, events: 138
lostBoth, events: 149136
$t_{Right} - t_{Front}$ [ns]

Raw events: 2000000

Clean events: 1852634

Efficiency Left: 0.577%

Efficiency Mid: 99.933%

Efficiency Right: 1.625%

Total efficiency: 99.994%

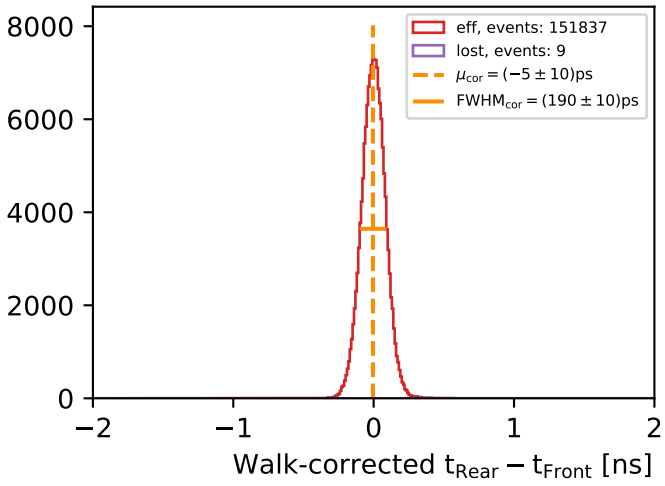

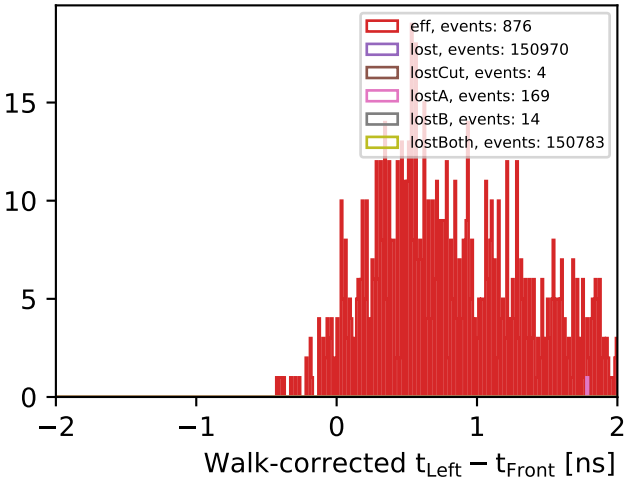

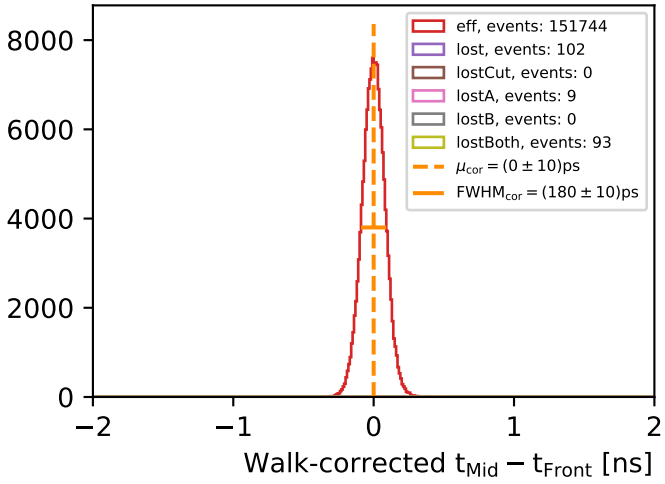

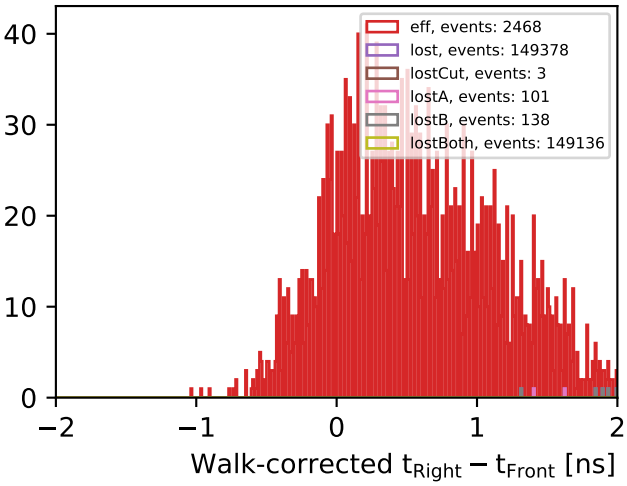

Channel time differences

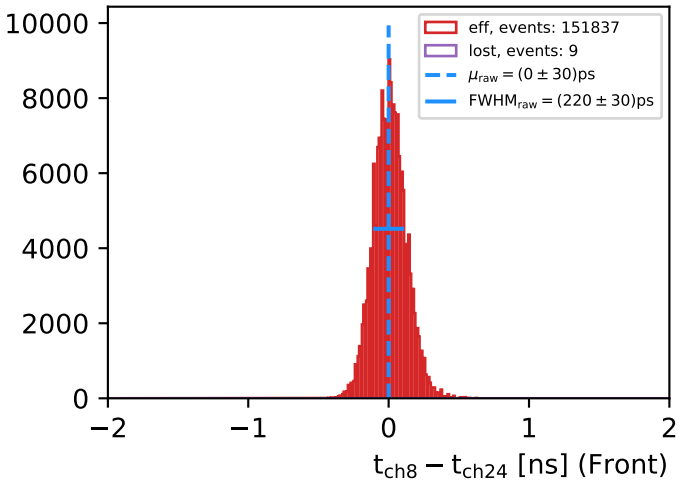
eff, events: 151837
lost, events: 9
$\mu_{raw} = (0 \pm 30)$ps
$FWHM_{raw} = (220 \pm 30)$ps
$t_{ch8} - t_{ch24}$ [ns] (Front)

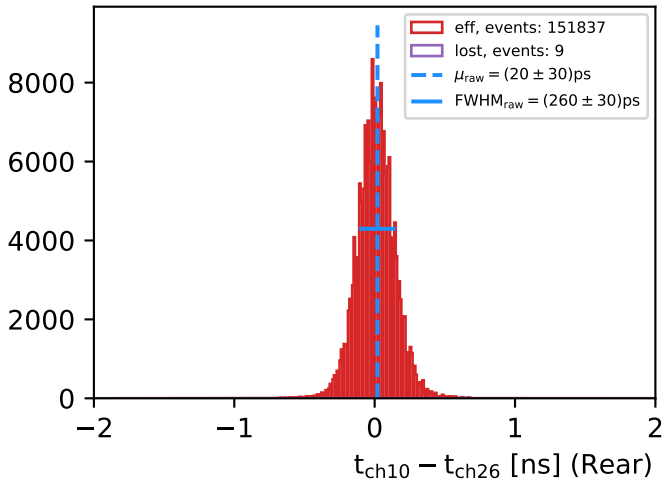
eff, events: 151837
lost, events: 9
$\mu_{raw} = (20 \pm 30)$ps
$FWHM_{raw} = (260 \pm 30)$ps
$t_{ch10} - t_{ch26}$ [ns] (Rear)

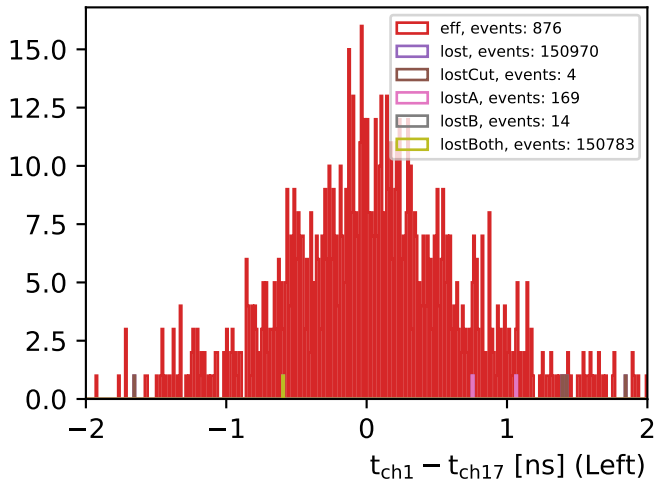
eff, events: 876
lost, events: 150970
lostCut, events: 4
lostA, events: 169
lostB, events: 14
lostBoth, events: 150783
$t_{ch1} - t_{ch17}$ [ns] (Left)

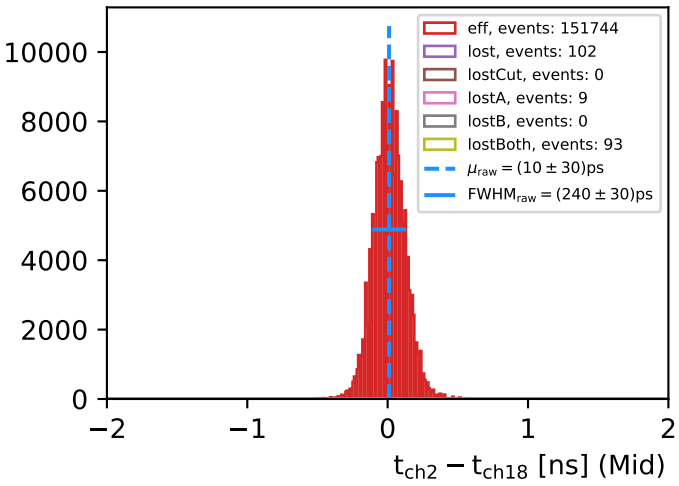
eff, events: 151744
lost, events: 102
lostCut, events: 0
lostA, events: 9
lostB, events: 0
lostBoth, events: 93
$\mu_{raw} = (10 \pm 30)$ps
$FWHM_{raw} = (240 \pm 30)$ps
$t_{ch2} - t_{ch18}$ [ns] (Mid)

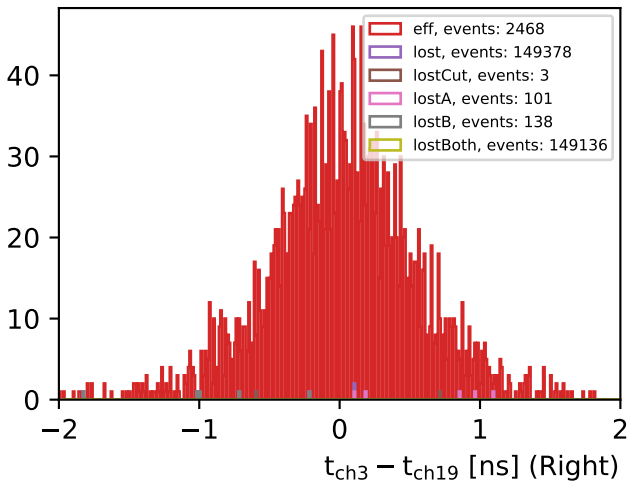
eff, events: 2468
lost, events: 149378
lostCut, events: 3
lostA, events: 101
lostB, events: 138
lostBoth, events: 149136
$t_{ch3} - t_{ch19}$ [ns] (Right)

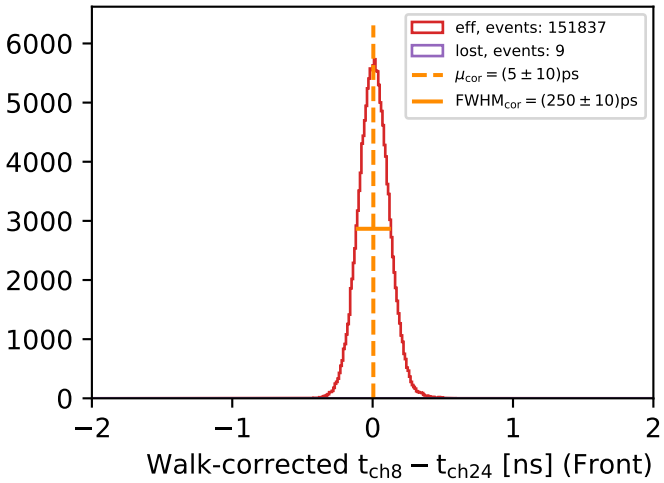
eff, events: 151837
lost, events: 9
$\mu_{cor} = (5 \pm 10)$ps
$FWHM_{cor} = (250 \pm 10)$ps
Walk-corrected $t_{ch8} - t_{ch24}$ [ns] (Front)

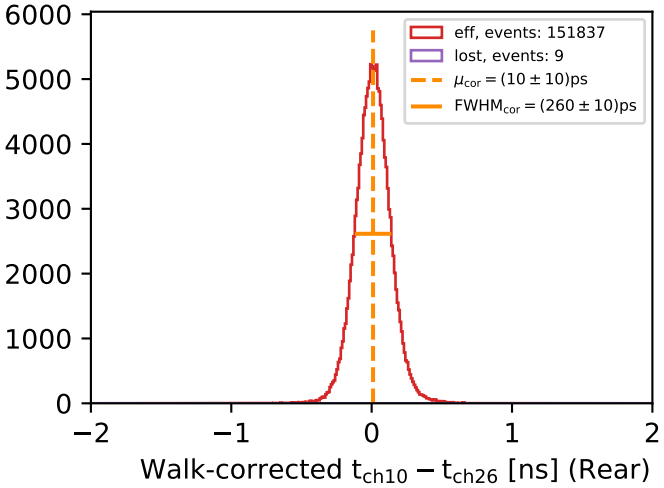
eff, events: 151837
lost, events: 9
$\mu_{cor} = (10 \pm 10)$ps
$FWHM_{cor} = (260 \pm 10)$ps
Walk-corrected $t_{ch10} - t_{ch26}$ [ns] (Rear)

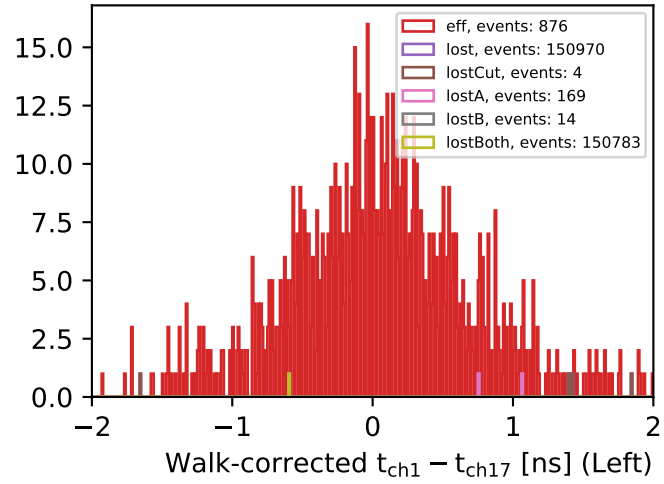
eff, events: 876
lost, events: 150970
lostCut, events: 4
lostA, events: 169
lostB, events: 14
lostBoth, events: 150783
Walk-corrected $t_{ch1} - t_{ch17}$ [ns] (Left)

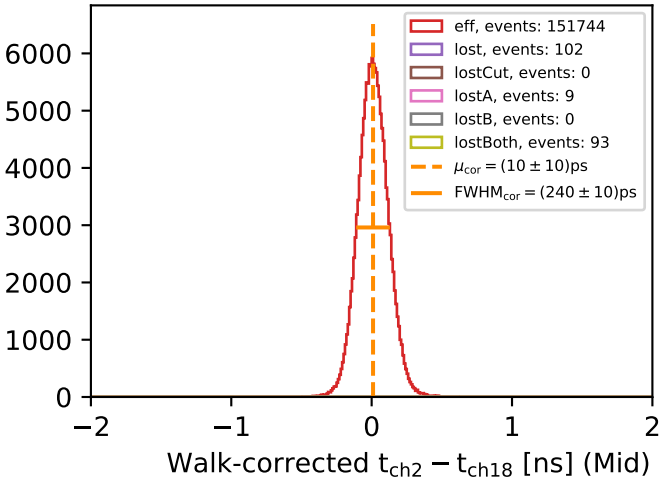
eff, events: 151744
lost, events: 102
lostCut, events: 0
lostA, events: 9
lostB, events: 0
lostBoth, events: 93
$\mu_{cor} = (10 \pm 10)$ps
$FWHM_{cor} = (240 \pm 10)$ps
Walk-corrected $t_{ch2} - t_{ch18}$ [ns] (Mid)

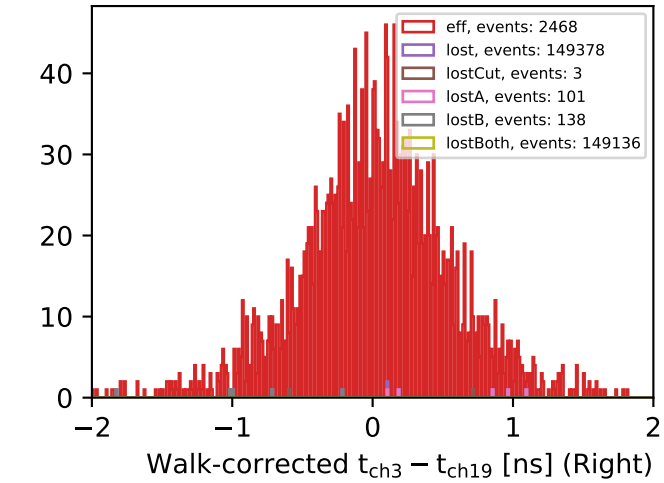
eff, events: 2468
lost, events: 149378
lostCut, events: 3
lostA, events: 101
lostB, events: 138
lostBoth, events: 149136
Walk-corrected $t_{ch3} - t_{ch19}$ [ns] (Right)

List of Figures

List of Tables

LIST OF CODES

BIBLIOGRAPHY

[1] Burbidge, E.M. and Burbidge, G.R. and Fowler, W.A. and Hoyle, F., "Synthesis of the Elements in Stars," *Rev. Mod. Phys.*, vol. 29, pp. 547–650, Oct. 1957. [Online]. Available: https://link.aps.org/doi/10.1103/RevModPhys.29.547

[2] Cameron, A.G.W., "Nuclear Astrophysics," *Annual review of nuclear science*, vol. 8, no. 1, pp. 299–326, Dec. 1958. [Online]. Available: https://www.annualreviews.org/content/journals/10.1146/annurev.ns.08.120158.001503

[3] Cosmos, "Origins of the elements reviewed," Sep. 2020, Accessed: Apr 04, 2023. [Online]. Available: https://cosmosmagazine.com/space/origin-of-the-elements-reviewed/

[4] Rolfs, C. and Barnes, C.A., "Radiative Capture Reactions in Nuclear Astrophysics," *Annual Review of Nuclear and Particle Science*, vol. 40, no. 1, pp. 45–78, Dec. 1990. [Online]. Available: https://www.annualreviews.org/content/journals/10.1146/annurev.ns.40.120190.000401

[5] Aliotta, M. and Boeltzig, A. and Depalo, R. and Gyürky, G., "Exploring Stars in Underground Laboratories: Challenges and Solutions," *Annual Review of Nuclear and Particle Science*, vol. 72, no. 1, pp. 177–204, Sep. 2022. [Online]. Available: https://www.annualreviews.org/content/journals/10.1146/annurev-nucl-110221-103625

[6] deBoer, R.J. *et al.*, "The $^{12}\mathbf{C}(\alpha,\gamma)^{16}\mathbf{O}$ reaction and its implications for stellar helium burning," *Rev. Mod. Phys.*, vol. 89, Sep. 2017. [Online]. Available: https://link.aps.org/doi/10.1103/RevModPhys.89.035007

[7] Lunkenheimer, S., "Feasibility Studies for Measuring the Astrophysical S-Factor of the Reaction $^{12}\mathbf{C}(\alpha,\gamma)^{16}\mathbf{O}$ via Electro-Disintegration at MAGIX," Ph.D. dissertation, Johannes Gutenberg University Mainz, Germany, Nov. 2021.

[8] A. Kozyreva, "Pair instability supernovae: Evolution, explosion, nucleosynthesis," Ph.D. dissertation, University of Bonn, Germany, Apr. 2014. [Online]. Available: https://astro.uni-bonn.de/~nlanger/thesis/Kozyreva_phd.pdf

[9] Woosley, S.E. and Heger, A. and Rauscher, T. and Hoffman, R.D., "Nuclear data needs for the study of nucleosynthesis in massive stars," *Nuclear Physics A*, vol. 718, pp. 3–12, May 2003. [Online]. Available: https://www.sciencedirect.com/science/article/pii/S0375947403006730

[10] Frisch, R. and Stern, O., "Über die magnetische Ablenkung von Wasserstoffmolekülen und das magnetische Moment des Protons. I," *Z. Phys*, vol. 85, pp. 4–16, Jan. 1933. [Online]. Available: https://link.springer.com/article/10.1007/BF01330773

[11] Frisch, R. and Stern, O., "Über die magnetische Ablenkung von Wasserstoffmolekülen und das magnetische Moment des Protons. II," *Z. Phys*, vol. 85, pp. 17–24, Jan. 1933. [Online]. Available: https://link.springer.com/article/10.1007/BF01330774

[12] J. C. Bernauer, "Measurement of the elastic electron-proton cross section and separation of the electric and magnetic form factor in the Q^2 range from 0.004 to 1 GeV/c," Ph.D. dissertation, Johannes Gutenberg University Mainz, Germany, Apr. 2010.

[13] Xiong, W. and Peng, C., "Proton Charge Radius from Lepton Scattering," Apr. 2023. [Online]. Available: https://arxiv.org/abs/2302.13818

[14] Bernauer, J.C. *et al.*, "High-Precision Determination of the Electric and Magnetic Form Factors of the Proton," *Phys. Rev. Lett.*, vol. 105, Dec. 2010. [Online]. Available: https://link.aps.org/doi/10.1103/PhysRevLett.105.242001

[15] Xiong, W. and Gasparian, A. and Gao, H. *et al.*, "A small proton charge radius from an electron–proton scattering experiment," *Nature*, vol. 575, Nov. 2019. [Online]. Available: https://www.nature.com/articles/s41586-019-1721-2

[16] Cui, Z.F. and Binosi, D. and Roberts, C.D. and Schmidt, S.M., "Pauli Radius of the Proton," *Chinese Physics Letters*, vol. 38, no. 12, Dec. 2021. [Online]. Available: https://iopscience.iop.org/article/10.1088/0256-307X/38/12/121401/meta

[17] Denig, A., "Precision hadron physics at the Mainz Microtron MAMI and MESA," *Journal of University of Science and Technology of China*, vol. 46, no. 7, pp. 608–616, 2016. [Online]. Available: http://justc.ustc.edu.cn/article/pdf/preview/2016-7-608.pdf

[18] Merkel, H., "Internal Target Experiments at the MESA accelerator," in *Proceedings of 54th International Winter Meeting on Nuclear Physics — PoS(BORMIO2016)*, vol. 272, 2016, p. 037. [Online]. Available: https://pos.sissa.it/272/037/

[19] Griffioen, K. and Carlson, C. and Maddox, S., "Consistency of electron scattering data with a small proton radius," *Physical Review C*, vol. 93, no. 6, Jun. 2016. [Online]. Available: https://journals.aps.org/prc/abstract/10.1103/PhysRevC.93.065207

[20] Bernauer, J.C., "The proton radius puzzle – 9 years later," *EPJ Web Conf.*, vol. 234, Apr. 2020. [Online]. Available: https://www.epj-conferences.org/articles/epjconf/abs/2020/10/epjconf_fccp2019_01001/epjconf_fccp2019_01001.html

[21] Wang, Y. *et al.*, "Low-Q^2 elastic electron-proton scattering using a gas jet target," *Phys. Rev. C*, vol. 106, p. 044610, Oct. 2022. [Online]. Available: https://link.aps.org/doi/10.1103/PhysRevC.106.044610

[22] Doria, L., "Search for New Physics with Intense Pion and Electron Beams," habilitation, Johannes Gutenberg University Mainz, Sep. 2018.

[23] Krasznahorkay, A.J. *et al.*, "Observation of Anomalous Internal Pair Creation in ^{8}Be: A Possible Indication of a Light, Neutral Boson," *Phys. Rev. Lett.*, vol. 116, p. 042501, Jan. 2016. [Online]. Available: https://link.aps.org/doi/10.1103/PhysRevLett.116.042501

[24] Aleksejevs, A. and Barkanova, S. and Kolomensky, Yu.G. and Sheff, B., "A Standard Model Explanation for the ATOMKI Anomaly," Feb. 2021. [Online]. Available: https://arxiv.org/abs/2102.01127

[25] Wong, C., "QED Meson Description of the Anomalous Particles at ~17 and ~38 MeV," *Universe*, vol. 10, no. 4, p. 173, Apr. 2024. [Online]. Available: https://arxiv.org/abs/2401.04142

[26] Doria, L. and Achenbach, P. and Christmann, M. and Denig, A. and Merkel, H., "Dark Matter at the Intensity Frontier: the new MESA electron accelerator facility," 2019. [Online]. Available: https://arxiv.org/abs/1908.07921

[27] Christmann, M., "Design Studies for the Beam-dump Experiment DarkMESA," Ph.D. dissertation, Johannes Gutenberg University Mainz, Germany, Dec. 2022.

[28] Achenbach, P. and Doria, L. and Battaglieri, M., "Summary Report of the 721th WE-Heraeus-Seminar : Light Dark Matter Searches," , 2022. [Online]. Available: http://doi.org/10.25358/openscience-6593

[29] Bjorken, J.D. and Essig, R. and Schuster, P. and Toro, N., "New fixed-target experiments to search for dark gauge forces," *Physical Review D*, vol. 80, no. 7, Oct. 2009. [Online]. Available: https://journals.aps.org/prd/abstract/10.1103/PhysRevD.80.075018

[30] Beranek, T. and Merkel, H. and Vanderhaeghen, M., "Theoretical framework to analyze searches for hidden light gauge bosons in electron scattering fixed target experiments," *Phys. Rev. D*, vol. 88, p. 015032, Jul. 2013. [Online]. Available: https://link.aps.org/doi/10.1103/PhysRevD.88.015032

[31] Schlimme, S. and Aulenbacher, K. and Baunack, S. and Berger, N. and Denig, A. and Doria, L. and Khoukaz, A. and Maas, F. and Merkel, H. and Sfienti, C. and Thiel, M., "The MESA physics program," Jul. 2024. [Online]. Available: https://arxiv.org/abs/2402.01027

[32] Berger, N. and Denig, A. and Maas, F. and Sfienti, C., "The MESA Experimental Program: A Laboratory for Precision Physics with Electron Scattering at Low Energy," *Nuclear Physics News*, vol. 31, no. 3, pp. 5–10, 2021. [Online]. Available: https://doi.org/10.1080/10619127.2021.1954434

[33] Dürr, S. *et al.*, "Ab Initio Determination of Light Hadron Masses," *Science*, vol. 322, no. 5905, pp. 1224–1227, Nov. 2008. [Online]. Available: https://doi.org/10.1126/science.1163233

[34] S. Kegel, "Systematic Investigations of the He-4 Monopole," Ph.D. dissertation, Johannes Gutenberg University Mainz, Germany, Nov. 2020.

[35] Bacca, S. and Barnea, N. and Leidemann, W. and Orlandini, G., "Role of the Final-State Interaction and Three-Body Force on the Longitudinal Response Function of ^{4}He," *Phys. Rev. Lett.*, vol. 102, Apr. 2009. [Online]. Available: https://link.aps.org/doi/10.1103/PhysRevLett.102.162501

[36] Bacca, S. and Barnea, N. and Leidemann, W. and Orlandini, G., "Isoscalar Monopole Resonance of the Alpha Particle: A Prism to Nuclear Hamiltonians," *Phys. Rev. Lett.*, vol. 110, Jan. 2013. [Online]. Available: https://journals.aps.org/prl/abstract/10.1103/PhysRevLett.110.042503

[37] Kegel, S. *et al.*, "Measurement of the α-Particle Monopole Transition Form Factor Challenges Theory: A Low-Energy Puzzle for Nuclear Forces?" *Phys. Rev. Lett.*, vol. 130, Apr. 2023. [Online]. Available: https://journals.aps.org/prl/abstract/10.1103/PhysRevLett.130.152502

[38] Epelbaum, E., "Probing the Helium Nucleus beyond the Ground State," *Physics*, vol. 16, p. 58, Apr. 2023. [Online]. Available: https://physics.aps.org/articles/v16/58

[39] Schlimme, S., private communication, Dec. 2023.

[40] Chernykh, M. and Feldmeier, H. and Neff, T. and von Neumann-Cosel, P. and Richter, A., "Pair Decay Width of the Hoyle State and its Role for Stellar Carbon Production," *Phys. Rev. Lett.*, vol. 105, Jul. 2010. [Online]. Available: https://journals.aps.org/prl/abstract/10.1103/PhysRevLett.105.022501

[41] Chernykh, M. and Feldmeier, H. and Neff, T. and von Neumann-Cosel, P. and Richter, A., "Structure of the Hoyle State in ^{12}C," *Phys. Rev. Lett.*, vol. 98, Jan. 2007. [Online]. Available: https://journals.aps.org/prl/abstract/10.1103/PhysRevLett.98.032501

[42] Molitor, M., "Machbarkeitsstudie zur Suche nach dunklen Photonen mit MESA," 2012.

[43] Hug, F. *et al.*, "Status of the MESA ERL Project," in *63rd ICFA Advanced Beam Dynamics Workshop on Energy Recovery Linacs*, 2020, p. MOCOXBS05. [Online]. Available: https://accelconf.web.cern.ch/linac2016/papers/mop106012.pdf

[44] Stoll, C. and Ledroit, B. and Meseck, A., "A Storage Ring for MESA," *JACoW*, vol. IPAC2021, p. MOPAB217, 2021. [Online]. Available: https://accelconf.web.cern.ch/ipac2021/papers/mopab217.pdf

[45] Simon, D., "Gesamtkonzept für den MESA-Teilchenbeschleuniger unter besonderer Berücksichtigung von Strahloptik und Kryogenik," Ph.D. dissertation, Johannes Gutenberg-Universität Mainz, Apr. 2021.

[46] Friederich, S., "Entwicklung einer hochbrillanten Photoemissionsquelle für spinpolarisierte Strahlen," Ph.D. dissertation, Johannes Gutenberg-Universität Mainz, Aug. 2019.

[47] Matejcek, C., "Strahldynamik der Niederenergie-Strahlführung von MESA unter Berücksichtigung von Raumladung und Multipol-Beiträgen höherer Ordnung," Ph.D. dissertation, Johannes Gutenberg-Universität Mainz, Feb. 2021.

[48] Heine, R.G. and Aulenbacher, K. and Hein, L.M. and Matejcek, C., "Current Status of the Milliampere Booster for the Mainz Energy-recovering Superconducting Accelerator," in *Proc. of International Particle Accelerator Conference (IPAC'16), Busan, Korea, May 8-13, 2016*, ser. International Particle Accelerator Conference, no. 7. Geneva, Switzerland: JACoW, Jun. 2016, paper TUPOW002, pp. 1741–1743, doi:10.18429/JACoW-IPAC2016-TUPOW002. [Online]. Available: https://accelconf.web.cern.ch/ipac2016/doi/JACoW-IPAC2016-TUPOW002.html

[49] Stengler, T., "Entwicklung eines supraleitenden Beschleunigermoduls für den rezirkulierenden Betrieb am Mainz Energy-Recovering Superconducting Accelerator (MESA)," Ph.D. dissertation, Johannes Gutenberg-Universität Mainz, Feb. 2020.

[50] Diefenbach, J., "A High Power Beamdump for the MAGIX Experiment," Mar. 2023, internal talk.

[51] Aulenbacher, K. and Heine, R. G. and Eichhorn, R., "MESA - Sketch of an Energy Recovery Linac for Nuclear Physics Experiments at Mainz," *Conf. Proc. C*, vol. 1205201, pp. 1993–1995, 2012. [Online]. Available: https://accelconf.web.cern.ch/IPAC2012/papers/tuppr073.pdf

[52] Becker, D. *et al.*, "The P2 experiment: A future high-precision measurement of the weak mixing angle at low momentum transfer," *The European Physical Journal A*, vol. 54, pp. 1–61, 2018. [Online]. Available: https://link.springer.com/article/10.1140/epja/i2018-12611-6

[53] Wilfert, M., "P2 - Overview," Feb. 2024, internal talk.

[54] Lauß, M. *et al.*, "Electron beam studies of light collection in a scintillating counter with embedded fibers," *Nuclear Instruments and Methods in Physics Research Section A: Accelerators,*

Spectrometers, Detectors and Associated Equipment, vol. 1012, p. 165617, 2021. [Online]. Available: https://www.sciencedirect.com/science/article/pii/S0168900221006021

[55] Christmann, M. *et al.*, "Detector response of Cherenkov radiators for calorimetry in the energy range below 14 MeV," *Nuclear Instruments and Methods in Physics Research Section A: Accelerators, Spectrometers, Detectors and Associated Equipment*, vol. 960, p. 163665, 2020. [Online]. Available: https://www.sciencedirect.com/science/article/pii/S0168900220302369

[56] Christmann, M. *et al.*, "Instrumentation and optimization studies for a beam dump experiment (BDX) at MESA — DarkMESA," *Nuclear Instruments and Methods in Physics Research Section A: Accelerators, Spectrometers, Detectors and Associated Equipment*, vol. 958, p. 162398, 2020, Proceedings of the Vienna Conference on Instrumentation 2019. [Online]. Available: https://www.sciencedirect.com/science/article/pii/S0168900219309787

[57] Lauß, M., "Entwicklung und Charakterisierung eines Veto-Detektors für das DarkMESA Experiment," Masterarbeit, Johannes Gutenberg-Universität Mainz, Feb. 2020.

[58] Pätschke, J., "Development of a Prototype Calorimeter for the DarkMESA Experiment," Bachelor's thesis, Johannes Gutenberg University Mainz, Apr. 2023.

[59] Manoussos, T., "Design of a Luminosity Monitoring System for MAGIX," Master's thesis, Johannes Gutenberg University Mainz, May 2022.

[60] Grieser, S. *et al.*, "A cryogenic supersonic jet target for electron scattering experiments at MAGIX@MESA and MAMI," *Nuclear Instruments and Methods in Physics Research Section A: Accelerators, Spectrometers, Detectors and Associated Equipment*, vol. 906, pp. 120–126, 2018. [Online]. Available: https://www.sciencedirect.com/science/article/pii/S0168900218309124

[61] Schlimme, B.S. *et al.*, "Operation and characterization of a windowless gas jet target in high-intensity electron beams," *Nuclear Instruments and Methods in Physics Research Section A: Accelerators, Spectrometers, Detectors and Associated Equipment*, vol. 1013, p. 165668, 2021. [Online]. Available: https://www.sciencedirect.com/science/article/pii/S0168900221006537

[62] Littich, M., "In preparation," Ph.D. dissertation, Johannes Gutenberg University Mainz, Germany.

[63] Frank, I. and Louckes, Jr., "Unique Sliding Seal for a Vacuum Chamber," *Review of Scientific Instruments*, vol. 28, no. 6, pp. 468–469, 1957. [Online]. Available: https://pubs.aip.org/aip/rsi/article-abstract/28/6/468/299421/Unique-Sliding-Seal-for-a-Vacuum-Chamber?redirectedFrom=fulltext

[64] Erskine, J.R. and Browne, C.P., "Inexpensive target chamber with port movable through zero degrees under vacuum," *Nuclear Instruments and Methods*, vol. 13, pp. 359–360, 1961. [Online]. Available: https://www.sciencedirect.com/science/article/abs/pii/0029554X61902270

[65] Hawrylak, R.A. and Cline, D. and Grube, D.F., "An improved strip sealed continuous rotation scattering chamber," *Nuclear Instruments and Methods*, vol. 36, pp. 237–240, 1965. [Online]. Available: https://www.sciencedirect.com/science/article/abs/pii/0029554X65904301

[66] Feldl, E. and Fetrow, C. and Moore, C.F., "A broad-range magnetic spectrograph system for routine angular distribution determinations," *Nuclear Instruments and Methods*, vol. 44, no. 1, pp. 98–102, 1966. [Online]. Available: https://www.sciencedirect.com/science/article/abs/pii/0029554X6690440X

[67] Borsay, F.L., "A vacuum chamber for nuclear scattering experiments," *Nuclear Instruments and Methods*, vol. 52, no. 2, pp. 338–340, 1967. [Online]. Available: https://www.sciencedirect.com/science/article/abs/pii/0029554X67902418

[68] McKnight, R.H., "A simple scattering chamber for measurements of the angular distribution of dissociation products produced by ion impact," *Review of Scientific Instruments*, vol. 46, no. 1, pp. 98–99, 1975. [Online]. Available: https://pubs.aip.org/aip/rsi/article-abstract/46/1/98/306712/A-simple-scattering-chamber-for-measurements-of?redirectedFrom=PDF

[69] Flynn, E.R. and Orbesen, S. and Sherman, J.D. and Sunier, J.W. and Woods, R., "A Q3D spectrometer with a helix detector system," *Nuclear Instruments and Methods*, vol. 128, no. 1, pp. 35–47, 1975. [Online]. Available: https://www.sciencedirect.com/science/article/abs/pii/0029554X75907715

[70] Gelbke, C.K., "A sliding seal scattering chamber for time-of-flight coincidence experiments," *Nuclear Instruments and Methods*, vol. 128, no. 1, pp. 175–177, 1975. [Online]. Available: https://www.sciencedirect.com/science/article/abs/pii/0029554X75907909

[71] Henneck, R. and Kretschmer, W. and Löh, H. and Muhr, G. and Stach, W., "A 14 cm diameter sliding seal chamber for the Erlangen double scattering spectrometer," *Nuclear Instruments and Methods*, vol. 158, pp. 391–394, 1979. [Online]. Available: https://www.sciencedirect.com/science/article/abs/pii/S0029554X79938254?via%3Dihub

[72] M. W. Kuss, "Konstruktion und Aufbau einer Streukammer mit gleitender Abdichtung für das Q-CLAM Spektrometer am neuen supraleitenden Darmstädter Elektronen-Linearbeschleuniger S-DALINAC," Master's thesis, Institut für Kernphysik, Technische Hochschule Darmstadt, Mär. 1990.

[73] Montagnoli, G. *et al.*, "Prisma-Fides Progress Report July 2013 - June 2014, Perspectives for 2015," INFN-Commissione III, Tech. Rep., Jul. 2014. [Online]. Available:

[74] S. Aulenbacher, "Sliding Seals/Scattering Chamber Status Quo," Dec. 2022, internal talk.

[75] Micron Semiconductor Limited, "Silicon Detectors – 2024 Catalog," p. 45, 2024, Version: MS022-1, Accessed: Jul 30, 2024. [Online]. Available: http://www.micronsemiconductor.co.uk/wp-content/uploads/2024/03/2024-MSL-Catalogue.pdf

[76] M. Friedl, "The CMS silicon strip tracker and its electronic readout," Ph.D. dissertation, Vienna, Tech. U., May 2001.

[77] Jones, L., "APV25-S1 - User Guide," RAL Microelectronics Design Group, Tech. Rep., Sep. 2001. [Online]. Available: https://cds.cern.ch/record/1069892/files/cer-002725643.pdf

[78] Biroth, M., private communication, Dec. 2023.

[79] Geimer, J., "Aufbau eines ortsauflösenden Siliziumdetektorsystems zum Nachweis von /alpha-Teilchen," Masterarbeit, Johannes Gutenberg-Universität Mainz, Jun. 2020.

[80] Schürg, H., "Versuchsaufbau zur Charakterisierung eines ortssensitiven Siliziumdetektors für das MAGIX-Experiment," Bachelorarbeit, Johannes Gutenberg-Universität Mainz, Apr. 2018.

[81] Schlaadt, J., "Konstruktion eines neuen Veto-Detektors für den Strahl-Halo am MAGIX-Experiment," Bachelorarbeit, Johannes Gutenberg-Universität Mainz, Aug. 2021.

[82] Höwelberend, F., "Spurparametrisierung und Fokalebenensimulation für die MAGIX-Spektrometer," Bachelorarbeit, Johannes Gutenberg-Universität Mainz, Sep. 2023.

[83] Müller, J., "Entwurf eines Spektrometers für Niederenergieexperimente an MESA," Diplomarbeit, Johannes Gutenberg-Universität Mainz, Jan. 2014.

[84] Caiazza, S.S. *et al.*, "The MAGIX focal plane time projection chamber," *Journal of Physics: Conference Series*, vol. 1498, no. 1, p. 012022, Apr. 2020. [Online]. Available: https://doi.org/10.1088/1742-6596/1498/1/012022

[85] Gülker, P. *et al.*, "Development of large area focal plane detectors for MAGIX," 2019. [Online]. Available: https://arxiv.org/abs/1906.05900

[86] Markus, D., "Effizienz und Auflösung des MAGIX TPC Prototypen," Masterarbeit, Johannes Gutenberg-Universität Mainz, Dez. 2021.

[87] Rausch, J., "Aufbau und Vermessung eines Spurendriftkammer-Prototypen für MAGIX," Masterarbeit, Johannes Gutenberg-Universität Mainz, Jul. 2019.

[88] Gülker, P., private communication, Dec. 2023.

[89] Steger, D., "Prototypentwicklung eines Kalibrierungssystems für die Spurendriftkammer am MAGIX," Bachelorarbeit, Johannes Gutenberg-Universität Mainz, Aug. 2022.

[90] Markus, D., private communication, Dec. 2023.

[91] De Geronimo, G. and Fried, J. and Li, S. and Metcalfe, J. and Nambiar, N. and Vernon, E. and Polychronakos, V., "VMM1 - An ASIC for micropattern detectors," in *2012 IEEE Nuclear Science Symposium and Medical Imaging Conference Record (NSS/MIC)*, 2012, pp. 633–639. [Online]. Available: https://ieeexplore.ieee.org/document/6551184

[92] Lupberger, M. *et al.*, "Implementation of the VMM ASIC in the Scalable Readout System," *Nuclear Instruments and Methods in Physics Research Section A: Accelerators, Spectrometers, Detectors and Associated Equipment*, vol. 903, pp. 91–98, 2018. [Online]. Available: https://www.sciencedirect.com/science/article/pii/S016890021830768X

[93] Emig, N., "Machbarkeitsstudie eines EPICS-basierten Slow Control Systems für das Experiment MAGIX," Bachelorarbeit, Johannes Gutenberg-Universität Mainz, Jan. 2017.

[94] Dalesio, L.R. and Kozubal, A.J. and Kraimer, M.R., "EPICS architecture," , Jan. 1991. [Online]. Available: https://www.osti.gov/biblio/6110347

[95] Dalesio, Leo R. *et al.*, "The Experimental Physics and Industrial Control System architecture: Past, present, and future," *Nucl. Instrum. Meth. A*, vol. 352, pp. 179–184, 1994. [Online]. Available: https://www.sciencedirect.com/science/article/pii/0168900294914931

[96] Knott, M. and Gurd, D. and Lewis, S. and Thuot, M., "EPICS: A control system software co-development success story," *Nuclear Instruments and Methods in Physics Research Section A: Accelerators, Spectrometers, Detectors and Associated Equipment*, vol. 352, no. 1, pp. 486–491, 1994. [Online]. Available: https://www.sciencedirect.com/science/article/pii/0168900294915776

[97] Piatek, S., "Low Light Detection: PMT versus SiPM," Dec. 2016. [Online]. Available: https://www.hamamatsu.com/eu/en/resources/webinars/detectors/low-light-detection-pmt-sipm.html

[98] Stöttinger, Y.A., "Measurement of the elastic electron deuteron cross-section and determination of the electric form factor in the region of low Q^2," Ph.D. dissertation, Johannes Gutenberg University Mainz, Germany, Jun. 2021.

[99] Eljen Technology, "Fast Timing Plastic Scintillator EJ-228, EJ-230 – Datasheet," Jan. 2016, Accessed: Jul 29, 2024. [Online]. Available: https://eljentechnology.com/images/products/data_sheets/EJ-228_EJ-230.pdf

[100] Saint Gobain Crystals, "BC-400, BC-404, BC-408, BC-412, BC-416 Premium Plastic Scintillators – Datasheet," Feb. 2018.

[101] Leo, W.R., *Techniques for nuclear and particle physics experiments: a how-to approach*, 2 ed. Berlin: Springer-Verlag Berlin Heidelberg GmbH, 1994. [Online]. Available: https://link.springer.com/book/10.1007/978-3-642-57920-2

[102] Shukla, P. and Sankrith, S., "Energy and angular distributions of atmospheric muons at the Earth," 2018. [Online]. Available: https://arxiv.org/pdf/1606.06907

[103] Eljen Technology, "General Purpose Plastic Scintillator EJ-200, EJ-204, EJ-208, EJ-212 – Datasheet," Jul. 2021, Accessed: Jul 29, 2024. [Online]. Available: https://eljentechnology.com/images/products/data_sheets/EJ-200_EJ-204_EJ-208_EJ-212.pdf

[104] Workman, R.L. *et al.*, "Review of Particle Physics," *PTEP*, vol. 2022, p. 083C01, 2022. [Online]. Available: https://academic.oup.com/ptep/article/2022/8/083C01/6651666?login=true

[105] Birks, J.B., *The Theory and practice of scintillation counting*. Elsevier, 1964. [Online]. Available: https://www.sciencedirect.com/book/9780080104720/the-theory-and-practice-of-scintillation-counting

[106] Tavernier, S., *Experimental Techniques in Nuclear and Particle Physics*. Springer, 2010. [Online]. Available: https://link.springer.com/book/10.1007/978-3-642-00829-0

[107] Grupen, C. and Buvat, I., *Handbook of Particle Detection and Imaging*. Springer, 2012. [Online]. Available: https://link.springer.com/referencework/10.1007/978-3-642-13271-1

[108] Hamamatsu Photonics K.K., "Photomultiplier Tube R1924A-03 – Datasheet," Apr. 2017, Version: DEPT.#22.

[109] Hamamatsu Photonics K.K., "Photomultiplier Tubes: Basics and Applications," Mar. 2017, Fourth Edition. [Online]. Available: https://www.hamamatsu.com/content/dam/hamamatsu-photonics/sites/documents/99_SALES_LIBRARY/etd/PMT_handbook_v4E.pdf

[110] Hamamatsu Photonics K.K., "DP-Type Socket Assemblies: C13003-01 – Datasheet," pp. 104–105, Sep. 2020, Version: TPMZ0002E02, Accessed: Jul 29, 2024. [Online]. Available: https://www.hamamatsu.com/content/dam/hamamatsu-photonics/sites/documents/99_SALES_LIBRARY/etd/PMT_TPMZ0002E.pdf

[111] Hamamatsu Photonics K.K., "Photomultiplier Tube R1924A – Datasheet," Mar. 2014, Version: TPMH1280E02.

[112] Demtröder, Wolfgang, *Experimentalphsyik 2: Elektrizität und Optik*. Springer, 2017, 7. Auflage. [Online]. Available: https://link.springer.com/book/10.1007/978-3-662-55790-7

[113] Zhang, John X.J. and Hoshino, K., *Molecular sensors and nanodevices: principles, designs and applications in biomedical engineering*. Academic Press, 2018. [Online]. Available: https://www.sciencedirect.com/book/9780128148624/molecular-sensors-and-nanodevices

[114] Schott AG, "Neutralfilter NG9 – Datasheet," Dec. 2020, Accessed: Jul 29, 2024. [Online]. Available: https://media.schott.com/api/public/content/c9564beaed1f48408d556eb0f8c01f25?v=17ec578c

[115] Polyanskiy, M.N., “Refractiveindex.info database of optical constants,” 2024. [Online]. Available: https://www.nature.com/articles/s41597-023-02898-2

[116] Garwin, R.L., “The design of liquid scintillation cells,” *Review of Scientific Instruments*, vol. 23, no. 12, pp. 755–757, 1952. [Online]. Available: https://pubs.aip.org/aip/rsi/article/23/12/755/298239

[117] Basavaraju, A. and Venkataramaiah, P. and Gopala, K. and Sanjeeviah, H., “Inner bremsstrahlung accompanying beta decay in Sr 90-Y 90,” *Physical Review C*, vol. 28, no. 1, p. 333, 1983. [Online]. Available: https://journals.aps.org/prc/abstract/10.1103/PhysRevC.28.333

[118] Epoxy Technology, “EPO-TEK 301-2 – Technical Data Sheet,” Feb. 2021, Version: Rev. XVIII, Accessed: Jul 29, 2024. [Online]. Available: https://www.epotek.com/docs/en/Datasheet/301-2.pdf

[119] Fechner, S., “Optimierung des Szintillator-Wrappings der MAGIX Triggerebene anhand der Lichtausbeute und Zeitauflösung,” Bachelorarbeit, Johannes Gutenberg-Universität Mainz, Mai 2022.

[120] Bent, K., “Entwicklung zweier Teststände zur Kalibration und Effizienzbestimmung der MAGIX Triggerdetektoren,” Bachelorarbeit, Johannes Gutenberg-Universität Mainz, Sep. 2023.

[121] I. Beltschikow, “MAGIX Triggerebene Slow Control Elektronik – Documentation,” Institute for Nuclear Physics, Johannes Gutenberg University Mainz, Oct. 2021, Version: 1.1.

[122] Kniel System-Electronic GmbH, “Double Output CAD 15.1,6 – Datasheet,” Jun. 2022, Version: 96350333.09, Accessed: Jul 29, 2024. [Online]. Available: https://kniel.de/download/96350333.09.pdf

[123] Kniel System-Electronic GmbH, “Double Output CAD 5.4 – Datasheet,” Jun. 2022, Version: 96350467.08, Accessed: Jul 29, 2024. [Online]. Available: https://kniel.de/download/96321237.07.pdf

[124] MYiR Tech Limited, “Z-turn Board – Overview,” Dec. 2014, Accessed: Jul 29, 2024. [Online]. Available: https://www.myirtech.com/download/Zynq7000/Z-turnBoard.pdf

[125] Kniel System-Electronic GmbH, “Single Output CAA 5.4 – Datasheet,” Jun. 2022, Version: 96350547.10, Accessed: Jul 29, 2024. [Online]. Available: https://kniel.de/download/96350556.09.pdf

[126] I. Beltschikow, “A1 Neutronendetektor Frontend-Elektronik – Dokumentation,” Institut für Kernphysik, Johannes Gutenberg-Universität Mainz, Mai 2019, Version: 1.1.

[127] Spreckels, R. *et al.*, “A highly segmented neutron polarimeter for A1,” *Nuclear Instruments and Methods in Physics Research Section A: Accelerators, Spectrometers, Detectors and Associated Equipment*, p. 169171, 2024. [Online]. Available: https://www.sciencedirect.com/science/article/pii/S0168900224000974

[128] Anghinolfi, F. *et al.*, “NINO, an ultra-fast, low-power, front-end amplifier discriminator for the Time-Of-Flight detector in ALICE experiment,” in *2003 IEEE Nuclear Science Symposium. Conference Record (IEEE Cat. No.03CH37515)*, vol. 1, 2003, pp. 375–379. [Online]. Available: https://ieeexplore.ieee.org/document/1352067

[129] Anghinolfi, F. *et al.*, “NINO: an ultra-fast and low-power front-end amplifier/discriminator ASIC designed for the multigap resistive plate chamber,” *Nuclear Instruments and Methods in*

Physics Research Section A: Accelerators, Spectrometers, Detectors and Associated Equipment, vol. 533, no. 1-2, pp. 183–187, 2004. [Online]. Available: https://www.sciencedirect.com/science/article/abs/pii/S0168900204014299

[130] Beltschikow, I., private communication, Apr. 2024.

[131] NXP Semiconductors, "BAP64Q Quad PIN diode attenuator – Datasheet," Feb. 2019, Version: Rev. 2.1, Accessed: Jul 29, 2024. [Online]. Available: https://www.nxp.com/docs/en/data-sheet/BAP64Q.pdf

[132] Radiall, "RF Coaxial Connectors – Full Line Catalog," Jun. 2020, Version: D1C004XE, Accessed: Jul 29, 2024. [Online]. Available: https://www.radiall.com/media/document_library/COAX_FullCatalog_light_20200626_D1C004XE_WEB.pdf

[133] LEMO SA, "Unipole & Multipole Connectors – Catalog," Jul. 2024, Version: CAT.UM.LEN.P1217, Accessed: Jul 29, 2024. [Online]. Available: https://web.lemo.com/img/resources/catalog/ROW/UK_English/unipole_multipole.pdf

[134] I. Beltschikow, "Double-NINO-Board-v1.1 – Schematic," Institute for Nuclear Physics, Johannes Gutenberg University Mainz, Oct. 2018, Version: 1.1.

[135] MYiR Tech Limited, "Z-turn Board V2 – Overview," Dec. 2022, Accessed: Jul 29, 2024. [Online]. Available: https://www.myirtech.com/download/Zynq7000/Z-turnBoardV2.pdf

[136] Keßler, H., "Charakterisierung der MAGIX Veto-Detektoren," Bachelorarbeit, Johannes Gutenberg-Universität Mainz, Jul. 2024.

[137] onsemi, "J-Series SiPM Sensors – Datasheet," Aug. 2021, Version: Rev. 7, Accessed: Jul 29, 2024. [Online]. Available: https://www.onsemi.com/pdf/datasheet/microj-series-d.pdf

[138] onsemi, "Biasing and Readout of ON Semiconductor SiPM Sensors – Manual," Apr. 2019, Version: Rev. 3 (AND9782/D), Accessed: Jul 29, 2024. [Online]. Available: https://www.onsemi.com/pub/collateral/and9782-d.pdf

[139] Gundacker, S. and Auffray, E. and Pauwels, K. and Lecoq, P., "Measurement of intrinsic rise times for various L(Y)SO and LuAG scintillators with a general study of prompt photons to achieve 10 ps in TOF-PET," *Physics in Medicine & Biology*, vol. 61, no. 7, p. 2802, Mar. 2016. [Online]. Available: https://iopscience.iop.org/article/10.1088/0031-9155/61/7/2802

[140] Luxium Solutions, "LYSO Scintillation Material – Datasheet," Apr. 2023, Accessed: Aug 02, 2024. [Online]. Available: https://www.luxiumsolutions.com/sites/default/files/2023-08/142266_Luxium_LYSO-Material-Data-Sheet_FIN.pdf

[141] R. G. Helmer, "LNE - LNHB/CEA Table de Radionucléides Co 60 – Datasheet," Laboratoire International Henri Becquerel, Mar. 2010, Accessed: Jul 30, 2024. [Online]. Available: http://www.lnhb.fr/nuclides/Co-60_tables.pdf

[142] Analog Devices, "AD8354 – Datasheet," Feb. 2017, Version: Rev. CF, Accessed: Aug 06, 2024. [Online]. Available: https://www.analog.com/media/en/technical-documentation/data-sheets/ad8354.pdf

[143] Wright, A.G. and Wright, T.G., *The Photomultiplier Handbook*. Oxford University Press, 2017. [Online]. Available: https://academic.oup.com/book/27426

[144] Engel, B., private communication, Dec. 2023.

[145] Kniel System-Electronic GmbH, “Double Output CAD 36.0,65 – Datasheet,” Jun. 2022, Version: 96321293.07, Accessed: Jul 29, 2024. [Online]. Available: https://kniel.de/download/96321293.07.pdf

[146] Rohde & Schwarz, “R&S RTM3000 Oscilloscope – User Manual,” Aug. 2022, Version: 10 (1335909002), Accessed: Jul 29, 2024. [Online]. Available: https://scdn.rohde-schwarz.com/ur/pws/dl_downloads/pdm/cl_manuals/user_manual/1335_9090_01/RTM3000_UserManual_en_10.pdf

[147] Analog Devices, “AD5671R/AD5675R – Datasheet,” Apr. 2018, Version: Rev. C, Accessed: Jul 29, 2024. [Online]. Available: https://www.analog.com/media/en/technical-documentation/data-sheets/ad5671r_5675r.pdf

[148] Schmitt, D., “Untersuchung der Effizienzgleichförmigkeit der MAGIX Triggerdetektoren,” Bachelorarbeit, Johannes Gutenberg-Universität Mainz, Aug. 2024.

[149] HAMEG Instruments, “10 MHz Function Generator HM8130 – Manual,” May 2005, Version: 45-8130-0010/04-05-2005-gw, Accessed: Jul 29, 2024. [Online]. Available: https://cdn.rohde-schwarz.com/hameg-archive/HM8130_D_En.pdf

[150] SIGLENT Technologies, “SDS1000X-E & SDS1000X-U – User Manual,” Aug. 2021, Version: EN05B, Accessed: Jul 29, 2024. [Online]. Available: https://siglentna.com/wp-content/uploads/dlm_uploads/2021/08/SDS1000X-ESDS1000X-U_UserManual_EN05B.pdf

[151] H. Merkel, “FPGA as TDC and for Trigger,” Mar. 2020, internal talk.

[152] Xilinx, “7 Series FPGAs Configurable Logic Block – User Guide,” Nov. 2014, Version: UG474 (v1.7), Accessed: Jul 30, 2024. [Online]. Available: https://www.eng.auburn.edu/~nelsovp/courses/elec4200/FPGA/ug474_7Series_CLB.pdf

[153] H. Merkel, “A Holistic Approach to Scintillator Readout,” May 2021, internal talk.

[154] Merkel, H., private communication, Dec. 2023.

[155] H. Merkel, “Programmable Trigger,” Jun. 2023, internal talk.

[156] H. Merkel, “Trigger Concepts,” Feb. 2024, internal talk.

[157] Python Software Foundation, “`socket` - Low-level networking interface,” Jul. 2024, Accessed: Aug 09, 2024. [Online]. Available: https://docs.python.org/3/library/socket.html#

[158] Merkel, H. *et al.*, “Search at the Mainz Microtron for Light Massive Gauge Bosons Relevant for the Muon $g-2$ Anomaly,” *Phys. Rev. Lett.*, vol. 112, Jun. 2014. [Online]. Available: https://link.aps.org/doi/10.1103/PhysRevLett.112.221802

[159] Cosmo, G. and Giani, S., “GEANT 4: an Object-Oriented toolkit for simulation in HEP,” CERN, Geneva, Tech. Rep., Oct. 1995. [Online]. Available: https://cds.cern.ch/record/303677/files/B00005944.pdf

[160] Geant4 Collaboration, “Introduction to Geant4,” Dec. 2023, Version: Rev 8.0, Accessed: Jul 30, 2024. [Online]. Available: https://geant4-userdoc.web.cern.ch/UsersGuides/IntroductionToGeant4/fo/IntroductionToGeant4.pdf

[161] Geant4 Collaboration, “Geant4 Installtion Guide Documentation,” Dec. 2023, Version: Rev 8.0, Accessed: Jul 30, 2024. [Online]. Available: https://geant4-userdoc.web.cern.ch/UsersGuides/InstallationGuide/fo/Geant4InstallationGuide.pdf

[162] Geant4 Collaboration, "Book For Application Developers," Dec. 2023, Version: Rev 8.0, Accessed: Jul 30, 2024. [Online]. Available: https://geant4-userdoc.web.cern.ch/UsersGuides/ForApplicationDeveloper/fo/BookForApplicationDevelopers.pdf

[163] Geant4 Collaboration, "Geant4 User's Guide for Toolkit Developers," Dec. 2023, Version: Rev 8.0, Accessed: Jul 30, 2024. [Online]. Available: https://geant4-userdoc.web.cern.ch/UsersGuides/ForToolkitDeveloper/fo/BookForToolkitDevelopers.pdf

[164] Geant4 Collaboration, "Physics Reference Manual," Dec. 2023, Version: Rev 8.0, Accessed: Jul 30, 2024. [Online]. Available: https://geant4-userdoc.web.cern.ch/UsersGuides/PhysicsReferenceManual/fo/PhysicsReferenceManual.pdf

[165] Geant4 Collaboration, "Guide For Physics Lists," Dec. 2023, Version: Rev 8.0, Accessed: Jul 30, 2024. [Online]. Available: https://geant4-userdoc.web.cern.ch/UsersGuides/PhysicsListGuide/fo/PhysicsListGuide.pdf

[166] Geant4 Collaboration, "Geant4 Examples," 2023, Accessed: Jul 30, 2024. [Online]. Available: https://geant4-userdoc.web.cern.ch/Doxygen/examples_doc/html/index.html

[167] Asai, M., "Introduction to Geant4," , 2000. [Online]. Available: https://cds.cern.ch/record/491492/files/p107.pdf

[168] Allison, J. *et al.*, "Recent Developments in Geant4," *Nuclear Instruments and Methods in Physics Research Section A: Accelerators, Spectrometers, Detectors and Associated Equipment*, vol. 835, pp. 186–225, 2016. [Online]. Available: https://www.sciencedirect.com/science/article/pii/S0168900216306957

[169] Berger, M.J. and Coursey, J.S. and Zucker, M.A. and Chang, J., "Stopping-Power & Range Tables for Electrons, Protons, and Helium Ions," NIST Standard Reference Database 124, NIST, Jul. 2017, Version: 2.0.1, Accessed: Aug 2, 2024. [Online]. Available: https://www.nist.gov/pml/stopping-power-range-tables-electrons-protons-and-helium-ions

[170] Eljen Technology, "Optical Cement EJ-500 – Datasheet," Jul. 2021, Accessed: Jul 29, 2024. [Online]. Available: https://eljentechnology.com/images/products/data_sheets/EJ-500.pdf

[171] Wacker Chemie AG, "Elastosil RT 601 A/B – Datasheet," Jun. 2024, Accessed: Jul 29, 2024. [Online]. Available: https://www.wacker.com/h/de-de/medias/ELASTOSIL-RT-601-AB-en-2024.06.16.pdf

[172] infochems Inc., "Elastosil RT 601 A – Datasheet," 2004, Accessed: Jul 29, 2024. [Online]. Available: http://www.infochems.co.kr/chemdb/product_content.asp?product_id=55209

[173] SAS Chambrelan, "Telescopic drawer slide D5VF – Datasheet," Jun. 2019, Accessed: Jul 29, 2024. [Online]. Available: https://chambrelan.com/guide/d5vf/

[174] Miluxor Schienen GmbH, "Teleskopschiene MX-DTP 30 – Datenblatt," Jan. 2023.

[175] SAS Chambrelan, "Telescopic drawer slide E1400 – Datasheet," Sep. 2023, Accessed: Jul 29, 2024. [Online]. Available: https://chambrelan.com/guide/e1400/

[176] Hamamatsu Photonics K.K., "Final Test Sheet – Photomultiplier Tube Type R1924A-03," Dec. 2020, JNO. 911615.

[177] Hamamatsu Photonics K.K., "Final Test Sheet – Photomultiplier Tube Type R1924A-03," Jan. 2022, JNO. 996470.

[178] Hamamatsu Photonics K.K., "Final Test Sheet – Photomultiplier Tube Type R1924A-03," Feb. 2022, JNO. 996471.

[179] Dytso, A. and Bustin, R. and Poor, H.V. and Shamai, S., "Analytical properties of generalized Gaussian distributions," *Journal of Statistical Distributions and Applications*, vol. 5, pp. 1–40, 2018.